(G 342)

Geophysics (II)

Third Year Geophysics

Dr. Ismail Sayed Ahmed

2022/2023

Section 1
POTENTIAL FIELD METHODS

Chapter 2
Gravity methods

2.1 INTRODUCTION

Gravity surveying measures variations in the Earth's gravitational field caused by differences in the density of sub-surface rocks. Although known colloquially as the 'gravity' method, it is in fact the variation of the *acceleration* due to gravity that is measured. Gravity methods have been used most extensively in the search for oil and gas, particularly in the early twentieth century. While such methods are still employed very widely in hydrocarbon exploration, many other applications have been found (Table 2.1), some examples of which are described in more detail in Section 2.7.

Micro-gravity surveys are those conducted on a very small scale – of the order of hundreds of square metres – and which are capable of detecting cavities, for example, as small as 1 m in diameter within 5 m of the surface.

Perhaps the most dramatic change in gravity exploration in the 1980s has been the development of instrumentation which now permits *airborne* gravity surveys to be undertaken routinely and with a high degree of accuracy (see Section 2.5.7). This has allowed aircraft-borne gravimeters to be used over otherwise inaccessible terrain and has led to the discovery of several small but significant areas with economic hydrocarbon potentials.

Table 2.1 Applications of gravity surveying

Hydrocarbon exploration
Regional geological studies
Isostatic compensation determination
Exploration for, and mass estimation of, mineral deposits
Detection of sub-surface cavities (micro-gravity)
Location of buried rock-valleys
Determination of glacier thickness
Tidal oscillations
Archaeogeophysics (micro-gravity); e.g. location of tombs
Shape of the earth (geodesy)
Military (especially for missile trajectories)
Monitoring volcanoes

2.2 PHYSICAL BASIS

2.2.1 Theory

The basis on which the gravity method depends is encapsulated in two laws derived by Sir Isaac Newton, which he described in *Principia Mathematica* (1687) · namely his Universal Law of Gravitation, and his Second Law of Motion.

The first of these two laws states that the force of attraction between two bodies of known mass is directly proportional to the product of the two masses and inversely proportional to the square of the distance between their centres of mass (Box 2.1). Consequently, the greater the distance separating the centres of mass, the smaller is the force of attraction between them.

Box 2.1 Newton's Universal Law of Gravitation

$$\text{Force} = \text{gravitational constant} \times \frac{\text{mass of Earth } (M) \times \text{mass } (m)}{(\text{distance between masses})^2}$$

$$F = \frac{G \times M \times m}{R^2} \qquad \text{(equation (1))}$$

where the gravitational constant $(G) = 6.67 \times 10^{-11}\ \text{N m}^2\ \text{kg}^{-2}$

Newton's law of motion states that a force (F) is equal to mass (m) times acceleration (Box 2.2). If the acceleration is in a vertical direction, it is then due to gravity (g).

Box 2.2 Newton's Second Law of Motion

$$\text{Force} = \text{mass } (m) \times \text{acceleration } (g)$$

$$F = m \times g \qquad \text{(equation (2))}$$

Equations (1) and (2) can be combined to obtain another simple relationship:

$$F = \frac{G \times M \times m}{R^2} = m \times g; \quad \text{thus } g = \frac{G \times M}{R^2} \quad \text{(equation (3))}.$$

This shows that the magnitude of the acceleration due to gravity on Earth (g) is directly proportional to the mass (M) of the Earth and inversely proportional to the square of the Earth's radius (R). Theoretically, acceleration due to gravity should be constant over the Earth. In reality, gravity varies from place to place because the Earth has the shape of a flattened sphere (like an orange or an inverted pear),

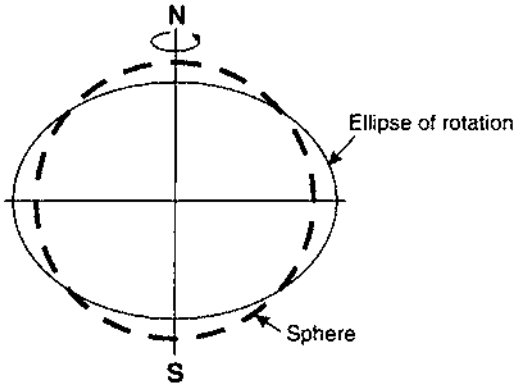

Figure 2.1 Exaggerated difference between a sphere and an ellipse of rotation (spheroid)

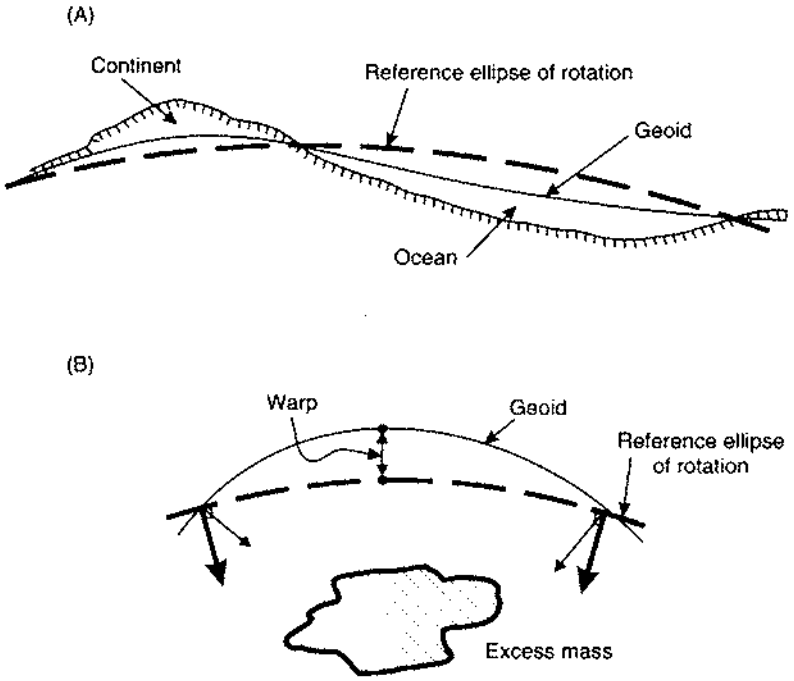

Figure 2.2 Warping of the geoid: (A) continental-scale effects, and (B) localised effects due to a sub-surface excess mass

rotates, and has an irregular surface topography and variable mass distribution (especially near the surface).

The shape of the Earth is a consequence of the balance between gravitational and centrifugal accelerations causing a slight flattening to form an oblate spheroid. Mathematically it is convenient to refer to the Earth's shape as being an *ellipse of rotation* (Figure 2.1).

The sea-level surface, if undisturbed by winds or tides, is known as the *geoid* and is particularly important in gravity surveying as it is horizontal and at right angles to the direction of the acceleration due

to gravity everywhere. The geoid represents a surface over which the gravitational field has equal value and is called an *equipotential surface*. The irregular distribution of mass, especially near the Earth's surface, warps the geoid so that it is not identical to the ellipse of rotation (Figure 2.2). Long-wavelength anomalies, which can be mapped using data from satellites (Wagner *et al.* 1977), relate to very deep-seated masses in the mantle (Figure 2.2A), whereas density features at shallow depths cause shorter-wavelength warps in the geoid (Figure 2.2B). Consequently, anomalies within the gravitational field can be used to determine how mass is distributed. The particular study of the gravitational field and of the form of the Earth is called *geodesy and is used to determine exact geographical locations and to* measure precise distances over the Earth's surface (*geodetic surveying*).

2.2.2 Gravity units

The first measurement of the acceleration due to gravity was made by Galileo in a famous experiment in which he dropped objects from the top of the leaning tower of Pisa. The normal value of g at the Earth's surface is 980 cm/s^2. In honour of Galileo, the c.g.s. unit of acceleration due to gravity (1 cm/s^2) is the *Gal*. Modern gravity meters (gravimeters) can measure extremely small variations in acceleration due to gravity, typically 1 part in 10^9 (equivalent to measuring the distance from the Earth to the Moon to within a metre). The sensitivity of modern instruments is about ten parts per million. Such small numbers have resulted in sub-units being used such as the milliGal (1 mGal = 10^{-3} Gals) and the microGal (1 μGal = 10^{-6} Gals). Since the introduction of SI units, acceleration due to gravity is measured in μm/s^2, which is rather cumbersome and so is referred to as the *gravity unit* (g.u.); 1 g.u. is equal to 0.1 mGal [10 g.u. = 1 mGal]. However, the gravity unit has not been universally accepted and 'mGal' and 'μGal' are still widely used.

2.2.3 Variation of gravity with latitude

The value of acceleration due to gravity varies over the surface of the Earth for a number of reasons, one of which is the Earth's shape. As the polar radius (6357 km) is 21 km shorter than the equatorial radius (6378 km) the points at the poles are closer to the Earth's centre of mass (so smaller value of R) and, therefore, the value of gravity at the poles is greater (by about 0.7%) than that at the equator (Figure 2.3) (see equation (3) under Box 2.2). Furthermore, as the Earth rotates once per sidereal day around its north–south axis, there is a centrifugal acceleration acting which is greatest where the rotational velocity is largest, namely at the equator (1674 km/h; 1047 miles/h) and decreases to zero at the poles (Figure 2.3). The centrifugal

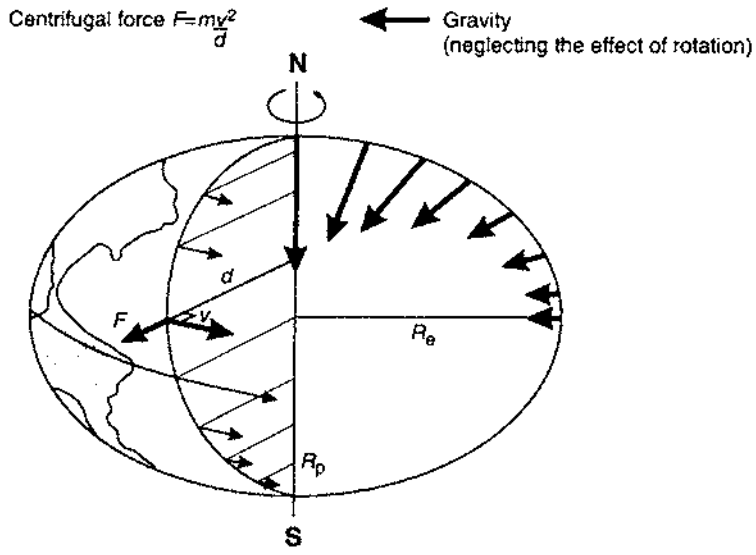

Figure 2.3 Centrifugal acceleration and the variation of gravity with latitude ϕ (not to scale)

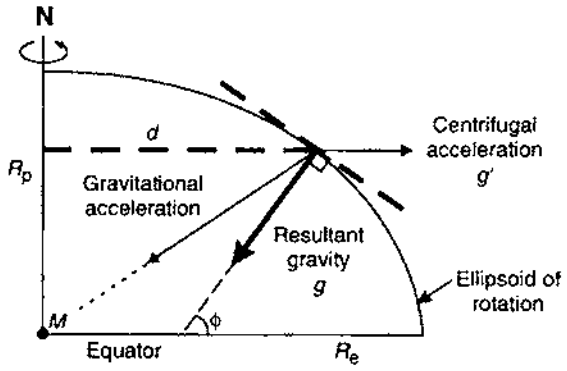

Figure 2.4 Resultant of centrifugal acceleration (g') and the acceleration due to gravity (g) (not to scale); the geographic (geodetic) latitude is given by ϕ. After Robinson and Coruh (1988)

acceleration, which is equal to the rotational velocity (ω) squared times the distance to the rotational axis (d), serves to decrease the value of the gravitational acceleration. It is exactly the same mechanism as that which keeps water in a bucket when it is being whirled in a vertical plane.

The value of gravity measured is the resultant of that acting in a line with the Earth's centre of mass with the centrifugal acceleration (Figure 2.4). The resultant acts at right-angles to the ellipsoid of rotation so that a plumb line, for example, hangs vertically at all locations at sea level. The angle ϕ in Figure 2.4 defines the geodetic (ordinary or geographic) latitude. The resultant gravity at the poles is 5186 mGal (51 860 g.u.) greater than at the equator and varies systematically with latitude in between, as deduced by Clairaut in 1743.

Subsequent calculations in the early twentieth century, based on Clairaut's theory, led to the development of a formula from which it was possible to calculate the theoretical acceleration due to gravity (g_ϕ) at a given geographic latitude (ϕ) relative to that at sea level (g_0). Parameters α and β are constants which depend on the amount of flattening of the spheroid and on the speed of rotation of the Earth.

Box 2.3 General form of the International Gravity Formula

$$g_\phi = g_0(1 + \alpha \sin^2 \phi - \beta \sin^2 2\phi)$$

In 1930 the International Union of Geodesy and Geophysics adopted the form of the *International Gravity Formula* (Nettleton 1971; p. 20) shown in Box 2.3. This became the standard for gravity work. However, refined calculations using more powerful computers and better values for Earth parameters resulted in a new formula – known as the *Geodetic Reference System 1967* (GRS67) becoming the standard (Woollard 1975) (Box 2.4). If gravity surveys using the 1930 gravity formula are to be compared with those using the 1967 formula, then the third formula (Kearey and Brooks 1991) in Box 2.4 should be used to compensate for the differences between them. Otherwise, discrepancies due to the differences in the equations may be interpreted wrongly as being due to geological causes.

Box 2.4 Standard formulae for the theoretical value of g at a given latitude ϕ

$$g_\phi(1930) = 9.78049\,(1 + 0.0052884 \sin^2 \phi - 0.0000059 \sin^2 2\phi)\ \text{m/s}^2$$

$$\mathbf{g_\phi(1967) = 9.78031846\,(1 + 0.005278895 \sin^2 \phi + 0.000023462 \sin^4 \phi)\ m/s^2}$$

$$g_\phi(1967) - g_\phi(1930) = (-172 + 136 \sin^2 \phi)\ \mu\text{m/s}^2\ \text{(g.u.)}$$

2.2.4 Geological factors affecting density

Gravity surveying is sensitive to variations in rock density, so an appreciation of the factors that affect density will aid the interpretation of gravity data. Ranges of bulk densities for a selection of different material types are listed in Table 2.2 and shown graphically in Figure 2.5.

It should be emphasised that in gravity surveys, the determination of densities is based on rocks that are accessible either at the surface, where they may be weathered and/or dehydrated, or from boreholes, where they may have suffered from stress relaxation and be far more

Table 2.2 Densities of common geologic materials (data from Telford *et al.* 1990)

Material type	Density range (Mg/m^3)	Approximate average density (Mg/m^3)
Sedimentary rocks		
Alluvium	1.96–2.00	1.98
Clay	1.63–2.60	2.21
Gravel	1.70–2.40	2.00
Loess	1.40–1.93	1.64
Silt	1.80–2.20	1.93
Soil	1.20–2.40	1.92
Sand	1.70–2.30	2.00
Sandstone	1.61–2.76	2.35
Shale	1.77–3.20	2.40
Limestone	1.93–2.90	2.55
Dolomite	2.28–2.90	2.70
Chalk	1.53–2.60	2.01
Halite	2.10–2.60	2.22
Glacier ice	0.88–0.92	0.90
Igneous rocks		
Rhyolite	2.35–2.70	2.52
Granite	2.50–2.81	2.64
Andesite	2.40–2.80	2.61
Syenite	2.60–2.95	2.77
Basalt	2.70–3.30	2.99
Gabbro	2.70–3.50	3.03
Metamorphic rocks		
Schist	2.39–2.90	2.64
Gneiss	2.59–3.00	2.80
Phylite	2.68–2.80	2.74
Slate	2.70–2.90	2.79
Granulite	2.52–2.73	2.65
Amphibolite	2.90–3.04	2.96
Eclogite	3.20–3.54	3.37

cracked than when *in situ*. Consequently, errors in the determination of densities are among the most significant in gravity surveying. This should be borne in mind when interpreting gravity anomalies so as not to over-interpret the data and go beyond what is geologically reasonable.

There are several crude 'rules of thumb' which can be used as general guides (Dampney 1977; Telford *et al.* 1990; Nettleton 1971, 1976). Sedimentary rocks tend to be the least dense (average density about $2.1 \pm 0.3\ Mg/m^3$). Within the three fundamental rock classifications there are crude trends and associations which are outlined in the next section. Commonly, units are quoted in terms of grams per cubic centimetre (g/cm^3) but are herein referred to in the SI derived units of Mg/m^3 which are numerically equivalent.

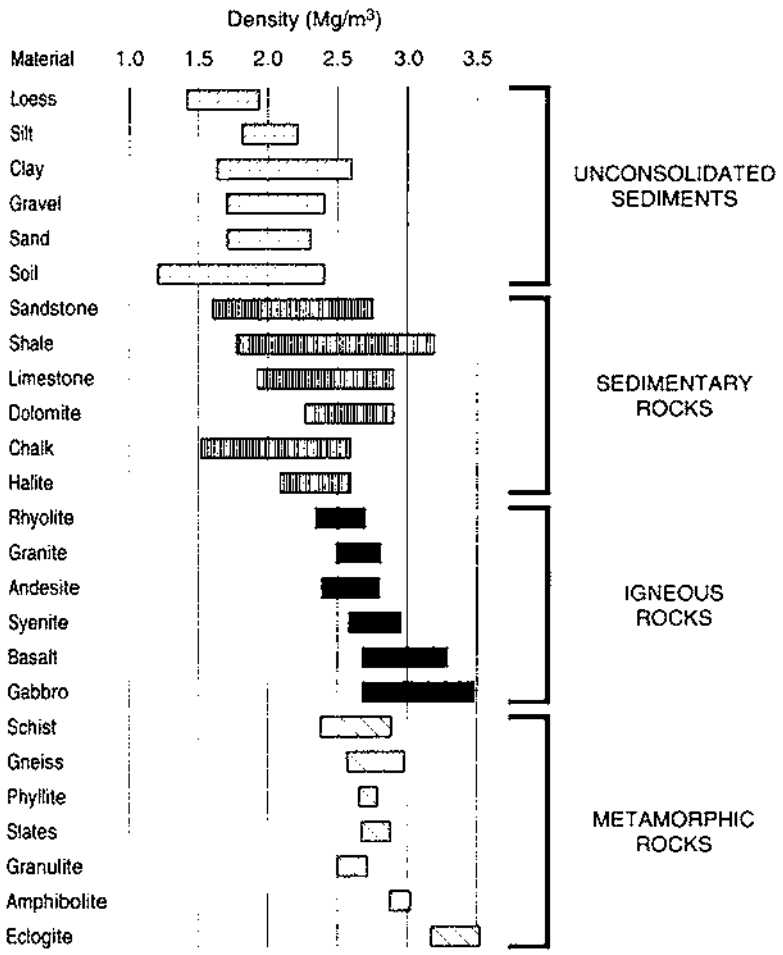

Figure 2.5 Variations in rock density for different rock types. Data from Telford *et al.* (1990)

2.2.4.1 Sedimentary rocks

At least seven factors affect the density of sedimentary materials: composition, cementation, age and depth of burial, tectonic processes, porosity and pore-fluid type. Any or all of these may apply for a given rock mass. The degree to which each of these factors affects rock density is given in Table 2.3; but experience shows that, under normal circumstances, the density contrast between adjacent sedimentary strata is seldom greater than 0.25 Mg/m^3.

Density varies depending on the material of which the rock is made, and the degree of consolidation. Four groups of materials are listed in order of increasing density in Table 2.4. Sediments that remain buried for a long time consolidate and lithify, resulting in reduced porosity and consequently an increased density.

Table 2.3 The effect of different physical factors on density

Factor	Approximate percentage change in density
Composition	35
Cementation	10
Age and depth of burial	25
Tectonic processes	10
Porosity and pore fluids	10

Table 2.4 Approximate average densities of sedimentary rocks

Material type	Approximate average Density (Mg/m^3)
Soils and alluvium	2.0
Shales and clays	2.3
Sandstones and conglomerates	2.4
Limestone and dolomite	2.6

In sandstones and limestones, densification is achieved not by volume change but by pore spaces becoming infilled by natural cement. In shales and clays, the dominant process is that of compaction and, ultimately, recrystallisation into minerals with greater densities.

2.2.4.2 Igneous rocks

Igneous rocks tend to be denser than sedimentary rocks although there is overlap. Density increases with decreasing silica content, so basic igneous rocks are denser than acid ones. Similarly, plutonic rocks tend to be denser than their volcanic equivalents (see Table 2.5).

Table 2.5 Variation of density with silica content and crystal size for selected igneous rocks; density ranges and, in parentheses, average densities are given in Mg/m^3. Data from Telford *et al.* (1990)

Crystal size	Silica content		
	Acid	Intermediate	Basic
Fine-grained (volcanic)	Rhyolite 2.35–2.70 (2.52)	Andesite 2.4–2.8 (2.61)	Basalt 2.70–3.30 (2.99)
Coarse-grained (plutonic)	Granite 2.50–2.81 (2.64)	Syenite 2.60–2.95 (2.77)	Gabbro 2.70–3.50 (3.03)

2.2.4.3 Metamorphic rocks

The density of metamorphic rocks tends to increase with decreasing acidity and with increasing grade of metamorphism. For example, schists may have lower densities than their gneissose equivalents. However, variations in density within metamorphic rocks tend to be far more erratic than in either sedimentary or igneous rocks and can vary considerably over very short distances.

2.2.4.4 Minerals and miscellaneous materials

As the gravity survey method is dependent upon contrast in densities, it is appropriate to highlight some materials with some commercial

Table 2.6 Densities of a selection of metallic and non-metallic minerals and some miscellaneous materials. Data from Telford *et al.* (1990)

Material type	Density range (Mg/m^3)	Approximate average density (Mg/m^3)
Metallic minerals		
Oxides, carbonate		
Manganite	4.2–4.4	4.32
Chromite	4.2 4.6	4.36
Magnetite	4.9 5.2	5.12
Haematite	4.9 5.3	5.18
Cuprite	5.7–6.15	5.92
Cassiterite	6.8–7.1	6.92
Wolframite	7.1 7.5	7.32
Uraninite	8.0 9.97	9.17
Copper	n.d.	8.7
Silver	n.d.	10.5
Gold	15.6–19.4	17.0
Sulphides		
Malachite	3.9 4.03	4.0
Stannite	4.3–4.52	4.4
Pyrrhotite	4.5–4.8	4.65
Molybdenite	4.4 4.8	4.7
Pyrite	4.9 5.2	5.0
Cobaltite	5.8 6.3	6.1
Galena	7.4–7.6	7.5
Cinnabar	8.0–8.2	8.1
Non-metallic minerals		
Gypsum	2.2 2.6	2.35
Bauxite	2.3–2.55	2.45
Kaolinite	2.2–2.63	2.53
Baryte	4.3–4.7	4.47
Miscellaneous materials		
Snow	0.05–0.88	n.d.
Petroleum	0.6–0.9	n.d.
Lignite	1.1 1.25	1.19
Anthracite	1.34 1.8	1.50

value for which the method can be used for exploration purposes. Gravity surveying becomes increasingly appropriate as an exploration tool for those ore materials with greatest densities. The densities of a selection of metallic and non-metallic minerals and of several other materials are listed in Table 2.6.

2.3 MEASUREMENT OF GRAVITY

2.3.1 Absolute gravity

Determination of the acceleration due to gravity in absolute terms requires very careful experimental procedures and is normally only undertaken under laboratory conditions. Two methods of measurement are used, namely the falling body and swinging pendulum methods. However, it is the more easily measured *relative* variations in gravity that are of interest and value to explorationists. More detailed descriptions of how absolute gravity is measured are given by Garland (1965), Nettleton (1976) and Robinson and Coruh (1988). A popular account of gravity and its possible non-Newtonian behaviour has been given by Boslough (1989); see also Parker and Zumberge (1989).

A network of gravity stations has been established worldwide where absolute values of gravity have been determined by reference to locations where absolute gravity has been measured, such as at the National Bureau of Standards at Gaithersburg, USA, the National Physical Laboratory at Teddington, England, and Universidad Nationale de Columbia, Bogata, Columbia. The network is referred to as the *International Gravity Standardisation Net 1971* (IGSN 71) (Morelli 1971) and was established in 1963 by Woollard and Rose (1963). It is thus possible to tie in any regional gravity survey to absolute values by reference to the IGSN 71 and form a primary network of gravity stations.

2.3.2 Relative gravity

In gravity exploration it is not normally necessary to determine the absolute value of gravity, but rather it is the relative variation that is measured. A base station (which can be related to the IGSN 71) is selected and a secondary network of gravity stations is established. All gravity data acquired at stations occupied during the survey are reduced relative to the base station. If there is no need for absolute values of g to be determined, the value of gravity at a local base station is arbitrarily designated as zero. Details of the data reduction procedure are given in Section 2.5.

The spacing of gravity stations is critical to the subsequent interpretation of the data. In regional surveys, stations may be located

with a density of 2–3 per km^2, whereas in exploration for hydrocarbons, the station density may be increased to 8 10 per km^2. In localised surveys where high resolution of shallow features is required, gravity stations may be spaced on a grid with sides of length 5–50 m. In micro-gravity work, the station spacing can be as small as 0.5 m.

For a gravity survey to achieve an accuracy of ± 0.1 mGal, the latitudinal position of the gravimeter must be known to within ± 10 m and the elevation to within ± 10 mm. Furthermore, in conjunction with multiple gravity readings and precision data reduction, gravity data can be obtained to within $\pm 5\,\mu$Gal (Owen 1983). The most significant causes of error in gravity surveys on land are uncertainties in station elevations. At sea, water depths are measured easily by using high-precision echo sounders. Positions are determined increasingly by satellite navigation; and in particular, the advent of the Global Positioning System (GPS) (Bullock 1988), with its compact hardware and fast response time, is resulting in GPS position-fixing becoming more precise. This is particularly true with reference to airborne gravity measurements.

2.4 GRAVITY METERS

No single instrument is capable of meeting all the requirements of every survey, so there are a variety of devices which serve different purposes. In 1749, Pierre Bouguer found that gravity could be measured using a swinging pendulum. By the nineteenth century, the pendulum was in common use to measure relative variations in gravity. The principle of operation is simple. Gravity is inversely proportional to the square of the period of oscillation (T) and directly proportional to the length of the pendulum (L) (Box 2.5). If the same pendulum is swung under identical conditions at two locations where the values of accelerations due to gravity are g_1 and g_2, then the ratio of the two values of g is the same as the ratio of the two corresponding periods of oscillation T_1 and T_2.

Box 2.5 Acceleration due to gravity from pendulum measurements

Gravity = constant × pendulum length/period^2 $\quad g = 4\pi^2 L / T^2$

$$\frac{(\text{Period}_1)^2}{(\text{Period}_2)^2} = \frac{\text{gravity}_2}{\text{gravity}_1} \quad \frac{T_2^2}{T_1^2} = \frac{g_2}{g_1}$$

Further, the size of the difference in acceleration due to gravity (δg) between the two locations is (to the first order) equal to the product of

gravity and twice the difference in periods ($T_2 - T_1$) divided by the first period (Box 2.6). This method is accurate to about 1 mGal if the periods are measured over at least half an hour. Portable systems were used in exploration for hydrocarbons in the 1930s.

Box 2.6 Differences in gravitational acceleration

$$\text{Gravity difference} = -2 \times \text{gravity} \times \frac{\text{difference in periods}}{\text{period}_1};$$

$$\delta g = -2g\,\frac{(T_2 - T_1)}{T_1}$$

Another method of determining relative gravity is that of the torsion balance (Figure 2.6). English physicist Henry Cavendish devised this system to measure the gravitational constant in 1791. The method was developed for geodetic purposes in 1880 by a Hungarian physicist, Baron Roland von Eötvös. After further modification it was used in exploration from 1915 to the late 1940s. The method, which measures variations in only the horizontal component of gravity due to terrain and not vertical gravity, is capable of very great sensitivity (to 0.001 mGal) but is awkward and very slow to use in the field. The method is described in more detail by Telford *et al.* (1990).

Since about the early 1930s, variations in relative gravity have been measured using gravity meters (gravimeters), firstly stable (static) and

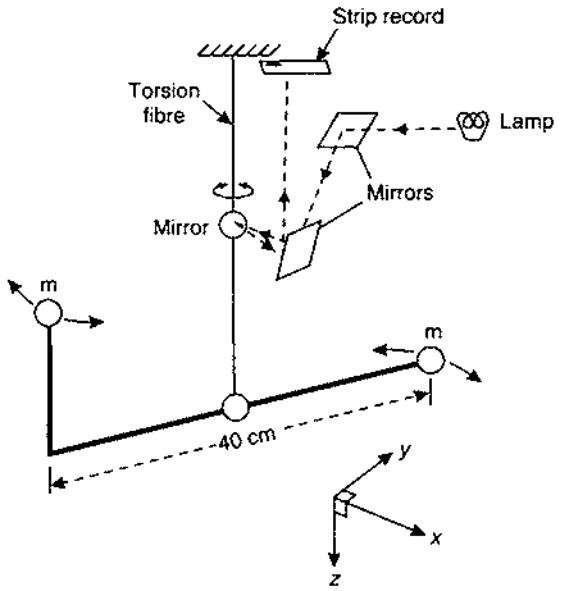

Figure 2.6 Schematic of a torsion balance

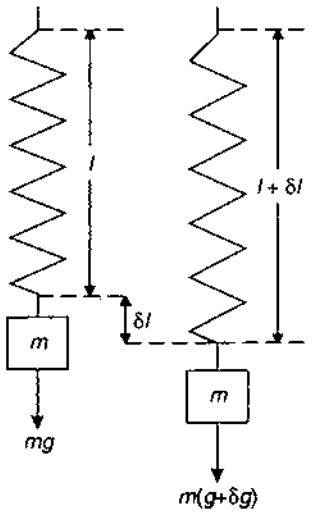

Figure 2.7 Extension (δl) of a spring due to additional gravitational pull (δg)

more recently unstable (astatic) types. Practical aspects of how to use such instruments have been detailed by Milsom (1989, Ch. 2). Gravimeters are sophisticated spring balances from which a constant mass is suspended (Figure 2.7). The weight of the mass is the product of the mass and the acceleration due to gravity. The greater the weight acting on the spring, the more the spring is stretched. The amount of extension (δl) of the spring is proportional to the extending force, i.e. the excess weight of the mass (δg). (Remember that weight equals mass times acceleration due to gravity.) The constant of proportionality is the elastic spring constant κ. This relationship is known as Hooke's Law (Box 2.7).

As the mass is constant, variations in weight are caused by changes in gravity (δg). By measuring the extension of the spring (δl), differences in gravity can then be determined. As the variations in g are very small (1 part in 10^8) the extension of any spring will also be extremely tiny. For a spring 30 cm long, changes in length of the order of 3×10^{-8} m (30 nanometres) have to be measured. Such small distances are even smaller than the wavelength of light (380–780 nm). Consequently, gravimeters use some form of system to amplify the movement so that it can be measured accurately.

Box 2.7 Hooke's Law

Extension to spring = mass $\times \dfrac{\text{change in gravity}}{\text{spring constant}}$	$\delta l = \dfrac{m\delta g}{\kappa}$
Change in gravity = constant $\times$ extension/mass	$\delta g = \kappa \delta l / m$

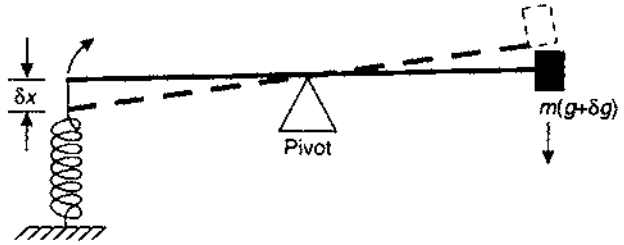

Figure 2.8 Basic principle of operation of a stable gravimeter

2.4.1 Stable (static) gravimeters

Stable gravimeters (Figure 2.8), which were developed in the 1930s, are less sensitive than their more modern cousins, the unstable gravimeters, which have largely superseded them. The stable gravimeter consists of a mass at the end of a beam which is pivoted on a fulcrum and balanced by a tensioned spring at the other end. Changes in gravity affect the weight of the mass which is counterbalanced by the restoring action of the spring. Different configurations of stable gravimeters are shown in Figure 2.9 and are discussed in more detail by Garland (1965), Nettleton (1976), Telford *et al.* (1990), and Parasnis (1986). A brief description of three stable gravimeters is given below.

2.4.1.1 Askania

A beam with a mass at one end is pivoted on a main spring S (Figure 2.9A). Changes in gravity cause the beam to tilt, so producing a deflection in a beam of light which is reflected off a mirror placed on the mass. A photoelectric cell, the output of which is displayed on a galvanometer, measures the displacement of the light beam. An auxiliary spring (AS) is retensioned using a micrometer to restore the mass to its rest position, which is indicted when the galvanometer reading is returned to zero (nulled).

2.4.1.2 Boliden

The Boliden gravimeter uses the principle that the capacitance of a parallel-plate capacitor changes with the separation of the plates (Figure 2.9B). The mass has the form of a bobbin with a plate at each end and is suspended by two springs between two other capacitor plates. With a change in gravity, the mass moves relative to the fixed plates, changing the capacitance between the upper plates; this movement can be detected easily using a tuned circuit. The lower plates are connected to a d.c. supply which supports the bobbin mass by electrostatic repulsion. With a change in gravity and the consequent displacement of the bobbin relative to the fixed plates, the original or

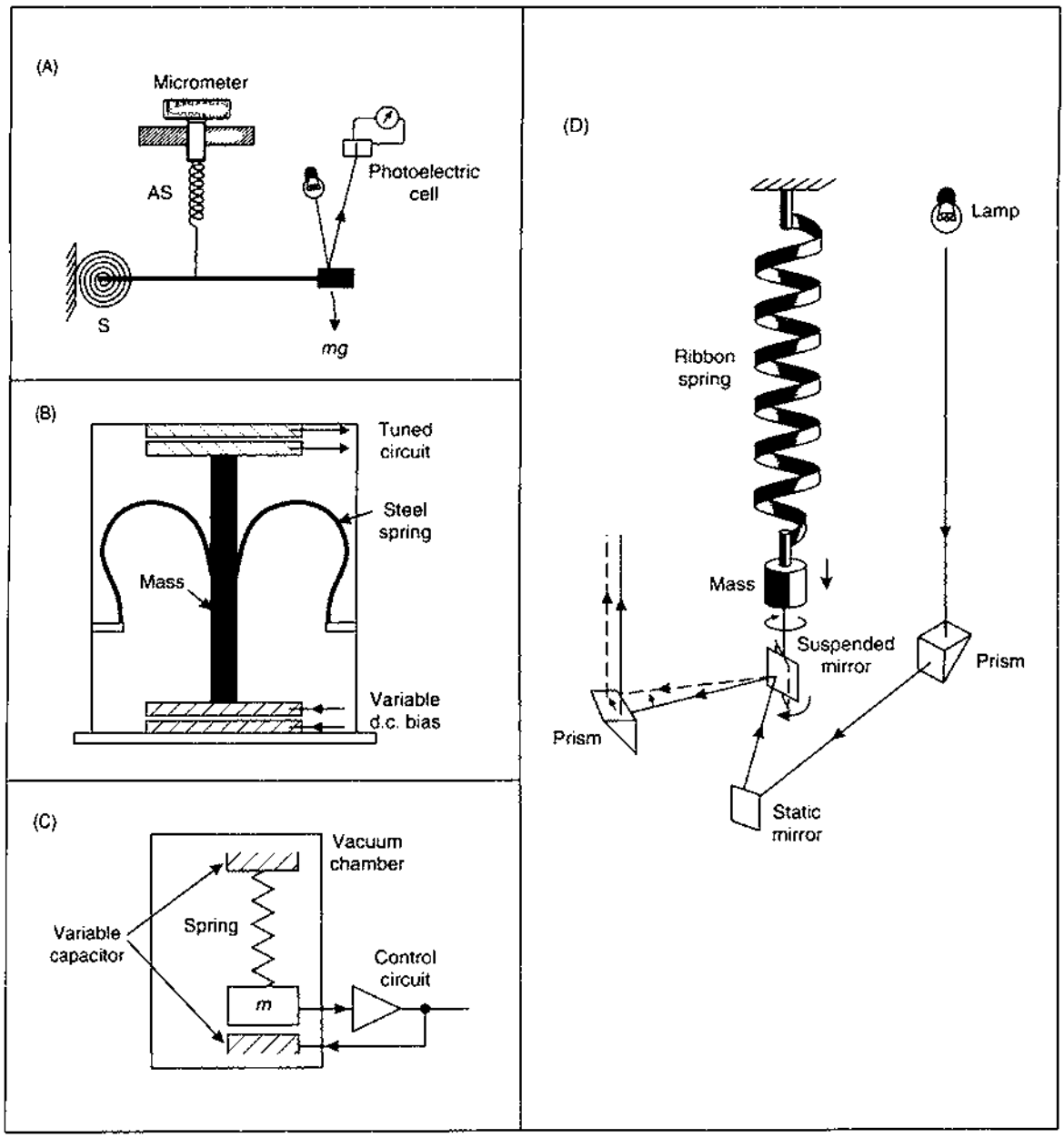

Figure 2.9 Types of stable gravimeter: (A) Askania; (B) Boliden; (C) Scintrex CG-3; and (D) Gulf (Hoyt). After Garland (1965), Telford *et al.* (1976), Robinson and Coruh (1988), by permission

a reference position can be obtained by changing the direct voltage between the lower pair of plates. The overall sensitivity is about 1 g.u. (0.1 mGal). A modern version has been produced by Scintrex (Model CG-3) which operates on a similar principle (see Figure 2.9C). Any displacement of the mass due to a change in gravity is detected by

a capacitor transducer and activates a feedback circuit. The mass is returned to its null position by the application of a direct feedback voltage (which is proportional to the change in gravity) to the plates of the capacitor which changes the electrostatic force between the plates and the mass (Robinson and Coruh 1988).

2.4.1.3 Gulf (Hoyt)

The Gulf gravimeter comprises a coiled helical ribbon spring which rotates as it changes length (Figure 2.9D). The rotation of the free end of the spring is much larger than the change in length and so is more easily measured. The range of measurement is quite small, being only 300 g.u. (30 mGal), although this can be overcome to some extent by retensioning the spring, and the accuracy of measurement is to within 0.2–0.5 g.u. (0.02–0.05 mGal).

2.4.2 Unstable (astatic) gravimeters

Since the 1930s, unstable gravimeters have been used far more extensively than their stable counterparts. In a stable device, once the system has been disturbed it will return to its original position, whereas an unstable device will move further away from its original position.

For example, if a pencil lying flat on a table is lifted at one end and then allowed to drop, the pencil will return to being flat on the table. However, if the pencil starts by being balanced on its end, once disturbed, it will fall over; i.e. it becomes unstable, rather than returning to its rest position. The main point of the instability is to exaggerate any movement, so making it easier to measure, and it is this principle on which the unstable gravimeter is based.

Various models of gravimeter use different devices to achieve the instability. The principle of an astatic gravimeter is shown in Figure 2.10. An almost horizontal beam hinged at one end supports a mass at the other. The beam is attached to a main spring which is connected at its upper end to a support above the hinge. The spring attempts to pull the beam up anticlockwise by its turning moment, which is equal to the restoring force in the spring multiplied by the perpendicular distance from the hinge (d). This turning moment is balanced by the gravitational turning moment which attempts to rotate the beam in a clockwise manner about the hinge and is equal to the weight of the mass (mg) times the length of the beam (l) multiplied by the cosine of the angle of the beam from the horizontal (θ) (i.e. $mgl\cos\theta$). If gravity changes, the beam will move in response but will be maintained in its new position because the main spring is a 'zero-length' spring. One virtue of such a spring is that it is pretensioned during manufacture so that the tension in the spring is proportional to its length. This means that if all forces were removed from the

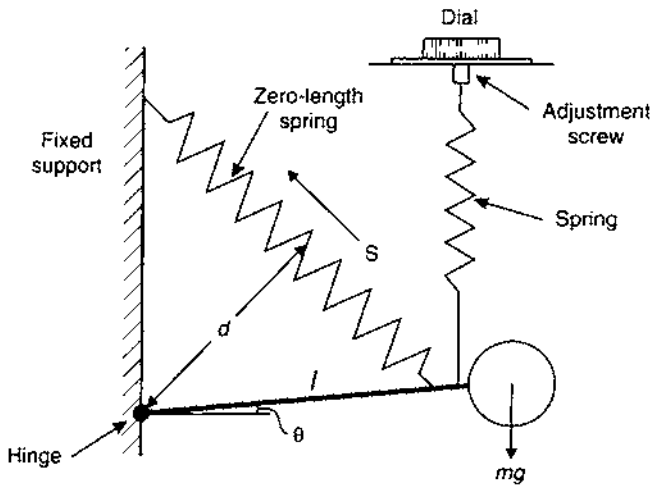

Figure 2.10 Principle of operation of an astatic gravimeter

spring it would collapse to zero length, something which is impossible in practice. Another virtue of the zero-length spring is that it results in an instrument which is linear and very responsive over a wide range of gravity values. Astatic gravimeters do not measure the movement of the mass in terms of changes in gravity but require the displaced mass to be restored to a null position by the use of a micrometer. The micrometer reading is multiplied by an instrumental calibration factor to give values of gravity, normally to an accuracy within 0.1 g.u. (0.01 mGal) and in some specialist devices to within 0.01 g.u. (0.001 mGal = 1 μGal).

2.4.2.1 Thyssen

Although obsolete, this gravimeter demonstrates the instability concept extremely well and is included for this reason. An extra mass is placed above a balanced beam (Figure 2.11) so producing the instability condition. If gravity increases, the beam tilts to the right and the

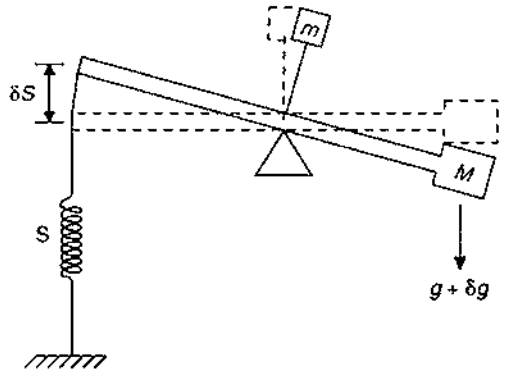

Figure 2.11 Schematic of a Thyssen gravimeter

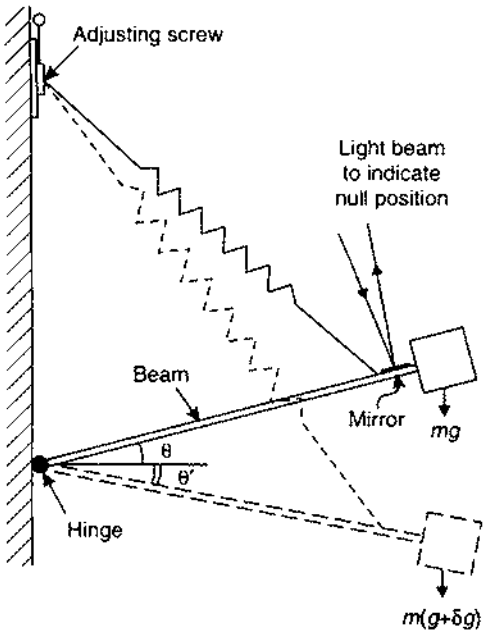

Figure 2.12 Schematic of a LaCoste-Romberg gravimeter. After Kearey and Brooks (1991), by permission

movement of the extra mass enhances the clockwise rotation about the pivot, and conversely for a reduction in gravity. When used, this type of gravimeter had a sensitivity of about 2.5 g.u. (0.25 mGal).

2.4.2.2 LaCoste–Romberg

This device is a development of LaCoste's long-period seismograph (LaCoste 1934) and is illustrated in Figure 2.12. The spring is made of metal with a high thermal conductivity but cannot be insulated totally to eradicate thermal effects and so has to be housed permanently in an enclosed container in which a stable temperature is maintained to within 0.002°C by a thermostat element. The null point is obtained by the observer viewing a scale through an eyepiece onto which a beam of light is reflected from the beam when it is in its rest position. In order to restore the position of the beam, the operator rotates a micrometer gauge on the outer casing which turns a screw which adjusts the beam position. The long length of the screw means that the gravimeter can be used worldwide without having to undergo any resets, which is a major advantage over other makes for surveys where this is important. When this type of gravimeter was manufactured in the 1930s it weighed a massive 30 kg, but modern technology has made it possible for the weight to be reduced to only about 2 kg, excluding the battery required to maintain the heating coils. The

springs can be clamped and so the gravimeter is more easily transportable than other makes and also less sensitive to vibration. It is possible for some models of LaCoste Romberg gravimeters to measure to 3 μGal.

2.4.2.3 Worden

Unlike the LaCoste–Romberg gravimeter, the Worden is made entirely of quartz glass springs, rods and fibres (Figure 2.13). The quartz construction makes it much easier to reduce thermal effects. Indeed, the whole assembly is housed in a glass vacuum flask and some models have an electrical thermostat. As the spring cannot be clamped, the Worden gravimeter is sensitive to vibration and has to be transported extremely carefully. The range of the instrument is about 20 000 g.u. (2000 mGal) with an accuracy to within 0.1–0.2 g.u. (0.01–0.02 mGal). However, quartz gravimeters such as the Worden can be quite difficult for inexperienced operators to read and a realistic accuracy may be more like 1 g.u. (0.1 mGal). The Worden gravimeter has two auxiliary springs, one for coarse and the other for fine adjustments.

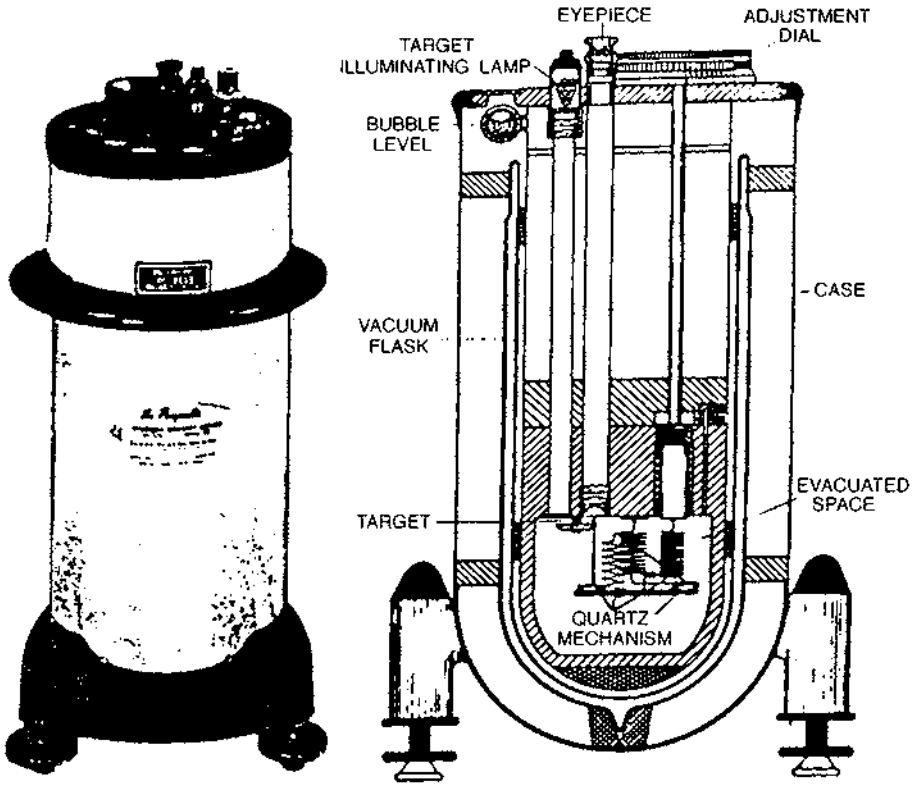

Figure 2.13 Cross-section through a Worden gravimeter (Texas Instruments Ltd). From Dunning (1970), by permission

2.4.2.4 Sodin

This is very comparable to the Worden and operates in similar ways. Further details are given by Robinson and Coruh (1988).

2.4.2.5 Vibrating string

If a mass is suspended on a fibre which is forced to oscillate by an a.c. circuit, then the frequency of vibration, which can be measured electronically, will vary with changes in gravity. For a fibre of length L, and mass per unit length m_s, from which a mass M is suspended, by measuring the frequency of vibration (f), gravity can be determined (Box 2.8). However, the technology is not sufficiently developed to provide the same resolution and accuracy as other gravimeters, but it does give the impression that even more compact and lightweight gravimeters may be forthcoming in the near future. There is potential for use in airborne survey systems.

Box 2.8 Determination of g using a vibrating string

$$\text{Gravity} = \frac{4 \times \text{string length}^2 \times \text{frequency}^2 \times \text{string mass}}{\text{suspended mass}};$$

$$g = \frac{4L^2 f^2 m_s}{M}$$

2.5 CORRECTIONS TO GRAVITY OBSERVATIONS

Gravimeters do not give direct measurements of gravity. Rather, a meter reading is taken which is then multiplied by an instrumental calibration factor to produce a value of observed gravity (g_{obs}). Before the results of the survey can be interpreted in geological terms, these raw gravity data have to be corrected to a common datum, such as sea level (geoid), in order to remove the effects of features that are only of indirect geological interest. The correction process is known as *gravity data reduction* or *reduction to the geoid*. The difference between the value of observed gravity (g_{obs}) and that determined either from the International Gravity Formula/Geodetic Reference System 67 for the same location, or relative to a local base station, is known as the *gravity anomaly*. The various corrections that can be applied are listed in Table 2.7 with the sections of this book in which each one is discussed.

Table 2.7 Corrections to gravity data

Correction	Book sections
Instrument drift	2.5.1
Earth tides	2.5.2
Eötvös	2.5.7
Latitude	2.2.3 and 2.5.3
Elevation	
Free-air correction	2.5.4
Bouguer correction	2.5.5
Terrain	2.5.6
Isostatic	2.5.8

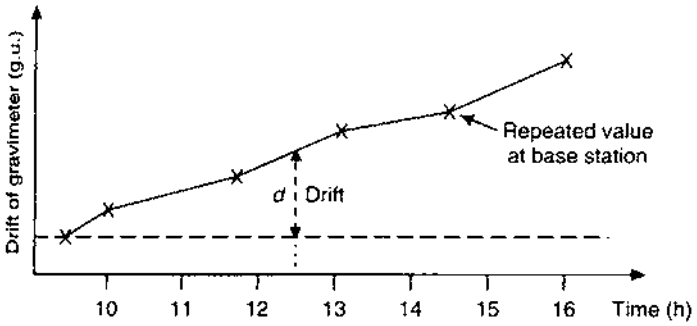

Figure 2.14 An instrumental drift curve

2.5.1 Instrumental drift

Gravimeter readings change (drift) with time as a result of elastic creep in the springs, producing an apparent change in gravity at a given station. The instrumental drift can be determined simply by repeating measurements at the same stations at different times of the day, typically every 1 2 hours. The differences between successive measurements at the same station are plotted to produce a *drift curve* (Figure 2.14). Observed gravity values from intervening stations can be corrected by subtracting the amount of drift from the observed gravity value. For example, in Figure 2.14 the value of gravity measured at an outlying station at 12.30 hours should be reduced by the amount of drift *d*. The range of drift of gravimeters is from a small fraction of one g.u. to about ten g.u. per hour. If the rate of drift is found to be irregular, return the instrument to the supplier it is probably faulty!

2.5.2 Tides

Just as the water in the oceans responds to the gravitational pull of the Moon, and to a lesser extent of the Sun, so too does the solid earth.

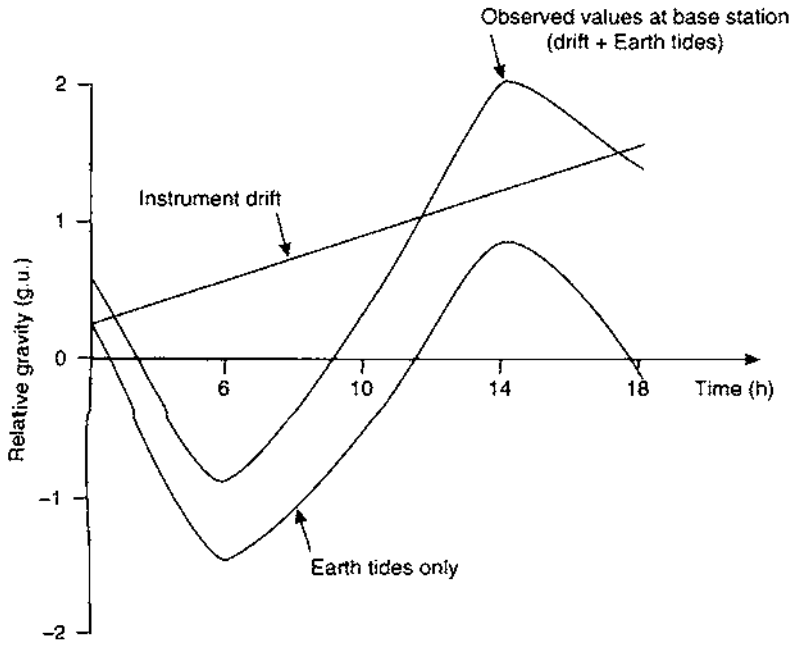

Figure 2.15 Graph of the effects of Earth tides and instrumental drift on the acceleration due to gravity

Earth tides give rise to a change in gravity of up to three g.u. with a minimum period of about 12 hours. Repeated measurements at the same stations permit estimation of the necessary corrections for tidal effects over short intervals, in addition to determination of the instrumental drift for a gravimeter (Figure 2.15). Alternatively, recourse can be made to published tide tables which are published periodically (e.g. *Tidal Gravity Corrections for 1991*, European Association of Exploration Geophysicists, The Hague).

2.5.3 Latitude

The latitude correction is usually made by subtracting the theoretical gravity calculated using the International Gravity Formula (g_ϕ) (Section 2.2.3) from the observed value (g_{obs}). For small-scale surveys which extend over a total latitude range of less than one degree, and not tied into the absolute gravity network, a simpler correction for latitude can be made. A local base station is selected for which the horizontal gravity gradient (δg_L) can be determined at a given degree of latitude (ϕ) by the expression in Box 2.9.

Box 2.9 Local latitude correction

$$\delta g_L = -8.108 \sin 2\phi \quad \text{g.u. per km N}$$

Note that the correction is negative with distance northwards in the northern hemisphere or with distance southwards in the southern hemisphere. This is to compensate for the increase in the gravity field from the equator towards the poles. For a latitude of 51°N, the local latitude correction is about 8 g.u./km. For gravity surveys conducted with an accuracy of ±0.1 g.u., the latitudinal position of the gravity station needs to be known to within ± 10 m, which is well within the capability of modern position-fixing.

2.5.4 Free-air correction

The basis of this correction is that it makes allowance for the reduction in magnitude of gravity with height above the geoid (see Figure 2.16 and Box 2.10), irrespective of the nature of the rock below. It is analogous to measuring gravity in the basket of a hot-air balloon in flight – hence the term *free-air correction*. The free-air correction is the difference between gravity measured at sea level and at an elevation of h metres with no rock in between. A value of 3.086 g.u./m

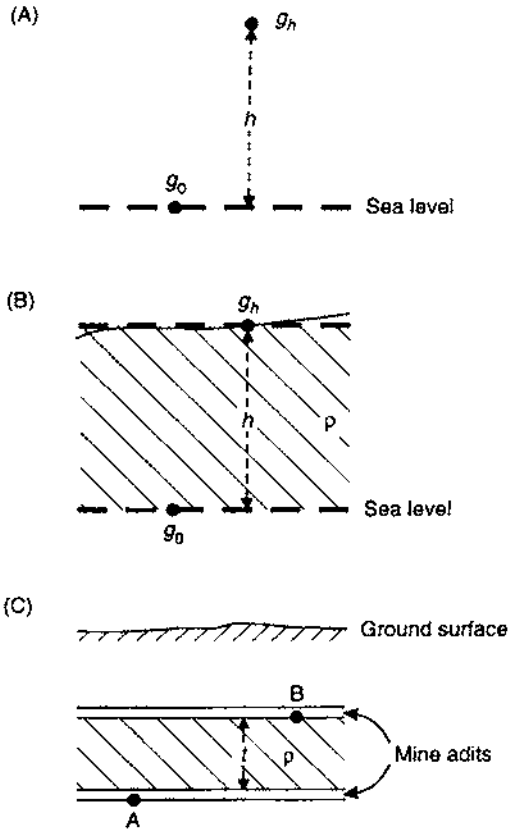

Figure 2.16 Schematic showing (A) the free-air correction, (B) the Bouguer correction, and (C) the Bouguer correction for measurements made underground

is accepted for most practical applications and is positive at elevations above sea level, and negative below. The free-air correction term varies slightly with latitude from 3.083 g.u./m at the equator to 3.088 g.u./m at the poles. With the normal measuring precision of modern gravimeters being around 0.1 g.u., elevations must be known to within 3–5 cm.

Box 2.10 Free-air correction (see also Figure 2.16)

Taking the Earth to be a sphere (rather than an oblate spheroid) with its mass concentrated at its centre of mass, then the value of gravity at sea level is:

$$g_0 = GM/R^2.$$

The value of gravity at a station at an elevation of h metres above sea level is:

$$g_h = GM/(R+h)^2 = \frac{GM}{R^2}\left(\frac{1-2h}{R}\cdots\right).$$

The difference in gravity between sea level and at h metres is the free-air correction:

$$\delta g_F = g_0 - g_h = \frac{2g_0 h}{R}.$$

With $g_0 = 9\,817\,855$ g.u., $R = 6\,371\,000$ M, and with h in metres,

$$\delta g_F = 3.082h \text{ g.u.}$$

Taking into account that the Earth is an oblate spheroid, rather than a sphere, the normally accepted value of the free-air correction is:

$$\boldsymbol{\delta g_F = 3.086h \text{ g.u.}}$$

The reduction in g with increasing height above the ground is important in airborne gravimetry. Anomalies detected by helicopter-mounted gravimeters will have decreased amplitudes and lengthened wavelengths compared with those obtained from land-based surveys. To compare land gravity survey data with airborne, it is necessary to correct for the free-air attenuation of the gravity anomaly by using *upward continuation*, which is discussed in Section 2.6.

The quantity calculated by applying both the latitude and the free-air corrections is called the *free-air anomaly* and is commonly

used to display corrected gravity data for oceans and continental shelves (see, e.g., Talwani *et al.* 1965).

2.5.5 Bouguer correction

Whereas the free-air correction compensates for the reduction in that part of gravity due only to increased distance from the centre of mass, the Bouguer correction (δg_B) is used to account for the rock mass between the measuring station and sea level (Figure 2.16).

The Bouguer correction calculates the extra gravitational pull exerted by a rock slab of thickness h metres and mean density ρ (Mg/m^3) which results in measurements of gravity (g_{obs}) being overestimated by an amount equal to $0.4192\rho h$ g.u. (Box 2.11). The Bouguer correction should be subtracted from the observed gravity value for stations above sea level. For an average rock density of 2.65 Mg/m^3, the Bouguer correction amounts to 1.12 g.u./m. For marine surveys, the Bouguer correction is slightly different in that the low density of sea water is effectively replaced by an equivalent thickness of rock of a specified density (Box 2.11).

Box 2.11 Bouguer correction

Bouguer correction (δg_B) $= 2\pi G\rho h = \beta\rho h$ (g.u.), where:

$$\beta = 2\pi G = 0.4192 \text{ g.u. m}^2 \text{ Mg}^{-1}$$

$$G = 6.67 \times 10^{-8} \text{ m}^3 \text{ Mg}^{-1} \text{ s}^{-2}.$$

Density (ρ) is in Mg m^{-3} and height (h) is in metres.

For marine surveys, the Bouguer correction is given by:

$$\delta g_B = \beta(\rho_r - \rho_w)h_w \text{ (g.u.)}.$$

where ρ_r and ρ_w are the densities of rock and sea water respectively, and h_w is the water depth in metres.

A further development of this correction has to be made for gravity measurements made underground (Figure 2.16C). In this case, the Bouguer correction has to allow for the extra gravitational pull ($=0.4191\rho t$ g.u.) on Station A caused by the slab of thickness t metres between the two stations A and B, whereas the value of gravity at Station A is underestimated by the equal but upward attraction of the same slab. The difference in gravity between the two stations is *twice* the normal Bouguer correction ($=0.8384\rho t$ g.u.). Allowances also have to be made for underground machinery, mine layout and the

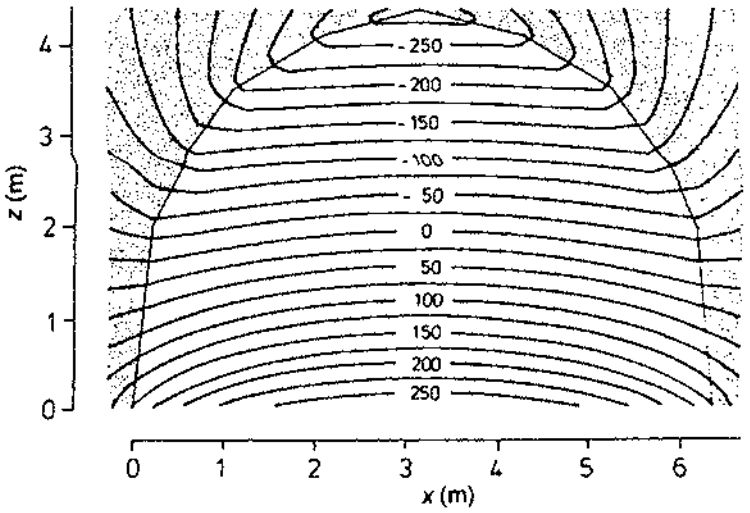

Figure 2.17 Micro-isogals for a typical gallery in a deep coal mine; the contour interval is 25 μGal and the density of the host rock is 2.65 Mg/m^3. From Casten and Gram (1989), by permission

variable density of local rocks, and this is sometimes referred to as the *Gallery correction* (Figure 2.17).

The Bouguer correction on land has to be modified by allowances for terrain roughness (see Section 2.5.6) in areas where there is a marked topographic change over a short distance, such as an escarpment of cliff. In such a situation the approximation of a semi-infinite horizontal slab of rock no longer holds true and more detailed calculations are necessary (Parasnis 1986; p. 72).

The free-air and Bouguer corrections are commonly combined into one *elevation correction* (δg_E) to simplify data handling (Box 2.12). It should be noted that in some cases, the resulting gravity anomaly may be misleading and the combined calculation should be used judiciously. For a density of 2.60 Mg/m^3, the total elevation correction is 2 g.u./m, which requires elevations to be known to an accuracy within 5 cm if gravity readings are to be made to within 0.1 g.u.

Box 2.12 Elevation correction

Elevation correction (δg_E) = (Free-air − Bouguer) corrections:

$$\delta g_E = \delta g_F - \delta g_B.$$

Substituting in the terms $\delta g_F = 3.086h$ and $\delta g_B = 0.4192\rho h$:

$$\boldsymbol{\delta g_E = (3.086 - 0.4192\rho)h \text{ (g.u.)}}$$

where ρ is the average rock density in Mg/m^3.

One of the main problems with the Bouguer correction is knowing which density to use. For example, a difference of 0.1 Mg/m^3 in density for a gravity measurement made at an elevation of 250 m will result in a discrepancy of more than 10 g.u. in the Bouguer correction. In many cases, it may be possible to obtain an estimate of rock densities from appropriate surface samples, or from borehole samples, if available. Caution should be used in the latter case as rock-core samples will relax mechanically, producing many cracks, and expanding slightly in response to the reduced pressure at the surface, giving rise to an underestimate of *in situ* density.

Nettleton (1939, 1940) found a very simple way of determining the appropriateness of the chosen density using a graphical method. Corrected gravity data should show no correlation with topography as all such effects should have been removed through the data reduction process. If a range of densities is chosen and the resulting elevation corrections computed along one gravity profile, the density that shows least correlation with topography is taken as the 'correct' one (Figure 2.18). It is known, however, that this method becomes less accurate if there is any topographic expression due to dipping beds with a significant density contrast to those above and below. Examples of where this might occur are in association with an inclined dense igneous intrusion, or in a marked structural feature with significant variations in density.

A generalised Nettleton method has been proposed by Rimbert *et al.* (1987) which allows for density to vary over a geographic area. The topographic data of an area are smoothed and reduced to produce a surface that lies just below the low topographic points on the survey, and which they refer to as the 'regional topography'. The density between the 'regional' and the actual topography is considered as constant (ρ_0) for a fixed radius around each station. The density below the 'regional' topography is taken as uniform throughout the area of the survey. The variations in density above the 'regional' topography are accounted for statistically but can be plotted in map form to demonstrate the areal variation in density which can be correlated independently with maps of the known geology. Rimbert *et al.* (1987) have achieved accuracies to within 3–4 g.u. with this method in an area in the south of France in which the observed gravity anomalies ranged from 40 to 150 g.u.

Another method to calculate density is to plot a graph of the latitude-corrected gravity data from an area without marked gravity anomalies, against station elevation (Reeves and MacLeod 1986). The resulting straight-line graph yields a gradient that is numerically equal to the elevation correction. Using the result in Box 2.16 and rearranging the equation to make density the subject of the equation, it is possible to solve and find a value for the density. Reeves and MacLeod used this method on data for a survey in Belgium, and produced a graphical elevation correction of 2.35 g.u./m which gave

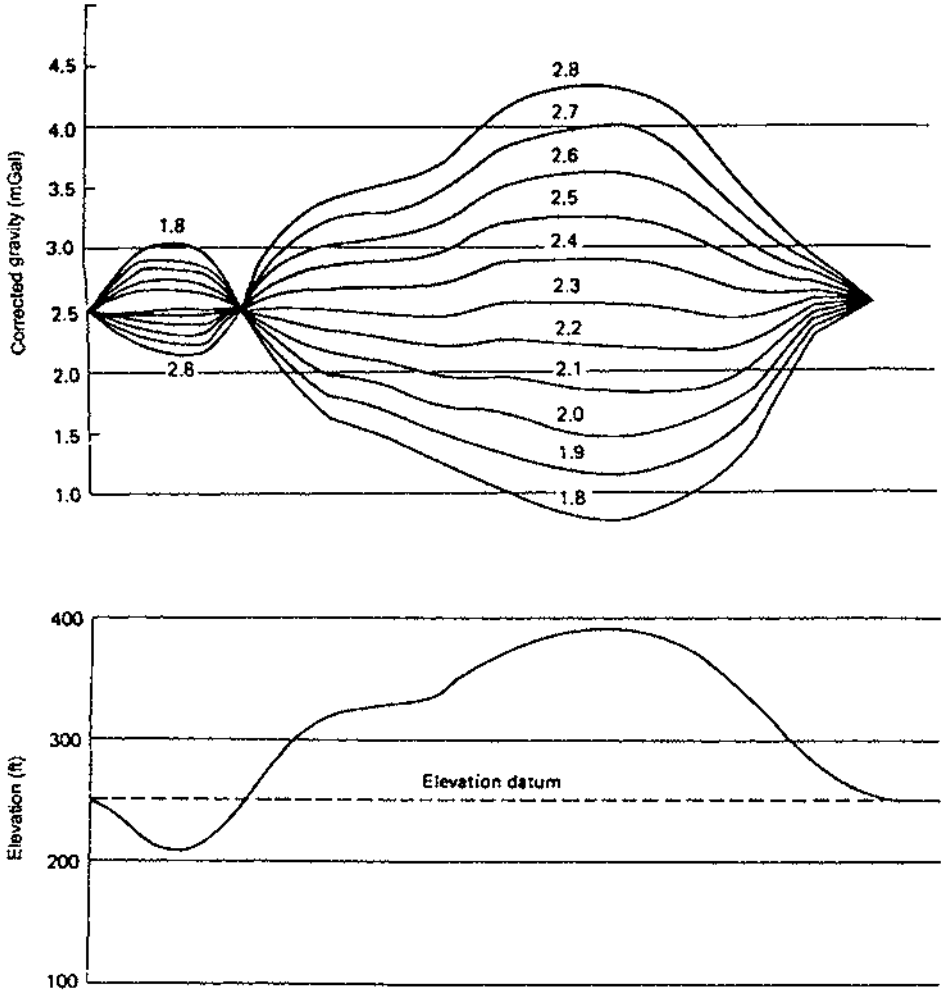

Figure 2.18 The Nettleton method for determining the density of near surface rock formations with the topography as shown. The most appropriate density is about 2.3 Mg/m^3 (least correlation with the topography). Corrections are referred to a height of 76 m. From Dobrin (1976), by permission

a density estimate of 1.74 Mg/m^3, compared with 1.6 Mg/m^3 determined using the Nettleton method.

The danger with a graphical method even if linear regression statistics are used to determine the gradient of the best straight-line fit through the data – is that a small difference in the graphical gradient can result in an unacceptably large density discrepancy, and this makes the method rather insensitive to small changes in density. For example, the data presented by Reeves and MacLeod, rather than showing a single trend with elevation, indicate two: data up to an elevation of 215 m yield a density of 1.43 Mg/m^3 and the remaining data up to 280 m yield a density of 1.79 Mg/m^3, a difference of 0.36 Mg/m^3. Densities should be determined to better than 0.1 Mg/m^3 if possible.

In underground gravity surveys, a similar method is employed (Hussein 1983). The vertical gravity gradient (i.e. δg_F) is obtained by measuring g at two or more elevations separated by only 1.5 - 3 m at the same location within an underground chamber. The density can then be calculated as described above. As the measurements of g are strictly controlled, the error in density can be minimised routinely to within 0.08 Mg/m^3 (Casten and Gram 1989).

Rock densities for depths below which it is not possible to sample can also be estimated using the relationship of density with P-wave velocities as described, for example, by Nafe and Drake (1963), Woollard (1950, 1959, 1975), Birch (1960, 1961), and Christensen and Fountain (1975).

2.5.6 Terrain correction

In flat countryside, the elevation correction (the combined free-air and Bouguer correction) is normally adequate to cope with slight topographic effects on the acceleration due to gravity. However, in areas where there are considerable variations in elevation, particularly close to any gravity station, a special *terrain correction* must be applied. The Bouguer correction assumes an approximation to a semi-infinite horizontal slab of rock between the measuring station and sea level. It makes no allowance for hills and valleys and this is why the terrain correction is necessary.

The effect of topography on g is illustrated in Figure 2.19. Consider a gravity station beside a hill as in Figure 2.19A. The slab of rock which comprises the hill (mass M) has its centre of mass above the plane on which the gravimeter is situated. There is a force of attraction between the two masses. If the force is resolved into horizontal and vertical components and the latter only is considered, then it can be seen that the measurement of g at the gravity station will be underestimated by an amount δg. Conversely, if the gravity station is adjacent to a valley, as indicated in Figure 2.19B, then the valley represents a mass deficiency which can be represented by a negative mass ($-M$). The lack of mass results in the measurement of g to be underestimated by an amount δg. Consequently, a gravity measurement made next to either a hill or a valley requires a correction to be added to it to make allowance for the variable distribution of mass. The correction effectively removes the effects of the topography to fulfil the Bouguer approximation of a semi-infinite rock slab.

Physical computation of the terrain correction is extremely laborious as it has to be carried out for each and every station in an entire survey. A special transparent template, known as a *Hammer chart* after its originator Sigmund Hammer (1939), consists of a series of segmented concentric rings (Figure 2.20). This is superimposed over a topographic map and the average elevation of each segment of the

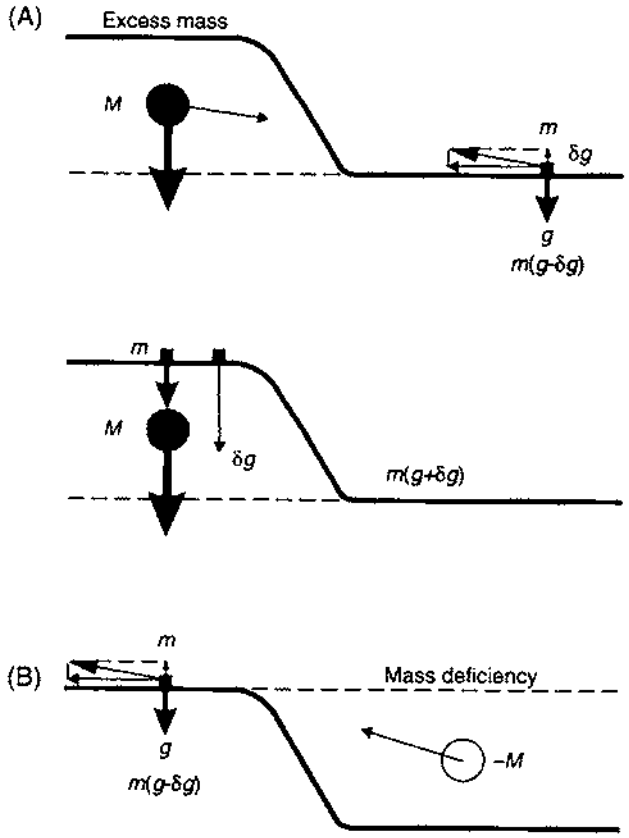

Figure 2.19 The effects of a hill and a valley on the measurement of gravity, illustrating the need for terrain corrections

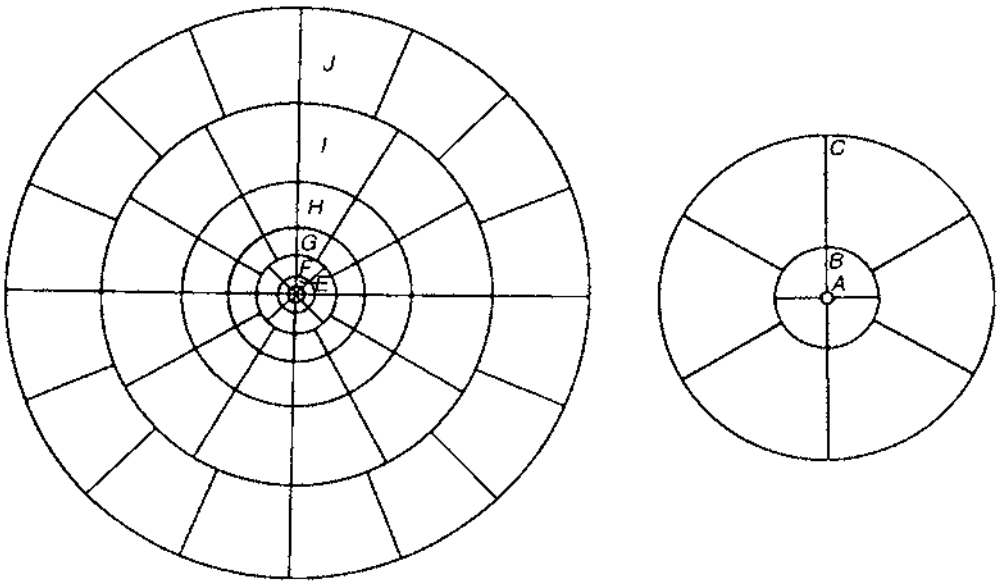

Figure 2.20 Hammer terrain correction chart with inner rings A–C shown expanded for clarity. After Dobrin (1976) and Milsom (1989), by permission

Table 2.8 Terrain corrections for Hammer zones B to M. From Milsom (1989), by permission

Zone	B	C	D	E	F	G
No. of compartments:	4	6	6	8	8	12
Correction (g.u.):	Heights (meters)					
0.01	0.5	1.9	3.3	7.6	11.5	24.9
0.02	0.7	2.6	4.7	10.7	16.3	35.1
0.03	0.8	3.2	5.8	13.1	19.9	43.1
0.04	1.0	3.8	6.7	15.2	23.0	49.8
0.05	1.1	4.2	7.5	17.0	25.7	55.6
0.06	1.2	4.6	8.2	18.6	28.2	60.9
0.07	1.3	5.0	8.9	20.1	30.4	65.8
0.08	1.4	5.4	9.5	21.5	32.6	70.4
0.09	1.5	5.7	10.1	22.9	34.5	74.7
0.10	1.6	6.0	10.6	24.1	36.4	78.7
0.20	2.4	8.7	15.1	34.2	51.6	111.6
0.30	3.2	10.9	18.6	42,1	63.3	136.9
0.40	3.9	12.9	21.7	48.8	73.2	158.3
0.50	4.6	14.7	24.4	54.8	82.0	177.4
0.60	5.3	16.5	26.9	60.2	90.0	194.7
0.70	6.1	18.2	29.3	65.3	97.3	210.7
0.80	6.9	19.9	31.5	70.1	104.2	225.6
0.90	7.8	21.6	33.7	74.7	110.8	239.8
1.00	8.7	23.4	35.7	79.1	117.0	253.2
	H	I	J	K	L	M
	12	12	16	16	16	16
0.01	32	42	72	88	101	125
0.02	46	60	101	124	148	182
0.03	56	74	125	153	186	225
0.04	65	85	144	176	213	262
0.05	73	95	161	197	239	291
0.06	80	104	176	216	261	319
0.07	86	112	191	233	282	346
0.08	92	120	204	249	303	370
0.09	96	127	216	264	322	391
0.10	103	134	228	278	338	413
0.20	146	190	322	394	479	586
0.30	179	233	396	483	587	717
0.40	206	269	457	557	679	828
0.50	231	301	511	624	759	926
0.60	253	330	561	683	832	1015
0.70	274	357	606	738	899	1097
0.80	293	382	648	790	962	1173
0.90	311	405	688	838	1020	1244
1.00	328	427	726	884	1076	1312

Note: These tables list the exact height differences which, assuming a density of 2000 kg/m^3 will produce the tabulated terrain effects. Thus, a height difference of 32 m between gravity station and average topographic level in one compartment of zone E would be associated with a terrain effect of 0.20, or possibly 0.19, g.u. Almost all commercial gravity meters have sensitivities of 0.1 g.u. but an additional decimal place is necessary if large 'rounding off' errors are to be avoided in summing the contributions from all the compartments. The inner radius of zone B is 2 m. Zone outer radii are: B: 16.6 m. C: 53.3 m. D: 170 m, E: 390 m, F: 895 m, G: 1530 m, H: 2.61 km, I: 4.47 km. J: 6.65 km. K: 9.9 km, L: 14.7 km, M: 21.9 km

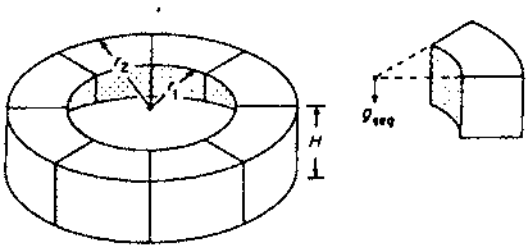

Figure 2.21 Segmented cylindrical ring used to compute terrain corrections. From Robinson and Coruh (1988), by permission

chart is estimated. The outer radius of the furthest zone is 21.9 km beyond which the effect of topography on g is negligible. In some cases, the range of the chart is extended to 50 km. Special tables (Table 2.8) are used to derive the terrain correction in g.u. for each segment, and then all the values are summed to produce a statistically weighted terrain correction for a given gravity station, each ring of the Hammer chart having a different weighting. For example, for a mean height difference of 34.7 m between the gravity station and a segment in zone D, a terrain correction of 0.95 g.u. can be determined from Table 2.8.

The terrain correction method works on the principle of determining the value of g at the centre of an annulus of inner and outer radii r_1 and r_2 (Figure 2.21) using the equation given in Box 2.13. Although topographic maps can be digitised and the terrain corrections calculated by computer (Bott 1959; Kane 1962) for the outer rings of the Hammer chart, it is still necessary to compute the terrain corrections for the innermost rings manually.

Box 2.13 Gravity of a Hammer chart segment (see Figure 2.21)

Gravity of a Hammer chart segment (δg_{seg}):

$$\delta g_{seg} = \frac{2\pi\rho G}{N}[r_2 - r_1 + (r_1^2 + z^2)^{1/2} - (r_2^2 + z^2)^{1/2}] \text{ (g.u.)}$$

where N is the number of segments in the ring, z is the modulus of the difference in elevation between the gravity station and mean elevation of the segment, and ρ is the Bouguer correction density (Mg/m^3).

There is no theoretical reason as to why the terrain correction needs to be calculated on the basis of a circular division of the terrain. It is computationally better for a regular grid to be used, in which case digitised topographic data can be used quite readily. Ketelaar (1976) has suggested a method in which the topography is represented by square prisms of side length D with an upper surface sloping at an

angle α. The terrain correction due to each prism can be calculated using the expression in Box 2.14. An example of computer analysis of terrain corrections for micro-gravity surveys has been given by Blizkovsky (1979) in which he also considers the gravitational effects of walls, vertical shafts and horizontal corridors. In micro-gravity surveys, an area of radius 2 m centred on the measurement station should be flat. For terrain effects of less than 1 μGal, height variations of less than 0.3 m in Hammer zone B and up to 1.3 m in zone C can be tolerated.

Box 2.14 Terrain correction for a square prism

Terrain correction due to a square prism of side length D:

$$\delta g_{\text{prism}(i,j)} = G\rho D(1 - \cos\alpha)K(i,j)$$

where $K(i,j)$ is the matrix of prism coordinates within the grid.

The calculation of terrain corrections is labour-intensive, time-consuming and adds considerably to the total cost of the survey. It is only undertaken when dictated by the roughness of the local topography. In built-up areas, care has to be taken in estimating the likely effect of neighbouring buildings. Modern, thin-walled buildings may contribute only a small effect (of the order of 1–5 μGal), but older thick-walled constructions may give rise to a terrain correction effect of 10–30 μGal. In these cases, it is preferable to position the gravimeter more than 2.5 m away from such a building in order to keep the effect to less than 5 μGal. Otherwise, specific calculations of the terrain corrections of the buildings concerned becomes necessary. An alternative approach is to measure the gravity effect around a comparable building, assuming one exists, away from the survey area and to carry out an empirical adjustment of the actual survey data. Budgetary constraints may preclude detailed data reduction, in which case the effectiveness of the micro-gravity survey may be jeopardised. Such considerations need to be made at the design stage of the survey. In some cases, the effects of adjacent buildings are assumed to be negligible and are ignored unjustifiably as they are thought to be too difficult to determine. Yet the magnitude of the anomalies being sought may be of the same order of magnitude as the terrain correction. There is scope for collaboration between geophysicists and members of the construction industry!

2.5.7 Eötvös correction

For a gravimeter mounted on a vehicle, such as a ship or a helicopter, the measured gravitational acceleration is affected by the vertical

component of the Coriolis acceleration which is a function of the speed and the direction in which the vehicle is travelling. To compensate for this, gravity data are adjusted by applying the Eötvös correction, named after the Hungarian geophysicist Baron von Eötvös who described this effect in the late 1880s.

There are two components to this correction. The first is the outward-acting centrifugal acceleration associated with the movement of the vehicle travelling over the curved surface of the Earth, and the second is the *change* in centrifugal acceleration resulting from the movement of the vehicle relative to the Earth's rotational axis. In the second case, an object that is stationary on the Earth's surface is travelling at the speed of the Earth's surface at that point as it rotates around the rotational axis in an east–west direction. If that same object is then moved at x km/h towards the east, its speed relative to the rotational velocity is increased by the same amount. Conversely, if it travels at a speed of y km/h in a westerly direction, its relative speed is slowed by the same amount. Any movement of a gravimeter which involves a component in an east–west direction will have a significant effect on the measurement of gravity. For shipborne gravimeters the Eötvös correction can be of the order of 350 g.u. For airborne gravity measurements, where speeds over 90 km/h (about 50 knots) are common, the Eötvös correction can be as high as 4000 g.u. The expression governing the Eötvös correction is given in Box 2.15, with a fuller mathematical explanation in Box 2.16.

Box 2.15 Eötvös correction

The Eötvös correction is given by:

$$\delta g_{EC} = 75.08\, V \cos\phi \sin\alpha + 0.0416\, V^2 \text{ (g.u.)}$$

or

$$\delta g_{EC} = 40.40\, V' \cos\phi \sin\alpha + 0.012\,11\, V'^2 \text{ (g.u.)}$$

where ϕ is the degree of geographic latitude, α is the azimuth in degrees, and V and V' are the speeds of the vehicle in knots and kilometres per hour respectively.

The error in the Eötvös correction $[d(\delta g_{EC})]$ in g.u. due to errors in speed (dV) and azimuth $(d\alpha)$ is:

$$d(\delta g_{EC}) = (0.705\, V' \cos\phi \cos\alpha)d\alpha + (40.40 \cos\phi \sin\alpha + 0.024\,22\, V')dV'.$$

At a latitude of 25°, a change of 0.1 knot (0.2 km/h) with a half a degree shift off course will result in over 7 g.u. difference in

Eötvös correction while on an easterly course ($\alpha = 90°$), or 3 g.u. on a northerly course ($\alpha = 0°$), assuming a speed of 10 km/h. Consequently, for an airborne survey to be accurate to within 10 g.u., extremely tight controls need to be kept on nagivation and on the general movement (roll, pitch, yaw, etc.) of the helicopter or plane; such accuracies are now thought to be routinely achievable (Hammer, 1982, 1984). From the last equation in Box 2.15, it can be seen that there is the greatest sensitivity to errors in speed in an east–west direction, and to errors in azimuth on a north–south course. Recent tests of airborne gravity have been discussed by Halpenny and Darbha (1995).

Box 2.16 Derivation of the Eötvös correction equation
(see Figure 2.22)

In general, the centrifugal acceleration a_1 is (velocity)$^2/d$. The total east–west speed of the vehicle is the linear speed of rotation of the Earth (v) plus the *east - west* component of the speed of the vehicle (V_E). Thus the centrifugal acceleration $a_1 = (v + V_E)^2/d$.

Centrifugal acceleration (a_2) along the radius vector, due simply to the movement of the vehicle in a *north south* direction, is $a_2 = V_N^2/R$.

However, it is the *change* in acceleration that is required, so the centrifugal acceleration acting on a static body (a_3) needs to be removed: $a_3 = v^2/d$.

The total change in acceleration acting in a vertical sense is:

$$\delta g_E = a_1 \cos\phi + a_2 - a_3 \cos\phi \quad \text{(equation (4))}.$$

We note that:

$$d = R\cos\phi$$
$$v = \omega R \cos\phi$$
$$V = (V_N^2 + V_E^2)^{1/2} \quad \text{(from Pythagoras' theorem)}$$
$$V_E = V \sin\alpha, \text{ where } \alpha \text{ is the bearing to True North.}$$

Substituting into equation (4) we obtain:

$$\delta g_E = \frac{(v + V_E)^2}{R\cos\phi}\cos\phi + \frac{V_N^2}{R} - \frac{v^2\cos\phi}{R\cos\phi}.$$

Simplifying, this becomes

$$\delta g_E = [(v + V_E)^2 + V_N^2 - v^2]/R$$

continued

continued

which reduces to

$$\delta g_E = [2\omega V_E + (V_E^2 + V_N^2)]/R.$$

Rewriting this in terms of ω, R, ϕ, and α using the above expressions, this becomes:

$$\delta g_E = 2\omega V \cos\phi \sin\alpha + V^2/R \quad \text{(equation (5))}.$$

Given the following values:

$$\omega = 7.2921 \times 10^{-5} \text{ radians/s}$$
$$R = 6.371 \times 10^8 \text{/cm}$$
$$1 \text{ knot} = 51.479 \text{ cm/s}$$
$$1 \text{ Gal} = 10^4 \text{ g.u.}$$

then equation (5) can be rewritten (in terms of g.u.) as:

$$\delta g_E = 2(7.2921 \times 10^{-5} \times 51.479 \times 10^4) V \cos\phi \sin\alpha + (51.479V)^2 \times 10^4/6.371 \times 10^8$$

Finally:

$$\delta g_E = 75.08\, V \cos\phi \sin\alpha + 0.0416\, V^2 \text{ (g.u.)}.$$

2.5.8 Isostatic correction

If there were no lateral variations in density in the Earth's crust, the fully reduced gravity data, after application of all the corrections so far outlined, would be the same. However, where there are lateral variations, a gravity anomaly results which is known as the *Bouguer anomaly* (discussed in more detail in Section 2.5.10). The average Bouguer anomaly in oceanic areas is generally positive, while over mountainous regions it is usually negative. These effects indicate that the rock beneath the oceans is more dense than normal while that beneath the mountains is less dense.

Two hypotheses were proved in the 1850s to account for this large-scale systematic variation in density (Figure 2.23). The geodesist G.B. Airy (1855) proposed that while mountain chains had deep roots, beneath the oceans the crust, which was assumed to have constant density everywhere, was thin. In contrast, an English Archdeacon J.H. Pratt (1859) thought that the crust extended to a uniform depth below sea level but that density varied inversely with the height of the topography.

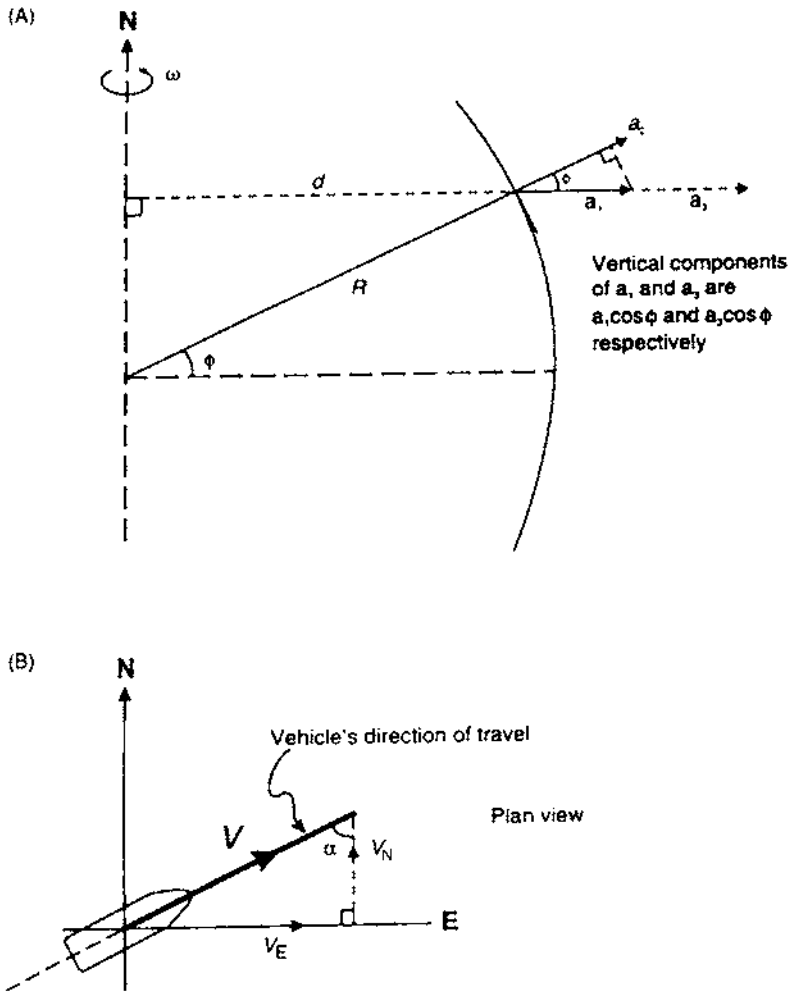

Figure 2.22 Schematic illustrating the components which contribute to the Eötvös correction (see box 2.16)

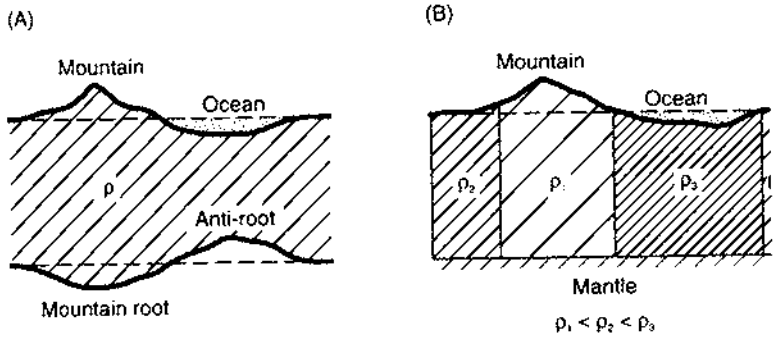

Figure 2.23 (A) Airy and (B) Pratt's models for isostacy

Airy's isostatic model is preferred geologically and seismologically, whereas Pratt's model is easier to use to calculate the isostatic (e.g. Rimbert *et al.* 1987), but the results are similar. Pratt's model has been developed by Heiskanen (1938) who suggested that density changes laterally with variable thickness of crust and that density increases gradually with depth. The aim of the isostatic correction is that effects on g of the large-scale changes in density should be removed, thereby isolating the Bouguer anomaly due to lateral variations in density in the upper crust (Hayford and Bowie 1912). The isostatic correction is discussed in more detail by Garland (1965), and the implications for isostatic rebound due to crustal loading and the viscosity of the mantle are discussed by Sharma (1986).

2.5.9 Miscellaneous factors

In Sections 2.5.1–2.5.8, calculable corrections to gravity data have been discussed. Gravimeters are sensitive not only to these factors but also to several others which tend to be erratic, temporal and difficult to quantify so that they may constitute gravitational noise. Such factors are: meteorological loading produced by atmospheric pressure changes; inertial acceleration caused by seismic and microseismic waves, including the effect of wind pressure on the gravimeter, and vibration from traffic and industrial machinery; and electrical noise from the gravimeter itself. Changes in atmospheric pressure can be corrected for by using -0.03 g.u. per millibar. Modern gravimeters used in micro-gravity surveys can filter out most noise above 10 Hz, and reject the microseismic noise between 0.1 and 2 Hz, so that standard deviations on gravity readings can be as small as 0.04 g.u. (4 μGal) (Thimus and van Ruymbeke, 1988).

2.5.10 Bouguer anomaly

The main end-product of gravity data reduction is the *Bouguer anomaly*, which should correlate only with lateral variations in density of the upper crust and which are of most interest to applied geophysicists and geologists. The Bouguer anomaly is the difference between the observed gravity value (g_{obs}), adjusted by the algebraic sum of all the necessary corrections (Σcorr; see Table 2.7 and Box 2.17), and that at some base station (g_{base}). The variation of the Bouguer anomaly should reflect the lateral variation in density such that a high-density feature in a lower-density medium should give rise to a positive Bouguer anomaly. Conversely, a low-density feature in a higher-density medium should result in a negative Bouguer anomaly.

Box 2.17 Bouguer anomaly

The Bouguer anomaly (Δg_B) is the difference between the observed value (g_{obs}), duly corrected, and a value at a given base station (g_{base}), such that:

$$\Delta g_B = g_{obs} + \Sigma(\text{corr}) - g_{base}$$

with

$$\Sigma(\text{corr}) = \delta g_L + (\delta g_F - \delta g_B) + \delta g_{TC} \pm \delta g_{EC} \pm \delta g_{IC} - \delta g_D$$

where the suffices refer to the following corrections:

L = latitude; F = free-air; B = Bouguer;
TC = terrain correction; EC = Eötvös correction;
IC = isostatic correction; and D = drift (including Earth tides).

2.6 INTERPRETATION METHODS

There are two approaches to the interpretation of Bouguer anomaly data. One is *direct* where the original data are analysed to produce an interpretation. The other is *indirect*, where models are constructed to

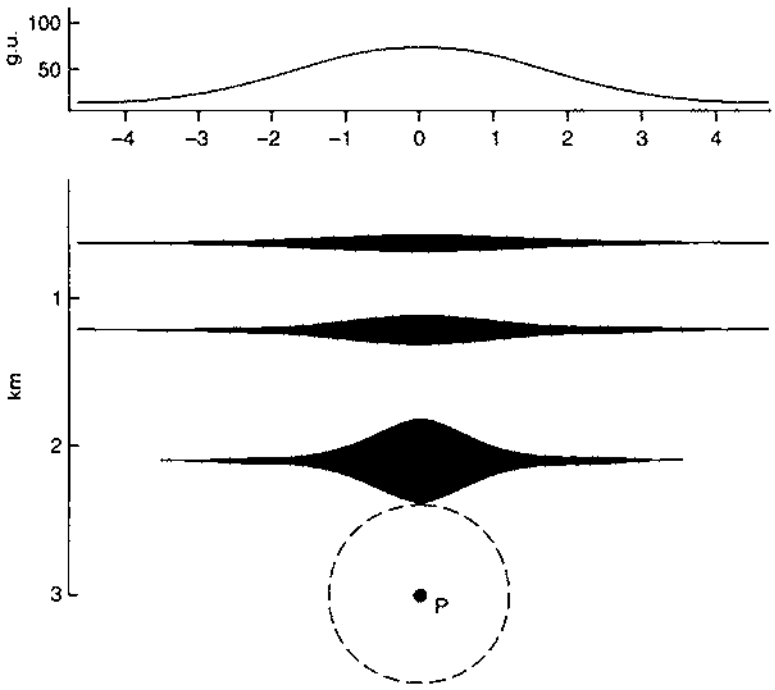

Figure 2.24 Ambiguity in geological models, all of which produce the gravity anomaly shown at the top. The lens-shaped bodies have a gravity anomaly identical to that of a sphere at P of radius 600 m and density contrast 1.0 Mg/m^3. The thickness of the bodies is exaggerated by a factor of 3. From Griffiths and King (1981), by permission

compute synthetic gravity anomalies which are compared in turn with the observed Bouguer anomaly. The model producing the best fit, however, will not be unique as several alternative models may be found which also produce an equivalent fit (Figure 2.24). It is because of this type of ambiguity, which has already been discussed in Section 1.2 (see also Figure 1.1), that different geophysical methods are used together to constrain the geologic model.

2.6.1 Regionals and residuals

Bouguer anomaly maps are rather like topographic maps with highs and lows, linear features and areas where the contours (*isogals*) are closely packed and others where they are further apart. There may be a gentle trend in the gravity data, reflecting a long-wavelength gravity anomaly attributable to deep-seated crustal features; this is known as a *regional anomaly*. Shorter-wavelength anomalies arising from shallower geological features are superimposed on the regional anomaly, and it is these anomalies that are often to be isolated for further analysis. Separation of the regional from the Bouguer anomaly will leave a *residual anomaly* (Figure 2.25).

There are a number of different methods with varying degrees of complexity and effectiveness by which residual anomalies can be isolated (Nettleton, 1954). These range from curve-sketching, which is purely subjective, through to computer-based analytical methods. Graphical methods include sketching in estimated regional trends by eye on a profile (Figure 2.25A) or calculating the residual from estimated isogals on a map. Figure 2.25B illustrates how the residual is calculated. The 5.0 mGal isogal, which has been highlighted, intersects several estimated regional isogals. At points A and B, the difference (i.e. the residual) between the 5.0 mGal line and those it crosses are respectively +0.2 and +0.4 mGal and contours are drawn of the same residual value.

An example of the quantitative analytical method consists in fitting a low-order polynomial expression to the Bouguer anomaly data and then subtracting the calculated values from those observed to produce residual values, which are then plotted in map form. A more sophisticated method is the application of Fourier analysis by which a power spectrum is obtained for the Bouguer anomaly (Spector and Grant 1970; Syberg 1972). This highlights the different wavelengths of anomaly present and so allows a form of filtering to be undertaken to remove the unwanted anomalies (e.g. Granser *et al.* 1989). Dobrin (1976), Grant and West (1965) and Telford *et al.* (1990) discuss the various techniques in more detail.

Although the analytical methods appear more rigorous and thorough, there are occasions when the manual interpretation can take into account known variations in local geology more readily than an automated system.

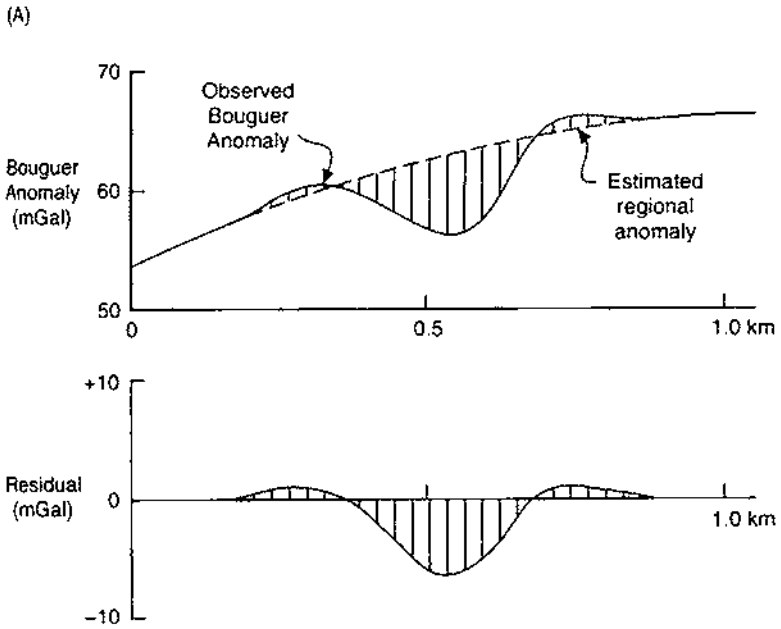

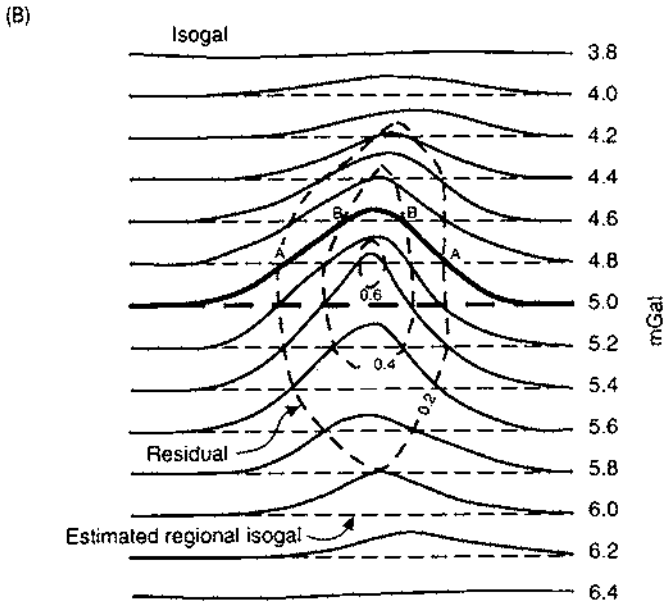

Figure 2.25 (A) Removal of a residual gravity anomaly from a regional profile, and (B) how a residual gravity map is constructed (see text for an explanation). After Dobrin (1976), by permission

2.6.2 Anomalies due to different geometric forms

Certain geologic structures can be approximated to models with known geometric forms (Nettleton, 1942). For example, a buried cavity may be represented by a sphere, a salt dome by a vertical cylinder, a basic igneous dyke by an inclined sheet or prism, etc. Another factor to be considered is whether the target to be modelled should be considered in two or three dimensions. If g is computed across a profile over a buried sphere, then that profile should hold true for any direction across the sphere. However, if the profile is across a buried horizontal cylinder, then the profile along the long-axis of the cylinder will be quite different from that across it. Also, if the strike length of the feature is greater than 20 times any other dimension, then it may be considered a two-dimensional body. Where this does not hold true, any profile will also sense the effects of the third dimension ('edge effects') and thus will not be modelled accurately if considered only in two dimensions.

Several common geometrical forms are illustrated in Figure 2.26, with their associated gravity profiles and the types of geologic features they approximate. The equations used to calculate the maximum anomaly for each geometric feature are given in Box 2.18. No attempt is made here to explain the derivations of these formulae, all of which are discussed much more fully by Dobrin (1976), Telford *et al.* (1990) and Parasnis (1986). The equations in Box 2.18 are intended only as guides to estimate the maximum values of the associated gravity anomalies. The use of the half-width ($x_{1/2}$) is discussed in more detail in Section 2.6.3 and 2.6.4.

The range of geometric forms given above is by no means complete. Details of other forms and their interpretations, such as by the use of characteristic curves, are given by Grant and West (1965) and Telford *et al.* (1990).

Calculation of gravity anomalies using the above methods should be regarded as a first step in the interpretation process. There are other, more sophisticated, and commonly computerised methods of gravity anomaly analysis. However, it is worth noting that for more complicated geological features of irregular shape which do not approximate to any of the geometrical forms, two other broad approaches can be adopted. The first is the use of graphical methods, and the second is an analytical approach. In the graphical methods, a template, which is divided into segments, is superimposed on an irregular cross-section of the geological feature to be modelled. The gravity at a point on the surface can be calculated by summing the effects of all the individual segments covering the cross-section of the feature.

Graphical methods can also be used for three-dimensional bodies. In this case, the appropriate template is superimposed on contours of the geological feature in the horizontal plane, thereby dividing it into

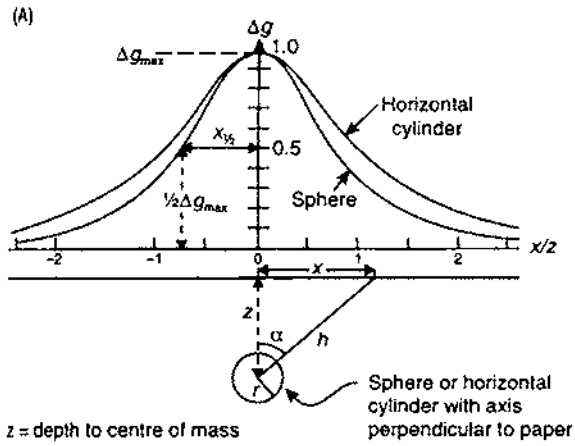

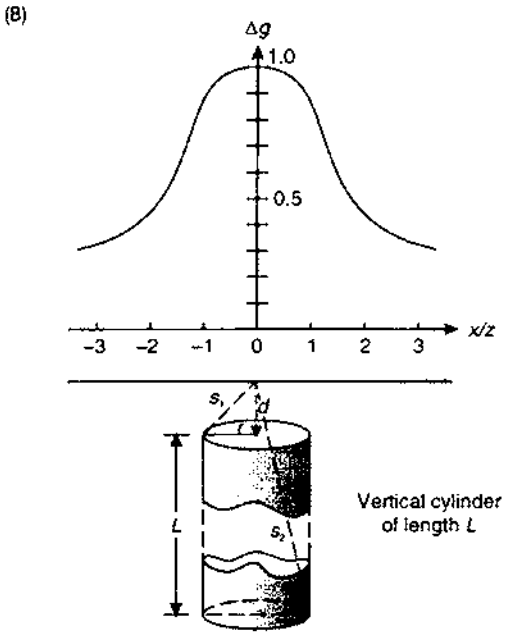

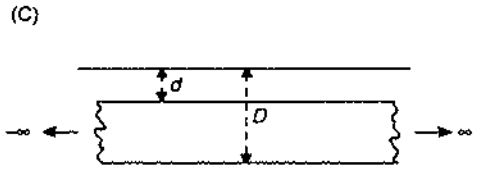

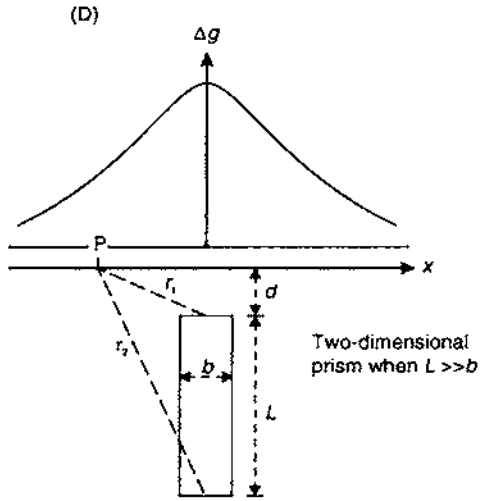

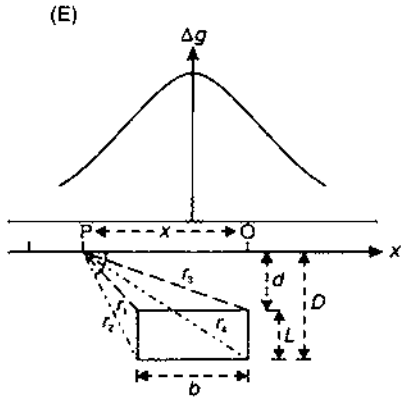

Figure 2.26 Representative gravity anomalies over given geometric forms: (A) a sphere or horizontal cylinder with its long axis perpendicular to the paper; (B) a vertical cylinder; (C) a semi-infinite horizontal slab (a Bouguer plate when $d = 0$); (D) a vertical rectangular prism; and (E) a horizontal rectangular prism

Box 2.18 Gravity anomalies associated with geometric forms
(see Figure 2.26)

Models	Maximum gravity anomaly	Notes
Sphere	$\Delta g_{max} = (4/3)\pi G\delta\rho r^3/z^2$	$z = 1.305x_{1/2}$ (m)
Horizontal cylinder	$\Delta g_{max} = 2\pi G\delta\rho r^2/z$	$z = x_{1/2}$
Vertical cylinder	$\Delta g_{max} = 2\pi G\delta\rho\,(s_1 - d)$ $\Delta g_{max} = 2\pi G\delta\rho r$ $\Delta g_{max} = 2\pi G\delta\rho\,(L + s_1 - s_2)$	If $L \rightarrow$ infinity If $d = 0$ If L finite $z = x_{1/2}\sqrt{3}$
Buried slab (Bouguer plate)	$\Delta g_{max} = 2\pi G\delta\rho\, L$	For $L = 1000$ m and $\delta\rho = 0.1$ Mg/m^3, $\Delta g_{max} = 42$ g.u.
Infinite slab	$\Delta g_{max} = 2\pi G\delta\rho\,(D - d)$	
Horizontal rectangular prism	$\Delta g_p = 2G\delta\rho\left[x\ln\left(\frac{r_1 r_4}{r_2 r_3}\right) + b\ln\left(\frac{r_2}{r_1}\right) + D(\phi_2 - \phi_4) - d(\phi_1 - \phi_3)\right]$	
Vertical rectangular prism	$\Delta g_{max} = 2G\delta\rho[b\ln(d/L)]$	$L \gg b$
Step	$\Delta g_{max} = 2G\delta\rho\,[x\ln(r_4/r_3) + \pi(D - d) - D\phi_4 + d\phi_3]$	

All distances are in metres unless stated otherwise; Δg_{max} in mGal and $\delta\rho$ in Mg/m^3, and the factor $2\pi G = 0.042$.

a pile of horizontal slabs each with a thickness equal to the contour interval.

Most computer-based analytical methods (e.g. Bott 1960) are based on the premise proposed by Talwani *et al.* (1959), that a cross-section of a two-dimensional body can be approximated by representing it by a multisided polygon (Figure 2.27A). This was developed by Talwani and Ewing (1960) for three-dimensional bodies (Figure 2.27B) which are approximated by a stack of polygonal laminae. The gravity effect of each lamina is computed and summed to give a total gravity anomaly. Enhancements of these methods have largely been centred on improving the ease of use of the software on computers that have dramatically increased in power and efficiency, and on the portability of software from mainframe machines to personal microcomputers (Busby 1987).

A development of the three-dimensional approach is to consider a geological body as a stack of cubic blocks of uniform size, each

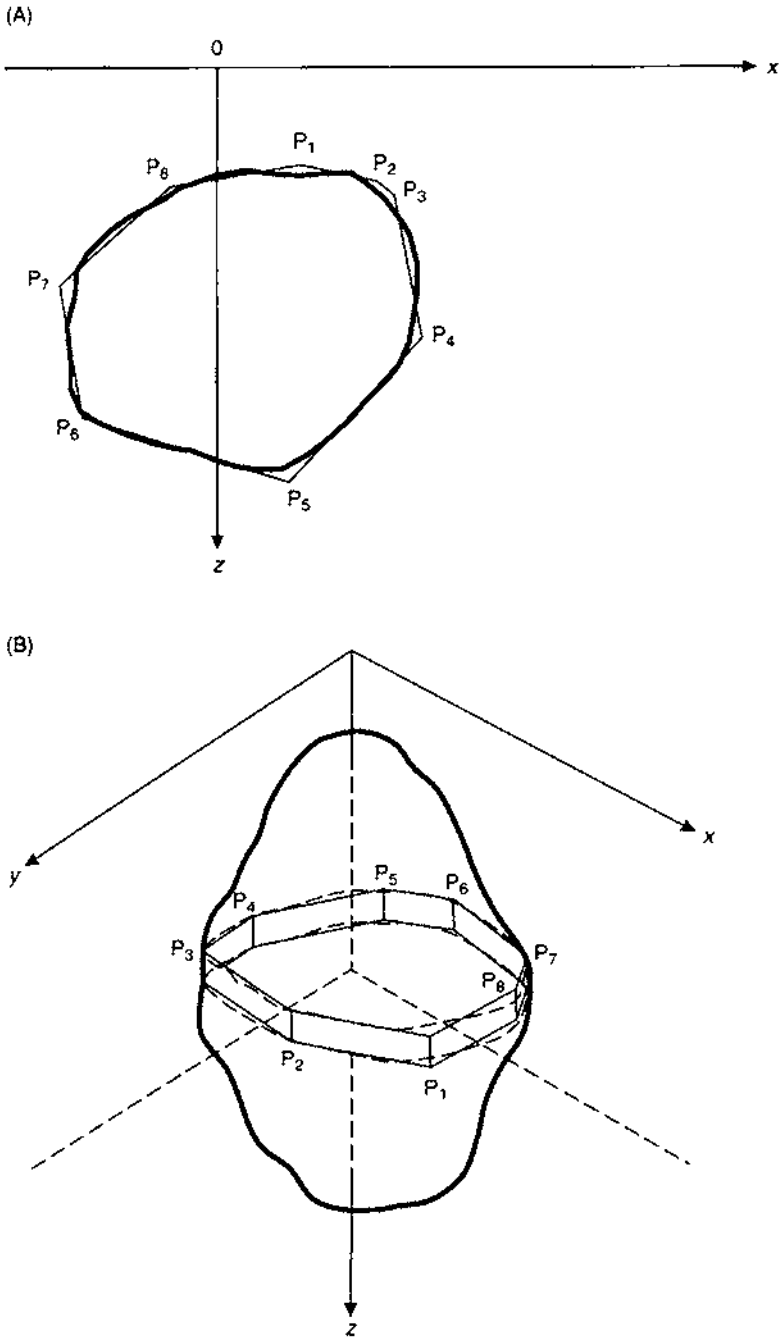

Figure 2.27 (A) Polygonal representation of an irregular vertical section of a two-dimensional geological feature. (B) Representation of an irregular three-dimensional geological feature by polygonal laminae

having a specified density contrast. Each little cube is considered as a point mass and thus the total gravity anomaly for the entire body is obtained by summing the constituent gravity components for each mini-cube. The resultant gravity anomaly is compared with that

(A)

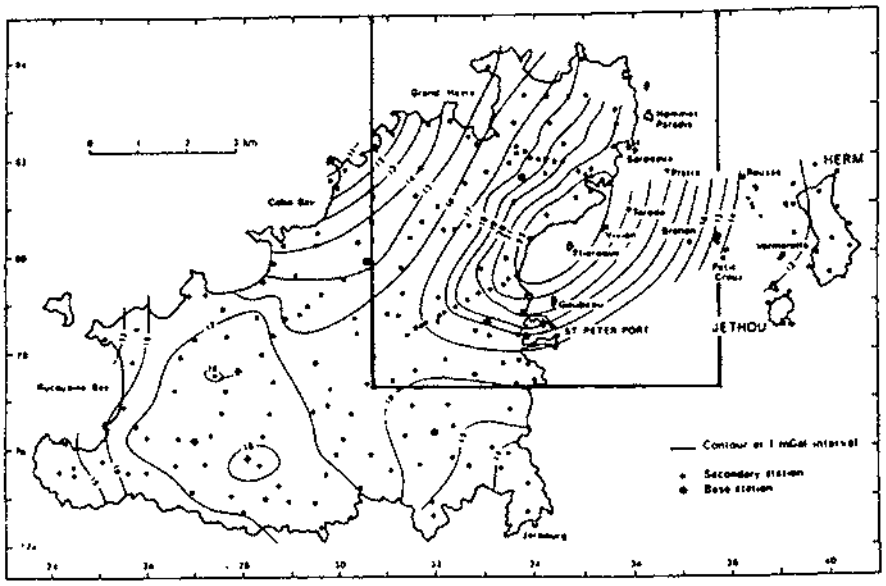

(B)

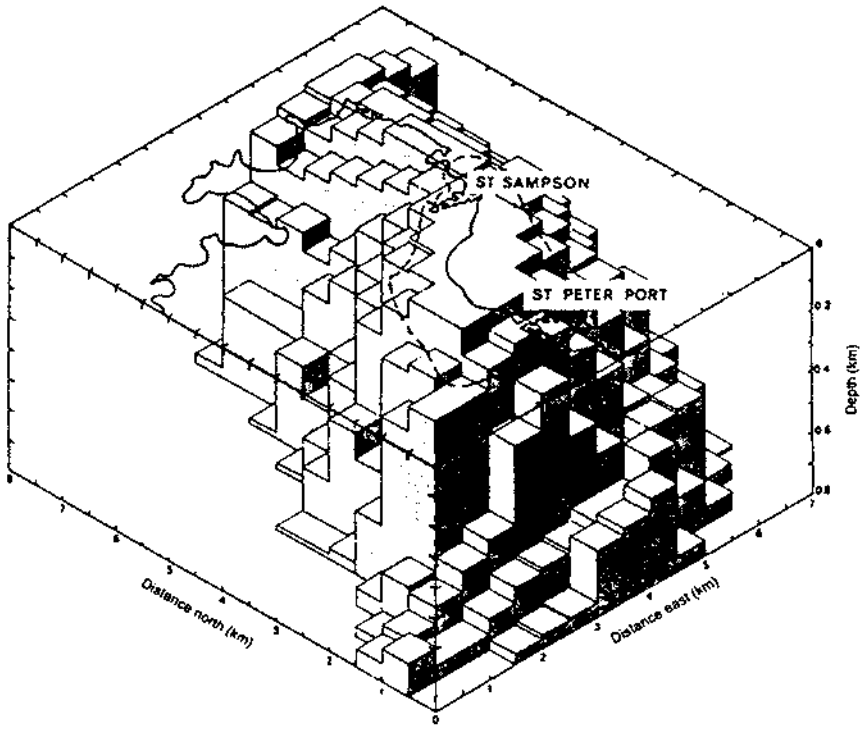

Figure 2.28 (A) Bouguer anomaly map for Guernsey, Herm and Jethou, Channel Islands, and (B) a three-dimensional model of the underlying St Peter Port Gabbro (density contrast 0.27 Mg/m^3, vertical exaggeration 5:1). The coastline and the outline of the gabbro outcrop are indicated. The gabbro is thus interpreted as a laccolith approximately 4 km in diameter and 0.8 km thick. From Briden *et al.* (1982), by permission

observed and, if necessary, the model is adjusted by trial-and-error or by automatic iterative methods (e.g. non-linear optimisation (Al-Chalabi 1972)) until the differences between the computed and observed anomalies are reduced to an acceptable, statistically defined level. Better resolution is obtained by reducing the size and increasing the number of individual cubes within the model. By having a regular cube size, the computation is eased considerably. An example of the application of this technique is given in Figure 2.28, where gravity data from Guernsey, Channel Islands, have revealed that a gabbro body, which outcrops to the north-east of the island near St Peter Port, has the form of a laccolith 0.8 km thick and about 4 km in diameter (Briden *et al.* 1982).

2.6.3 Depth determinations

Of major importance in the interpretation of any gravity data is the determination of depth to the centre of mass and/or to the top of the body causing the anomaly. The maximum depth at which the top of any particular geological body can be situated is known as the *limiting depth*. Methods of obtaining this information depend on which interpretational technique and model are being used. Let us consider various *direct* or *forward* methods where the actual gravity anomaly data are used to derive depths and also estimates of anomalous masses of the features causing the anomalies.

The commonest rules of thumb concern the use of the half-width of the anomaly; that is, the half-width ($x_{1/2}$) of the anomaly where the amplitude is half the maximum value (see Figure 2.26). Some workers define the half-width as the entire width of the anomaly at half peak amplitude and the form of the depth and mass determination equations will differ accordingly. Whichever formulae are used, care should be taken when calculating the limiting depth. The causative body has finite size and its mass is not concentrated at its centre of mass, and thus any estimate of depth will be overestimated. Also, the method will only give an approximation of depth in cases where all the constituent components have the same sense of density contrast (i.e. all negative or all positive). These formulae will also not be effective for compact mineral bodies. Formulae for a selection of given geometric forms are given in Box 2.19A and an example of one calculation is given in Box 2.19B.

Several basic 'rules', known as the *Smith Rules* after their originator (Smith 1959, 1960), have become established in the calculation of limiting depths. Two rules (1 and 2 in Box 2.20) use a *gradient–amplitude ratio* method. Consider any geological body that gives an isolated gravity anomaly (Figure 2.30) entirely of either sign with a maximum gravity (Δg_{max}) that varies along the line of the profile and thus has a horizontal gradient which reaches a maximum value at $\Delta g'_{max}$. The Smith Rules describe the various relationships between

the limiting depth d to the top of any geological body and the maximum gravity (Δg_{max}) and its horizontal gradient ($\Delta g'_{max}$) as listed in Box 2.20.

Box 2.19A Depth estimates for given geometric forms

Form	Formula	Notes
Sphere	$z = 1.305x_{1/2}$	z is depth to centre of mass
	$d = z - r$	d is depth to top of sphere of radius r
		$r^3 = \lvert\Delta g_{max}\rvert z^2/(0.028\delta\rho)$ from Box 2.18
Horizontal cylinder	$z = x_{1/2}$	z is depth to cylinder axis
	$d = z - r$	d is depth to top of cylinder of radius r
		$r^2 = \lvert\Delta g_{max}\rvert z/(0.042\delta\rho)$ from Box 2.18
Vertical cylinder	$z = 1.732x_{1/2}$	z is depth to top end of cylinder (overestimates z)
Thin dipping sheet	$z \approx 0.7x_{1/2}$	z is depth to top of sheet
	$z \approx x_{1/2}$	When $z \approx$ dip length of sheet
		When $z \gg$ dip length of sheet
		When length of sheet is very large or sheet dips at less than 60°, *no solution is possible*
Thick prism	$z = 0.67x_{1/2}$	z is depth to prism top = prism width, and depth to prism base is twice width
	$z = 0.33x_{1/2}$	When depth to prism base is 10 times prism width
		In both cases, estimates of z are unreliable

Box 2.19B Example of calculation for a sphere

An air-filled cavity in rock of density 2.5 Mg/m^3 can be modelled by a sphere of radius r and depth to centre of mass, z (m). The resultant gravity anomaly is shown in Figure 2.29. Given $\Delta g_{max} = 0.048$ mGal, $x_{1/2} = 2.2$ m, and $\delta\rho = 2.5$ Mg/m^3:

$$z = 1.305 \times 2.2\,\text{m} = 2.87\,\text{m}.$$

Radius of sphere = r:

$$r^3 = 0.048 \times (2.87)^2/(0.0286 \times 2.5) = 5.53\,\text{m}^3.$$

continued

continued

So $r = 1.77$ m. Depth to top of sphere $d = 2.87 - 1.77 = 1.10$ m. *An air-filled cavity of this size so close to the surface could constitute a hazard*

Box 2.20 Smith Rules

(1) Where the entire anomaly has been isolated:

$$d \leqslant C.\ \Delta g_{max}/\Delta g'_{max}$$

where $C = 0.65$ for a 2-D body and $C = 0.86$ for a 3-D body.

(2) When only part of an anomaly is isolated, for any point x:

$$d \leqslant K\ \Delta g_x/\Delta g'_x$$

where $K = 1.00$ for a 2-D body and $K = 1.50$ for a 3-D body.

(3) For a maximum density contrast $\delta\rho_{max}$ and a maximum value of the second horizontal gradient ($\Delta g''_{max}$) (that is, the rate of change of $\Delta g'$ with x):

$$d \leqslant 5.4\ G\delta\rho_{max}/\Delta g''_{max}.$$

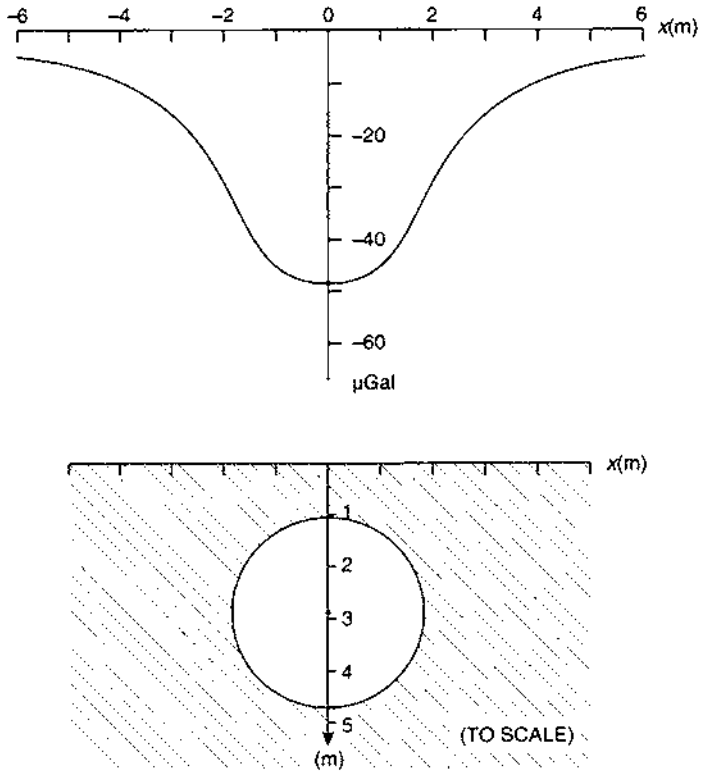

Figure 2.29 Gravity anomaly over an air-filled cavity of radius 1.77 m and 2.87 m depth to centre, in rock of density 2.5 Mg/m^3

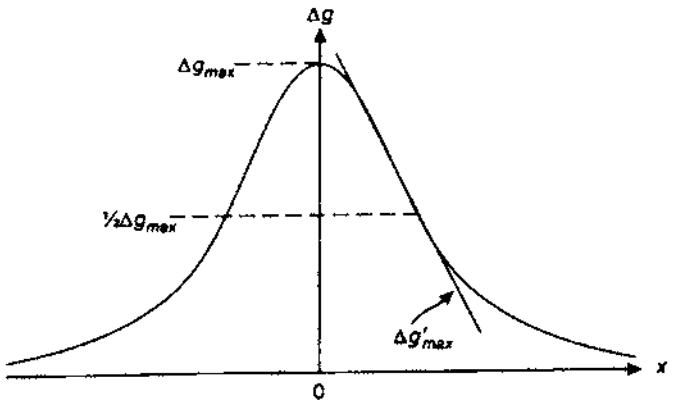

Figure 2.30 Limiting depth calculations: half-width method and gradient–amplitude ratio method (see text for details)

The third Smith Rule adopts a second-derivative method which uses the rate at which the gravity gradient changes along the profile. It is thought that second-derivative methods produce more accurate estimates of limiting depths. Second derivatives are discussed in more detail in Section 2.6.5.

2.6.4 Mass determination

Anomalous mass is the difference in mass between a geological feature and the host rock. There are two basic methods of calculating either an excess mass due to a high-density body or a mass deficiency caused by a body with a lower density.

The first method uses a rule of thumb based on the gravity anomaly half-width ($x_{1/2}$) and an assumption that the geological feature approximates to a given geometric form, such as a sphere (Box 2.21). The anomalous mass can be calculated by subtracting the mass due to a sphere (density times volume) from the mass estimated using gravity data. In the example below, the actual mass of an air-filled cavity is negligible, so the mass deficiency calculated is the mass of the missing rock.

Box 2.21 Mass of a sphere

Total mass $M \approx 255\ \Delta g_{max} (x_{1/2})^2$ tonnes

where Δg_{max} is in mGal and $x_{1/2}$ in metres.

Example
For an air-filled cavity described in Box 2.19B, the total mass deficiency of the sphere is equal to the mass of the rock that

continued

continued

would have been in the cavity, times its density (2.5 Mg/m^3):

Mass = density × volume = $2.5 \times (4/3)\pi\ 1.77^3 = 58$ tonnes.

Using the gravity data:

$$\text{Mass} \approx 255 \times 0.048 \times 2.2^2 = 59 \text{ tonnes.}$$

The second method is based on Gauss's Theorem in potential theory (Grant and West 1965) and is particularly important for two reasons. First, the total anomalous mass of a geological feature can be calculated from the associated gravity anomaly without any assumptions being necessary about the body's shape or size. Secondly, the total anomalous mass can be very important in the determination of tonnage of ore minerals (Hammer, 1945). For this method to work effectively, it is important that the regional gravity field be removed and that the entire residual anomaly be isolated clearly. The survey area is divided into a series of rings each of which is further divided into segments of area δA. The gravity effect of each segment is determined and the total for each ring is obtained and summed together (Box 2.22). Having determined the excess mass, it is then a simple matter to calculate the actual mass (M) if the densities of the host rock (ρ_0) and the anomalous body (ρ_1) are known.

Box 2.22

(1) Total anomalous mass (M_E):

$$M_E = 23.9\Sigma(\Delta g \delta A) \text{ tonnes}$$

where Δg is in mGal and δA in metres.

(2) Actual mass of a geological body (M):

$$M = M_E \frac{\rho_1}{(\rho_1 - \rho_0)} \text{ tonnes } (\rho_1 > \rho_0).$$

Parasnis (1966) gives an example where the total anomalous mass of the Udden sulphide orebody in northern Sweden was calculated to be 568 820 tonnes. Assuming the densities of the ore and host rock to be 3.38 and 2.70 Mg/m^3 respectively, the actual mass of the ore was found to be 2.83 million tonnes, a value consistent with drillhole estimates.

2.6.5 Second derivatives

2.6.5.1 Second vertical derivative (SVD) maps

One of the problems inherent within the interpretation of Bouguer anomaly maps is that it is difficult to resolve the effects of shallow structures from those due to deeper seated ones. The removal of the effect of the regional field from the Bouguer anomaly data results in an indeterminate and non-unique set of residuals. It is possible to separate the probable effects of shallow and deeper structures by using second vertical derivatives.

The gravity field (g) which is measured by gravimeters varies with height; that is, there is a vertical gradient ($\delta g/\delta z = g'$). Over a non-uniform earth in which density varies laterally, the vertical gradient changes and the *rate* of change ($\delta g'/\delta z$) is thus the second vertical derivative of the gravity field ($\delta^2 g/\delta z^2$. This quantity is very sensitive to the effects of shallow features (and to the effects of noise and topography).

As an illustration of how the gravity effects of shallow and deep structures can be separated, consider two equal point masses (m) at two different depths, say at depths of 1 unit and 4 units. The value of g for a point mass at a depth z is simply equal to the product of the gravitational constant (G) and the mass divided by the depth z squared, so $g = Gm/z^2$). If this is differentiated twice with respect to z, it becomes $g'' = 6Gm/z^4$. This tells us that the second derivative of the two masses, g'', is inversely proportional to z^4. Hence the ratio of the two derivatives will be, for $z_1 = 1$ and $z_4 = 4$, $g''_1/g''_4 = 256$.

It is possible to compute and plot maps of the second vertical derivative of Bouguer anomaly data. The zero-contour should indicate the edges of local geological features. The contours have units where 10^{-6} mGal/cm$^2 \equiv 10^{-9}$ cm^{-1} s$^{-2} \equiv 1$ E cm^{-1}. (E stands for an Eötvös unit = 10^{-6} mGal/cm, which is a measure of gravitational gradient.)

It should be emphasised that it is not possible to undertake any quantitative analyses of SVD maps except to produce characteristic profiles over known geometric forms. The main advantage of SVD maps is to highlight and clarify features spatially, as can be seen from Figures 2.31 and 2.32. In the first of these, the Bouguer anomaly map appears to have a consistent trend in the direction of the gravity gradient (increasingly positive to the east) with isogals aligned in a NW–SE direction. There is no obvious major feature evident on the Bouguer anomaly map. In contrast, the SVD map shows a major ENE–WSW linear feature with three closures, and it has picked out the outline of the Cement field in Oklahoma extremely well. Figure 2.32 illustrates the case when a single Bouguer anomaly is really the envelope of several smaller anomalies. In this atypical and rather extreme case, several deep boreholes were drilled on the large minimum indicated on both the Bouguer and the residual anomaly maps;

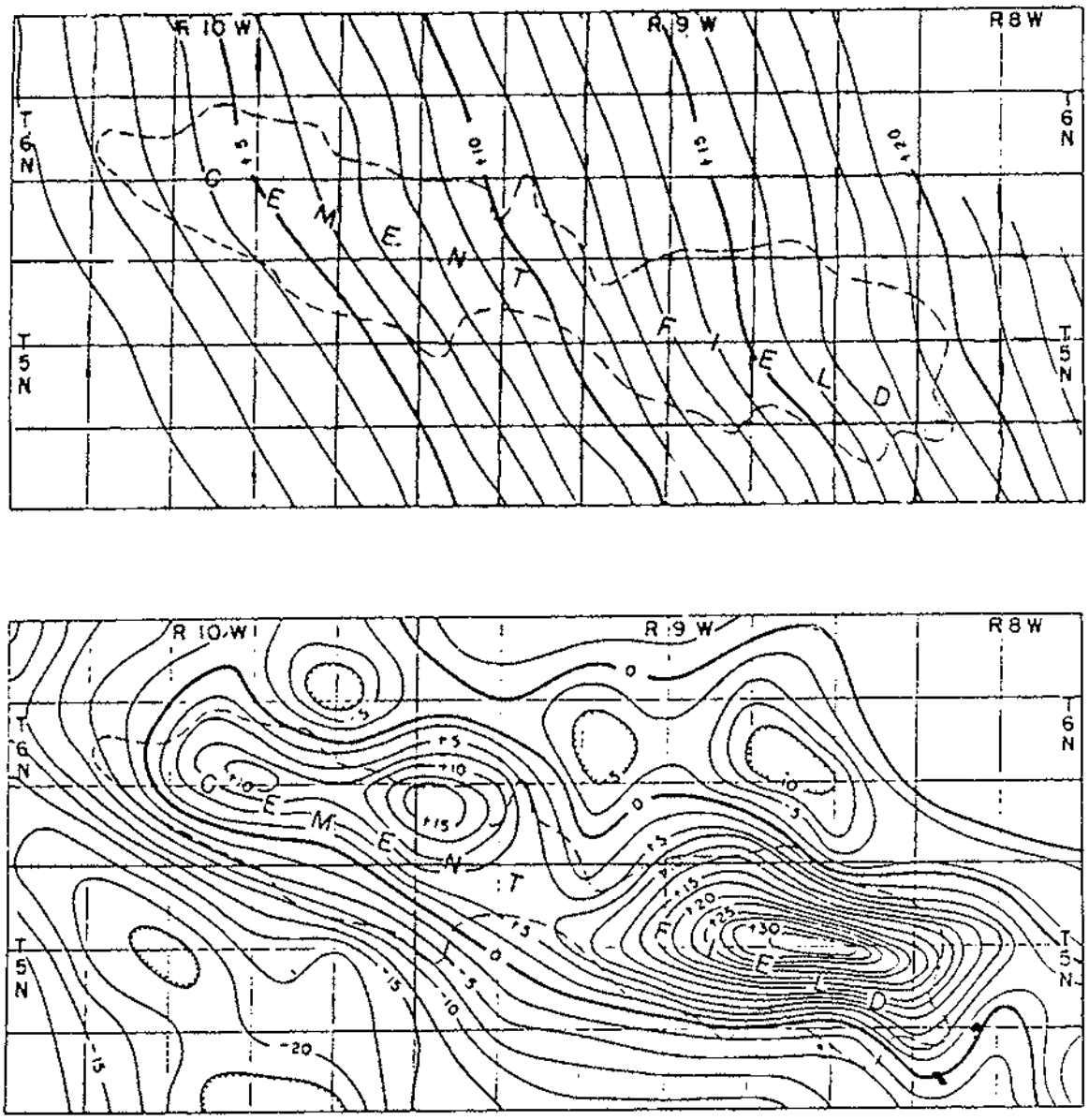

Figure 2.31 Observed Bouguer anomaly (contour interval 1 mGal) and second vertical derivative (contour interval 2.5×10^{-15} c.g.s.u.) maps over a Cement field in Oklahoma. From Elkins (1951), by permission

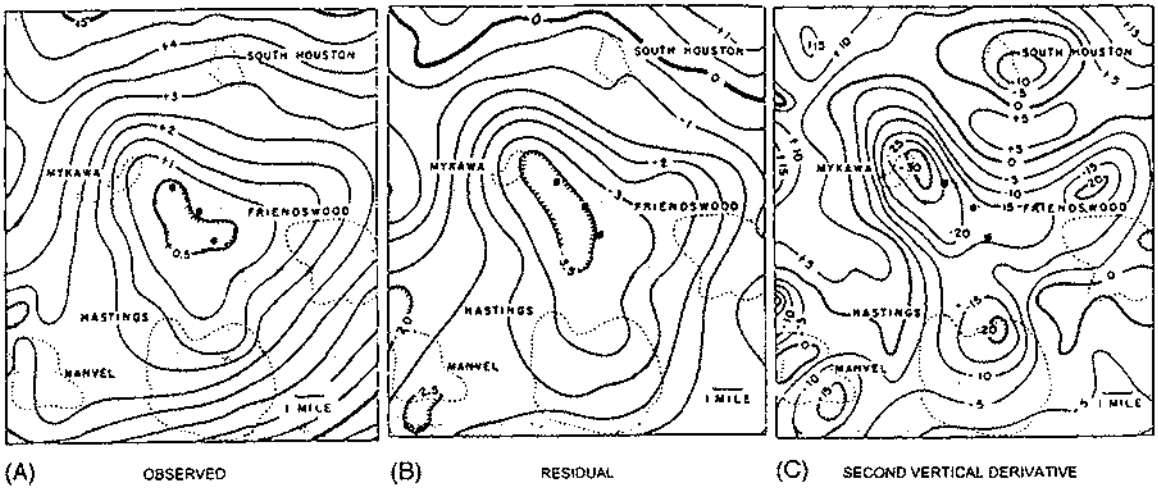

Figure 2.32 (A) Observed gravity, (B) residual gravity (contour interval 0.5 mGal), and (C) second vertical derivative (contour interval 5×10^{-15} c.g.s.u.) maps for Mykawa, Texas Gulf Coast. • indicate dry boreholes. From Elkins (1951), by permission

they were found to be dry, having missed the appropriate target, presumed to be a single salt dome. In contrast, the SVD map highlights three salt domes accurately.

Unfortunately, SVD also amplifies noise and so can produce many second-derivative anomalies that are not related to geology. Consequently, in some cases, SVD analyses provide no real advantage over the Bouguer anomaly map. An example of where extraneous anomalies shroud the geologically related features is given in Figure 2.33. Although it is possible to see on the SVD map the two main features present on the Bouguer anomaly map of the J-jaure titaniferous iron-ore region in Sweden, the SVD map also has a number of small maxima and minima that are of no structural interest. To resolve which anomalies are of geological importance, it is necessary to go back to the original gravity map and to any other source of geological information. It may even be prudent to refer back to the raw observations and corrections.

2.6.5.2 *Downward and upward continuation*

The effect on gravity of a geological mass at considerable depth is far less than if it were close to the surface (see Figure 2.24). the *principle of continuation* is the mathematical projection of potential field data (gravity or magnetic) from one datum vertically upwards or downwards to another datum. Effectively, the continuation process simulates the residual Bouguer anomaly at levels below or above sea level as if the gravity data had been obtained at those levels.

Upward continuation is relatively straightforward as the projection is usually into free space. Upward continuation serves to filter out the shorter-wavelength anomalies and reduce their amplitudes and decrease noise.

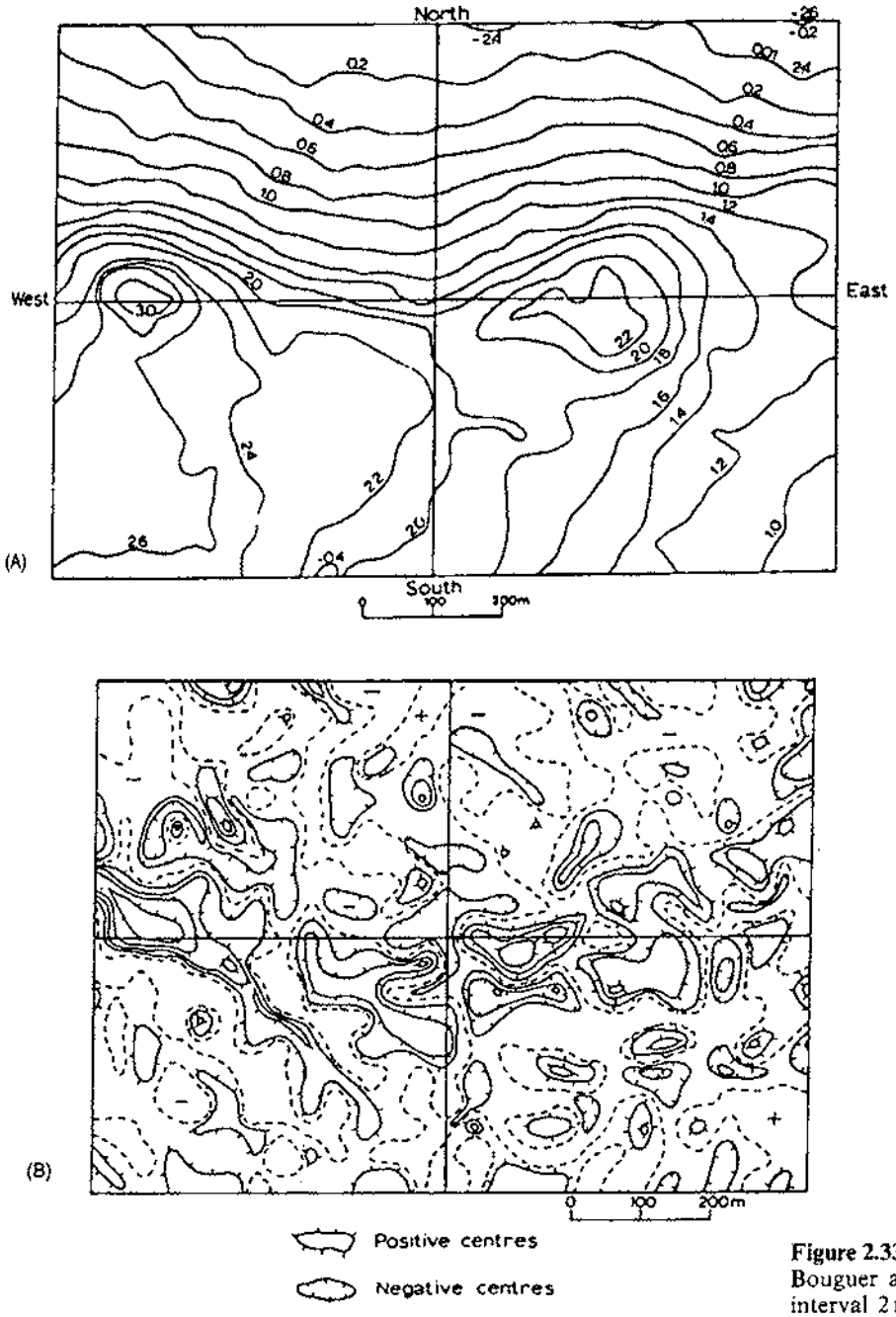

Figure 2.33 An example where the Bouguer anomaly map (A) (contour interval 2 mGal) exhibits more detail than the corresponding second vertical derivative map (B) for the J-jaure titaniferous iron-ore region in Sweden. Contours: 0 (dashed), ± 0.1, ± 0.2, ± 0.4 in units of 0.0025 mGal/m^2). From Parasnis (1966), by permission

Downward continuation is far more problematical as there is an inherent uncertainty in the position and size of the geological features as represented by the Bouguer gravity data. Furthermore, downward continuation aims to reduce each anomaly's wavelength and increase its amplitude. This mathematical amplification will also work on noise within the data and the resultant information may prove unsuitable for further analysis.

Continuation also forms a method of gravitational stripping (Hammer, 1963) where the gravity effects of upper layers are necessarily removed to reveal the anomalies due to deeper seated geological structures (e.g. Hermes 1986; Abdoh *et al.* 1990). The method uses the concept of an equivalent stratum (Grant and West, 1965). The Bouguer gravity field is continued downwards to a level that corresponds to a previously identified interface, such as from seismic reflection surveys, and an equivalent topographic surface is constructed at that level. This equivalent stratum should account for any residual anomalies at the surface arising from the interface. Continuation is discussed in much more detail by Grant and West (1965) and by Telford *et al.* (1990).

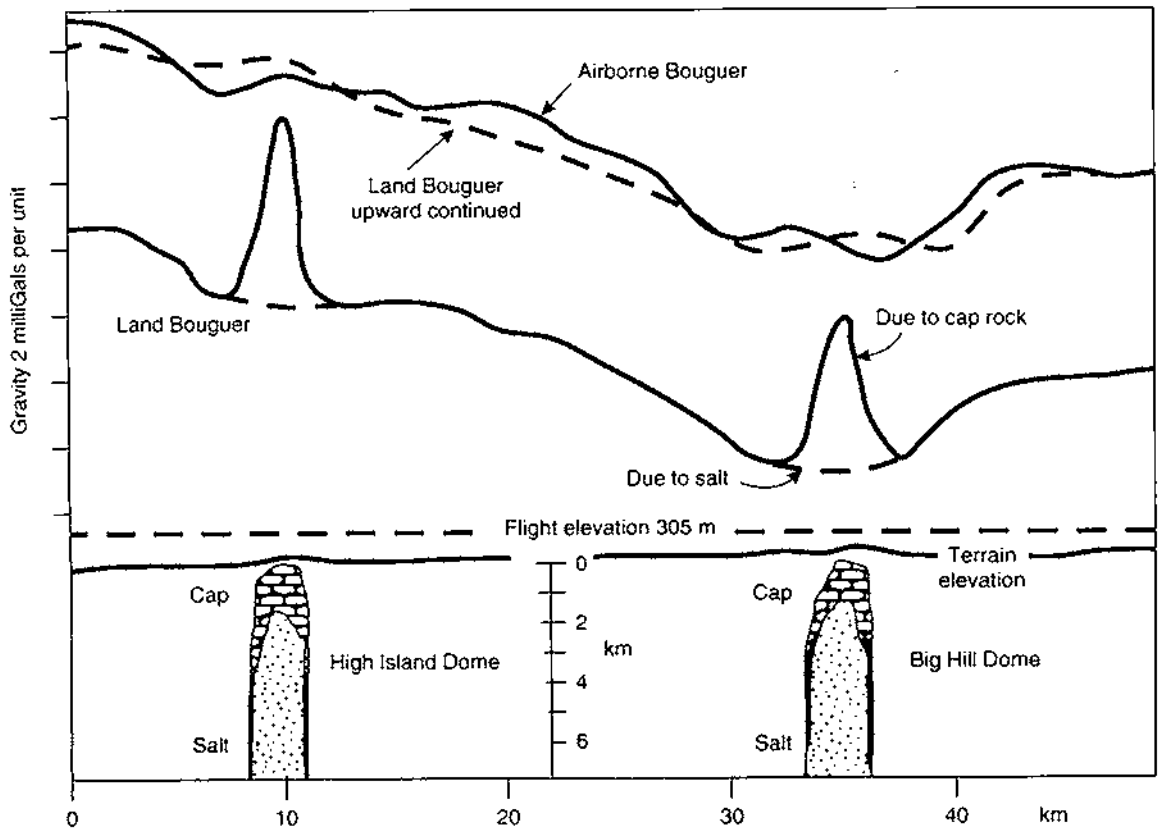

Figure 2.34 Comparison of airborne and upward continued land Bouguer gravity data with those obtained by airborne gravity surveying. From Hammer (1984), by permission

Upward continuation is used in comparisons of ground-based gravity anomalies with airborne data. It is usual to continue ground data upwards rather than to work downwards so as not to amplify noise. An example of such a comparison is shown in Figure 2.34 (Hammer 1982, 1984). Two gravity minima associated with low-density salt have shorter-wavelength maxima superimposed which are due to the high-density cap rocks. These maxima attenuate with increased elevation and the agreement between the upwardly continued land Bouguer data and the airborne is better than 5 g.u. except in the immediate vicinity of the cap rocks.

One of the major considerations in the interpretation of particularly regional gravity data is the amount of computer processing required. Considerable effort has been expended in developing computer-based methods of data enhancement. For example, image processing of data on computer-compatible tapes (CCTs) permits considerable manipulation of the data for display purposes to aid analysis and interpretation. Processes include edge enhancement to highlight lineaments (e.g. Thurston and Brown 1994), amplitude displays and spectral modelling (Figure 2.35). It is usually only economically viable to undertake such sophisticated processing on very large data sets.

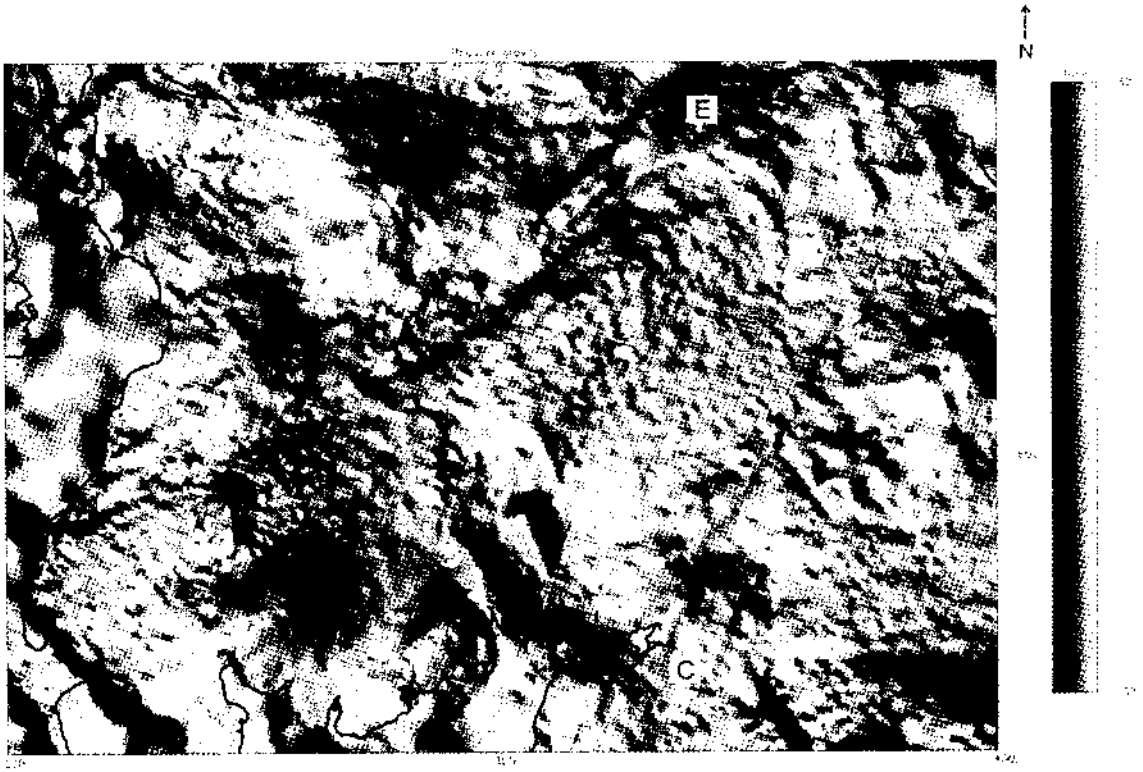

Figure 2.35 Structural analysis, based on lineations from a series of colour and greyscale shaped-relief images of geophysical data can provide a basis for reassessment of regional structure, mineralisation potential and fracture patterns. This image is of observed regional Bouguer gravity data, over an area of 200 km × 140 km of the Southern Uplands, Scotland (C: Carlisle; E: Edinburgh). The data have been reduced to Ordnance Datum using a density of 2.7 Mg/m^3, interpolated to a square grid of mesh size 0.5 km and displayed as a greyscale shaded-relief image. Sun illumination azimuth and inclination are NE and 45° respectively. A series of NE trending features parallel to the regional strike and the Southern Uplands fault have been suppressed by the NE illumination, whereas subtle NW trending features linked to development of the Permian basins are enhanced and seen to be more extensive. For comparison, see Figure 3.48. Image courtesy of Regional Geophysics Group, British Geological Survey

2.6.6 Sedimentary basin or granite pluton?

It is very important in the interpretation of gravity data for hydrocarbon exploration to be able to distinguish between a sedimentary basin (a good possible hydrocarbon prospect) and a granitic pluton (no prospect for hydrocarbons), as both can produce negative gravity anomalies of comparable magnitude.

For example, Arkell (1933) interpreted a minimum in an initial Bouguer gravity survey in the Moray Firth, north-east Scotland, as being due to a granite pluton. It was only after further geological work (Collette, 1958) and gravity work (Sunderland, 1972) that it was realised that the minimum was due to a sedimentary basin. Simultaneously, the Institute of Geological Sciences undertook seismic reflection surveys and initiated some shallow drilling. It was not until 1978 that the Beatrice Field was discovered (McQuillin *et al.* 1984). Had the 1933 interpretation been different, the history of the development of the North Sea as a major hydrocarbon province might have been very different.

In 1962, Bott proposed a set of criteria to distinguish between a sedimentary basin and a granite boss as interpretations of gravity minima. His argument was based on the second vertical derivative of the gravity anomaly due to a semi-infinite two-dimensional horizontal slab with a sloping edge. He found that the ratio of the moduli of the maximum and minimum second vertical derivative ($|g''_{max}|/|g''_{min}|$) provides a means of distinguishing between the two geological structures, as outlined in Box 2.23 and illustrated in Figure 2.36. McCann and Till (1974) have described how the method can be computerised, and the application of Fourier analysis to Bott's method. Some authors calculate the second *horizontal* derivative ($\delta^2 g/\delta x^2$) (e.g. Kearey and Brooks 1991; figure 6.19) which responds in exactly the same way as the *vertical* derivative except that the maxima and minima are reversed, as are the criteria in Box 2.23. In order for the method to work, the gravity anomaly attributed to the appropriate geological feature (sedimentary basin or granitic pluton) needs to be clearly isolated from adjacent anomalies due to other features. The method is not applicable, however, in cases where extensive tectonic activity has deformed either a sedimentary basin by basin-shortening or a granitic pluton by complex faulting, thereby changing the gradients of the flanks of both types of model.

Box 2.23 Bott criteria (see also Figure 2.36)

(1) For a sedimentary basin:

$$|g''_{max}|/|g''_{min}| > 1.0.$$

Basin sides slope *inwards*.

continued

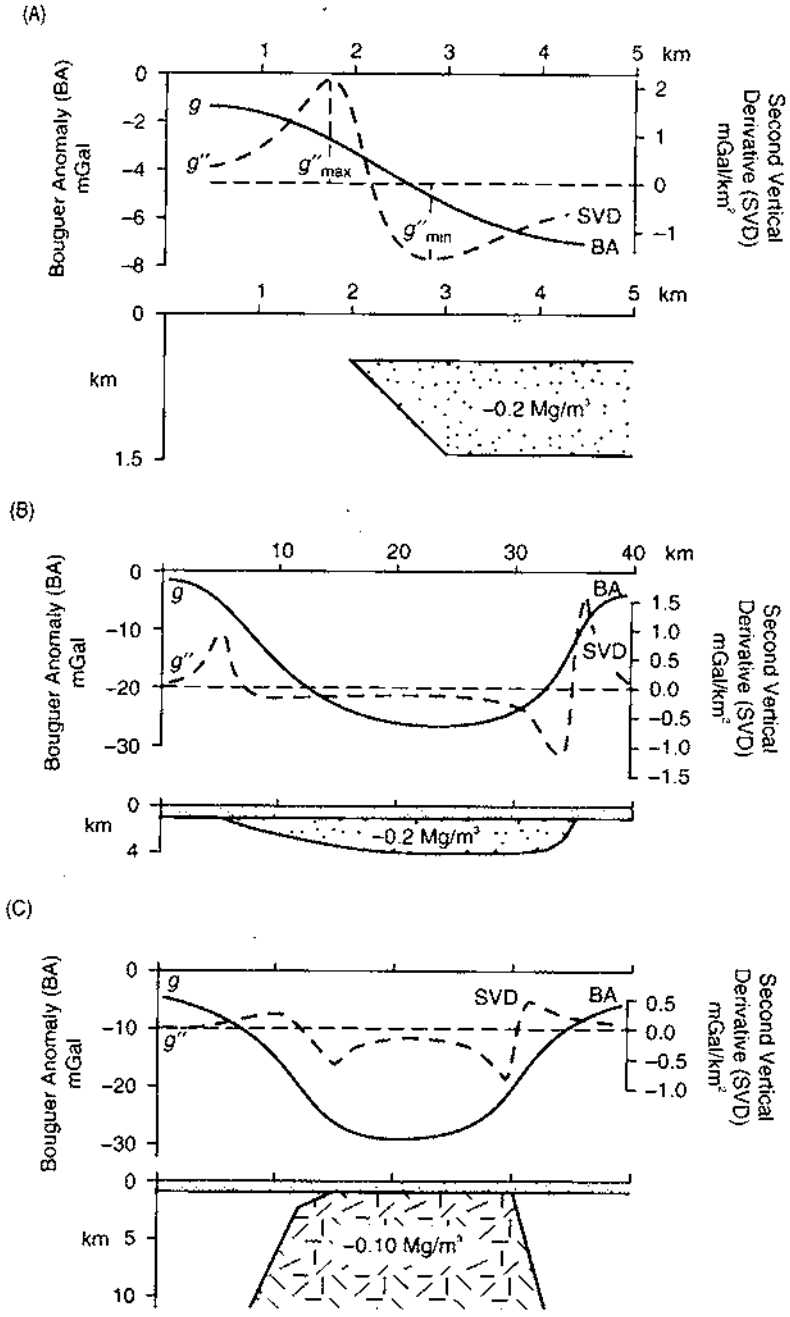

Figure 2.36 Bott criteria to distinguish between the Bouguer gravity profile over (A) a horizontal prism, (B) a sedimentary basin, and (C) a granitic pluton. After Bott (1962), by permission

continued

(2) For a granite pluton:

$$|g''_{max}|/|g''_{min}| \leq 1.0.$$

Granite pluton sides slope *outwards*.

The vertical variation of density of sediments with depth in a sedimentary basin can be represented in a number of ways. Moving away from Bott's uniform density model, consideration of the variation in density in terms of exponential and hyperbolic density contrast has been given by Rao *et al.* (1993) and Rao *et al.* (1994), for example.

2.7 APPLICATIONS AND CASE HISTORIES

In this section, a limited number of case histories are described to illustrate the diversity of applications to which the gravity method can be put. Other geophysical methods are discussed as appropriate, where they have been used in conjunction with, or to contrast with, the gravity results. These other methods are explained in their respective chapters.

2.7.1 Exploration of salt domes

2.7.1.1 Mors salt dome, Denmark (waste disposal)

An original interpretation of the Bouguer anomaly (Figure 2.37) over the Mors salt dome in northern Jutland was made in 1974, five years before any seismic results were known (Sharma, 1986). The investigation was connected to a feasibility study for the safe disposal of radioactive waste in the salt dome, but the methodology is identical had the study been for hydrocarbons.

The salt dome was approximated by a sphere. The values of $\Delta g_{max} \approx 16$ mGal and the half-width ≈ 3.7 km were obtained from profiles across the feature (Figure 2.38A) used to determine the depth to the centre of mass ($z = 4.8$ km). In order to calculate the depth to the top of the sphere, an estimate of the density contrast of the salt with the surrounding material had to be made. For a density contrast ($\delta\rho$) of -0.25 Mg/m^3, this gave the radius of the sphere as 3.8 km and thus depth to the top of the sphere is about 1 km (4.8 km minus 3.8 km); with $\delta\rho = -0.2$ Mg/m^3, the radius is 4.1 km and depth to the top is 0.7 km (4.8 km -4.1 km). This was later found to be in good agreement with the seismic results (Figure 2.38B). If the salt dome approximated to a vertical cylinder of length 5300 m, depth to top 700 m, and radius 4400 m, and density contrast -0.2 Mg/m^3, the expected value of Δg_{max} is around 19 mGal, compared with an observed value of 16–18 mGal; but this is still close enough to be a reasonable approximation to the actual shape.

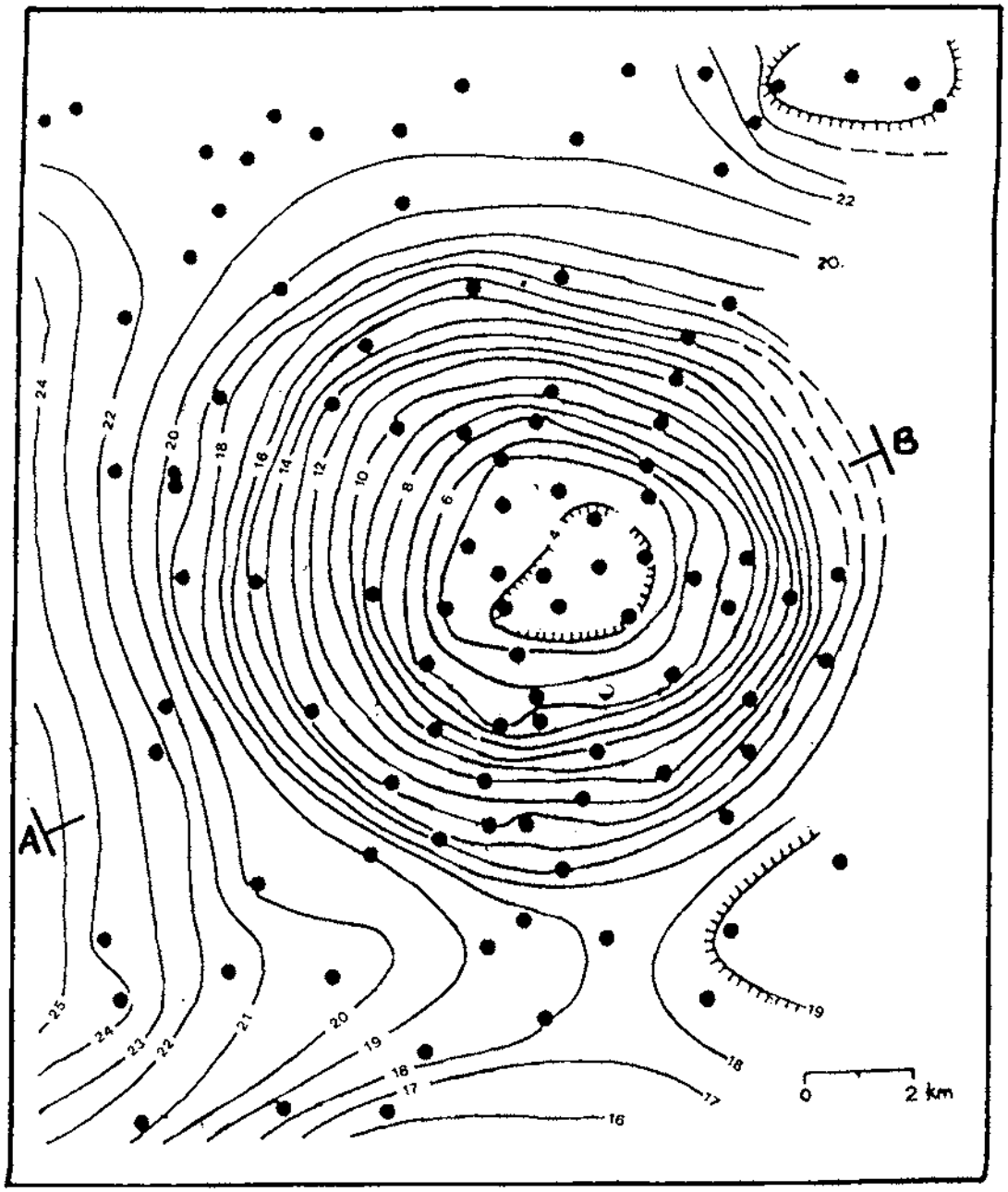

Figure 2.37 Bouguer anomaly map of the Mors salt dome, Jutland, Denmark. Solid dots represent observation points. Contour interval = 1 mGal. From Saxov (1956) and Sharma (1986). by permission

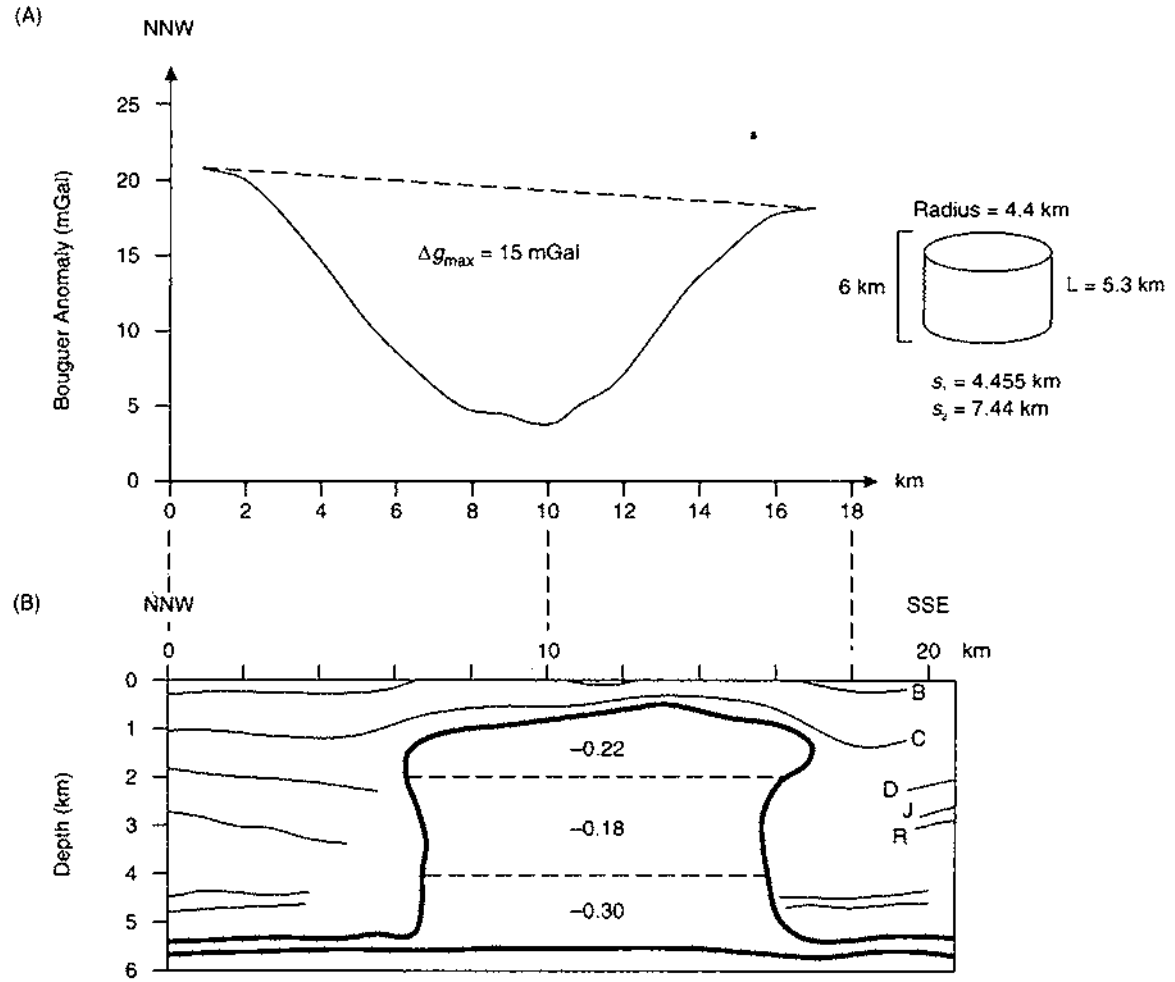

Figure 2.38 (A) Bouguer anomaly profile and (B) corresponding seismic section across profile A B in Figure 2.37. After Kreitz (1982), LaFehr (1982) and Sharma (1986), by permission

Uncertainty in the density contrast is the biggest problem in interpretation. Subsequent drilling into the salt dome and the use of the seismic profiles undertaken radially across the salt dome enabled the geological model to be enhanced. It was found that the density contrast within the salt dome could be divided into three sections with slightly different density contrasts (Figure 2.38B). The seismic sections did not give a very good image of the top of the salt dome, which is mushroom-shaped and so causes the slight discrepancies between the sphere and vertical cylinder approximations. The combined use of seismic data and gravity modelling has resulted in a much more realistic geological model.

However, it should always be remembered that any geophysical model is only a crude approximation of what can be a very complex geological structure. Consider how well (or otherwise) a vertical cylinder

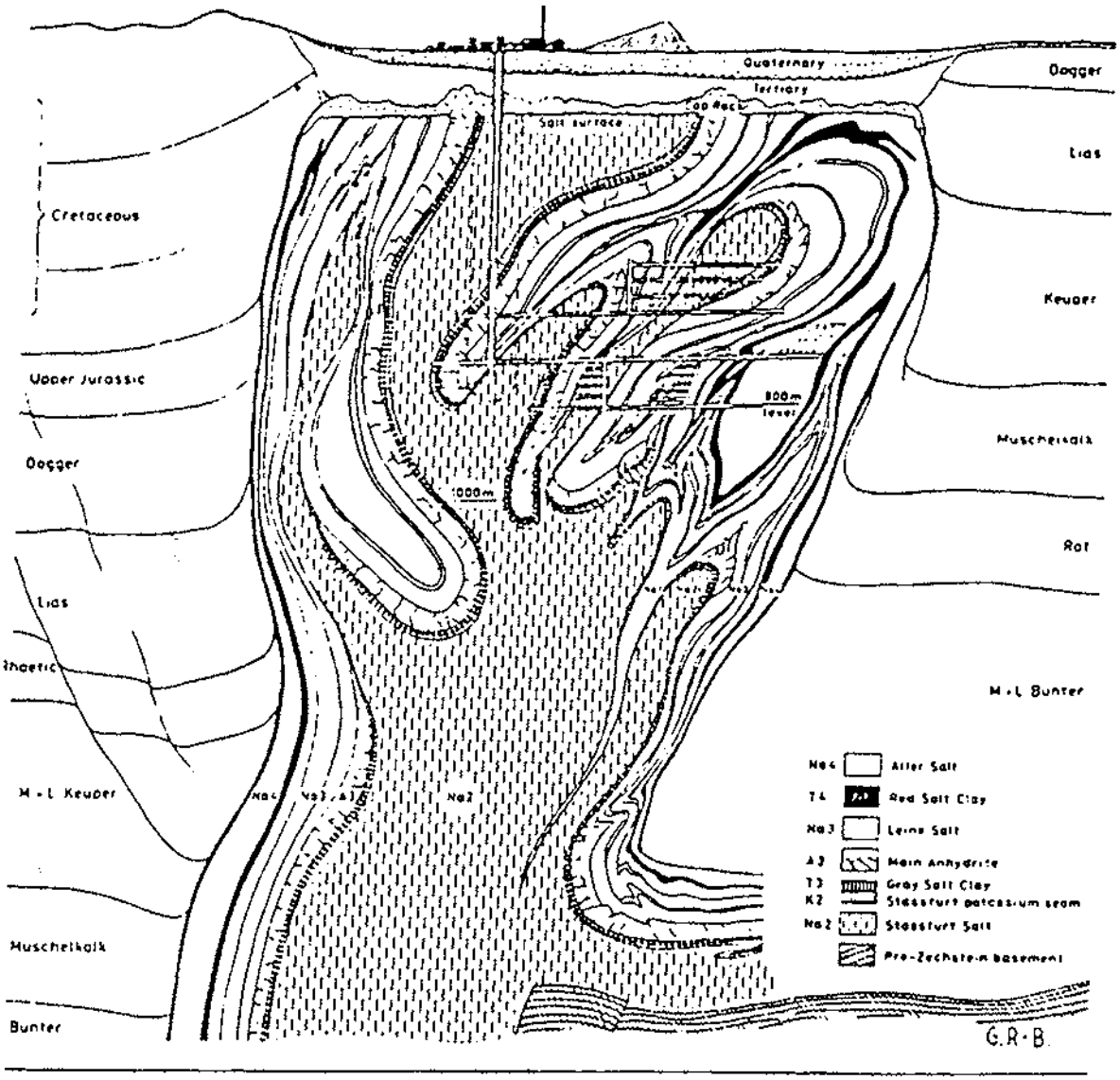

model would represent the salt dome illustrated in Figure 2.39. It is clear that much fine geological detail would not be resolvable unambiguously by the interpretation of geophysical data (Sorgenfrei 1971; Richter-Bernburg 1982).

Figure 2.39 Schematic cross-section through a salt dome structure in north-west Germany, illustrating known complexities in contrast to the usual assumed geophysical model of a vertical cylinder with a uniform density distribution. From Sorgenfrei (1971) and Richter-Bernburg (1982), by permission

2.7.1.2 Salt domes in NW Germany (hydrocarbons)

Another example of gravity anomalies over salt domes is given in Figure 2.40, which is taken from part of a survey over north-west Germany (Hermes, 1986). The intention was to derive the gravity field

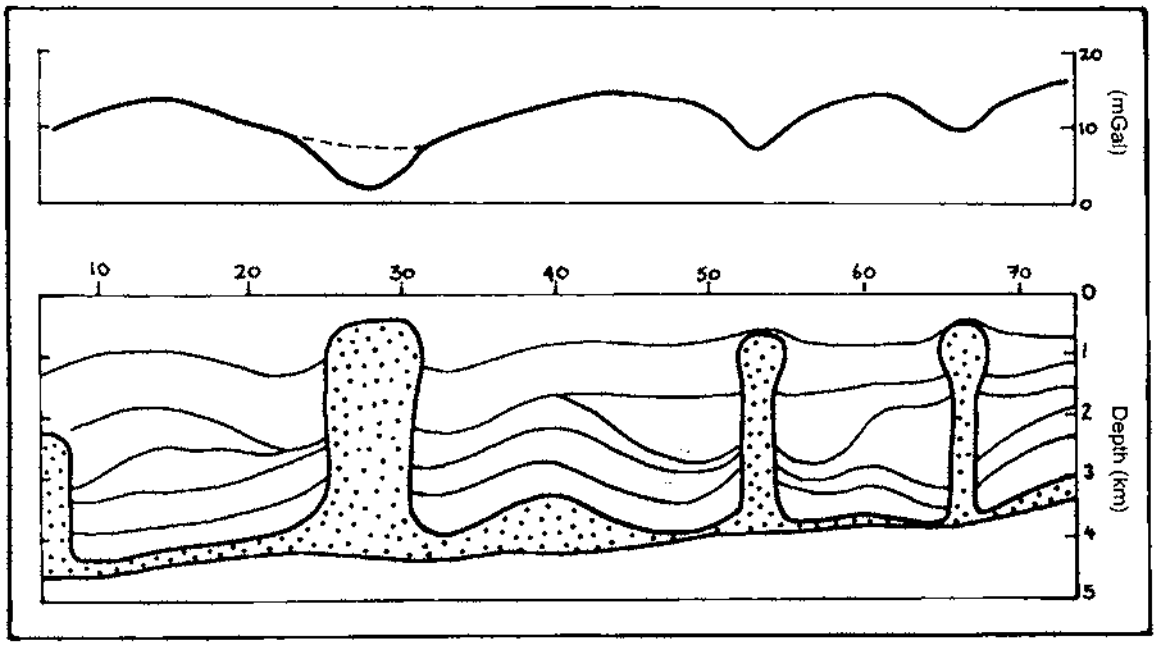

Figure 2.40 A typical Bouguer anomaly profile compared with the corresponding sub-surface geology associated with the Zechstein in northern Germany. From Hermes (1986), by permission

due to the pre-Zechstein and remove it, akin to gravity stripping, to be able to investigate what lies beneath it. Seismic reflection profiling has been singularly unsuccessful both in penetrating through this layer and in producing much useful information. The amplitudes of the Bouguer anomaly minima are clearly associated with the size of the salt domes, the smallest having the lowest amplitude (≈ 5 mGal). The largest minimum is a compound anomaly comprising a minimum associated with the syncline through which the low-density salt has risen. This emphasises the fact that the Bouguer anomaly map of this area is strongly influenced by the structures within the post-Zechstein and by the salt domes and walls. To determine the gravity effect of the pre-Zechstein it is thus essential that these effects be removed. Gravity stripping appears to succeed where filtering methods have been less successful.

2.7.2 Mineral exploration

Gravity surveys fulfil two roles in exploration for minerals: (1) for search and discovery of the ore body, and (2) as a secondary tool to delimit the ore body and to determine the tonnage of ore.

2.7.2.1 Discovery of the Faro lead–zinc deposit, Yukon

An integrated airborne and land geophysical exploration programme, of which gravity surveying was an integral part, led to the discovery of

the Faro lead–zinc deposit in the Yukon, northern Canada (Brock 1973). Gravity was found to be the best geophysical method to delimit the ore body (Figure 2.41). It was also used to obtain an estimate of the tonnage (44.7 million tonnes), which compared very well with a tonnage proven by drilling of 46.7 million tonnes (Tanner and Gibb 1979). In contrast, vertical magnetic mapping provided an anomaly with too shallow gradients to be used, as Figure 2.41 shows.

2.7.2.2 Pyramid ore body, North West Territories

The Pyramid lead–zinc ore body, at Pine Point in the North West Territories, Canada, was discovered using the 'induced polarisation' (IP) method (Seigel *et al.* 1968). For further details of IP, see Chapter 9. Gravity was used to optimise development drilling since the gravity anomalies (Figure 2.42) correlated extremely well with the distribution of the mineralisation within the ore body. Additionally, the gravity data were used successfully to estimate total ore tonnage. Electrical resistivity (see Chapter 7) produced low-amplitude anomalies with a broad correlation with the position of the ore body, and a TURAM electromagnetic survey (see Chapters 10 and 11) was singularly unsuccessful and produced virtually no anomaly at all. The induced polarisation chargeability produced a spectacular anomaly.

2.7.2.3 Sourton Tors, Dartmoor, SW England

This is an example of where gravity did not work at all in association with a known occurrence of mineralisation (Figure 2.43), whereas electrical, electromagnetic and magnetic methods all produced significant anomalies (Beer and Fenning 1976; Reynolds 1988). The reason for the failure of the gravity method in this case is twofold:

- The scale of mineralisation, which is a stockwork of mineralised veins, was of the order of only a few metres wide.
- The sensitivity of the gravimeter was insufficient to resolve the small density contrast between the sulphide mineralisation and the surrounding rocks.

Had a gravimeter capable of measuring anomalies of the order of tens of μGal, and the station interval been small enough, then the zone of mineralisation may have been detectable. At the time of the survey (1969), such sensitive gravimeters were not as widely available as they are today.

2.7.3 Glacier thickness determination

For a regional gravity survey to be complete in areas such as Antarctica and Greenland, measurements have to be made over ice

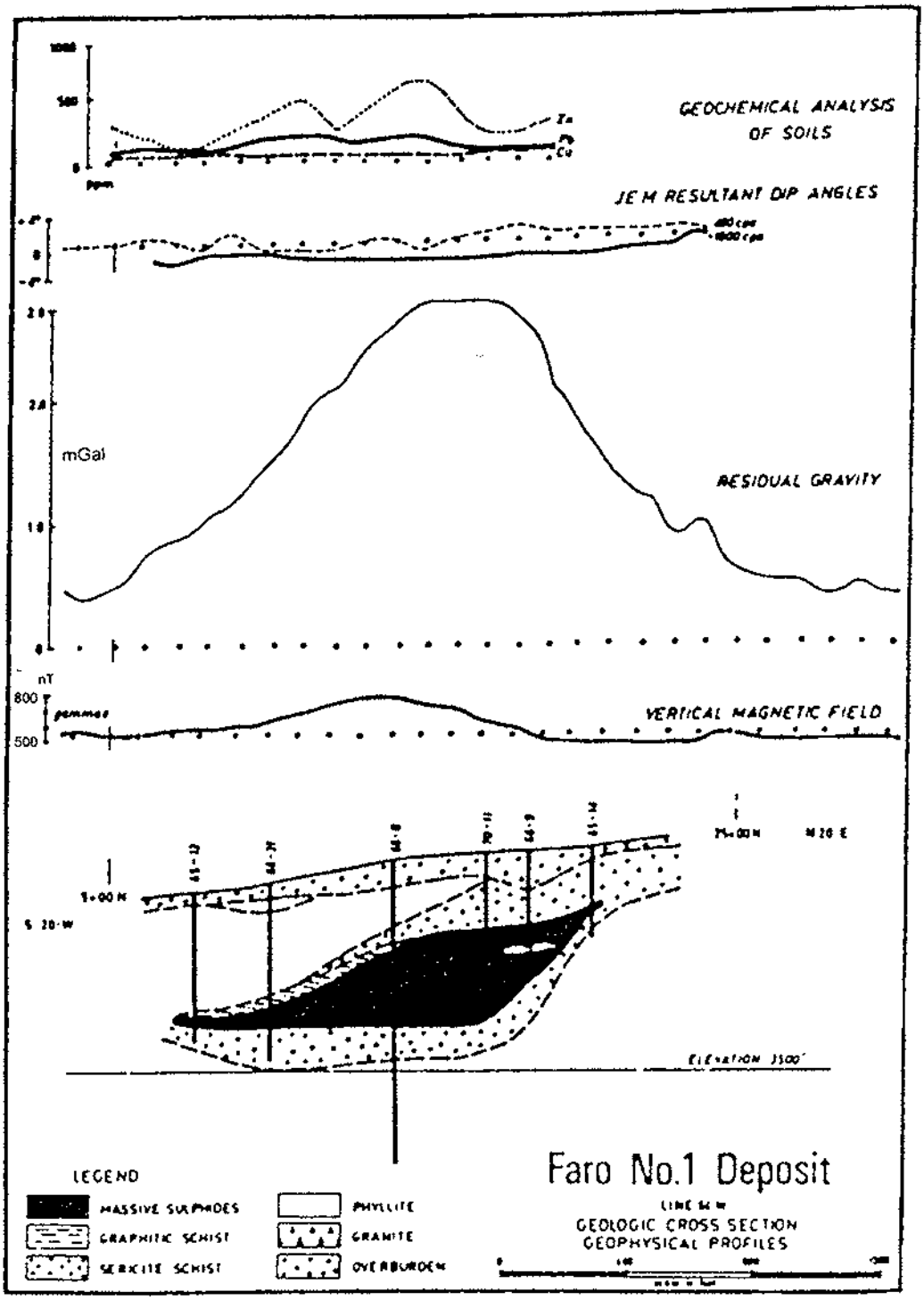
GEOCHEMICAL ANALYSIS OF SOILS
JEM RESULTANT DIP ANGLES
mGal
RESIDUAL GRAVITY
nT
VERTICAL MAGNETIC FIELD
ELEVATION 3500'
LEGEND
MASSIVE SULPHIDES
GRAPHITIC SCHIST
SERICITE SCHIST
PHYLLITE
GRANITE
OVERBURDEN
Faro No.1 Deposit
GEOLOGIC CROSS SECTION
GEOPHYSICAL PROFILES

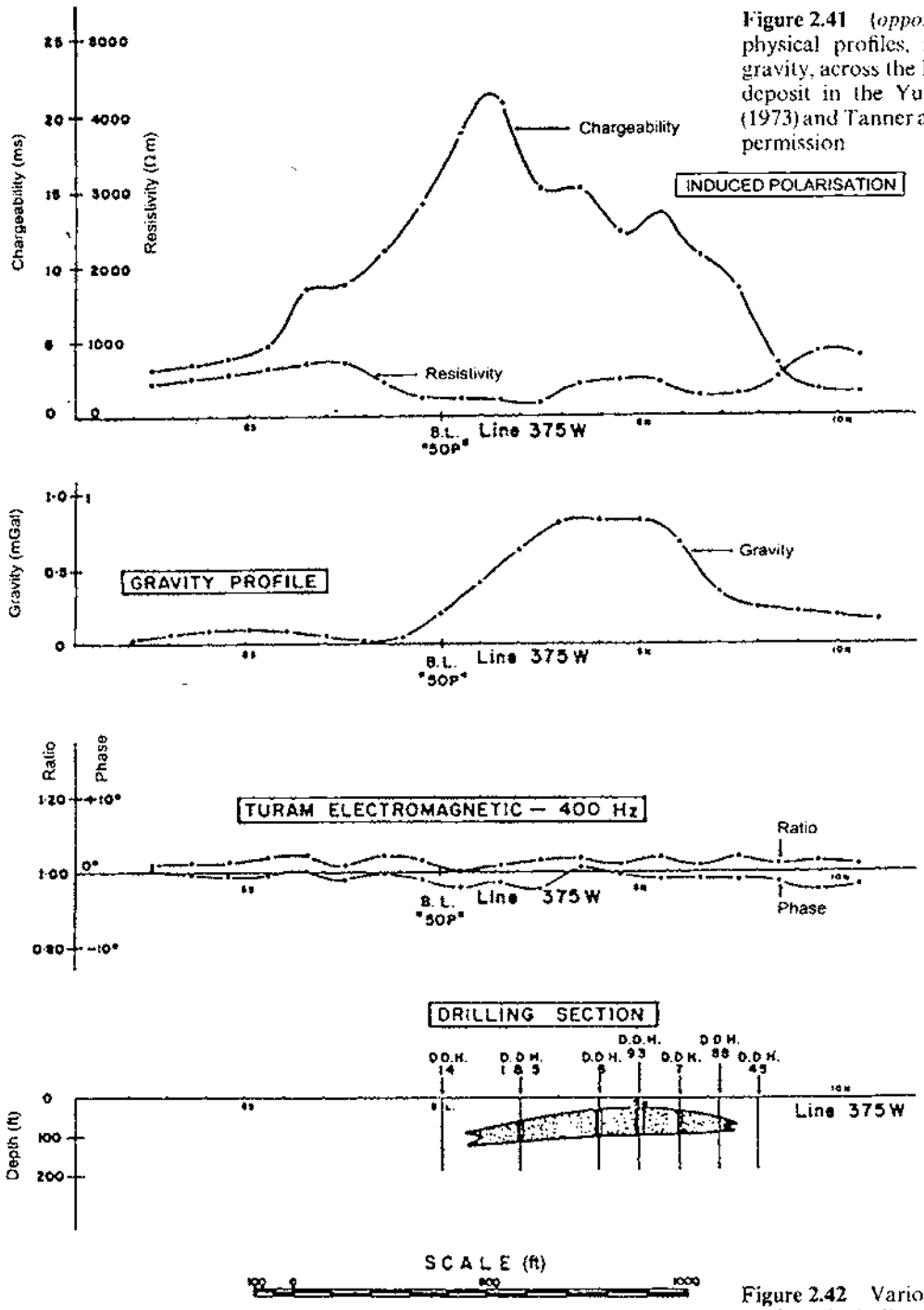

Figure 2.41 (*opposite*) Various geophysical profiles, including residual gravity, across the Faro lead–zinc ore deposit in the Yukon. From Brock (1973) and Tanner and Gibb (1979), by permission

Figure 2.42 Various geophysical profiles including residual gravity, across Pyramid no. 1 ore body. From Seigel *et al.* (1968), by permission

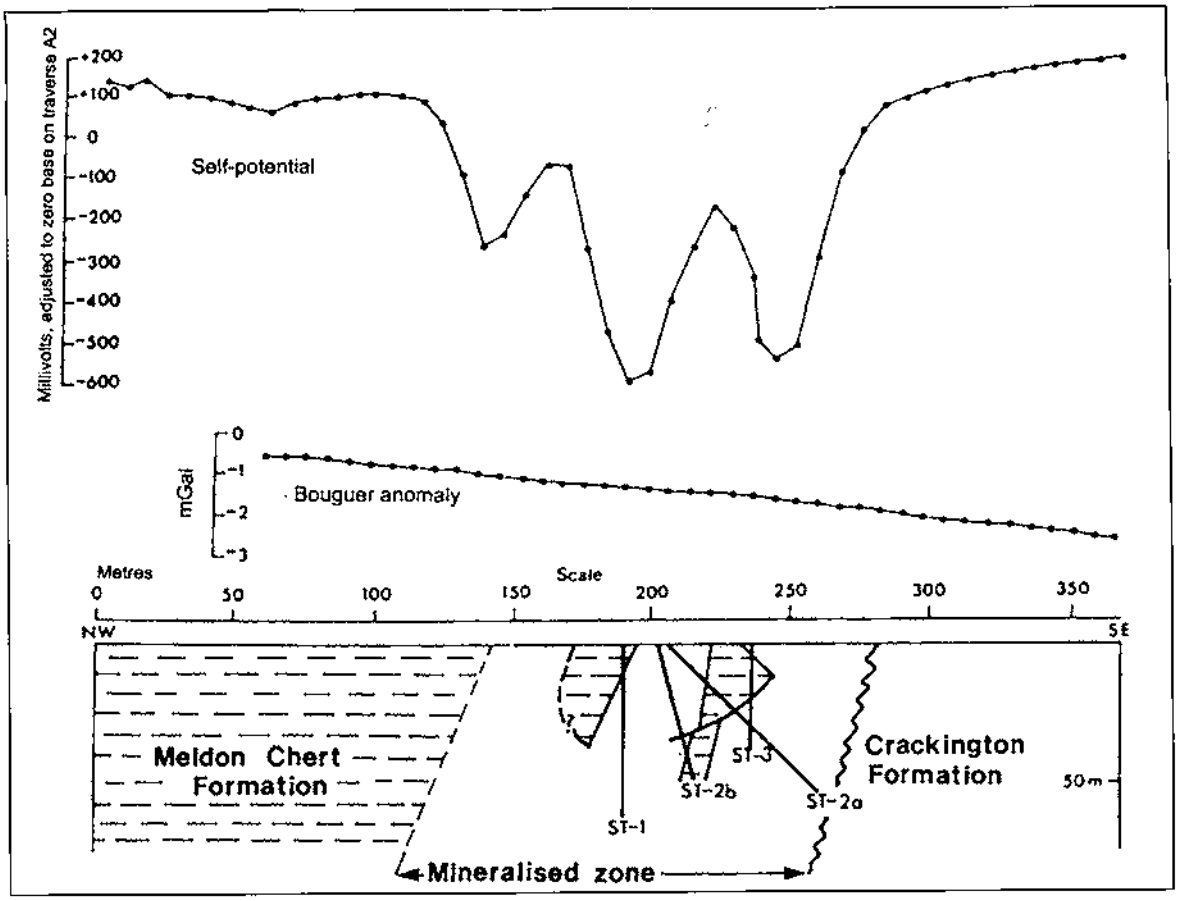

Figure 2.43 A Bouguer gravity profile across mineralised zones in chert at Sourton Tors, north-west Dartmoor, showing no discernible anomalies. From Beer and Fenning (1976), by permission

sheets and valley glaciers. Very often, these areas have incomplete information about the depth or volume of ice. The large density difference between ice (0.92 Mg/m^3) and the assumed average rock density (2.67 Mg/m^3) means that easily measured gravity anomalies can be observed and the bottom profile of the ice mass (i.e. the sub-glacial topography) can be computed.

An example of this has been given by Grant and West (1965) for the Salmon Glacier in British Columbia (Figure 2.44), in which a gravity survey was undertaken in order to ascertain the glacier's basal profile prior to excavating a road tunnel beneath it. A residual gravity anomaly minimum of almost 40 mGal was observed across the glacier, within an accuracy of ± 2 mGal due to only rough estimates having been made for the terrain correction. An initial estimate of local rock densities was 2.6 Mg/m^3 and the resultant depth profile across the glacier proved to be about 10% too deep (Figure 2.44B) compared with depths obtained by drilling. Considering the approxi-

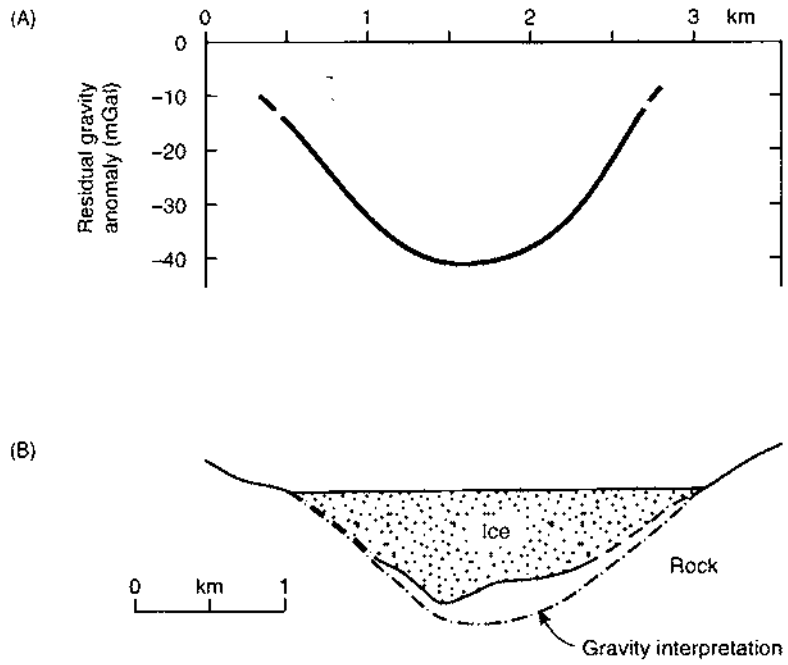

Figure 2.44 A residual gravity profile across Salmon Glacier, British Columbia, with the resulting ice thickness profile compared with that known from drilling. After Grant and West (1965), by permission

mations taken in the calculations, the agreement was considered to be fair. In addition, it was found that the average density of the adjacent rocks was slightly lower (2.55 Mg/m^3). This could have indicated that there was a significant thickness of low-density glacial sediments between the sole of the glacier and bedrock. However, had more detailed modelling been undertaken on data corrected fully for terrain, the discrepancy could have been reduced.

Increasingly, ice thickness measurements are being made by seismic reflection surveying (see Chapter 5), electromagnetic VLF measurements (see Chapter 9, Section 9.6.6.3) and radio echosounding (see Chapter 9, Section 9.7.4.2). Comparisons between the various geophysical methods indicate that agreements of ice thickness within 10% can be readily obtained. Gravity measurements over large ice sheets (e.g. Renner *et al.* 1985; Herrod and Garrett 1986) can be considerably less accurate than standard surveys for three reasons:

- The largest errors are due to the imprecise determination of surface elevations. Currently, heights can be determined to within 5–10 m.
- Inaccurate corrections for sub-ice topography vary by hundreds of metres, in areas without radio echosounding control. An error in estimated ice thickness/bedrock depth of 100 m can introduce an error of ± 74 g.u.
- As in all gravity surveys, the estimate of the Bouguer correction density is also of critical importance. Major ice sheets obscure the

local rock in all but a few locations, and the sub-ice geology, and its associated densities, may vary significantly.

Another glaciological application of the gravity method is the use of a gravimeter to measure oceanic tidal oscillations by the vertical movements of floating ice shelves in the Antarctic (Thiel *et al.* 1960; Stephenson 1984). The resulting tidal oscillation pattern can be analysed into the various tidal components and hence relate the mechanical behaviour of the ice shelf to ocean/tidal processes. If tidal oscillations are not found at particular locations, this may indicate that the ice shelf is grounded. Independent measurements with tilt meters, strain gauges and radio echosounding should be used to confirm such a conclusion (Stephenson and Doake 1982).

2.7.4 Engineering applications

The size of engineering site investigations is normally such that very shallow (<50 m) or small-scale (hundreds of square metres) geological problems are being targeted. Consequently, the resolution required for gravity measurements is of the order of μGals. The use of gravity is commonly to determine the extent of disturbed ground where other geophysical methods would fail to work because of particularly high levels of electrical or acoustic noise, or because of the presence of a large number of underground public utilities (Kick 1985). Additionally, gravity is used to assess the volume of anomalous ground, such as the size of underground cavities or of ice lenses in permafrost. There are often no records of where ancient quarrying or mining has been undertaken and the consequent voids may pose considerable hazards to people and to property. The increasing development of higher latitudes brings its own engineering problems, and the application of gravity surveying, amongst other applied geophysical methods, is playing a growing and important role in site investigations in these areas. Furthermore, it is also true to say that with the increased use of geophysical methods, the very geological phenomena under investigation are becoming better studied and better known.

2.7.4.1 Detection of back-filled quarries

Where there is sufficient density contrast between infill material and the surrounding rock, small-scale gravity surveys can be used successfully to locate backfilled quarries (Poster and Cope 1975), as the following example demonstrates.

A proposed new railway section in Newcastle-upon-Tyne, England, was routed through a built-up area which contained a number of backfilled, late-nineteenth century sandstone quarries. The design of the section of railway included a cut-and-cover tunnel, and so it was

extremely important to determine the position of the old quarry faces very accurately. The nature of the loose infill material (density 1.65 M_g/m^3) provided a strong contrast in physical properties with the local sandstone (of density 2.1 Mg/m^3) and a number of geophysical methods could have been employed. However, the site was criss-crossed by a large number of underground pipes and cables, and the superficial material contained significant amounts of scrap metal, all of which made it impractical to use electrical, electromagnetic or magnetic methods. High levels of acoustic noise which were generated by large volumes of traffic during the working day, and the lack of space due to extensive building cover, precluded the use of seismic methods. Consequently, the gravity method was selected and operated between the hours of midnight to 6 a.m., thus avoiding the problems of vibrations arising from both traffic and from heavy industrial plant, and ensuring better access through the reduction in the number of parked cars.

The contrast in density between the infill material and the local sandstone (0.5 Mg/m^3) produced small but detectable residual gravity anomalies of the order of 0.7 mGal. The gravity data were reduced and interpreted with the aid of data from one borehole and a preliminary archaeological investigation. A map of the residual gravity anomalies (Figure 2.45) clearly illustrates the locations of the faces of two quarries.

2.7.4.2 Detection of massive ice in permafrost terrain

The thawing of massive ice masses and associated ice-rich permafrost can cause severe engineering and environmental problems. The detection and identification of such ground phenomena is thus extremely important.

Kawasaki *et al.* (1983) provide an example of the use of gravity surveying to detect the presence and the volume of massive ice within an area of permafrost at Engineer Creek, near Fairbanks, Alaska, along the route of a proposed road cut. It is well known that large bodies of massive ice, such as occur within pingos, give rise to significant gravity anomalies (Mackay 1962; Rampton and Walcott 1974). Permafrost without discrete segregated ice has a density of about 1.6 Mg/m^3, compared with the density of solid ice (0.88 0.9 Mg/m^3) and with that of typical Alaskan soils (1.35–1.70 Mg/m^3) and should give rise to detectable residual gravity anomalies if measured with a sufficiently sensitive gravimeter.

Kawasaki and colleagues demonstrated that, although massive ice can be detected by correlation with the gravity minima along the profile shown in Figure 2.46, the measurements were also sensitive to variations of density within the schist bedrock.

The gravity method is considered an excellent tool for detailed investigation of construction sites where massive ice is suspected, but

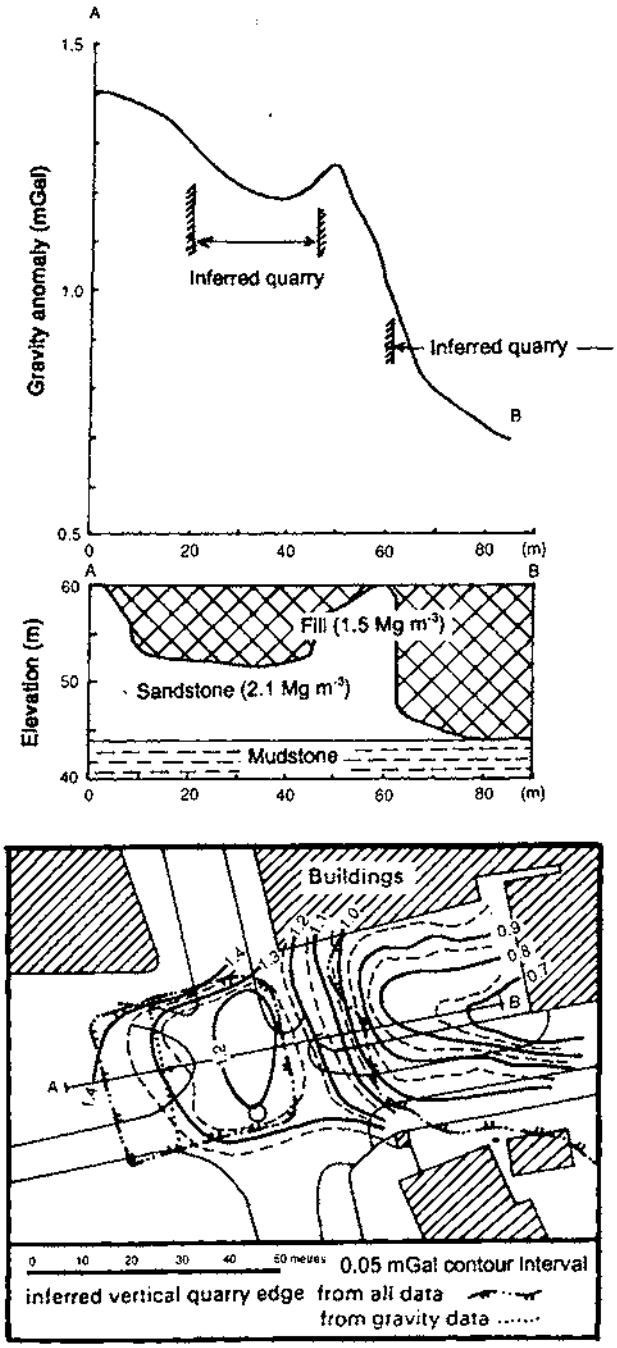

Figure 2.45 The top shows a residual gravity profile across infilled sandstone quarries in Newcastle-upon-Tyne. The cross-section and plan are also shown. After Poster and Cope (1975), by permission

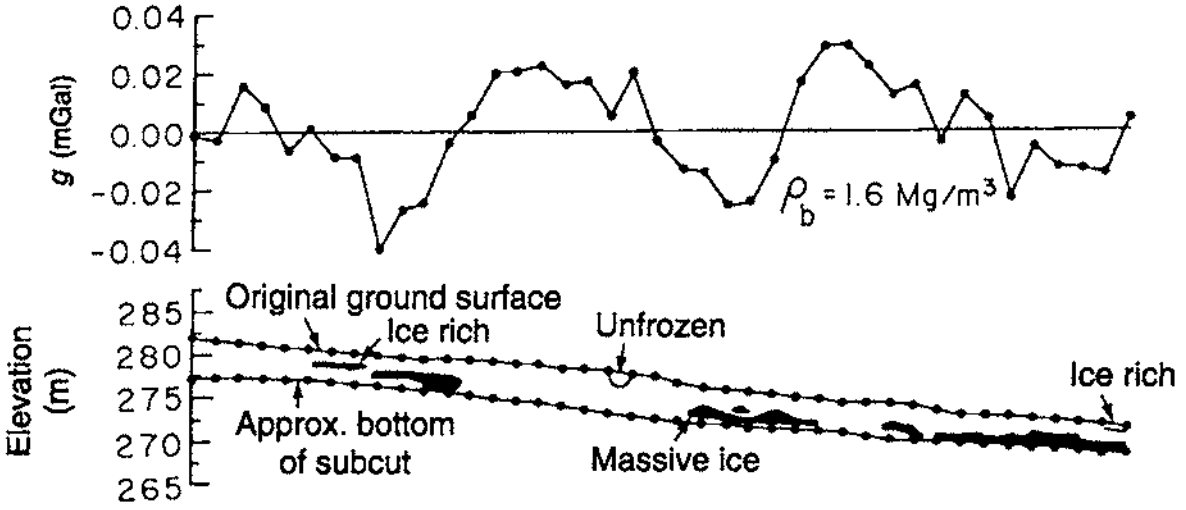

Figure 2.46 Gravity profile across massive ground ice in a road cut at Engineer Creek, near Fairbanks, Alaska. After Kawasaki *et al.* (1983), by permission

it is too slow a method for use as a reconnaissance tool over long profiles. Other geophysical methods such as electrical resistivity, electromagnetic ground conductivity and ground-penetrating radar are more efficient, particularly for reconnaissance (Osterkamp and Jurick 1980).

2.7.5 Detection of underground cavities

Hidden voids within the near-surface can become serious hazards if exposed unwittingly during excavation work, or if they become obvious by subsidence of the overlying ground (Figure 2.47). The detection of suspected cavities using gravity methods has been achieved in many engineering and hydrogeological surveys (e.g. Colley 1963). Gravimetry is increasingly of interest to archaeologists searching, for example, for ancient crypts or passages within Egyptian pyramids, such as has been achieved within the Kheops (see *First Break*, 1987 5(1): 3) with what is called 'endoscopic micro-gravity' (see also Lakshmanan 1991).

2.7.5.1 Hidden natural cavities

An example of the application of micro-gravimetry to the detection of underground cavities has been given by Fajklewicz (1986). Over many years he has investigated the gravity effect of both natural and man-made cavities and has helped to develop a method of detection based on calculating the vertical gradient of the gravity field. He has found that the amplitude of the gravity anomaly is commonly greater than that predicted (Figure 2.48) for reasons that are still not clear.

Figure 2.47 Catastrophic failure of the roof of an ancient flint mine in chalk in Norwich. Photo courtesy of Eastern Daily Press

A micro-gravity survey was carried out in the town of Inowrocław, Poland, where karst caverns occur to depths of around 40 m in gypsum, anhydrite, limestone and dolomite. The cavities develop towards the ground surface and have resulted in the damage and destruction of at least 40 buildings within the town. The density contrast between the cavity and the surrounding material in Figure 2.48A is $-1.8\ \mathrm{Mg/m^3}$ and for Figure 2.48B is $-1.0\ \mathrm{Mg/m^3}$, slightly lower due to the presence of rock breccia within the cavity. Fajklewicj has demonstrated that the cavity in Figure 2.48B should not have been detectable assuming that its gravity field is due entirely to a spherical cavity at the depth shown. Even the theoretical anomaly from the vertical gravity gradient is too broad to indicate the presence of a cavity, yet the observed anomaly is quite marked.

A similar approach can be taken using horizontal gravity gradients ($\Delta g/\Delta x$ or $\Delta g/\Delta y$), in which case the point at which the gravity anomaly reaches a minimum or maximum, the gradient goes through zero, and that point should lie over the centre of the body causing the anomaly (Butler 1984). An example of this (Figure 2.49) is given by Casten and Gram (1989) for a test case where gravity data were measured in a deep coal mine along an inclined drift which was known to pass at right-angles over a pump room.

Furthermore, micro-gravimetry can be used to determine the rate and extent of the development of strength-relaxation around underground excavations, as shown in Figure 2.50 (Fajklewicz 1986;

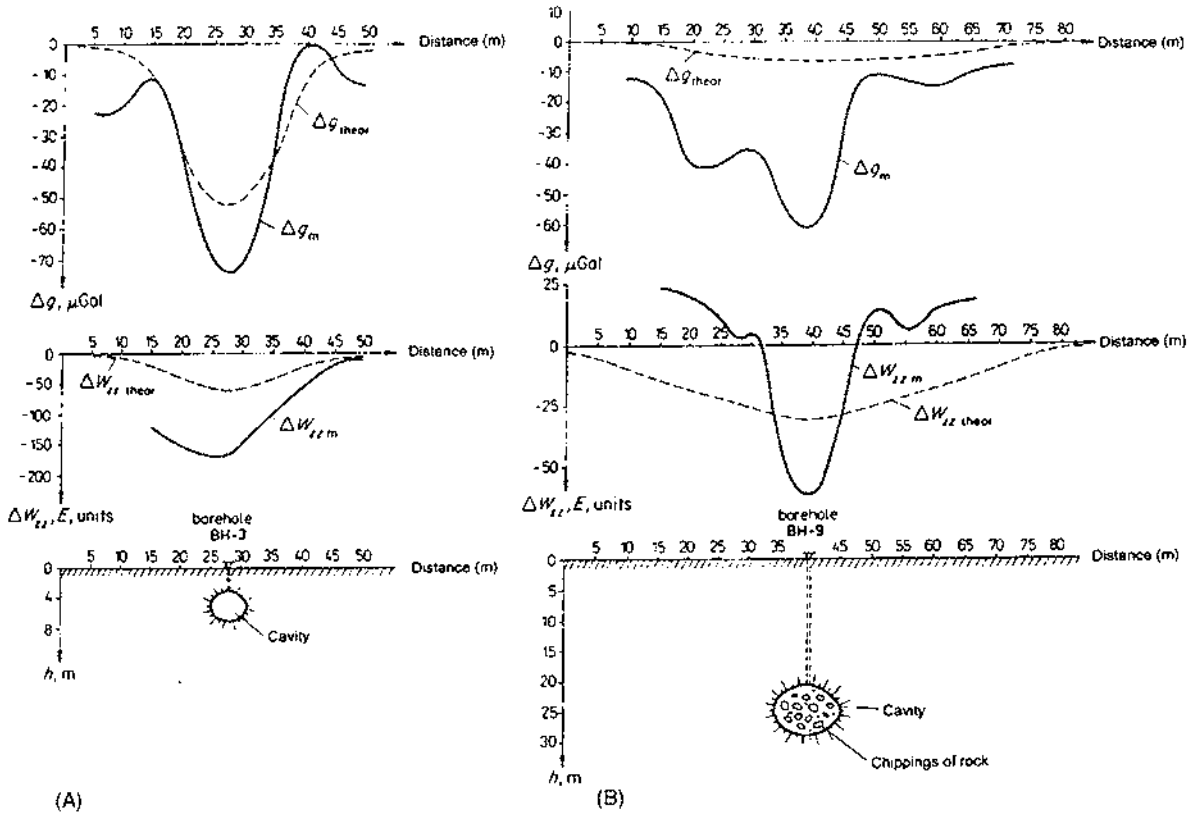

Figure 2.48 Δg_m and $\Delta W_{zz,m}$ micro-gravity anomalies and gravity gradient anomalies respectively–over (A) an air-filled cavity (BH-3), and (B) one partially infilled by rock fragments (BH-9). Curves labelled with suffix 'theor' represent the theoretical anomalies based on the parameters of the cavity alone. From Fajklewicz (1986), by permission

Gluško *et al.* 1981). As the rock relaxes mechanically it cracks, thereby reducing its bulk density. As the cracking continues and develops, so the changes in density as a function of time can be detected using highly sensitive micro-gravimeters, and then modelled.

2.7.5.2 *Archaeological investigations*

Blizkovsky (1979) provides an example of how a careful micro-gravity survey revealed the presence of a suspected crypt within the St 'Venceslas church, Tovacov, Czechoslovakia, which was later proven by excavation work. The dataset consisted of 262 values measured on a $1\,m^2$ or $4\,m^2$ grid to an accuracy of $\pm 11\,\mu$Gal, corrected for the gravity effect of the walls of the building (Figure 2.51). Two significant gravity minima with relative amplitudes of $-60\,\mu$Gal were located which indicated mass deficiencies associated with the previously unknown crypts.

2.7.6 Hydrogeological applications

Gravity methods are not used as much as electrical methods in hydrogeology but can still play an important role (Carmichael

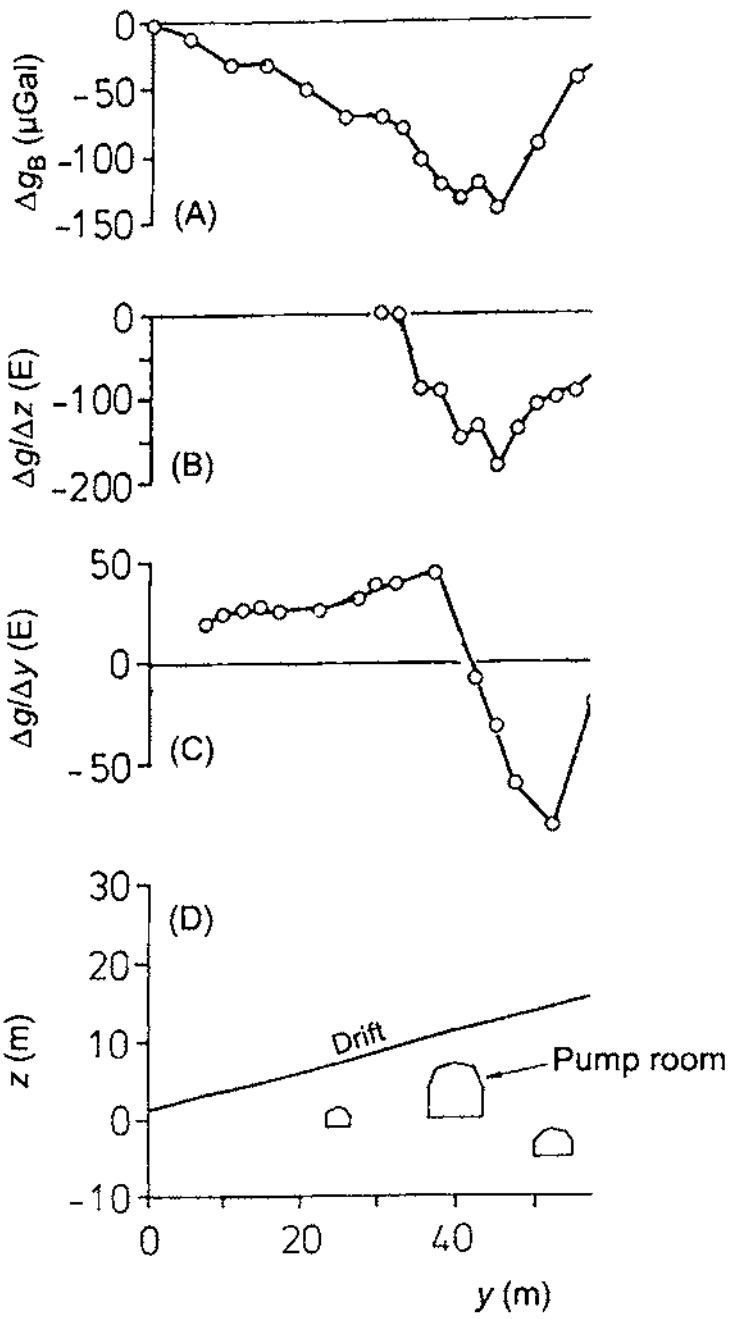

Figure 2.49 A micro-gravity survey within a deep coal mine as measured along a drift cut over a pump room and other known cavities. (A) shows observed residual gravity profiles; (B) observed and computed vertical gravity gradients; (C) observed horizontal gravity gradient, and (D) underground positions of known cavities from mine plans. From Casten and Gram (1989), by permission

and Henry 1977). Their more normal use is to detect low-density rocks that are thought to be suitable aquifers, such as alluvium in buried rock valleys (Lennox and Carlson 1967; van Overmeeren 1980).

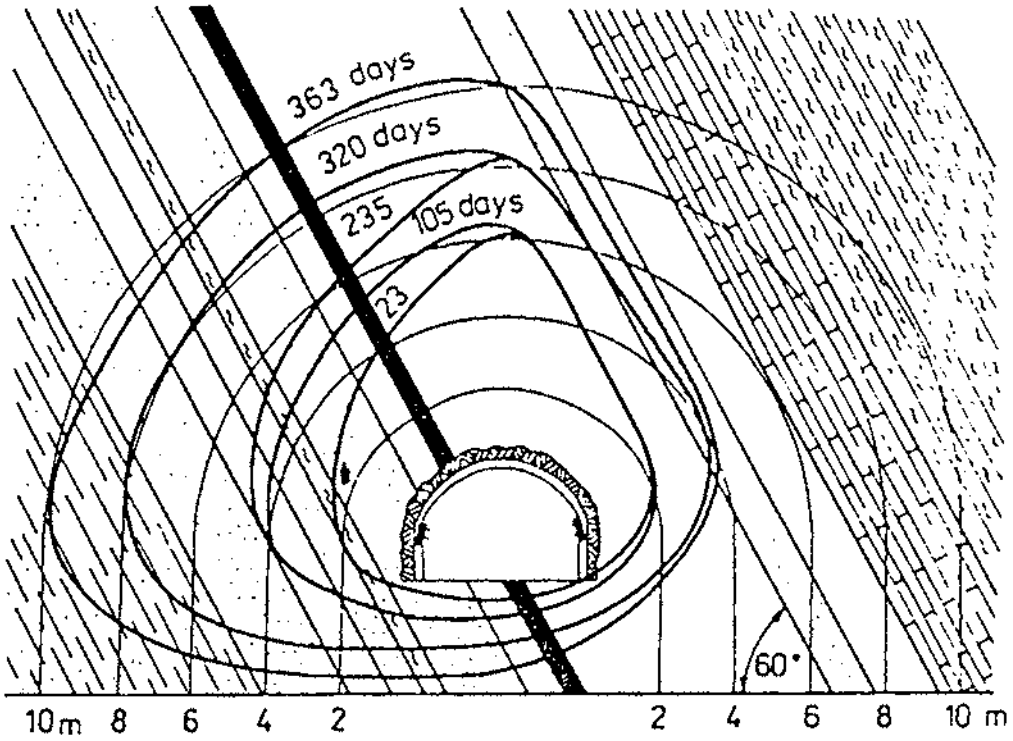

Figure 2.50 The time-dependent strength-relaxation around an underground gallery at 540 m depth as deduced from micro-gravity surveying in the Tchesnokov Colliery in the Don Basin over a period of 363 days. From Gluško *et al.* (1981) and Fajklewicz (1986), by permission

Buried valleys, which have been incised into either bedrock or glacial till and are associated with the South Saskatchewan River, have been identified by their gravity effects (Hall and Hajnal 1962). The Bouguer anomaly across the current river valley shows a minimum considerably wider than the present-day valley (Figure 2.52), thus indicating the presence of low-density material – subsequently found by drilling to be silts and sand.

Rather than interpret Bouguer anomalies, it is possible to use a gravimeter to monitor the effect of changing groundwater levels. For example, in a rock with a porosity of 33% and a specific retention of 20%, a change in groundwater level of 30 m could produce a change in g of 170 μGal. It is possible, therefore, to use a gravimeter to monitor very small changes in g at a given location. The only changes in gravity after corrections for instrument drift and Earth tides should be the amount of water in the interstices of the rock. Consequently, for an aquifer of known shape, a measured change in gravity, in conjunction with a limited number of water-level observations at a small number of wells, can be translated into an estimate of the aquifer's specific yield. Similarly, repeated gravity measurements have been used to estimate the volume of drawdown, degree of saturation of the steam zone (Allis and Hunt 1986) and the volume of

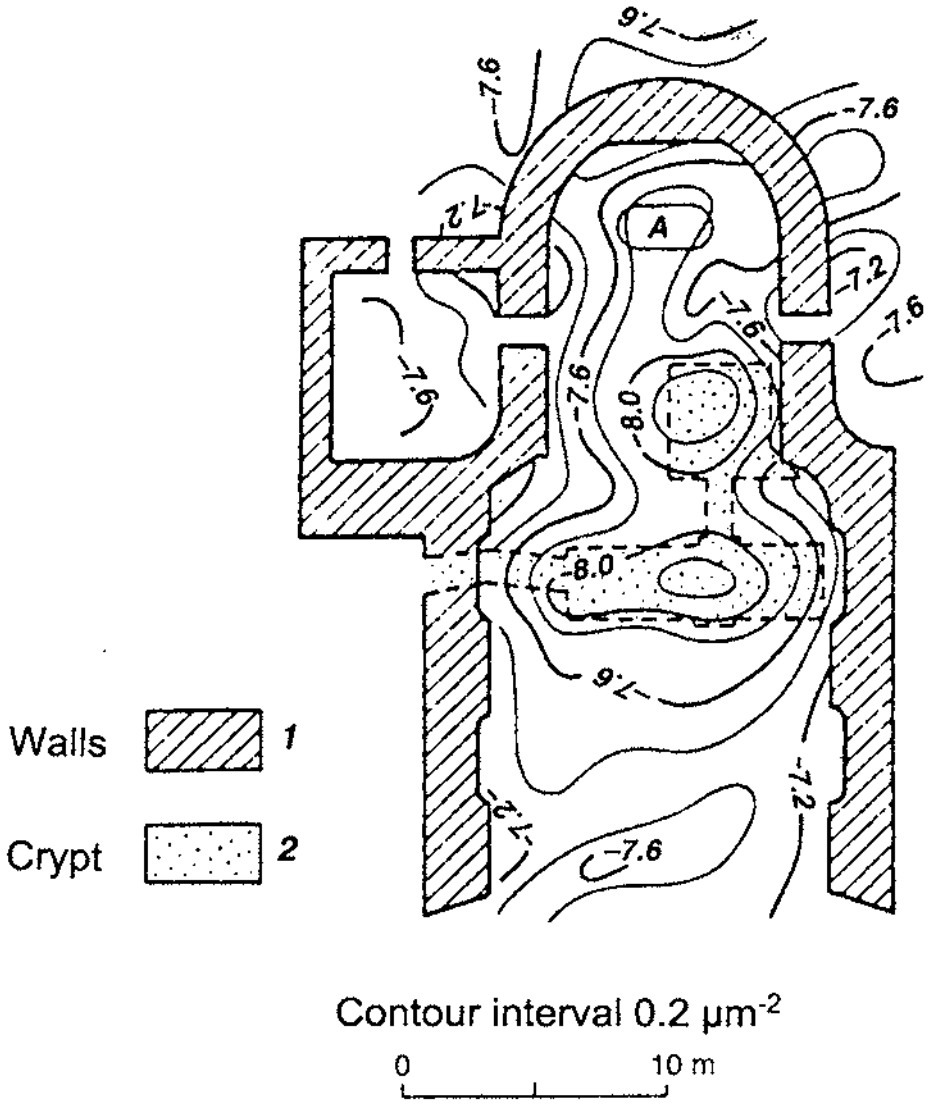

Figure 2.51 Micro-gravity map of St 'Venceslas Church, Tovacov, Czechoslovakia showing marked anomalies over previously unknown crypts. From Blizkovskt (1979), by permission

recharge of the Wairakei geothermal field, North Island, New Zealand (Hunt 1977).

2.7.7 Volcanic hazards

With the advent of highly accurate surveying equipment and methods, and the availability of very sensitive gravimeters, it is possible to monitor small changes in the elevations of the flanks of active volcanoes – ultimately with a view to predicting the next eruption. Such studies are often accompanied by seismic monitoring

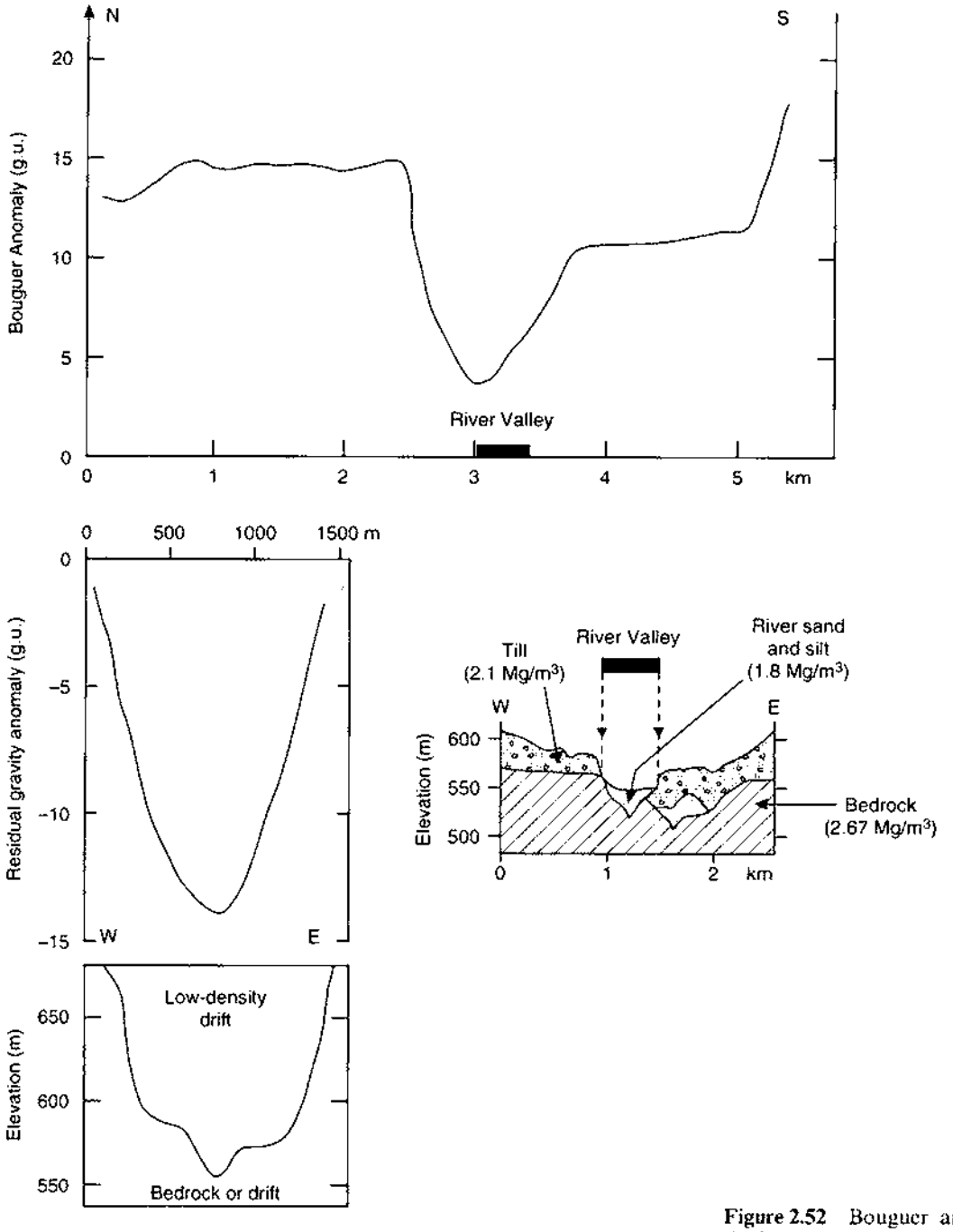

Figure 2.52 Bouguer anomaly over the South Saskatchewan River Valley, and the corresponding geological cross-section across the gravity minimum. After Hall and Hajnal (1962), by permission

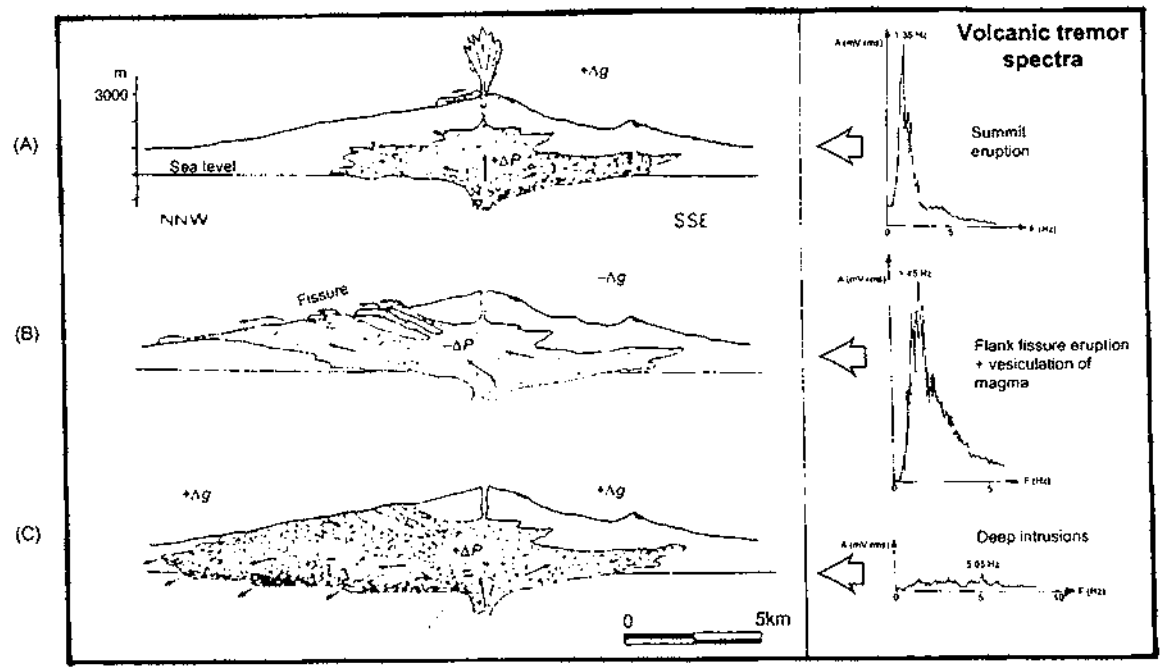

Figure 2.53 Sketches of the stages of fissure eruptions on Mt Etna, Sicily, with gravity trends and typical volcanic tremor spectra. From Sanderson *et al.* (1983) and Cosentino *et al.* (1989), by permission

(e.g. Cosentino *et al.* (1989). Sanderson *et al.* (1983) carried out such a gravity monitoring and levelling programme on Mount Etna, Sicily, during the period August 1980 to August 1981, during which time a flank eruption took place (17–23 March 1981) from which a lava flow resulted which narrowly missed the town of Randazzo. A series of schematic diagrams is shown in Figure 2.53 to illustrate the three clear stages of the fissure eruption.

Changes in gravity in association with elevation increases were interpreted as the injection of new magma at depth during the intrusion of a new dyke at about 1.5 km depth (Figure 2.53A). Gravity decreases were observed when eruptions took place because of the reduction in material (Figure 2.53B). Where increases in gravity were observed without an increase in elevation, this was interpreted as being due to the density of the magma increasing by the enforced emplacement of new material at depth (Figure 2.53C). The magnitude of the gravity changes (≈ 2–$25\,\mu$Gal) coupled with the known variations in elevation ($< \approx 20$ cm) provide a means of determining where within the volcano's plumbing the intrusions of new material and/or density changes are taking place.

Rymer and Brown (1987, 1989) have summarised the micro-gravity effects resulting from vertical movements of the magma/rock interface, vesiculation cycles with the magma column and radial changes in the dimensions of the magma body for Poás volcano in Costa Rica

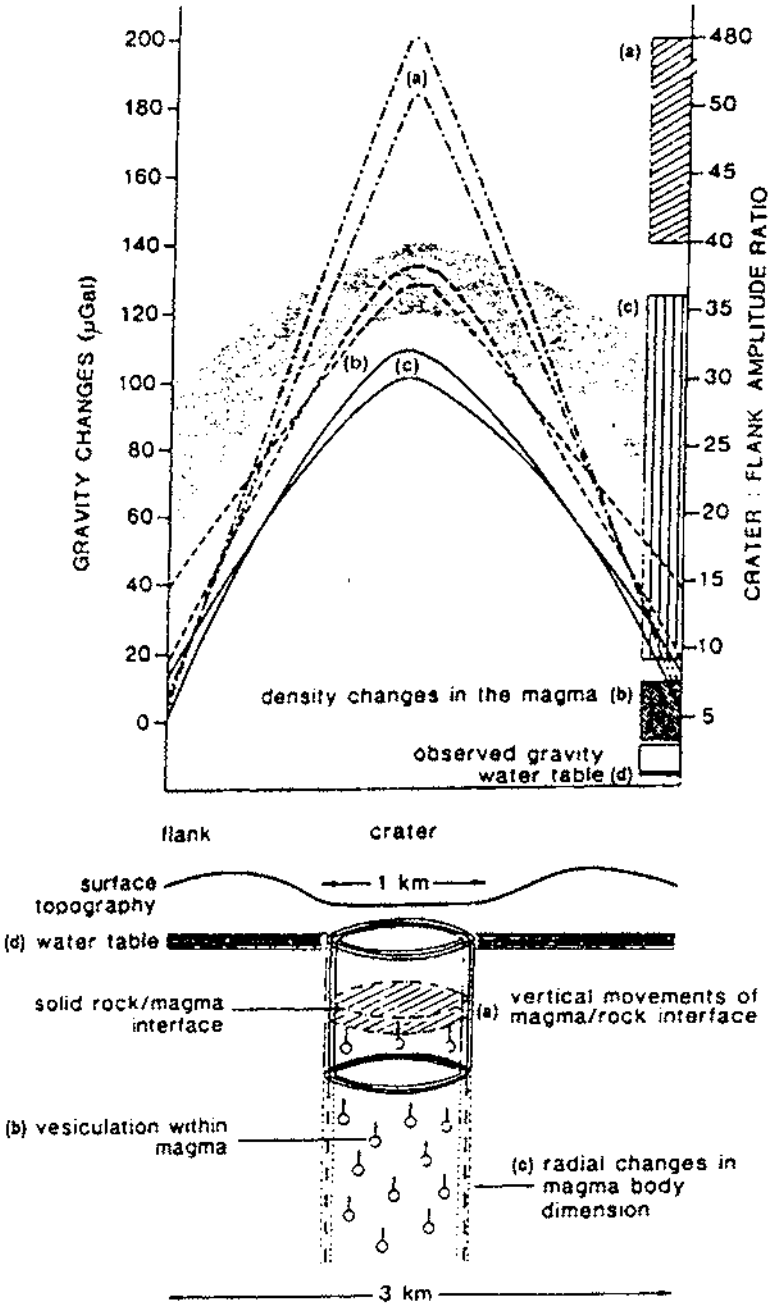

Figure 2.54 The top shows a schematic of the various gravity effects produced at the flank and summit of Poás volcano, Costa Rica (the observed range of gravity effects is shaded) and the ratio of the two (shown alongside in the vertical bar) as caused by different geological processes within the volcano (lower diagram). The processes are: (a) vertical movements of the magma/rock interface; (b) vesiculation cycles within the magma column; (c) radial changes in dimension of the magma column, and (d) variations in the level of the water table. From Rymer and Brown (1987), by permission

(Figure 2.54). The individual internal processes in this particular volcano can be clearly differentiated by using the ratio of the gravity effects measured at the volcano flank and summit. However, not all sub-terrainian activity is associated with seismic signatures. Indeed,

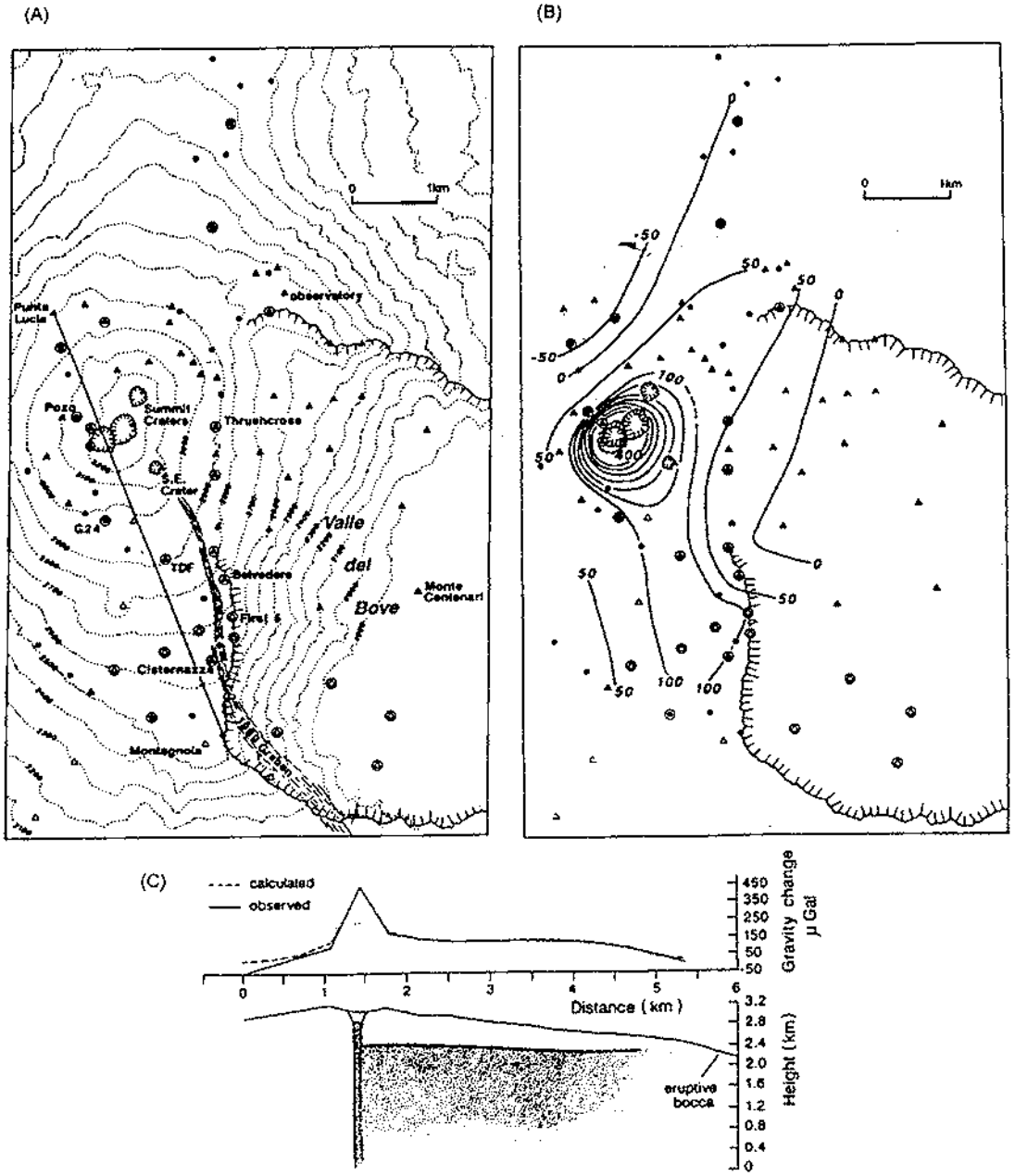

Figure 2.55 Maps showing (A) the locations of micro-gravity and ground deformation monitoring stations and (B) a contoured micro-gravity map of the summit area of Mt Etna, Sicily. The contour interval is 50 μGal. (C) Cross-section through the summit area of the Mt Etna along the profile indicated in (A). The best-fitting model for the observed gravity changes involved a dyke 4 m wide and a feeder pipe 50 m in diameter filling with magma at some time between the two sets of observations in June 1990 and June 1991. From Rymer (1993) and Rymer *et al.* (1993), by permission

Rymer (1993) reported on an increase in gravity at Mt Etna between June 1990 and June 1991 with no corresponding seismic activity. Large increases in gravity were observed around the summit craters and along an elongated zone following the line of a fracture formed during a previous eruption in 1989 (Figure 2.55). Surface elevation changes surveyed between 1990 and 1991 were only of the order of less than 3 cm. The gravity changes were an order of magnitude larger than would have been expected on the basis of elevation changes alone, which suggested that there must have been some sub-surface increase in mass. This was calculated to be of the order of 10^7 Mg and was caused by the intrusion of magma into fractures left by the 1989 eruption. The magma migrated passively into the pre-existing fractures so there was no corresponding seismic activity. Consequently, the micro-gravity measurements, in conjunction with elevations surveys, produced the only evidence of an impending eruption. The eruption of Mt Etna lasted for 16 months from 1991 to 1993, during which time lava poured out of the vent at a rate of $10\,m^3/s$, making this the largest eruption there for 300 years (Rymer 1993; Rymer *et al.* 1993).

Micro-gravity monitoring coupled with the distinctive patterns of the frequency of seismic activity (volcanic tremor spectra) are beginning to provide a very comprehensive model for volcanic eruptions, such as those at Mt Etna, and their associated processes. Many other volcanoes now have active monitoring programmes utilising gravity, seismic, and thermal investigations. Monitoring gas emissions is also proving to be a valuable additional indicator of impending volcanic activity (e.g. Pendick 1995, on the work of S. Williams). If these data can be obtained for individual volcanoes in conjunction with thermal radiation as measured by satellite, then the probability of identifying recognisable precursors to eruptions may be enhanced significantly, leading to a better prediction of volcanic activity and mitigation of potential hazards (Rymer and Brown 1986; Eggers 1987).

Chapter 3
Geomagnetic methods

3.1 INTRODUCTION

It is thought that the Chinese first used lodestone (magnetite-rich rock) in primitive direction-finding as early as the second century BC. It was not until the twelfth century in Europe that reference was made to the use of a magnetic compass for navigation. The first scientific analysis of the Earth's magnetic field and associated phenomena was published by the English physicist William Gilbert in 1600 in his book *De Magnete*. Measurements of variations in the Earth's magnetic field were made in Sweden to locate iron ore deposits as early as 1640. In 1870, Thalén and Tiberg developed instruments to measure various components of the Earth's magnetic field accurately and quickly for routine prospecting.

In 1915, Adolf Schmidt made a balance magnetometer which enabled more widespread magnetic surveys to be undertaken. As with many geophysical methods, advances in technology were made during the Second World War which enabled more efficient, reliable and accurate measurements to be made thereafter. In the 1960s, optical absorption magnetometers were developed which provided the means for extremely rapid magnetic measurements with very high sensitivity, ideally suited to airborne magnetic surveys. Since the early 1970s, magnetic gradiometers have been used which measure not only the total Earth's magnetic field intensity but also the magnetic gradient between sensors. This provides extra information of sufficient resolution which can be invaluable in delimiting geological targets.

Geomagnetic methods can be used in a wide variety of applications (Table 3.1) and range from small-scale investigations to locate pipes and cables in the very near surface, and engineering site investigations, through to large-scale regional geological mapping to determine gross structure, such as in hydrocarbon exploration. Commonly in the larger exploration investigations, both magnetic and gravity methods are used to complement each other. Used together prior to seismic surveys, they can provide more information about the sub-surface, particularly the basement rocks, than either technique on its own. Subsequent seismic reflection surveys are then used to provide more detailed imaging of the

Table 3.1 Applications of geomagnetic surveys

Locating
- Pipes, cables and metallic objects
- Buried military ordnance (shells, bombs, etc.)
- Buried metal drums of contaminated or toxic waste
- Concealed mineshafts and adits

Mapping
- Archaeological remains
- Concealed basic igneous dykes
- Metalliferous mineral lodes
- Geological boundaries between magnetically contrasting lithologies, including faults
- Large-scale geological structures

sub-surface, which is of more value to hydrocarbon exploration. The range of magnetic measurements which can now be made is extremely large, especially in the area of palaeomagnetism which will not be dealt with here. Palaeomagnetism is discussed in detail by Tarling (1983), for example.

3.2 BASIC CONCEPTS AND UNITS OF GEOMAGNETISM

3.2.1 Flux density, field strength and permeability

Around a bar magnet, a magnetic flux exists, as indicated by the flux lines in Figure 3.1, and converges near the ends of the magnet, which are known as the magnetic poles. If such a bar magnet is suspended in free air, the magnet will align itself with the Earth's magnetic field with one pole (the positive north-seeking) pointing towards the Earth's north pole and the other (the negative south-seeking) towards the south magnetic pole. Magnetic poles always exist in pairs of opposite sense to form a *dipole*. When one pole is sufficiently far removed from the other so that it no longer affects it, the single pole is referred to as a *monopole*.

If two magnetic poles of strength m_1 and m_2 are separated by a distance r, a force exists between them (Box 3.1). If the poles are of the same sort, the force will push the poles apart, and if they are of opposite polarity, the force is attractive and will draw the poles towards each other. Note the similarity of the form of the expression in Box 3.1 with that for the force of gravitational attraction in Box 2.1; both gravity and magnetism are *potential fields* and can be described by comparable potential field theory.

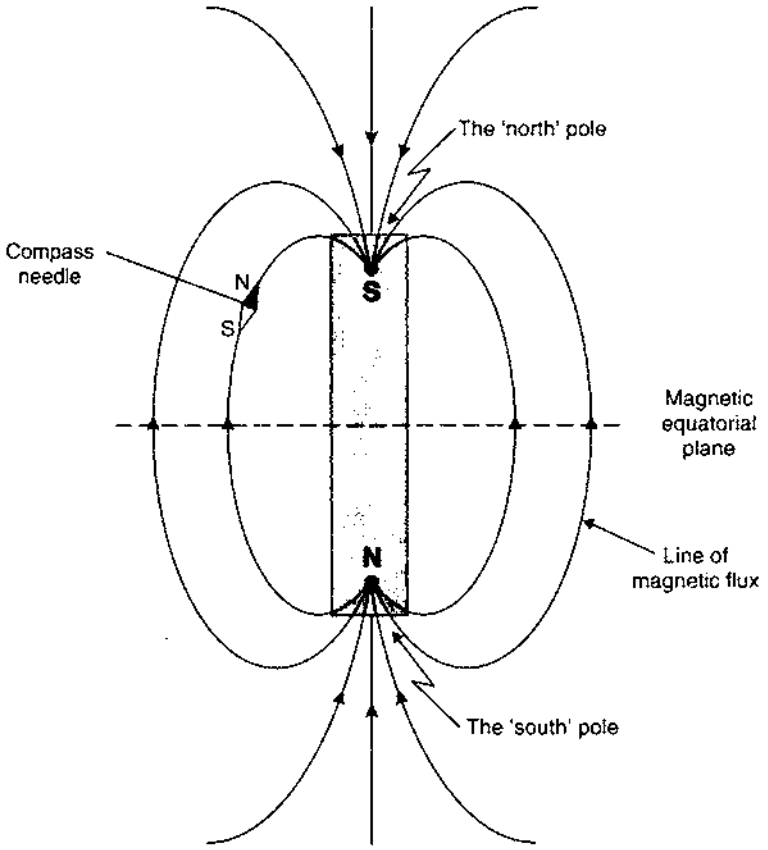

Figure 3.1 Lines of magnetic flux around a bar magnet

Box 3.1 Force between two magnetic poles

$$F = \frac{m_1 m_2}{4\pi\mu r^2}$$

where μ is the magnetic permeability of the medium separating the poles; m_1 and m_2 are pole strengths and r the distance between them.

The closeness of the flux lines shown in Figure 3.1, the flux per unit area, is the *flux density* $\boldsymbol{B}$ (and is measured in weber/m^2 = teslas). $\boldsymbol{B}$, which is also called the 'magnetic induction', is a vector quantity. (The former c.g.s. units of flux density were gauss, equivalent to 10^{-4} T.) The units of teslas are too large to be practical in geophysical work, so a sub-unit called the nanotesla (nT = 10 ^{9} T) is used instead, where 1 nT is numerically equivalent to 1 gamma in c.g.s. units (1 nT is equivalent to 10^{-5} gauss).

The magnetic field can also be defined in terms of a force field which is produced by electric currents. This *magnetising field strength* $\boldsymbol{H}$ is defined, following Biot Savart's Law, as being the field strength at the centre of a loop of wire of radius r through which a current $\boldsymbol{I}$ is flowing such that $\boldsymbol{H} = \boldsymbol{I}/2r$. Consequently the units of the magnetising field strength $\boldsymbol{H}$ are amperes per metre (A/m).

The ratio of the flux density $\boldsymbol{B}$ to the magnetising field strength $\boldsymbol{H}$ is a constant called the *absolute magnetic permeability* (μ). Practically, the magnetic permeability of water and air can be taken to be equal to the *magnetic permeability of free space* (a vacuum), denoted μ_0 which has the value $4\pi \times 10^{-7}$ Wb A^{-1} m^{-1}. For any medium other than a vacuum, the ratio of the permeabilities of a medium to that of free space is equal to the *relative permeability* μ_r, such that $\mu_r = \mu/\mu_0$ and, as it is a ratio, it has no units.

3.2.2 Susceptibility

It is possible to express the relationship between $\boldsymbol{B}$ and $\boldsymbol{H}$ in terms of a geologically diagnostic parameter, the *magnetic susceptibility* κ (see Box 3.2 and Section 3.3.1). Susceptibility is in essence a measure of how susceptible a material is to becoming magnetised. For a vacuum, $\mu_r = 1$ and $\kappa = 0$. Although susceptibility has no units, to rationalise its numerical value to be compatible with the SI or rationalised system of units, the value in e.g.s. equivalent units (e.g. unrationalised units such as e.m.u. – electromagnetic units) should be multiplied by 4π. Some materials have negative susceptibilities (see Section 3.3).

Box 3.2 Relationship between magnetic flux density $\boldsymbol{B}$, magnetising force $\boldsymbol{H}$, and susceptibility κ

Given:

$$\boldsymbol{B} = \mu \boldsymbol{H}$$

[units: μ(Wb/Am), $\boldsymbol{H}$(A/m) = Wb/m^2 = teslas]

Since $\mu = \mu_r \mu_0$:

$$\boldsymbol{B} = \mu_r \mu_0 \boldsymbol{H}.$$

Rearranging to introduce $k = \mu_r - 1$:

$$\begin{aligned} \boldsymbol{B} &= \mu_0 \boldsymbol{H} + \mu_0(\mu_r - 1)\boldsymbol{H} \\ &= \mu_0 \boldsymbol{H} + \mu_0 k \boldsymbol{H} = \mu_0 \boldsymbol{H} + \mu_0 \boldsymbol{J}. \end{aligned}$$

Hence:

$$\boldsymbol{B} = \mu_0 \boldsymbol{H}(1 + k) \quad \text{and} \quad \boldsymbol{J} = k\boldsymbol{H}.$$

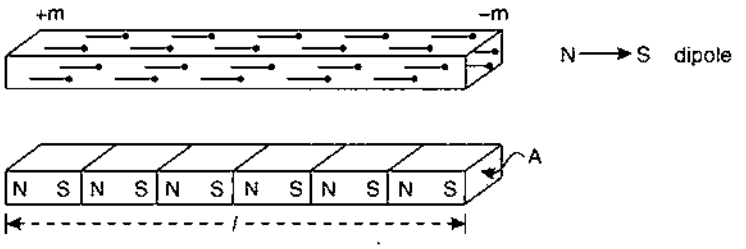

Figure 3.2 Schematic of a uniformly magnetised bar magnet as a collection of aligned dipoles producing a pole strength of $+m$ and as a series of minor bar magnets

3.2.3 Intensity of magnetisation

From the last expressions given in Box 3.2, it is clear that for a vacuum, $\boldsymbol{B} = \mu_0 \boldsymbol{H}$ (as $k = 0$). The penultimate expression in Box 3.2 indicates that in a medium other than a vacuum, an extra magnetising field strength of $k\boldsymbol{H}$, called the *intensity of magnetisation* $\boldsymbol{J}$, is induced by the $\boldsymbol{H}$.

Another way of visualising the intensity of magnetisation is to examine a bar magnet of length l and cross-sectional area A which is uniformly magnetised in the direction of the long axis. The bar magnet can be thought of as consisting of a series of much smaller bar magnets or dipoles all aligned parallel to the long axis of the whole bar magnet (Figure 3.2). The magnetic intensities due to all the individual north and south poles will cancel out except at the end faces of the whole magnet, thus giving the whole magnet an overall magnetisation. The surface concentration of free poles, or pole strength m per unit area, is a measure of the intensity of magnetisation $\boldsymbol{J}$ (Box 3.3). The stronger the magnetisation, the greater will be the concentration of free poles. Furthermore, if a body of volume V is

Box 3.3 Intensity of magnetisation, $\boldsymbol{J}$ (amps/metre)

$$\boldsymbol{J} = \boldsymbol{m}/A$$

where $\boldsymbol{m}$ is the pole strength (amp . metre) and A is the cross-sectional area of the bar magnet (metre^2).
In terms of the *magnetic moment*, $\boldsymbol{M}$ (amp . metre^2):

$$\boldsymbol{J} = \boldsymbol{M}/V = \boldsymbol{m}.l/V$$

where l is the length of the dipole, V is the volume of the magnetised body, and $\boldsymbol{M} = \boldsymbol{m}.l$.

The intensity of the induced magnetisation, $\boldsymbol{J}_i$ in rock with susceptibility κ, caused by the Earth's magnetic field $\boldsymbol{F}$ (tesla) in the sense of the flux density, i.e. the $\boldsymbol{B}$-field, is given by:

$$\boldsymbol{J}_i = k.\boldsymbol{F}/\mu_0$$

where μ_0 is the permeability of free space, and $\boldsymbol{F} = \mu_0 \boldsymbol{H}$, with $\boldsymbol{H}$ being the magnetising force.

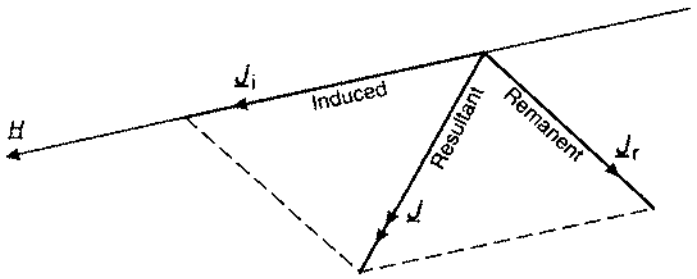

Figure 3.3 Vectorial summation of induced and remanent intensities of magnetisation

magnetised uniformly with intensity J, then that body is said to have a magnetic moment M which is defined as the product of the magnetic pole strength m and the length l separating the poles (Box 3.3). The intensity of magnetisation, which is thus the magnetic moment per unit volume, is of fundamental importance in describing the magnetic state of any rock mass.

3.2.4 Induced and remanent magnetisation

So far the discussion has centred upon a magnetisation that is induced by an applied field H where the induced intensity of magnetisation is denoted by J_i. In many cases, in the absence of an applied field (H), there is still a measurable intensity of magnetisation which is sustained by the internal field strength due to permanently magnetic particles. The intensity of this *permanent* or *remanent magnetisation* is denoted by J_r.

A rock mass containing magnetic minerals will have an induced as well as a remanent magnetisation. These magnetisations may have different directions and magnitudes of intensity (Figure 3.3). The magnitude and orientation of the resultant J dictate both the amplitude and shape of a magnetic anomaly, respectively. Consequently, interpretation of magnetic data is complicated by having greater degrees of freedom of the magnetic parameters and physical properties compared with gravity, which is largely dependent upon only rock density.

3.2.5 Diamagnetism, paramagnetism and ferromagnetism

All atoms have a magnetic moment as a result of the orbital motion of electrons around the nucleus and the spin of the electrons. According to quantum theory, two electrons can exist in the same electron shell (or state) as long as they spin in opposite directions. The magnetic moments of two such electrons, called *paired electrons*, will cancel out. In the majority of substances, when there is no external applied magnetic field, the spin magnetic moments of adjacent atoms are distributed randomly so there is no overall magnetisation. In a *diamagnetic* material, such as halite, all the electron shells are complete

and so there are no unpaired electrons. When an external magnetic field is applied, a magnetisation is induced. The electrons orbit in such a way so as to produce a magnetic field which opposes the applied field, giving rise to a weak, negative susceptibility.

Unpaired electrons in incomplete electron shells produce unbalanced spin magnetic moments and weak magnetic interactions between atoms in *paramagnetic* materials such as fayerite, amphiboles, pyroxenes, olivines, garnets and biotite. In an external applied field, the magnetic moments align themselves into the same direction, although this process is retarded by thermal agitation. The result is a weak positive susceptibility but one which decreases inversely with the absolute temperature according to the Curie–Weiss Law. Paramagnetism is generally at least an order of magnitude stronger than diamagnetism.

In *ferromagnetic* materials, the susceptibility is large but is dependent upon temperature and the strength of the applied magnetic field. The spin moments of unpaired electrons are coupled magnetically due to the very strong interaction between adjacent atoms and overlap of electron orbits. A small grain in which magnetic coupling occurs forms what is called a single *magnetic domain* and has dimensions of the order of one micron. This gives rise to a strong 'spontaneous magnetisation' which can exist even when there is no external applied field. The magnetic coupling can be such that the magnetic moments are aligned either parallel or antiparallel (Figure 3.4).

Truly ferromagnetic materials occur only rarely in nature but include substances such as cobalt, nickel and iron, all of which have parallel alignment of moments. Ferromagnetism disappears when the temperature of the material is raised above the *Curie temperature* T_C as inter-atomic magnetical coupling is severely restricted and the material thereafter exhibits paramagnetic behaviour. In *antiferromagnetic* materials, for example hematite, the moments are aligned in

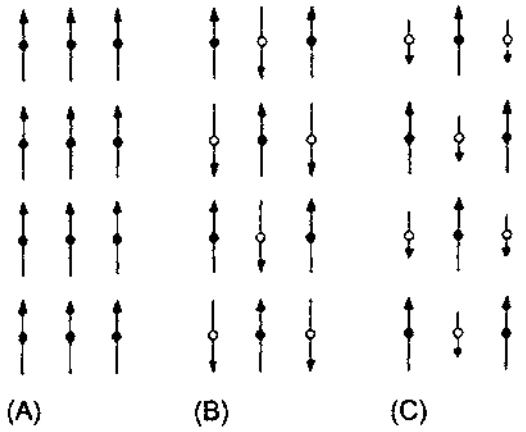

Figure 3.4 Schematic of magnetic moments in (A) ferromagnetic, (B) antiferromagnetic, and (C) ferrimagnetic crystals. After Nagata (1961), by permission

an antiparallel manner. Although the magnetic fields of the oppositely orientated dipoles cancel each other out, crystal lattice defects result in a net residual moment or *parasitic (anti)-ferromagnetism*. In ferrimagnetic materials, of which magnetite, titanomagnetite and ilmenite are prime examples, the sub-lattices are unequal and antiparallel. This results in a net magnetisation. Spontaneous magnetisation and large susceptibilities are characteristics of ferrimagnetic materials, such as in the case of pyrrhotite. Although the temperature dependence of ferrimagnetic behaviour is complex, ferrimagnetism disappears at temperatures above the Curie point. The majority of naturally occurring magnetic minerals exhibit either ferrimagnetic or imperfectly antiferromagnetic characteristics.

The Curie temperature varies with different minerals and will be different for whole rocks depending upon the composition of magnetic minerals present. In a granite rhyolite, for example, the Curie temperature for titanomagnetite is between 463 and 580°C, whereas for ilmenite-hematite series it is in the range 130–220°C. Oxidation of the iron–titanium oxides generally causes a rise in the Curie temperature. When low-temperature oxidation occurs, i.e. at temperatures lower than 300°C, in addition to increases in the Curie temperature, the intensity of magnetisation decreases. In order of increasing oxidation and decreasing intensity of magnetisation, titanomagnetite ($T_C = 100$ 200°C) alters to titanomaghemite (150–450°C) then to magnetite (550–580°C) and ultimately to hematite (650 680°C) (Petersen 1990). Hematite has the lowest intensity of magnetisation. The alteration of magnetic minerals is important to remember when it comes to the interpretation of magnetic anomalies. Rocks which should display large susceptibilities and greatest intensities of magnetisation may exhibit much weaker magnetic properties owing to geochemical alteration of the magnetic minerals.

For a multidomain material in a field-free space ($\boldsymbol{H} = 0$), the spontaneous magnetisation of the magnetic domains within a crystal is related to the crystal axes (Figure 3.5). The magnetisation directions of all domains cancel each other out so there is no net magnetisation intensity ($\boldsymbol{J} = 0$). On increasing the applied magnetic field ($\boldsymbol{H}$), the domain walls can move easily and reversibly should $\boldsymbol{H}$ be reduced at this point. As $\boldsymbol{H}$ increases, so the various domains reorientate themselves parallel to the applied field, but in discrete steps called *Barkhausen jumps*, which are permanent. When there is no further increase in magnetisation intensity with increasing applied field strength, all the domains are orientated parallel to the applied field direction and the material is said to be magnetically *saturated*. On reducing $\boldsymbol{H}$ to zero following saturation, only some of the magnetic domains are able to return to their former orientation, which results in a remanent magnetisation $\boldsymbol{J}_r$.

If the magnetic permeability (μ) of a medium is independent of the magnetising force ($\boldsymbol{H}$), the material is said to be linear in its behaviour.

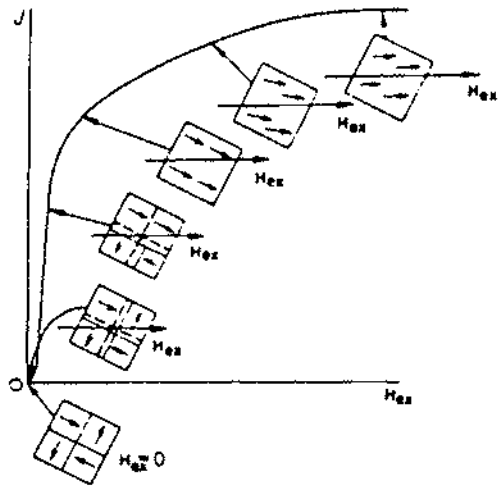

Figure 3.5 Process of magnetisation of a ferromagnetic substance according to domain theory. From Sharma (1986), by permission

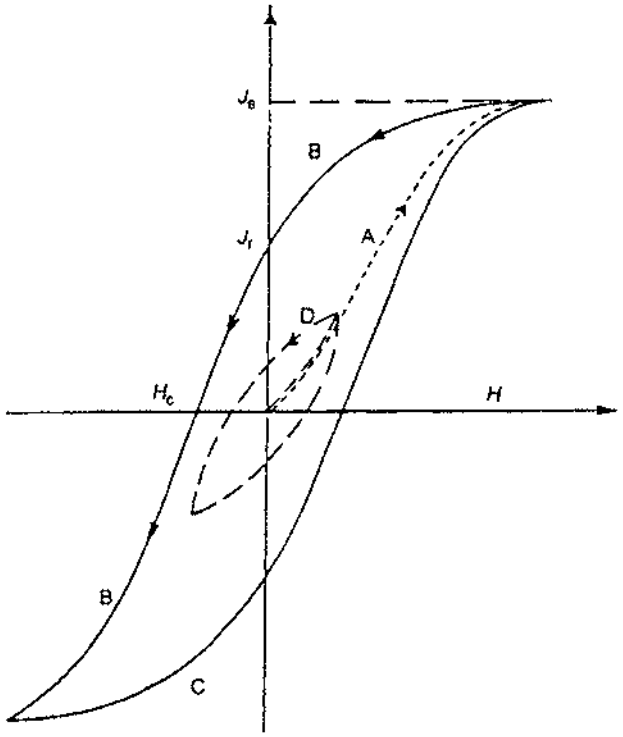

Figure 3.6 Hysteresis loop illustrating a cycle of magnetisation (curves A, B, C) of a ferromagnetic material. Small loop (D) shows the magnetisation cycle without saturation. From Sharma (1986), by permission

However, if a ferromagnetic or ferrimagnetic material, such as magnetite or pyrrhotite, with grains larger than 10 microns is placed in an increasing applied magnetic field, its magnetic intensity ***J*** increases to the point of saturation following a hysteresis loop (Figure 3.6). The physical processes by which this happens have already been described

in terms of domain theory. After reaching saturation, the applied field $\boldsymbol{H}$ is reduced to zero at which point the intensity of magnetisation is that attributed to the remanent magnetisation. To eliminate this magnetisation, a negative field, $-\boldsymbol{H}_c$, the *coercive force*, has to be applied. The *coercivity*, $\boldsymbol{H}_c$, is an indication as to the 'hardness' or permanence of the magnetisation. Consequently, larger magnetic grains, which thus contain more magnetic domains, are easier to magnetise (and therefore have a higher susceptibility), than fine grains which are magnetically hard as indicated by a relatively high coercivity and low susceptibility. On increasing the applied magnetic field to full saturation, the hysteresis loop is completed. It follows that, for minerals that exhibit a nonlinear behaviour, no unique value of susceptibility exists. Values cited for such materials are usually for weak values of $\boldsymbol{H}$ and prior to saturation ever having been reached. For much more detailed discussion of rock magnetism, see the monographs by Nagata (1961), Stacey and Banerjee (1973) and O'Reilly (1984).

3.3 MAGNETIC PROPERTIES OF ROCKS

3.3.1 Susceptibility of rocks and minerals

Magnetic susceptibility is an extremely important property of rocks and is to magnetic exploration methods what density is to gravity surveys. Rocks that have a significant concentration of ferro- and/or ferri-magnetic minerals tend to have the highest susceptibilities. Consequently, basic and ultrabasic rocks have the highest susceptibilities, acid igneous and metamorphic rocks have intermediate to low values, and sedimentary rocks have very small susceptibilities in general (Table 3.2 and Figure 3.7). In this compilation of data, specific details of rock types are not available and so the values cited should be taken only as a guide. Metamorphic rocks are dependent upon their parent material and metapsammites are likely to have different susceptibilities compared with metapelites, for example.

Whole rock susceptibilities can vary considerably owing to a number of factors in addition to mineralogical composition. Susceptibilities depend upon the alignment and shape of the magnetic grains dispersed throughout the rock. If there is a marked orientation of particles, such as in some sedimentary and metamorphic rocks, a strong physical anisotropy may exist. The variation of magnetic properties as a function of orientation and shape of mineral grains is known as the *magnetic fabric*. Magnetic fabric analysis provides a very sensitive indication as to the physical composition of a rock or sediment, which in turn can be important in interpreting physical processes affecting that rock. For example, it is possible to correlate magnetic fabric variation in estuarine sediments with sonograph

Table 3.2 Susceptibilities of rocks and minerals (rationalised SI units)

Mineral or rock type	Susceptibility*
Sedimentary	
Dolomite (pure)	−12.5 to +44
Dolomite (impure)	20000
Limestone	10 to 25000
Sandstone	0 to 21000
Shales	60 to 18600
Average for various	**0 to 360**
Metamorphic	
Schist	315 to 3000
Slate	0 to 38000
Gneiss	125 to 25000
Serpentenite	3100 to 75000
Average for various	**0 to 73000**
Igneous	
Granite	10 to 65
Granite (m)	20 to 50000
Rhyolite	250 to 37700
Pegmatite	3000 to 75000
Gabbro	800 to 76000
Basalts	500 to 182000
Oceanic basalts	300 to 36000
Peridotite	95500 to 196000
Average for acid igneous	**40 to 82000**
Average for basic igneous	**550 to 122000**
Minerals	
Ice (d)	−9
Rocksalt (d)	−10
Gypsum (d)	−13
Quartz (d)	−15
Graphite (d)	−80 to −200
Chalcopyrite	400
Pyrite (o)	50 to 5000
Hematite (o)	420 to 38000
Pyrrhotite (o)	1250 to 6.3×10^6
Ilmenite (o)	314000 to 3.8×10^6
Magnetite (o)	70000 to 2×10^7

(d) = diamagnetic material; (o) = ore; (m) = with magnetic
*$\kappa \times 10^6$ rationalised SI units; to convert to the unrationalised c.g.s. units, divide by 4π
Data from Parasnis (1986), Sharma (1986), Telford *et al.* (1990)

images of the estuary floor. In conjunction with Thematic Mapper images obtained from low-flying aircraft and simultaneous water sampling from boats, it is possible to establish a detailed model of estuarine sediment dynamic processes, as has been achieved for Plymouth Sound in south-west England (Fitzpatrick 1991). For further details of the magnetic fabric method, see the discussions by Lowrie (1990) and Tarling (1983), for example.

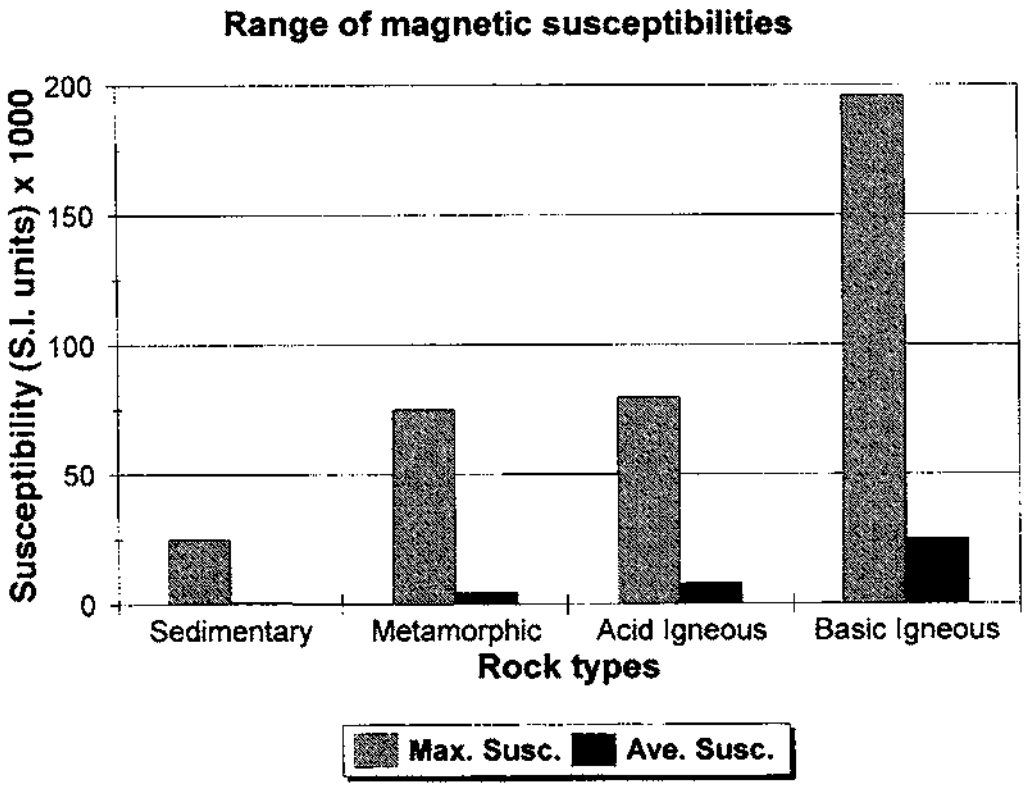

Figure 3.7 Susceptibilities of major rock types

For magnetic ore bodies with extremely high susceptibilities ($\kappa \geqslant 10^6$ SI), the measured susceptibility – more correctly referred to as the *apparent susceptibility* κ_a can be reduced substantially by a shape demagnetisation effect (see Box 3.4). This involves a *demagnetisation factor* N_x which depends on a direction x. For a sphere, $N_x = 1/3$ in all directions. In the case of a thin sheetlike body with a high true susceptibility ($\kappa \sim 10^6$ SI): $N_x \sim 1$ in the transverse direction, giving a susceptibility $\kappa_a \approx 0.5K$; and $N_z \sim 0$ in the longitudinal direction, so that $\kappa_a \approx \kappa$. Demagnetisation factors are discussed further by Parasnis (1986) and Sharma (1986).

Box 3.4 Apparent susceptibility κ_a and the demagnetisation factor N_x

$$\kappa_a = \kappa/(1 + N_x\kappa)$$

Susceptibilities can be measured either in the field using a handheld susceptibility meter such as the kappameter, or on samples returned to a laboratory where they can be analysed more accurately.

3.3.2 Remanent magnetisation and Königsberger ratios

In addition to the induced magnetisation, many rocks and minerals exhibit a permanent or *natural remanent magnetisation* (NRM) of intensity J_r when the applied field H is zero. The various processes by which rocks can acquire a remanent magnetisation are listed in Table 3.3 and discussed in more detail by Merrill (1990), Sharma (1986) and Tarling (1983).

Table 3.3 Types of remanent magnetisation (RM). After Merrill (1990), by permission

Type of RM	Process
Natural (NRM)	Acquired by a rock or mineral under natural conditions
Thermal (TRM)	Acquired by a material during cooling from a temperature greater than the Curie temperature to room temperature (e.g. molten lava cooling after a volcanic eruption)
Isothermal (IRM)	Acquired over a short time (of the order of seconds) in a strong magnetic field at a constant temperature (e.g. such as by a lightning strike)
Chemical (CRM)	Also crystallisation RM; acquired at the time of nucleation and growth or crystallisation of fine magnetic grains far below the Curie point in an ambient field
Thermal chemical (TCRM)	Acquired during chemical alteration and cooling
Detrital (DRM)	Also depositional RM; acquired by the settling out of previously magnetised particles to form ultimately consolidated sediments which then have a weak net magnetisation, but prior to any chemical alteration through diagenetic processes
Post-depositional (PDRM)	Acquired by a sediment by physical processes acting upon it after deposition (e.g. bioturbation and compaction)
Viscous VMR	Acquired after a lengthy exposure to an ambient field with all other factors being constant (e.g. chemistry and temperature)
Anhysteretic (ARM)	Acquired when a peak amplitude of an alternating magnetic field is decreased from a large value to zero in the presence of a weak but constant magnetic field

Primary remanent magnetisations are acquired by the cooling and solidification of an igneous rock from above the Curie temperature (of the constituent magnetic minerals) to normal surface temperature (TRM) or by detrital remanent magnetisation (DRM). Secondary remanent magnetisations, such as chemical, viscous or post-depositional remanent magnetisations, may be acquired later on in the rock's history. This is especially true of igneous rocks which have later undergone one or more periods of metamorphism, particularly thermal metamorphism.

The intensity of the remanent magnetisation J_r may swamp that of the induced magnetisation J_i, particularly in igneous and thermally metamorphosed rocks. The ratio of the two intensities (J_r/J_i) is called the *Königsberger ratio*, Q, which can be expressed in terms of the Earth's magnetic field at a given locality and the susceptibility of the rocks (Box 3.5). Just as susceptibility can vary within a single rock type, so too can the Königsberger ratio. However, similar rock types have characteristic values of Q, some of which are listed in Table 3.4. Nagata (1961) has made four broad generalizations on the basis of Q:

- $Q \sim 1$ for slowly crystallised igneous and thermally metamorphosed rocks in continental areas;
- $Q \sim 10$ for volcanic rocks;

Table 3.4 Examples of values of the Königsberger ratio

Rock type	Location	Q
Basalt	Mihare volcano, Japan	99–118
Oceanic basalts	Northeast Pacific	15–105
Oceanic basalts	Mid-Atlantic Ridge	1–160
Sea-mount basalts	North Pacific	8–57
Cainozoic basalts	Victoria, Australia	5
Early tertiary basalts	Disko, West Greenland	1–39
Tholeiite dykes	England	0.6–1.6
Dolerite sills	North England	2–3.5
Dolerite	Sutherland, Scotland	0.48–0.51
Quartz dolerite	Whin Sill, England	2–2.9
Gabbro	Småland, Sweden	9.5
Gabbro	Minnesota, USA	1–8
Gabbro	Cuillin Hills, Scotland	29
Andesite	Taga, Japan	4.9
Granite	Madagascar	0.3–10
Granite plutons	California, USA	0.2–0.9
Granodiorite	Nevada, USA	0.1–0.2
Diabase	Astano Ticino, Switzerland	1.5
Diabase dykes	Canadian Shield	0.2–4
Magnetite ore	Sweden	1–10
Magnetite ore	South India	1–5

- $Q \sim 30$–50 for many rapidly quenched basaltic rocks;
- $Q < 1$ in sedimentary and metamorphic rocks, except when iron ore is involved.

Box 3.5 Königsberger ratio, Q

$$Q = J_r/\kappa(F/\mu_0)$$

where J_r is the intensity of remanent (NRM) magnetisation, κ is the susceptibility, μ_0 is the permeability of free space and F is the magnitude of the Earth's magnetic field (in tesla) at a given location in the same sense as the B-field (flux density).

It is also very important to consider that not only may J_r exceed J_i, but the direction of remanent magnetisation may be quite different from that of the ambient induced field at a location. Consequently, the resultant magnetisation (i.e. the vectorial sum of the remanent and induced magnetisations) will give rise to characteristic magnetic anomalies (refer back to Figure 3.3) when reversely magnetised rocks are present.

3.4 THE EARTH'S MAGNETIC FIELD

3.4.1 Components of the Earth's magnetic field

The geomagnetic field at or near the surface of the Earth originates largely from within and around the Earth's core. Currents external to the Earth in the ionosphere and magnetosphere associated with the Van Allen radiation belts (Figure 3.8), currents induced in the Earth by external field variations and the permanent (remanent) and steady-state induced magnetisations of crustal rocks, also contribute to the overall geomagnetic field. The magnetosphere is vital for the survival of life on Earth as it forms the primary force field which protects the planet from harmful radiation from the Sun. The various components of the geomagnetic field affect exploration surveys in a variety of ways which will be discussed in turn.

3.4.1.1 The main dipole field

The main component of the geomagnetic field is called the *dipolar field* as it behaves, to a first-order approximation, like a dipolar electromagnet located at the centre of the Earth but inclined at 11.5° to the rotational axis (Figure 3.9).

The *geomagnetic poles*, the positions on the Earth's surface through which the axis of the best-fitting dipole passes – which are located in Hayes Peninsula in northern Greenland and near the Russian Vostok research station in Greater Antarctica – are not the same as the

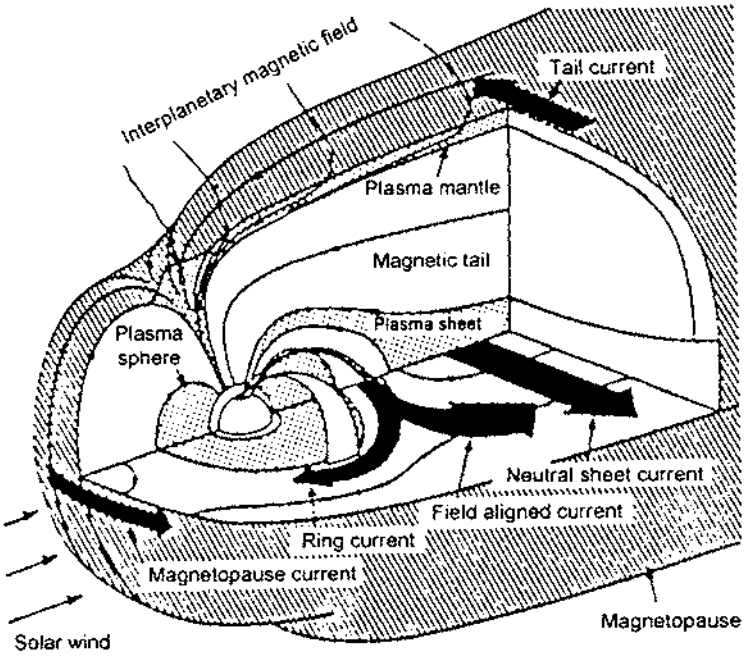

Figure 3.8 The geomagnetic field showing the magnetosphere, magnetopause and Van Allen radiation belts. From James (1990), by permission

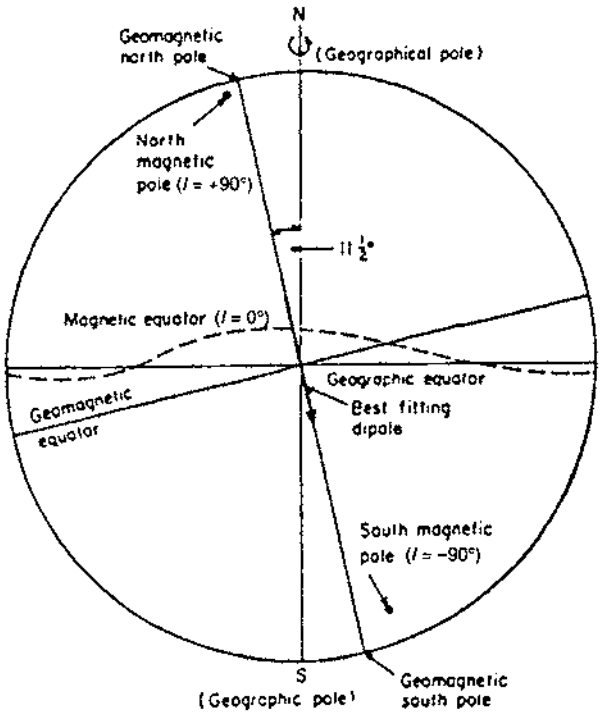

Figure 3.9 The field due to an inclined geocentric dipole. From McElhinny (1973), by permission

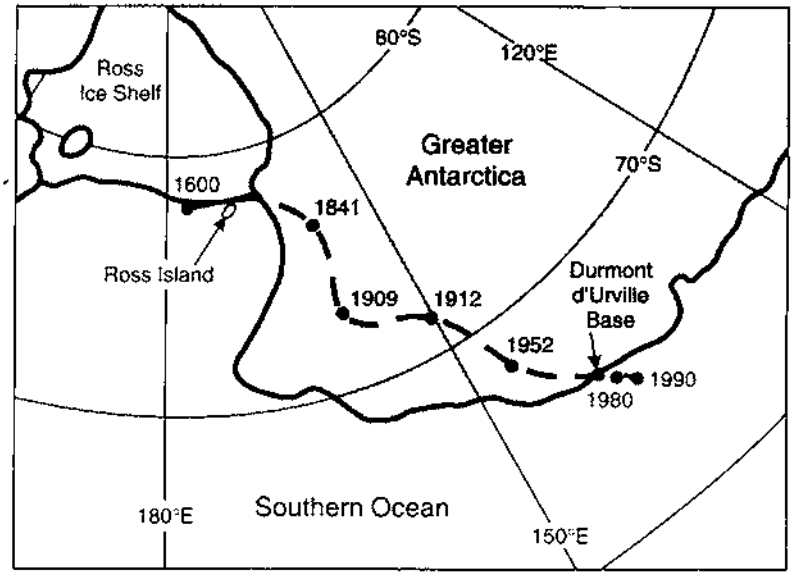

Figure 3.10 Location of the south magnetic pole and its drift since the year 1600

magnetic or *dip poles*. These are located where the magnetic field is directed vertically. The north magnetic pole is currently just north of Bathurst Island in the Canadian Arctic Archipelago and was discovered on 1 June 1831 by James Clark Ross and his uncle Sir John Ross. The south magnetic pole is currently about 150 km offshore from the French Research Station Durmont d'Urville on the Adélie Coast of Greater Antarctica. James Ross came extremely close to locating the south magnetic pole in 1841 but as it was then inland (Figure 3.10) he was thwarted by icebergs and the land ice. It was only on 15 January 1909 that Alistair Mackay, Edgeworth David and Douglas Mawson reached the south magnetic pole after an epic sledge journey from their base on Ross Island.

The geomagnetic field is produced by electric currents induced within the conductive liquid outer core as a result of slow convective movements within it (Figure 3.11). It is for this reason that the analogy of the Earth's field to that induced by an electromagnet is preferred to that of a permanently magnetised bar magnet. The liquid core behaves as a geodynamo but the precise nature of the processes involved has yet to be resolved. Models to explain the disposition of the magnetic field must also account for the slow but progressive change in field intensity and westward drift in direction known as the *secular variation*. Furthermore, the model must also explain how the Earth's magnetic field goes through reversals of magnetic polarity. The study of how the Earth's magnetic field has changed through geological time is known as *palaeomagnetism*. The use of magnetic reversals to provide global chronometric calibration of geological events is known as *magnetostratigraphy* (Tauxe, 1990).

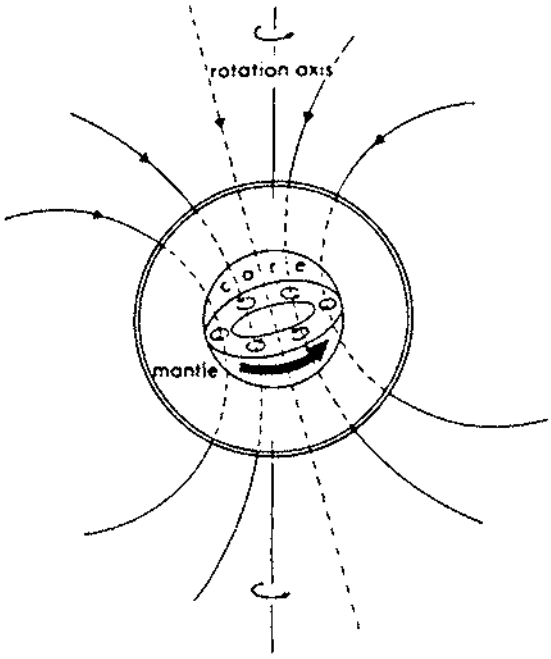

Figure 3.11 Schematic of the cause of the majority of the Earth's magnetic field. From Sharma (1986), by permission

The geomagnetic field can be described in terms of the declination, D, inclination, I, and the total force vector $\boldsymbol{F}$ (Figure 3.12). A freely suspended magnetised needle will align itself along the $\boldsymbol{F}$ vector so that at the magnetic (dip) north, the inclination is 90°; i.e. the needle will point vertically downwards. At the south magnetic (dip) pole, the needle will point vertically upwards. At the magnetic equator, the needle will lie horizontally (Figure 3.13). Furthermore, the vertical component of the magnetic intensity of the Earth's magnetic field varies with latitude, from a minimum of around 30 000 nT at the magnetic equator to 60 000 nT at the magnetic poles.

3.4.1.2 The non-dipolar field

While the single dipole field approximates to the Earth's observed magnetic field, there is a significant difference between them, which is known as the *non-dipole field*. The total intensity for the non-dipole field is shown in Figure 3.14, from which several large-scale features can be seen with dimensions of the order of several thousand kilometres and with amplitudes up to 20 000 nT, about one-third of the Earth's total field. Using the method of spherical harmonic analysis, it can be demonstrated that the non-dipole field and the associated large-scale features can be represented by a fictitious set of 8–12 small dipoles radially located close to the liquid core. These dipoles serve to simulate the eddy currents associated with the processes within the liquid core.

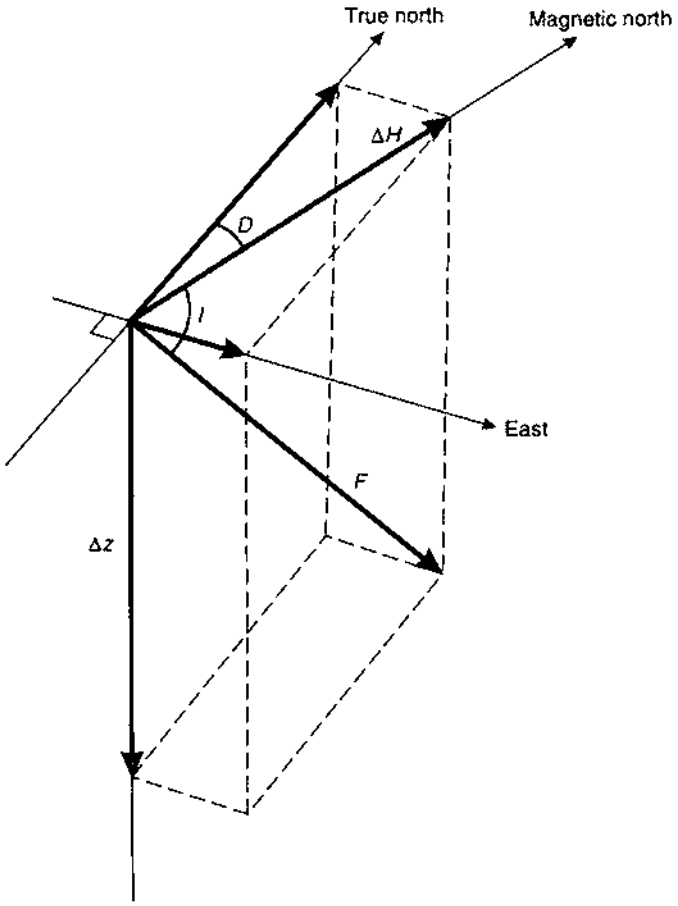

Figure 3.12 Elements of the magnetic field: inclination I, declination D, and total magnetic force F

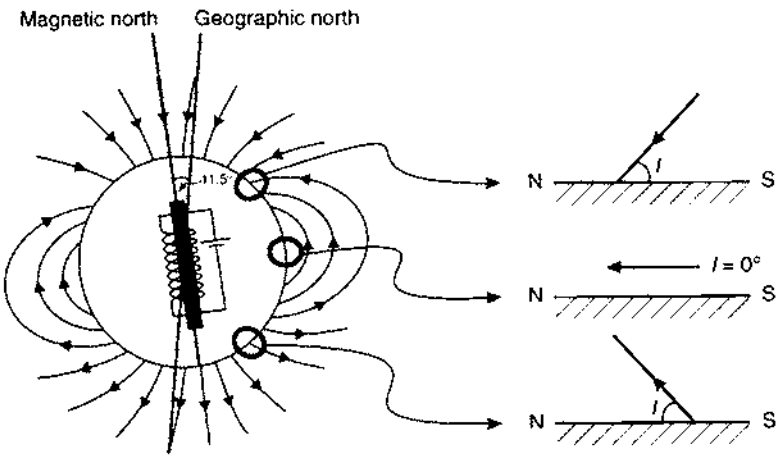

Figure 3.13 Variation of inclination with latitude

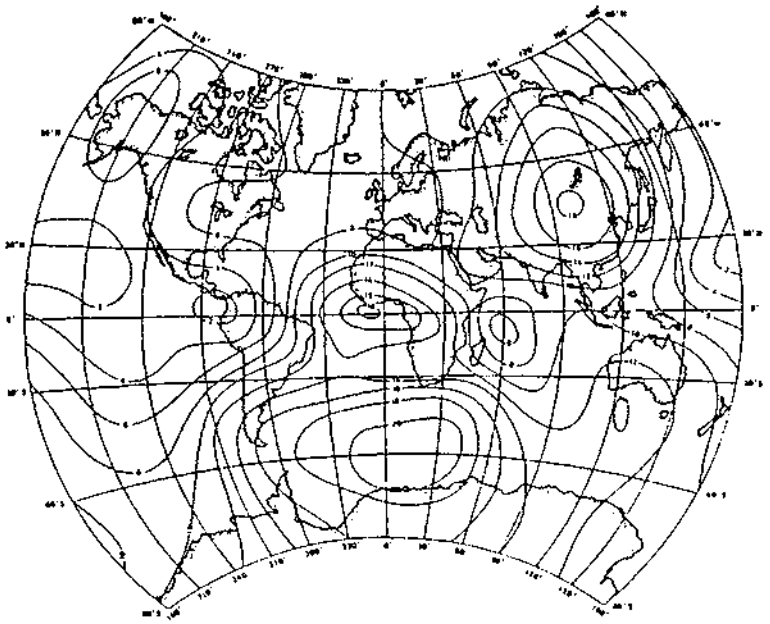

Figure 3.14 Variation in the intensity of the non-dipole field for epoch 1980. From Sharma (1986), by permission

A further use of the spherical harmonic analysis is that it provides a means whereby the spatial distribution and intensity of the total magnetic field can be calculated for the whole globe. The total field, which is calculated every five years, is called the *International Geomagnetic Reference Field* (IGRF) and the year of calculation is known as the *epoch*. It has to be recalculated regularly because of the secular variation (see, for example, IAGA (1987) and Peddie (1982)). Consequently, it is possible to obtain a theoretical value for the field strength of the Earth's magnetic field for any location on Earth (Figure 3.15). It can be seen from this figure that instead of the anticipated two maxima consistent with a truly dipolar field, there are in fact four maxima. The significance of the IGRF in processing magnetic data is discussed in Section 3.6.3.

Data used in the computation of revisions of the International Geomagnetic Reference Field have been obtained by satellite (e.g. during 1965–71, Polar Orbiting Geophysical Observatory series, POGO; October 1979 to June 1980, MAGSAT). However, at satellite orbit ranges, perturbations in the earth's magnetic field caused by magnetic materials in the crust are not resolvable. Surface or airborne measurements can detect considerable high-amplitude small-scale features within the crust down to a depth of 25–30 km where the Curie isotherm is reached. These features may be caused by induction due to the Earth's field or remanent magnetisation or a mixture of both.

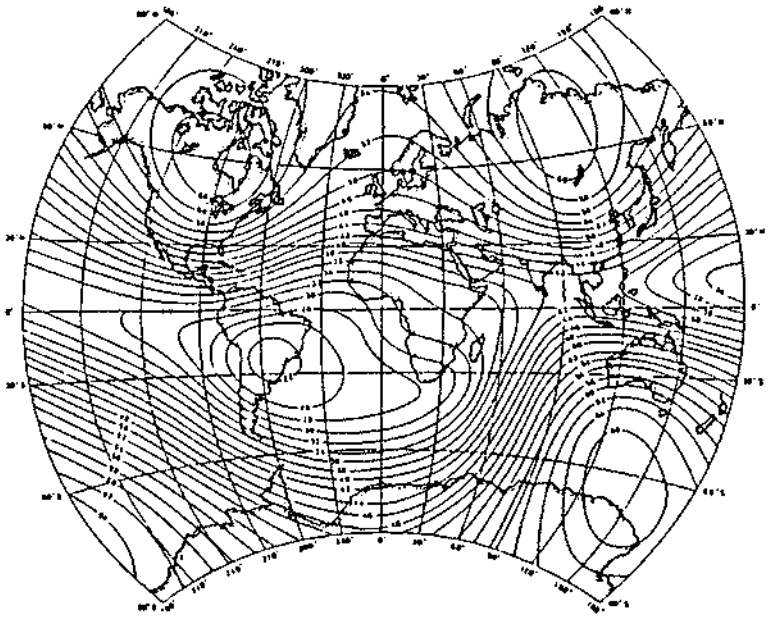

Figure 3.15 Total field intensity derived using the IGRF epoch 1980. From Sharma (1986), by permission

3.4.2 Time variable field

Observations of the Earth's magnetic field have been made for over four centuries at London and Paris. From these data, it is clear that the geomagnetic and magnetic pole positions drift with time, known as the secular variation in the magnetic field (Figure 3.16). In addition, the intensity of the main magnetic field is decreasing at about 5% per century. These rates of change, although very significant on a geological time scale, do not affect data acquisition on a typical exploration survey unless it covers large geographical areas and takes many months to complete, or if such surveys are being used to compare with historical data.

The Earth's magnetic field changes over a daily period, the *diurnal variations*. These are caused by changes in the strength and direction of currents in the ionosphere. On a magnetically 'quiet' (Q) day, the changes are smooth and are on average around 50 nT but with maximum amplitudes up to 200 nT at the geomagnetic equator. The changes are least during the night when the background is almost constant, and decrease in amplitude from dawn to midday whereupon they increase to the daily maximum about mid-late afternoon before settling down to the night-time value.

Magnetically disturbed (D) days are marked by a rapid onset of fluctuations of the order of hundreds of nanoteslas followed by slower but still erratic fluctuations with decreasing amplitude. These

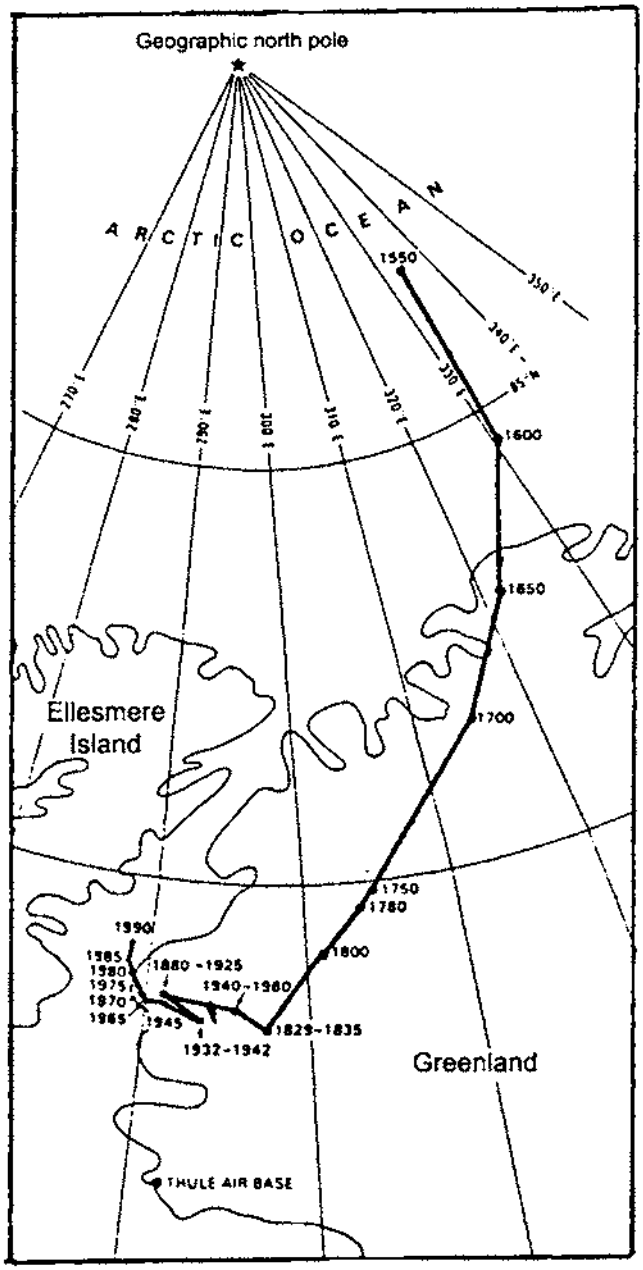

Figure 3.16 Drift of the north magnetic pole position from 1550 to 1990. From James (1990), by permission

disturbances, which are called *magnetic storms*, may persist for several hours or even days. Such frenetic magnetic activity is caused by sunspot and solar activity resulting in solar-charged particles entering the ionosphere. This may happen on fine sunny days and not necessarily in stormy weather. Magnetic observatories around the

world provide an advance warning service to advise of the probability of magnetic storm activity. In severe storms, all magnetic surveying has to stop as it is not practicable to correct for such extreme fluctuations. In minor disturbances, if a continuous-reading base station magnetometer is used, the diurnal variations can be corrected. In aeromagnetic surveys, it is necessary to specify contractually what constitutes a magnetic storm. Survey data adversely affected by magnetic disturbances may have to be reflown and this obviously has cost implications. Practical details of how to correct for diurnal variations are given in Section 3.6.2.

3.5 MAGNETIC INSTRUMENTS

The earliest known device which responded to the Earth's magnetic field was a magnetised spoon used by Chinese geomancers (diviners) in the first century AD. Compass needles were introduced for navigation around the year 1000 in China and in Europe about 200 years later. The first accurate measurement of the inclination of the Earth's field was made at Radcliffe in London in 1576 by Robert Norman. He described his instruments and collected data in his book *The Newe Attractive* (1581), which was the first book ever to be devoted to geomagnetism.

Magnetometers used specifically in geophysical exploration can be classified into three groups: the torsion (and balance), fluxgate and resonance types, of which the last two have now completely superseded the first. Torsion magnetometers are still in use at 75% of geomagnetic observatories, particularly for the measurement of declination. Magnetometers measure horizontal and/or vertical components of the magnetic field (F_h and F_z respectively) or the total field F_t (see Figure 3.12).

3.5.1 Torsion and balance magnetometers

Historically the first to be devised (1640), these comprise in essence a magnetic needle suspended on a wire (torsion type) or balanced on a pivot. In the Earth's magnetic field the magnet adopts an equilibrium position. If the device is taken to another location where the Earth's magnetic field is different from that at the base station, or if the magnetic field changes at the base station, the magnet will align itself to the new field and the deflection from the rest position is taken as a measure of the Earth's magnetic field. The Swedish mine compass, Hotchkiss superdip, and Thalén-Tiberg magnetometer are all early examples of this type of device. In 1915, Adolf Schmidt devised his variometer in which a magnetic beam was asymmetrically balanced on an agate knife edge (Figure 3.17) and zeroed at a base station.

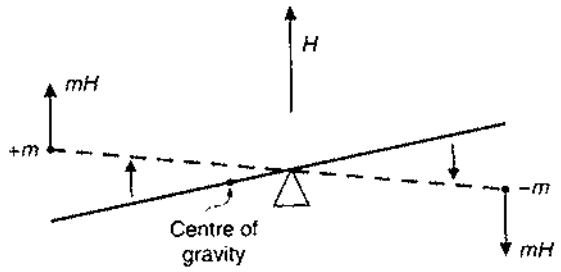

Figure 3.17 Basic principle of operation of a torsion or balance-type magnetometer

Deflections from the rest position at other locations were then read using a collimating telescope. To be used it had to be orientated at right-angles to the magnetic meridian so as to remove the horizontal component of the Earth's field. The device was calibrated using Helmholtz coils so that the magnitude of the deflection was a measure of the vertical component of the field strength.

A development of the Schmidt variometer was the compensation variometer. This measured the force required to restore the beam to the rest position. In exploration work, the greatest precision with a balance magnetometer was only 10 nT at best. For further details of these devices, see the descriptions by Telford *et al.* (1990).

3.5.2 Fluxgate magnetometers

The fluxgate magnetometer was developed during the Second World War to detect submarines. It consists of two parallel cores made out of high-permeability ferromagnetic material. Primary coils are wound around these cores in series but in opposite directions (Figure 3.18). Secondary coils are also wound around the cores but in the opposite sense to the respective primary coil. A current alternating at 50

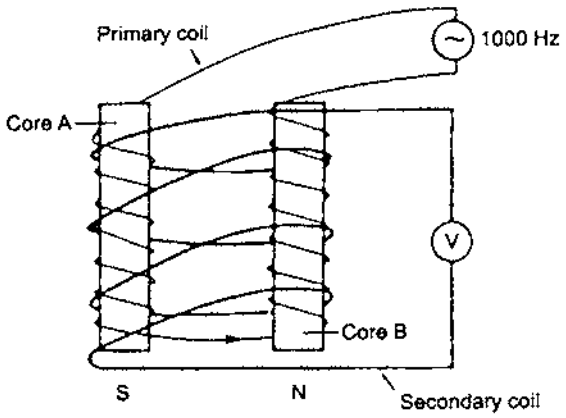

Figure 3.18 Basic operating principle of the fluxgate magnetometer

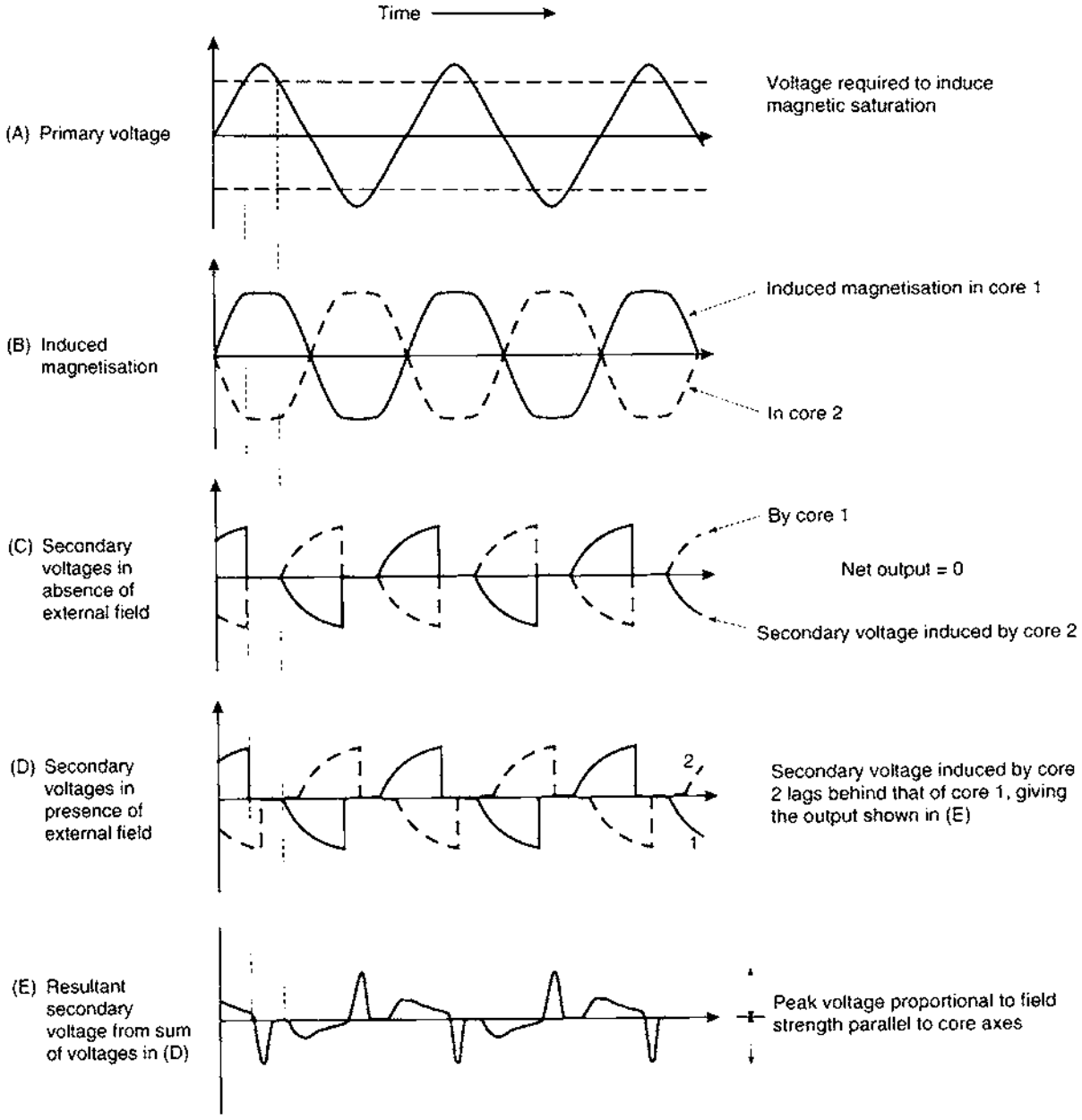

Figure 3.19 Response characteristics of primary and secondary circuits in a fluxgate magnetometer

1000 Hz (Figure 3.19A) is passed through the primary coils which drives each core through a B H hysteresis loop (cf. Figure 3.6) to saturation at every half-cycle (Figure 3.19B) in the absence of an external field, so inducing a magnetic field in each core. The generated alternating magnetic field induces an in-phase voltage within the secondary coils. This voltage reaches its maximum when the rate of

change of the magnetic field is fastest (Figure 3.19C). As the coils are wound in opposing directions around the two cores, the secondary voltages are in phase but have opposite polarity (Figure 3.19C) so that the sum of the two voltages is at all times zero. However, when the cores are placed in the Earth's magnetic field, a component of that field will be parallel to the orientation of the cores. Consequently, the core whose primary field is reinforced by the ambient external field will reach saturation earlier than the other core whose magnetic field is opposed by the external field. This has the effect of shifting the phases of the secondary voltages (Figure 3.19D) so that the sum of the two secondary voltages is now non-zero (Figure 3.19E). The peak amplitude of the pulsed output of the combined secondary coils is proportional to the magnitude of the external field component (Primdahl 1979).

The fluxgate magnetometer can be used to measure specific magnetic components with the same attitude as the sensor cores. As the fluxgate magnetometer is relatively insensitive to magnetic field gradients, it has the advantage that it can be used in areas where very steep gradients would militate against the use of resonance-type devices which are affected. Some portable fluxgate magnetometers suffer from temperature effects owing to inadequate thermal insulation, which can reduce the resolution to only $\pm$ 10 to 20 nT, this being inadequate for ground exploration surveys. They are used quite widely in airborne surveys where better thermal insulation can be ensured and additional devices can be used to aid the consistent orientation of the sensor cores. In such cases, an accuracy to within $\pm$ 1 nT can be achieved. In addition, fluxgate instruments can provide a continuous output which is another advantage for airborne applications. Fluxgate magnetometers can also be used in down-hole logging applications in mineral exploration.

3.5.3 Resonance magnetometers

There are two main types of resonance magnetometer: the *proton free-precession magnetometer*, which is the best known, and the *alkali vapour magnetometer*. Both types monitor the precession of atomic particles in an ambient magnetic field to provide an absolute measure of the total magnetic field, $\boldsymbol{F}$.

The proton magnetometer has a sensor which consists of a bottle containing a proton-rich liquid, usually water or kerosene, around which a coil is wrapped, connected to the measuring apparatus (Figure 3.20). Each proton has a magnetic moment $\boldsymbol{M}$ and, as it is always in motion, it also possesses an angular momentum $\boldsymbol{G}$, rather like a spinning top. In an ambient magnetic field such as the Earth's ($\boldsymbol{F}$), the majority of the protons align themselves parallel with this field with the remainder orientated antiparallel (Figure 3.21A). Consequently, the volume of proton-rich liquid

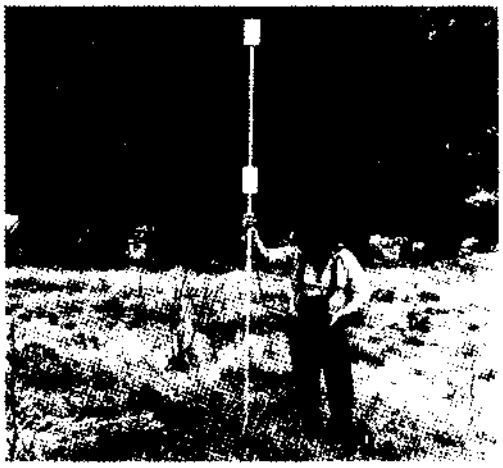

(A)

(B)

Figure 3.20 (A) A nuclear proton precession magnetometer in use, and (B) a caesium vapour magnetometer. Courtesy of Geometrics

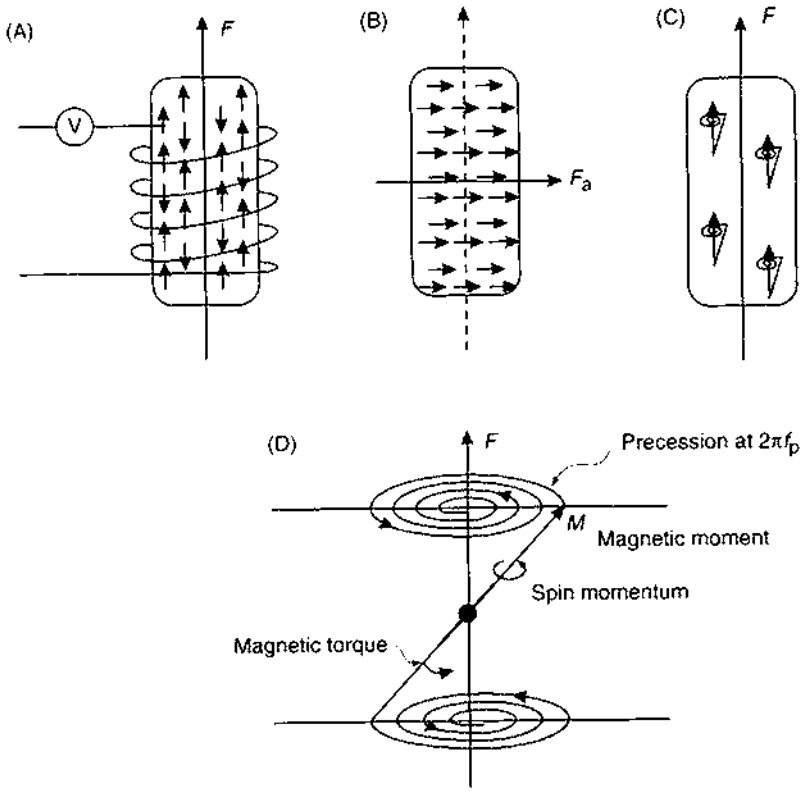

Figure 3.21 Basic operating principles of a proton magnetometer. After Kearey and Brooks (1991), by permission

acquires a net magnetic moment in the direction of the ambient field ($\boldsymbol{F}$).

A current is applied to the coil surrounding the liquid, generating a magnetic field about 50 to 100 times stronger than, and at right-angles to, the Earth's field. The protons align themselves to the new magnetic direction (Figure 3.21B). When the applied field is switched off, the protons precess around the pre-existent ambient field $\boldsymbol{F}$ (Figure 3.21C) at the *Larmor precession frequency* (f_p) which is proportional to the magnetic field strength $\boldsymbol{F}$ (Box 3.6). As protons are charged particles, as they precess they induce an alternating voltage at the same frequency as f_p into the coil surrounding the sensor bottle. Interaction between adjacent protons causes the precession to decay within 2–3 seconds, which is sufficient time to measure the precession frequency. To obtain a value of $\boldsymbol{F}$ to within ± 0.1 nT, frequency must be measured to within ± 0.004 Hz, which is quite easily achieved. This resolution is equivalent to 1 part in 10^6, which is 100 times less sensitive than in gravity measurements.

Box 3.6 Magnetic field strength, F, and precession frequency, f_p

$$F = 2\pi f_p/\Phi_p$$

where Φ_p is the gyromagnetic ratio of the proton, which is the ratio of the magnetic moment and spin angular momentum (see Figure 3.21); and

$$\Phi_p = 0.26753 \text{ Hz/nT and } 2\pi/\Phi_p = 23.4859 \text{ nT/Hz}.$$

Thus:

$$F = 23.4859 f_p.$$

For example, for $F = 50\,000$ nT, $f_p = 2128.94$ Hz.

One of the limiting factors of the proton magnetometer is that its accuracy is reduced in areas of high magnetic gradient. As the sensor bottle is of the order of 15 cm long, a strong field gradient of 500 nT/m, for example, means that there is a 75 nT difference in field strength between the top and bottom of the sensor and the rate of damping is increased. The accuracy of measurement of the precession frequency is thus reduced. As a guide, if the gradient is 400 nT/m, the precision is at best 1 nT; for 200 nT/m it is 0.5 nT.

As the precession frequency is only a function of field strength, there is no need to orientate the field sensor. Modern proton magnetometers give a direct readout of the field strength in nanoteslas and data can be automatically output into a datalogger for subsequent downloading into a computer.

Proton magnetometers are used extensively not only in land surveys but also at sea and in airborne investigations. In marine surveys, the magnetometer sensor bottle, which is located in a sealed unit called a 'fish', is deployed two or three ship's lengths astern so as to be sufficiently removed from magnetic interference from the ship. In the case of aircraft, two techniques are used. One is to tow the sensor bottle at least 30 m below and behind the aircraft in what is called a 'bird', or place it in a non-magnetic boom called a 'stinger' on the nose, on the tail fin or on a wingtip of the aircraft. In the fixed mode, special magnetic compensation measures can be taken to annul the magnetisation of the aircraft; the excellence of the compensation is called the *figure of merit* (FOM) rating. The fitting of active compensation systems in modern aircraft has improved FOM values and reduced the time taken for compensation, and so helped to improve the cost-effectiveness of airborne surveys. In addition to ground, marine and airborne applications, proton magnetometers can be deployed down boreholes, and can be particularly useful in mineral exploration programmes.

A limitation on proton magnetometers, particularly in airborne surveys, is the rate at which measurements can be made. As the proton

precession and measurement take a finite time (of the order of a second or longer), continuous readings are not possible and this can be restricting in some situations.

One manufacturer (GEM Systems Inc.) has produced a modified precession instrument that utilises the Overhauser Effect. An electron-rich fluid containing free radicals is added to a standard hydrogen-rich liquid. The combination increases the polarisation by a factor of 5000 in comparison with standard liquids. Overhauser proton precession uses a radio-frequency (RF) magnetic field and so needs only minimal power, in contrast with high-power direct current fields used in traditional proton precession magnetometers. Polarisation and magnetisation can occur simultaneously and thus rapid sampling of the total field strength (two readings per second) can be achieved.

The second type of resonance magnetometer is the *alkali vapour magnetometer* or *optical absorption magnetometer*, which utilises the optical pumping technique (Bloom 1962). The principle on which this method is based is illustrated in Figure 3.22. Under normal conditions of temperature and pressure, electrons exist at certain energy states (A and B) around the nucleus of the atom. According to quantum physics, it is only possible to transfer an electron from a lower energy state (A) to one with higher energy (B) in discrete jumps. If a vapour of an element such as rubidium or caesium is illuminated by a light whose filament is made of the same element, the light emitted is at the correct wavelength for incident photons to be absorbed by the vapour and the low-energy state electrons excited up to higher levels. If the incident light is circularly polarised, only electrons in the A_1 orbit will be excited or 'optically pumped' up to the B orbit. At this point, the excess photons will be transmitted through the excited vapour and will be detected by the photocell as an increase in light intensity.

A small alternating current is passed through a coil at a frequency of between 90 and 300 kHz to induce a magnetic field around the

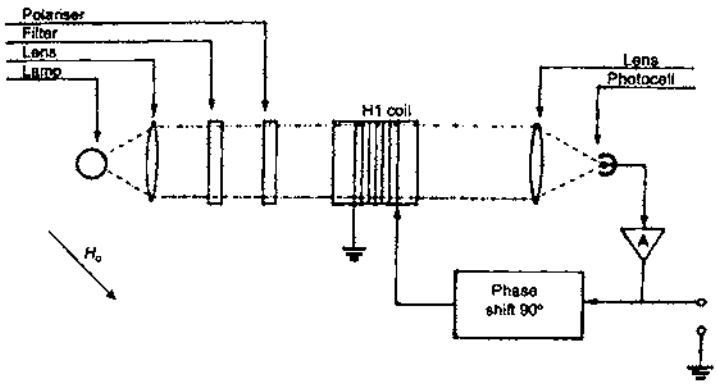

Figure 3.22 Optical pumping – principle of the alkali vapour magnetometer. From James (1990), by permission

alkali vapour cell. The frequency is tuned until it is locked into the Larmor frequency for the alkali vapour concerned. This small magnetic field energises some electrons back into their vacant A ground states. The consequence of this is that the light intensity at the photocell diminishes as photons are absorbed by the alkali vapour in the cell until saturation is reached again. Photons will continue to be absorbed until all the available electrons have been excited to the B state, when the light at the photocell will again be at its most intense. Consequently, the cycled optical pumping produces a light at the photocell that flickers at the Larmor precession frequency, which can easily be measured. As the precession frequency is dependent upon the ambient field strength of the Earth (see Box 3.6), the total field strength can be determined from a measurement of the precession frequency. The factor $2\pi/\Phi_p$ is approximately equal to 0.2141 and 0.1429 nT/Hz for rubidium and sodium respectively, which give corresponding precession frequencies of 233.5 and 350 kHz in a field of 50 000 nT. As long as the light beam axis is not parallel or antiparallel to the Earth's magnetic field (when no signals would be produced), the precession frequency can be measured with sufficient accuracy so that the magnetic field strength can be determined to within ± 0.01 nT. The measurement time is extremely small, and so alkali vapour magnetometers can be used as virtually continuous reading instruments, which makes them ideally suited to airborne surveys.

For land-based archaeological or environmental geophysical applications, self-oscillating split-beam caesium vapour magnetometers have been developed, largely from military ordnance detection instruments (e.g. the Geometrics G-822L magnetometer). Sampling rates of up to 10 readings per second are possible with a sensitivity of 0.1 nT.

3.5.4 Cryogenic (SQUID) magnetometers

The most sensitive magnetometer available is the cryogenic magnetometer which operates using processes associated with superconductivity, details of which have been given by Goree and Fuller (1976). These magnetometers are perhaps better known as *SQUID* (Superconducting QUantum Interference Device) magnetometers. Used extensively in palaeomagnetic laboratories, the SQUID magnetometer has also been developed for use in aeromagnetic surveying since the early 1980s, particularly as a gradiometer. SQUIDs can have a measurement sensitivity of 10^{-5} nT/m; this means that two sensors need only be placed 25 cm or less apart, thus making it possible to have the entire sensor system in a very small space. This has great advantages in mounting the equipment in aircraft, in borehole probes and in submarine devices where space is at a premium. Measurement accuracy of the total field strength is within ± 0.01 nT.

Technical difficulties over the use of liquid helium, which has to be maintained at a temperature of 4.2 K for superconductivity to occur, limit the widespread deployment of SQUID magnetometers. They are rarely, if ever, used in surface magnetic measurements.

3.5.5 Gradiometers

A gradiometer measures the difference in the total magnetic field strength between two identical magnetometers separated by a small distance. In airborne work, typical separations between sensors is 2 m to 5 m for stingers (Figure 3.23) and up to 30 m for birds. In ground instruments, a separation of 0.5 m is common. The magnetic field gradient is expressed in units of nT/m and taken to apply at the mid-point between the sensors. A major advantage of gradiometers is that because they take differential measurements, no correction for diurnal variation is necessary as both sensors will be equally affected. As gradiometers measure the vertical magnetic gradient, noise effects from long-wavelength features are suppressed and anomalies from shallow sources are emphasised. For detailed high-resolution surveys exploring for mineral targets, magnetic gradiometry is the preferred method (Hood 1981).

Fluxgate and resonance-type magnetometers are commonly used in ground surveys. Where continuous-reading devices are required, such as when automatic datalogging is being used, fluxgate gradiometers are preferable (e.g. Sowerbutts and Mason 1984). A detailed although dated comparison of the different types of gradiometers and magnetometers has been made by Hood *et al.* (1979).

Self-oscillating split-beam caesium vapour gradiometers have also been developed for small-scale land-based surveys, such as Geomet-

Figure 3.23 Eurocopter AS315 about to lift a 3-axis magnetic gradiometer system. Courtesy of Aerodat Inc., Canada

rics Inc.'s G-858 instrument. These instruments can sample at up to 10 readings per second with a sensitivity of 0.05 nT. An additional feature of this particular instrument is that it can be connected to a Differential Global Positioning System for the simultaneous logging of position and magnetic data. The system was first tested at Stanford University, USA, in March 1993. As with any geophysical instruments, it is always best to check with equipment manufacturers for the latest technical specifications.

3.6 MAGNETIC SURVEYING

3.6.1 Field survey procedures

As with every geophysical survey, the keeping of detailed and accurate field notes cannot be emphasised too strongly, even if dataloggers or memory-magnetometers are used. Orderly record-keeping permits more efficient and accurate data processing. Practical details of how magnetic surveys should be undertaken have been given by Milsom (1989).

In the vast majority of cases where the magnetic targets have a substantial strike length, survey profiles should, where possible, be conducted across strike with tie-lines along strike. In cases such as some archeological and engineering site investigations where the targets are more equidimensional, such as the ruins of a Roman villa or a brick-lined mineshaft, north south and east–west orientations are commonly used.

In ground-based surveys, it is important to establish a local base station in an area away from suspected magnetic targets or magnetic noise and where the local field gradient is relatively flat. A base station should be quick and easy to relocate and re-occupy. The precise approach to the survey will depend on the type of equipment. If a manual push-button proton magnetometer is deployed, the exact time of occupation of each station is needed and at least three readings of the total field strength should be recorded. Each of the three values should be within ± 1 or 2 nanoteslas; an average of these three readings is then calculated. As the survey progresses, the base station must be re-occupied every half or three-quarters of an hour in order to compile a diurnal variation curve for later correction (see next section). Next to each data entry, where required, should be any comments about the terrain or other factors that may be considered to be important or relevant to subsequent data processing and interpretation.

If a continuous-reading base-station magnetometer is used to measure the diurnal variation, it is still worth returning to base every 2–3 hours, just in case the base magnetometer fails.

When dataloggers or memory magnetometers are used, regular checks on the recording of data are vital. It is all very well occupying

hundreds of stations and taking perhaps several thousand measurements only to find that the logger is not functioning or the memory has been corrupted.

One golden rule is always to check your data as they are collected and at the end of each survey day. This serves two purposes. First, it provides a data quality check and allows the operator to alter the survey in response to the magnetic values measured. For example, if a 50 m station interval was selected at the outset and the field values indicate a rapid change over a much shorter interval, the separation between stations must be reduced in order to collect enough data to image the magnetic anomaly. Secondly, it provides a check on the consistency of the data. Odd anomalous values may indicate something of geologic interest which may need to be followed up, or may highlight human error. In either case, the next day's survey can take this into account and measurements can be made to check out the oddball values.

In the case of aeromagnetic or ship-borne surveys, the specifications are often agreed contractually before an investigation begins. Even so, there are guidelines as to what constitutes an adequate line separation or flying height, orientation of survey line, and so on. As an example, Reid (1980) compiled a set of criteria based on avoidance of spatial aliasing (Tables 3.5 and 3.6). For example, if a mean flying height over magnetic basement (h) of 500 m is used with a flight line spacing (δx) of 2 km, then $h/\delta x = 0.5/2 = 0.25$, which would indicate that 21% aliasing would occur in measurements of the total field and

Table 3.5 Degree of aliasing (Reid 1980)

$h/\delta x$	F_T	F_G
0.25	21	79
0.5	4.3	39
1	0.19	5
2	0.0003	0.03
4	0	0

F_T and F_G are the aliased power fraction (per cent) expected from surveys of total field and vertical gradient respectively

Table 3.6 Maximum line spacings (Reid 1980)

Survey type	Intended use	δx_{max}
Total field	Contour map	$2h$
Total field	Computation of gradient, etc., maps	h
Vertical gradient	Gradient contour maps	h
Total field	Modelling of single anomalies	$h/2$

as much as 79% if the vertical magnetic gradient were being measured (Table 3.5). Neither value is acceptable. The larger the value of $h/\delta x$, the less aliasing will occur; a survey is considered reasonably designed if $h/\delta x \geqslant 0.5$, depending on survey type. At this minimum value, about 5% maximum aliasing is acceptable if contouring is to be undertaken on total field data. Other maximum flight line spacings are given in Table 3.6. There have been examples of commercially flown surveys in Egypt, for instance, where the flying height was 400 m above ground, but with 1 km thickness of sedimentary cover over magnetic basement (hence $h = 1.4$ km) and the line spacing was 21 km. This gives a value of $h/\delta x \approx 0.07$, resulting in more than 65% aliasing. The contour maps of these surveys, which covered thousands of square kilometers, are virtually useless. To have been contoured adequately, the flight line spacing for data acquired at a flying height of 1.4 km above basement should have been no more than 2.8 km; i.e. from Table 3.6, $\delta x \leqslant 2h$.

The choice of survey parameters will also affect the success (or otherwise) of subsequent computer contouring. These guidelines can also apply to surface surveys using a proton magnetometer where $h = 3$ m (1 m of overburden over a magnetic target, plus 2 m for the magnetometer sensor pole) for example. In this case, an acceptable maximum line spacing would be 6 m if a contour map of the total field were required. Survey design parameters and automated contouring have been described briefly in Chapter 1 and in detail by Hood *et al.* (1979) and by Reid (1980).

3.6.2 Noise and corrections

All magnetic data sets contain elements of noise and will require some form of correction to the raw data to remove all contributions to the observed magnetic field other than those caused by sub-surface magnetic sources. In ground magnetometer surveys, it is always advisable to keep any magnetic objects (keys, penknives, some wristwatches, etc.), which may cause *magnetic noise*, away from the sensor. Geological hammers put next to the sensor bottle of a proton magnetometer will have a significant effect, as demonstrated by students trying to simulate a magnetic storm so that they could abandon the survey and retire to the nearest hostelry! It is also essential to keep the sensor away from obviously magnetic objects such as cars, metal sheds, power lines, metal pipes, electrified railway lines, walls made of mafic rocks, etc.

The most significant correction is for the *diurnal variation* in the Earth's magnetic field. Base station readings taken over the period of a survey facilitate the compilation of the diurnal 'drift' as illustrated in Figure 3.24. Measurements of the total field made at other stations can easily be adjusted by the variation in the diurnal curve. For example, at point A in Figure 3.24, the ambient field has increased by

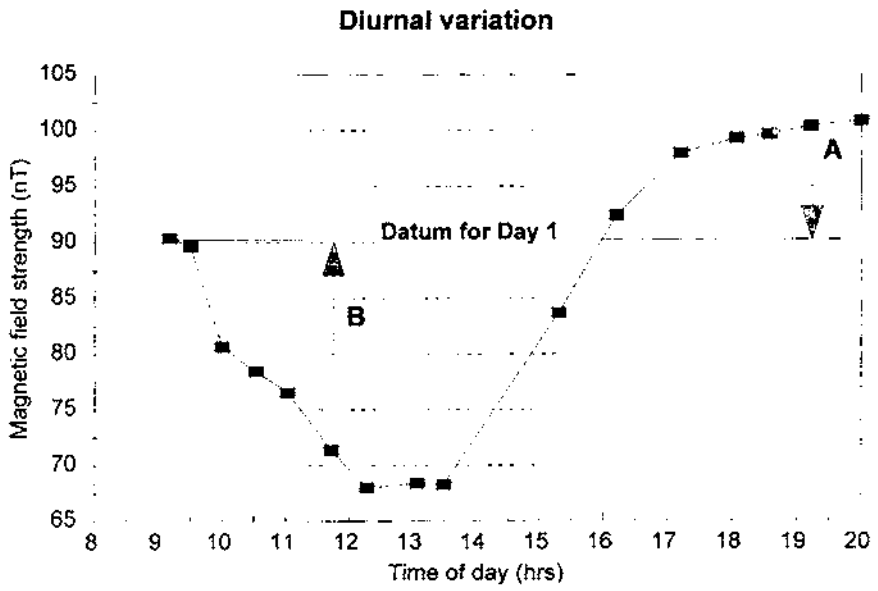

Figure 3.24 Diurnal drift curve measured using a proton magnetometer

10 nT and thus the value measured at A should be reduced by 10 nT. Similarly, at B, the ambient field has fallen by 19 nT and so the value at B should be increased by 19 nT. Further details of diurnal corrections have been given by Milsom (1989). Gradiometer data do not need to be adjusted as both sensors are affected simultaneously and the gradient remains the same between them.

In airborne and shipborne surveys, it is obviously not possible to return to a base station frequently. By designing the survey so that the track lines intersect (Figure 3.25), the dataset can be appropriately corrected. Some surveys use profiles and tie-lines at the same spacing to give a regular grid. Other surveys have tie-lines at 10 times the inter-profile line spacing. In addition to checking on diurnal variations, tie-lines also serve as a useful control on navigational and measurement accuracy. A flow chart depicting the reduction of aeromagnetic data is given in Figure 3.26. In regional surveys, a further tie is to a local Geomagnetic Observatory, if there is one within 150 km, at which all the magnetic components are measured and which can provide diurnal variations. It would then have to be demonstrated that the curve obtained from the observatory applied in the survey area.

The degree of data processing is dependent upon the resolution required in the final dataset. For a broad reconnaissance survey, a coarser survey with lower resolution, say several nanoteslas, may be

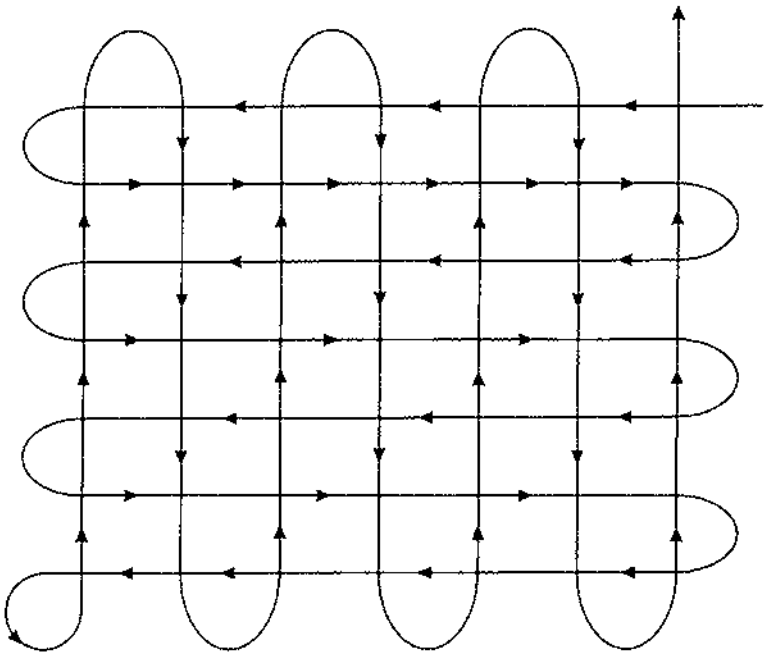

Figure 3.25 Tracks of a shipborne or airborne magnetic survey. Some surveys, rather than having equal spacings between all tracks, have tie-lines at 10 times the normal interline spacing

all that is required. In detailed surveys, however, an accuracy to within 0.1 nT will need a finer survey grid, more accurate position-fixing and diurnal drift corrections.

Rarely, a *terrain correction* may need to be applied when the ground over which a survey is conducted is both magnetic and topographically rough. Unlike the gravity case where terrain corrections, though laborious, are relatively easy to calculate, corrections for terrain for magnetic data are extremely complex. If the rough terrain is made up largely of low-susceptibility sedimentary rocks, there will be little or no distortion of the Earth's magnetic field. However, if the rocks have a significant susceptibility, a terrain factor may have to be applied. Anomalous readings as large as 700 nT have been reported by Gupta and Fitzpatrick (1971) for a 10 m high ridge of material with susceptibility $\kappa \approx 0.01$ (SI). Furthermore, magnetic readings taken in a gulley whose walls are made of basic igneous rocks will be anomalous owing to the magnetic effects of the rocks above the magnetic sensor. Considerable computational effort (see Sharma, 1986, appendix C) then has to be applied to correct the data so that they are interpretable. Similar geometric effects can also occur in radiometric surveys.

Another way of correcting for the effect of topography, or of reducing the data to a different reference plane, is by *upward continuation*. This permits data acquired at a lower level (e.g. on the ground) to be processed so that they can be compared with airborne surveys. The effect of this is to lessen the effects of short-wavelength high-

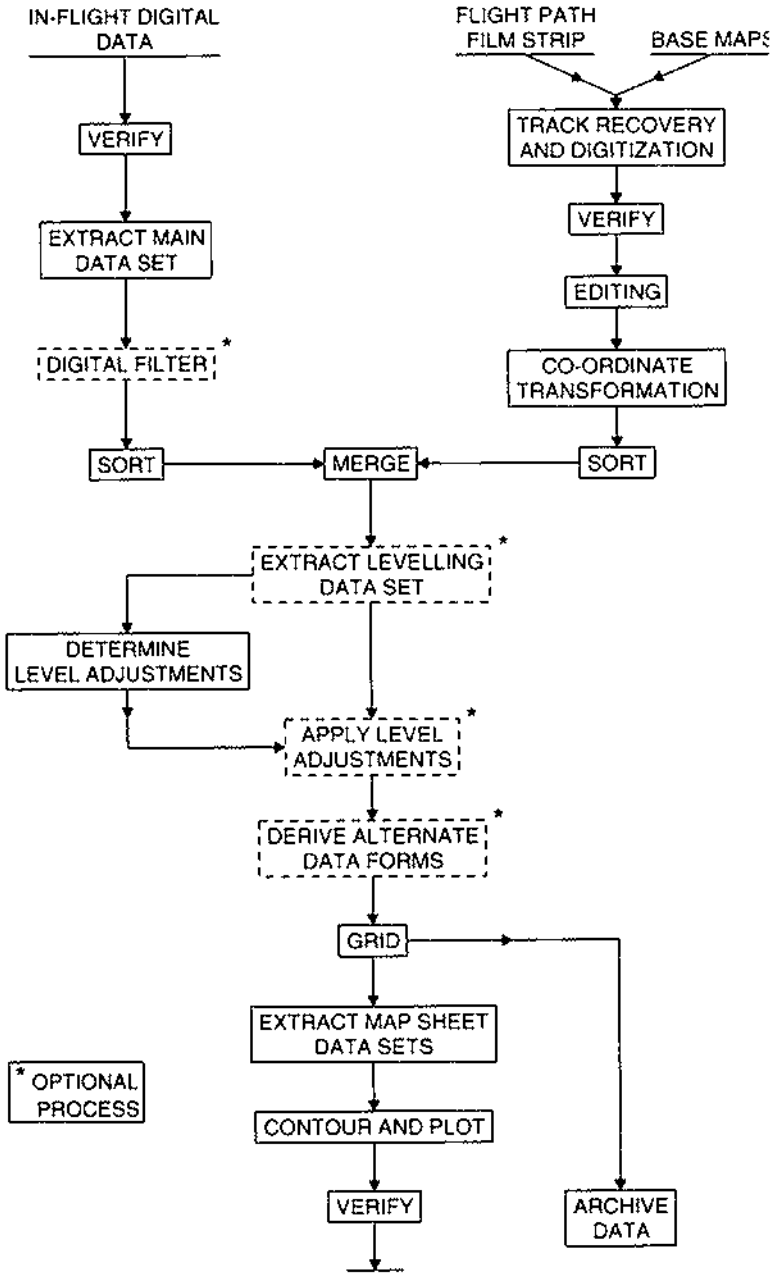

Figure 3.26 Flow chart of reduction processes on aeromagnetic data. From Hood *et al.* (1979), by permission

amplitude features as the magnetic force is indirectly proportional to the square of the distance between source and sensor (see Box 3.1). The rate of change of the field with elevation (akin to the gravitational free-air correction) is between 1.5 and 3.5 nT/100 m, with the maximum gradient being at the poles. In areas where the range of

elevations of the ground surface is large, such as in the Rockies or Andes, and Himalayas, maintaining a constant terrain clearance is not practicable (or safe!). Indeed, in areas of extreme altitude, airborne surveys are not possible as the ground can be higher than the flying ceiling of available aircraft owing to the rarified atmosphere. Different flying heights can be specified for particular areas within a survey region and the various datasets processed to the same flying height or alternative datum.

In some regions, metal pipes can become inductively magnetised by currents in the atmosphere (Campbell 1986) or are cathodically protected by passing a large direct current (1–7 amps) through them to reduce internal corrosion. The presence of such pipes can contribute a significant anomaly on high-resolution aeromagnetic data (Gay 1986). In hydrocarbon exploration over sedimentary basins up to 6 km depth, basement faulting, which affects basement-controlled traps and reservoirs, can be identified from their respective magnetic anomalies which can have amplitudes of only several nanoteslas. There is then a problem over differentiating between a geologically significant fault and a cathodically protected pipe as their respective magnetic anomalies may appear to be similar.

Iron pipes have a permanent magnetisation acquired at the foundry at the time of manufacture. Being magnetisable, they also acquire a magnetisation induced by the Earth's magnetic field. Current injected into the pipes will also generate a magnetic field according to the right-hand rule. This states that a conductor carrying electrical current, indicated by the thumb on the right hand, will generate a magnetic field in the direction indicated by the coiled fingers of the right hand (Figure 3.27A). The injection of current at specific points along a pipe has one marked effect (Figures 3.27B and C). The polarity of the magnetic anomaly will be reversed either side of the injection point as the current is flowing in opposite directions away from it and into the ground. The point at which the polarity reverses (Figure 3.27B) indicates the position of current injection. The figure shows the magnitudes and senses of the western and eastern anomaly peaks for each survey line. Lines 9–13 have a positive western peak and corresponding negative eastern peak while lines 14–17 south of the injection point have a negative western peak and positive eastern peak (Figure 3.27C). The magnitude of the anomaly will also decrease away from the injection point. The magnitudes determined for survey lines south of the injection point are slightly larger than those for northern lines as the flying height was 40 m lower to the south. Mean flying height was 257 m. These characteristics are diagnostic of cathodically protected pipes and can be used to tell them apart from linear fault structures whose polarity does not switch along its length, although its magnitude may vary along the strike of the fault. Having identified a linear anomaly as being due to a cathodically protected pipe, the anomaly can be filtered out of the dataset.

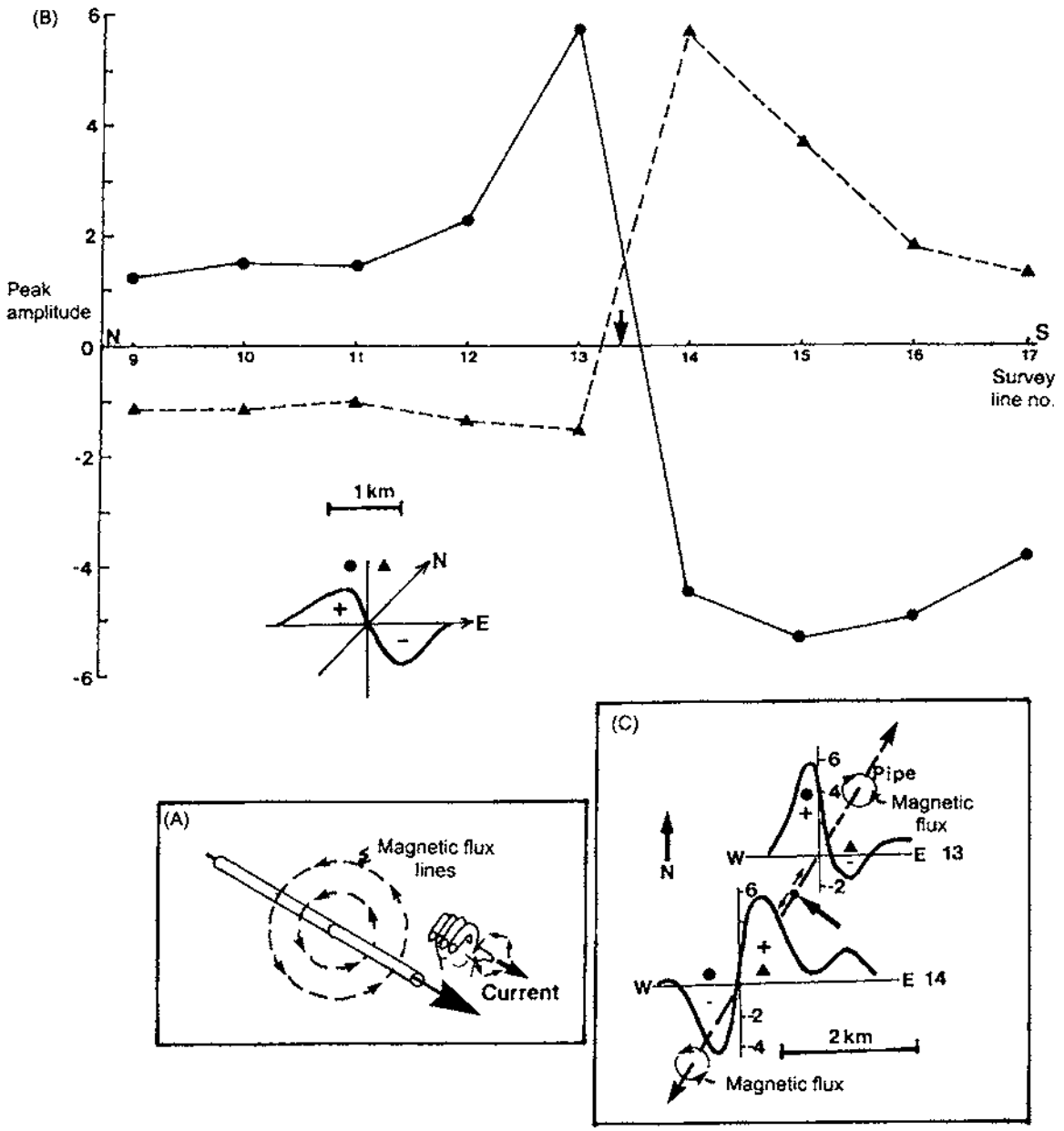

3.6.3 Data reduction

In order to produce a magnetic anomaly map of a region, the data have to be corrected to take into account the effect of latitude and, to a lesser extent, longitude. As the Earth's magnetic field strength varies from 25 000 nT at the magnetic equator to 69 000 nT at the poles, the

increase in magnitude with latitude needs to be taken into account. Survey data at any given location can be corrected by subtracting the theoretical field value F_{th}, obtained from the International Geomagnetic Reference Field, from the measured value, F_{obs}. This works well in areas where the IGRF is tied-in at or near to Geomagnetic Observatories, but in many places the IGRF is too crude. Instead, it is better to use a local correction which can be considered to vary linearly over the magnetic survey area. Regional latitudinal (ϕ) and longitudinal (θ) gradients can be determined for areas concerned and tied to a base value (F_0), for example, at the south-east corner of the survey area. Gradients northwards ($\delta F/\delta\phi$) and westwards ($\delta F/\delta\theta$) are expressed in nT/km and can easily be calculated for any location within the survey area. For example, in Great Britain, gradients of 2.13 nT/km north and 0.26 nT/km west are used. Consequently, the anomalous value of the total field (δF) can be calculated arithmetically, as demonstrated by the example in Box 3.7.

Another method of calculating the anomalous field δF is to determine statistically the trend of a regional field to isolate the higher-frequency anomalies, which are then residualised in the same way that gravity residuals are calculated. The regional field is subtracted from the observed field to produce a residual field (δF) (Figure 3.28A). If the survey is so laterally restricted, as in the case of small-scale archaeological, engineering or detailed mineral prospecting surveys (e.g. $< 500\,\text{m} \times 500\,\text{m}$ in area), the use of regional gradients is not practicable. Instead, profile data can be referred to a local base station (F_b) which is remote from any suspected magnetic sources. In this case, the anomalous field δF is obtained by subtracting the base value (F_b) from every diurnally corrected observed value F_{obs} along the profile ($\delta F = F_{obs} - F_b$), as illustrated in Figure 3.28B.

Box 3.7 Anomalous total field strength δF

$$\delta F = F_{obs} - (F_0 + \delta F/\delta\phi + \delta F/\delta\theta) \quad (\text{nT})$$

where F_{obs} is the measured value of F at a point within the survey area with coordinates (x, y); F_0 is the value at a reference point ($x = 0$; $y = 0$); $\delta F/\delta\phi$ and $\delta F/\delta\theta$ are the latitudinal and longitudinal gradients respectively (in units of nT/km).

Example: For a station 15 km north and 18 km west of a reference station at which $F_0 = 49\,500$ nT with gradients $\delta F/\delta\phi = 2.13$ nT/km north, and $\delta F/\delta\theta = 0.26$ nT/km west, and the actual observed field $F_{obs} = 50\,248$ nT, the magnetic anomaly δF is:

$$\delta F = 50\,248 - (49\,500 + 2.13 \times 15 + 0.26 \times 18)\,\text{nT}$$
$$= 711\,\text{nT}$$

Figure 3.27 (*opposite*) Variation in magnetic anomalies associated with a cathodically protected pipe in north-east Oklahoma, USA. (A) Right-hand rule applied to a pipe through which a current is passed to show direction of magnetic flux lines. (B) Peak amplitudes for western and eastern parts of profile anomalies, of which two for lines 13 and 14 are shown in (C). Note the relative amplitudes of the anomalies on lines 13 and 14 either side of the current injection point (arrowed). Data from Gay (1986), by permission

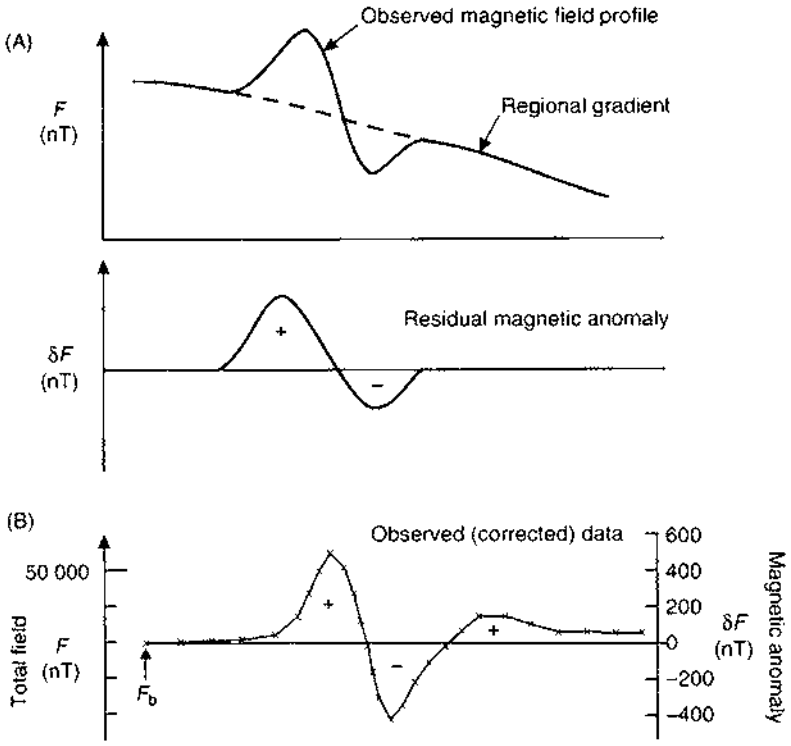

Figure 3.28 Magnetic residuals (A) Subtraction of a regional field gradient, and (B) reference to a local arbitrary base station

3.7 QUALITATIVE INTERPRETATION

Once magnetic data have been fully corrected and reduced to their final form, they are usually displayed either as profiles (Section 3.7.1) or as maps (Section 3.7.2) and the interpretation procedures are different for the two cases. However, it must always be borne in mind that, although the techniques used are similar to those for gravity surveys, there are two important complications. First, the Earth's magnetic field is dipolar, which means that a single anomaly can have the form of a positive peak only, a negative peak only or a doublet consisting of both positive and negative peaks. Secondly, the single largest unknown is whether there is any remanent magnetisation and, if there is, its intensity and direction (J_r) need to be ascertained. It must also be remembered that many geophysical interpretations may fit the observed data and that a given interpretation may not be unique (see Chapter 1, and Figure 1.1 in particular). For this reason, it is always useful to use other geophysical methods in the same area to help constrain the interpretations. If some geological information already exists for the area, then this should be used to help with the

geophysical interpretations. However, a word of warning: be careful that some geological information may itself be an interpretation and should not be considered to be the only solution. The geophysics may disprove the geological hypothesis!

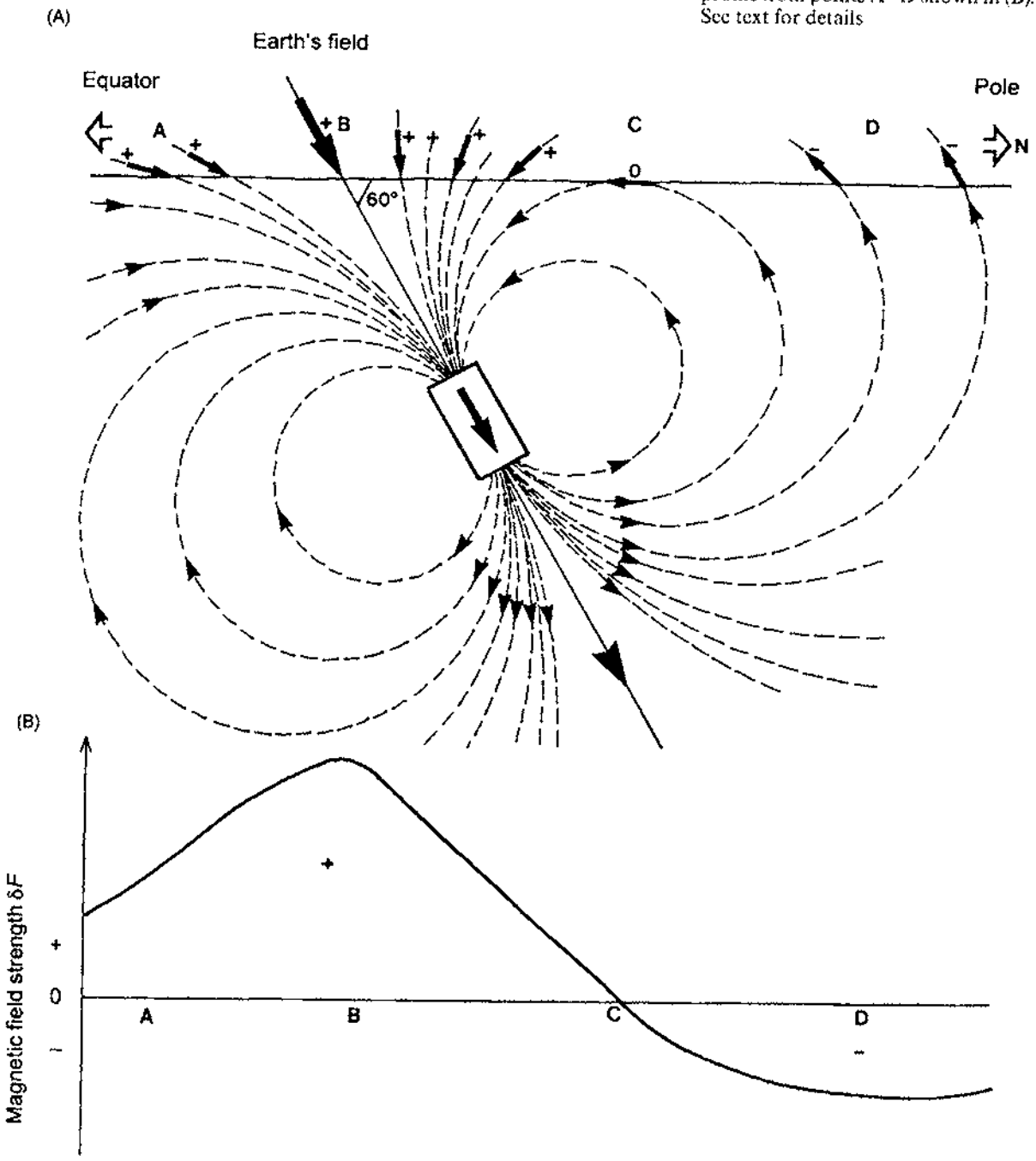

Figure 3.29 The magnetic field generated by a magnetised body inclined at 60° parallel to the Earth's field (A) would produce the magnetic anomaly profile from points A–D shown in (B). See text for details

A magnetisable body will have a magnetisation induced within it by the Earth's magnetic field (Figure 3.29A). As magnetisation is a vector quantity, the anomaly shape will depend on the summation of the vectors of the Earth's field $\boldsymbol{F}$ (with intensity J) and the induced field (J_i) from the sub-surface body and from any remanent magnetisation (J_r). It can be seen from Figure 3.29 (A and B) how any magnetic anomaly is produced. The maximum occurs when the induced field is parallel to the Earth's field; the anomaly goes negative when the induced field vector is orientated upwards as at D. As the magnetic data have been corrected to remove the effect of the Earth's magnetic

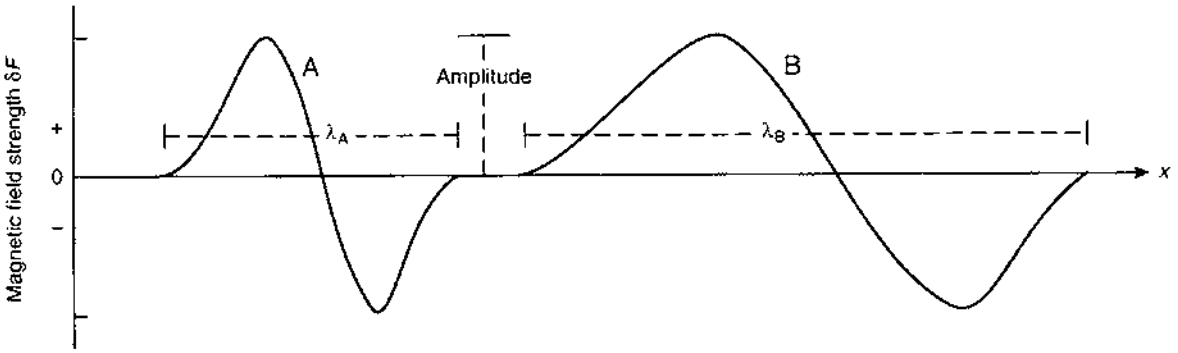

Figure 3.30 Two magnetic anomalies arising from buried magnetised bodies (see text for details)

Table 3.7 Guidelines to qualitative interpretation of magnetic profiles and maps

Applies to:	Magnetic character	Possible cause
Segments of a profile and areas of maps	Magnetically quiet Magnetically noisy	Low κ rocks near surface Moderate–high κ rocks near surface
Anomaly	Wavelength	Short ⇒ near-surface feature Long ⇒ deep-seated feature
	± amplitude	Indicative of intensity of magnetisation
Profile*	Anomaly structure† and shape	Indicates possible dip and dip direction Induced magnetisation indicated by negative to north and positive to south in northern hemisphere and vice versa in southern hemisphere; if the guideline does not hold, it implies significant remanent magnetisation present
Profile and maps	Magnetic gradient	Possible contrast in κ and/or magnetisation direction
Maps	Linearity in anomaly	Indicates possible strike of magnetic feature
Maps	Dislocation of contours	Lateral offset by fault
Maps	Broadening of contour interval	Downthrow of magnetic rocks

*Can be determined from maps also; †Structure = composition of anomaly, i.e. positive peak only, negative peak only or doublet of positive and negative peaks; κ = magnetic susceptibility

field, the anomaly will be due to the vectors associated with the source body. The sign convention is positive downwards, negative upwards. Where there is no remanent magnetisation, a magnetised body in the northern hemisphere will always have a negative anomaly on its northern side and a positive anomaly on its southern side. The opposite is true for the southern hemisphere.

For the two anomalies shown in Figure 3.30, anomaly A has a short wavelength compared with anomaly B, indicating that the magnetic body causing anomaly A is shallower than the body causing B. As the amplitude of anomaly B is identical to that of anomaly A, despite the causative body being deeper, this must suggest that the magnetisation of body B is much greater than for body A, as amplitude decreases with increasing separation of the sensor from the magnetised object.

Some general guidelines for the qualitative interpretation of magnetic profiles and maps are listed in Table 3.7, and an example in Figure 3.31. The list of guidelines should be used like a menu from which various combinations of parameters apply to specific anomalies. For instance, a short-wavelength high-amplitude doublet anomaly with negative to the north, and positive to the south, with an

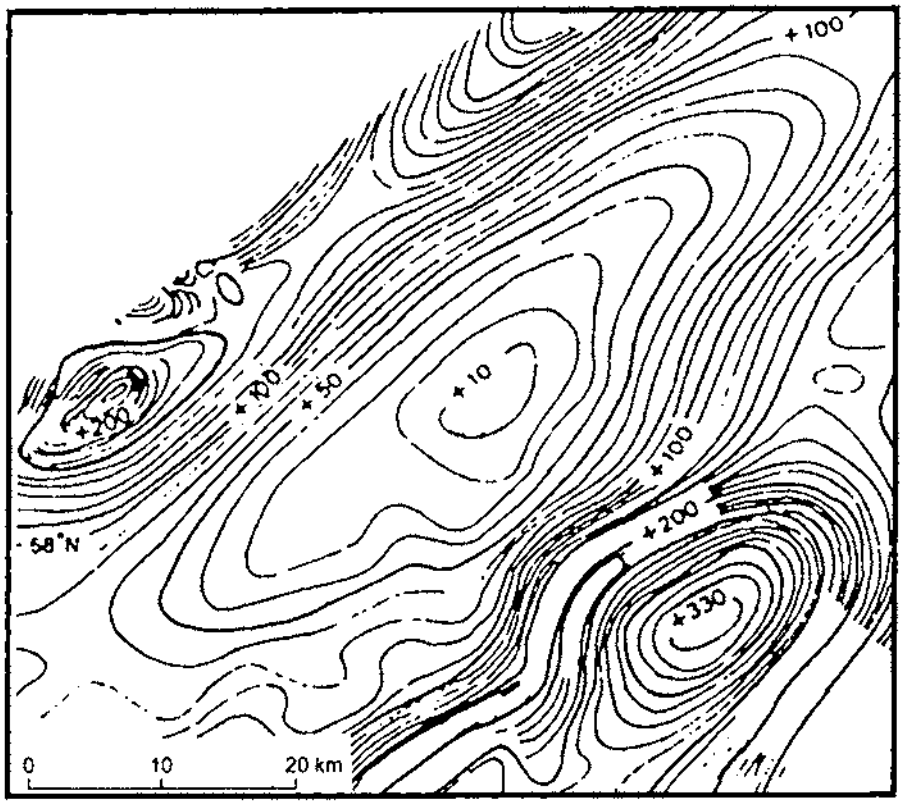

Figure 3.31 Magnetic anomaly map associated with a fault-bounded sedimentary basin with upthrown horst block to south-east – Inner Moray Firth, Scotland. After McQuillin *et al.* (1984), by permission

elongation in the east–west direction in the mid-latitudes of the northern hemisphere, suggests a near-surface, moderate-to-high susceptibility magnetic feature with induced magnetisation in a sheet-like body with an east–west strike and northerly dip.

3.7.1 Profiles

The simplest interpretation technique is to identify zones with different magnetic characteristics. Segments of the profile with little variation are termed magnetically 'quiet' and are associated with rocks with low susceptibilities. Segments showing considerable variation are called magnetically 'noisy' and indicate magnetic sources in the sub-surface. The relative amplitudes of any magnetic anomalies (both

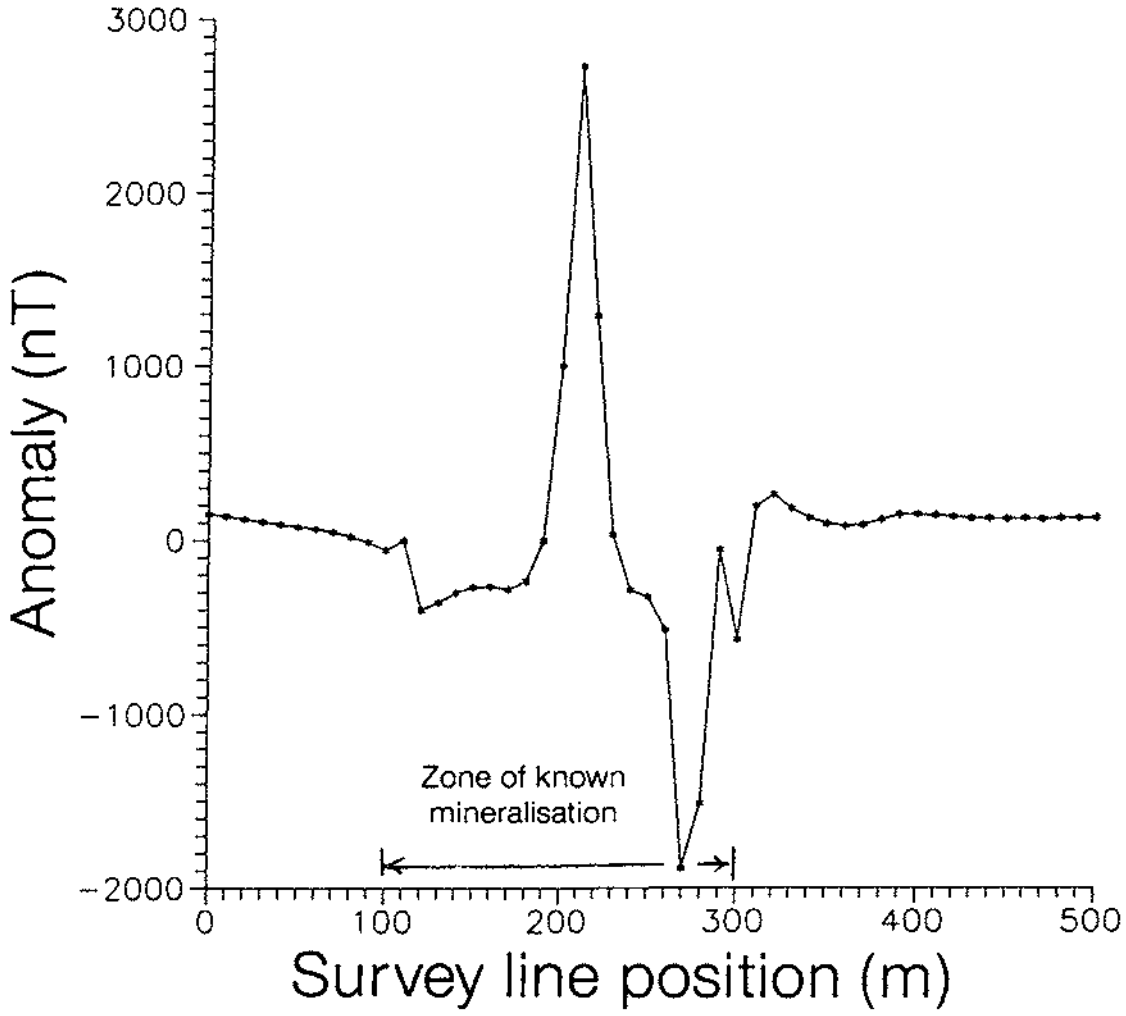

Figure 3.32 Magnetic zonation of a proton magnetiometer profile across Sourton Common, north Dartmoor, England

positive and negative) and the local magnetic gradients can all help to provide an indication of the sub-surface.

Figure 3.32 illustrates the differences between noisy and quiet zones in a profile over Sourton Tors, north Dartmoor, England, where the magnetically noisy segments indicate metalliferous mineralisation. The negative occurring as the northern part of the doublet indicates that there is little remanent magnetisation and that the anomaly is due largely to induction ($J_i \gg J_r$).

Figure 3.33 shows a profile measured at Kildonnan, Isle of Arran, Scotland, across a beach section over a series of vertical dolerite dykes. Two of the three dykes (A and B) give rise to large positive anomalies, while a third dyke (C) produces a broader low. All the dykes have virtually identical geochemistry and petrology and hence

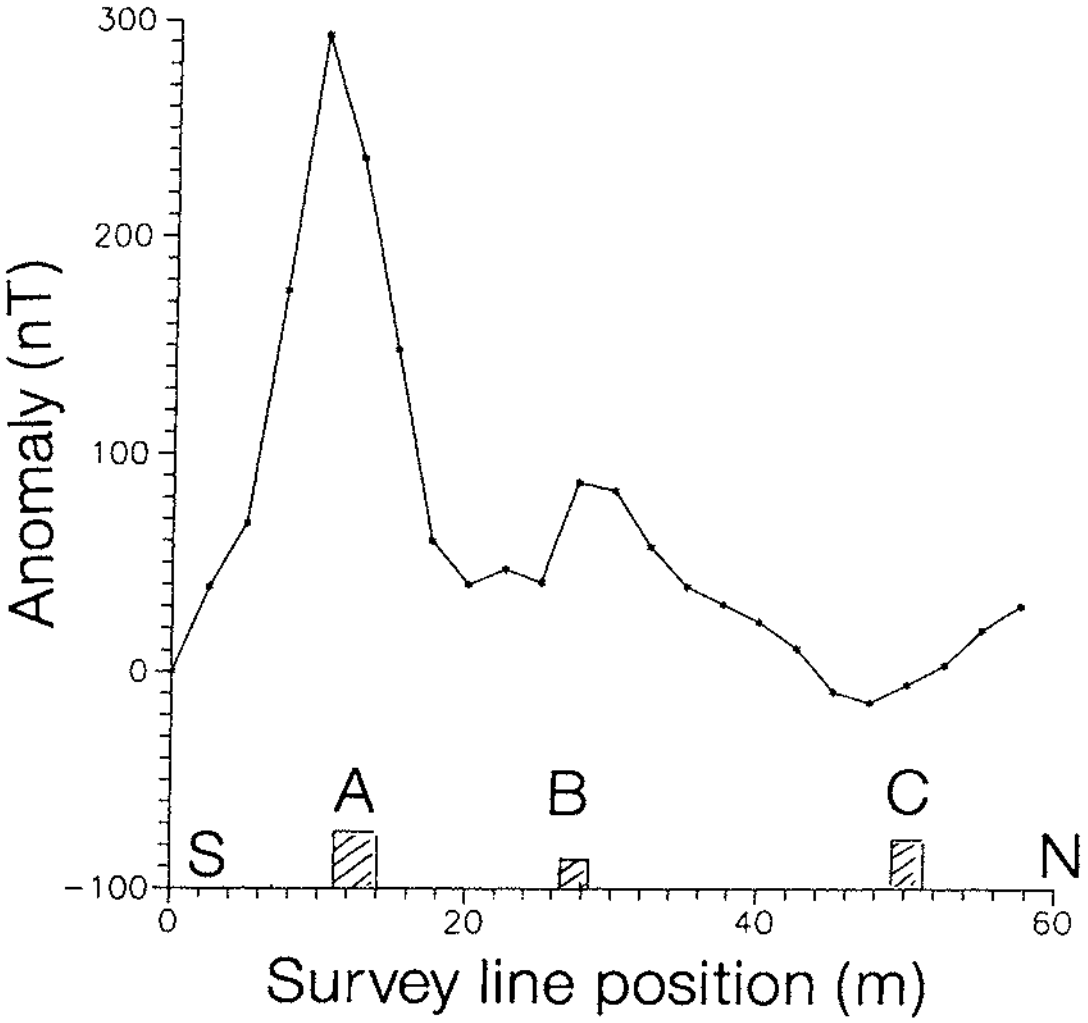

Figure 3.33 Proton magnetometer profile across three vertical dolerite dykes at Kildonnan, Isle of Arran, Scotland, which have been intruded during a period when the Earth's magnetic polarity changed

similar susceptibilities. The difference in magnetic character associated with dyke C compared with dykes A and B is attributed to there having been a magnetic reversal between the intrusion of dyke C relative to the other two. It is well known that in the British Tertiary Igneous Province, which includes the western isles of Scotland, a phase of doleritic intrusion occurred which lasted 10 million years and straddled a magnetic reversal (Dagley *et al.* 1978). Some dykes are normally magnetised and others have a reversed polarity. The different magnetic characters therefore provide a means of identifying which dykes were associated with which phase of the intrusion episode, whereas it is virtually impossible to make such an identification in the field on the basis of rock descriptions.

Having identified zones with magnetic sources, and possibly having gained an indication of direction of dip (if any) of magnetic

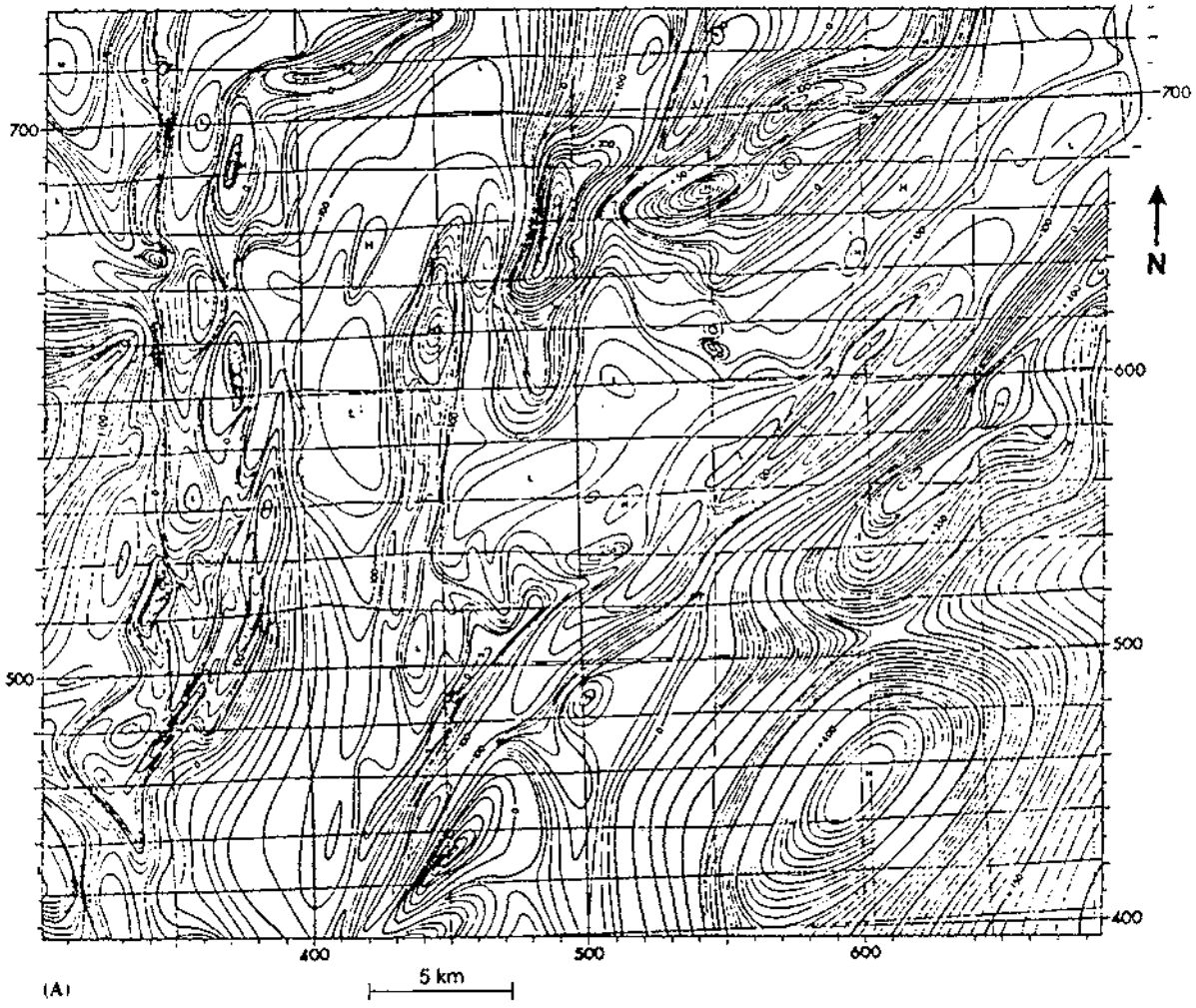

Figure 3.34 (A) Aeromagnetic map of the south-east part of the Shetland Islands, Scotland (Flinn 1977); (B) *(opposite)* zonation of (A) in terms of magnetic characteristics

targets and relative intensities, either more detailed fieldwork can be undertaken to obtain more information and/or the existing data can be interpreted using quantitative methods (see Section 3.8).

3.7.2 Pattern analysis on aeromagnetic maps

Magnetic data acquired over a grid with no spatial aliasing are displayed as contoured maps, as three-dimensional isometric projections, or as image-processed displays (see Section 3.8.3). The various displays can be interpreted in terms of the guidelines in Table 3.7. Commonly, even such a basic level of interpretation can yield important information about the sub-surface geology very quickly. One major advantage of airborne surveys is that they can provide information about the geology in areas covered by water.

An aeromagnetic survey was acquired over the south-eastern part of the Shetland Islands, north-east Scotland, and described in detail by Flinn (1977). The original aeromagnetic data were extracted from part of a British Geological Survey map and are shown in Figure 3.34A. The corresponding pattern analysis for the same area is shown in Figure 3.34B and compares very well with Flinn's

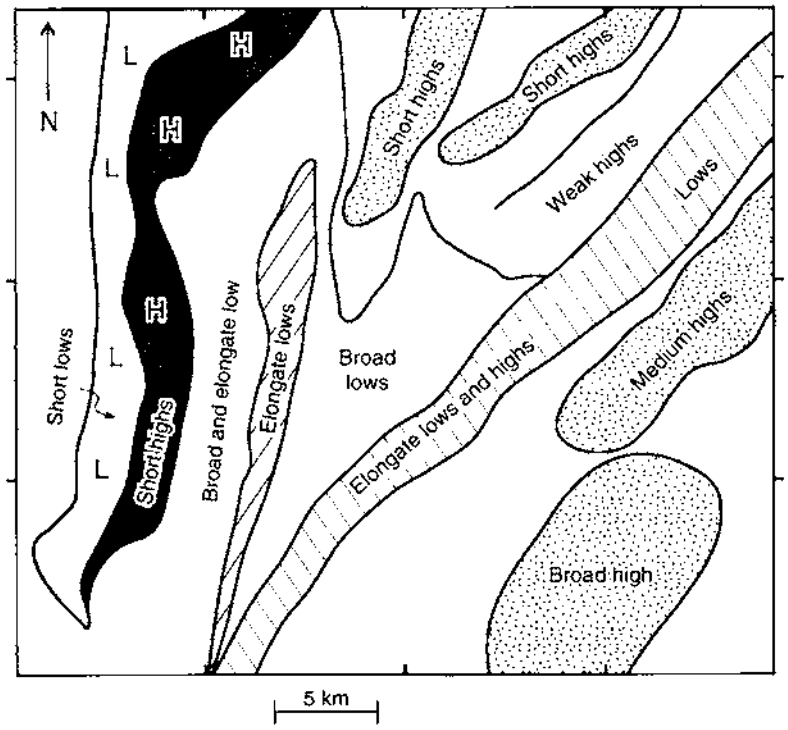

(B)

interpretation (Figure 3.35). Magnetic lows in band A are associated with psammites and migmatised psammites which have been heavily injected by pegmatite. The lows in band B correspond to gneissified semipelites and psammites intruded by granites and pegmatites. The short-wavelength but large-amplitude highs just east of band A are attributed to the magnetic pelitic schist and gneiss. In the central part of Figure 3.34A, truncation of NE–SW trending contours can be seen to be associated with the Whalsay Sound Fault. Other faults, such as the Lunning Sound Fault and the Nesting Fault, separate zones of differing magnetic character and lie parallel to the local aeromagnetic contours. A series of three localised positive highs in the south-east corner (h, i and j along the thrust beneath the Quarff Nappe;

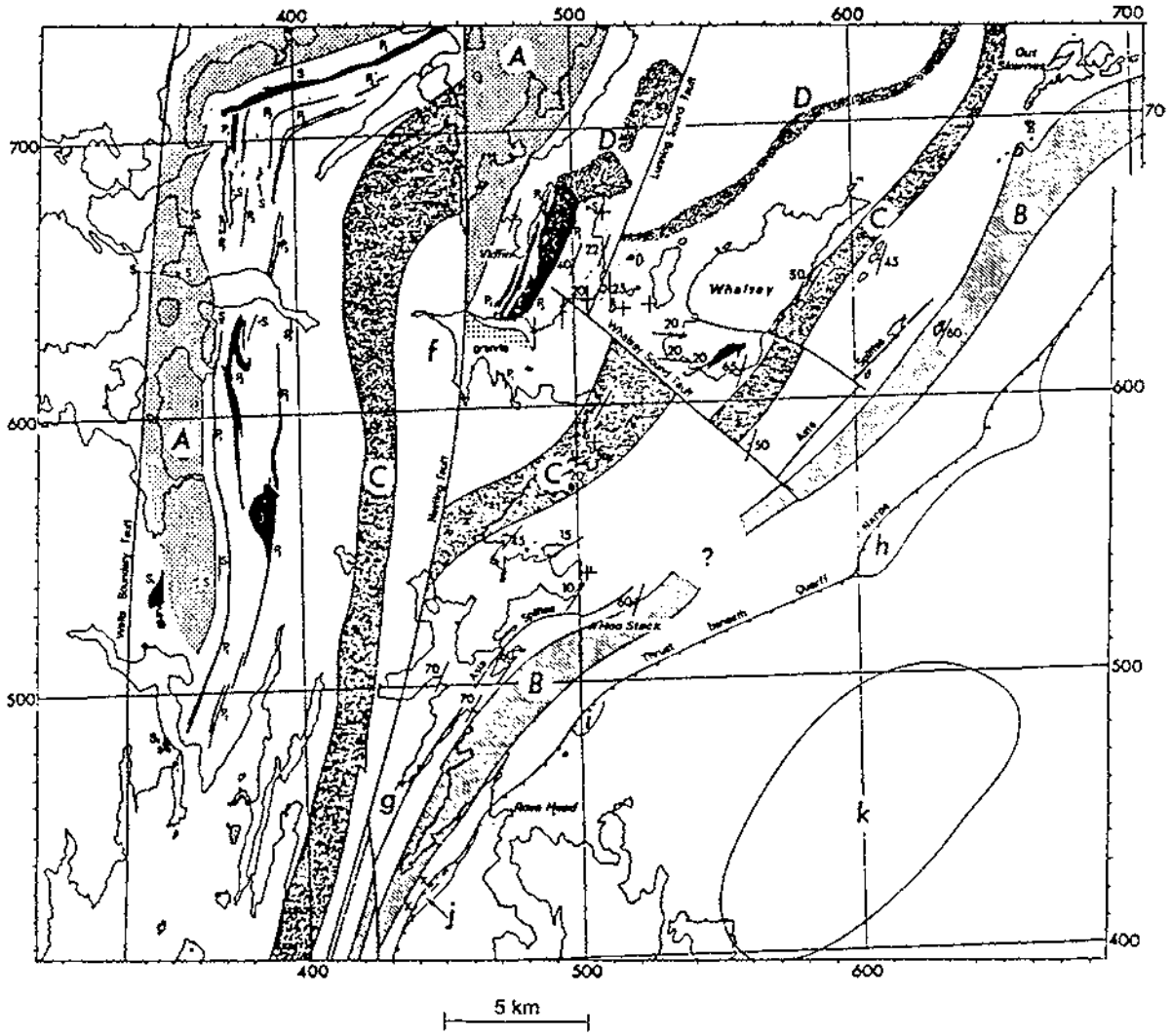

Figure 3.35 Geological interpretation of the aeromagnetic map shown in Figure 3.34 of the south-east part of the Shetland Islands, Scotland. From Flinn (1977), by permission

Figure 3.35) is thought to be due to phyllites with 4% hematite which in itself cannot explain the anomaly amplitudes. However, suitably orientated remanent magnetisation could account for these magnetic features. The large-amplitude anomaly (k) in the south-east corner is attributed to a large buried intrusive which is also evident on gravity data. However, this and similar anomalies in the vicinity with similar character all occur over sea and have not been sampled and so the exact nature of the rock remains unknown.

More detailed discussions on the interpretation of aeromagnetic maps have been given, for example, by Vacquier *et al.* (1951), Nettleton (1976) and Hinze (1985).

3.8 QUANTITATIVE INTERPRETATION

The essence of quantitative interpretation is to obtain information about the depth to a particular magnetic body, its shape and size, and details about its magnetisation in two possible ways. One is direct, where the field data are interpreted to yield a physical model. The other is the inverse method, where models are generated from which synthetic magnetic anomalies are generated and fitted statistically against the observed data. The degree of detail is limited by the quality and amount of available data and by the sophistication of either the manual methods or the computer software that can be used.

3.8.1 Anomalies due to different geometric forms

Just as with gravity data, magnetic data can be interpreted in terms of specific geometric forms which approximate to the shapes of subsurface magnetised bodies. This tends to be true where profiles are to be interpreted only in terms of two dimensions. Three-dimensional models are far more complex and can be used to approximate to irregularly shaped bodies (see Section 3.8.3). Detailed mathematical treatments of the interpretation of magnetic data have been given by Grant and West (1965), Telford *et al.* (1990) and Parasnis (1986), among others.

The commonest shapes used are the sphere and the dipping sheet, both of which are assumed to be uniformly magnetised and, in the simplest cases, have no remanence. Total field anomalies (δF) for various types of model are illustrated in Figures 3.36–3.39; except where otherwise stated, the field strength is 50 000 nT, inclination $I = 60°$, declination $D = 0°$, and susceptibility $\kappa = 0.05$ (SI).

In the example of a uniformly magnetised sphere (Figure 3.36), the horizontal and vertical components are shown in addition to the total field anomaly. The anomalies associated with vertical bodies of various thicknesses are shown in Figure 3.37. The anomaly produced by a 50 m thick vertical dyke (Figure 3.37A) is both wider and has

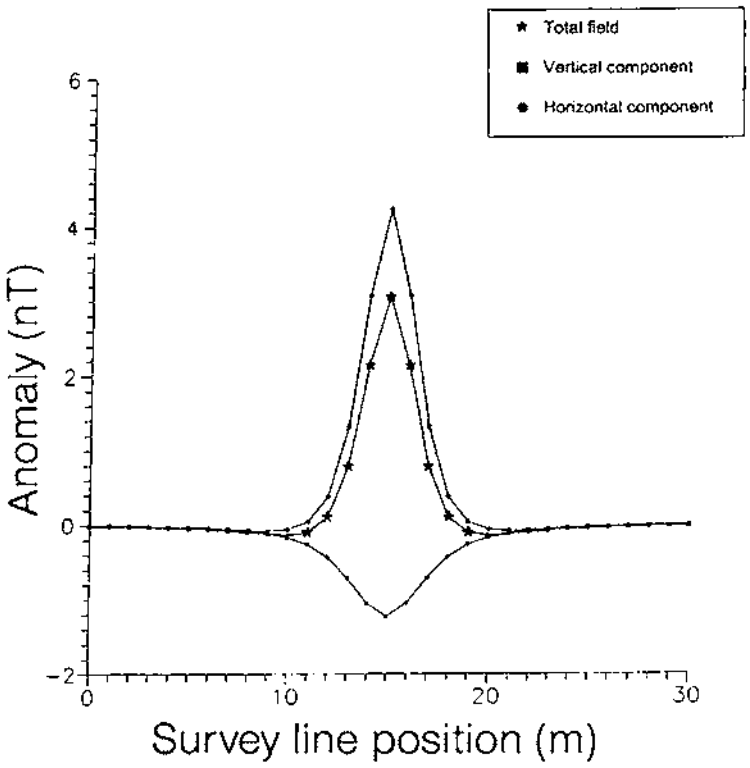

Figure 3.36 Horizontal and vertical components and the total field over a uniformly magnetised sphere with a radius of 1 m and whose centre lies at 3 m depth at position $x = 15$ m

a significantly larger amplitude (830 nT) than that of the 5 m thick dyke (peak amplitude 135 nT). Notice also that the anomaly shape changes considerably with strike direction, from being a positive–negative doublet when the dyke is striking east–west (with the negative on the northern side) to being a single symmetric positive peak when the dyke strikes north south. In all cases, when an inductively magnetised body of regular shape is orientated north–south, its anomaly is symmetric. For a 70 m thick, 400 m long magnetised slab with its top 30 m below ground, a symmetric M-shaped anomaly is produced with the strike in a north–south direction (Figure 3.37B). When striking east–west, the positive negative doublet is stretched to form an inflection in the middle; again the negative is on the northern side.

The effects on anomaly shape caused by changing the depth to the top of a vertical magnetised dyke are illustrated in Figure 3.38. With increasing depth, the anomaly decreases in amplitude and widens. At any given latitude, the anomaly shape will also be affected by any dip (α) of a sheet-like body, such as the inductively magnetised sheet (5 m thick) striking east–west (dip direction is towards the north) indicated in Figure 3.39. With zero dip, the body behaves like a thin horizontal slab with its northern edge off the scale of the figure.

If one end of a thick horizontal slab is sufficiently far enough away from the other, the model effectively becomes a vertical boundary separating two contrasting magnetic media (Figure 3.40A). The anomaly produced when the boundary strikes east–west has a significantly larger field strength (peaking around 1870 nT) than when in the other orientation. Furthermore, the single peak is effectively the positive peak of Figure 3.37C isolated from its negative partner.

The direction and degree of dip of a fault plane in a magnetised body also has a distinctive anomaly shape (Figure 3.40B). The negative anomaly is associated with the downthrown side. The anomaly shape is very similar to half of the M-shaped anomaly in Figure 3.37B.

Anomalies produced over a near-semicylindrical low-susceptibility body within magnetised basement, to simulate a buried rock valley

(A)

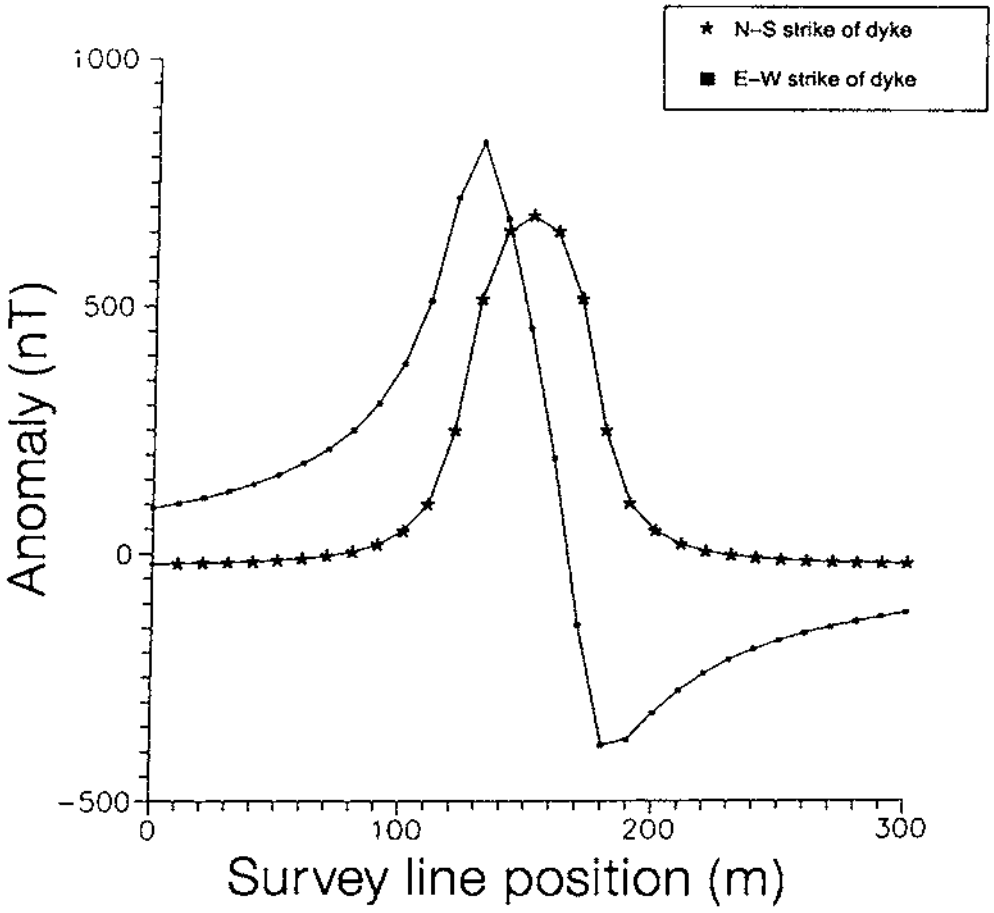

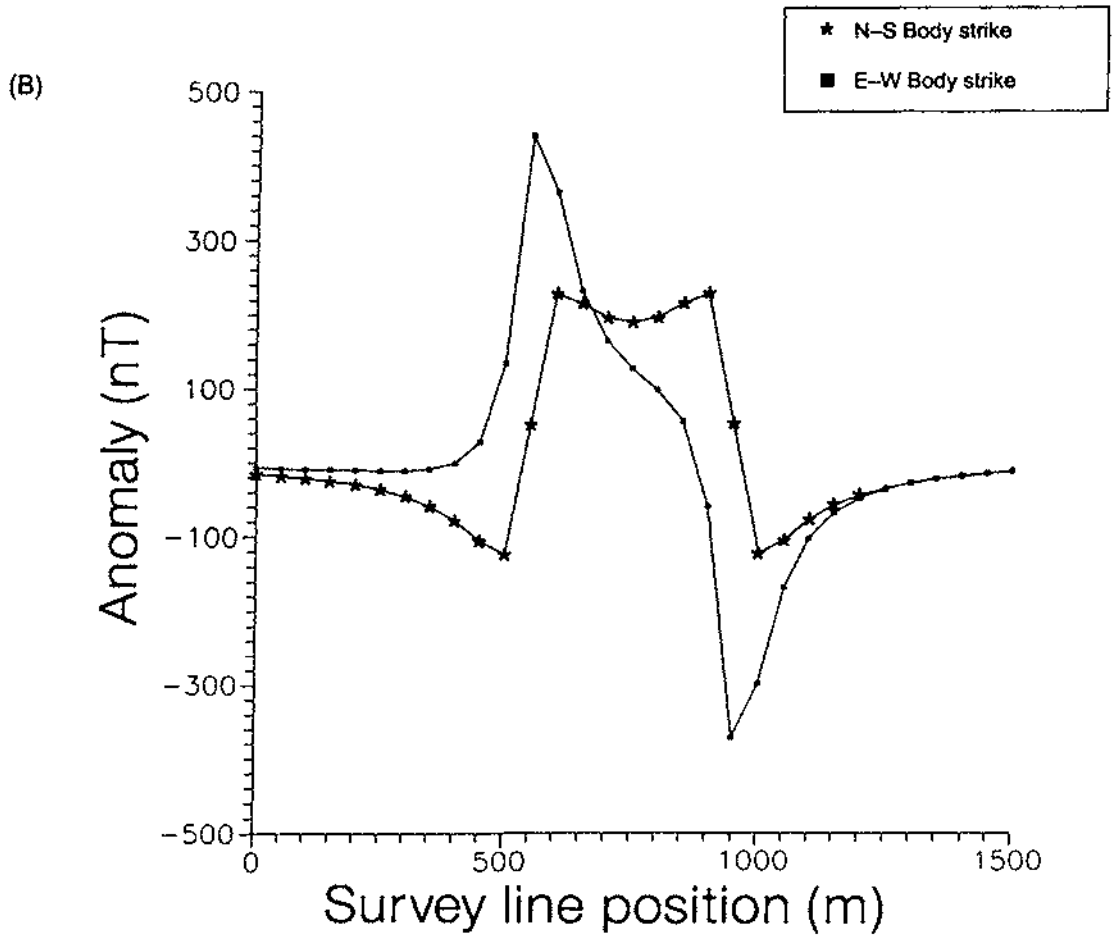

Figure 3.37 Total field anomalies over a vertical sheet-like body. (A) (*previous page*) 50 m and (B) 400 m wide. In (A), the magnetic anomaly arising from a 5 m wide body is given for comparison

infilled by sediments in magnetic bedrock, are shown in Figure 3.41. The symmetric anomaly is obtained when the semicylinder is orientated north–south. When this body is orientated north–south, the negative anomaly is on the southern side and so can be distinguished from the anomaly over a thin vertical dyke. Furthermore, the minimum anomaly amplitude is far greater in the case of the low-susceptibility semicylinder than for a vertical dyke.

One of the largest effects on anomaly shape for a given geological structure is latitude. Anomalies in the northern hemisphere over a 5 m thick dyke dipping at 45° to the north decrease in amplitude (partly a function of the reduced field strength towards the magnetic equator) and the negative minimum becomes more pronounced (Figure 3.42A). If the same geological structure exists at different latitudes in the southern hemisphere, this trend continues (Figure 3.42B) but with the slight growth of the now northern positive anomaly. These curves

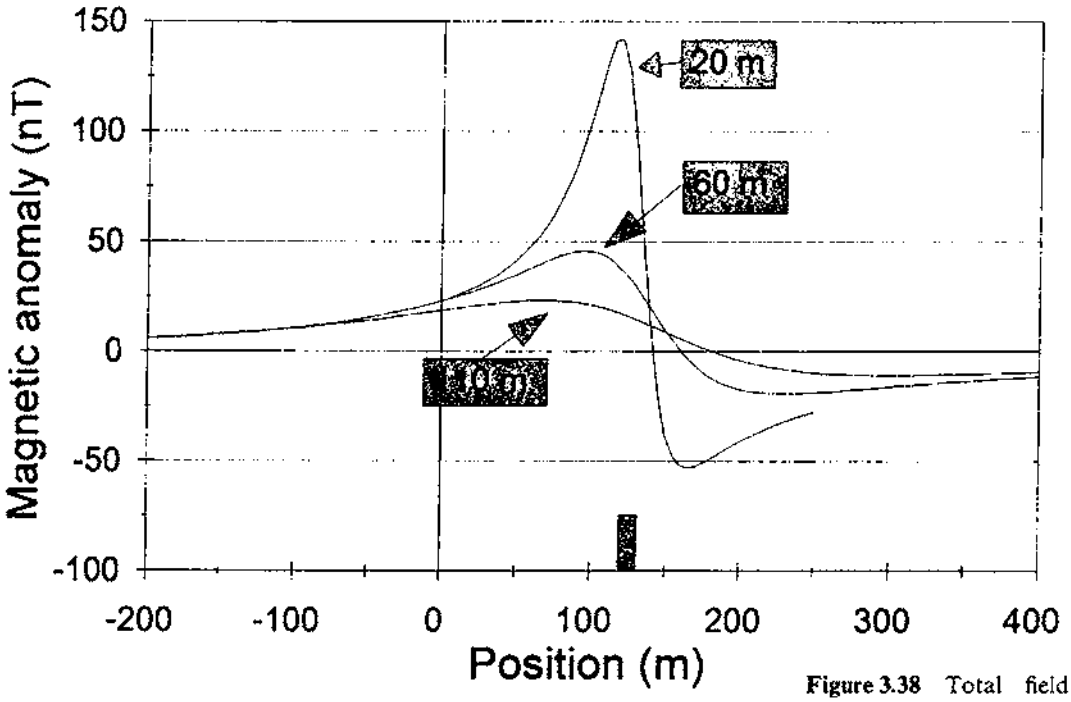

Figure 3.38 Total field anomalies over a 10 m wide vertical sheet-like body orientated east–west and buried at depths of 20 m, 60 m and 110 m; the position of the magnetised body is indicated

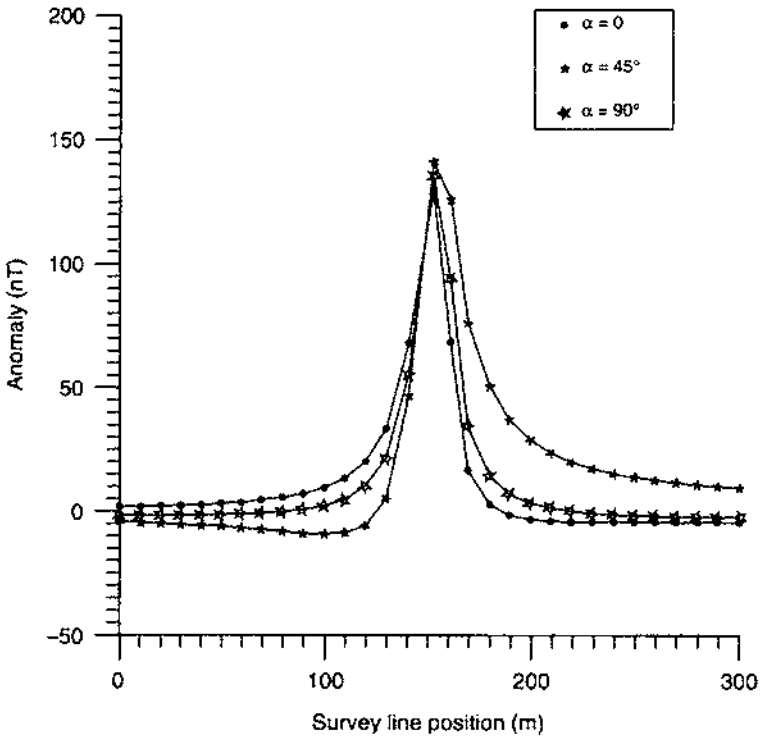

Figure 3.39 Total field anomalies over a thin dyke (5 m wide) dipping to the north at angles from $\alpha = 90°$ to $\alpha = 0°$; body strike is east west

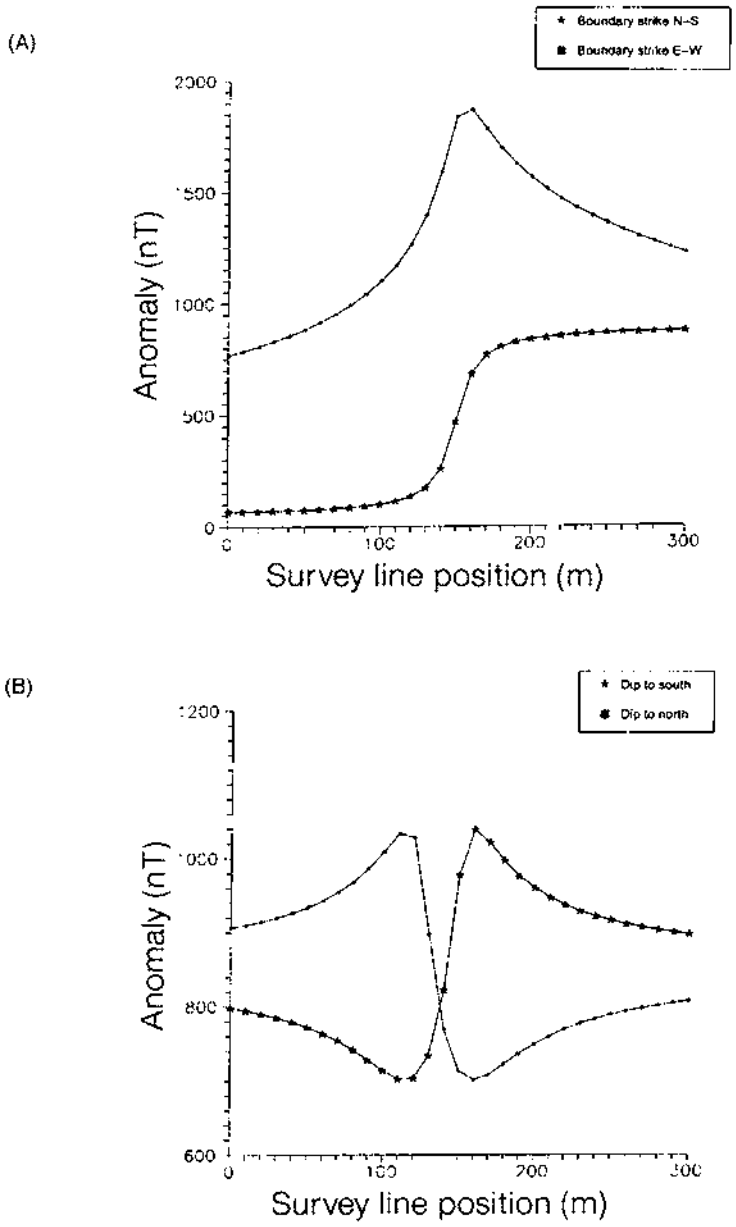

Figure 3.40 Total field anomalies over (A) a vertical contact between contrasting magnetised bodies, and (B) over a fault plane dipping at 45° to the south and to the north for a north south fault strike direction

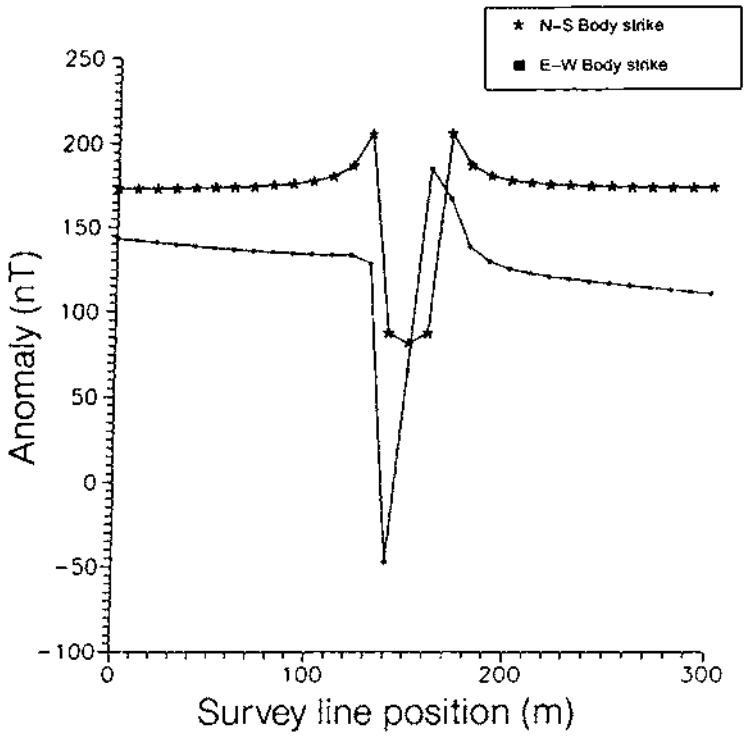

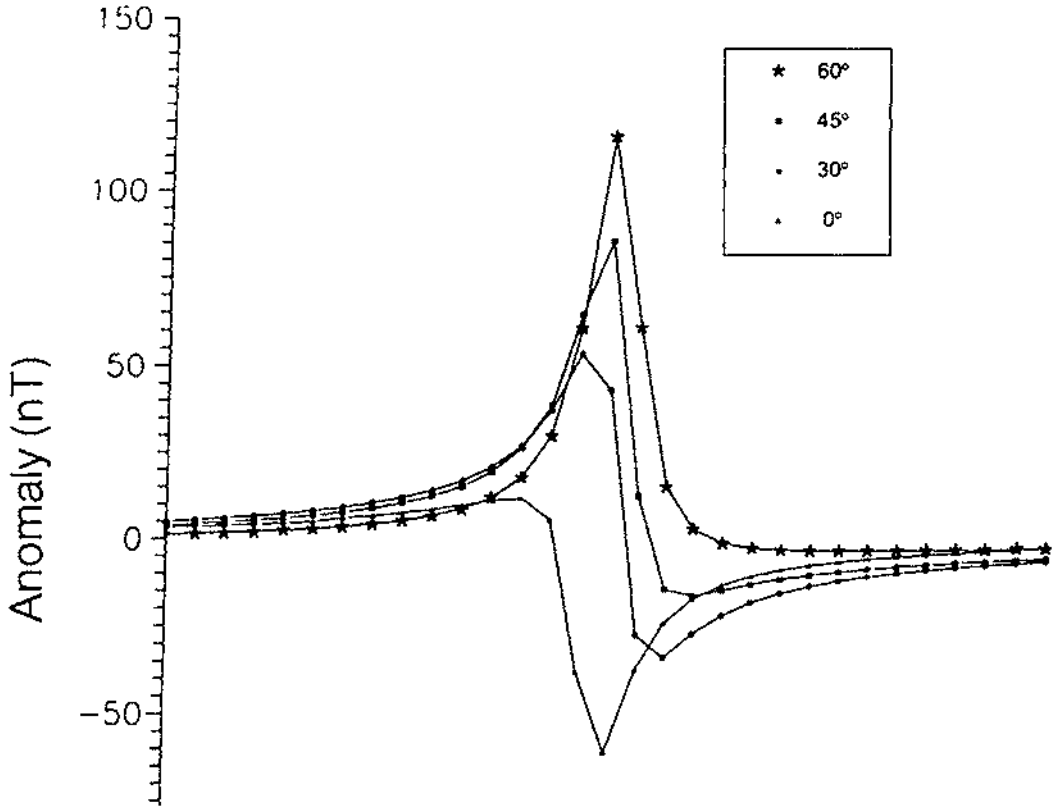

Figure 3.41 Total field anomalies over a semicylindrical body of low susceptibility within a magnetised basement

were calculated along the 0° Greenwich meridian where the field strengths in the southern hemisphere are significantly less than at equivalent latitudes in the northern hemisphere. Profiles along other lines of longitude would produce anomalies of similar shapes but with different amplitudes. It is also worth remembering that a given geological model, which produces a significant magnetic anomaly at one latitude and strike direction, may produce only a negligible anomaly at a different latitude and strike (Figure 3.42B) and so could be overlooked.

Figure 3.42 Total field anomalies over a 5 m thick dyke dipping at 45° to the north with an east west strike direction but with different magnetic inclinations along the 0° Greenwich Meridian, with (A) (*previous page*) the northern hemisphere, and (B) (*below*) the southern hemisphere, taking into account changes in magnetic field strengh with latitude. (C) (*next page*) The total field anomaly for a vertical dyke but at two different magnetic latitudes and directions to illustrate how the magnetic anomaly over a magnetised body can become insignificant by only changing the magnetic latitude (inclination) and strike direction

(B)

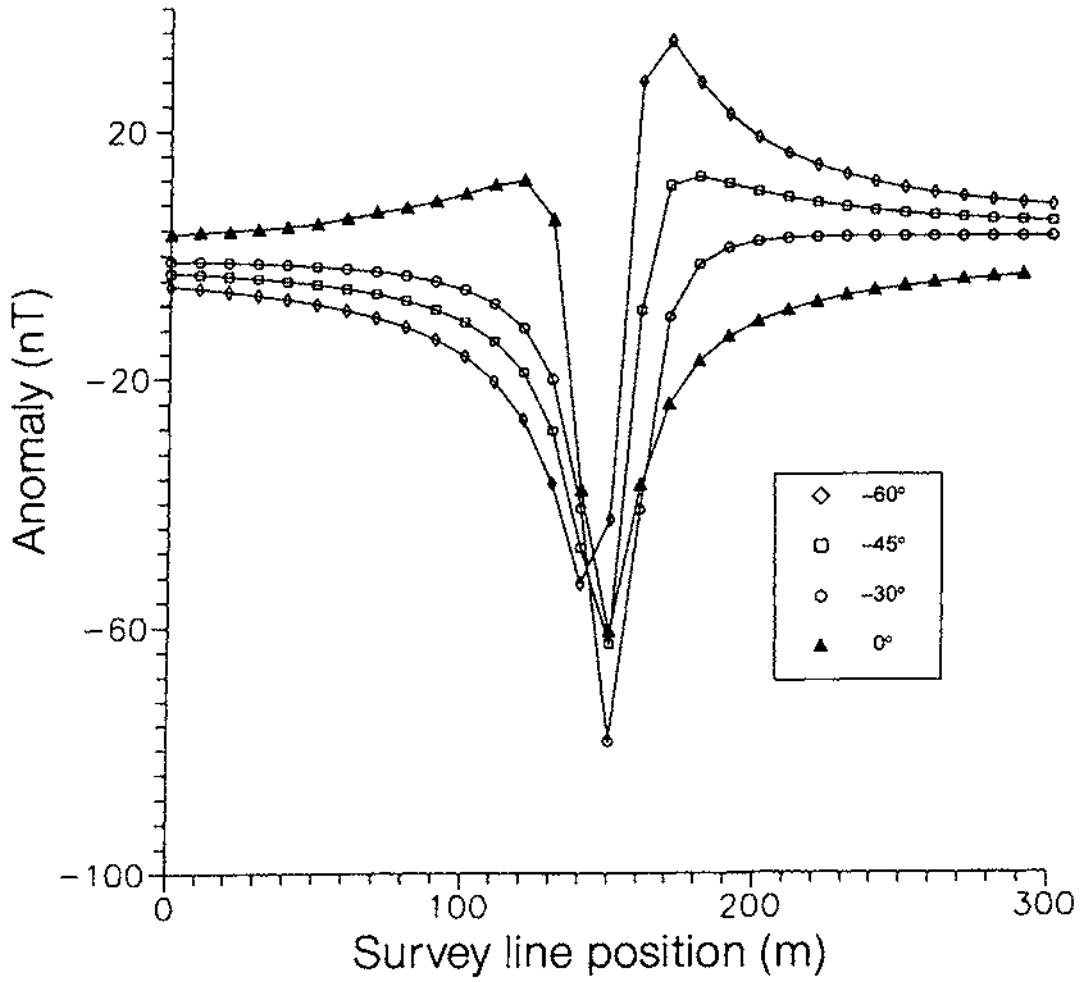

(C)

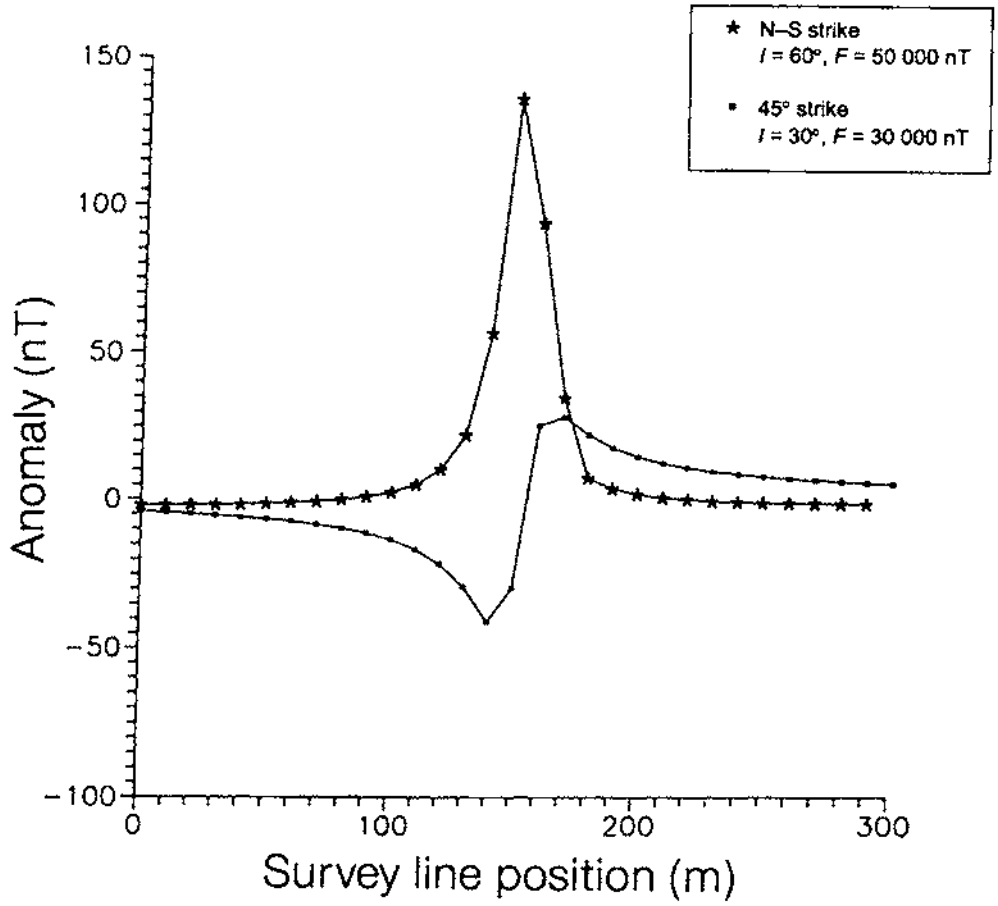

In all the above cases, it was assumed that there was no remanent magnetisation, yet if present, it can affect the shape of an anomaly significantly (Green 1960). In Figure 3.43, four profiles are illustrated, one where there is no remanent magnetisation, and three others where the intensity of remanent magnetisation is constant at 0.12 A/m (giving a strength of 150 nT). A schematic vector diagram is shown to illustrate the effects of remanence and the significance of the vertical component in high magnetic latitudes ($>45°$). When the direction of permanent magnetisation is antiparallel to the Earth's field (A), the resultant amplitude is $F'_a (\ll F)$, so the anomaly amplitude is substantially reduced. In the case B, where the remanent magnetisation is at right-angles to the Earth's field, the resultant F'_b ($<F$) has a smaller vertical component than F and so the amplitude is slightly reduced. In

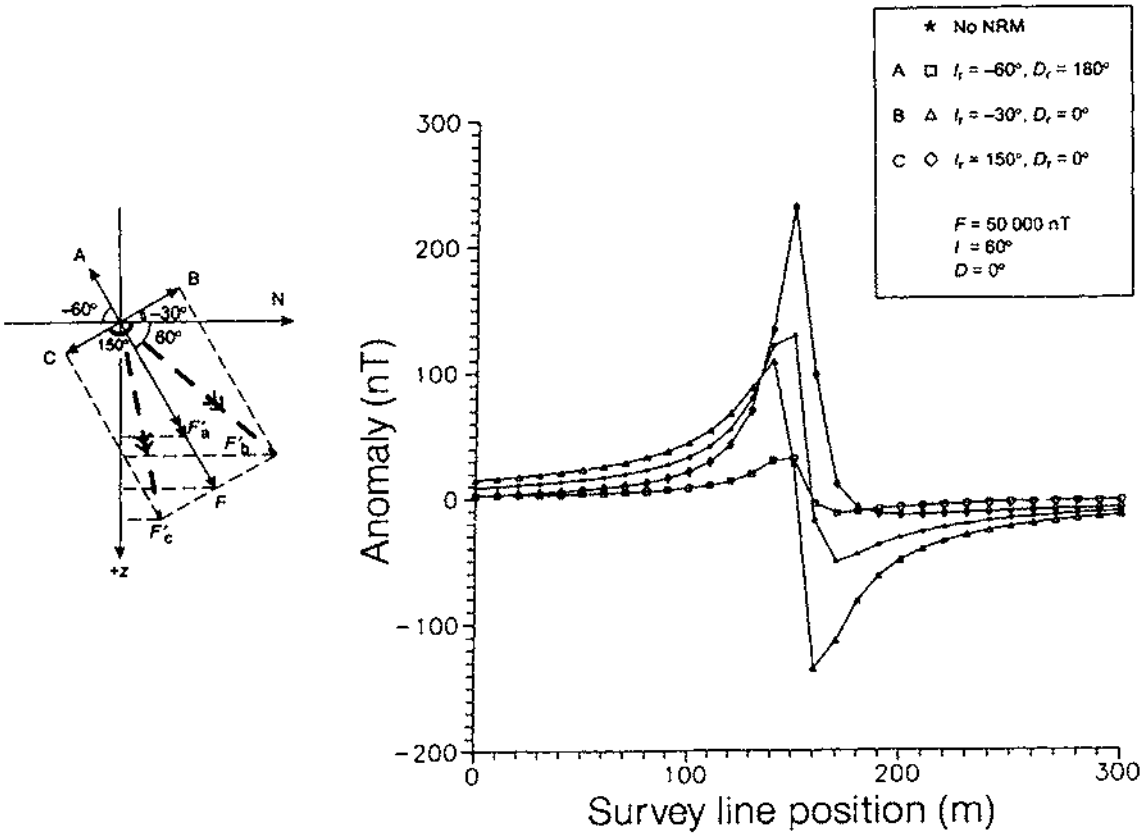

Figure 3.43 Total field anomalies over a vertical dyke striking east-west with either no remanent magnetisation (*), or remanent magnetisation of 150 nT in three directions as indicated by the schematic vector diagram

case C, where the remanent magnetisation is also at right-angles to the Earth's field but has the same positive downwards sense, F'_c, although the same magnitude as F'_b, has a larger vertical component than even the Earth's field and so the anomaly amplitude is increased substantially. In low magnetic latitudes ($< 45°$), the horizontal vector component becomes more important than the vertical component when considering remanent magnetisation.

A range of different anomaly shapes demonstrating the effects of strike, latitude, dip, depth and body size has been provided above for comparison. When a field profile is to be interpreted, there is usually some background information available about the local geology (how else was the survey designed?). Consequently, many of the variables can be constrained so that a reasonable interpretation can be produced. The biggest unknown in many cases is the presence or otherwise of any remanance. Commonly it is assumed to have no effect unless found otherwise from measurements of remanence of

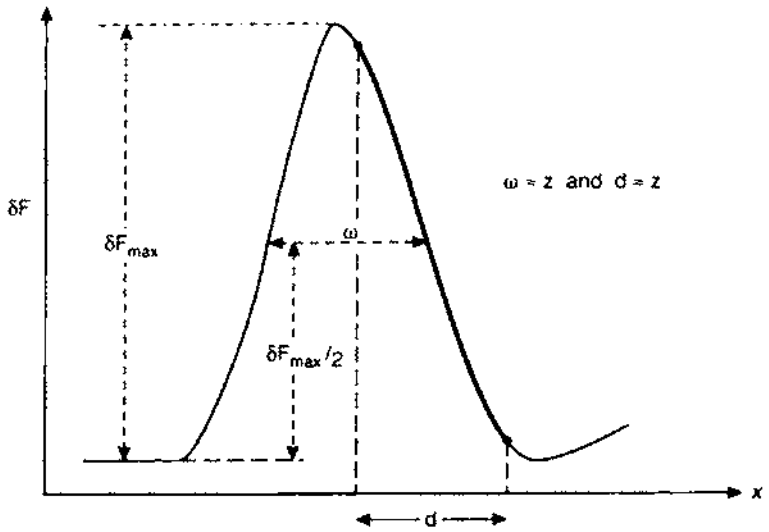

Figure 3.44 Simple graphical methods to estimate the depth to the top of a magnetised body

retrieved rock samples. However, to obtain a more exact interpretation it is necessary to model the observed data using computer methods (see Section 3.8.3).

3.8.2 Simple depth determinations

It is possible to obtain a very approximate estimate of depth to a magnetic body using the shape of the anomaly. By referring to either a simple sphere or horizontal cylinder, the width of the main peak at half its maximum value ($\delta F_{max}/2$) is very crudely equal to the depth to the centre of the magnetic body (Figure 3.44). In the case of a dipping sheet or prism, it is better to use a gradient method where the depth to the top of the body can be estimated. The simplest rule of thumb to determine depth is to measure the horizontal extent, d, of the approximately linear segment of the main peak (Figure 3.44). This distance is approximately equal to the depth (to within $\pm 20\%$).

A more theoretically based graphical method was devised by Peters (1949) and is known as Peters' Half-Slope method (Figure 3.45). A tangent (Line 1) is drawn to the point of maximum slope and, using a right-angled triangle construction, a line (Line 2) with half the slope of the original tangent is constructed. Two further lines with the same slope as Line 2 are then drawn where they form tangents to the anomaly (Lines 3 and 4). The horizontal distance, d, between these two tangents is a measure of the depth to the magnetic body (see Box 3.8).

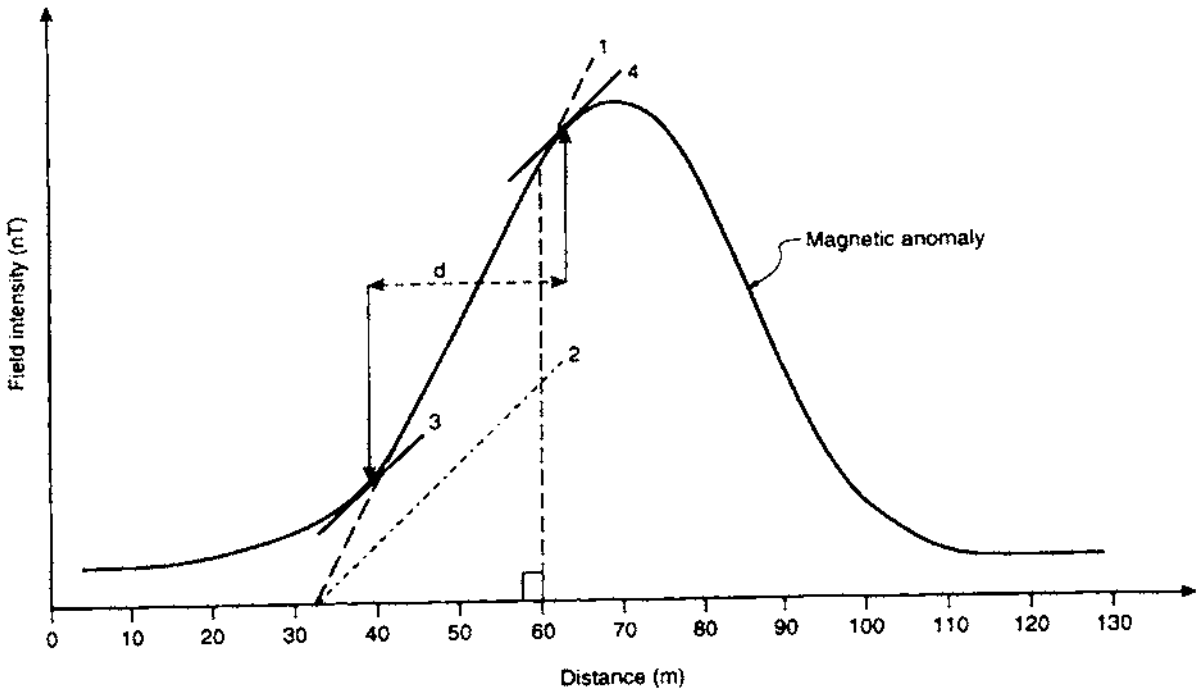

Figure 3.45 Peters' Half-Slope method of determining the depth to the top of a magnetised dyke (see text for further details)

Box 3.8 Peters' Half-Slope method of depth determination (see Figure 3.45)

The depth (z) to the top of the magnetised body is:

$$z = (d \cos \alpha)/n$$

where d is the horizontal distance between half-slope tangents; $1.2 \leqslant n \leqslant 2$, but usually $n = 1.6$; α is the angle subtended by the normal to the strike of the magnetic anomaly and true north.

Example: If $d = 24$ m, $n = 1.6$ and $\alpha = 10^{\circ}$, then $z \approx 15$ m.

Parasnis (1986) derived alternative methods of depth determination for a magnetised sheet of various thicknesses and dips using the anomaly shape as well as amplitude. Given an asymmetric anomaly (Figure 3.46) over a dipping dyke of known latitude, dip and strike directions, the position of, and the depth to, the top of the dyke can be determined from the anomaly shape. If the maximum and minimum *numerical* values are denoted δF_{max} and δF_{min} respectively (i.e. irrespective of sign), the position of the centre of the top edge of the dyke is

located at the position of the station where the anomaly amplitude equals the sum of the maximum and minimum values (taking note of their respective signs, positive or negative) and which lies between the maximum and minimum values. For example, if $\delta F_{max} = 771\,\text{nT}$ and $\delta F_{min} = -230\,\text{nT}$, the position of the centre of the dyke would be located where $\delta F = 771 - 230\,\text{nT} = 541\,\text{nT}$. Expressions from which the depth to the top of the dipping sheet can be derived (see Box 3.9) relate the amplitudes of the minimum and maximum values and their respective separations. Expressions for thick dipping sheets and other models are much more complicated

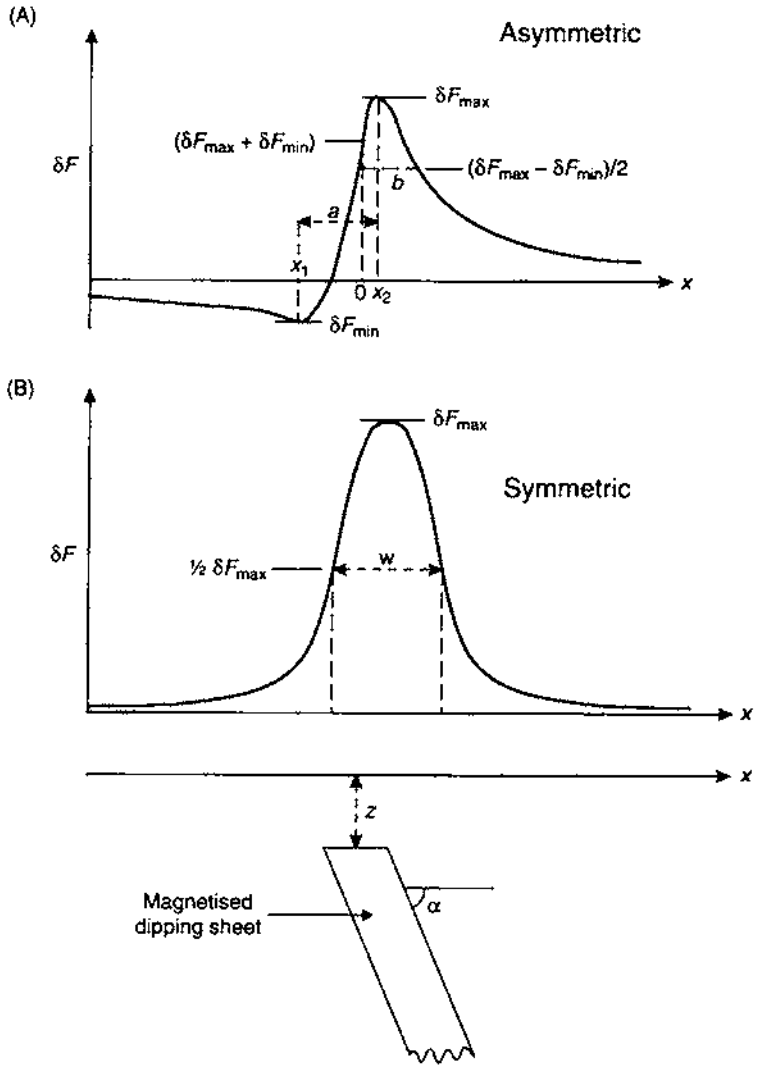

Figure 3.46 Parasnis' method of determining the position of the centre of, and the depth to the top of, a magnetised thin sheet. (A) An asymmetric profile, and (B) a symmetric profile

to calculate and are not discussed further here. Derivations of mathematical expressions and full descriptions of methods to determine shape parameters for a variety of dipping sheet-like bodies have been given by Gay (1963), Åm (1972), Parasnis (1986) and Telford *et al.* (1990), for example. Manual calculation of parameters has been largely superseded by the ease with which computer methods can be employed.

Box 3.9 Depth estimations (see Figure 3.46 for definitions of parameters)

Thin sheet (depth to top of body z)

Asymmetric anomaly:

$$z = (-x_1.x_2)^{1/2} (x_1 \text{ or } x_2 \text{ is negative})$$

$$\text{and } z = (a^2 - b^2)^{1/2}.|C|/2.(1 + C^2)^{1/2}$$

where $1/C = \tan(I + i - \alpha)$; $|C|$ is the magnitude of C; I = inclination of the Earth's magnetic field; i = inclination of any remanent magnetisation; and α = angle of dip of the sheet.

Symmetric anomaly:

$$z = w/2$$

where w = anomaly width at $\delta F_{max}/2$.

3.8.3 Modelling in two and three dimensions

Manual calculations of depths to the top of a particular magnetised body may provide an approximate figure provided an individual anomaly can be isolated from the background adequately. One common problem is when two magnetised bodies are so close to each other spatially that their magnetic anomalies overlap to form a complex anomaly (Figure 3.47). Sometimes such an anomaly may be misinterpreted as being due to a much thicker body with lower susceptibility than the actual cause, and so gives rise to an erroneous interpretation. Geological control may help, but having the ability to generate models quickly by computer is a great boon. 'What if...?' models can be constructed to test to see what anomaly results if different configurations of magnetised bodies are considered. A basis for many computer programs was provided by Talwani *et al.* (1959) and Talwani (1965). In essence, two-dimensional modelling requires that the body being modelled has a lateral extent at least 20 times its width so that the end effects can be ignored. For many geological features this restriction is adequate and anomalies from such bodies can be analysed successfully. In

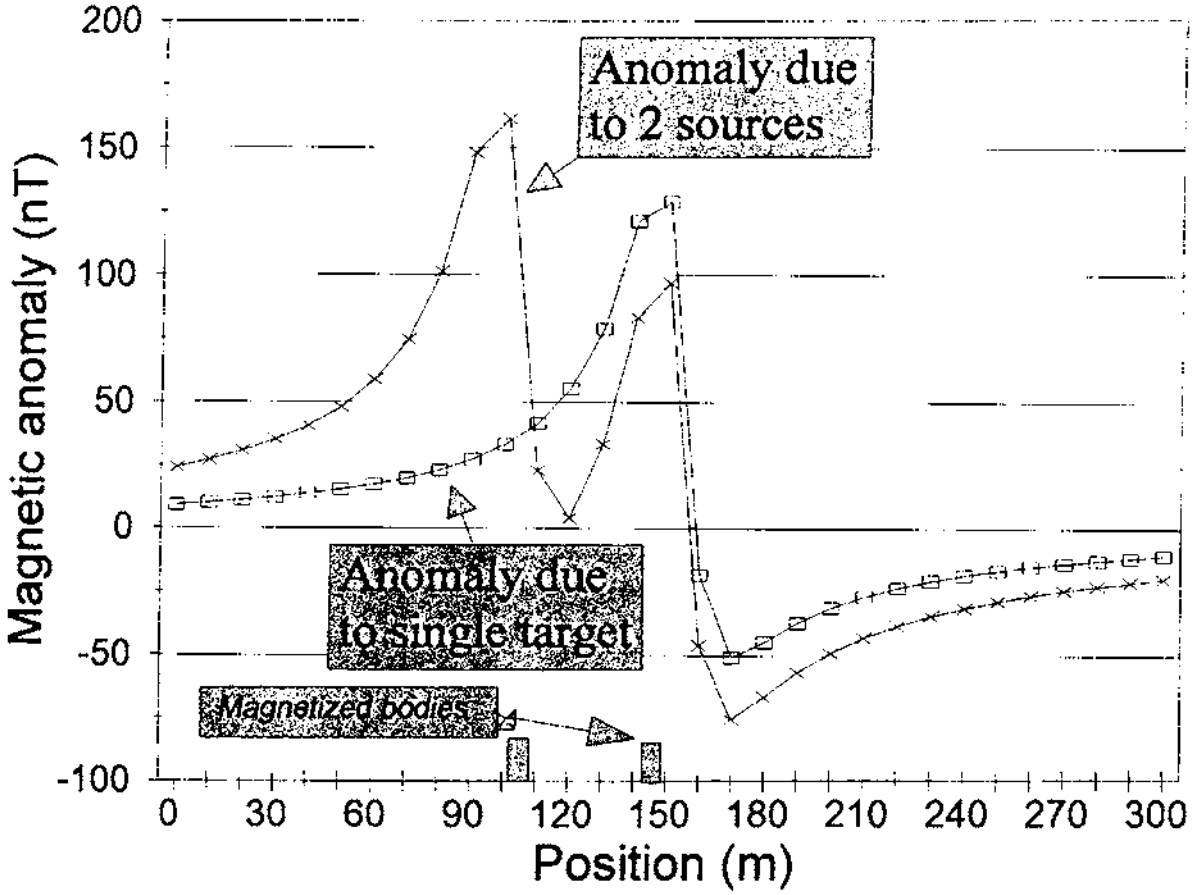

Figure 3.47 Total magnetic anomalies over two identical 5 m wide vertical dykes whose centres are separated by 45 m (their locations are indicated), and in contrast, the magnetic anomaly arising from just one of the dykes (at position 145 m), ignoring the other

many other cases, it is necessary to use more sophisticated computer methods.

With any set of profile data and the analysis of anomalies, it is absolutely essential that there be sufficient data to image the correct shape of the anomaly. Too few data leads either to incorrect evaluation of amplitude maxima or minima (consider the effects on simple depth determinations if the peak positions are not adequately defined), or in more extreme cases to severe aliasing (see Chapter 1). Limitations can be caused by too few field data values and/or by computer models producing too few point values at too large a station interval. It is therefore essential that, if computer methods are to be employed, the user is aware of what the software is actually trying to do and how it does it, and that adequate field data, both in number of values and data quality, are used.

A wide variety of computer methods exist, ranging from simple two-dimensional packages that can be run on low-cost personal

computers and laptops, up to extremely sophisticated 2.5-dimensional and three-dimensional modelling packages on more powerful workstations. Two-and-a-half dimensional modelling is an extension of two-dimensional modelling but allows for end effects to be considered (e.g. Busby 1987). Some packages provide a statistical analysis on the degree of fit between the computer-generated anomaly and the observed data. Others allow successive iterations so that each time the software completes one calculation it generates better input parameters automatically for the next time round, until certain quality parameters are met. For example, a computer program may run until the sum of the least-squares errors lies within a defined limit.

One other factor that needs to be borne in mind with magnetic modelling is that some software packages compute the anomaly for each body and then sum them arithmetically at each station. This ignores the fact that adjacent magnetised bodies will influence the magnetic anomalies of the other bodies. Consequently, the computed anomalies may be over-simplifications; and even if statistical parameters of the degree of fit are met, the derived model may still be only a crude approximation. In the majority of cases involving small-scale surveys in archaeology or site investigations, these problems are not likely to be as significant.

Modelling in three dimensions permits the construction of irregularly shaped bodies made up of a stack of magnetised polygons and takes into account edge effects. An example of three-dimensional interpretation of magnetic (and gravity) data is given in Section 3.9.1.

In addition to the spatial modelling, another method of assisting interpretation is the use of spectral analysis. The magnetic field is expressed by Fourier analysis as an integral of sine and/or cosine waves each with its own amplitude and phase. In this, the amplitude or power spectrum is plotted as a function of wavelengths (from short to long), expressed in terms of wavenumber (1/wavelength). A number of methods exist to determine the power spectrum (e.g. Spector and Parker 1979; García-Abdeslem and Ness 1994). They attempt to isolate the regional field so that the residual anomalies can be identified. Once the frequency of the residuals has been determined, the dataset can be filtered to remove the regional field, thus facilitating the production of anomaly maps on which potential target features may be highlighted. It is also possible to produce susceptibility maps from this type of analysis. From the form of the Fourier spectrum, estimates of depth to the magnetised bodies can be made (Hahn *et al.* 1976). The power spectrum yields one or more straight-line segments, each of which corresponds to a different magnetised body. A recent example of such an analysis of aeromagnetic data associated with the Worcester Graben in England has been described by Ates and Kearey (1995). Further analysis of magnetic data in the wavenumber domain has been discussed by Xia and Sprowl (1992), for example.

3.8.4 Recent developments

There have been two important developments in the display and processing of magnetic data. Where a large dataset exists for a regional aeromagnetic survey, say, the data have been displayed conventionally as a contoured anomaly map. With the advent since the 1970s of image processing using computers, it is possible to digitise and process data recorded previously in analogue form. Instead of contouring, the area covered is divided into rectangular cells each of which is assigned a total field strength value. These cells are manipulated and displayed as individual pixels. The resultant display is a colour image with blue indicating negative anomalies and red the positive anomalies. Shades of colour indicate intensities, so dark red indicates a high-amplitude positive anomaly while deep blue a high-amplitude negative anomaly. Image-processing software analogous to that used to process satellite image data, such as Landsat, is used to analyse the aeromagnetic (or indeed gravity) data (Figure 3.48).

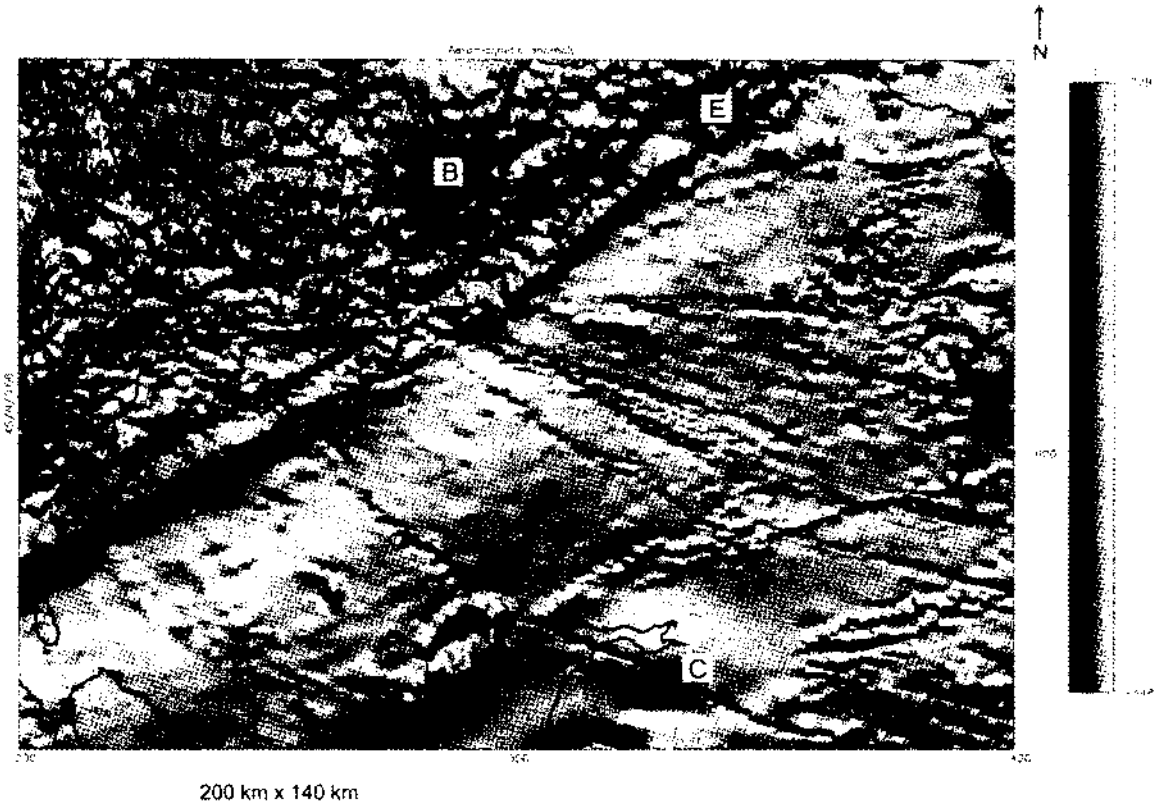

Figure 3.48 This image shows total field aeromagnetic data collected over an area of 200 km × 140 km of the Southern Uplands, Scotland (B: Bathgate; C: Carlisle; E: Edinburgh). The data were acquired in analog form along flight lines spaced approximately 2 km apart with tie lines about 10 km apart and with a mean terrain clearance of 305 m. The data were digitised, interpolated to a square grid of mesh size 5.0 km and displayed as a greyscale shaded-relief image. Sun illumination azimuth and inclination are N and 45° respectively. East–west lineations through the high-amplitude Bathgate anomaly are related to quartz-dolerite Permo-Carboniferous dykes. Numerous Teritiary dykes can be mapped trending NW–SE across the Southern Uplands. For comparison, see Figure 2.35. Image courtesy of Regional Geophysics Group, British Geological Survey

Lineaments suggestive of faults can be identified using edge filters. Spatial filters can be applied to resolve the data into regional and residual datasets and zoom facilities allow the accurate expansion of subsets of data for high-resolution analysis of much smaller areas, thus permitting the identification of any low-amplitude anomalies. Green (1983), for example, has discussed digital image processing in detail.

Image-processing methods need not be restricted to datasets covering very large areas. The only prerequisite for image processing to be possible is that there must be a large enough dataset. Dataloggers attached to magnetometers and memory-backed magnetometers or gradiometers can also be used for ground surveys where very high spatial discrimination is required (Sowerbutts and Mason 1984). Scollar *et al.* (1986) have reviewed the various data processing and display methods used in archaeology where very high resolution is also required.

Sowerbutts (1987) mapped the largely concealed Butterton Dyke in central England using a microcomputer-based fluxgate gradiometer. More than 16 800 magnetic measurements were made in one day by one person. Data were recorded at 0.5 m intervals along 317 parallel traverses 1 m apart and the results plotted as a contour map and as an isometric display (Figure 3.49). The lines of the olivine dolerite dykes are obvious. The survey produced an extremely accurate map of the dyke, which was totally concealed in the area of the survey, and demonstrated that the dyke was not terminated by a fault, as previously thought, but died out naturally.

Calculating depths to magnetic features is still the most significant aspect of magnetic surveys. Since Peters' classic paper in 1949 there has been a steady stream of publications describing new or modified methods of depth determination. In the 1980s, one technique, known as the Euler Deconvolution method, was developed to process magnetic data and convolve them to a point source at depth (Thompson 1982). The method operates on the data directly and provides a mathematical solution without recourse to any geological constraints. This has the advantage that the Euler-derived interpretation is not constrained by any preconceived geological ideas and thus can be used critically to appraise geological, and particularly structural, interpretations.

Euler's method utilises the magnetic field strength at any point in terms of the gradient of the total magnetic field, expressed in Cartesian coordinates. Furthermore, these gradients are related to different magnetic sources by a function termed the Structural Index, N. Euler's equation is given in Box 3.10. Considering the equation asterisked, a series of seven equations can be determined from observed data by evaluating this equation in at least seven places within a window placed on the data. This provides seven equations to solve for three unknowns using a least-squares procedure. The output

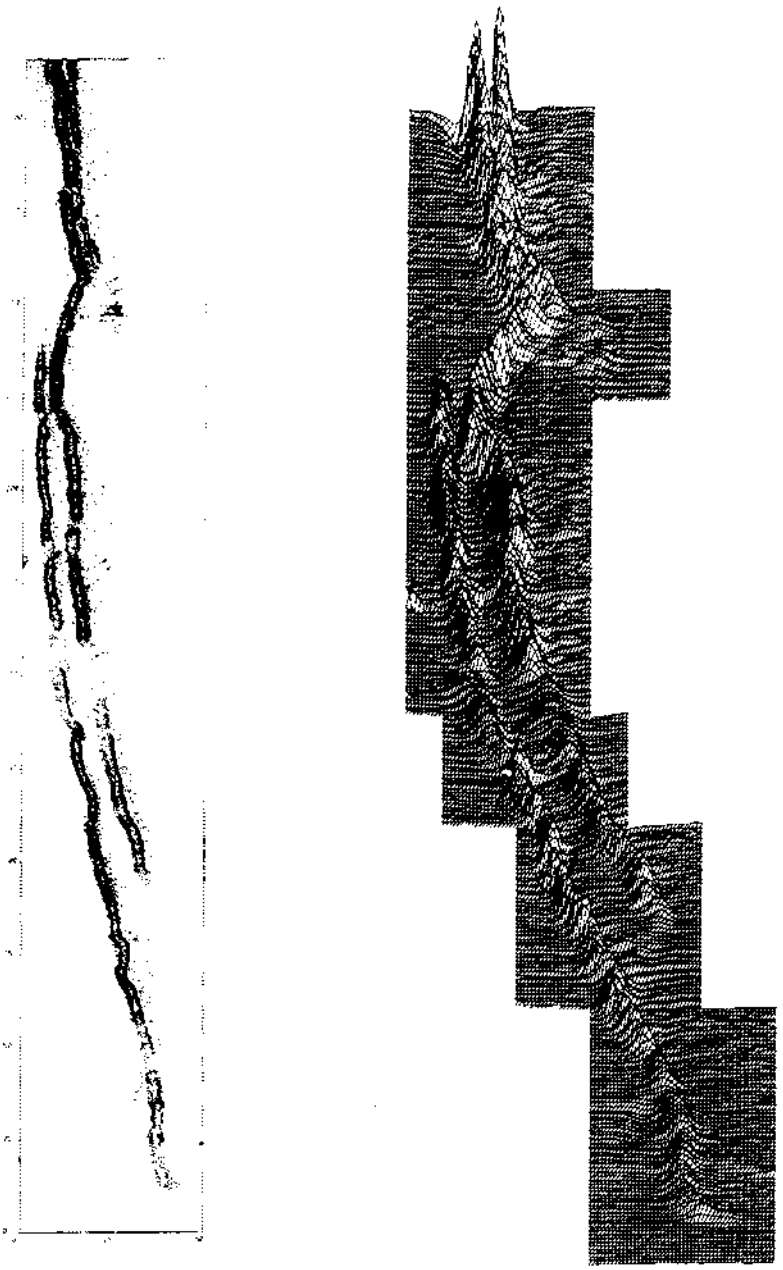

Figure 3.49 Butterton Dyke anomalies displayed as a magnetic gradient contour map with a contour interval of 20 nT/m (positives values, solid; negative values, dashed). From Sowerbutts (1987), by permission

consists of determinations of the depth to the magnetic body (z_0) producing the anomaly which can be plotted on a map as a circle, the increasing size of which indicates greater depth. Solutions that lie outside predetermined statistical bounds are rejected, thus constraining the possible number of solutions.

Box 3.10 Euler's equation

$$(x - x_0)\frac{\delta T}{\delta x} + (y - y_0)\frac{\delta T}{\delta y} - z_0\frac{\delta T}{\delta z} = N(B - T)$$

where x_0, y_0, z_0 are the coordinates of a magnetic source whose total field intensity T and regional value B are measured at a point (x, y, z); N is the degree of homogeneity and referred to as the Structural Index.

For two dimensions (x, z), Euler's equation reduces to:

$$x_0\frac{\delta T}{\delta t} + z_0\frac{\delta T}{\delta z} + NB = x\frac{\delta T}{\delta x} + NT\,(*)$$

The only unknowns are x_0, z_0 and N; gradients of T with respect to x and z can be derived from the measured magnetic data; $\delta T/\delta y$ is assumed to be equal to zero.

Structural indices N:		
Vertical geological contact	Edge of large tank	0– <0.5
Infinite sheet		0
Thick step		0.5
Irregular sill	Metal sheet	1
Vertical cylinder	Well/drum	2 2.25
Cylinder with unknown orientation	Drum	2.5
Horizontal cylinder	Pipeline/drum	2–2.75
Point dipole		3
Sphere	Tank	3

Reid *et al.* (1990) have used Euler's method to aid the interpretation of an area in south-central England. A simplified geological map of the survey area is given in Figure 3.50 with the aeromagnetic survey data. The Euler solutions have been plotted in Figure 3.50C which has been interpreted to form a structural map shown in Figure 3.50D. The Euler display has picked out the two north–south striking boundary faults marking the central block. Depth solutions for the Eastern Boundary Fault were within 0.3 km of those derived by other means. The magnetic anomalies over the central block yield very few

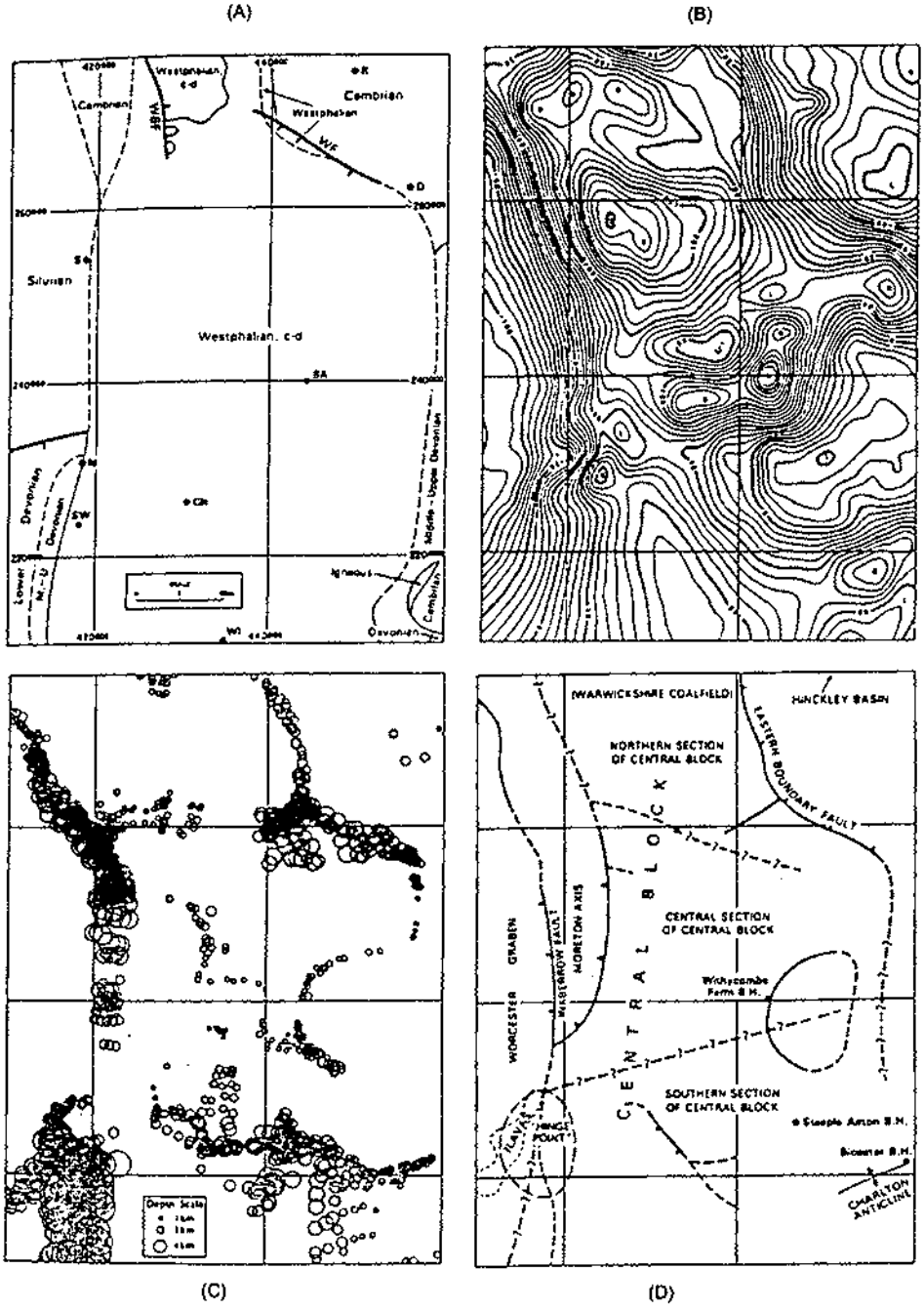

Figure 3.50 (A) Simplified geological map of the south-central part of England. (B) Aeromagnetic map of the area shown in (A). (C) Euler solutions derived from the aeromagnetic data calculated for a structural index of 1. (D) structural interpretation of the Euler solutions. From Reid *et al.* (1990), by permission

Euler solutions and this may be due to overlapping anomalies making Euler solutions statistically unacceptable and so have been rejected. Alternatively, there are insufficient data to represent the area adequately. In the south-west corner, there is a strong cluster of solutions with large depth values. This has been interpreted as being due to a magnetic body intruded at a depth of about 10 km. The main benefit of using the Euler method appears to be the delimitation of lineaments due to faults or major linear intrusions, and these features are best imaged by the Euler solutions if they are dipping, rather than vertical. The technique offers a method of independent interpretation which can be used to appraise existing geological models.

Euler's method has been incorporated into commercially available software (GRIDEPTH [Registered trademark of the Simon–Robertson Group plc] Geosoft Ltd) and has been demonstrated to be applicable to the location of near-surface utilities (pipes, drums, etc.) in addition to regional structural features. Examples of the use of the method in locating buried man-made targets have been given by Yaghoobian *et al.* (1992). They have described a detailed magnetic survey carried out at the Columbia Test Site, University of Waterloo, Canada, and corresponding Euler analysis. The results are shown in Figure 3.51. This example is perhaps too contrived to demonstrate the effectiveness in a real situation with a typical amount of background noise, but it does serve to show that the method works. Where there is a significant background noise problem, accurate depths and/or locations may be hard to achieve, especially if the measured data yield only weak signals. With careful analysis and selection of processing parameters (especially the Structural Index and GRIDEPTH window size) best-possible solutions may be obtained. It is also important that the field data be of as high quality as can be achieved and that appropriate filtering to remove obvious noise is undertaken before Euler analysis.

In addition to Euler analysis, increasing attention is being paid to the use of three-dimensional analytic signals (Nabighian 1984; Roest *et al.* 1992; MacLeod *et al.* 1993). The general principle behind the method is illustrated schematically in Figure 3.52. Given a magnetic anomaly (in the case illustrated, this arises from a square prism magnetised in an arbitrary direction), the three derivatives can be obtained from which the analytic signal is derived (Box 3.11). The amplitude of the three-dimensional analytic signal of the total magnetic field produces maxima over magnetic sources irrespective of their magnetisation direction (MacLeod *et al.* 1993; Parlowski *et al.* 1995). The three-dimensional analytic signal can be calculated readily from an accurately gridded dataset. A 3×3 filter can be applied to obtain the horizontal gradients ($\delta T/\delta x$ and $\delta T/\delta y$). A fast Fourier transform (FFT) can be used to obtain the vertical gradient ($\delta T/\delta z$). Alternatively, if a gradiometer has been used to acquire the data, the vertical gradient is a measured parameter.

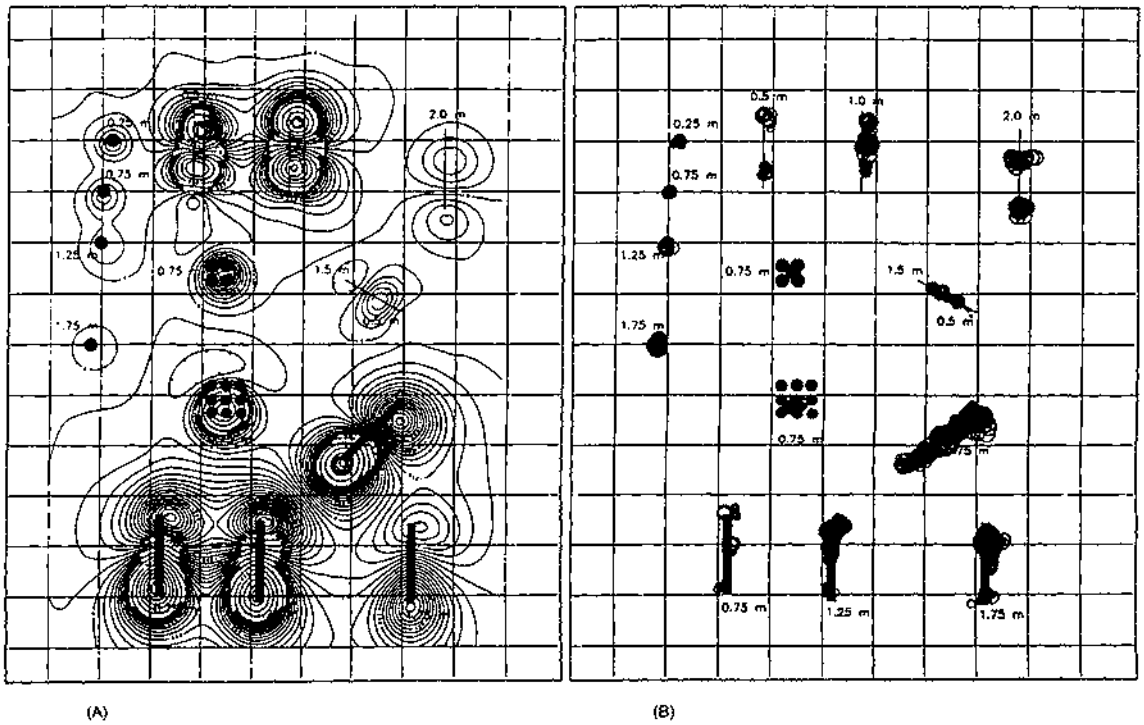

Figure 3.51 (A) Total magnetic field anomaly map over the Columbia Test Site, University of Waterloo, Canada, with the known depths to the various targets listed. (B) The Euler solutions calculated from (A). From Yaghoobian *et al.* (1992), by permission

From the form of the resultant analytic signal, solutions are obtained as to the location (x, y, z) of the source. These are shown graphically as circles, much the same as from Euler solutions. The distance between the inflection points of the analytic signal anomaly is directly proportional to the depth to the top of the magnetic source. It has been demonstrated that both Euler and analytic solutions can be used to produce an integrated model of the causative magnetised structure: the analytic signal can be used to delineate the magnetic contrasts and give estimates of their approximate depths, while the Euler solution yields more detailed interpretation at depth (Roest *et al.* 1992; Parlowski *et al.* 1995). It should be noted that the use of analytic signals can also be applied to gravity data or a combination of potential-field data.

Box 3.11 The amplitude of the three-dimensional analytic signal (MacLeod et al. 1993)

The amplitude of the analytic signal ($|A(x, y)|$) at any location (x, y) is given by:

$$|A(x, y)| = [(\delta T/\delta x)^2 + (\delta T/\delta y)^2 + (\delta T/\delta z)^2]^{1/2}$$

where T is the measured field at (x, y).

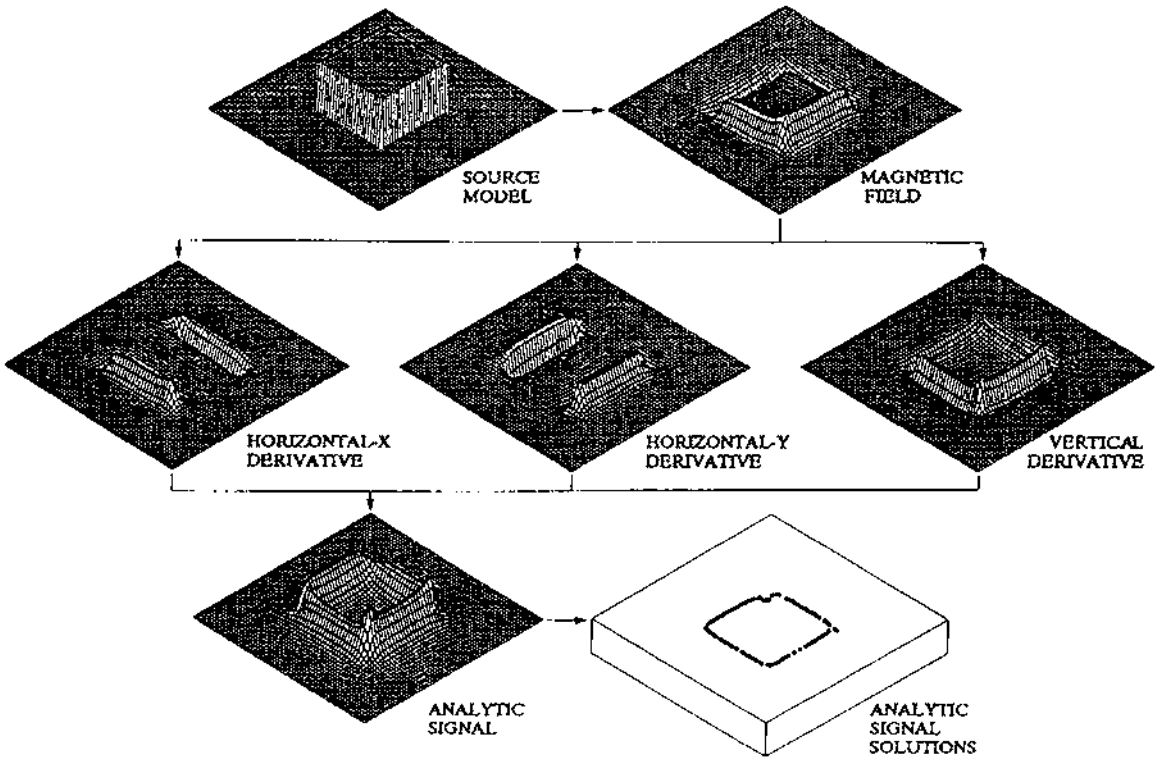

Figure 3.52 Schematic outline of the analytic signal method. Horizontal and vertical derivatives are calculated from the total field anomaly over a square prism and combined to yield the absolute value of the analytic signal. The locations of the maxima and the shape of this signal can be used to find body edges and corresponding depth estimates. From Roest *et al.* (1992), by permission

In shallow environmental applications, sources at very shallow depth (< 1 m) give rise to extremely high frequency signals which are difficult to resolve using these techniques. It is probably more cost-effective to dig with a shovel on the position of magnetic anomalies to locate the target source than to go through the analytic procedures outlined above. However, as soon as the depth is beyond easy excavatability, the value in the use of analytic solutions increases. Accuracies in depth determination are of the order of 30% of the target depth. This figure is one that may be improved upon in time with future developments and experience.

3.9 APPLICATIONS AND CASE HISTORIES

3.9.1 Regional aeromagnetic investigations

An aeromagnetic survey over the Lizard Peninsula in Cornwall, which was interpreted in conjunction with gravity data (Rollin 1986), provides an example of three-dimensional interpretation. The Lizard Complex comprises what is thought to be an ophiolite suite made up of a lower tectonic sheet of hornblende schists and metasediments and

structurally overlain by peridotite and gabbro. This upper sheet shows lateral variation from harzburgite peridotite, gabbro and a dyke complex in the east to therzolite peridotite and cumulate complex to the west. Comparison of the simplified geological map with the corresponding aeromagnetic map (Figure 3.53) demon-

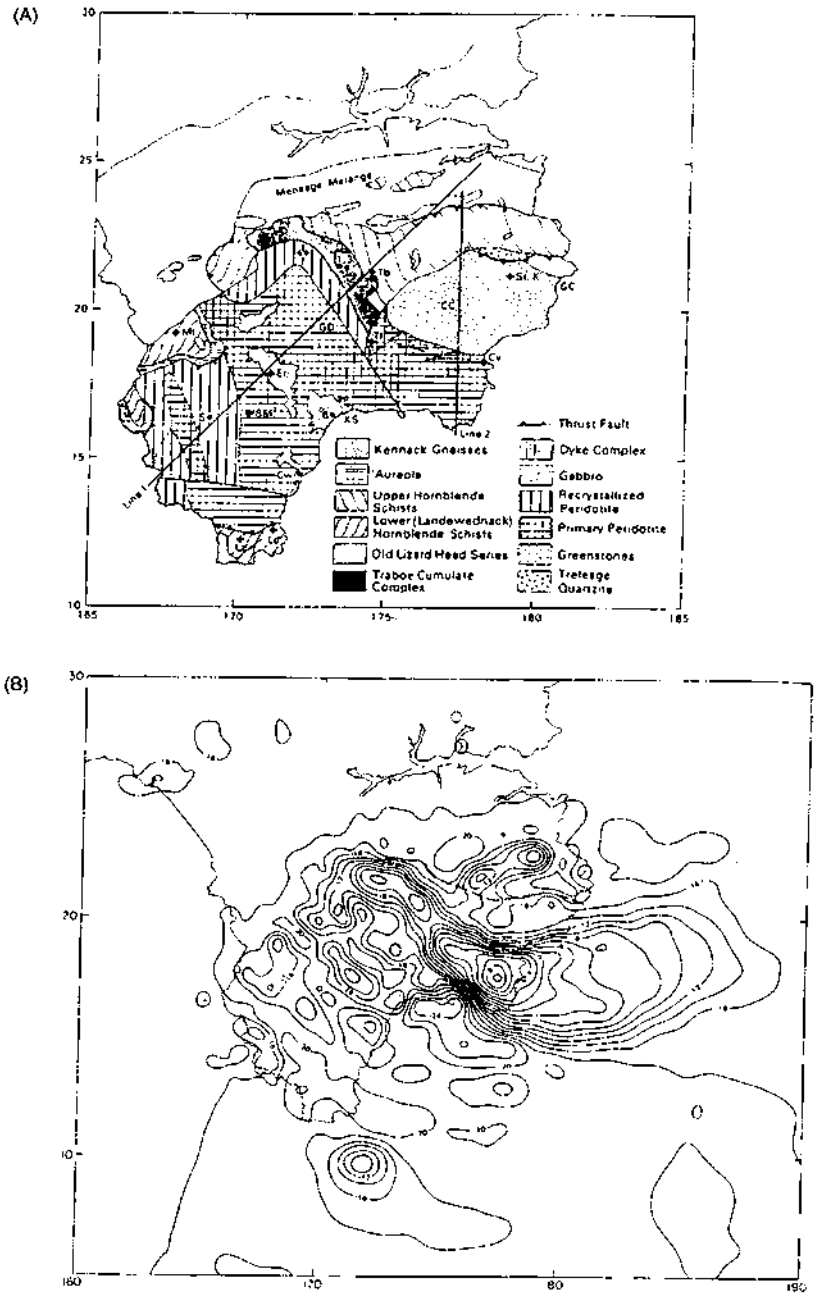

Figure 3.53 (A) Simplified geological map of the Lizard Peninsula, south Cornwall, and (B) the corresponding aeromagnetic map. From Rollin (1986), by permission

strates the correlation of the most prominent magnetic feature, a magnetic high which extends offshore to the east, onshore across the harzburgite peridotite south of Coverack north-westwards with diminishing amplitude over the Traboe Cumulate Complex. Western Lizard is characterised by small localised anomalies over the western peridotite. These features correlate with small outcrops of interlayered basic gneiss. A summary of the tectonic units and their respective schematic geophysical responses are shown in Figure 3.54. From this it can be seen that the lherzolite peridotite has a much smaller magnetic effect than the harzburgite peridotite while they both have comparable effects on the gravity field. It was found that the harzburgite peridotite was depleted particularly in TiO_2 compared with the lherzolite peridotite. Low concentrations of titanium in these rocks are indicative of complex geochemical processes which affected the formation of magnetite during serpentinisation.

When modelling these aeromagnetic anomalies, Rollin found that it was necessary to investigate the remanent magnetisation which is

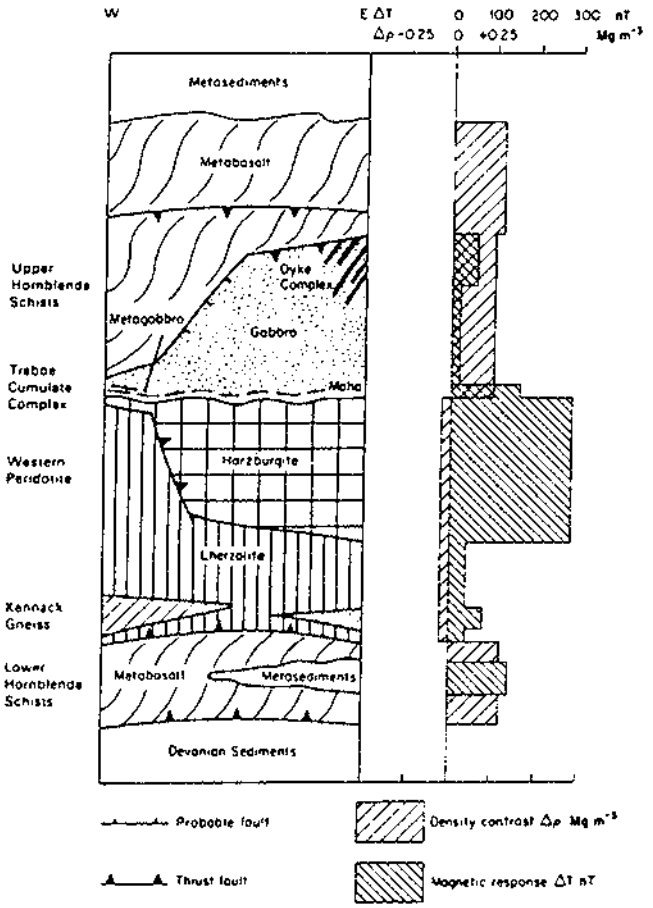

Figure 3.54 Tectonics units of the Lizard and a schematic representation of their geophysical responses. From Rollin (1986), by permission

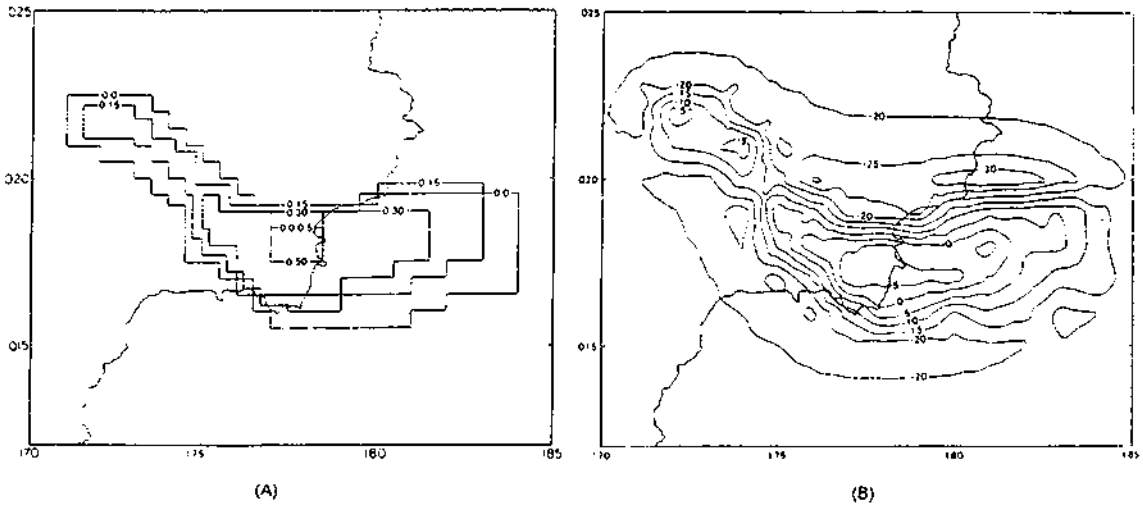

Figure 3.55 Three-dimensional modelling of the south-east part of the Lizard. (A) Stacked horizontal polygons, and (B) the resulting calculated magnetic anomaly. From Rollin (1986), by permission

significant, as might be expected for such a suite of rocks. On the basis of field and laboratory measurements, the overall Königsberger ratio (remanent:induced magnetisation) was taken to be 0.43 with a declination and inclination of the remanent magnetisation of 286° and 75° respectively, with a resultant magnetisation up to 220 nT and a mean susceptibility of 0.0774 (SI). A simple three-dimensional model comprising stacked horizontal polygons was then constructed for the eastern area, which produced a calculated anomaly (Figure 3.55)

Δρ Mg m^{-3}	ΔT nT	
0.29	220-250	Traboe Complex
-0.05	25-100	Peridotite
-0.05	75-100	Gneiss-Schist
0.29	0	Hornblende schist
0.15	0	Meneage
0.24	50	Gabbro

± ± ± Observed and calculated (+) gravity anomaly

• • • Observed and calculated (•) magnetic anomaly

Figure 3.56 Aeromagnetic and gravity anomaly profiles along Line 2 (Figure 3.53A) across the south-eastern part of the Lizard. From Rollin (1986), by permission

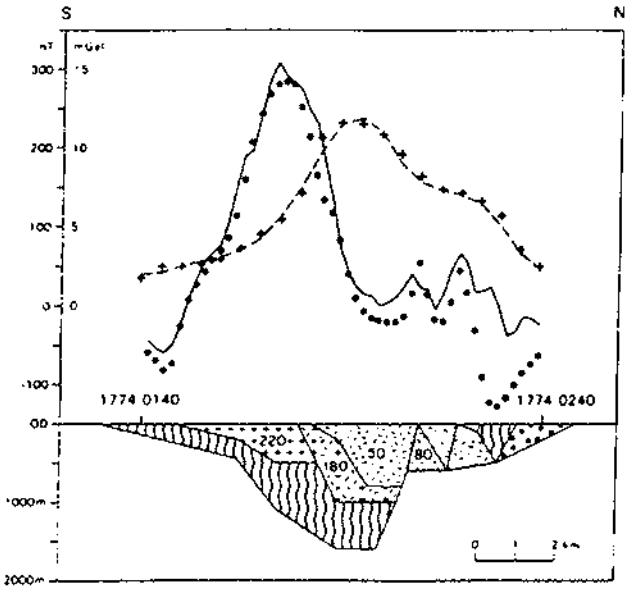

comparable to the observed aeromagnetic anomaly. The magnetic interpretation indicated that the Traboe Complex has a thickness of only 150 m while the eastern harzburgite peridotite is about 500 m thick (Figure 3.56). Independent gravity modelling gave the thickness of the eastern peridotite as 560 m, which is in reasonable accord with the magnetic interpretation.

3.9.2 Mineral exploration

In Finland, in regions of Pre-Cambrian basement comprising black graphite-schists, the location of sulphide ores is becoming increasingly difficult. The easy-to-find ores have already been identified. The more difficult ones, such as pyrrhotite-rich black schists and associated mineralisation, have been more easily eroded by glacial ice than the surrounding rocks and have become buried beneath a veneer of overburden, commonly up to 30 m thick. The overburden is characterised by high resistivities so the relatively conductive ore zones can be located using electrical methods. However, this is not always practicable so magnetic methods have also been used in conjunction with geochemical surveys. Furthermore, it is difficult to discriminate between the geophysical anomalies produced by economic sulphide mineralisation and those caused by the black schists and other rocks. Consequently, the identification of copper ores is particularly difficult.

The Saramäki orebody, located about 370 km north-east of Helsinki, forms a compact copper mass with some cobalt, and occurs in geological complexes comprising serpentinites, dolomites, skarns, quartzites and black schists, in a country rock of mica schist. The exploration strategy has been discussed in detail by Ketola (1979). The whole mineralised complex can be traced using aerogeophysical methods for over 240 km. The specific orebody, which was located in 1910 by drilling, is 4 km long, 200–400 m wide and extends down to about 150 m. Average copper content is 3.8% with 0.2% cobalt.

Problems with identification of the orebody can be seen by reference to Figure 3.57. The electrical resistivity (SLINGRAM) anomalies are caused by the black schists. The whole skarn zone forms a denser block (0.23 Mg/m^3 higher) compared with the country rock and so the sub-units within the mineralised zone cannot be differentiated using gravity. Susceptibility measurements made using the boreholes suggested that the mineralised zone was magnetised heterogeneously and that its upper part influenced the magnetic anomaly. In addition it was found by two-dimensional modelling that the main magnetised zones had significant remanent magnetisation. If remanence is ignored, the dip of the two main zones is inconsistent with the known dips, derived from drilling, even though the computed anomaly fits the observed one very well (Figure 3.58A). By incorporating remanence, with inclination 45° and declination 90° (compared

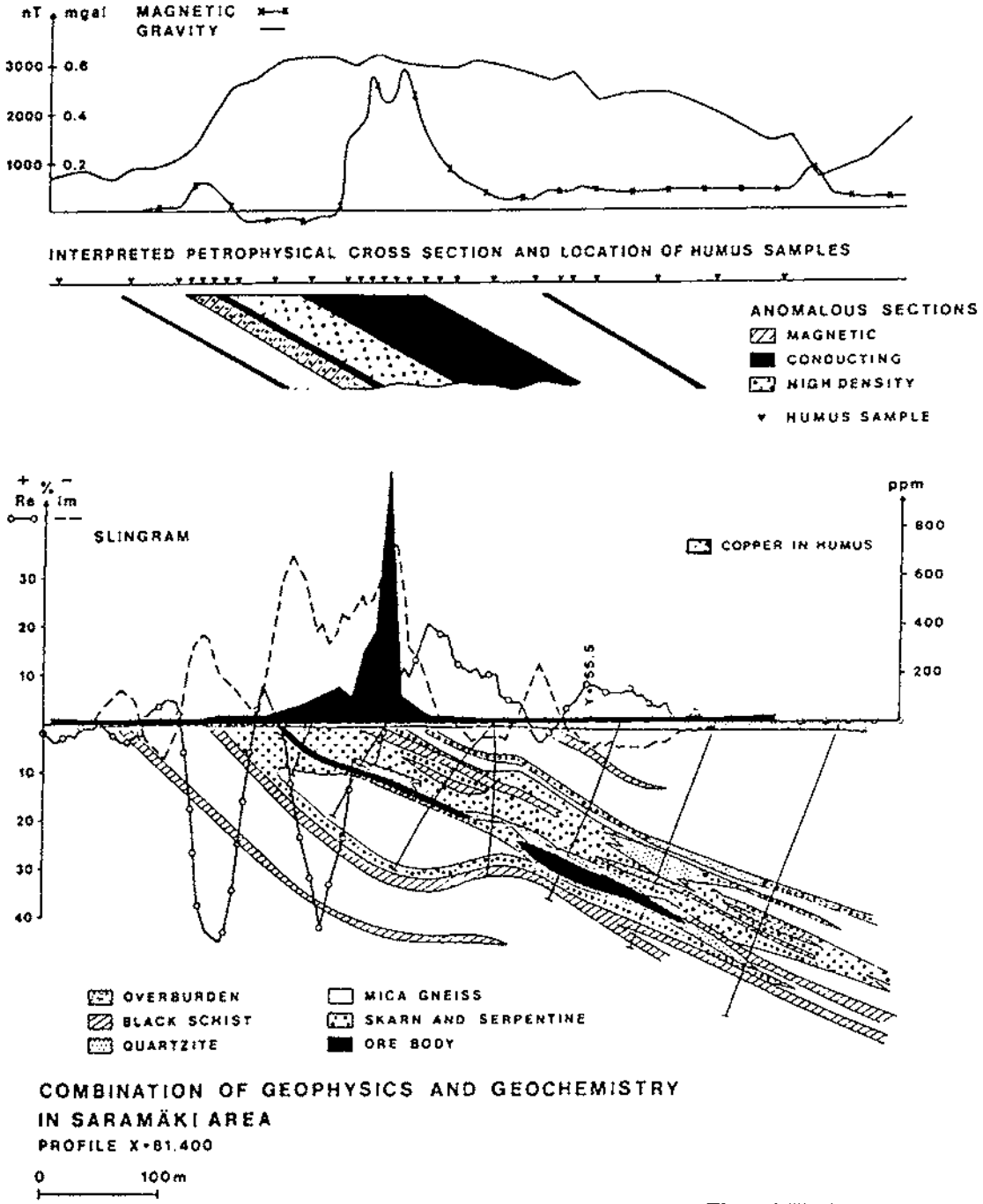

Figure 3.57 Magnetic, gravity and SLINGRAM electrical data with a geological cross-section for the Saramäki orebody, Finland. From Ketola (1979), by permission

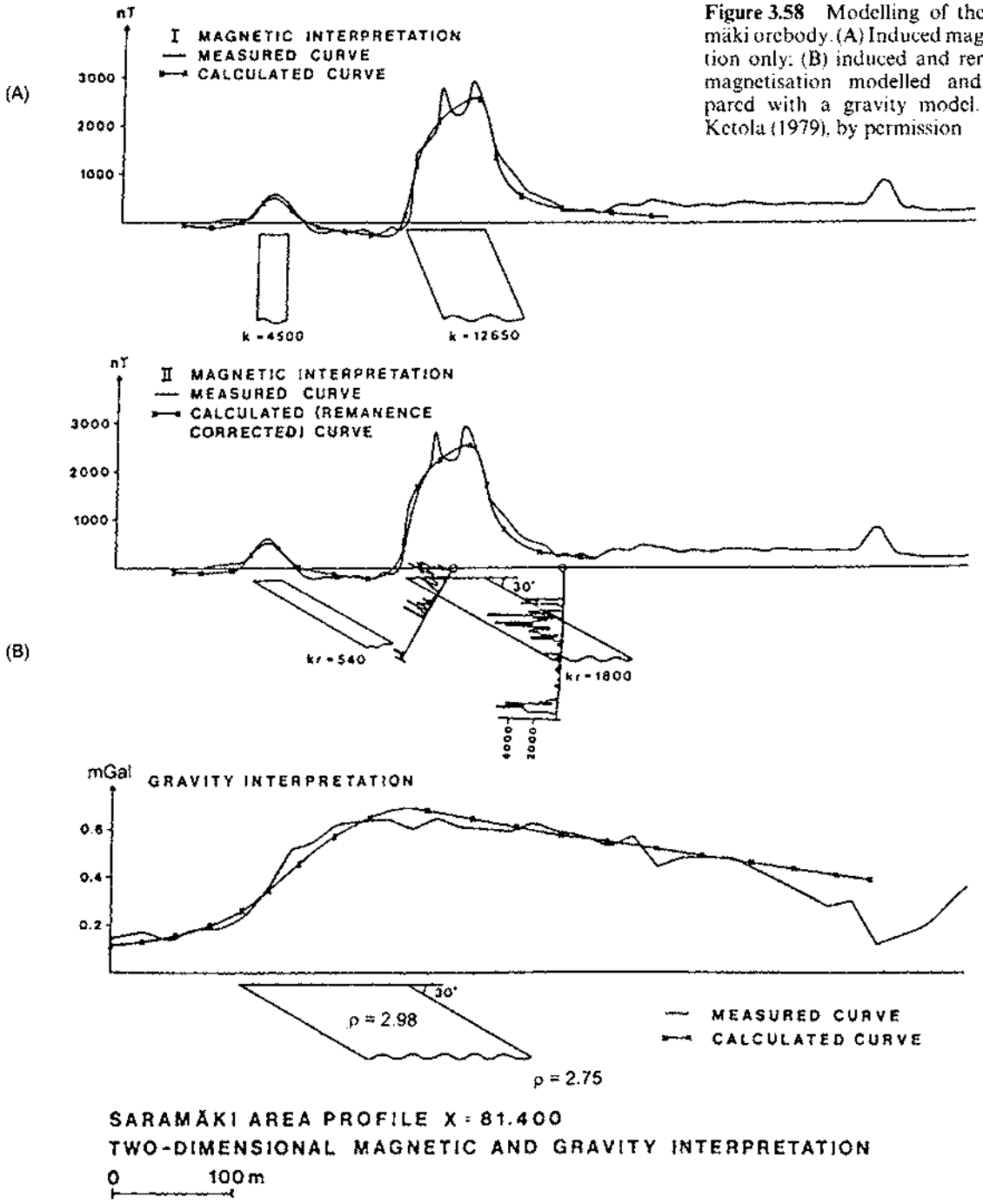

Figure 3.58 Modelling of the Saramäki orebody. (A) Induced magnetisation only; (B) induced and remanent magnetisation modelled and compared with a gravity model. From Ketola (1979), by permission

with 75° and 7°, respectively for the Earth's field), geologically compatible models were then produced which were also in accord with those used in the gravity modelling (Figure 3.58B).

Ketola concluded from this and other similar examples in Finland that geophysical or geochemical methods alone were insufficient to resolve these complex orebodies. It was necessary to use a wide variety of geophysical and geochemical techniques together, in conjunction with drilling, to provide a successful differentiation of the sub-surface geology.

Other illustrations of magnetic anomalies over mineralised bodies have been shown in Figure 1.9D, for a lode at Wheel Fanny, north-west Devon, where the course of the lode is picked out clearly by the linear magnetic anomalies. Figure 3.32 illustrates a ground magnetometer profile over sulphide mineralisation at Sourton Tors, north-west Dartmoor, Devon.

3.9.3 Engineering applications

3.9.3.1 Detection of underground pipes

Sowerbutts (1988) has provided a clear example of how high-resolution magnetic gradient surveys can identify not only the location of underground metal pipes but also the position of joints between individual sections of pipe. If joints can be located remotely, the amount of excavation required to examine and repair a pipe can be minimised, saving time, money and inconvenience.

The magnetic anomaly along a pipe consists of a series of smaller anomalies each of which corresponds to an individually cast segment of pipe which behaves like a magnetic dipole. For a pipe buried close to the surface and away from extraneous magnetic sources, a clear repetition of anomalies can be identified (Figure 3.59A). In the case illustrated, the pipe had a diameter of 0.5 m and was made of ductile iron in 6.3 m long sections and buried at a depth of 0.5 m. Magnetic highs, with gradients up to 4000 nT/m, are centred between 0.5 m and 1.0 m along from the socket end. For a pipe orientated east west, a typical negative (north) and positive (south) anomaly doublet is produced along a profile aligned north south in the northern hemisphere (cf. Figure 3.37A). A magnetised body orientated north–south produces a more symmetric positive-only or negative-only anomaly, and this is also seen in pipes orientated north–south (Figure 3.59B). For a smaller 76 mm diameter pipe (Figure 3.59C) this anomaly doublet effect is clearly repeated along the line of this north–south orientated pipe. In an urban environment, identifying the anomalies associated specifically with the buried pipe can be very difficult. Other magnetic materials are likely to be nearby and this can obscure or defocus the pipeline anomaly (Figure 3.59D). In the last case, the pipe was 0.15 m diameter and buried about 1.5 m down. Local metal grids

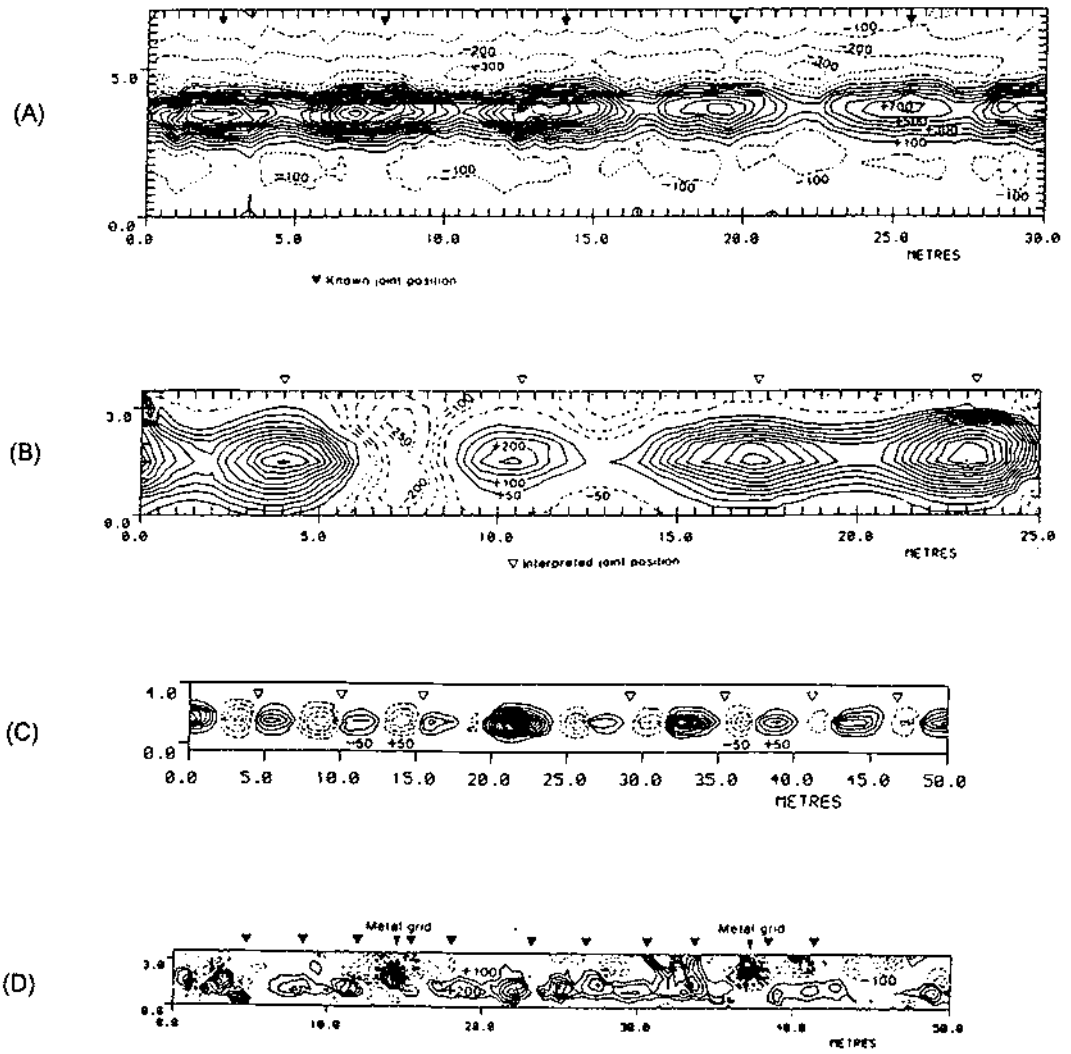

Figure 3.59 Magnetic gradiometer anomalies over buried pipelines: (A) Ductile iron pipe, diameter 0.5 m buried at 0.5 m depth, E–W trend of pipe; contour interval 200 nT/m. (B) Cast iron pipe, N–S trend of pipe; contour interval 50 nT/m. (C) 76 mm diameter cast iron gas pipe trending N–S. (D) 0.15 m diameter pipe, buried about 1.5 m down, in an urban environment with extraneous magnetic anomalies caused by adjacent metal grids. From Sowerbutts (1988), by permission

produce large magnetic anomalies. The anomaly pattern associated with this pipe is now irregular and complex, and it is not possible to identify pipe joints. Even seamless steel pipes with welded joints can be identified in areas with a quiet magnetic background.

A further example of the use of magnetometry to locate near-surface pipes has been given by Geometrics Inc., who acquired data over a test site at Stanford University, USA, using a caesium magnetometer. The data were contoured and displayed as both a map and an isometric projection which are shown with a map of the utilities in Figure 3.60. The correlation between buried objects and the corresponding magnetic anomalies is obvious.

(A)

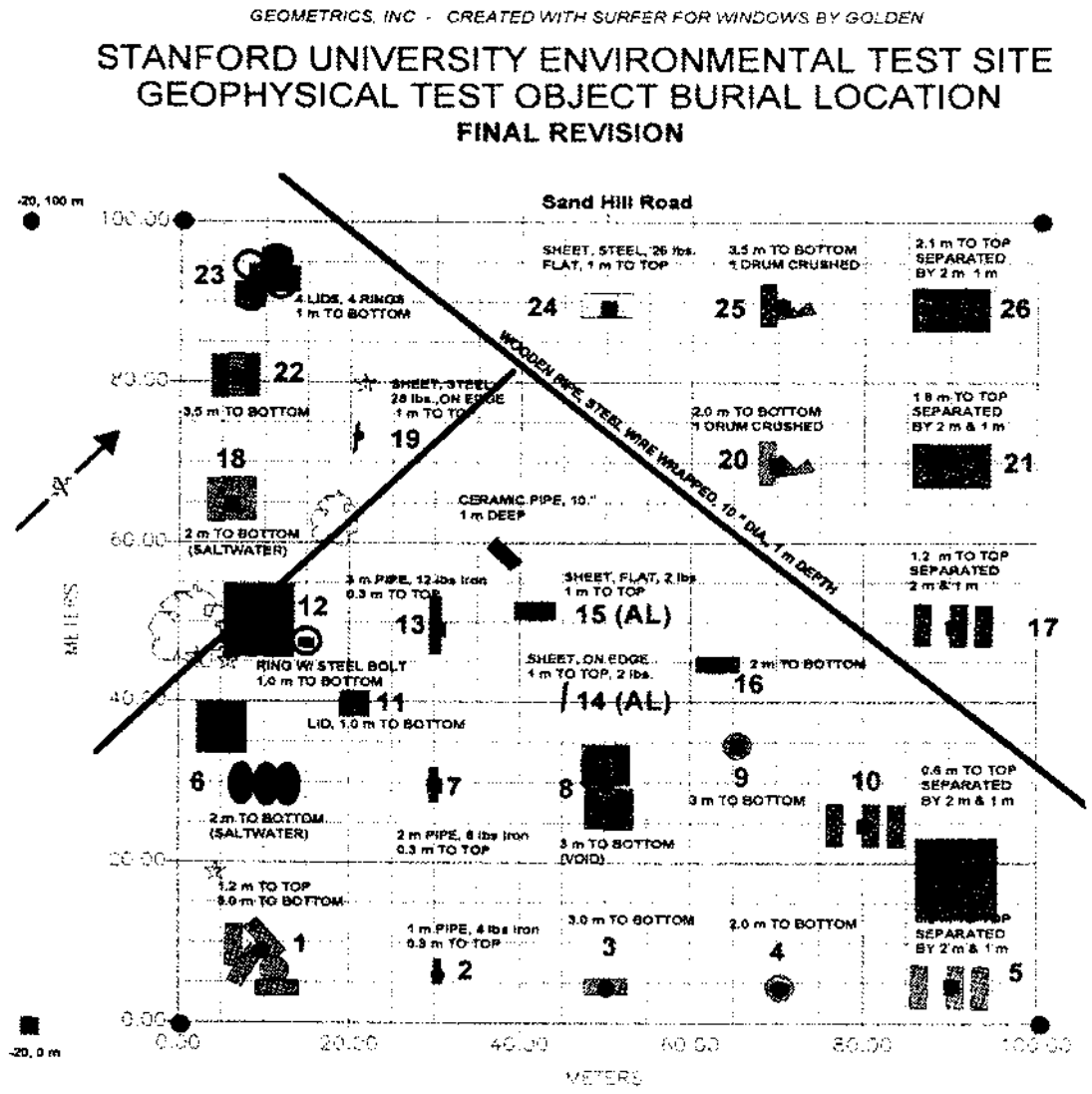
GEOMETRICS, INC - CREATED WITH SURFER FOR WINDOWS BY GOLDEN
STANFORD UNIVERSITY ENVIRONMENTAL TEST SITE
GEOPHYSICAL TEST OBJECT BURIAL LOCATION
FINAL REVISION
Sand Hill Road
WOODEN PIPE, STEEL WIRE WRAPPED, 10" DIA, 1 m DEPTH
METERS
0.00
20.00
40.00
60.00
80.00
100.00
CORNER IRON STAKE, 1/2 " X 3 FT
55 GALLON STEEL DRUM, 35 lbs.
DRUM LOCKING RING
METAL SHEET, 48" X 28" FLAT AND ON EDGE
55 GALLON PLASTIC DRUM
DRUM LID
IRON PIPE, 3/4" NO JOINTS
OBJECT LOCATION
UNKNOWN
TREE OR STUMP
SALTWATER IS 2.8 lbs. ROCKSALT PER 55 GALLONS WATER - OBJECT SIZES NOT TO SCALE

(B)

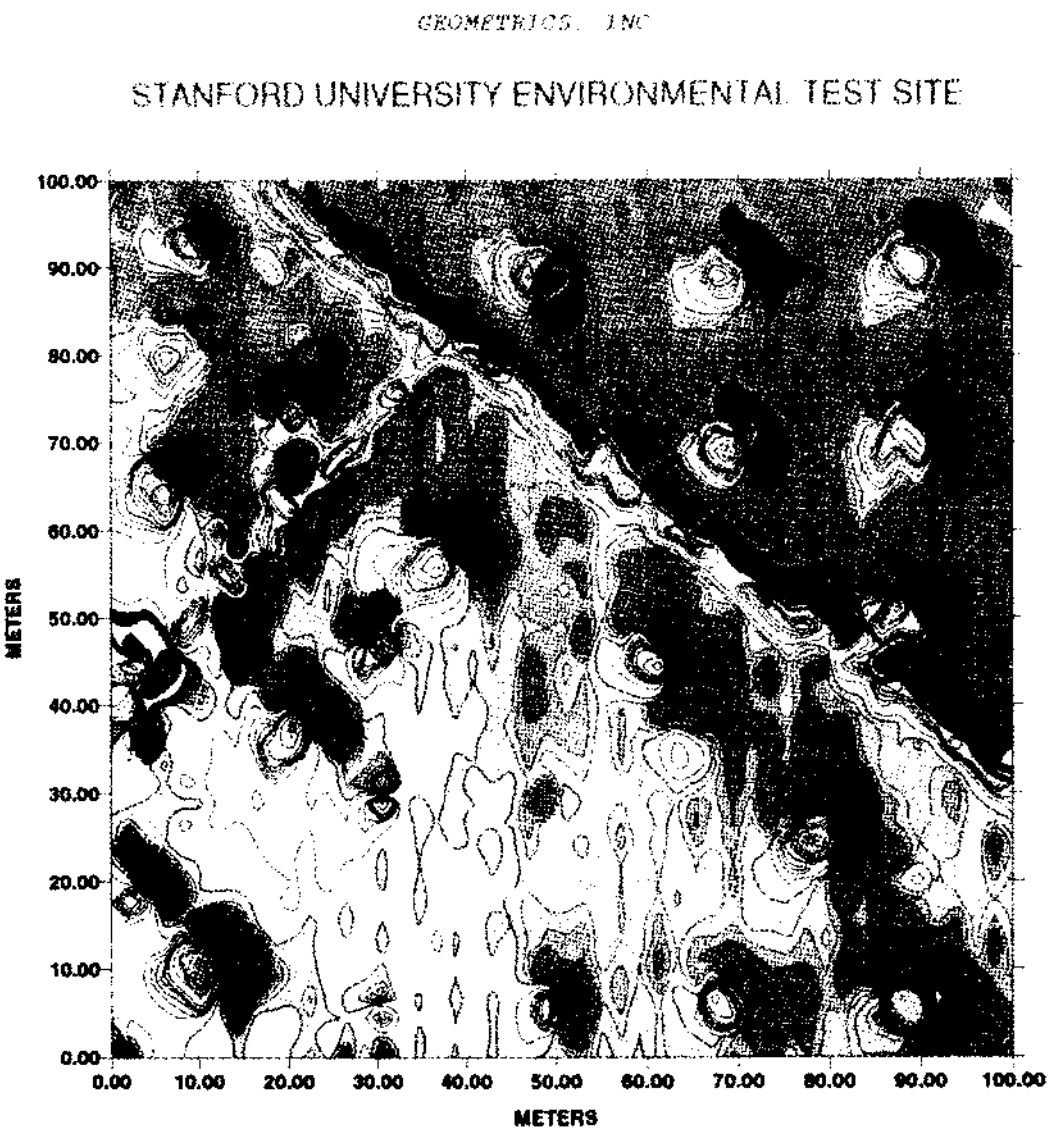
GEOMETRICS, INC
STANFORD UNIVERSITY ENVIRONMENTAL TEST SITE
METERS
100.00
90.00
80.00
70.00
60.00
50.00
40.00
30.00
20.00
10.00
0.00
0.00
10.00
20.00
30.00
40.00
50.00
60.00
70.00
80.00
90.00
100.00
METERS
G-822L CESIUM MAGNETOMETER DATA
VARIABLE CONTOUR INTERVAL
FINAL MAGNETIC CONTOUR MAP

(C)

GEOMETRICS, INC

STANFORD UNIVERSITY ENVIRONMENTAL TEST SITE

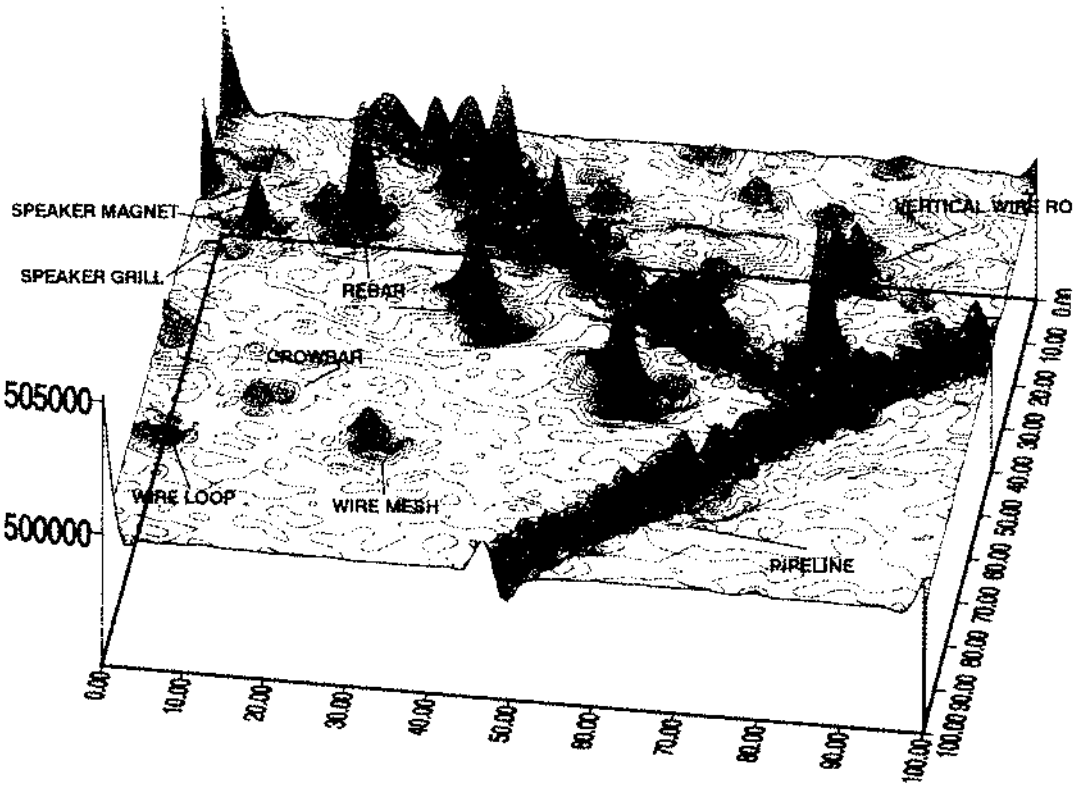

G-822L CESIUM MAGNETOMETER DATA

20 GAMMA CONTOUR INTERVAL

INTERSECTING PIPELINES

[illegible] WINSURF BY GOLDEN

Anomalies have been produced which have been characteristic of induced magnetisation in many cases, but what has not been considered is that pipes acquire a permanent magnetisation on cooling during manufacture. It may be necessary to examine the orientation of the pipes as they cool at their respective foundries (hence determine the inclination and declination of permanent magnetisation). Having ascertained the permanent magnetisation, and knowing where these pipes have been buried, it should then be possible to determine more accurately the magnetic anomaly due to each segment of pipe.

Figure 3.60 (*previous pages*) (A) Map of the Stanford University, USA, environmental test site showing the details of the various buried targets. (B) Magnetic anomaly map produced using a caesium magnetometer sampling at 10 readings per metre along survey lines at 2 m spacings. (C) Isometric projection of the data in (B). Courtesy of Geometrics Inc.

3.9.3.2 Detection of buried infill

In areas where clay infills hollows in bedrock such as chalk, the slight contrast in magnetic susceptibility can still be sufficient for magnetic survey methods to be useful.

In many engineering investigations, an arbitrary spacing or grid of boreholes is used that in all too many cases is inadequate to indicate the actual variation on ground conditions. To drill holes at small enough separations may be prohibitively expensive as well as being unnecessarily intrusive. In such cases, geophysical methods can be used to image the ground variability.

McDowell (1975) has provided an example of how magnetic mapping of magnetic anomalies with only 15 nT amplitudes provided a clearer picture of a clay with flints cover over chalk in Upper Enham, Hampshire. A magnetic anomaly map (Figure 3.61A) of the site shows the possible clay infill and clearly demonstrates that the inter-borehole separation was far too large to provide a representative impression of ground conditions. Should a contractor have started excavations on the basis of ground conditions predicted by the borehole data, a claim for compensation could have justifiably been made to recompense the additional work required to cope with the unexpected variations in ground conditions. The cost of the claim probably would have exceeded that of the geophysical survey in the first place! The magnetic profile across the clay pipe, which is orientated north–south, shows a form similar to that illustrated in Figure 3.41 but with opposite polarity, as the clay with flints has the slightly higher magnetic susceptibility than the chalk.

3.9.4 Detection of buried containers

There are many situations where it is imperative that potentially harmful objects, such as bombs or drums of toxic waste, be located passively. Drilling holes to locate drums of poisonous waste, or using electromagnetic signals to detect hidden bombs, could have devastating consequences. As both types of object will produce a magnetic anomaly, it is possible to use magnetic methods to locate them without risk. The amplitudes of magnetic anomalies detectable for

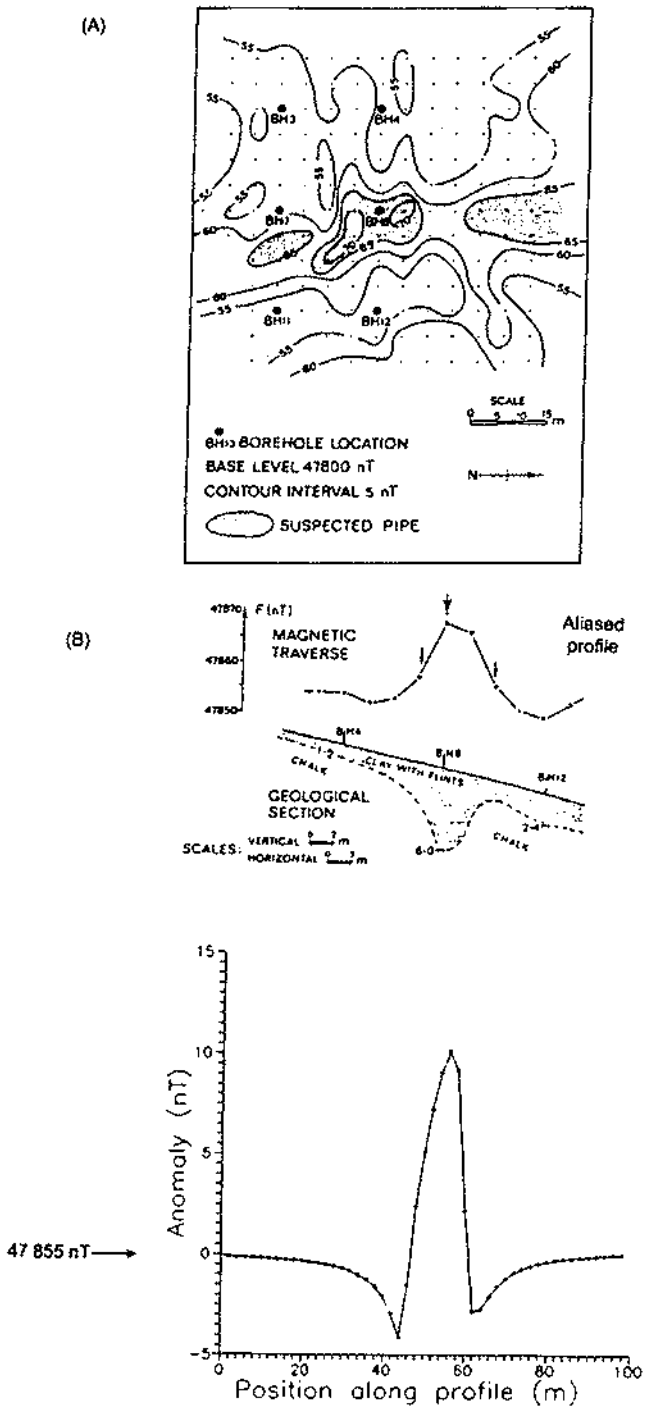

Figure 3.61 Megnetic anomalies over a clay-with-flints infill over chalk at Upper Enham, Hampshire, showing (A) how the magnetic survey resolved the variable ground conditions far better than the inadequately spaced boreholes, and (B) the shape of the profile across the clay pipe infill, which trends N–S, compared with a modelled anomaly (cf. Figure 3.41). (A) and (B) from McDowell (1975), by permission

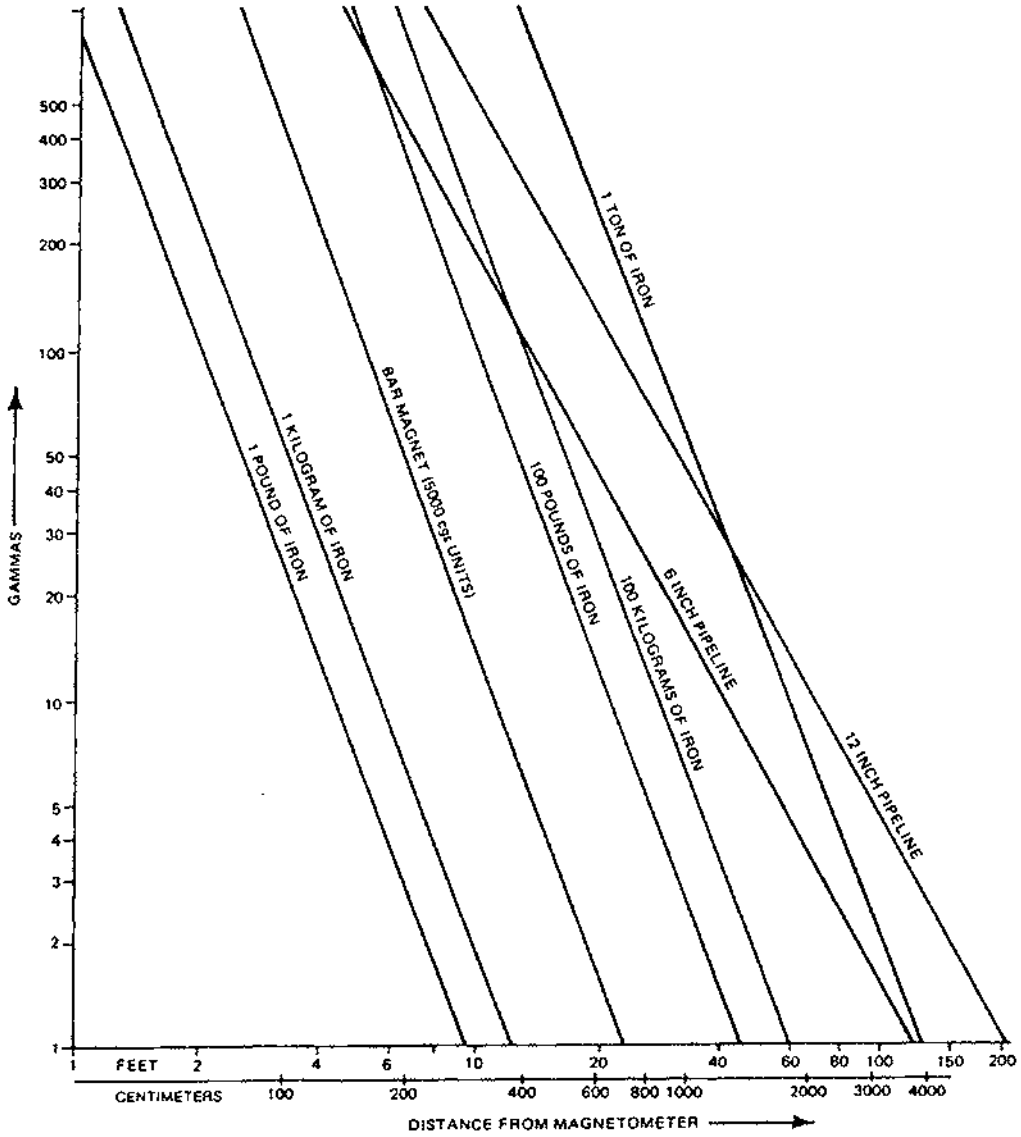

Figure 3.62 Minimum detectable anomaly amplitudes for different types of ordnance at various depths of burial. Note that the distances cited are those between the sensor and the target, not the depth below ground of the target. From Breiner (1981), by permission

various types of ordnance of different size and depth of burial are illustrated in Figure 3.62, assuming a maximum detectability of 0.1 nT. However, in practice, the smallest anomaly likely to be discernible above background noise is likely to be around 1 nT. This means that it would technically be possible to detect a 1000 lb bomb buried at a depth of 22 m.

Metal drums also give rise to strong magnetic anomalies and, if dumped together in a random way, will produce large-amplitude but highly variable anomalies that will stand out from background noise. An example of the kind of anomaly produced is shown in Figure 3.63.

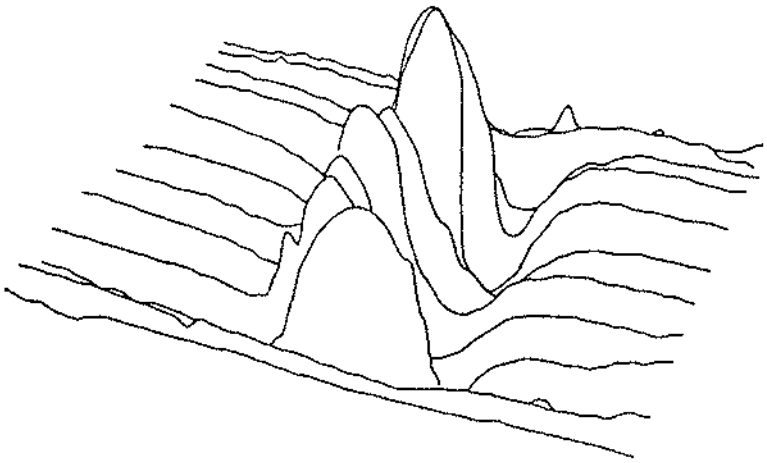

Figure 3.63 Magnetic anomaly over a trench containing metal drums of waste. From Evans (1982), by permission

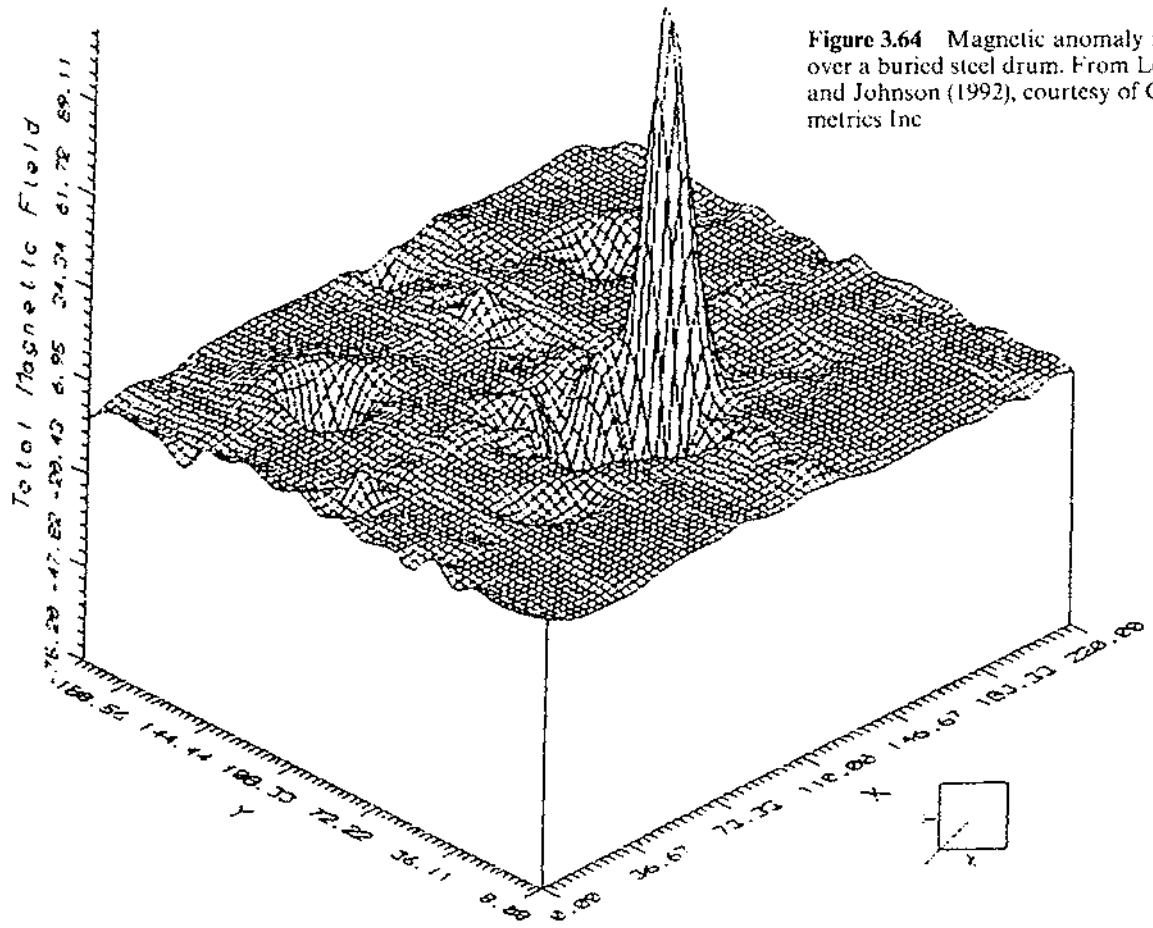

Figure 3.64 Magnetic anomaly map over a buried steel drum. From Leech and Johnson (1992), courtesy of Geometrics Inc

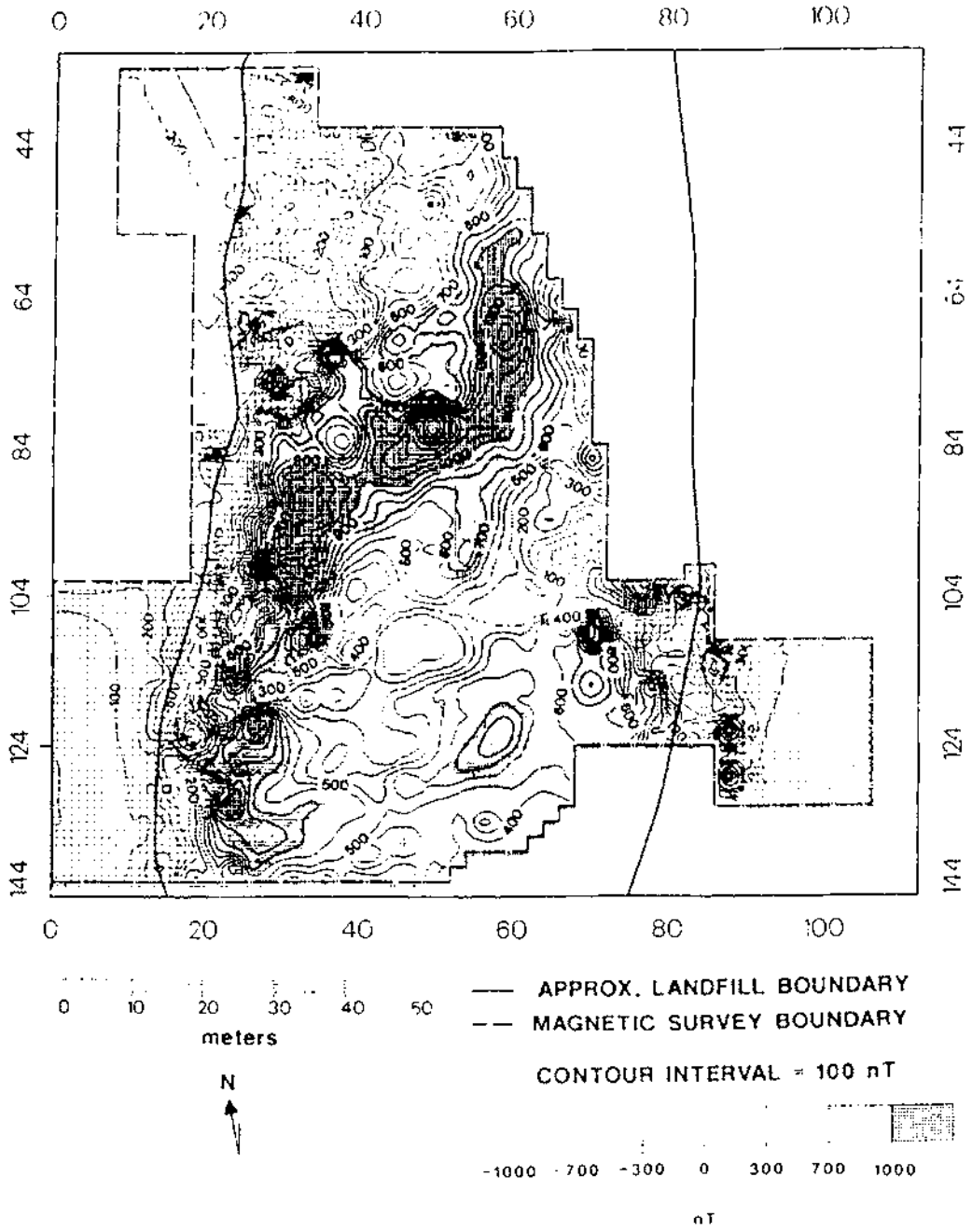

Figure 3.65 Contour map of total field magnetic intensity data measured at 1 m height, at the Thomas Farm landfill site, USA. From Roberts *et al.* (1990), by permission

To resolve the number of drums and their possible size, it may be preferable to use a gradiometer survey and datalogger so that the anomalies can be imaged with greater resolution. The magnetic anomaly over a buried steel drum is shown in Figure 3.64, from which it can be seen that local anomaly amplitudes are as high as several thousand nanoteslas, and field gradients several thousand nanoteslas per metre (Leech and Johnson 1992). The main difficulty with locating illegally buried drums of toxic waste is that they are usually dumped in ground with other rubbish which would help to mask their anomalies. However, by careful analysis of the anomaly shapes, amplitudes, orientations and overall characteristics, it should be possible to differentiate between various buried objects, if not actually identify them.

3.9.5 Landfill investigations

One of the aspects of landfills is that they are likely to contain large amounts of ferrometallic debris deposited at irregular angles. Consequently, a magnetic anomaly map produced over a former landfill will show a considerable amount of high-frequency noise from near-surface ferrometallic objects. There is perhaps a tendency to think that such noise is likely to dominate the magnetic anomaly map to produce a highly chaotic and largely unhelpful anomaly map.

One aspect of old closed landfills is that their previous tipping history may have been lost, or was never recorded. It might be useful to be able to obtain some idea as to whether a site has had different tipping sequences, such as periods of waste of a similar character being tipped and then having another type of waste with different magnetic properties. Consequently, the magnetic method lends itself to the rapid surveying of closed landfills in order to assess previous tipping histories and the zonation of waste types within a site.

An example of a magnetic survey over the Thomas Farm landfill in the USA has been given by Roberts *et al.* (1990). The site was surveyed on a 2×2 m grid with a sensor height at 1 m above the ground. Roberts and co-workers demonstrated that, by careful data processing, the high-frequency noise could be filtered out to reveal longer-wavelength anomalies more closely associated with broad types of waste. An example of one of their maps is given in Figure 3.65. In this case, the lateral extent of the landfill was already known. The magnetic anomaly map reveals several zones with quite distinctive magnetic anomaly characters. For example, note the band of strong magnetic anomalies (> 1000 nT) orientated NE–SW. To the south-east of this the magnetic anomalies are broader in wavelength and have low positive amplitudes, whereas those anomalies found north-west of this band are slightly higher frequency but predominantly negative. The actual wastes were domestic refuse in the north-west and brush, wood-cuttings and construction debris in the southern part.

Chapter 5
Seismic refraction surveying

5.1 INTRODUCTION

Seismic refraction experiments can be undertaken at three distinct scales: global (using earthquake waves), crustal (using explosion seismology), and near-surface (engineering applications). For the purposes of this book, emphasis is placed on shallow investigations. Discussion of passive seismic refraction in earthquake studies can be found in other texts, such as those by Brown and Mussett (1981), Gubbins (1990) and Kearey and Vine (1990).

The major strength of the seismic refraction method is that it can be used to resolve lateral changes in the depth to the top of a refractor

and the seismic velocity within it. The most commonly derived geophysical parameter is the seismic velocity of the layers present. From such values, a number of important geotechnical factors can be derived, such as assessing rock strength, determining rippability (the ease with which ground can be ripped up by an excavator), and potential fluid content. In addition to the more conventional engineering applications of foundation studies for dams and major buildings etc., seismic refraction is increasingly being used in hydrogeological investigations to determine saturated acquifer thickness, weathered fault zones etc. The location of faults, joints, and other such disturbed zones using seismic refraction is of major importance in the consideration of the suitability of potential sites for the safe disposal of particularly toxic hazardous wastes.

5.2 GENERAL PRINCIPLES OF REFRACTION SURVEYING

5.2.1 Critical refraction

The seismic refraction method is based on the principle that when a seismic wave (P- and/or S-wave) impinges upon a boundary across which there is a contrast in velocity, then the direction of travel of that wave changes on entry into the new medium. The amount of change of direction is governed by the contrast in seismic velocity across the boundary according to Snell's Law as described in Chapter 4 (see Boxes 4.8 and 5.1 and Figures 4.7 and 5.1). The critical angle for a given boundary for P-waves may be different from that for S-waves as the respective ratio in velocities between the two layers for P- and S-waves may not be the same.

Box 5.1 Snell's Law (see Figure 5.1)

Snell's Law:

$\sin i / \sin r = V_1/V_2$ for general refraction
$\sin i_c = V_1/V_2$ for critical refraction

where i_c is the angle at which critical refraction occurs, and V_2 is greater than V_1. V_1 and V_2 are the seismic velocities of the upper and lower layers respectively; i and r are the angles of incidence and refraction.

The refraction method is dependent upon there being an increase in velocity with depth. If, however, the lower medium has a velocity lower than that from which the wave is emerging (i.e. V_2 is less than V_1, a *velocity inversion*) then the refracted wave will bend towards the normal. This gives rise to a situation known as a *hidden layer*, which is discussed in more detail in Section 5.4.4.

(A)

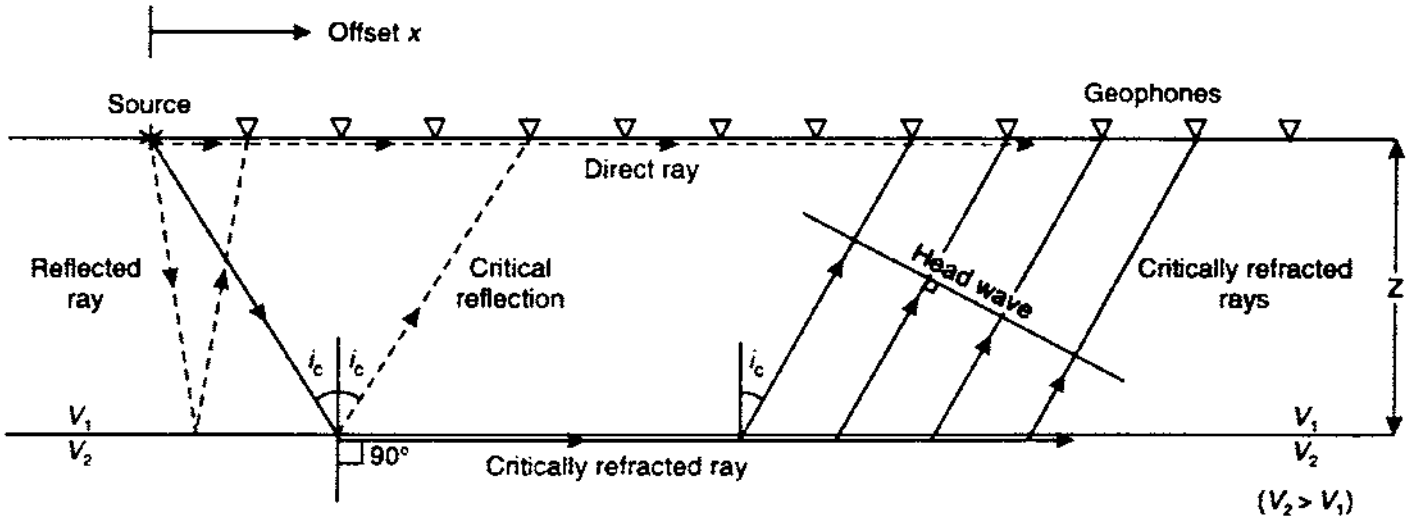

(B)

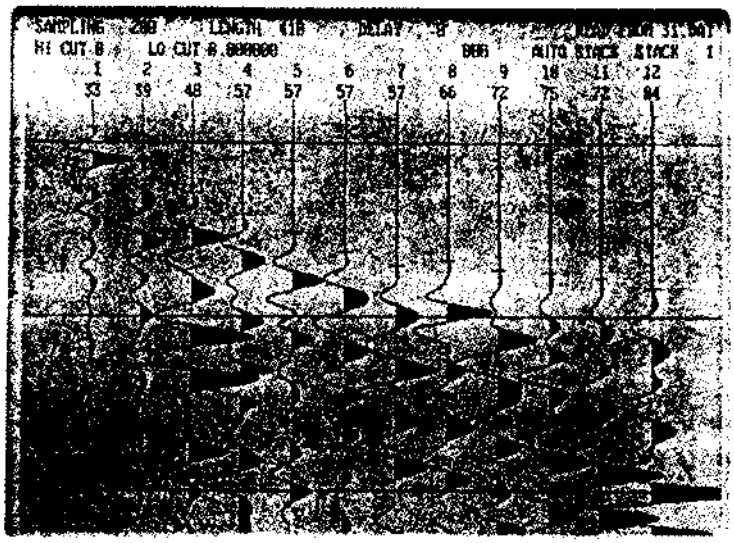

It is assumed in the refraction method that the thickness of each layer present is greater than the wavelength of the incident energy, and that each successive layer is as thick as, or is thicker than, the one lying above it. A further assumption is that the raypaths are constrained to lie in the vertical plane of the refraction profile line such that there is no seismic energy (refracted or reflected) arising from boundaries out of that plane – a phenomenon known as *side-swipe*. In some engineering applications, this factor is significant and has to be considered during data acquisition.

In a refraction survey, only the P-wave is usually considered. There are occasions when the additional use of S-waves is beneficial to the overall interpretation. For the purposes of the discussion which follows, we shall confine our considerations to P-waves only.

The basic components of a seismic refraction experiment are shown schematically in Figure 5.1A. A source, such as a sledge hammer on

(C)

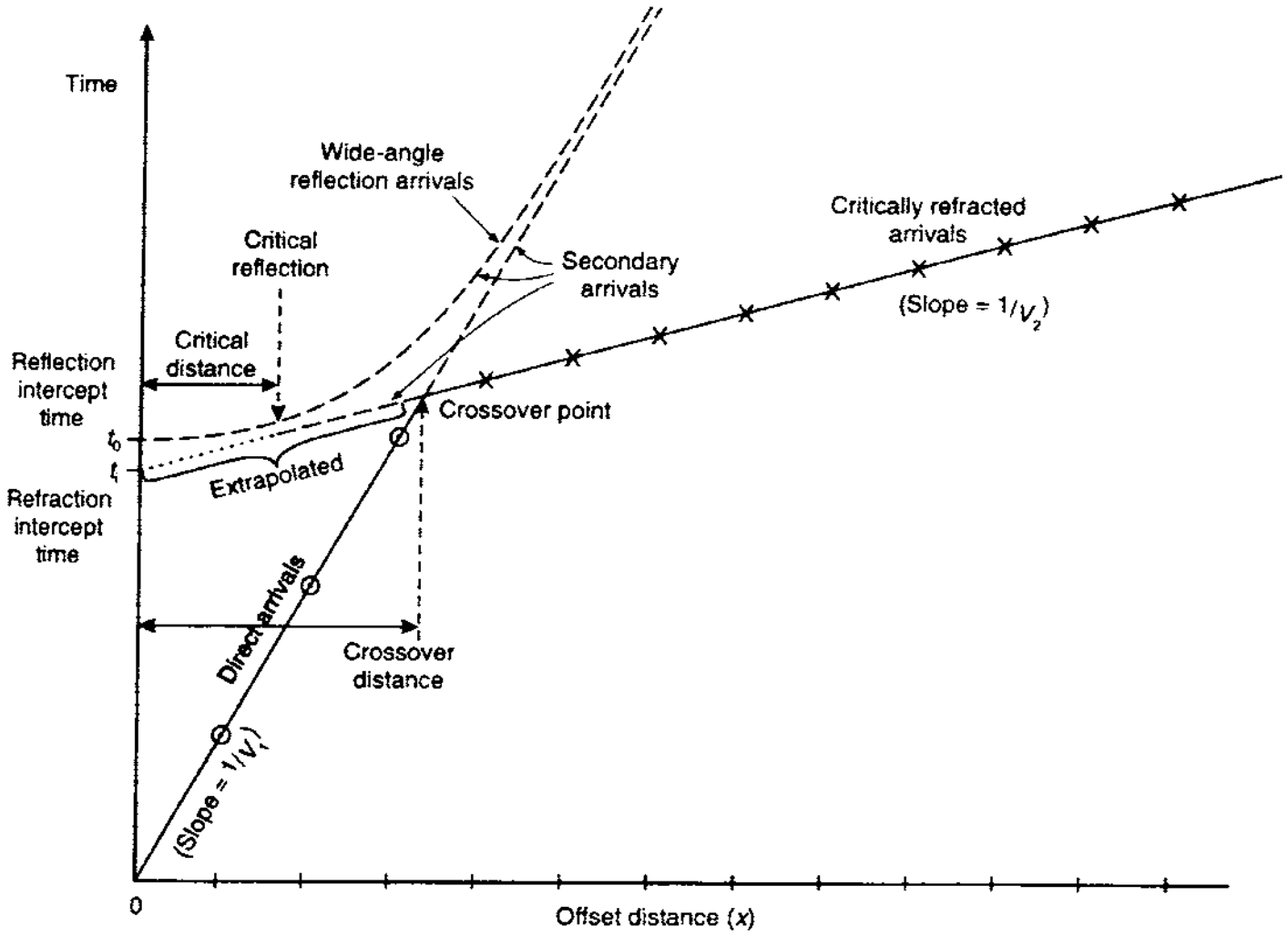

Figure 5.1 (A) (*opposite*) Raypath diagram showing the respective paths for direct, reflected and refracted rays. (B) (*opposite*) Example of a seismic refraction record as seen on the display of an EG&G Smartseis seismograph, with first arrivals picked on each trace (indicated by the small cross line). (C) (*top*) Arrival times plotted on a time–distance graph.

a baseplate or shotgun blanks in a buffalo gun, is used to generate the P-waves. The waves produced travel in three principal ways: directly along the top of the ground surface (direct wave); by reflection from the top of the refractor; and, of greatest importance, by critical refraction along the top of the refractor(s). The arrival of each wave is detected along a set of geophones and recorded on a seismograph, with the output of each geophone being displayed as a single trace. The onset of each arrival for each geophone is identified (Figure 5.1B) and the associated travel time is measured and plotted on a time–distance graph (Figure 5.1C).

At a distance called the *critical distance*, the reflected arrival is coincident with the first critically refracted arrival and the travel times of the two are identical. The critical distance is thus the offset at which the reflection angle equals the critical angle. This distance should not be confused with the *crossover distance*, which is the offset at which the critically refracted waves precede the direct waves. The crossover

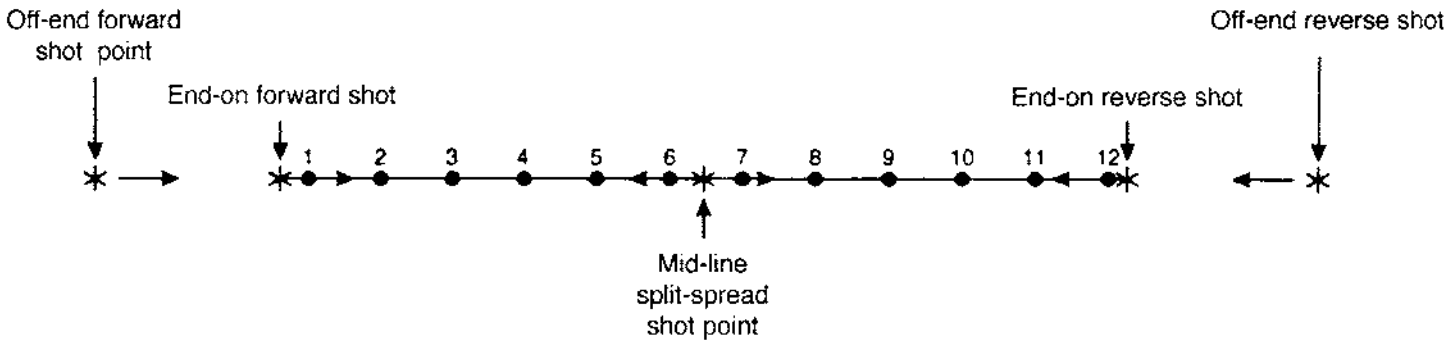

Figure 5.2 Geophone spread for a refraction survey with shot locations indicated

point marks the change in gradient of the time–distance graph from the slope of the direct arrivals segment to that for the refracted signals. While the travel time hyperbola associated with reflected arrivals is shown in Figure 5.1C, only direct and refracted arrival times are usually considered in the refraction analysis.

5.2.2 Field survey arrangements

5.2.2.1 Land surveys

For a seismic refraction survey on land, the basic layout is shown in Figure 5.2. A number of geophones, usually 12 or 24, are laid out along a cable with a corresponding number of takeouts along a straight line. This set of geophones constitutes a 'spread'; it should be noted that this is not a geophone 'array' (see Chapter 6). The seismic source (shot), whatever type it happens to be for a given survey, is located in one of five locations. The simplest case is for the shot to be positioned at the start and the end of the spread ('end-on' shots). A source located at a discrete distance off the end of the spread is known as an 'off-end' shot. A source positioned at a location along the spread is known as a 'split-spread' shot; usually this is either at mid-spread or at a quarter or three-quarters along a spread. Shots are usually fired into a spread from each end (end-on and off-end shots) in forward and reverse directions. The positioning of shots relative to a given spread is to achieve adequate coverage of the refractor surface and to provide adequate lateral resolution. As will be described in later sections, for each shot, appropriate travel times can be picked on each trace on the seismic record obtained. With each shot location into the same spread, additional data are acquired to provide sufficient information for detailed data reduction and analysis.

5.2.2.2 Water-borne surveys

Seismic refraction can also be undertaken in an aquatic environment but special systems are required. There are two main methods of

detecting the critically refracted signals: one is to use a bottom-drag hydrophone cable and the other is to use sonobuoys. Each will be described briefly in turn.

A bottom-drag cable is similar to a normal reflection hydrophone streamer but is usually only 55 m long. A boat housing all the shot-firing and seismograph recording systems tows the cable on to station, when the cable is allowed to sink to the river/seabed. In some cases, divers are used to anchor the cable to the substrate as required. Shots are fired as necessary and then the cable is towed to the next station and the process repeated. By careful operation of the boat and the positioning of the bottom-tow cable, long seismic refraction lines can be acquired.

The sonobuoy method does away with hydrophone streamer cables and is not limited by streamer cable lengths. The sonobuoy consists of a flotation device containing batteries which, when in contact with seawater, are activated, causing a radio telemetering antenna to be raised and one or more hydrophones to be suspended on cables from below. When a shot is fired from the survey ship, the signals received by the hydrophones are radioed back to the ship where they are recorded. The offset between the shot and the sonobuoy is determined from the travel time of the direct wave through the water. In the case of inshore surveys, land-based surveying methods can be used to track the sonobuoy. One advantage of the sonobuoy method if used during a major marine seismic reflection survey is that the sonobuoys are expendable and sink after a finite period. The refraction data can, however, be acquired while the reflection survey is in progress.

A third method of marine seismic refraction surveying requires at least two ships, one towing the hydrophone streamer and the other firing the shots. If reverse shooting is to be used, a third ship may be required – two ships steam in opposite directions firing shots in sequence while a third ship steams along the profile track towing a hydrophone streamer.

In hydrocarbon exploration, the use of multiship surveys and the slow rate of data acquisition make this an extremely expensive operation. Similarly, water-borne refraction surveys in harbours and estuaries takes considerably longer to acquire than a comparable line-meterage of reflection profiling. Marine refraction surveys are very valuable in investigations for proposed tunnel routes under harbours for sewerage schemes, for example.

5.3 GEOMETRY OF REFRACTED RAYPATHS

The basic assumption for seismic refraction interpretation is that the layers present are horizontal or only dipping at shallow angles and are, in the first instance, planar surfaces.

5.3.1 Planar interfaces

5.3.1.1 Two-layer case

In Figure 5.3, it can be seen that the raypath taken by a signal originating from the source S travels to A where it undergoes critical refraction and travels towards and ultimately beyond position B. The headwave originating from the refractor at B travels through layer 1 where it is detected by a geophone at G. The geophone is offset from the shot by a distance x. The total travel time taken is the sum of the three component travel times, details of which are presented in Box 5.2. The time–distance graph for the two-layer case (Figure 5.1C) is used to calculate the velocities of the two layers, V_1 and V_2, from the gradients of the two straight-line segments (gradient $= 1/V$). The extrapolation of the segment from the critically refracted arrivals on to the time axis gives an intercept time t_i from which the depth to the refractor (z) can be calculated (Box 5.2, equation 8), given values of V_1 and V_2 derived from the time–distance graph.

Box 5.2 Travel time calculations for a two-layer case
(see Figures 5.1 and 5.3)

Total travel time is:

$$T_{SG} = T_{SA} + T_{AB} + T_{BG} \tag{1}$$

where:

$$T_{SA} = T_{BG} = z/(V_1 \cos i_c) \tag{2}$$

$$T_{AB} = (x - 2z \tan i_c)/V_2 . \tag{3}$$

Substituting expressions (2) and (3) into (1), we obtain:

$$T_{SG} = z/(V_1 \cos i_c) + (x - 2z \tan i_c)/V_2 + z/(V_1 \cos i_c)$$

which simplifies to:

$$T_{SG} = (1/V_2)x + 2z (\cos i_c)/V_1 . \tag{4}$$

This has the form of the general equation of a straight line, $y = mx + c$, where m = gradient and c = intercept on the y-axis on a time–distance graph. So, from equation (4), the gradient is $1/V_2$ and c is the refraction time intercept t_i (see Figure 5.1) such that $t_i = 2z (\cos i_c)/V_1$.

Remember that $\sin i_c = V_1/V_2$ (Snell's Law), and hence:

$$\cos i_c = (1 - V_1^2/V_2^2)^{1/2} \text{ (from } \sin^2 \theta + \cos^2 \theta = 1).$$

continued

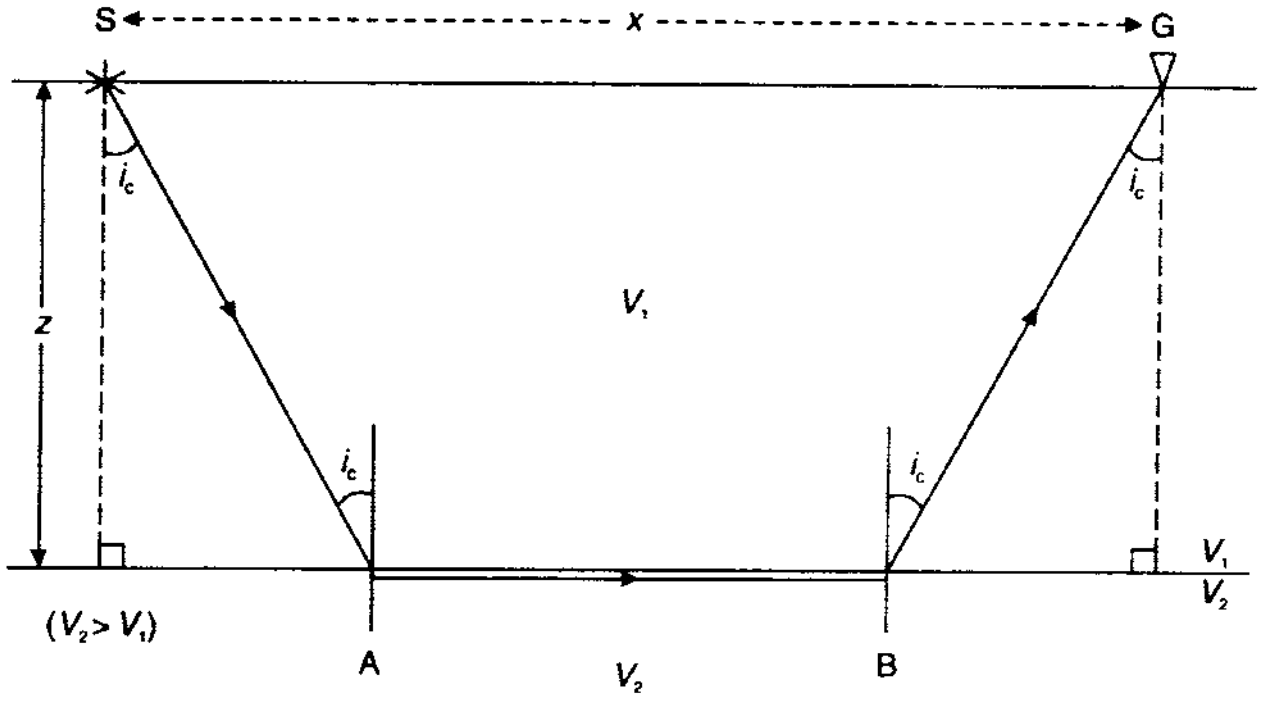

Figure 5.3 Simple raypath for a two-layer structure

continued

An alternative form to equation (4) is:

$$T_{SG} = x(\sin i_c)/V_1 + 2z(\cos i_c)/V_1 \qquad (5)$$

or

$$T_{SG} = x/V_2 + t_i \qquad (6)$$

where

$$t_i = 2z(V_2^2 - V_1^2)^{1/2}/V_1 V_2 \qquad (7)$$

$$z = t_i V_1 V_2 / 2(V_2^2 - V_1^2)^{1/2} \qquad (8)$$

On Figure 5.1, it can be seen that the travel times for the direct and critically refracted ray are the same at the crossover distance. Consequently, solving equation (1) in Box 5.3 in terms of the crossover distance x_{cross} provides an additional means of calculating the depth to the refractor. Furthermore, equation (2) in Box 5.3 shows that the depth to the refractor is always less than half the crossover distance.

Box 5.3 The use of crossover distance to calculate refractor depth

Travel time of direct ray at the crossover distance is x_{cross}/V_1. Travel time of critically refracted ray at the crossover distance is (from equation (6) in Box 5.2) given by:

$$T = x_{cross}/V_2 + 2z(V_2^2 - V_1^2)^{1/2}/V_1 V_2.$$

continued

continued

Hence, at the crossover point:

$$x_{cross}/V_1 = x_{cross}/V_2 + 2z(V_2^2 - V_1^2)^{1/2}/V_1V_2. \quad (1)$$

Solving for x_{cross} and reorganising gives:

Depth to the refractor:

$$z = \tfrac{1}{2}x_{cross}[(V_2 - V_1)/(V_2 + V_1)]^{1/2} \quad (2)$$

Crossover distance:

$$x_{cross} = 2z[(V_2 + V_1)/(V_2 - V_1)]^{1/2}$$

5.3.1.2 Three-layer case

The simple raypath geometry for critical refraction to occur in a three-layer model with horizontal interfaces is shown in Figure 5.4A and its corresponding travel time–distance graph in Figure 5.4B. The expressions governing the travel time–velocity relationships are given in Box 5.4. The effect of reducing the thickness of layer 2 on the time–distance graph is to reduce or even remove completely the straight-line segment corresponding to refracted arrivals from the top of layer 2 (Lankston 1990). The signal travels from the source down to the first refractor (at A), where it is refracted into the second medium through to the second interface (at B), at which point it is then critically refracted. From there the generated head wave from the lowest refractor travels back from C through the overlying layers to arrive at the geophone at G.

Box 5.4 Travel time calculations for a three-layer case
(see Figure 5.4)

Total travel time is:

$$T_{SG} = T_{SA} + T_{AB} + T_{BC} + T_{CD} + T_{DG}$$

where:

$$T_{SA} = T_{DG} = z_1/V_1 \cos\theta_1$$
$$T_{AB} = T_{CD} = z_2/V_2 \cos\theta_c$$
$$T_{BC} = (x - 2z_1 \tan\theta_1 - 2z_2 \tan\theta_c)/V_3.$$

Combining these gives:

$$T_{SG} = x/V_3 + (2z_2 \cos\theta_c)/V_2 + (2z_1 \cos\theta_1)/V_1 \quad (1)$$

$$T_{SG} = x/V_3 + t_2 \quad (2)$$

continued

continued

where

$$\frac{\sin\theta_1}{V_1} = \frac{\sin\theta_c}{V_2} = \frac{1}{V_3} \text{ from Snell's Law.}$$

Thicknesses of refractors are given by:

$$z_1 = t_1 V_1 V_2 / 2(V_2^2 - V_1^2)^{1/2}$$

$$z_2 = t_2 V_2 V_3 / 2(V_3^2 - V_2^2)^{1/2} - z_1 V_2 (V_3^2 - V_1^2)^{1/2} / V_1 (V_3^2 - V_2^2)^{1/2}$$

The analysis works by determining V_1, V_2, t_1 and t_2 from the travel time graph for the top two layers, and hence the thicknesses of the first two refractors can be calculated using the equations in Box 5.4. The thicknesses of refractors are usually underestimated by about 3%, with the percentage inaccuracy increasing the larger the number of layers involved.

5.3.1.3 Multilayer case

The general expressions governing the travel time–velocity relationships for the situation where more than three horizontal planar layers are present are given in Box 5.5. The form of the equations and of the analysis of the travel time graphs follow the procedures explained for a three-layer case, but are extended to the relevant total number of layers.

Box 5.5 Travel time calculations for a multilayer case

The total travel time T_{SG} in an n-layer case is given by:

$$T_{SG} = x/V_n + \sum_{i=1}^{n-1} [(2z_i \cos\theta_i)/V_i]$$

where $\sin\theta_i = V_i/V_n$.

Note that θ_i are not critical angles except for θ_{n-1}.

In engineering applications, it is unusual to have more than three or at most four layers present; commonly only two-layer cases are used, with any variations in velocity within the first layer being taken into account by consideration of the value of the first layer velocity being an average. Commonly, in areas of alluvial fill or over glacial

(A)

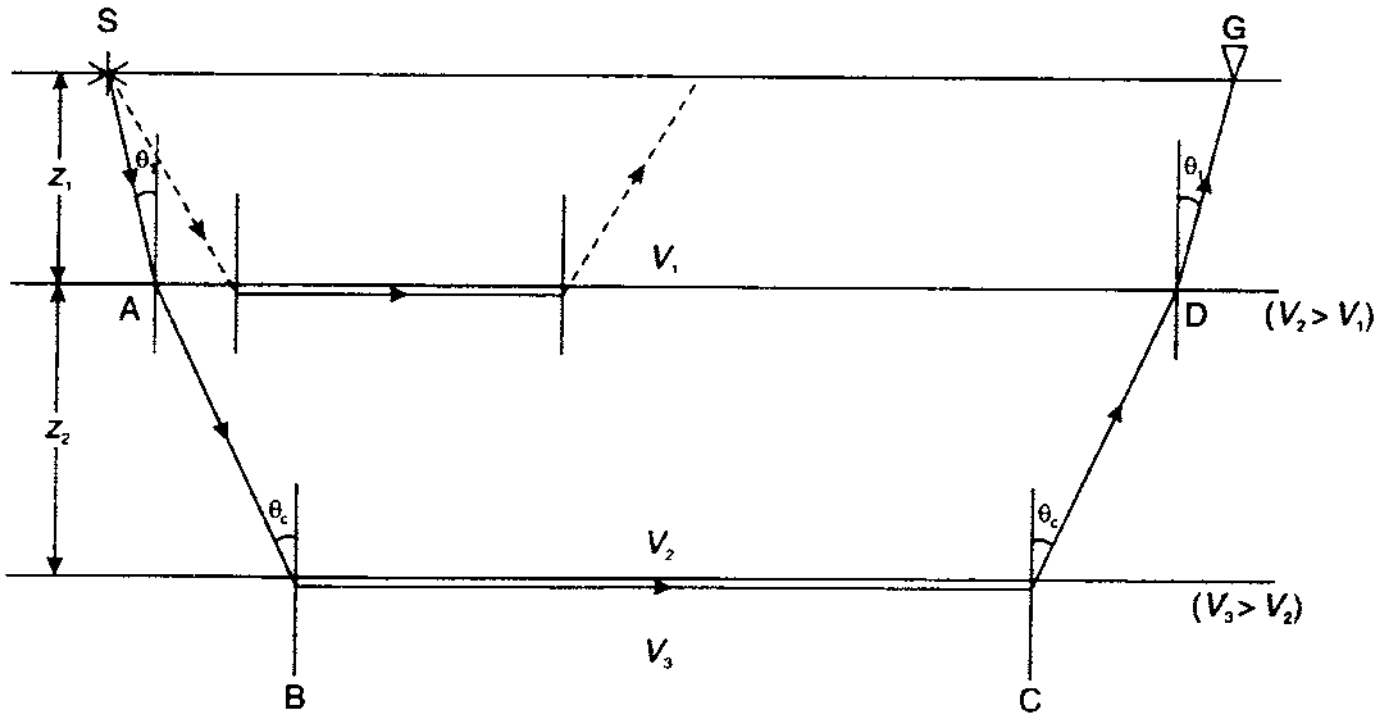
S
G
z_1
θ_1
V_1
A
D
$(V_2 > V_1)$
z_2
θ_c
θ_c
V_2
$(V_3 > V_2)$
V_3
B
C

(B)

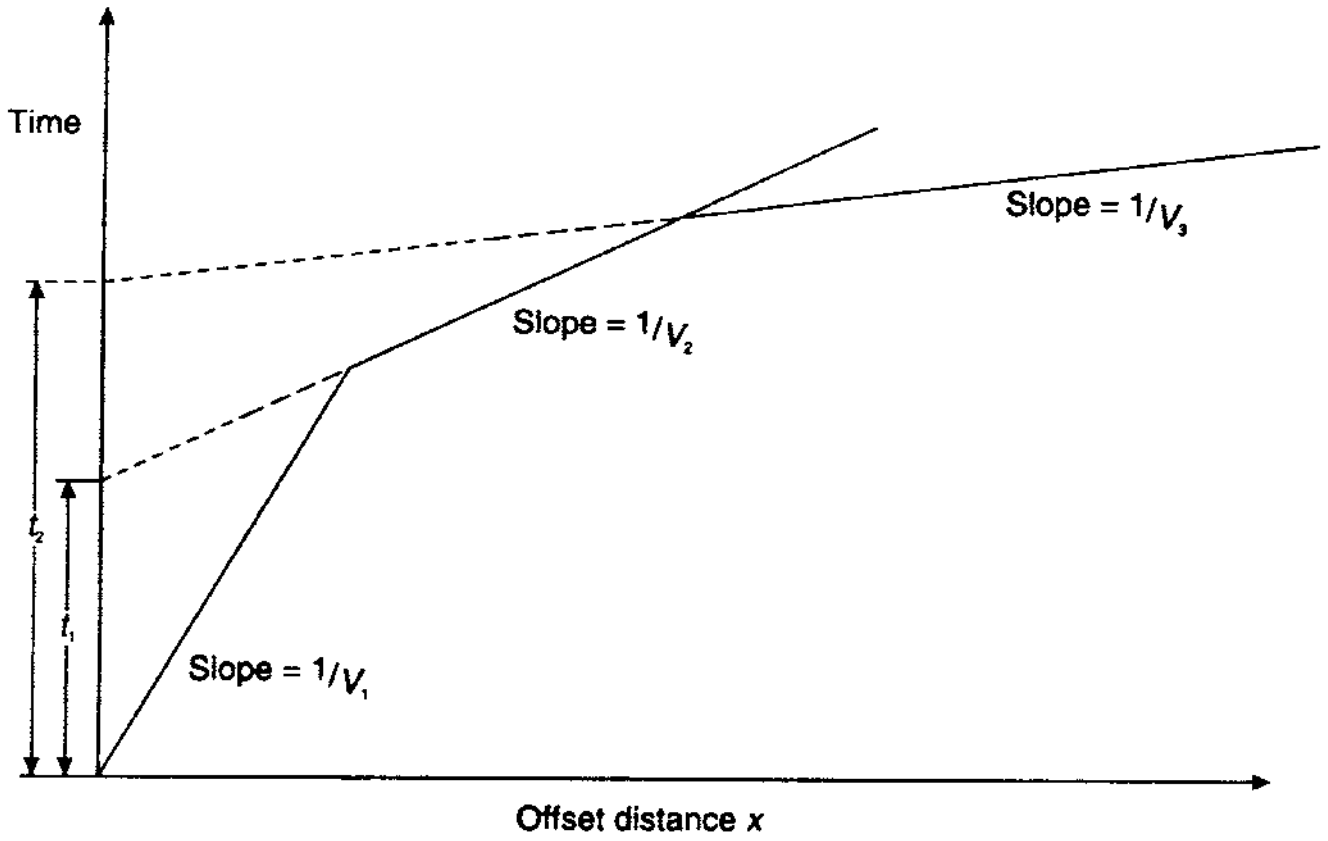
Time
Slope = $1/V_3$
Slope = $1/V_2$
t_2
t_1
Slope = $1/V_1$
Offset distance x

sediments, the local lateral and vertical variations in velocity can be significant. It is often advisable to undertake micro-spreads, with geophone intervals as small as 1 m, in order to measure the near-surface velocities along a spread. If it is known from desk study work that the area has Quaternary and/or Recent sediment cover, the survey design should include micro-spreads in order to provide better control on the determination of local velocities. The variation in near-surface velocities makes it quite inappropriate to quote calculated values of velocity to the nearest metre per second. Careful thought should be given to determining the statistical significance of variations in P-wave velocities determined from refraction surveys. Calculated values of velocity should be quoted to perhaps the nearest 50 m/s, for example, with an estimation of the standard deviation as calculated from a relevant statistical analysis. If due consideration is not given to careful analysis of the variation of velocities, any depth estimates arising from the refraction survey are likely to be inaccurate, possibly being as much as 30 -40% of the actual refractor depth. Depths determined to a refractor should be quoted with *realistic* error bars, not 'hoped-for' values!

Where refraction surveys are carried out as part of a hydrocarbon exploration programme or for crustal research, larger numbers of refractors can be encountered. However, there still needs to be a very careful appraisal of the errors and inaccuracies involved in whatever analysis is undertaken.

Figure 5.4 (*opposite*) (A) Simple raypath diagram for refracted rays, and (B) their respective travel time distance graphs for a three-layer case with horizontal planar interfaces

5.3.1.4 Dipping-layer case

When a refractor lies at an angle to the horizontal, the simple geometries so far described are complicated by the *angle of dip*. It is no longer adequate to undertake only one direction (forward) of shooting; it becomes necessary to carry out both forward and reverse shooting in order to determine all the parameters required to solve for the refractor geometry. Furthermore, the refractor velocities determined in the case of dip are referred to as *apparent* velocities, as the values of velocity determined from the inverse gradients of the straight-line segments on the travel time–distance graphs are higher in the upslope direction (V_u) and lower in the downslope direction (V_d).

The raypath geometry for a dipping two-layer case is shown in Figure 5.5A with its travel time–distance graph in Figure 5.5B. Following the logic used in discussing the two-layer planar refractor in Section 5.3.1.1, a set of equations can be produced (Box 5.6) that relate velocity, layer thickness and angle of refractor dip from which the geometry of the dipping refractor can be determined. The depths (d_a and d_b) to the refractor vertically below the spread end-points can easily be calculated from the derived values of perpendicular depths (z_a and z_b) using the expression $d = z/\cos\alpha$.

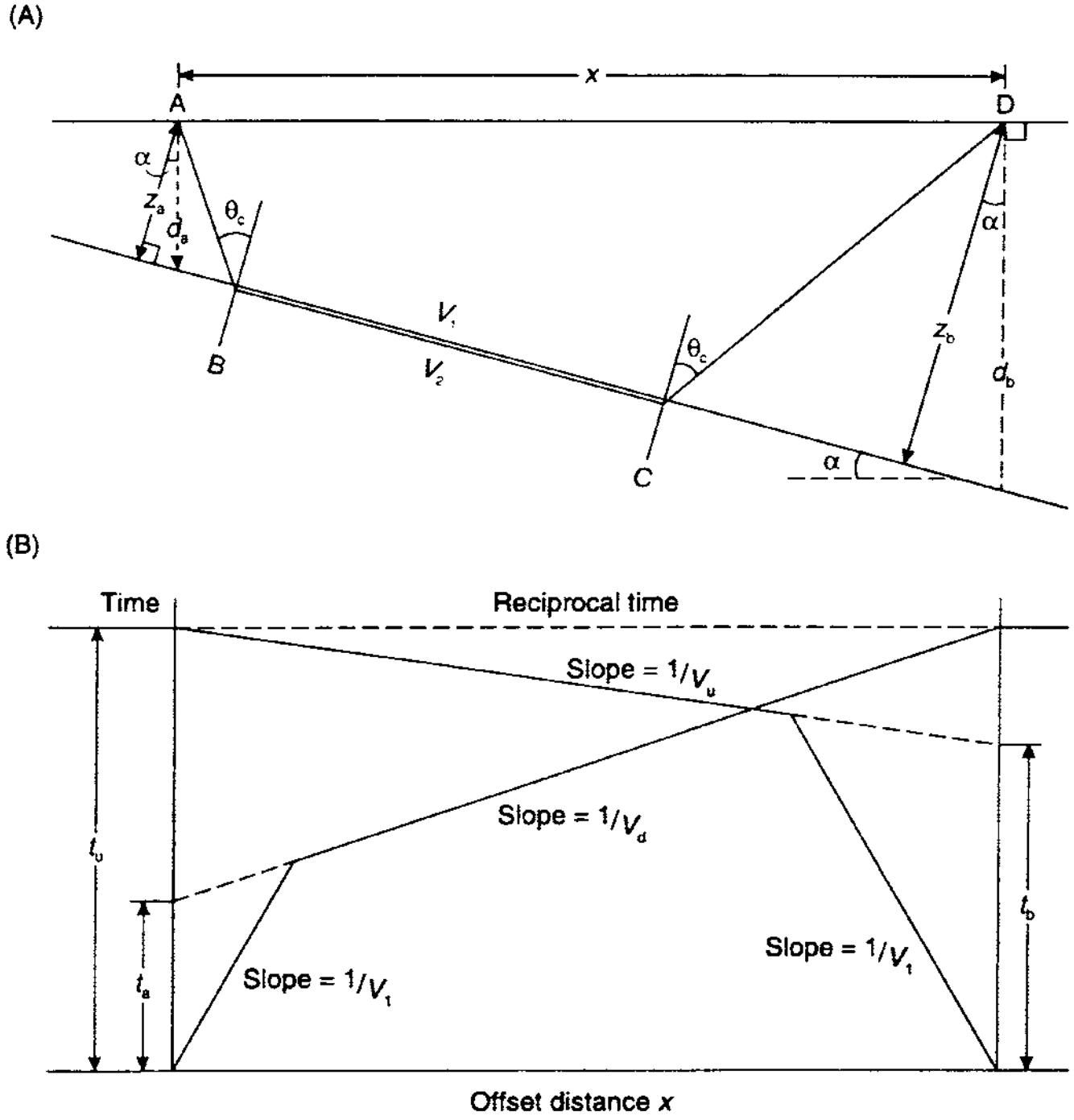

Figure 5.5 (A) Raypath geometry over a refractor dipping at an angle α, and (B) the respective travel time-distance graph for the forward (down- dip) and reverse (up-dip) shooting directions.

It should also be noted that the total travel times obtained from both forward and reverse shooting should be the same ($T_{AD} = T_{DA}$) and these are hence also known as 'reciprocal times'. When undertaking forward and reverse shooting, the reciprocity of the measured travel times should be checked. If the total travel times are not the same, the picking of first arrivals and the offsets of the geophones should be checked for errors.

Box 5.6 Travel time calculations for a dipping refractor
(see Figure 5.5)

Total travel time over a refractor dipping at an angle α is given by:

$$T_{ABCD} = (x \cos \alpha)/V_2 + [(z_a + z_b) \cos i_c]/V_1$$

where V_2 is the refractor velocity, and z_a and z_b are the distances perpendicular to the refractor.

The down-dip travel time t_d is given by:

$$t_d = x\,[\sin(\theta_c + \alpha)]/V_1 + t_a \qquad (1)$$

where $t_a = 2z_a(\cos \theta_c)/V_1$.

$$t_u = x\,[\sin(\theta_c - \alpha)]/V_1 + t_b \qquad (2)$$

where $t_b = 2z_b(\cos \theta_c)/V_1$.

Equations (1) and (2) above can be written in terms of the apparent up-dip velocity (V_u) and down-dip velocity (V_d) such that:

$t_d = x/V_d + t_a$, where $V_d = V_1/\sin(\theta_c + \alpha)$

$t_u = x/V_u + t_b$, where $V_u = V_1/\sin(\theta_c - \alpha)$.

An approximate relationship between true and apparent velocities for shallow angles of dip ($\alpha < 10°$) is given by:

$$V_2 \approx (V_d + V_u)/2.$$

5.3.1.5 The case of a step discontinuity

So far the refractor has been assumed to be planar and continuous. There are situations where a step discontinuity may occur in the refractor, such as in an old backfilled quarry where a former quarry face has been covered over with backfill material (Figure 5.1B). In such a situation, the refractor velocity should remain the same along its length, the only perturbation arising from the distortion is raypath (Figure 5.6).

If the step discontinuity has been caused by a normal fault, for example, there may be an additional complication of the refractor velocity having different magnitudes across the fault plane; if the

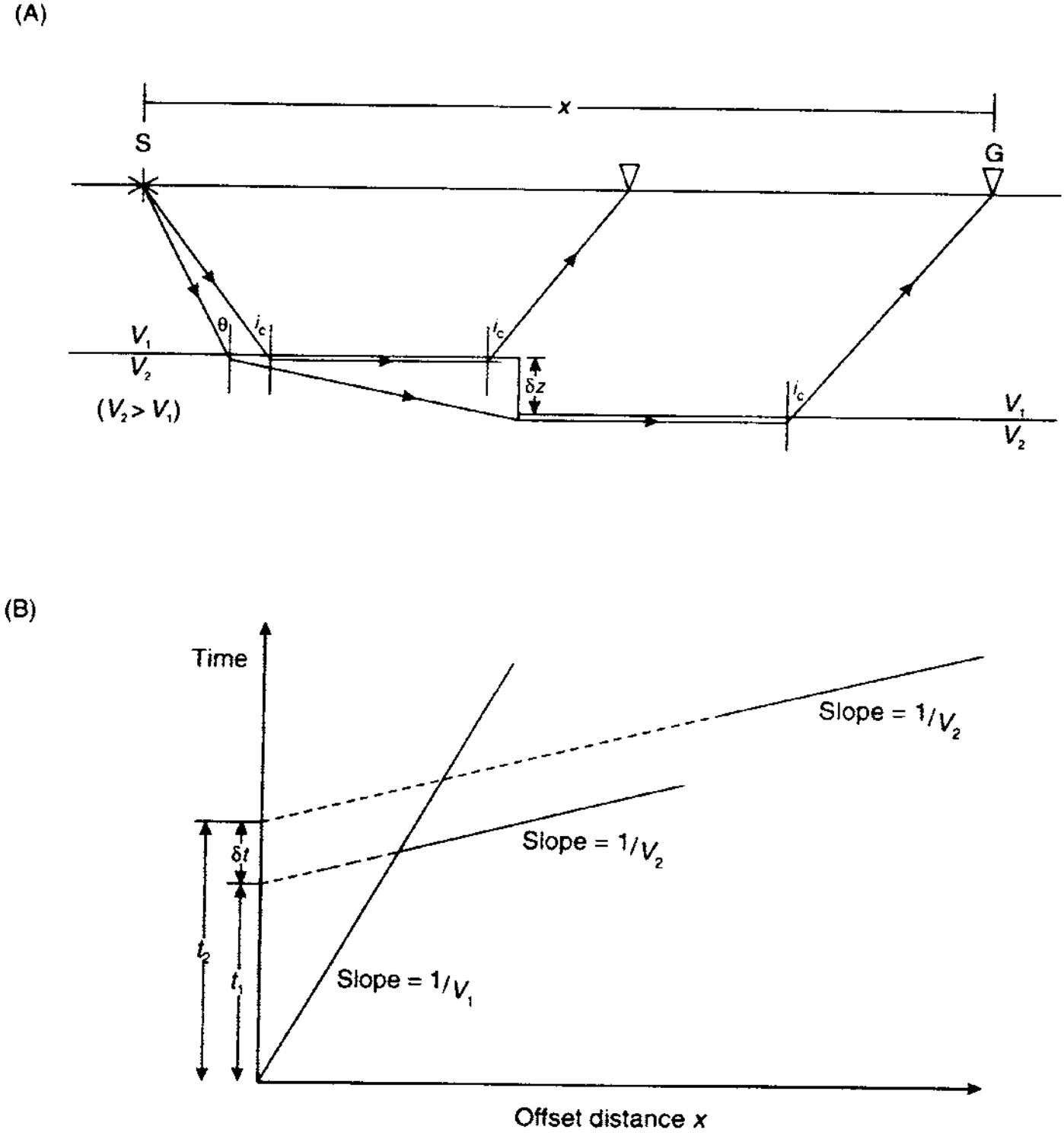

throw on the fault is significant, different geological materials may now be juxtaposed with consequent difference in seismic velocities. Indeed, the presence of a lateral change in refractor velocity in a two-layer case may give rise to a travel time–distance graph from a single end-on forward shot identical to that produced by three horizontal layers but with uniform layer velocities. The easiest way to discriminate between the two cases is to carry out an off-end forward

Figure 5.6 (A) Raypath geometry over a refractor with a step discontinuity but no lateral change in layer velocity, and (B) the corresponding travel time–distance graph

shot. If the crossover point on the travel time–distance graph is shifted laterally (i.e. along the x-axis), this indicates that the three-layer case is correct. If, instead, the crossover point is shifted vertically on the time axis (i.e. there is a delay time) then this is indicative of a two-layer case, such as across a fault plane at which there is no topographic effect on the refractor but where there is a significant velocity contrast. This situation has been discussed in more detail by Lankston (1990).

Where the size of the step discontinuity is small with respect to the depth of the refractor, then a simple equation (Box 5.7) can be used to estimate the difference in depth to the refractor. While the delay time (δt) may be observed on a time–distance graph from a shot in a forward direction, commonly the amplitudes of the refracted signals from a reverse shot are very small and it may not be possible to obtain satisfactory data from a reverse shot.

Box 5.7 Determination of depth to a refractor with a step discontinuity (see Figure 5.7)

The step size (δz) in a discontinuity in a refractor is given by:

$$\delta z = \delta t \, V_1 V_2 / (V_2^2 - V_1^2)^{1/2}.$$

5.3.2 Irregular (non-planar) interfaces

The preceding discussion has been for planar layers that are either horizontal or dipping uniformly and with no lateral variation in velocity in the refractor or vertical variation in velocity within the surface layer. It is important whenever a refraction survey is designed and then executed that consideration be given to the type of layer case present as judged from the quality and nature of travel time–distance data obtained. In a significant number of cases the simple models are obviously not appropriate, as in the situation of a refraction survey over a buried rock valley, for instance. It becomes necessary to carry out interpretation on the basis that the refractor is no longer planar or necessarily horizontal, but irregular in form, but where the wavelength of variation in refractor elevation is greater than the depth to the refractor. When an irregular refractor is encountered, it is usually analysed on the basis of only a two-layer case, details of which are given in the next section.

5.4 INTERPRETATIONAL METHODS

Before any detailed interpretation can begin it is important to inspect the travel time–distance graphs obtained, (a) as a check on quality the of data being acquired, and (b) in order to decide which

Table 5.1 Travel time anomalies (see Figure 5.7)

(i)	Isolated spurious travel time of a first arrival, due to a mispick of the first arrival or a mis-plot of the correct travel time value
(ii)	Changes in velocity or thickness in the near-surface region
(iii)	Changes in surface topography
(iv)	Zones of different velocity within the intermediate depth range
(v)	Localised topographic features on an otherwise planar refractor
(vi)	Lateral changes in refractor velocity

Figure 5.7 (*opposite*) Travel time anomalies and their respective causes. (A) Bump and cusp in layer 1. (B) Lens with anomalous velocity (V_2') in layer 2. (C) Cusp and bump at the interface between layers 2 and 3. (D) Vertical but narrow zone with anomalous velocity (V_3') within layer 3. After Odins (1975) in Greenhaigh and Whiteley (1977), by permission

interpretational method to use simple solutions for planar layers and for a dipping refractor, or more sophisticated analysis for the case of an irregular refractor. Checks to be considered are listed in Table 5.1, and some of the associated time anomalies ((iii)–(vi)) are illustrated in Figure 5.7. Indiscriminate smoothing of 'cusps' in travel time data can obscure what might be important features and result in serious errors in interpretation.

Several different interpretational methods have been published, falling into two approaches: delay-time and wavefront construction methods. Examples of the former are Gardner (1939, 1967), Wyrobek (1956), Barry (1967), and Palmer (1980), and those of the latter are Thornburgh (1930), Hales (1958), Hagedoorn (1959), Schenck (1967), Hill (1987), Vidale (1990), and Aldridge and Oldenburg (1992). However, two methods emerge as the most commonly used, namely Hagedoorn's 'plus–minus' method (Hagedoorn 1959) and the generalised reciprocal method (GRM) (Palmer 1980), which are described in Sections 5.4.2 and 5.4.3 respectively. The more recent publications tend to be modifications of earlier methods or new computational procedures.

5.4.1 Phantoming

The sub-surface coverages of a dipping refractor obtained by forward and reverse shooting overlap along only part of the refractor and are not totally coincident, as shown in Figure 5.8 (Lankston 1990). The apparent velocities obtained up-dip and down-dip are in fact derived from different segments of the refractor. If the interface is planar, then the use of such apparent velocities to derive layer thicknesses and dip angles is justified.

In order to increase the sub-surface coverage, and depending on the suitability of the local geology, both the shot locations and the geophone spread have to be moved along the line of the profile. If there is no lateral variation in refractor velocity, then the resultant travel time–distance graph from a headwave generated from shot at increased offset is delayed in travel time but has the same gradient as that from the end-on shot (Figure 5.9). The observed parallelism of the two travel time graphs indicates that the difference in travel time is

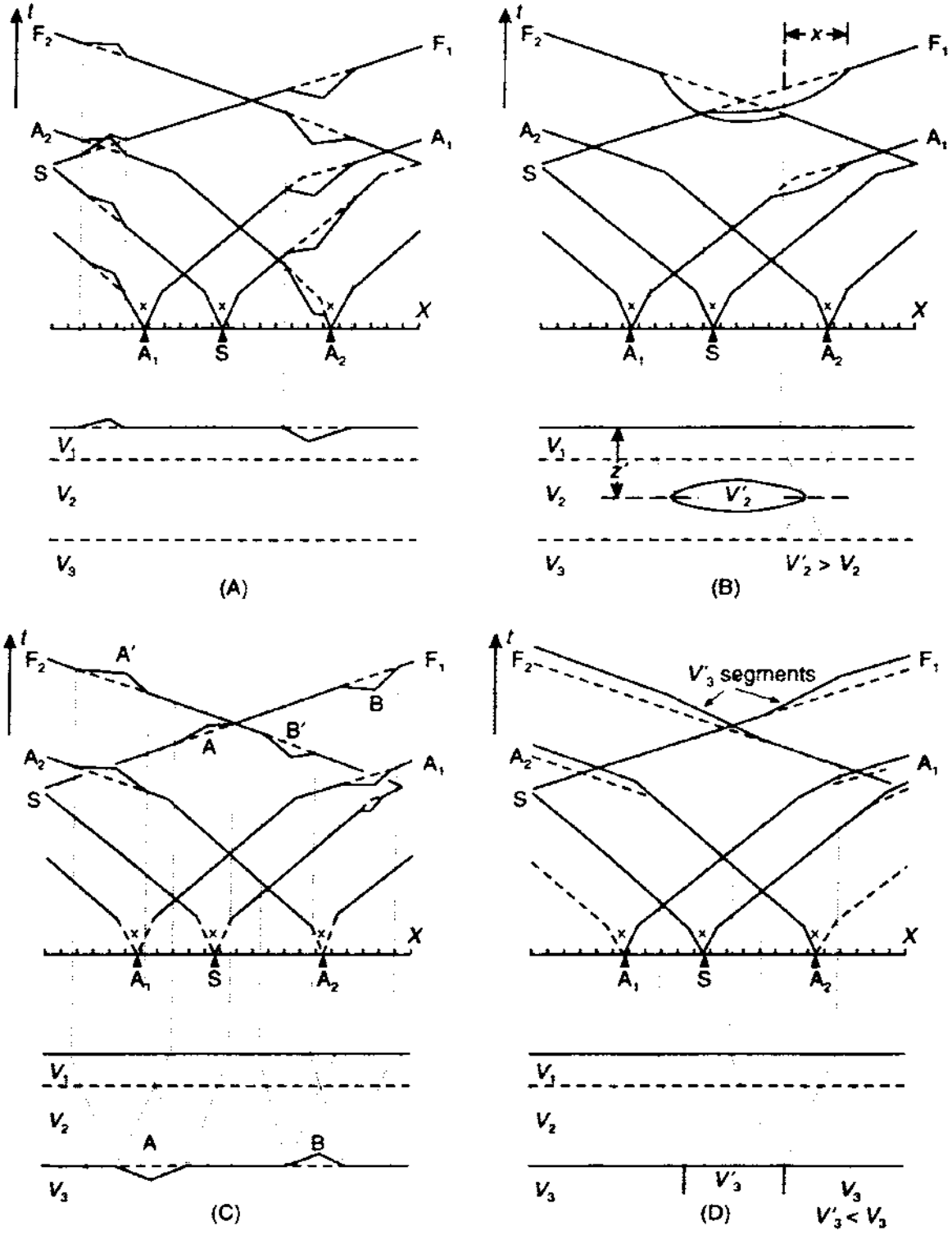
t
F2
F1
A2
A1
S
X
A1
S
A2
V1
V2
V3
(A)
x
z
V'2
V'2 > V2
(B)
A'
B
A
B'
(C)
V'3 segments
V'3
V3
V'3 < V3
(D)

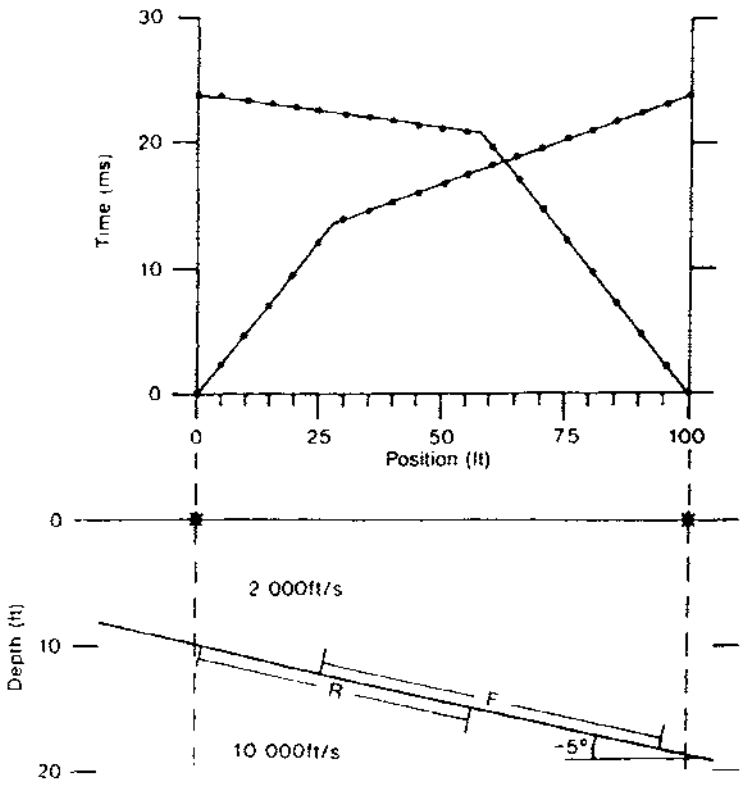

Figure 5.8 Overlapping zones of sub-surface coverage from forward and reverse shooting over a dipping refractor, and corresponding travel time distance graphs. From Lankston (1990), by permission

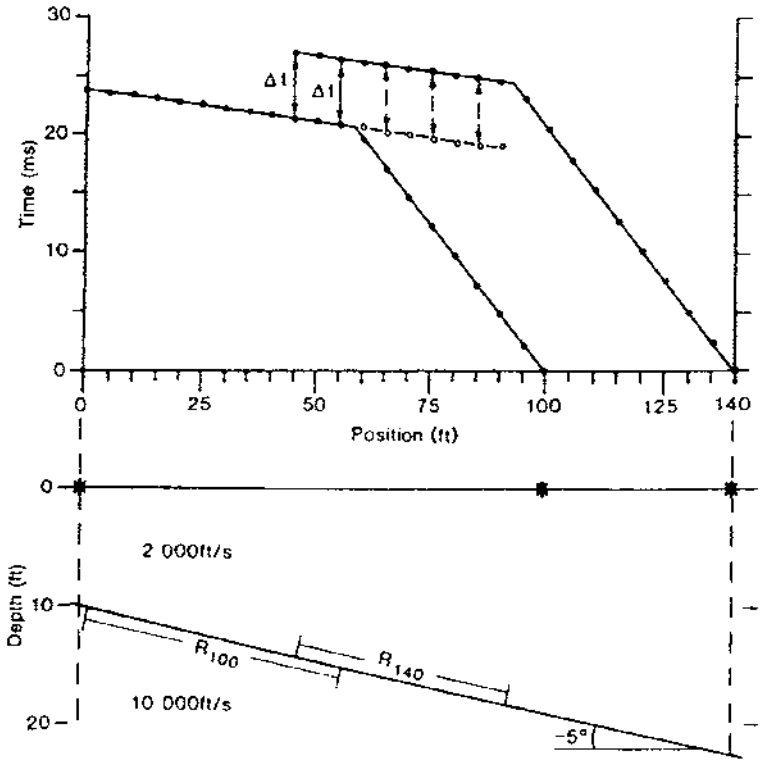

Figure 5.9 Travel time–distance graphs and sub-surface coverages from two overlapping reverse direction spreads; open circles denote phantom arrivals. From Lankston (1990), by permission

a constant for each geophone location. By substracting this time difference from the headwave arrivals from the refractor in the second, offset shot, then the reduced travel times are those that would have been recorded from the first shot over the distance between the end-on shot and the crossover distance.

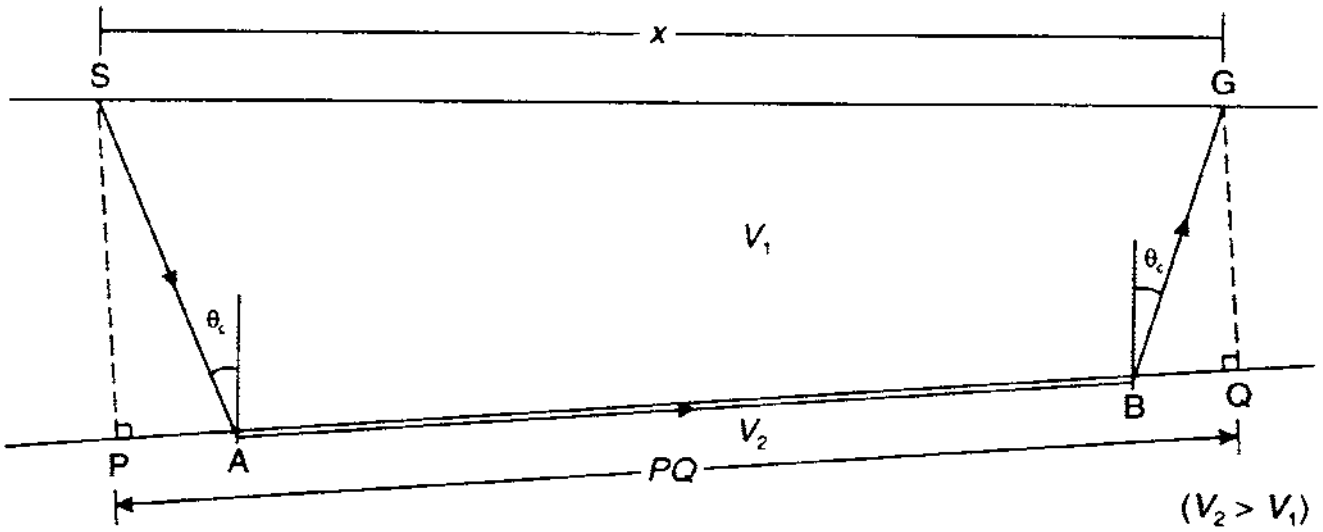

Figure 5.10 The principle of delay time (see text for details)

The time-shifted arrivals are known as *phantom arrivals* (Redpath 1973) and the process of time-shifting is referred to as *phantoming*. This process provides a means of obtaining real first-arrival information between the end-on shot and the original crossover distance which could not have been recorded from the first shot. The phantom arrivals, therefore, remove the necessity to extrapolate the travel time graph from beyond the crossover point back to the zero-offset point to obtain the intercept time, as indicated previously in Figure 5.1.

5.4.2 Hagedoorn plus–minus method

In Hagedoorn's method, it is assumed that the layers present are homogenous, that there is a large velocity contrast between the layers, and that the angle of dip of the refractor is less than 10°. The method uses intercept times and delay times in the calculation of the depth to a refractor below any geophone location. Referring to Figure 5.10, the delay time (δt) is the difference in time between (1) the time taken for a ray to travel along a critically refracted path from the source via the sub-surface media and back to the surface (T_{SG} along SABG), and (2) the time taken for a ray to travel the equivalent distance of the source geophone offset (x) along the refractor surface (i.e. T_{PQ} along the projection PQ of the refracted raypath on to the refractor surface). The total delay time (δt) is effectively the sum of the 'shot-point delay time' (δt_s) and the 'geophone delay time' (δt_g). In cases where the assumptions on which the method is based are realistic, it is sufficiently accurate to consider the distance PQ to be approximately the same as the source–geophone offset (SG). The mathematical equations relating the various delay times and velocities are given in Box 5.8.

Box 5.8 Determination of delay times (see Figure 5.10)

The total delay time is given by:

$$\delta t = T_{SG} - T_{PQ}$$

and

$$T_{SG} = (SA + BG)/V_1 + AB/V_2 \quad \text{and} \quad T_{PQ} = PQ/V_2 .$$

Thus:

$$\begin{aligned} \delta t &= (SA + BG)/V_1 - (PA + BQ)/V_2 \\ &= (SA/V_1 \quad PA/V_2) + (BG/V_1 - BQ/V_2) \\ &= \delta t_s + \delta t_g \approx T_{SG} - x/V_2 . \end{aligned}$$

Alternatively:

$$T_{SG} = x/V_2 + \delta t_s + \delta t_g \qquad (1)$$

where δt_s and δt_g are the shot-point and geophone delay times.

In the case of a horizontal refractor, $\delta t = t_i$, the intercept time on the corresponding time distance graph (see Figure 5.1 and Box 5.2, equation 6).

Hagedoorn's plus–minus method of analysing refraction data from both forward and reverse shooting provides a means of determining the delay times and hence the layer velocities and the depth to the refractor beneath any given geophone.

In Figure 5.11A, A and B are the locations of the forward and reverse shot points, and G is an arbitrary location of a geophone in between. Using equation (1) from Box 5.8, the travel time for a refracted ray from a shot point to any geophone G can be defined in terms of the respective delay times (see Box 5.9). Hagedoorn's 'plus term' (T^+) is the sum of the travel times from shot to the geophone from each end, minus the overall travel time between one shot point and the other (Box 5.9, equation 4). Hagedoorn's 'minus term' (T^-) is the difference in travel times taken by rays from each shot point to a given geophone.

T values can be plotted on a graph either against offset distance directly, in which case the velocity is determined from the slope which is $2/V_2$, or against $(2x - L)$ in which case the velocity is simply the inverse slope $(1/V_2)$. Values of the first layer velocity can be obtained in the conventional way from the inverse slope of the time–distance graph $(1/V_1)$. In each case, the T term provides

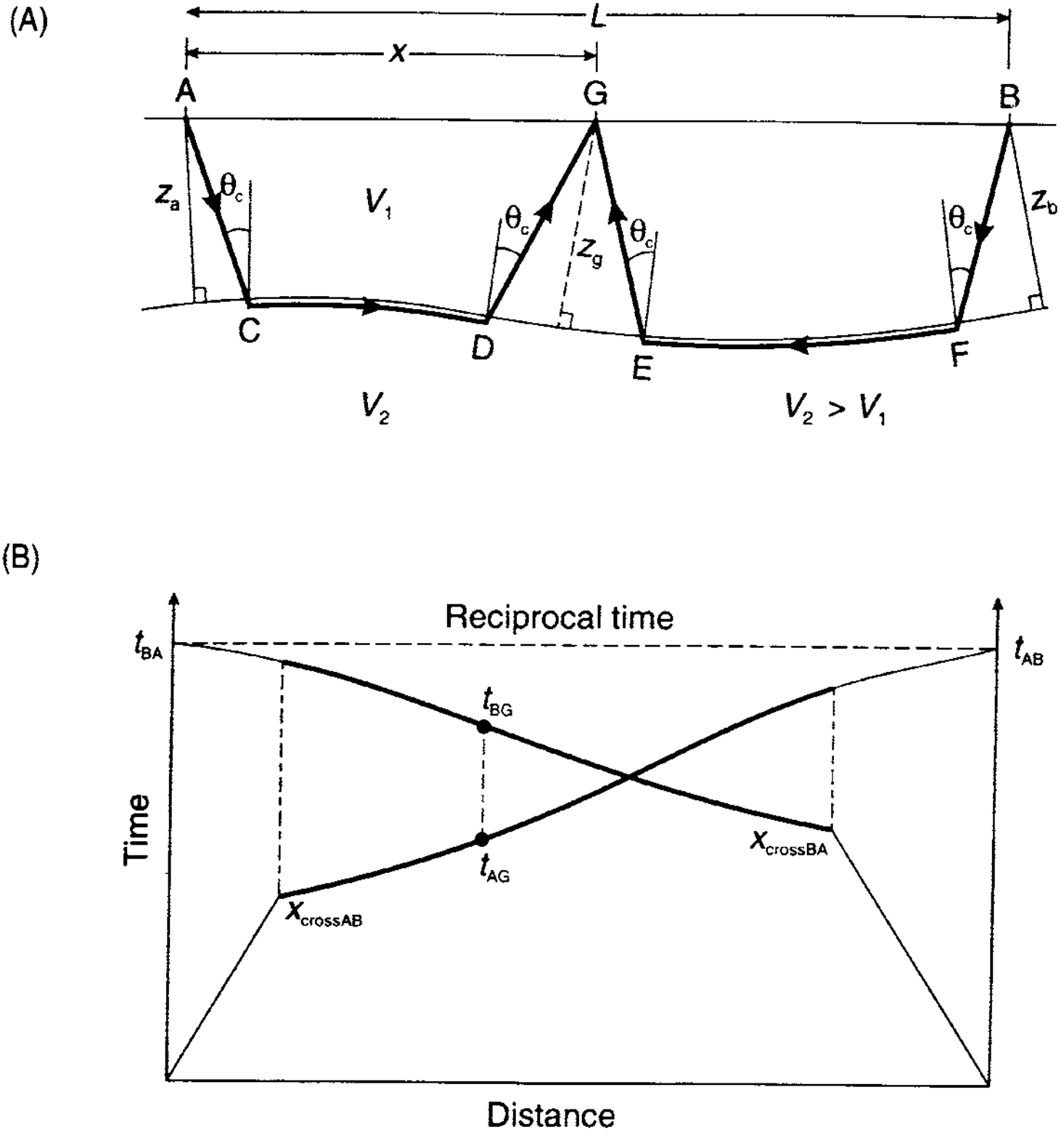

Figure 5.11 (A) Raypath geometry for forward and reverse shots over a refractor with irregular surface topography, and (B) the corresponding travel time–distance graphs. The segments between respective crossover distances are highlighted by thicker lines as it is these segments that are used in Hagedoorn's plus-minus analysis

a means of examining the lateral variation in refractor velocity with a lateral resolution equal to the geophone separation. Better accuracy of the estimate of velocity can be achieved, whichever graphical method is used, by carrying out linear regression analysis over the appropriate segments of the graph to determine the slope(s) most accurately and to provide some means of determining standard deviations.

Once values of layer velocities have been calculated, the depth (z_g) perpendicular to the refractor below each geophone can be computed using the T^- term. Calculations are made easier if velocities are expressed in km/s and time in milliseconds as depths are then given in metres. Given the assumptions made, the accuracy of depth calculation should be to within 10%.

An example of the graphical output from the plus minus method is shown in Figure 5.12.

Box 5.9 Hagedoorn plus – minus terms (see Figure 5.11)

The travel time of a refracted ray at any geophone G is given by:

$$t_{AG} = x/V_2 + \delta t_g + \delta t_a \quad (1)$$

$$t_{BG} = (L - x)/V_2 + \delta t_g + \delta t_b \quad (2)$$

$$t_{AB} = L/V_2 + \delta t_a + \delta t_b \quad (3)$$

Hagedoorn's plus term T^+ is given by:

$$T^+ = t_{AG} + t_{BG} - t_{AB} = 2\delta t_g = 2z_g(\cos\theta_c)/V_1 . \quad (4)$$

Therefore, the depth to the refractor beneath any geophone (z_g) is given by:

$$z_g = (T^+)V_1/2\cos\theta_c = (T^+)V_1V_2/2(V_2^2 - V_1^2)^{1/2}. \quad (5)$$

Hagedoorn's minus term T^- is given by:

$$T^- = t_{AG} - t_{GB} = (2x - L)/V_2 + \delta t_a - \delta t_b. \quad (6)$$

The Hagedoorn plus–minus method is readily adapted for calculation using a programmable calculator (Cummings 1988), or a personal computer using either stand-alone proprietary software (e.g. GREMIX from Interpex Ltd; and van Overmeeren 1987) or a computer spreadsheet (e.g. Morris 1992), such as Lotus 1–2–3, Microsoft's Excel or Borland's Quattro-Pro. Seismograph manufacturers are also providing their own interpretational software with their instruments.

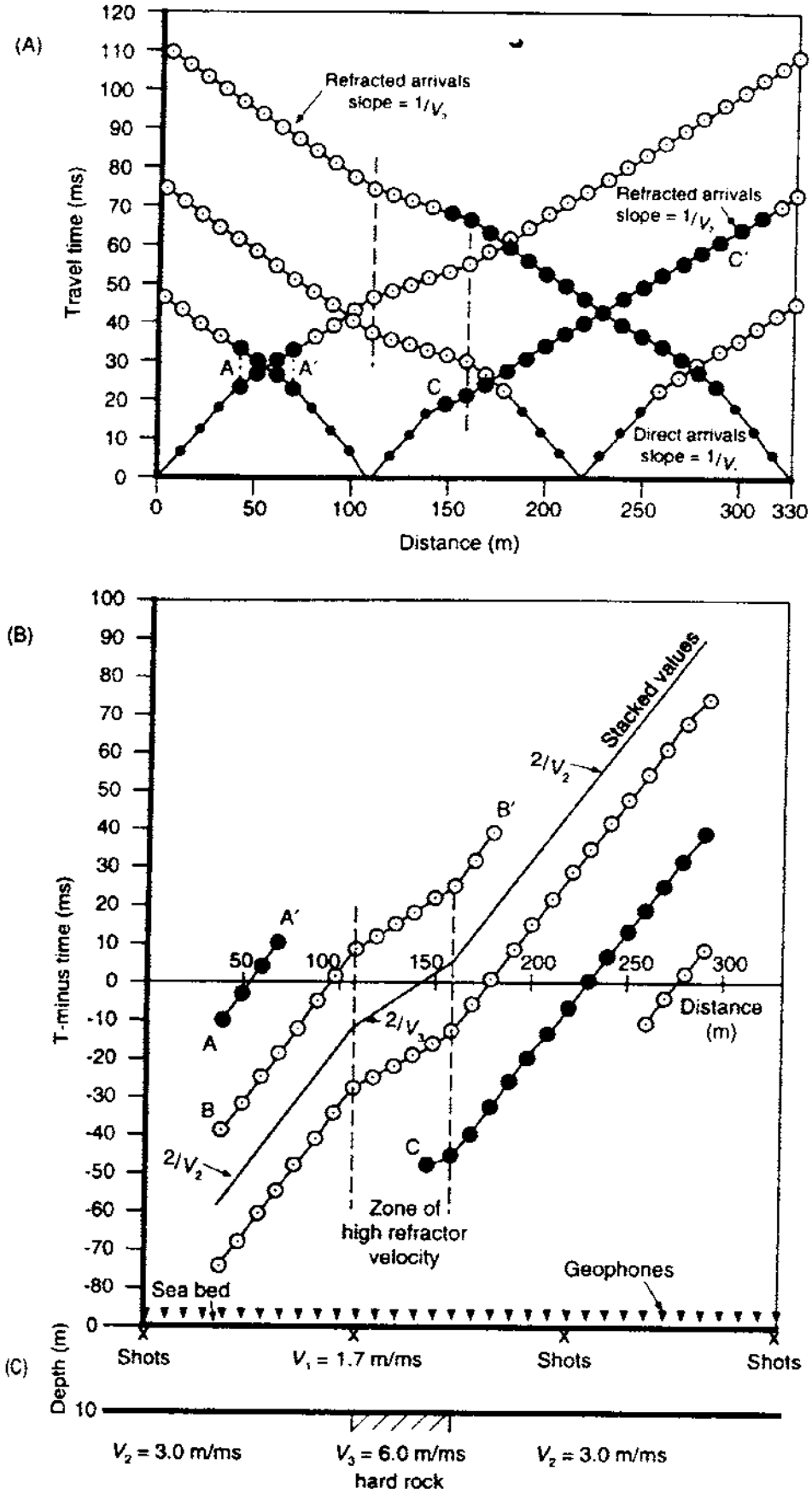

Figure 5.12 (A) Composite travel time-distance graphs; (B) Hagedoorn T^- graph; and (C) calculated depths to a refractor. After Gardener (1992), by permission

The interpretation procedure is very straightforward. Having picked the first-arrival times, the values are put into their respective spreadsheet cells for their given offset distance. By inspection of the time–distance (T X) graphs the reciprocal times can be found and checked; the distances between end-to-end shots and hence the values of the distance L are known from the survey layout. The T–X graphs are inspected to separate out which portions of which graph are to be used in the analysis (i.e. which data give information about V_1 and which about V_2, etc.). Velocities are found using linear regression analysis on the relevant portions of the T–X graph (for V_1) and of the T^{-}–distance graphs (for V_2). These values are then used with the T^{+} term to derive values of depth to the refractor at each geophone location. All the graphical output and the calculations can be achieved using just one software package, thus making it very convenient to carry out the analysis.

The plus–minus method assumes also that the refractor is uniform between the points of emergence on the interface (i.e. between D and F in Figure 5.11A). If this assumption does not hold but the method is used, then the non-planarity of the refractor is smoothed and an oversimplified interpretation would be obtained. This smoothing is overcome by the generalised reciprocal method which is discussed in the next section.

5.4.3 Generalised reciprocal method (GRM)

The generalised reciprocal method (Palmer 1980) is an inversion technique which uses travel-time data from both forward and reverse shots and which provides a graphical solution to resolve the geometry of sub-surface refractors. The method uses refraction migration to obtain the detailed structure of a refractor and information about any localised lateral variations within it. Refraction migration uses the offset (migration) distance which is the horizontal separation between a point on the refractor where a ray is critically refracted and that at the surface where the ray emerges.

It has been pointed out (Sjögren 1984), however, that the migration distance does not satisfactorily define narrow zones with low seismic velocities. As such zones are often the targets for refraction surveys, it is important that the interpretational method is capable of resolving them. Palmer (1991) has demonstrated that the migration distance selected to define the refractor surface is not necessarily the same as that which provides the optimum information about refractor velocities. Consequently, if the GRM is used to its full effect, it can be used successfully to define narrow low-velocity zones (see also Section 5.5.1). In order to increase the accuracy of the GRM, Zanzi (1990) has proposed that consideration should be given to nonlinear corrections in the case of an irregular refractor.

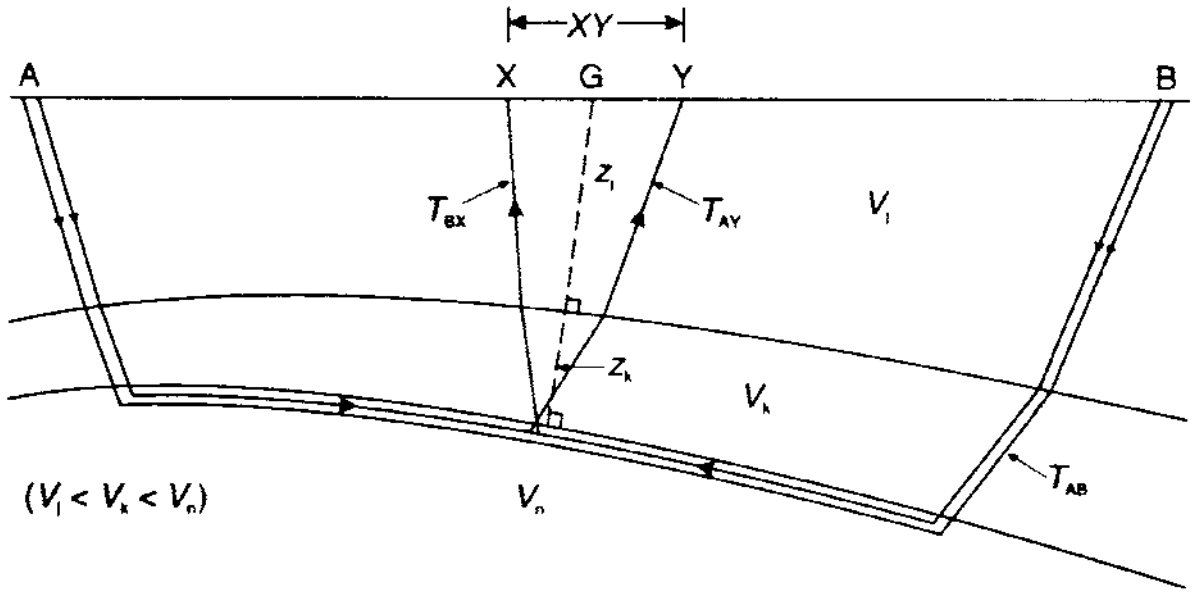

Figure 5.13 Schematic summary of parameters used in the generalised reciprocal method (GRM)

A principal difference of the GRM compared with the plus–minus method is that the critically refracted rays emerge at or very near the same point on the refractor, thereby removing the smoothing problem discussed in the previous section. They arrive at two different geophone locations separated by a distance XY (Figure 5.13).

Two functions are computed within the generalised reciprocal method: the velocity analysis function (t_v) and the time–depth function (t_G). The latter is determined with respect to a position G (Figure 5.13) at the mid-point between the points of emergence at the surface of forward and reverse rays at Y and X, respectively. Both functions are expressed in units of time and are detailed in Box 5.10. Equations (1) and (2) in that box are similar to Hagedoorn's T^- and T^+ terms, respectively, when the points X and Y are coincident (see Box 5.9). In cases where the maximum angle of dip is less than 20°, the GRM, as detailed here, provides estimates of refractor velocities to within 5%.

Both the velocity analysis and time–depth functions are evaluated and presented for a range of XY values from zero to one considerably larger than the optimum value. The increment in values of XY is usually taken as being equivalent to the geophone separation. Thus, if geophones are spaced at 5 m intervals, XY is incremented in steps of 5 m.

Box 5.10 GRM velocity analysis and time functions (Figure 5.13)

The **refractor velocity analysis function** (t_v) is given by:

$$t_v = (T_{AY} - T_{BX} + T_{AB})/2 \qquad (1)$$

where the distances AY and BX can be defined in terms of the

continued

continued

XY and AG, such that:

$$AY = AG + XY/2 \qquad \text{and} \qquad BX = AB - AG + XY/2.$$

A graph of t_v plotted as a function of distance x has a slope $= 1/V_n$, where V_n is the seismic velocity in the refractor (which is the nth layer).

The **time–depth function** (t_G) is given by:

$$t_G = [T_{AY} + T_{BX} - (T_{AB} + XY/V_n)]/2. \tag{2}$$

The time depth function, plotted with respect to position G, is related to the thicknesses (z_{jG}) of the overlying layers, such that:

$$t_G = \sum_{j=1}^{n-1} z_{jG}(V_n^2 - V_j^2)^{1/2}/V_n V_j \tag{3}$$

where z_{jG} and V_j are the perpendicular thickness below G and velocity of the jth layer, respectively.

The optimum distance XY (XY_{opt}) is related to layer thickness z_{jG} and seismic velocities V_j and V_n by:

$$XY_{opt} = 2\sum_{j=1}^{n-1} z_{jG} \tan\theta_{jn} \tag{4}$$

where $\sin\theta_{jn} = V_j/V_n$.

Given a value of XY_{opt}, an average velocity (V') of all the layers above the refractor (layer n) is given by:

$$V' = [V_n^2 XY_{opt}/(XY_{opt} + 2t_G V_n)]^{1/2}. \tag{5}$$

At the optimum value of XY, both the forward and reverse rays are assumed to have been critically refracted at or very near the same point on the refractor. The optimum value of XY in the analysis of velocity is determined as being that which gives a time–depth function which approximates most closely to a straight line. Where there are lateral variations in refractor velocity, the optimum value of XY may differ with distance (see, for example, the case history in Section 5.5.1). In the selection of the optimum value of XY for the time–depth function, the graph which exhibits most detail should be the one chosen. In general, the optimum value of XY should be the same for both the velocity analysis and time–depth functions.

Having determined the value(s) of refractor velocity from the velocity analysis function (t_v), and hence determined the optimum value of XY, then equation (3) in Box 5.10 can be used to calculate the perpendicular depth to the refractor below each geophone position. This depth value is, however, the locus of depths centred on any given

geophone position. Hence, an arc is drawn centred on a given geophone location with a radius equivalent to the calculated depth. The refractor surface is constituted by drawing the tangent to the constructed arcs, so that the true geometry of the refractor is migrated to the correct location in space. A further example of the application of this method is given in Section 5.5.1 (Lankston 1990).

5.4.4 Hidden-layer problem

A *hidden layer* or *blind zone* occurs when a layer that is present is not detected by seismic refraction. There are four causes of this problem: velocity inversion; lack of velocity contrast; the presence of a thin bed; and inappropriate spacing of geophones (Figure 5.14). In the situation where a layer with a lower velocity underlies one with a higher velocity, then the lower-lying layer may not be detected using seismic refraction methods. No critical refraction can occur in such a situation and thus no headwaves from the interface are produced. If there is little velocity contrast, then it may be extremely difficult to identify the arrivals of headwaves from the top of this zone. In addition, in the case where velocities increase with depth, but the thickness of a layer is less than one wavelength of the incident wave, then the thin bed would not be evident on the corresponding time distance graph and would therefore effectively be hidden. Furthermore, the portion of travel time graph arising from this thin bed may not be sampled if the geophone interval is too large (Lankston 1990).

The hidden-layer problem precludes seismic refraction surveys from being undertaken where there is known to be a velocity inversion, such as where there is a layer of strongly cemented material in less consolidated material at shallow depth, such as hard-pan or duricrust. The only way seismic refraction can be undertaken in such circumstances is for each shot and geophone to be located below this hard, higher-velocity layer. This solution can lead to considerable logistical problems and reduced production rates, with a corresponding increase in cost.

5.4.5 Effects of continuous velocity change

So far it has been assumed that each layer has a uniform velocity both horizontally and vertically. In reality there are some materials where a uniform velocity is not observed. Examples of such materials are: sedimentary sequences in which grain size varies as a function of depth (fining-up and fining-down sequences), or where the degree of cementation increases with depth; some igneous bodies where fractionation has occurred, giving rise to more dense material at depth; and in polar regions over snowfields, where the degree of compaction from snow to ice increases with depth (firnification). In these situations, there is a gradual change in velocity with depth (e.g. Kirchner

(A)

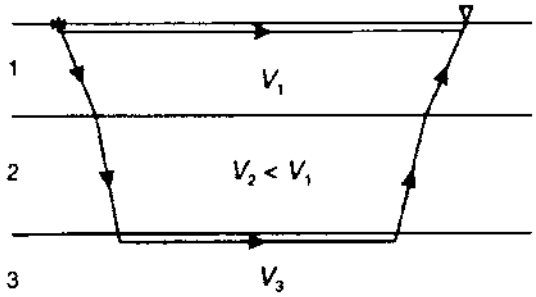
1
V_1
2
$V_2 < V_1$
3
V_3

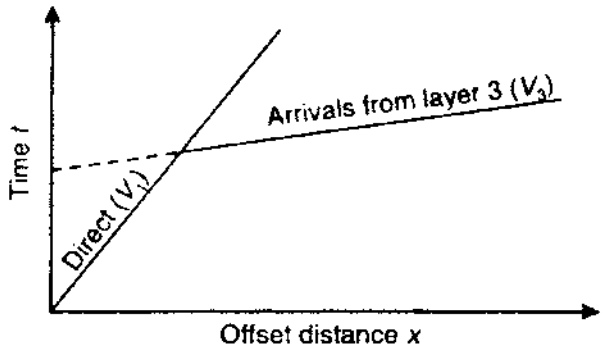
Time t
Arrivals from layer 3 (V_3)
Direct (V_1)
Offset distance x

(B)

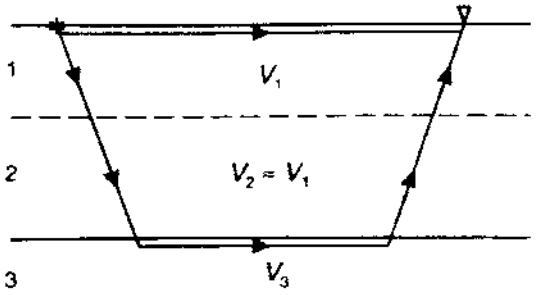
1
V_1
2
$V_2 \approx V_1$
3
V_3

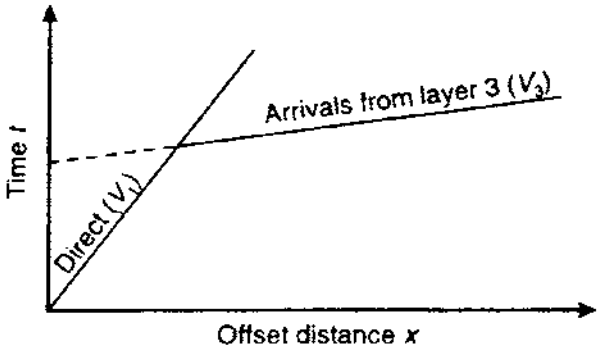
Time t
Arrivals from layer 3 (V_3)
Direct (V_1)
Offset distance x

(C)

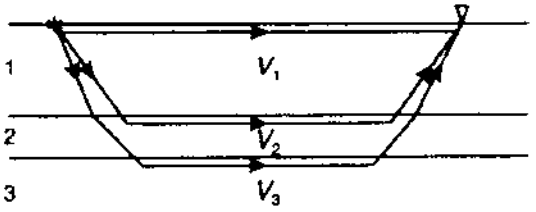
1
V_1
2
V_2
3
V_3

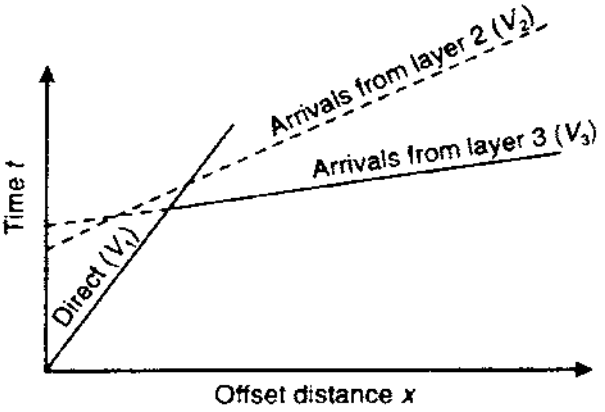
Time t
Arrivals from layer 2 (V_2)
Arrivals from layer 3 (V_3)
Direct (V_1)
Offset distance x

(D)

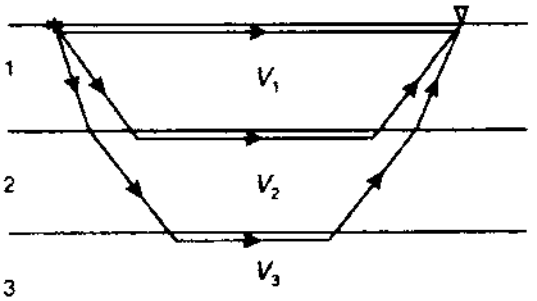
1
V_1
2
V_2
3
V_3

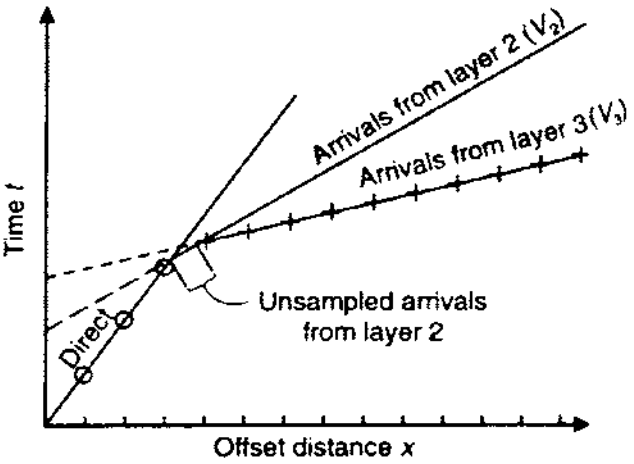
Time t
Arrivals from layer 2 (V_2)
Arrivals from layer 3 (V_3)
Unsampled arrivals from layer 2
Direct
Offset distance x

and Bentley 1979; Beaudoin *et al.* 1992; King and Jarvis 1992) and hence there is no obvious crossover point on the time–distance graph. Instead, the graph is curved, and the change from one so-called layer to another is gradational, making the usual methods of analysis inappropriate.

Figure 5.14 (*opposite*) Depiction of the 'hidden layer' problem due to: (A) velocity inversion ($V_2 < V_1$); (B) lack of velocity contrast ($V_2 \approx V_1$) and (C) a thin layer (layer 2) sandwiched between layers 1 and 3. In (D) the distance between geophones is too large to permit the identification of layer 2.

5.5 APPLICATIONS AND CASE HISTORIES

5.5.1 Rockhead determination for a proposed waste disposal site

Lankston (1990) has provided an example of the use of seismic refraction surveying with respect of a municipality granting a permit for a waste disposal site. The proposed location was an isolated site adjacent to a major river. Basalt, which was exposed along the side of the site farthest from the river, formed the underlying bedrock. Overlying bedrock was alluvium and windblown sand that in areas formed dunes 1–2 m high. Owing to the presence of loose sand at the surface, a sledge-hammer source was ineffective so explosives were used. The geophone interval was 50 ft (15.2 m). Each refraction spread was surveying using one long and one short offset shot at each end plus one mid-spread shot. Each successive spread overlapped with the previous one by two geophone positions.

Figure 5.15 Travel time distance graphs for forward-direction shots. The first breaks for the far-offset shots (shown as crosses) for the leftmost spread arrive earlier than those from the near-offset shot (shown by squares) for this spread. This occurs when the distance between the shotpoint and the refractor decreases significantly bewteen the near- and far-offset shots. Form Lankston (1990), by permission. See text for details

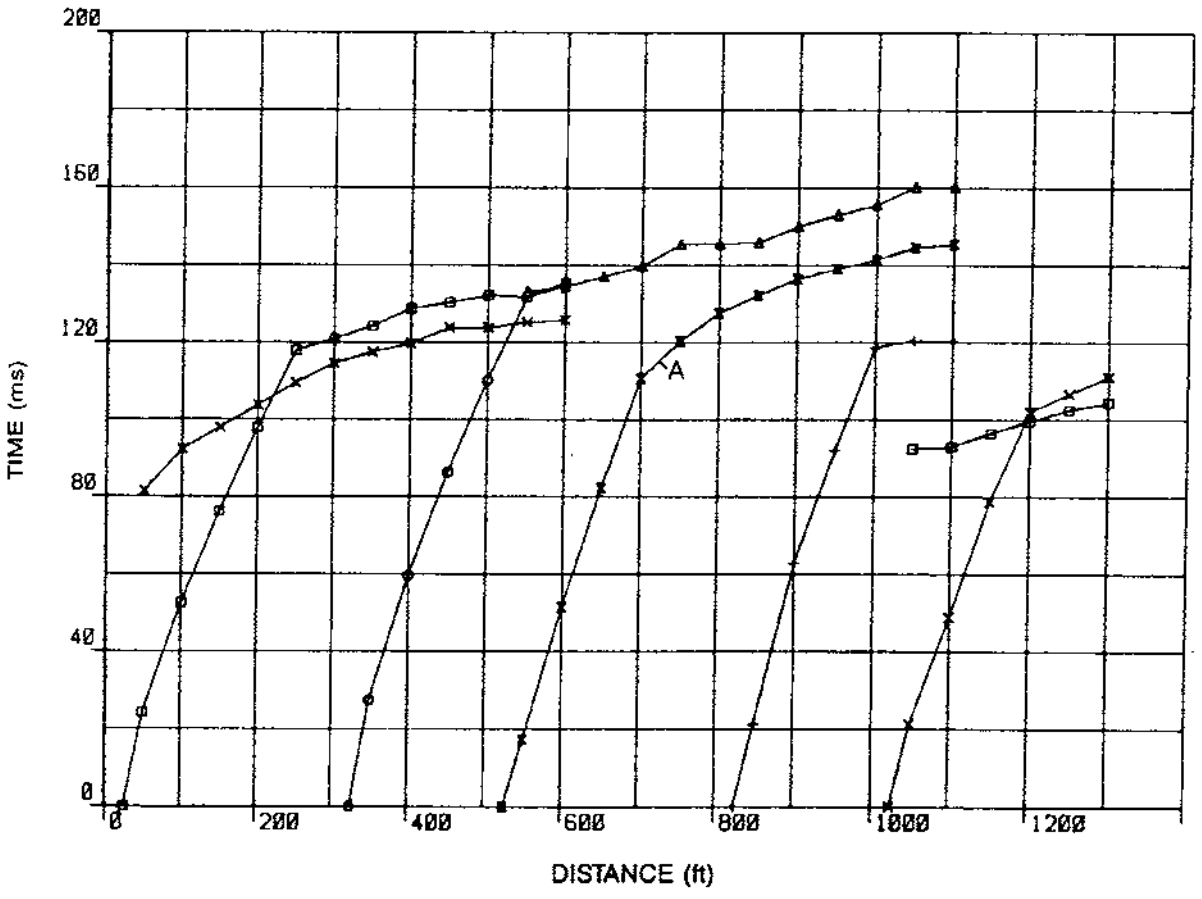

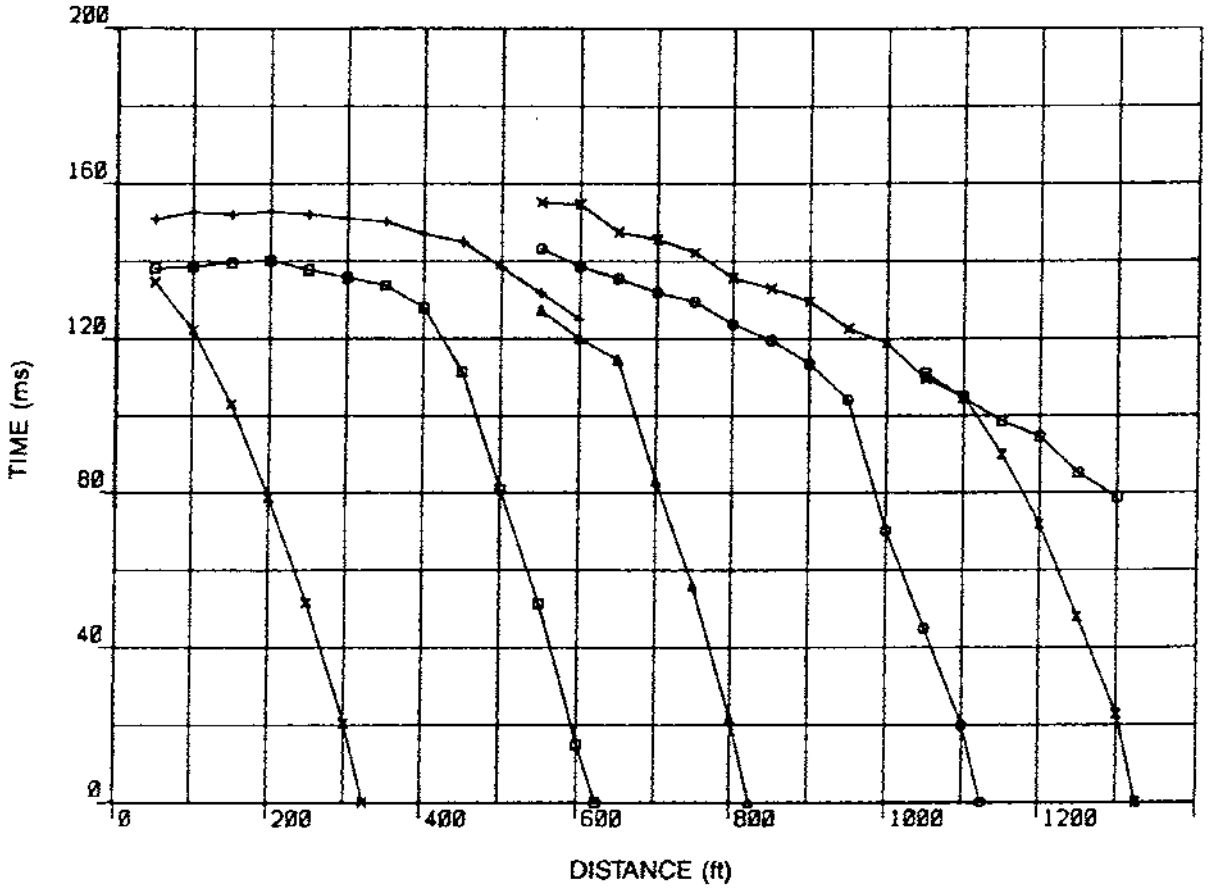

Figure 5.16 Travel time–distance graphs for the reverse-direction shots. From Lankston (1990), by permission

The forward-direction travel time–distance graphs along one survey line are shown in Figure 5.15. The data are indicative of a two-layer case, with good parallelism evident in the high-velocity, deeper layer arrivals, except between 700 and 800 ft (213 m and 244 m) along the line. It is evident that the geophone interval is too large to provide the required resolution here. It is a good example of the occurrence of the problem illustrated in Figure 5.14D. The presence of an intermediate layer is indicated at 750 and 800 ft (indicated by the letter A in Figure 5.15).

The reverse-direction travel time graphs for the same survey line are given in Figure 5.16. However, these data do not help to resolve the problem over the presence of an intermediate layer – or to what extent the feature occurs laterally.

The data were phantomed (Figure 5.17) using the method described by Lankston and Lankston (1986). Forward data from the shot at 325 ft (99 m) and reverse data from the shot at 1125 ft (343 m) were used. Between each observed (or phantomed) point on the travel time–distance graph, travel times were interpolated in order to improve the resolution of the optimum XY value using the general reciprocal method. The resulting velocity analysis is shown in Figure 5.18. Applying Palmer's (1980) criterion of least detail, the curve for $XY = 0$ was considered to be the best for defining the refractor's velocities. Applying Palmer's (1980) maximum detail criterion to the

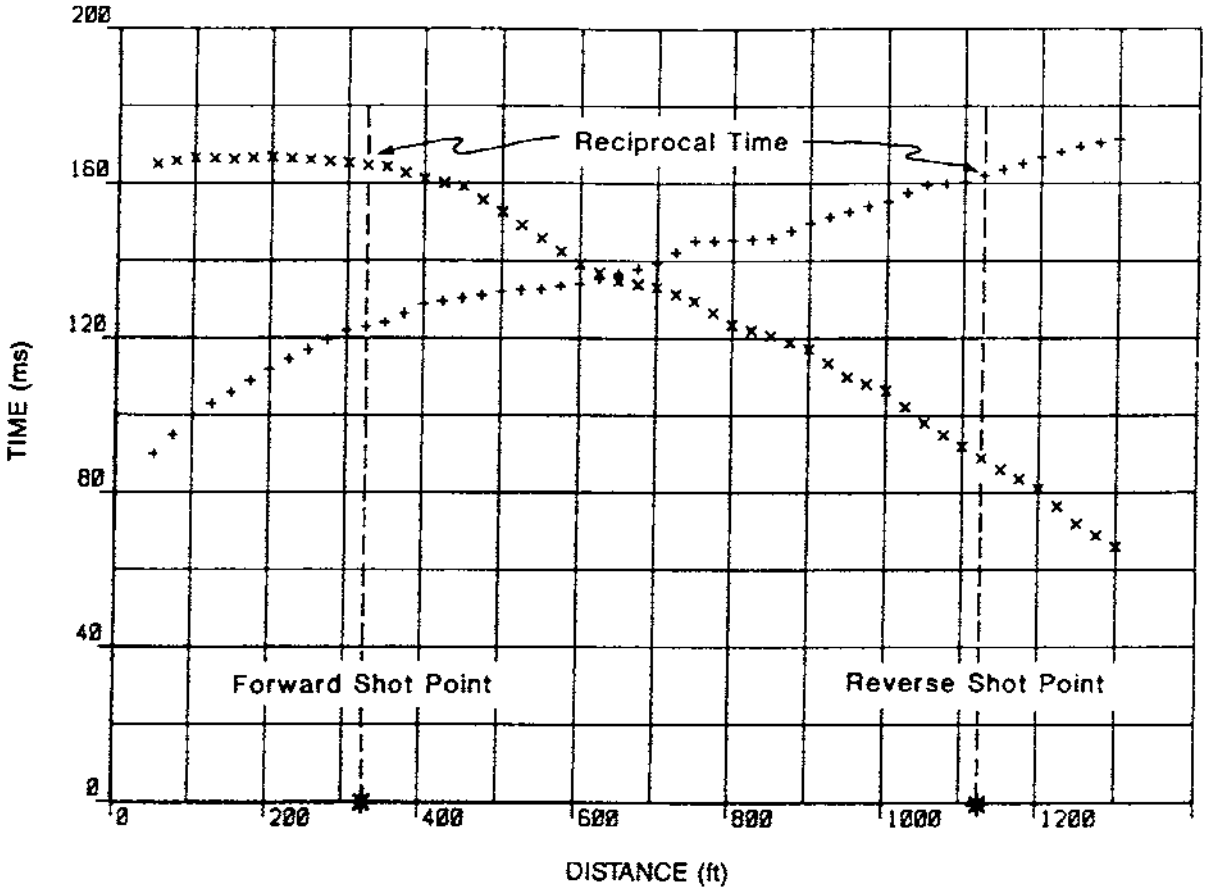

Figure 5.17 Forward- and reverse-direction travel time–distance graphs after intra-line phantoming and interpolation of new arrivals at locations halfway between observed arrivals. The reciprocal time as interpreted from the forward and reverse direction experiments is indicated. From Lankston (1990), by permission

time–depth data in Figure 5.19, an optimum $XY = 0$ was also chosen. In generating the time–depth graphs, the refractor velocity was required; three values were interpreted along the refractor as indicated in Figure 5.20.

With such a large inter-geophone spacing (50 ft), quantifying any change in the optimum XY value on the basis of the data acquired was not possible. However, had the layer thicknesses and velocities been known, the optimum XY value could have been predicted. By working backwards in this example from the interpreted velocities and depths, the optimum XY value was predicted to be equal to about 6 m (20 ft).

Having determined the refractor velocities and, from micro-spreads, the velocities of the near-surface layers, within the constraints of the actual survey, the depth of the refractor below each geophone position was determined. The uppermost layer was determined to have a velocity of 305 m/s (1000 ft/s) and a thickness of 3.1 m (10 ft) along the length of the survey line. The second layer was assigned a velocity of 550 m/s (1800 ft/s). The calculated depth to the refractor is shown graphically below the appropriate geophone as an arc whose radius is equal to the calculated depth at that point (Figure 5.21). The actual surface of the refractor is then indicated by the envelope of tangents to the circular arcs. Also indicated in Figure 5.21

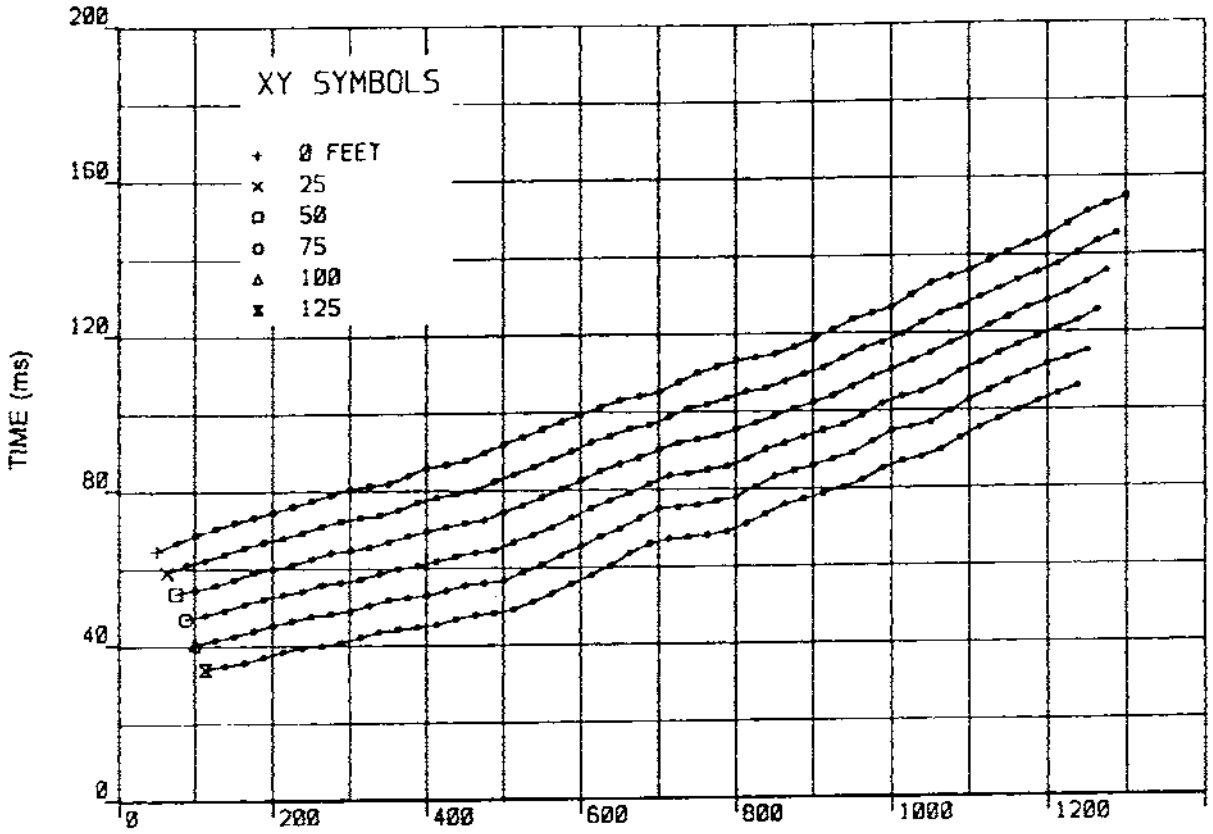

Figure 5.18 Velocity analysis curves for XY spacings from zero to 48 m (125 ft). From Lankston (1990), by permission

are the three values of refractor velocity. As it was known that the bedrock was basalt and that its structure was generally flat-lying, then the interpreted structure depicted in Figure 5.21 appears to be reasonable, with the three intra-refractor velocities corresponding to layers within the basalt.

Having produced the interpretation shown in Figure 5.21, this does not necessarily reflect the true geological picture. Earlier, it was suggested that there was an intermediate layer whose presence was intimated in the data in Figure 5.15 (at A). This has not been taken into account in the final model. If it had been, the depression evident in the refractor surface at 750 ft along the profile (which corresponds to the location of A) would have had a greater calculated depth to its surface.

In this example, Lankston (1990) reported that at the intersection of cross lines, the interpreted depths to the refractor agreed to within 5%. It was also stated that the final model produced was a fair reflection of the geological structure and that the survey had achieved the client's objectives.

5.5.2 Location of a buried doline

Palmer (1991) has described a seismic refraction survey over a known collapsed doline (sink hole) in Silurian metasediments in central

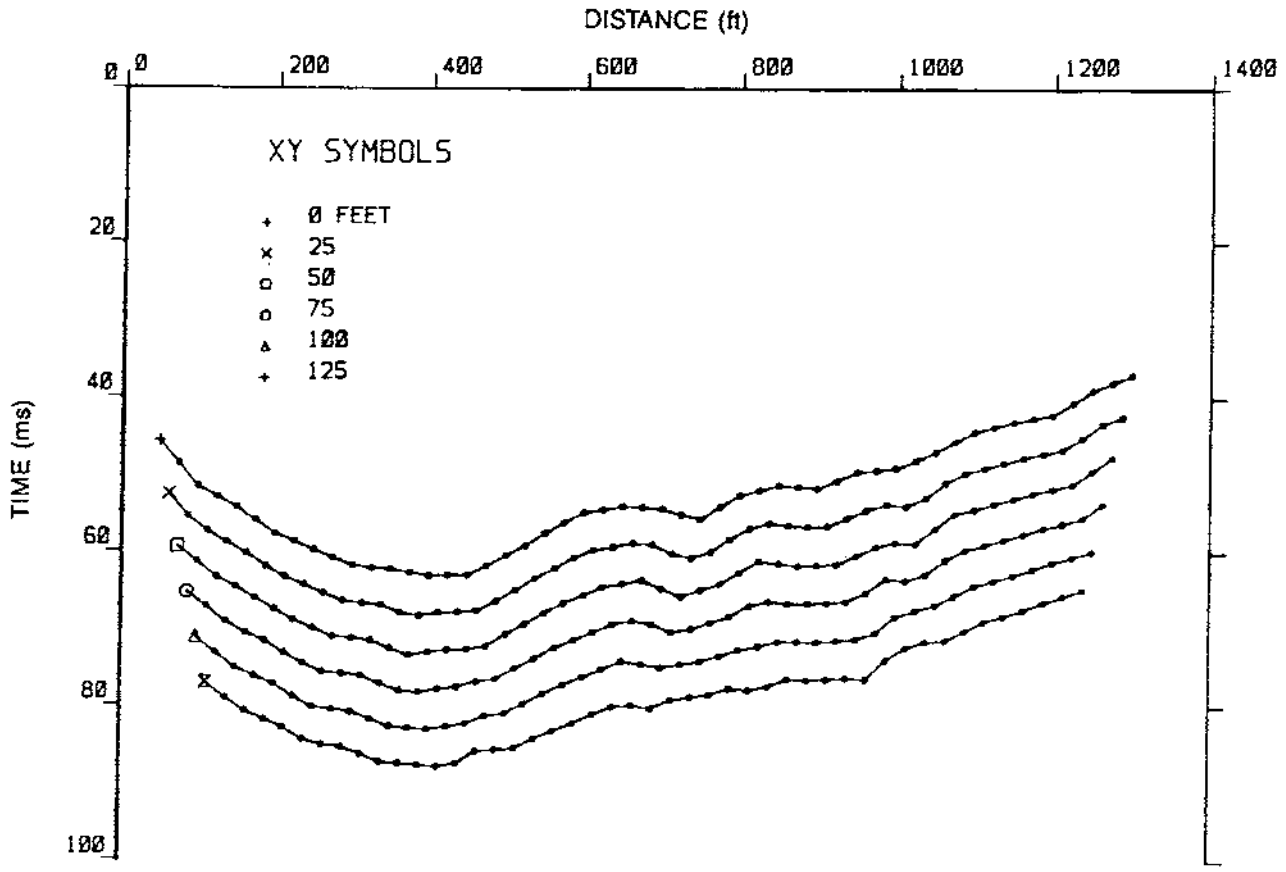

Figure 5.19 Time-depth curves for XY spacings fron zero to 48 m (125 ft). Refractor velocities used to generate these curves are indicated in Figure 5.20. From Lankston (1990), by permission

eastern Australia. In contrast to the previous example, the geophone interval was 2.5 m with a shot point interval nominally of 30 m. The travel time–distance graphs obtained are shown in Figure 5.22.

The refractor velocity analysis for shots at stations 12 and 83 are shown in Figure 5.23 for values of XY from zero to 15 m, in increments of 2.5 m. Velocity analysis for the refractor revealed values of 2750 m/s between stations 24 and 46, and 2220 m/s between stations 46 and 71. Palmer determined that the optimum value of XY was 5 m. The travel time–depth graphs over the same spread and range of XY values are shown in Figure 5.24. From these graphs the optimum value of XY was confirmed as being 5 m. A deepening of the refractor is evident between stations 40 and 52.

Evaluating equation (5) in Box 5.10 with an optimum value of XY of 5 m, a time-depth of 15 ms is obtained and a refractor velocity of 2500 m/s, with an average seismic velocity of 600 m/s for the material above the refractor. This latter value is comparable to that determined directly from travel time–distance graphs. The similarity of the near-surface velocities determined using the two approaches suggests strongly that there is no hidden-layer problem. Using these velocities, a depth section was produced (Figure 5.25).

In Figure 5.25, the arcs, representing the loci of the refractor surface beneath stations 39 and 46, all intersect in a cluster beneath station 39.

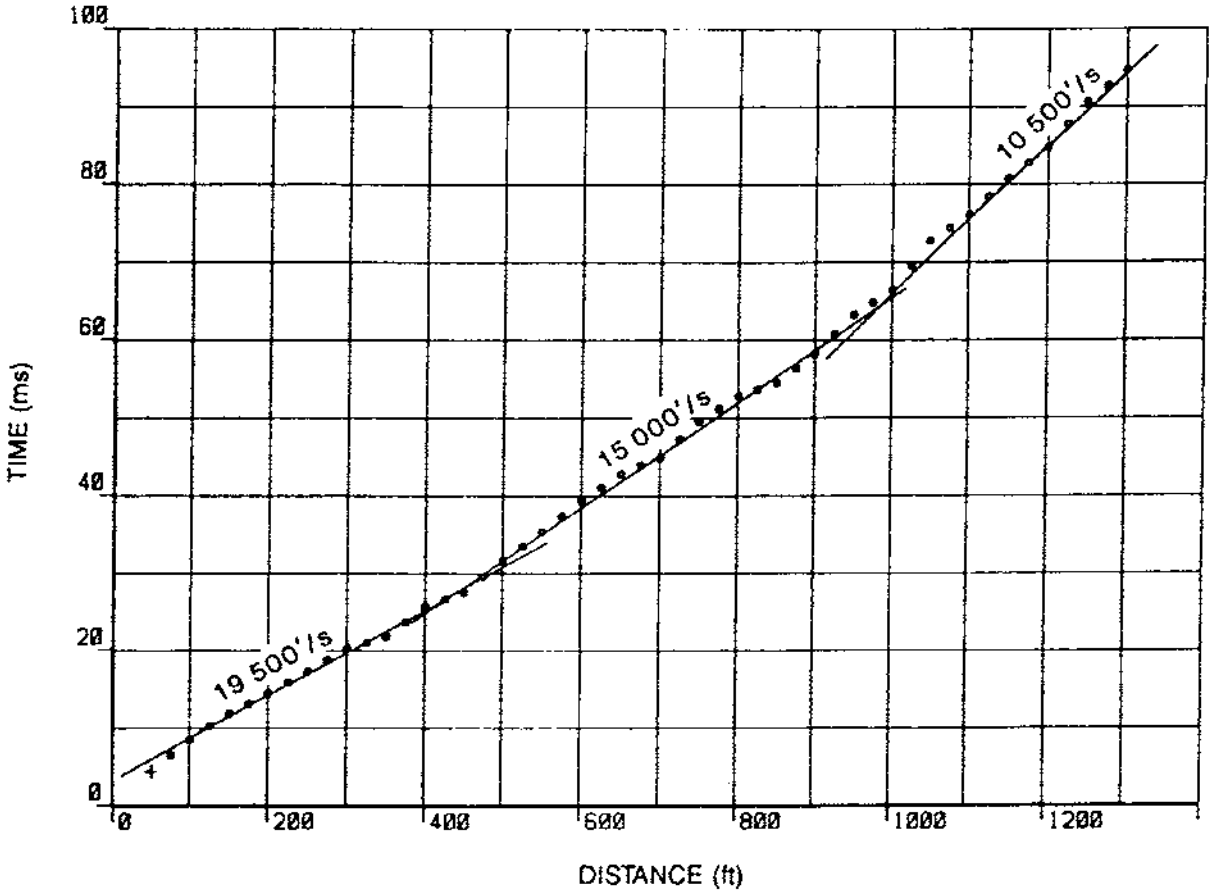

Figure 5.20 Velocity analysis curve for the $XY = 0$ case; the refractor is interpreted to have two lateral velocity changes. From Lankston (1990), by permission

Similarly, the arcs from stations 47 and 54 cluster beneath station 53. Such clusters indicate that all arrivals associated with the collapsed doline at these locations are diffractions from the edges. The refractor surface shown in Figure 5.25 is the minimum equivalent refractor rather than a true image of the doline. A drill hole sited near station 47 intersected almost 50 m of siliceous sandstone and voids. It was concluded that, with the large vertical extent of the doline relative to its 30 m diameter, and a roughly circular plan section, most of the seismic energy probably travelled around the doline rather than underneath it. Consequently, the minimum equivalent refractor was thought to be a hemisphere with a diameter of about 30 m.

From this analysis using the GRM, it was also concluded that there was no low-velocity zone associated with the collapsed doline. If a value for XY of zero was used in the velocity analysis function, it was possible to infer a seismic velocity of about 750 m/s between stations 44 and 47. This in itself would warrant further investigation. However, as it was thought that the seismic energy travelled around the doline, the volume beneath the feature was thought not to have been adequately sampled. Nevertheless, it was concluded that any low-velocity zone, if there was one, would have been of only limited lateral extent.

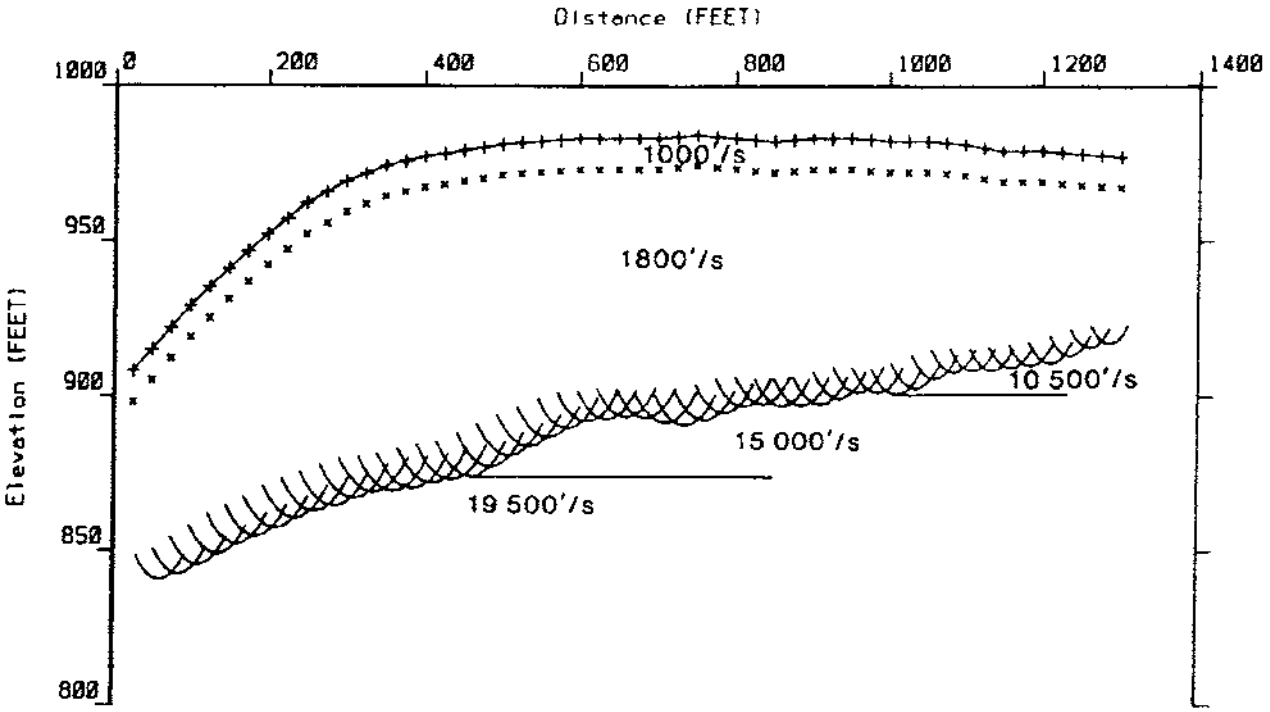

Figure 5.21 Final migrated section. The refractor surface is the envelope of the tangents to the suite of arcs. The arcs are mathematically circular, but they appear elliptical because of vertical exaggeration of the elevation scale. The ground surface is denoted by the continuous curve. The small crosses represent the interface between the 305 m/s (1000 ft/s) unit and the underlying 550 m/s (1800 ft/s) unit. The positions of the lateral velocity changes from Figure 5.20 are shown and have been interpreted as being due to layering with the basalt. From Lankston (1990), by permission

Another feature of this example is that it demonstrates the ability of the GRM to take diffractions into account without having to recognise them beforehand. In this respect, the migrated depth section (Figure 5.25) is very useful in revealing the clusters of arcs that are indicative of the diffractions. Furthermore, inclusion of the drilling results also helped to elucidate the mechanism of wave propagation in the vicinity of the collapsed doline. The combined interpretation that resulted was more realistic than if either the refraction survey or the drilling had been used in isolation.

5.5.3 Assessment of rock quality

There is an increasing requirement for geophysical surveys carried out during geotechnical investigations to provide direct information about rock quality or other geotechnical parameters. With the paucity of information to correlate geophysical results with actual rock properties, this is still difficult to achieve. Much more research needs to be done to address this. However, New (1985) has described one detailed study designed specifically to investigate this matter.

As part of the United Kingdom's radioactive waste management research programme, the Transport and Road Research Laboratory undertook a short programme of seismic velocity measurements at Carwynnan, Cornwall. The site was an experimental excavation in massive granite towards the north-western margin of the Carnmenellis Granite boss. The Cornubian batholith, of which the Carnmenellis

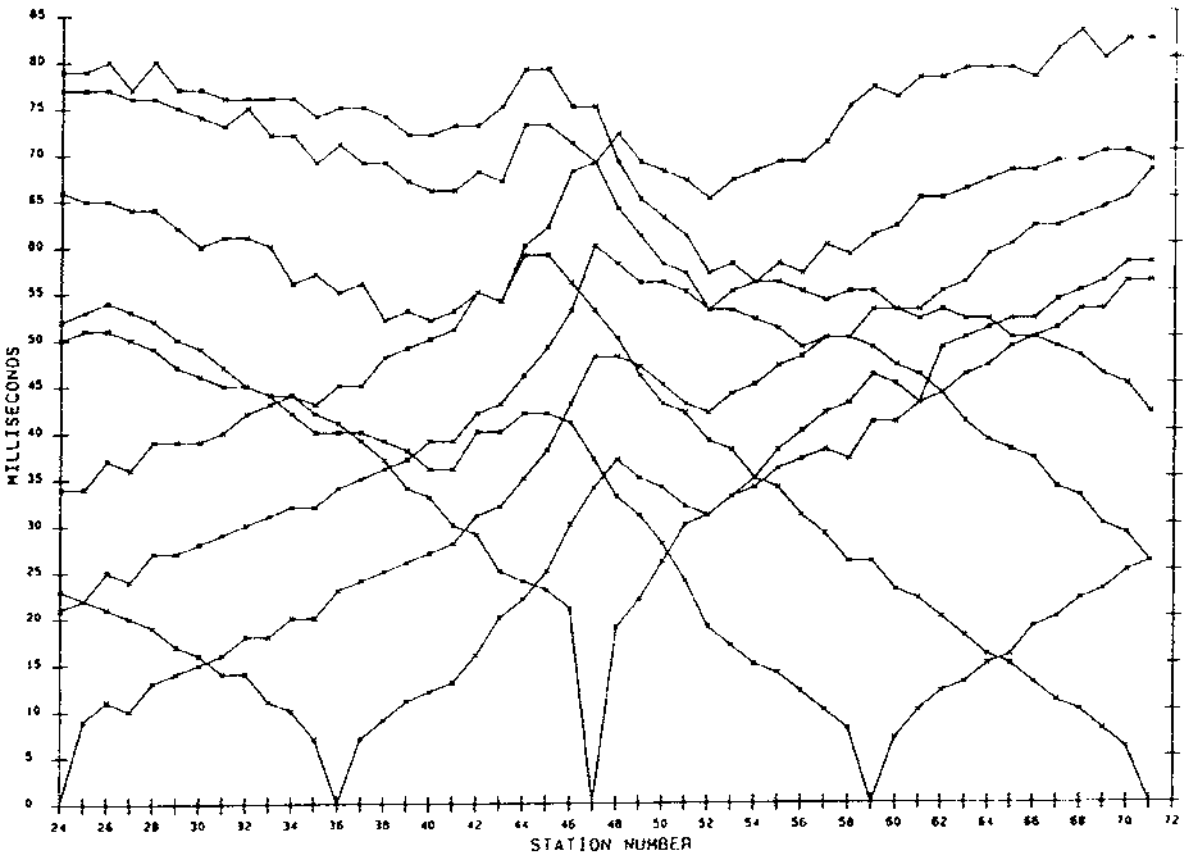

Figure 5.22 Travel time-distance graphs recorded over a collapsed doline in eastern Australia; the inter-geophone spacing is 2.5 m. From Palmer (1991), by permission

boss is part, is predominantly coarse-grained biotite–muscovite granite with phenocrysts of potassium feldspar. The rock is generally very strong and is weakly weathered. A predominant sub-vertical joint set, with a 120° strike direction and a joint spacing usually greater than 1 m, was found throughout the test site area.

The survey was undertaken within three horizontal headings at a depth of 30 m below ground level. Twenty reference points were fixed along three sides of a rectangular section of rock some 900 m^2 in area. Transmitting and receiving locations were numbered from 0 to 19 (Figure 5.26A). Geophones were bolted rigidly to the rock and surveyed in to an accuracy of ± 0.5 cm. The seismic source used was a sledge hammer.

The travel times and waveforms of the seismic signal were recorded and analysed using Fourier processing and a representative velocity (V_R) determined for each cell of a grid calculated for the rock mass. Contoured values of V_R were displayed in map form (Figure 5.26B). It is obvious that rock affected by the excavation of the headings has a reduced seismic velocity (< 5000 m/s) in comparison with that for undisturbed rock (≈ 5500 m/s).

A site-specific rock classification system was used to derive a numerical classification value (C) for each area of wall between reference points. This parameter depended upon:

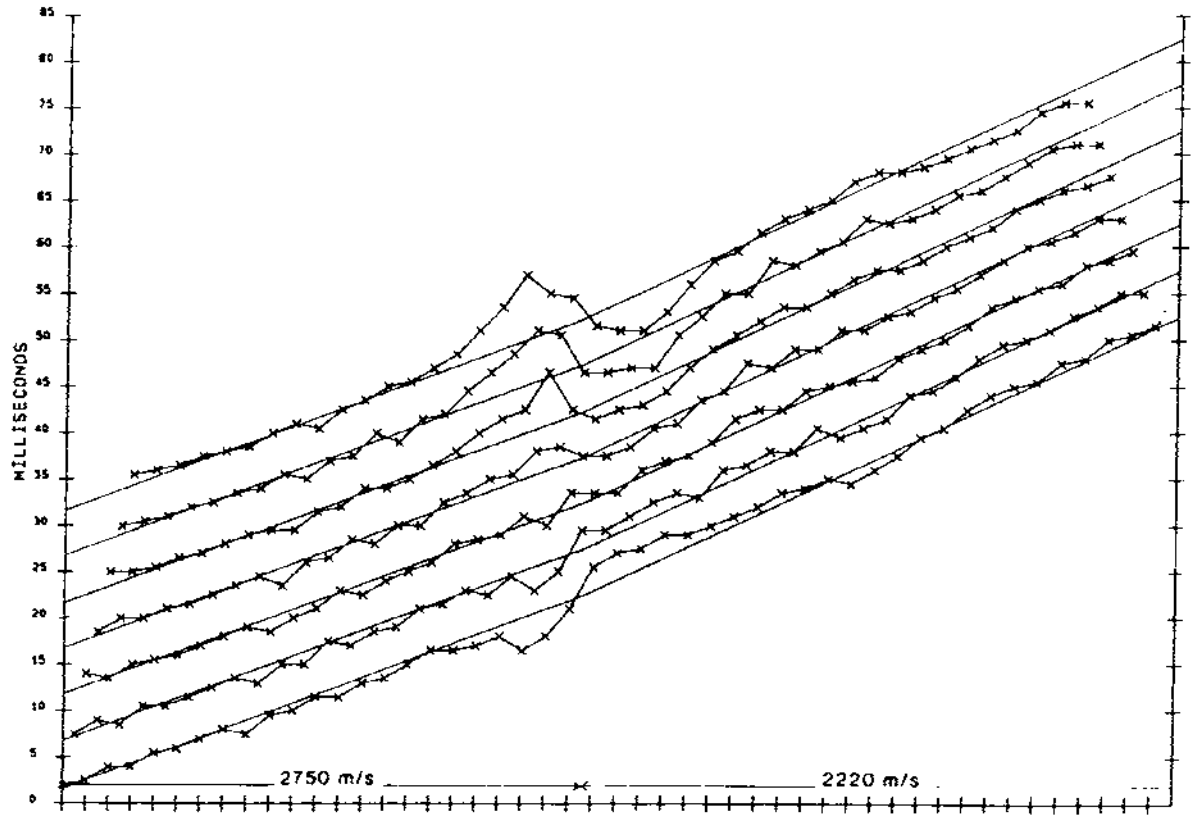

Figure 5.23 The GRM velocity analysis function computed with XY values from zero, the lower set of points, to 15 m, the upper set of points, in increments of 2.5 m. The reciprocal time has been increased by 10 ms for each XY value for clarity of display. From Palmer (1991), by permission

- the spacing of the joints;
- the condition of the joints (aperture, filling etc.);
- the general intact rock condition;
- the degree of excavation-induced blast damage;
- the density of shot holes in a given area – these were drilled to depths of between 1 m and 3 m.

The representative seismic velocity (V_R) was plotted as a function of the derived rock quality classification number (C) (Figure 5.27) for each pair of reference points.

It is clear from Figure 5.27 that there is a correlation between the seismic velocity and the rock quality. Indeed, New (1985) calculated the correlation as $V_R = 48.4\,C + 4447$ (with a correlation factor $r^2 = 0.86$). The very lowest velocities were found to be associated with a damaged and weathered area of rock with several major joints at the western extremity of the survey area. The north-western and south-western walls of the test area had been affected by heavy blast damage and extensively drilled compared with the smaller heading along the south-eastern wall.

This experiment, although limited in extent, did demonstrate that classification of rock using seismic methods can satisfactorily indicate the engineering properties of a rock mass. See also papers by Sjögren *et al.* (1979) and Gardener (1992).

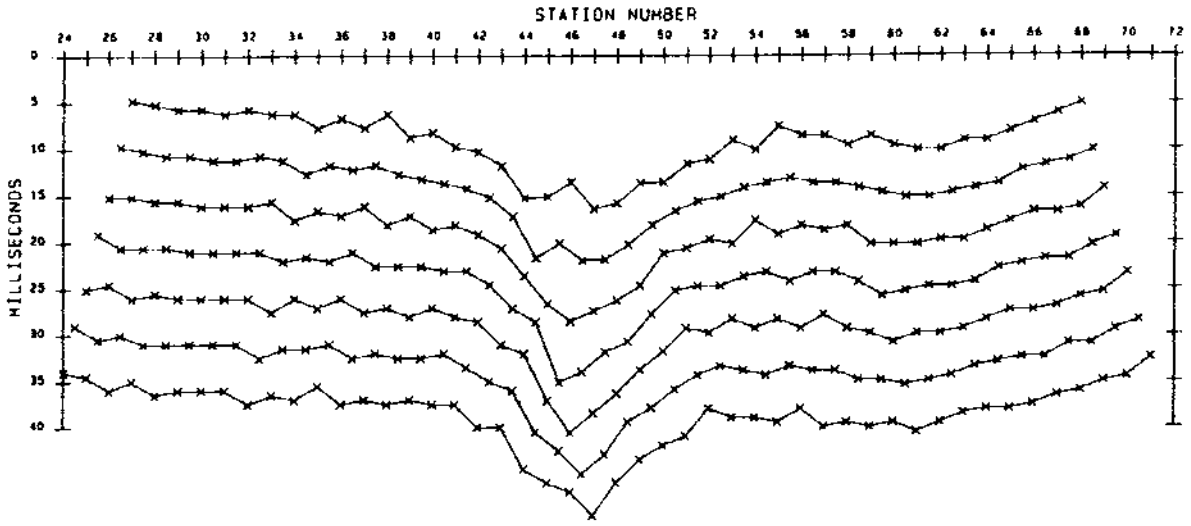

Figure 5.24 The GRM travel time–depth function computed with XY values from zero, the lower set of points, to 15 m, the upper set of points, in increments of 2.5 m. The reciprocal time has been increased by 10 ms for each XY value for clarity of display. From Palmer (1991), by permission

A very well-known application of seismic velocities is the determination of rippability – the ease with which the ground may be excavated using machines. In 1958, the Caterpillar Tractor Company developed the use of seismic velocities determined from surface refraction experiments to produce a practical chart (Figure 5.28) of rippability. Using this, contractors can estimate the ease (or otherwise) of excavating a given tract of ground using a mechanical device. Obviously, the chart is not exhaustive, but it provides general guidelines for practical use. Similarly, rippability is also a function of vehicle size, power and machine type. More specific charts relate geological material and rippability to machine types (Caterpillar Tractor Co. 1988). Other charts have been produced by other bulldozer manufacturers (e.g. Komatsu). However, disputes have arisen because the determination of rippability is not precise and contractors have found that ground reported to be rippable was patently not so, or their production rates were considerably slower than expected because of greater difficulty in excavating the ground. The estimation of rock rippability, including the use of seismic velocities, has been reviewed extensively by MacGregor *et al.* (1994).

Figure 5.25 The depth section computed with $XY = 5$ m and an average velocity in the overburden of 600 m/s; the position of the collapsed doline is evident. From Palmer (1991), by permission

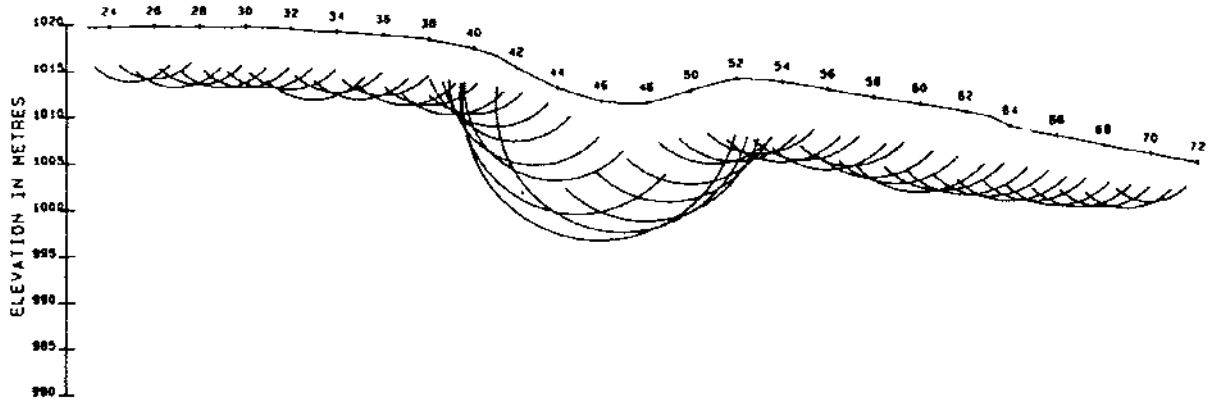

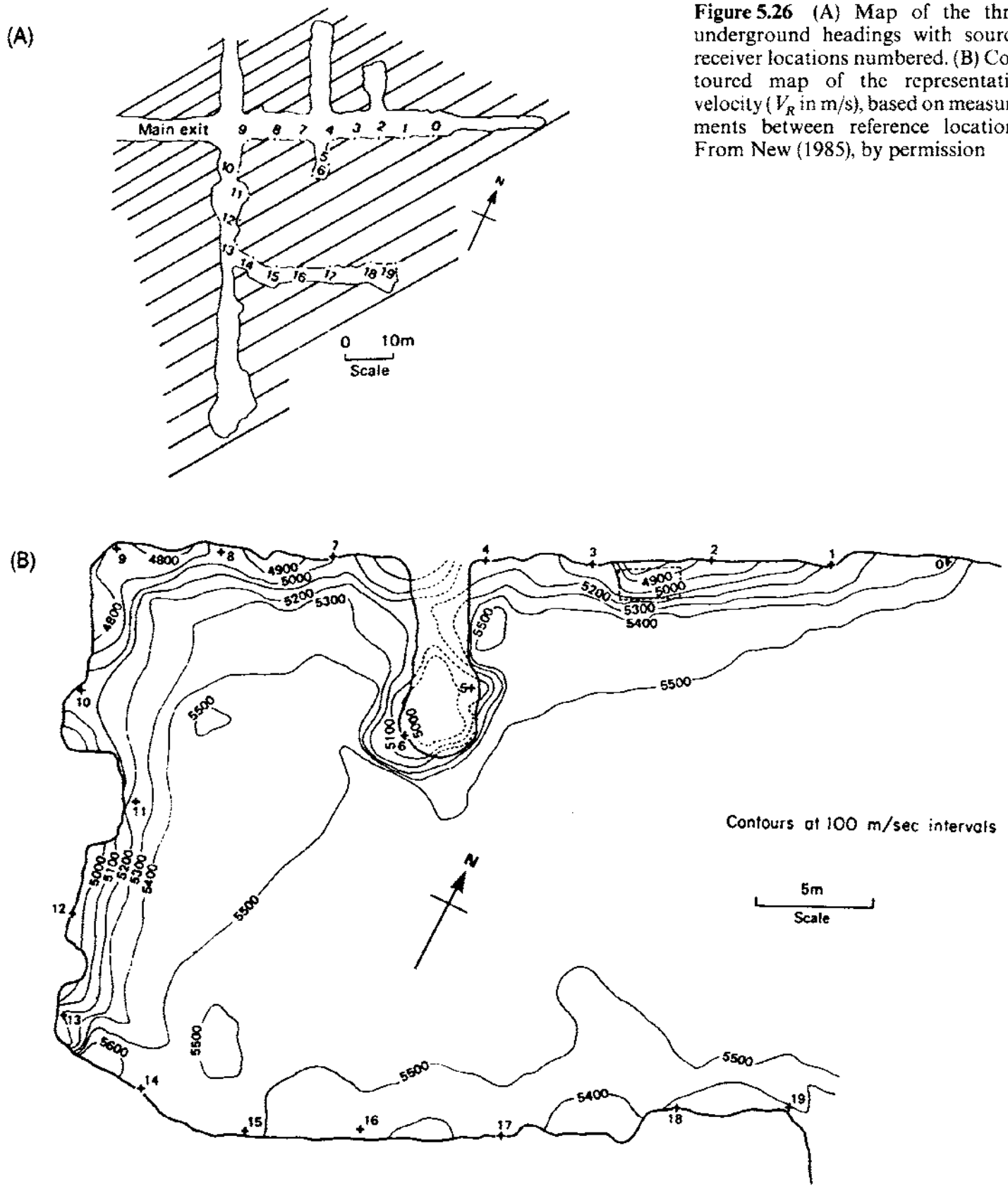

Figure 5.26 (A) Map of the three underground headings with source-receiver locations numbered. (B) Contoured map of the representative velocity (V_R in m/s), based on measurements between reference locations. From New (1985), by permission

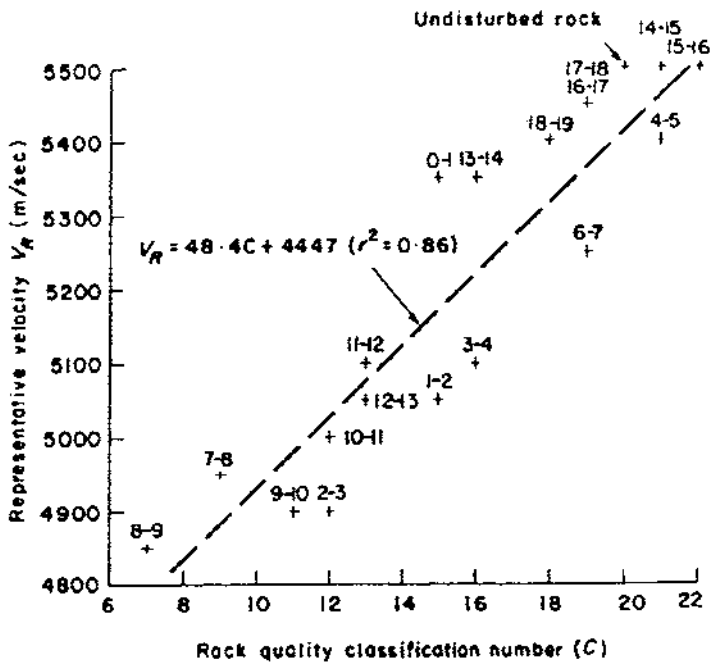

Figure 5.27 Correlation of representative velocity with rock quality classification. From New (1985), by permission

5.5.4 Landfill investigations

Refraction rather than reflection seismology has been used on landfills for three principal reasons:

- most landfills are too shallow for reflection seismology to be of much use;
- landfill material is highly attenuating and thus it is difficult to put much energy into the material and detect any significant signals;
- the cost of seismic reflection surveys is much greater than that of refraction surveys.

Even refraction surveys are seldom used over closed landfills (Reynolds and McCann 1992). One of the reasons for this is the difficulty in energy input – a hammer source may not be powerful enough and shotgun shells cannot be used where there is an active generation of methane gas! The general use of seismic methods on landfills is thus quite rare.

For selected sites where conditions permit, refraction seismology can be used to determine (1) the depth of fill; (2) P-wave velocities of the fill and substrates; (3) the location of old quarry walls that may delimit the edge of a landfill; and (4) the state of a clay cap, if it is of sufficient thickness. An example of a seismic refraction record with displaced first arrivals due to a vertical step associated with a step within an old backfilled quarry is shown in Figure 5.29.

Knight *et al.* (1978) have described the results of a seismic refraction survey carried out at a waste disposal site at Lucas Heights near

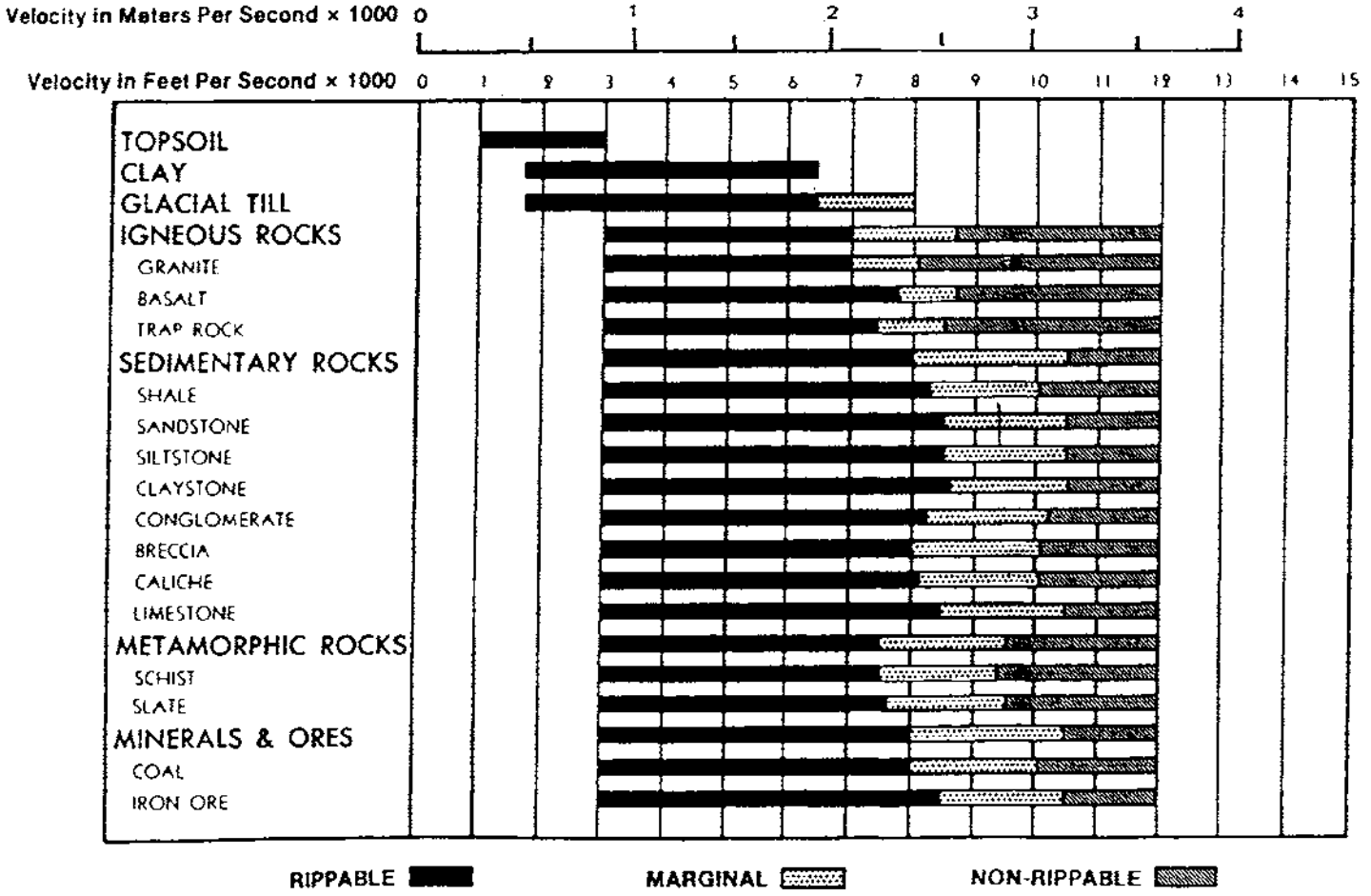

Figure 5.28 Typical chart of ripper performances related to seismic P-wave velocities. © Caterpillar Tractor Company, by permission

Sydney, Australia, to determine the depth of the fill material and the properties of the underlying bedrock. The fill material was made up of glass, metal and plastic, with small quantities of paper, cardboard and wood. At the base of the fill was a 'brown viscous sludge' at a depth of about 4 m below ground surface. The depth of fill was 6.5 m and it was underlain by sand containing a second water table and shale at a depth of 19 m. Their results were generally of poor quality because of the high attenuation of the seismic energy in the fill material. With a geophone interval of 3 m, the close-spaced survey indicated a P-wave velocity of 450 m/s for the fill material and 1900 m/s for the underlying sand.

Nunn (1978) described a refraction survey to determine the depth of fill at a landfill site at Brownhills, Warwickshire, UK. The fill material was colliery spoil and domestic waste. The actual site was an old lake bed over a shallow depression in Etruria Marl. The fill material was underlain by an unknown thickness of glacial drift deposits, interbedded clays, sands and gravels, which were known to vary both laterally and vertically. Nunn found P-wave velocities of 500 m/s for unsaturated fill material, and 1300 m/s for saturated fill below the water

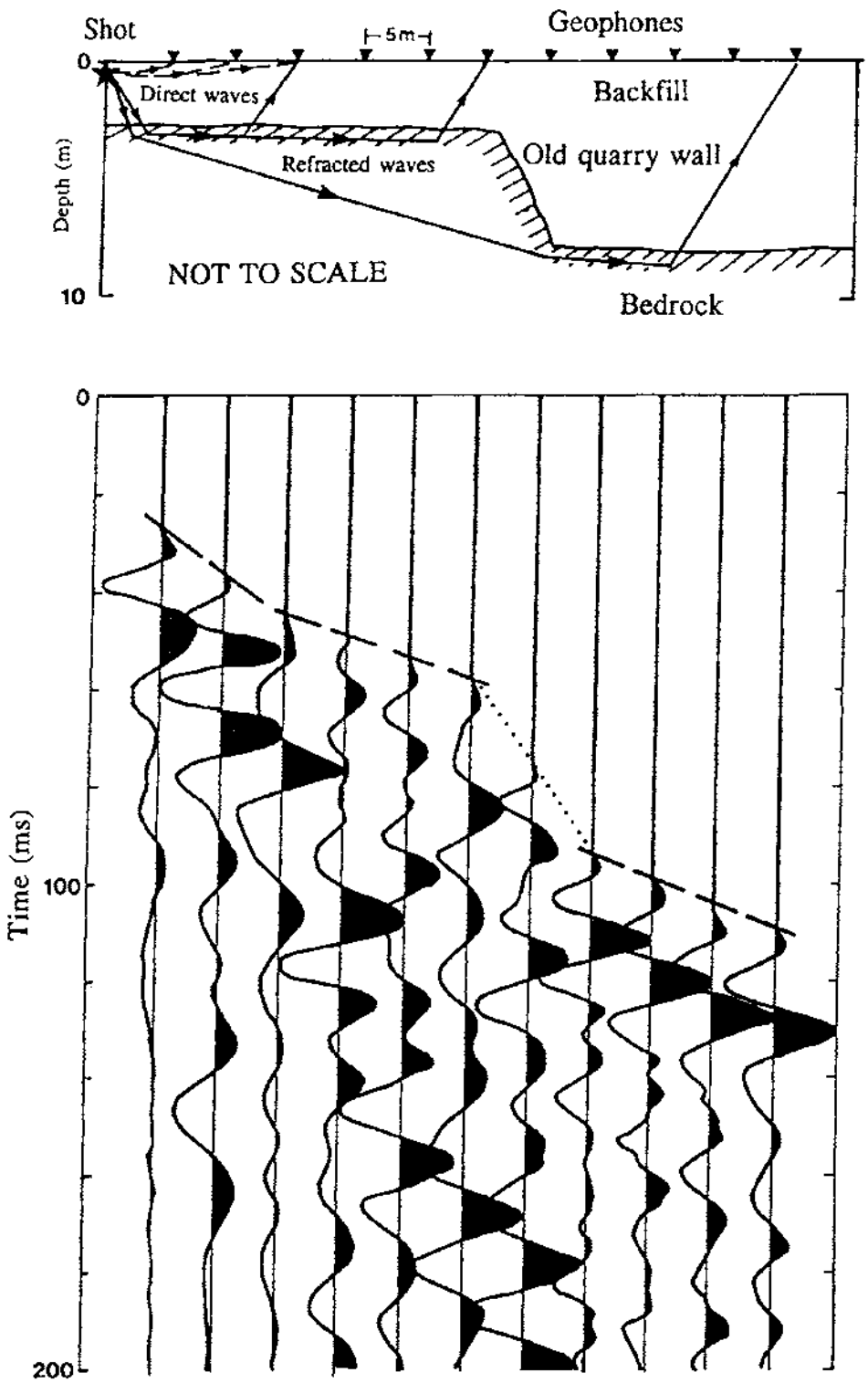

Figure 5.29 Seismic section over a buried quarry face within a landfill site backfilled with marl with the corresponding refraction record; the lines of the first breaks are indicated by the dashed and dotted lines. From Reynolds and McCann (1992), by permission

table. There was no direct evidence of the saturated drift layer in the results and thus it was thought that this layer was 'hidden'.

As far as the assessment of the geotechnical properties of a landfill is concerned, the work of Baoshan and Chopin (1983) on the measurement of shear waves in a tailings deposit at four tailings dam sites in China is of particular significance. Surface to borehole and cross-hole

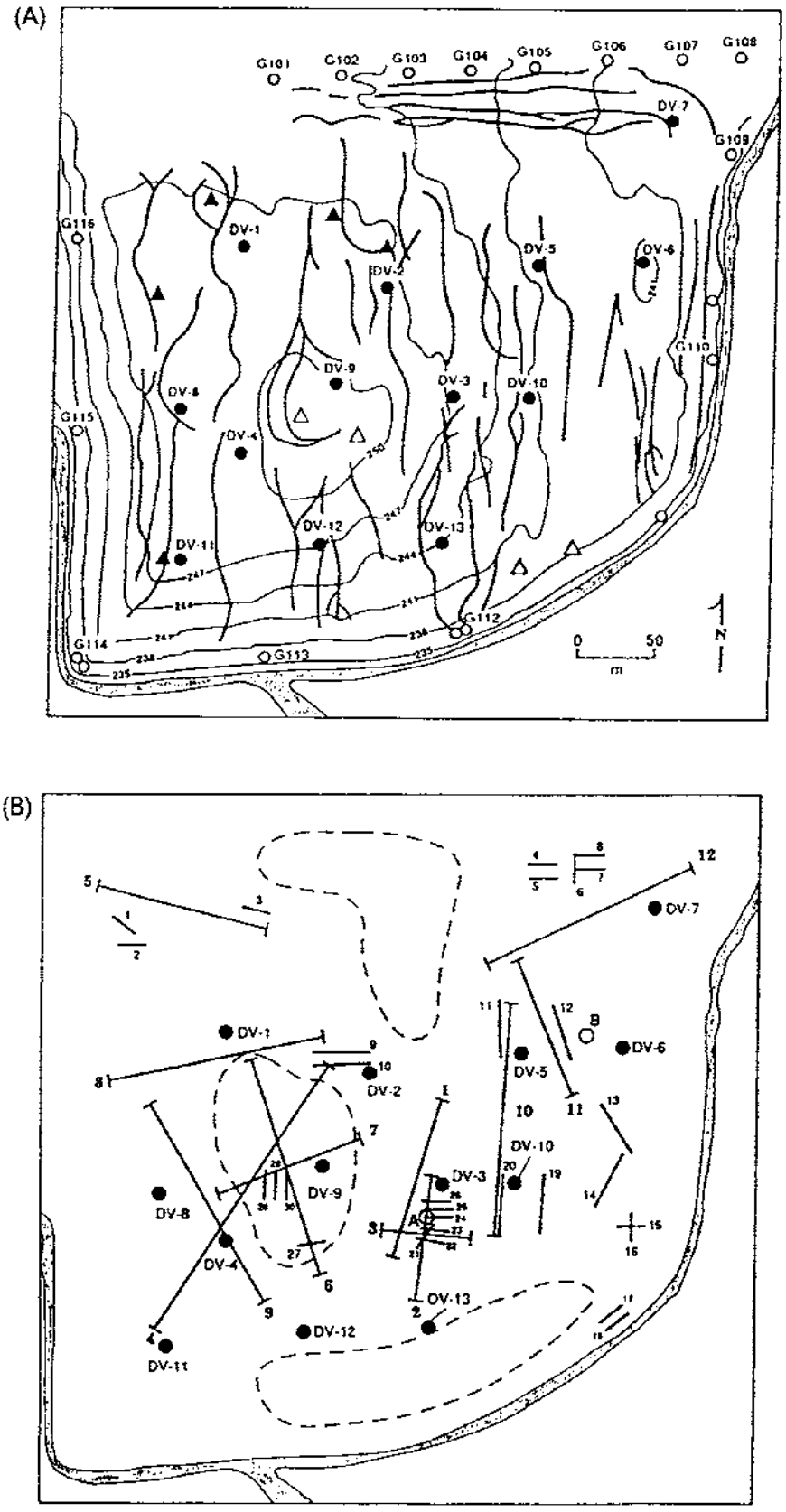

Figure 5.30 Map of the Mallard North landfill, showing (A) topography, major fissures, shallow/deep gas vents, and monitoring wells, and (B) lines of resistivity soundings, seismic refraction profiles, and azimuthal resistivity arrays marked ('A' and 'B'). Areas of cover replacement during the experiment are also shown in (B). From Carpenter *et al.* (1991), by permission

seismic measurements were made to determine the shear wave velocity (V_s). Their results showed excellent correlation between V_s and the geotechnical properties of the tailings material.

An integral part of the successful management of an enclosed landfill is the maintenance of the integrity of the compacted clay cap overlying the waste material. As long as this impermeable layer remains intact, gases are kept beneath (to vent in a controlled manner through appropriate outlets) and rain water/snow melt is kept out to run off into surface drains. However, erosion can occur into this clay cap and it can also degrade through differential settlement of the waste beneath.

Carpenter *et al.* (1991) reported on their use of both seismic refraction and electrical resistivity surveys to examine the integrity of a clay cap over a municipal landfill at Mallard North, near Chicago, USA. They demonstrated that detailed mapping of P-wave velocities could be used to identify areas where the clay cap had been fractured (giving rise to low P-wave velocities) compared with the intact clay cap (with higher P-wave velocities). Similarly, variability in electrical resistivity with azimuth around a central point indicated the orientation of fractures within the clay cap. Maps of the site and of their survey locations are shown in Figure 5.30.

Carpenter and co-workers found that average P-wave velocities determined along survey lines parallel and perpendicular to fractures were around 370 ± 20 m/s and 365 ± 10 m/s, respectively, compared with a value of 740 ± 140 m/s over unfractured clay cap. They also reported difficulty in obtaining refracted arrivals in some areas owing to the P-wave velocity in the underlying waste being lower than that for the clay cover. It is thought that where clay caps are of the order of 1.5–2 m thick, as in this case, electrical resistivity sub-surface imaging could provide a quick and reliable method of measuring the thickness non-intrusively.

Section 3
ELECTRICAL METHODS

Chapter 7

Electrical resistivity methods

7.1 INTRODUCTION

Electrical resistivity methods were developed in the early 1900s but have become very much more widely used since the 1970s, due primarily to the availability of computers to process and analyse the data. These techniques are used extensively in the search for suitable groundwater sources and also to monitor types of groundwater pollution; in engineering surveys to locate sub-surface cavities, faults and fissures, permafrost, mineshafts, etc.; and in archaeology for mapping out the areal extent of remnants of buried foundations of ancient buildings, amongst many other applications. Electrical resistivity methods are also used extensively in downhole logging. For the purposes of this chapter, applications will be confined to the use of direct current (or very-low-frequency alternating current) methods.

Electrical resistivity is a fundamental and diagnostic physical property that can be determined by a wide variety of techniques, including electromagnetic induction. These methods will be discussed in their respective chapters. That there are alternative techniques for the determination of the same property is extremely useful as some methods are more directly applicable or more practicable in some circumstances than others. Furthermore, the approaches used to determine electrical resistivity may be quite distinct – for example, ground contact methods compared with airborne induction techniques. Mutually consistent but independent interpretations give the interpreter greater confidence that the derived model is a good approximation of the sub-surface. If conflicting interpretations result, then it is necessary to go back and check each and every stage of the data acquisition, processing and interpretation in order to locate the problem. After all, the same ground with the same physical properties should give rise to the same model irrespective of which method is used to obtain it.

7.2 BASIC PRINCIPLES

7.2.1 True resistivity

Consider an electrically uniform cube of side lenght L through which a current (I) is passing (Figure 7.1). The material within the cube resists the conduction of electricity through it, resulting in a potential drop (V) between opposite faces. The resistance (R) is proportional to the length (L) of the resistive material and inversely proportional to the cross-sectional area (A) (Box 7.1); the constant of proportionality is the 'true' *resistivity* (symbol: ρ). According to Ohm's Law (Box 7.1) the ratio of the potential drop to the applied current (V/I) also defines the resistance (R) of the cube and these two expressions can be combined (Box 7.2) to form the product of a resistance (Ω) and

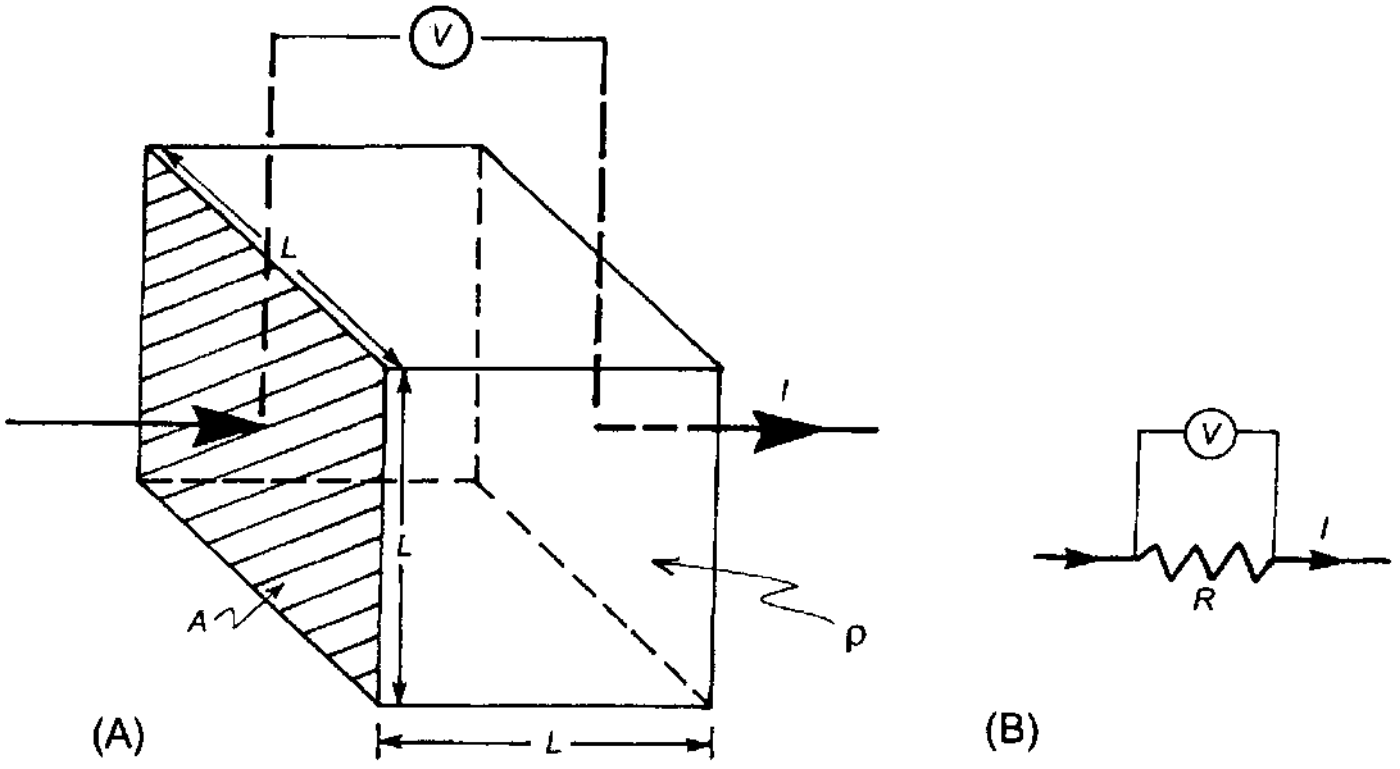

Figure 7.1 (A) Basic definition of resistivity across a homogeneous block of side length L with an applied current I and potential drop between opposite faces of V. (B) The electrical circuit equivalent, where R is a resistor

a distance (area/length; metres); hence the units of resistivity are ohm-metres (Ω m). The inverse of resistivity ($1/\rho$) is conductivity (σ) which has units of siemens/metre (S/m) which are equivalent to mhos/metre ($\Omega^{-1}\,m^{-1}$). It should be noted that Ohm's Law applies in the vast majority of geophysical cases unless high current densities (J) occur, in which case the linearity of the law may break down.

If two media are present within the resistive cube, each with its own resistivity (ρ_1 and ρ_2), then both proportion of each medium and their geometric form within the cube (Figure 7.2) become important considerations. The formerly isotropic cube will now exhibit variations in electrical properties with the direction of measurement (known as *anisotropy*); a platey structure results in a marked anisotropy, for example. A lower resistivity is usually obtained when measured parallel to limitations in phyllitic shales and slates compared with that at right-angles to the laminations. The presence and orientation of elongate brine pockets (with high conductivity) strongly influence the resistivity of sea ice (Timco 1979). The amount of anisotropy is described by the *anisotropy coefficient*, which is the ratio of maximum to minimum resistivity and which generally lies in the range 1–2. Thus it is important to have some idea of the form of electrical conductors with a rock unit. Detailed discussions of anisotropy have been given, for example, by Maillet (1947), Grant and West (1965) and Telford *et al.* (1990) (see also Section 7.3.3).

Box 7.1 True resistivity (see Figure 7.1)

Resistance (R) is proportional to length (L) divided by area (A):

$$R \propto L/A.$$

This can be written as $R = \rho L/A$, where ρ is the true resistivity.

Ohm's Law

For an electrical circuit, Ohm's Law gives $R = V/I$, where V and I are the potential difference across a resistor and the current passing through it, respectively.

This can be written alternatively in terms of the electric field strength (E; volts/m) and current density (J; amps/m^2) as:

$$\rho = E/J\ (\Omega\,\mathrm{m})$$

Box 7.2 Resistivity

$$\rho = \frac{VA}{IL}\ (\Omega/\mathrm{m})$$

There are three ways in which electric current can be conducted through a rock: electrolytic, electronic (ohmic) and dielectric conduction. *Electrolytic conduction* occurs by the relatively slow movement of ions within an electrolyte and depends upon the type of ion, ionic concentration and mobility, etc. *Electronic conduction* is the process by which metals, for example, allow electrons to move rapidly, so carrying the charge. *Dielectric conduction* occurs in very weakly conducting materials (or insulators) when an external alternating current is applied, so causing atomic electrons to be shifted slightly with respect to their nuclie. In most rocks, conduction is by way of

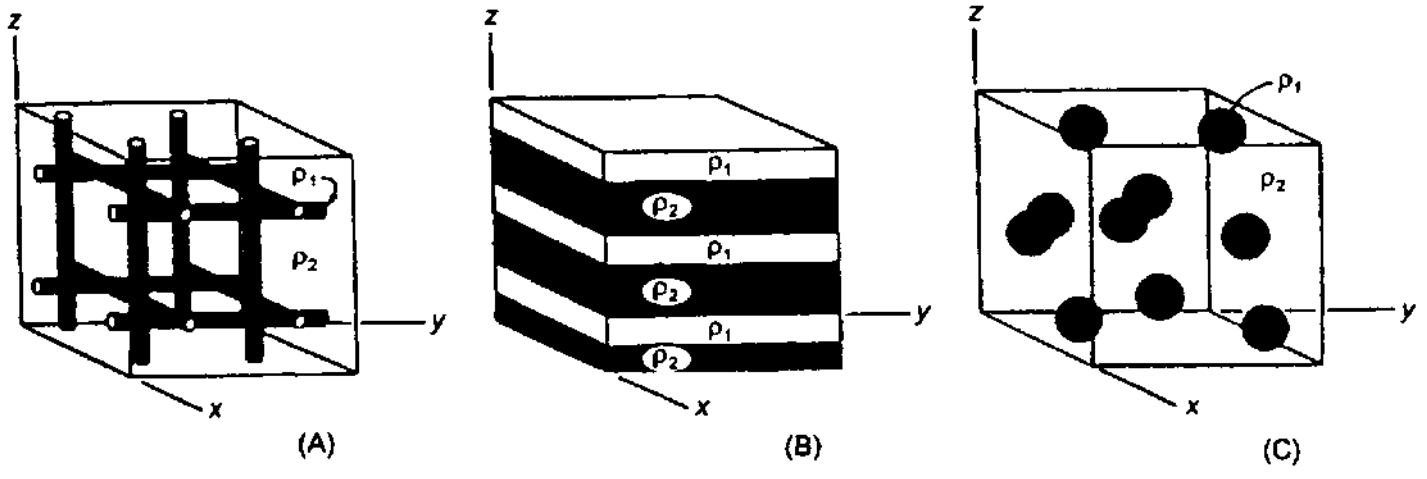

Figure 7.2 Three extreme structures involving two materials with true resistivities ρ_1 and ρ_2. After Grant and West (1965), by permission

pore fluids acting as electrolytes with the actual mineral grains contributing very little to the overall conductivity of the rock (except where those grains are themselves good electronic conductors). At the frequencies used in electrical resistivity surveying dielectric conduction can be disregarded. However, it does become important in 'spectral induced polarisation' and in 'complex resistivity' measurements (see Chapter 9).

The resistivity of geological materials exhibits one of the largest ranges of all physical properties, from $1.6 \times 10^{-8}\,\Omega$m for native silver to $10^{16}\,\Omega$m for pure sulphur. Igneous rocks tend to have the highest resistivities; sedimentary rocks tend to be most conductive, largely due to their high pore fluid content; and metamorphic rocks have intermediate but overlapping resistivities. The age of a rock also is an important consideration: a Quaternary volcanic rock may have a resistivity in the range 10–200 Ωm while that of an equivalent rock but Precambrian in age may be an order of magnitude greater. This is a consequence of the older rock having far longer to be exposed to secondary infilling of interstices by mineralisation, compaction decreasing the porosity and permeability, etc.

In sedimentary rocks, the resistivity of the interstitial fluid is probably more important than that of the host rock. Indeed, Archie (1942) developed an empirical formula (Box 7.3) for the effective resistivity of a rock formation which takes into account the porosity (ϕ), the fraction (s) of the pores containing water, and the resistivity of the water (ρ_w). Archie's Law is used predominantly in borehole logging. Korvin (1982) has proposed a theoretical basis to account for Archie's Law. Saline groundwater may have a resistivity as low as 0.05 Ωm and some groundwater and glacial meltwater can have resistivities in excess of 1000 Ωm.

Resistivities of some common minerals and rocks are listed in Table 7.1, while more extensive lists have been given by Telford *et al.* (1990).

Box 7.3 Archie's Law

$$\rho = a\phi^{-m}s^{-n}\rho_w$$

where ρ and ρ_w are the effective rock resistivity, and the resistivity of the pore water, respectively; ϕ is the porosity; s is the volume fraction of pores with water; a, m and n are constants where $0.5 \leqslant a \leqslant 2.5, 1.3 \leqslant m \leqslant 2.5$, and $n \approx 2$.
The ratio ρ/ρ_w is known as the Formation Factor (F).

Some minerals such as pyrite, galena and magnetite are commonly poor conductors in massive form yet their individual crystals have high conductivities. Hematite and sphalerite, when pure, are virtual insulators, but when combined with impurities they can become very

Table 7.1 Resistivities of common geologic materials

Material	Nominal resistivity (Ω m)
Sulphides:	
Chalcopyrite	1.2×10^{-5}–3×10^{-1}
Pyrite	2.9×10^{-5}–1.5
Pyrrhotite	7.5×10^{-6}–5×10^{-2}
Galena	3×10^{-5}–3×10^{2}
Sphalerite	1.5×10^{7}
Oxides:	
Hematite	3.5×10^{-3}–10^{7}
Limonite	10^{3}–10^{7}
Magnetite	5×10^{-5}–5.7×10^{3}
Ilmenite	10^{-3}–5×10
Quartz	3×10^{2}–10^{6}
Rock salt	3×10–10^{13}
Anthracite	10^{-3}–2×10^{5}
Lignite	9–2×10^{2}
Granite	3×10^{2}– $\times 10^{6}$
Granite (weathered)	3×10–5×10^{2}
Syenite	10^{2}–10^{6}
Diorite	10^{4}–10^{5}
Gabbro	10^{3}–10^{6}
Basalt	10–1.3×10^{7}
Schists (calcareous and mica)	20–10^{4}
Schist (graphite)	10–10^{2}
Slates	6×10^{2}–4×10^{7}
Marble	10^{2}–2.5×10^{8}
Consolidated shales	20–2×10^{3}
Conglomerates	2×10^{3}–10^{4}
Sandstones	1–7.4×10^{8}
Limestones	5×10–10^{7}
Dolomite	3.5×10^{2}–5×10^{3}
Marls	3–7×10
Clays	1–10^{2}
Alluvium and sand	10–8×10^{2}
Moraine	10–5×10^{3}
Sherwood sandstone	100–400
Soil (40% clay)	8
Soil (20% clay)	33
Top soil	250–1700
London clay	4–20
Lias clay	10–15
Boulder clay	15–35
Clay (very dry)	50–150
Mercia mudstone	20–60
Coal measures clay	50
Middle coal measures	>100
Chalk	50–150
Coke	0.2–8
Gravel (dry)	1400
Gravel (saturated)	100
Quaternary/Recent sands	50–100

Table 7.1 (*continued*)

Material	Nominal resistivity (Ω m)
Ash	4
Colliery spoil	10–20
Pulverised fuel ash	50 ·100
Laterite	800–1500
Lateritic soil	120–750
Dry sandy soil	80–1050
Sand clay/clayey sand	30–215
Sand and gravel	30–225
Unsaturated landfill	30· 100
Saturated landfill	15–30
Acid peat waters	100
Acid mine waters	20
Rainfall runoff	20–100
Landfill runoff	<10–50
Glacier ice (temperate)	2×10^6–1.2×10^8
Glacier ice (polar)	5×10^4 3×10^5 *
Permafrost	10^3– > 10^4

* – 10°C to – 60°C, respectively; strongly temperature-dependent. Based on Telford *et al.* (1990) with additional data from McGinnis and Jensen (1971), Reynolds (1987a). Reynolds and Paren (1980, 1984) and many commercial projects.

good conductors (with resistivities as low as 0.1 Ω m). Graphite dispersed throughout a rock mass may reduce the overall resistivity of otherwise poorly conducting minerals. For rocks that have variable composition, such as sedimentary rocks with gradational facies, the resistivity will reflect the varying proportions of the constituent materials. For example, in northern Nigeria it is possible, on the basis of the interpreted resistivities, to gauge whether a near-surface material is a clayey sand or a sandy clay. Resistivities for sandy material are about 100 Ω m and decrease with increasing clay content to about 40 Ω m, around which point clay becomes the dominant constituent and the values decrease further to those more typical of clay: well-formed and almost sand-free clay has a value in the range 1 10 Ω m (Reynolds 1987a).

The objective of most mordern electrical resistivity surveys is to obtain true resistivity models for the sub-surface because it is these that have geological meaning. The methods by which field data are obtained, processed and interpreted will be discussed later.

The *apparent resistivity* is the value obtained as the product of a measured resistance (R) and a *geometric factor* (K) for a given electrode array (see Section 7.3.2), according to the expression in Box 7.2. The geometric factor takes into account the geometric spread of electrodes and contributes a term that has the unit of length (metres). Apparent resistivity (ρ_a) thus has units of ohm-metres.

7.2.2 Current flow in a homogeneous earth

For a single current electrode implanted at the surface of a homogeneous medium of resistivity ρ, current flows away radially (Figure 7.3). The voltage drop between any two points on the surface can be described by the potential gradient $(-\delta V/\delta x)$, which is negative because the potential decreases in the direction of current flow. Lines of equal voltage ('equipotentials') intersect the lines of equal current at right-angles. The current density (J) is the current (I) divided by the area over which the current is distributed (a hemisphere; $2\pi r^2$), and so the current density decreases with increasing distance from the current source. It is possible to calculate the voltage at a distance (r) from a single current point source (Box 7.4). If, however, a current sink is added, a new potential distribution occurs (Figure 7.4) and a modified expression is obtained to describe the voltage at any point (Box 7.5).

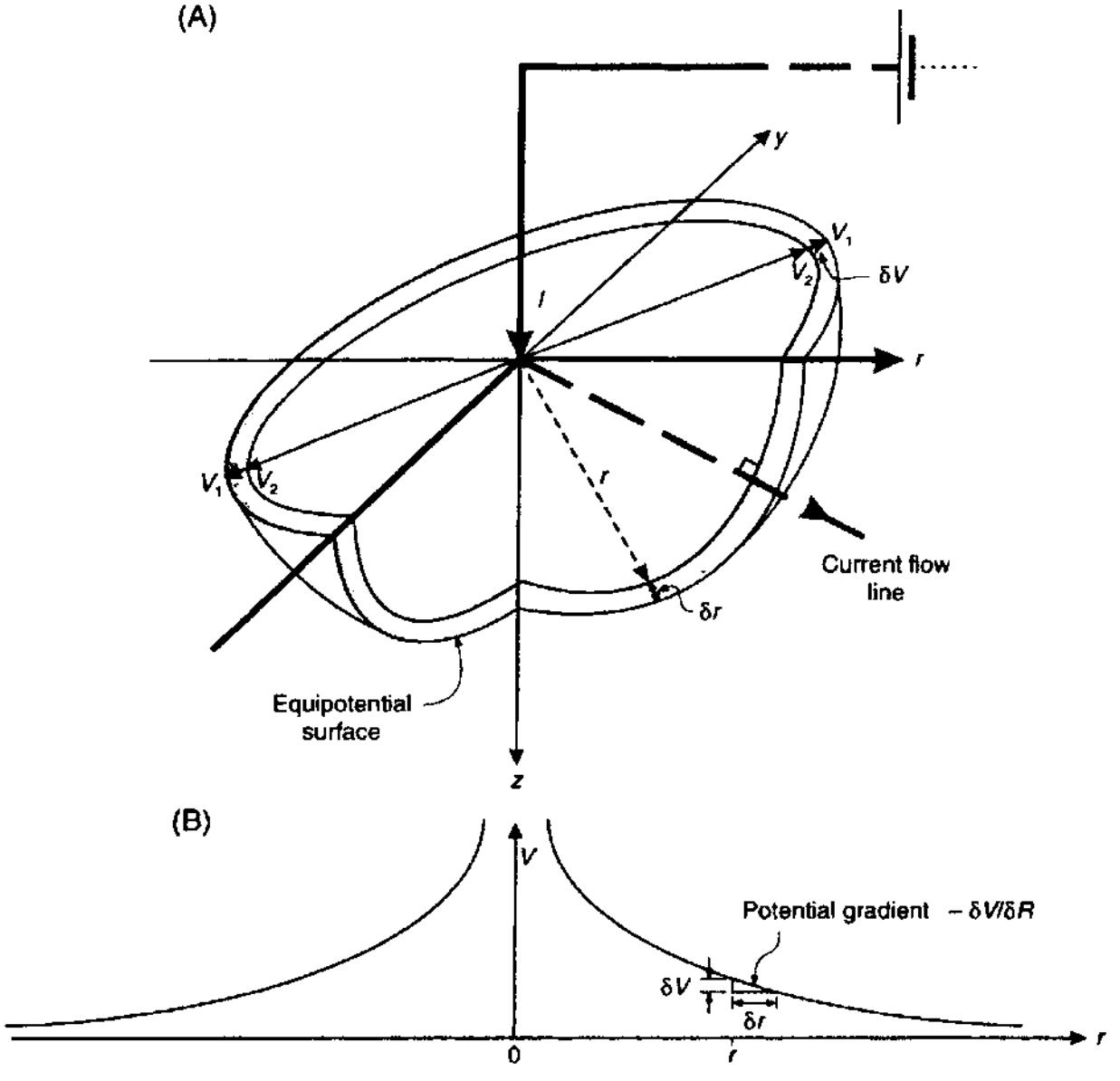

Figure 7.3 (A) Three-dimensional representation of a hemispherical equipotential shell around a point electrode on a semi-infinite, homogeneous medium. (B) Potential decay away from the point electrode

Box 7.4 (See Figure 7.3)

The potential difference (δV) across a hemispherical shell of incremental thickness δr is given by:

$$\frac{\delta V}{\delta r} = -\rho . \boldsymbol{J} = -\rho \frac{I}{2\pi r^2}.$$

Thus the voltage V_r at a point r from the current point source is:

$$V_r = \int \delta V = -\int \rho \frac{I}{2\pi r^2} \delta r = \frac{\rho I}{2\pi} \cdot \frac{1}{r}.$$

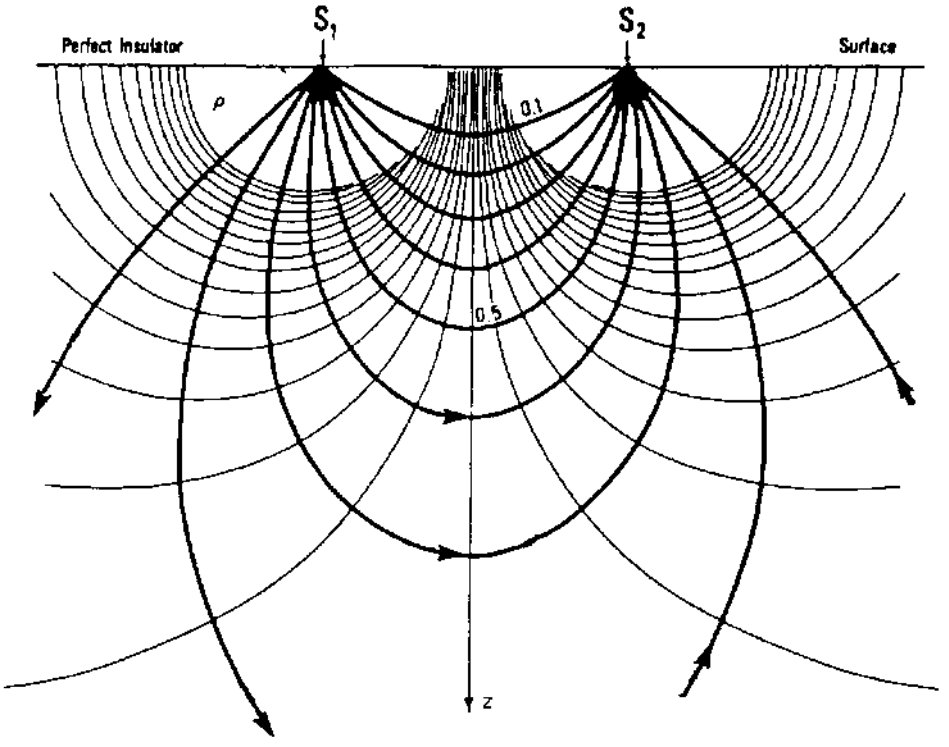

Figure 7.4 Current and equipotential lines produced by a current source and sink. From van Nostrand and Cook (1966), by permission

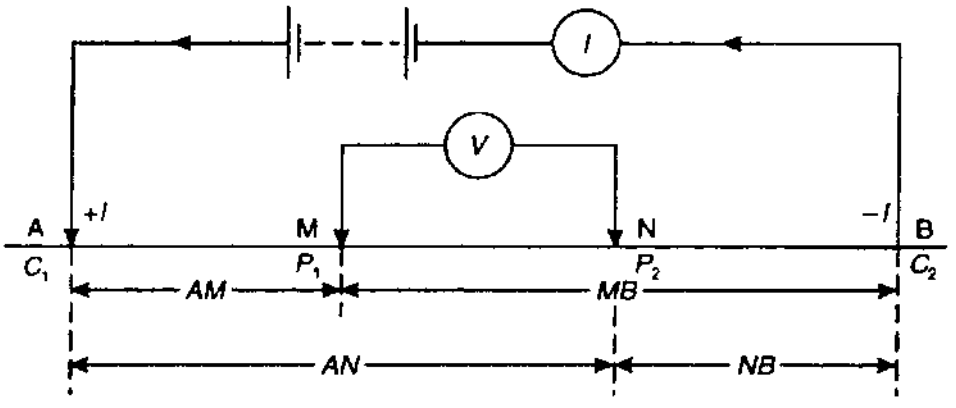

Figure 7.5 Generalised form of electrode configuration in resistivity surveys

Box 7.5 (See Figure 7.5)

For a current source and sink, the potential V_P at any point P in the ground is equal to the sum of the voltages from the two electrodes, such that: $V_P = V_A + V_B$ where V_A and V_B are the potential contributions from the two electrodes, A(+I) and B(−I).

The potentials at electrode M and N are:

$$V_M = \frac{\rho I}{2\pi}\left[\frac{1}{AM} - \frac{1}{MB}\right], \quad V_N = \frac{\rho I}{2\pi}\left[\frac{1}{AN} - \frac{1}{NB}\right].$$

However, it is far easier to measure the potential difference, δV_{MN}, which can be rewritten as:

$$\delta V_{MN} = V_M - V_N = \frac{\rho I}{2\pi}\left\{\left[\frac{1}{AM} - \frac{1}{MB}\right] - \left[\frac{1}{AN} - \frac{1}{NB}\right]\right\}$$

Rearranging this so that resistivity ρ is the subject:

$$\rho = \frac{2\pi\delta V_{MN}}{I}\left\{\left[\frac{1}{AM} - \frac{1}{MB}\right] - \left[\frac{1}{AN} - \frac{1}{NB}\right]\right\}^{-1}$$

7.3 ELECTRODE CONFIGURATIONS AND GEOMETRIC FACTORS

7.3.1 General case

The final expression in Box 7.5 has two parts, namely a resistance term (R; units Ω) and a term that describes the geometry of the electrode configuration being used (Box 7.6) and which is known as the *geometric factor* (K; units m). In reality, the sub-surface ground does not conform to a homogeneous medium and thus the resistivity obtained is no longer the 'true' resistivity but the *apparent resistivity* (ρ_a) which can even be negative. It is very important to remember that the apparent resistivity is not a physical property of the sub-surface

Box 7.6 The geometric factor (see Figure 7.5)

The geometric factor (K) is defined by the expression:

$$K = 2\pi\left[\frac{1}{AM} - \frac{1}{MB} - \frac{1}{AN} + \frac{1}{NB}\right]^{-1}.$$

Where the ground is not uniform, the resistivity so calculated is called the *apparent resistivity* (ρ_a):

$$\rho_a = RK, \text{ where } R = \delta V/I.$$

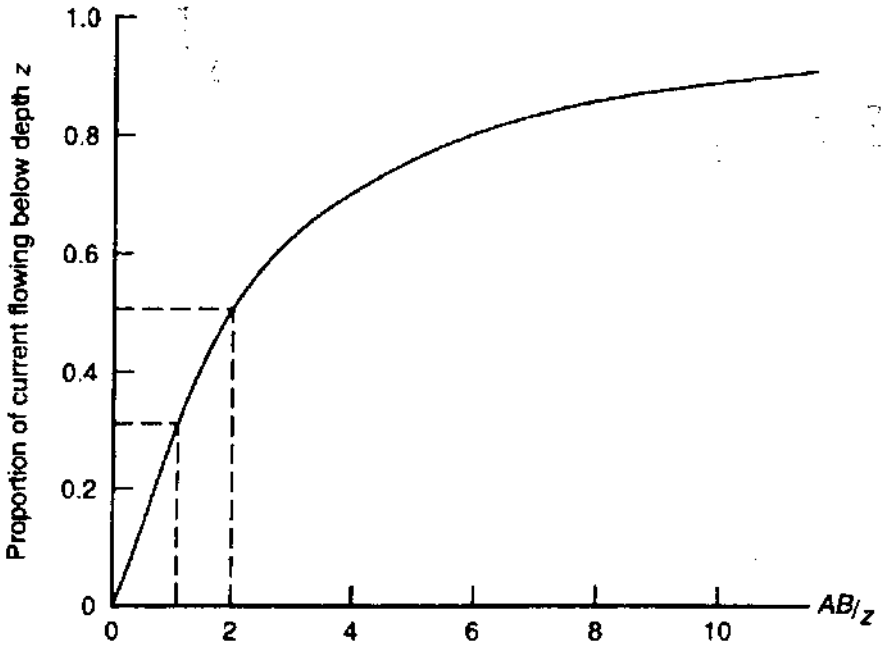

Figure 7.6 Proportion of current flowing below a depth z (m); AB is the current electrode half-separation

media, unlike the true resistivity. Consequently, all field resistivity data are apparent resistivity while those obtained by interpretation techniques are 'true' resistivities.

Figure 7.6 shows that, in order for at least 50% of the current to flow through an interface at a depth of z metres into a second medium, the current electrode separation needs to be at least twice – and preferably more than three times – the depth. This has obvious practical implications, particularly when dealing with situations where the depths are of the order of several hundreds of metres, so requiring very long cable lengths that can produce undesirable inductive coupling effects. For very deep soundings where the electrode separation is more than several kilometres, telemetering the data becomes the only practical solution (e.g. Shabtaie *et al.* 1980, 1982). However, it should be emphasised that it is misleading to equate the depth of penetration with the current electrode separation as a general rule of thumb in the region of a resistivity survey. This aspect is discussed in Section 7.3.3.

7.3.2 Electrode configurations

The value of the apparent resistivity depends on the geometry of the electrode array used, as defined by the geometric factor K. There are three main types of electrode configuration, two of which are named after their originators – Frank Wenner (1912a,b) and Conrad Schlumberger – and a range of sub-types (Table 7.2 and Figure 7.7). The geometric factors for these arrays are given in Box 7.7 and a worked example for the Wenner array is given in Box 7.8. Arrays highlighted in bold in Table 7.2 are those most commonly used.

Table 7.2 Electrode configurations (see also Figure 7.7)

Wenner arrays	**Standard Wenner**
	Offset Wenner
	Lee-partitioning array
	Tripotential (α, β and γ arrays)
Schlumberger array	**Standard Schlumberger**
	Brant array
	Gradient array
Dipole–dipole arrays	**Normal** (axial or polar)
	Azimuthal
	Radial
	Parallel
	Perpendicular
	Pole–Dipole
	Equatorial
	Square (special form of equatorial)

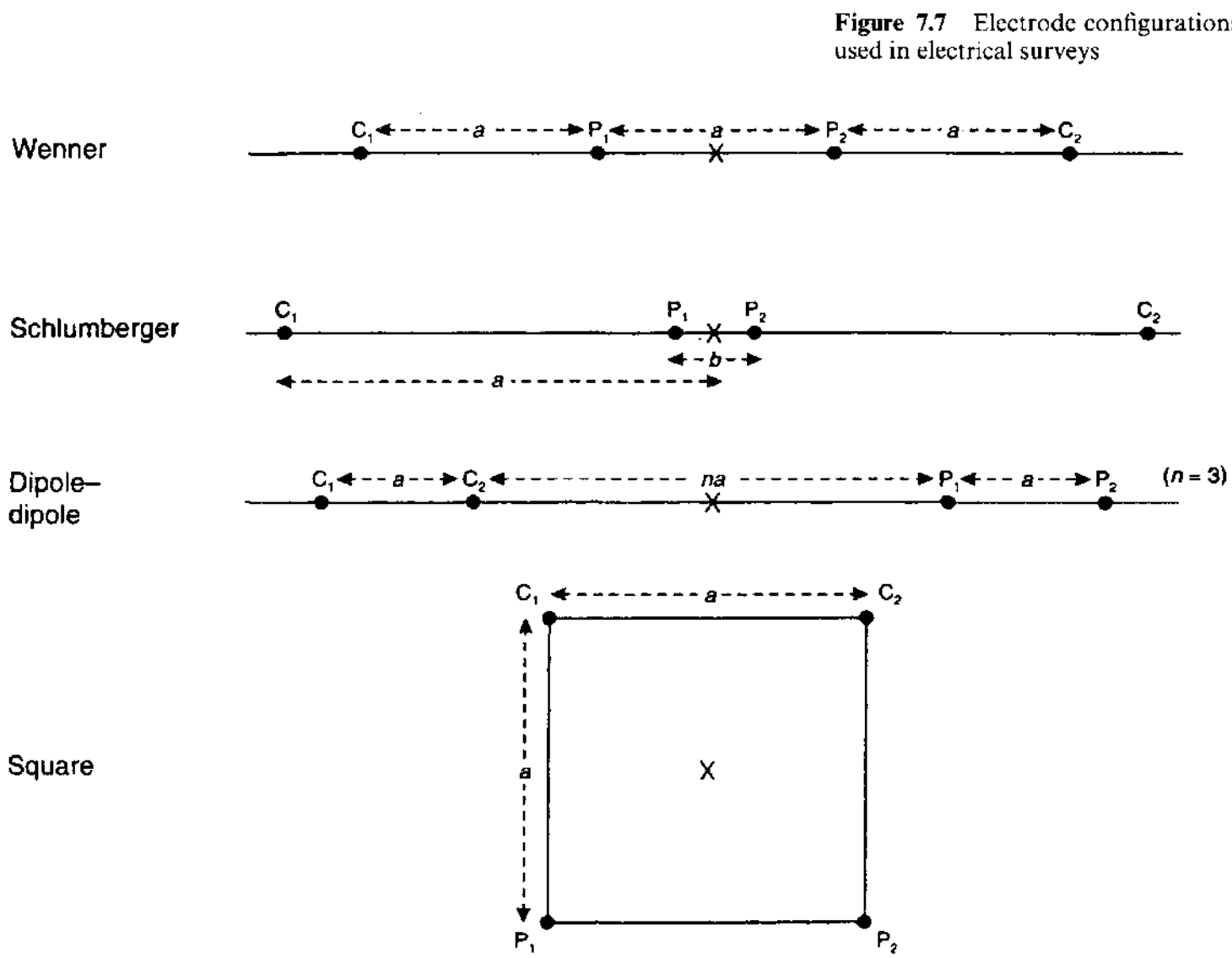

Figure 7.7 Electrode configurations used in electrical surveys

Dipole–dipole arrays have been used extensively by Russian geophysicists since 1950, and especially in Canada, particularly for 'induced polarisation' surveys (see Chapter 9) in mineral exploration, and in the USA in groundwater surveys (Zohdy 1974). The term 'dipole' is misapplied in a strict sense because the inter-electrode separation for each of the current or potential electrode pairs should be insignificant with respect to the length of the array, which it is not. However, the term is well established in its usage.

Box 7.7 Apparent resistivities for given geometric factors for electrode configurations in Figure 7.7

Wenner array: $\rho_a = 2\pi a R$ (alpha/beta arrays)
$\rho_a = 3\pi a R$ (gamma rays)

Two-electrode: $\rho_a = 2\pi s R$

Lee array: $\rho_a = 4\pi a R$

Schlumberger array: $$\rho_a = \frac{\pi a^2}{b}\left[1 - \frac{b^2}{4a^2}\right] R; \quad a \geqslant 5b$$

Gradient array: $$\rho_a = 2\pi \frac{L^2}{a}\frac{1}{G} R$$

$$\text{where } G = \frac{1 - X}{(Y^2 + (1 - X)^2)^{3/2}} + \frac{1 + X}{(Y^2 + (1 + X)^2)^{3/2}}$$

$$\text{and } X = x/L,\ Y = y/L$$

Dipole–dipole array: $\rho_a = \pi n(n + 1)(n + 2) a R$

Pole–dipole array: $\rho_a = 2\pi n(n + 1) a R$

Square array: $\rho_a = \pi a(2 + \sqrt{2}) R$

These different types and styles of electrode configuration have particular advantages, disadvantages and sensitivities. Factors affecting the choice of array type include the amount of space available to lay out an array and the labour-intensity of each method. Other important considerations are the sensitivity to lateral inhomogeneities (Habberjam and Watkins 1967a; Barker 1981) and to dipping interfaces (Broadbent and Habberjam 1971).

A graphic example of the different responses by the three main electrode configurations is given by so-called 'signal contribution sections' (Barker 1979) shown in Figure 7.8. These sections are contoured plots of the contribution made by each unit volume of the sub-surface to the voltage measured at the surface.

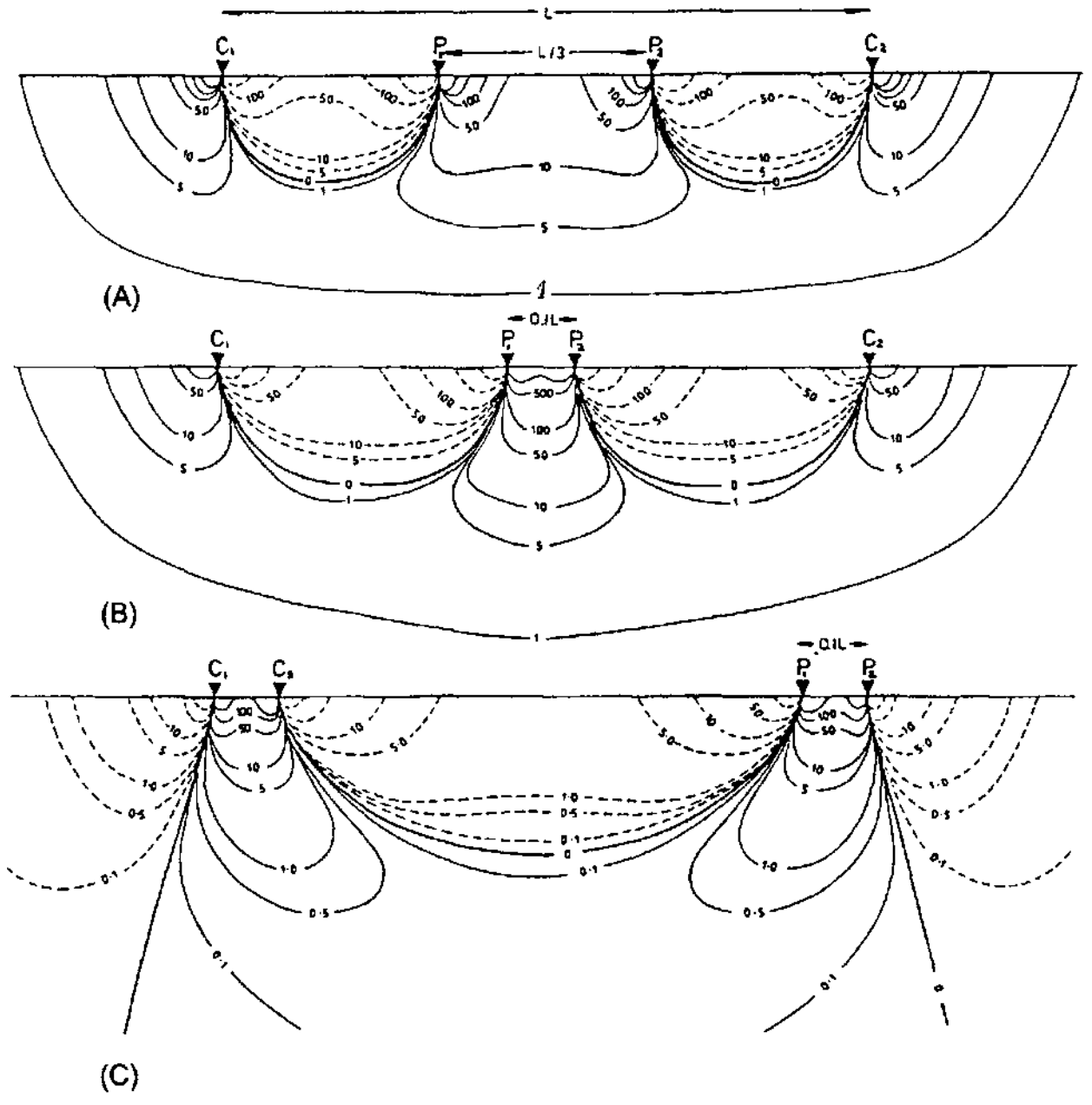

Figure 7.8 Signal contribution sections for: (A) Wenner, (B) Schlumberger and (C) dipole–dipole configurations. Contours indicate the relative contributions made by discrete volume elements of the sub-surface to the total potential difference measured between the two potential electrodes P_1 and P_2. From Barker (1979), by permission

Box 7.8 Worked example of how to calculate a geometric factor

Using the expression previously defined in Box 7.6 (see also Figure 7.5), and substituting in the correct values for the *Wenner array*:

$$K = 2\pi\left[\frac{1}{a} - \frac{1}{2a} - \frac{1}{2a} + \frac{1}{a}\right]^{-1} = 2\pi\left[\frac{2}{a} - \frac{2}{2a}\right]^{-1}$$

$$= 2\pi a.$$

Hence, as $\rho_a = KR$, $\rho_a = 2\pi aR$.

Figure 7.8A shows the signal contribution for a Wenner array. In the near-surface region, the positive and negative areas cancel each other out and the main response, which originates from depth, is largely flat (see the 1 unit contour). This indicates that for horizontally, layered media, the Wenner array has a high vertical resolution. The Schlumberger array has almost as high a vertical resolution, but note that the form of the signal contribution at depth is now concave upwards (Figure 7.8B). For the dipole–dipole array (Figure 7.8C), the lobate form of the signal contribution indicates that there is a poor vertical resolution and that the array is particularly sensitive to deep lateral resistivity variations, making it an unsuitable array for depth sounding (Bhattacharya and Patra 1968). Nevertheless, this sensitivity can be utilised in resistivity profiling (see Section 7.4.3).

A modified electrode array (Lee partitioning array) was devised by Lee (Lee and Schwartz 1930) in an attempt to reduce the undesirable effects of near-surface lateral inhomogeneities. An alternative tripotential method was proposed by Carpenter (1955) and by Carpenter and Habberjam (1956) which combined the apparent resistivities obtained for the alpha, beta and gamma rays (Figure 7.9). The

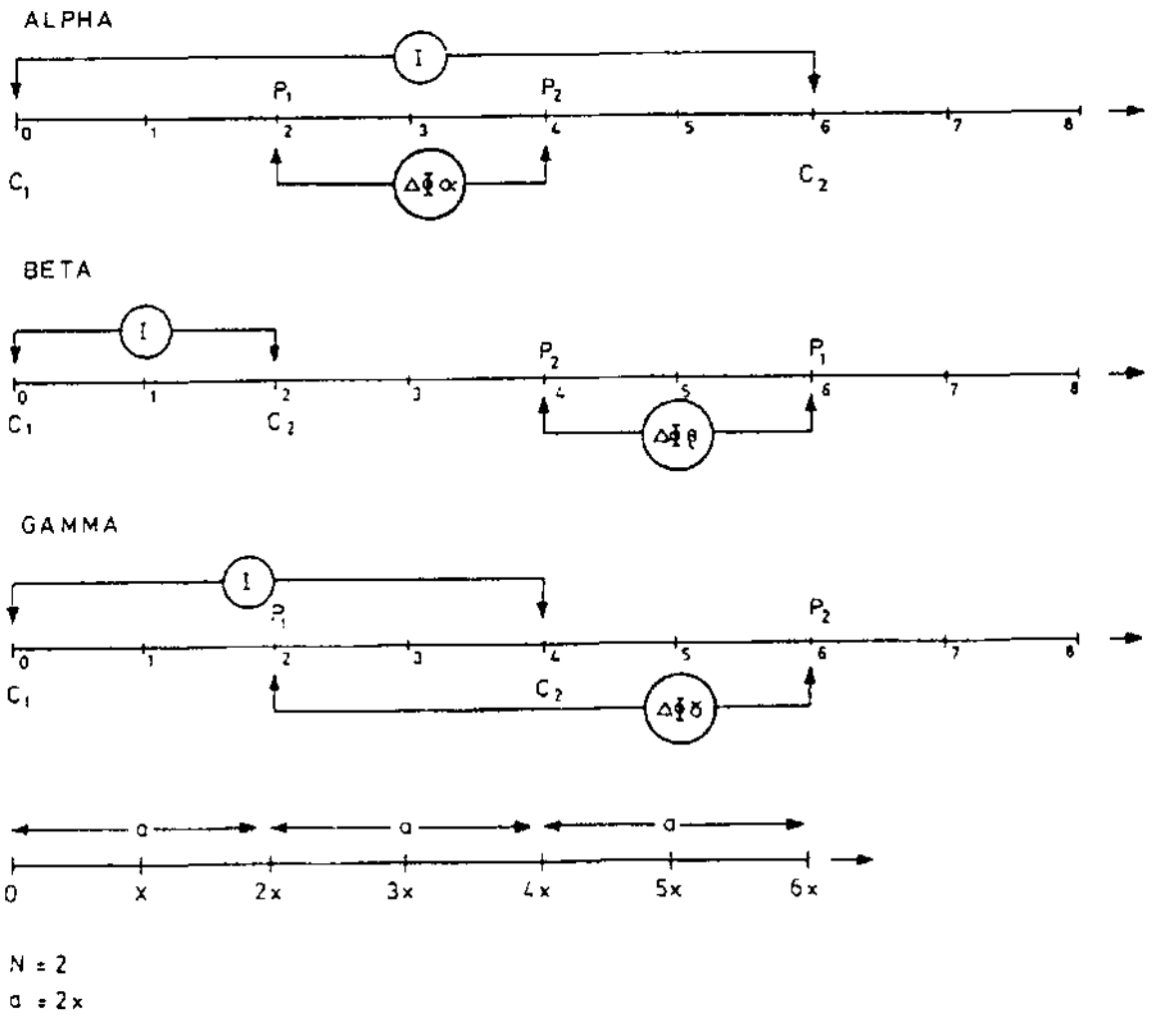

Figure 7.9 Wenner tripotential electrode configurations for $N = 2$. x is the fixed interelectrode separation, and the active electrode separation is $2x$. From Ackworth and Griffiths (1985), by permission

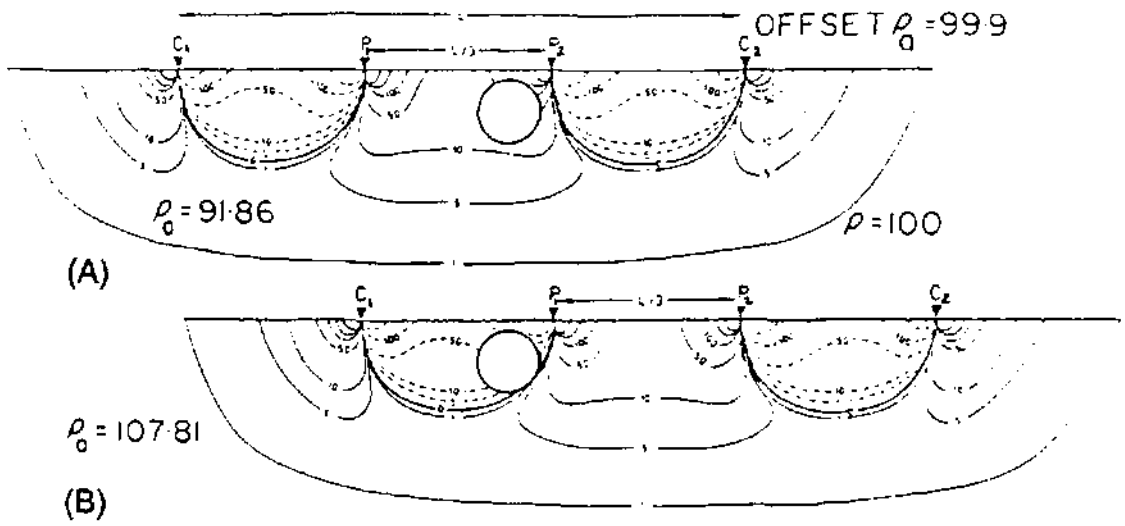

Figure 7.10 (A) Signal contribution section for a Wenner array with a conducting sphere (negative K) in a positive region in a medium with resistivity 100 Ω m. (B) Offset Wenner electrodes in which the sphere is now in a negative region. Distortion of contours due to the presence of the sphere is not shown. From Barker (1981), by permission

method has been discussed further by Ackworth and Giffiths (1985). A smoothing technique using the tripotential method was produced by Habberjam and Watkins (1967a).

An alternative technique, called the *Offset Wenner* method (Barker 1981), has been readily adopted for its ease of use. The method is extremely simple in concept. Figure 7.10 shows a single contribution section for a standard Wenner array. A conducting sphere buried in a semi-infinite homogeneous medium with true resistivity of 100 Ω m is located in a positive region of the signal contribution section (Figure 7.10A). The corresponding apparent resistivity, calculated using an exact analytical method (Singh 1976), is 91.86 Ω m. Offsetting the Wenner array one spacing to the right (Figure 7.10B), the previously positive areas are now negative and vice versa, and the buried sphere is located in a negative region resulting in an apparent resistivity of 107.81 Ω m. The average of these two apparent resistivities is 99.88 Ω m, thereby reducing the error due to a lateral inhomogeneity from around ± 8% to only 0.1 %.

One array that is seldom used, but which has two major advantages, is the square array. This is a special form of the equatorial dipole–dipole array for $n = 1$. The square array is particularly good for determining lateral azimuthal variations in resistivity. By swapping P_1 and C_2, the square is effectively rotated through 90° and thus the apparent resistivity can be determined for two orthogonal directions. For ground that is largely uniform, the two resistivities should be the same, but where there is a difference in resistivity due to a form of anisotropy (*transverse anisotropy* as it is measured only in the $x - y$ plane), the two resistivities will differ. The ratio of the two resistivities is an indication of the transverse anisotropy. Profiles and maps of transverse anisotropy can be interpreted qualitatively to indicate anomalous ground. The second advantage of the square array is that it lends itself to rapid grid mapping. By moving two electrodes at

Table 7.3 Comparison of dipole–dipole, Schlumberger, square and Wenner electrode arrays

Criteria	Wenner	Schlumberger	Dipole–dipole	Square
Vertical resolution	√√√	√√	√	√√
Depth penetration	√	√√	√√√	√√
Suitability to VES	√√	√√√	√	×
Suitability to CST	√√√	×	√√√	√√√
Sensitivity to orientation	Yes	Yes	Moderate	No
Sensitivity to lateral inhomogeneities	High	Moderate	Moderate	Low
Labour intensive	Yes (no*)	Moderate (no*)	Moderate (no*)	Yes
Availability of interpretational aids	√√√	√√√	√√	√

√ = poor; √√ = moderate; √√√ = good; × = unsuitable
* When using a multicore cable and automated electrode array

a time, the square can be moved along the transect. By increasing the dimensions of the square, and thus generally increasing the depth penetration and repeating the same survey area, three-dimensional models of the resistivity distribution can be obtained. Of all the electrode configurations, the square array is the least sensitive to steeply dipping interfaces (Broadbent and Habberjam 1971) and thus it can cope in situations where the sub-surface media are not horizontally-layered. Being a particularly labour-intensive field method, it is best restricted to small-scale surveys where the electrode separation is only of the order of a few metres. This technique has particular value in 3-D mapping of buried massive ice and in shallow archaeological investigations, for example.

A general guide to the suitability of the dipole–dipole, Schlumberger, square and Wenner electrode configurations is given in Table 7.3. An important consideration for the suitability of a given array is the scale at which it is to be deployed. For example, a square array is not really appropriate for depth sounding ('vertical electrical sounding'; VES) or for 'constant separation traversing' (CST) with a large square side; whereas it is perhaps better than either the Wenner or Schlumberger arrays for applications concerned with very shallow depths (< 2 m), such as in archaeological investigations. While the main electrode configurations are now well established in their major applications, small-scale mini-resistivity surveys have yet to realise their full potential.

7.3.3 Media with contrasting resistivities

A geological section may show a series of lithologically defined interfaces which do not necessarily coincide with boundaries identified electrically. For example, in an unconfined sandstone aquifer,

there is a capillary zone above the water table making the boundary from 'dry' to 'saturated' a rather diffuse one. Furthermore, different lithologies can have the same resistivity and thus would form only one electric unit.

A geoelectric unit is characterised by two basic parameters: the *layer resistivity* (ρ_i) and the *layer thickness* (t_i) for the ith layer ($i = 1$ for the surface layer). Four further electrical parameters can be derived for each layer from the respective resistivity and thickness; these are called the *longitudinal conductance* (S_L; units mS); *transverse resistance* (T; units $\Omega\,m^2$); *longitudinal resistivity* (ρ_L; units Ωm); and *transverse resistivity* (ρ_T; units Ωm). They are defined in Box 7.9 for the model shown in Figure 7.11. The sums of all the longitudinal conductances and of the transverse resistances for a layered ground are called the Dar Zarrouk 'function' and 'variable', respectively. (The curiously named Dar Zarrouk parameters were so called by Maillet (1947) after a place near Tunis where he was a prisoner of war.)

The importance of the longitudinal conductance for a particular layer is that it demonstrates that it is not possible to know both the true layer conductivity (or resistivity) *and* the layer thickness, so giving rise to layer *equivalence*. For example, a layer with a longitudinal conductance of 0.05 mS can have a resistivity of 100 Ωm and thickness 5 m. Layers with the combination of resistivity 80 Ωm and thickness 4 m, and 120 Ωm and 6 m, are all equivalent electrically. Equivalence needs to be considered during interpretation of sounding curves (see Section 7.5.4) and generally in the interpretation of electrical data, whether obtained by contact electrical or electromagnetic induction methods.

Box 7.9 Dar Zarrouk parameters

For a given layer:

Longitudinal conductance	$S_L = h/\rho = h.\sigma$
Transverse resistance	$T = h.\rho$
Longitudinal resistivity	$\rho_L = h/S$
Transverse resistivity	$\rho_T = T/h$
Anisotropy	$A = \rho_T/\rho_L$.

For n layers:

$$S_L = \sum_{i=1}^{n} (h_i/\rho_i) = \frac{h_1}{\rho_1} + \frac{h_2}{\rho_2} + \frac{h_3}{\rho_3} + \cdots \frac{h_n}{\rho_n}$$

$$T = \sum_{i=1}^{n} (h_i\rho_i) = h_1\rho_1 + h_2\rho_2 + h_3\rho_3 + \cdots h_n\rho_n$$

Where a point current source is located close to a plane boundary between two homogeneous media, the lines of current flow (and hence

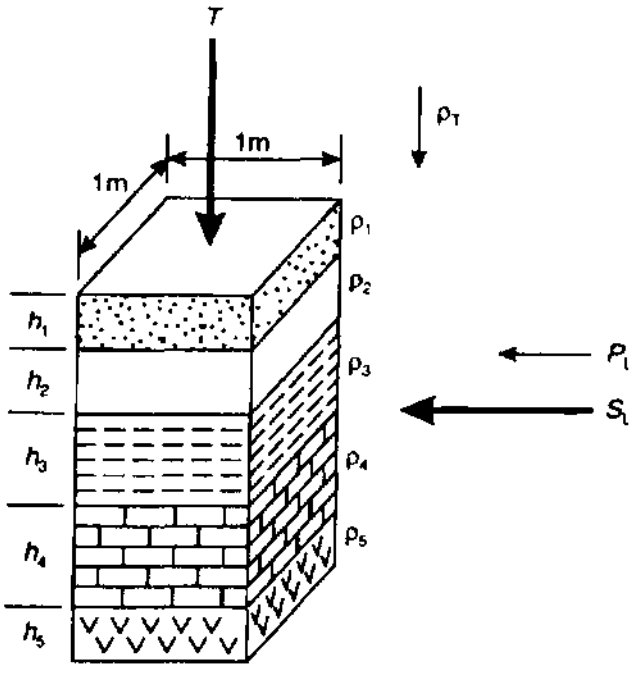

Figure 7.11 Thickness (h) and true resistivity (ρ) of component layers with an indication of the total longitudinal conductance (S_L) and total transverse resistance (T); subscripts L and T refer to longitudinal and transverse, respectively

of equipotential) are refracted at the boundary in proportion to the contrast in resistivity between the two media (Figure 7.12 and Box 7.10). In a homogeneous material with no boundaries in the vicinity, current flow lines are symmetrically radial. If a boundary is nearby, the current flow lines will become distorted (Figure 7.12B): current flowing towards a medium with a higher resistivity will diverge from the radial pattern and current densities adjacent to the boundary will decrease, whereas the current converges on approaching a medium with a lower resistivity with a consequent increase in current densities. The potential at a point adjacent to a plane boundary can be calculated using optical image theory (Figure 7.12C). If a current source of strength S is placed in one medium of resistivity ρ_1, the source's image point lies in the second medium of resistivity ρ_2 (where $\rho_2 > \rho_1$) but has a reduced strength kS, where k is dependent upon the resistivity contrast between the two media and lies in the range ± 1. This k factor is akin to the reflection coefficient in optics and in reflection seismology, and has the form given in Box 7.11. If the current passes from a lower resistivity medium to one with a higher resistivity, k is positive; if it passes into a medium with a lower resistivity, k is negative.

Box 7.10 (See Figure 7.12A)

Refraction of current flow at a plane boundary:

$$\tan\theta_2/\tan\theta_1 = \rho_1/\rho_2.$$

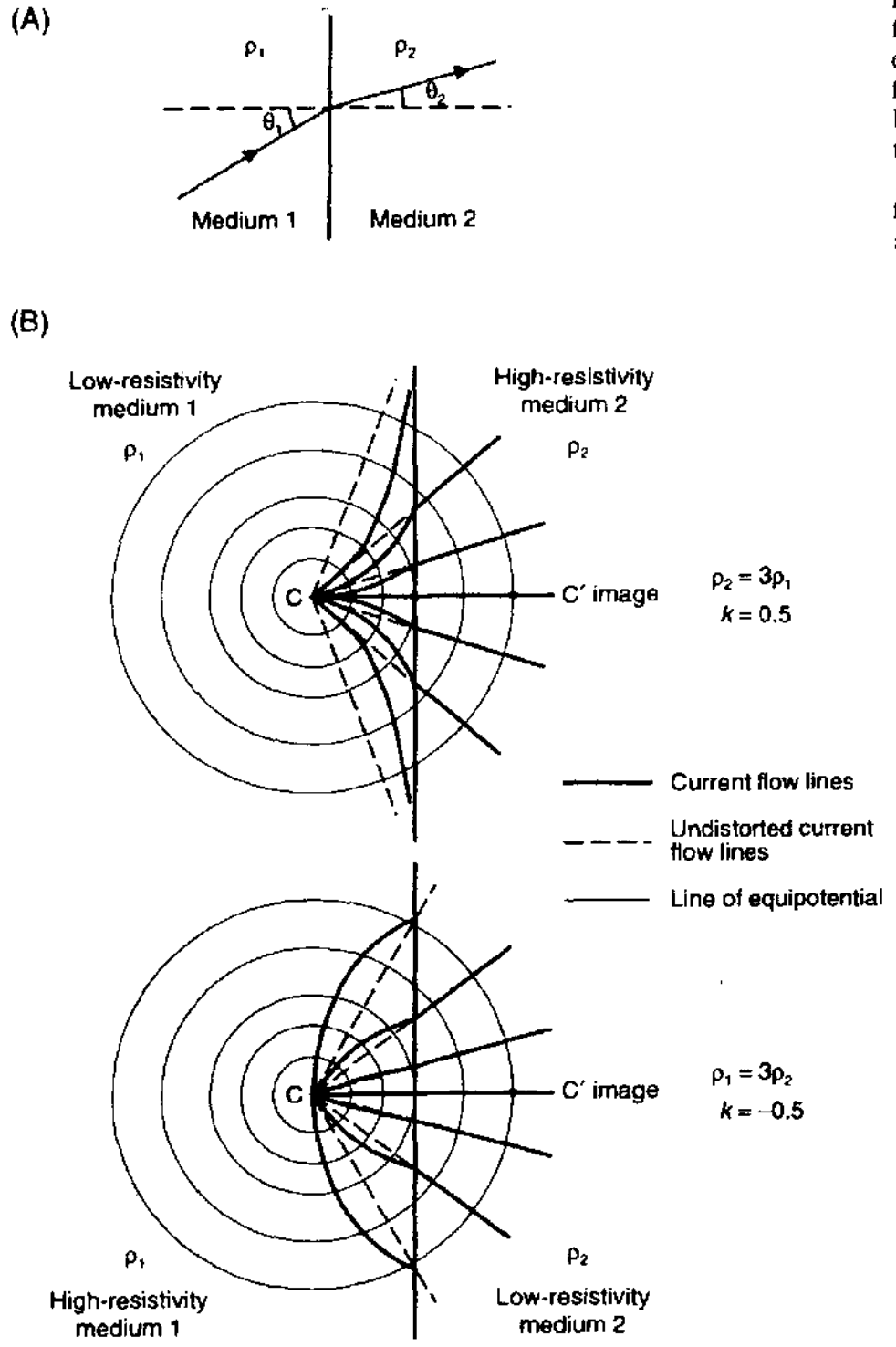

Figure 7.12 (A) Refraction of current flow lines, and (B) Distortion of equipotential and current flow lines from a point electrode across a plane boundary between media with contrasting resistivities (Telford *et al.* 1990). (C) Method of optical images for the calculation of a potential at a point (see text for details)

Box 7.11 Electrical reflection coefficient, k (see Figure 7.12C)

Potential at P:

$$V = \frac{I\rho_1}{4\pi}\left[\frac{1}{r_1} + \frac{k}{r_2}\right].$$

Potential at Q:

$$V' = \frac{I\rho_2}{4\pi}\left[\frac{1 - k}{r_3}\right].$$

At the interface $V = V'$ and $r_1 = r_2 = r_3$. Hence:

$$\frac{\rho_1}{\rho_2} = \frac{1-k}{1+k}$$

or

$$k = \frac{\rho_2 - \rho_1}{\rho_2 + \rho_1}$$

In the case when the boundary is vertical, different types of anomaly will be produced dependent upon the electrode configuration used and whether it is developed at right-angles or parallel (broadside) to the boundary. Examples of the types of anomalies produced are illustrated in Figure 7.13. The cusps and discontinuity in (A), (B) and (C) are due to the positioning of the electrodes relative to the vertical boundary with each cusp occurring as one electrode crosses the boundary. In the case of the Wenner array, it can be explained in detail (Figures 7.13D and E) as follows.

As the array is moved from the high-resistivity medium towards the low-resistivity medium (case (i) in Figure 7.13), the current flow lines converge towards the boundary, increasing the current density at the boundary but decreasing the potential gradient at the potential electrodes. The apparent resistivity gradually falls from its true value until a minimum is reached when the current electrode C_2 is at the boundary (ii). Once C_2 has crossed into the low-resistivity unit (iii), the current density increases adjacent to the boundary but within the low-resistivity medium, causing the potential gradient between the potential electrodes to rise. When the entire potential electrode dipole has crossed the boundary (iv), the current density is highest in the high-resistivity medium, causing the potential gradient across $P_1 - P_2$ to fall dramatically. With the current electrode C_1 now into the low-resistivity unit (v), the current adjacent to the boundary is divergent. This results in an elevated potential gradient between P_1 and P_2 which falls to a normal value when the entire collinear array is sufficiently far away from the boundary. At this point the current flow is radial once more. The magnitude of the cusps and discontinuities is

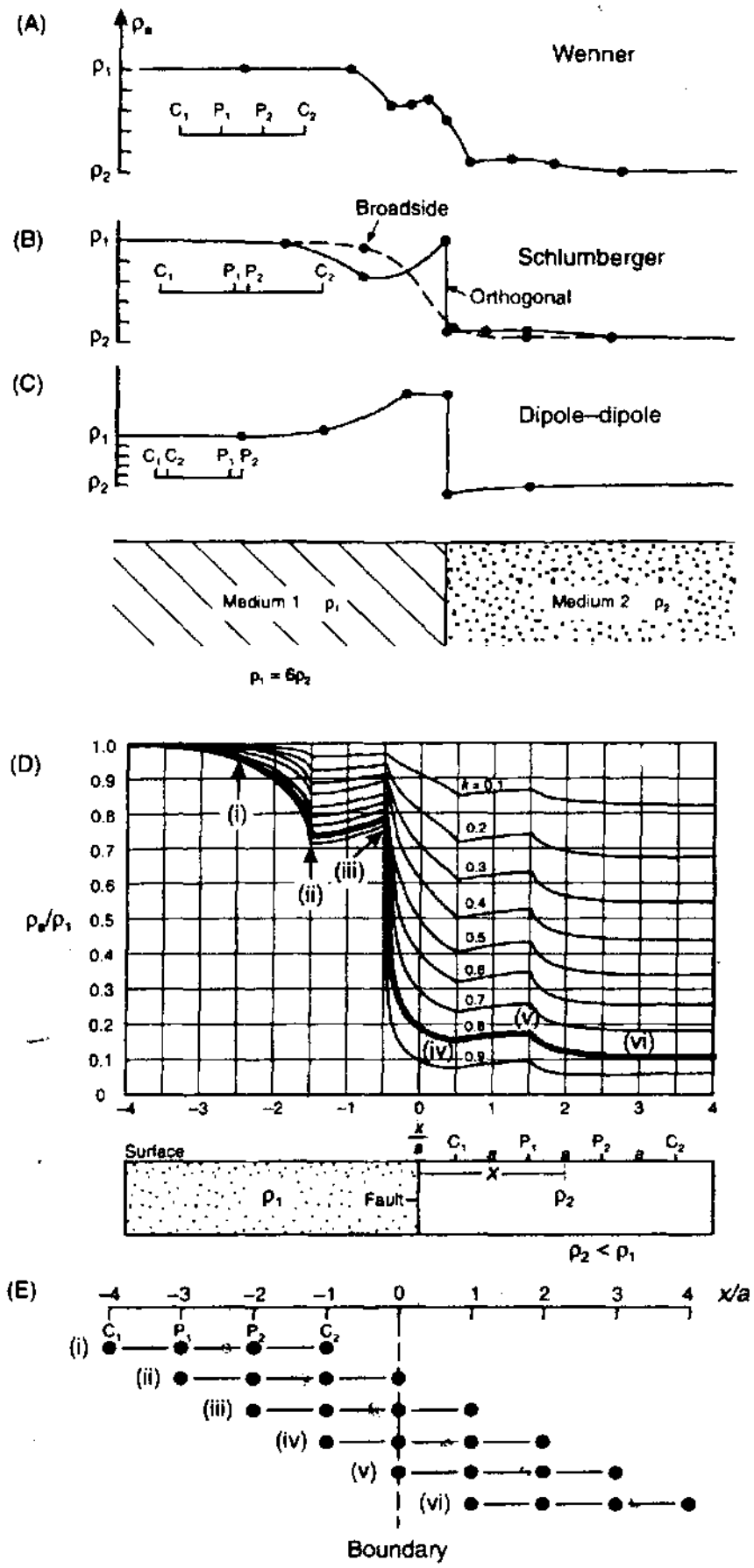

Figure 7.13 Apparent resistivity profiles measured over a vertical boundary using different electrode arrays: (A) Wenner (with its characteristic W-shaped anomaly), (B) Schlumberger, and (C) dipole–dipole. After Telford *et al.* (1990), by permission of Cambridge University Press. (D) Profile shapes as a function of resistivity contrast. From van Nostrand and Cook (1966), by permission. (E) Plan view of successive moves of a Wenner array with electrode positions indicated for six marked points in (D)

Figure 7.14 (*opposite*) Apparent resistivity profiles across a thin vertical dyke using (A) a dipole–dipole array and (B) a Wenner array. (C) Computed normalised resistivity profiles across a thin vertical dyke with different resistivity contrasts. After van Nostrand and Cook (1976), by permission

(A)

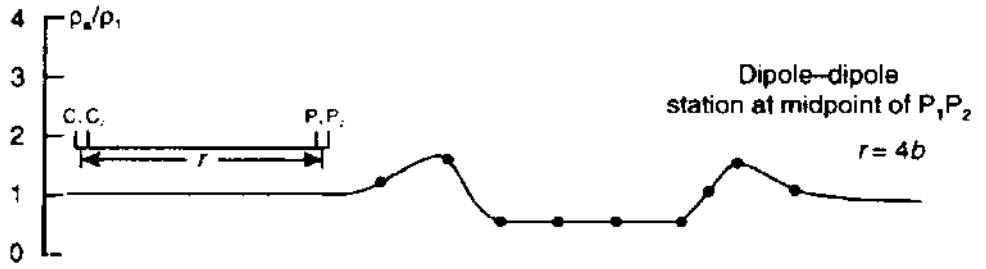
4
3
2
1
0
ρ_a/ρ_1
C₁C₂
P₁P₂
r
Dipole–dipole
station at midpoint of P₁P₂
r = 4b

(B)

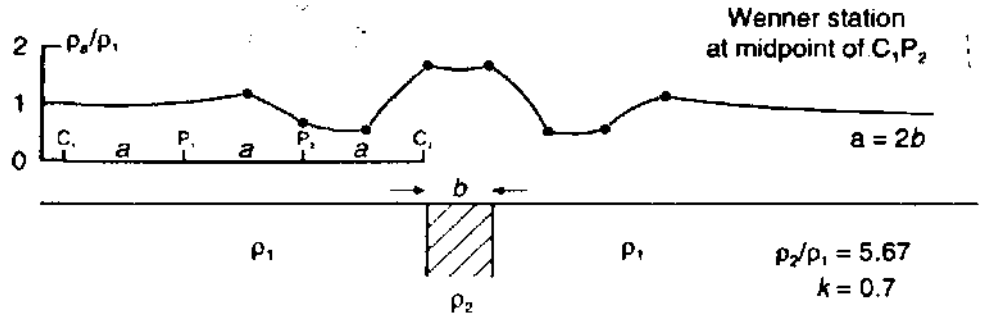
2
1
0
ρ_a/ρ_1
C₁
a
P₁
a
P₂
a
C₂
Wenner station
at midpoint of C₁P₂
a = 2b
b
ρ₁
ρ₂
ρ₁
ρ₂/ρ₁ = 5.67
k = 0.7

(C)

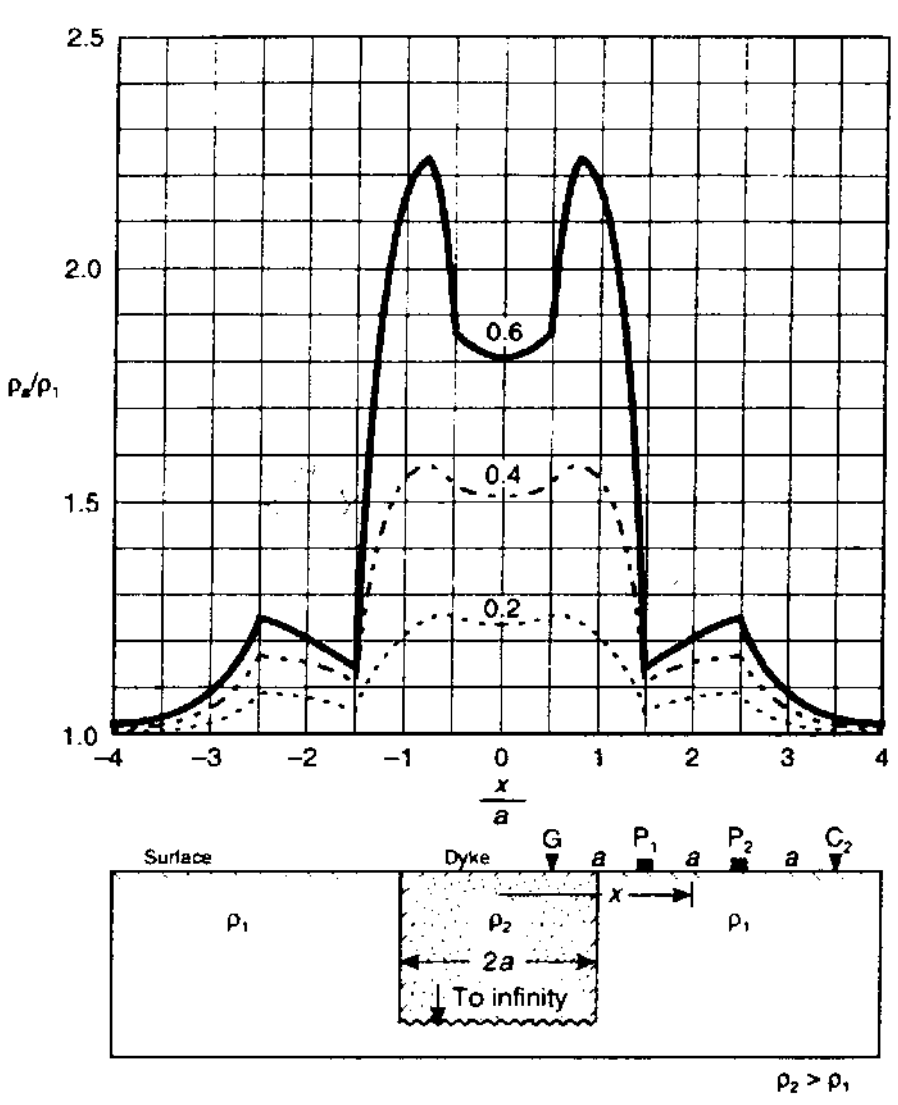
2.5
2.0
1.5
1.0
ρ_a/ρ_1
0.6
0.4
0.2
−4
−3
−2
−1
0
1
2
3
4
x/a
Surface
Dyke
G
P₁
P₂
C₂
a
a
a
x
ρ₁
ρ₂
ρ₁
2a
To infinity
ρ₂ > ρ₁

dependent upon the resistivity contrast between the two media. However, if the array is orientated parallel to the boundary such that all electrodes cross it simultaneously, the cusping is reduced. (Figure 7.13B, dashed line).

The anomaly shape is similarly varied over a vertical dyke (Figure 7.14) in which the width of the anomaly varies not only with electrode configuration but also with the ratio of the dyke width to electrode separation. An example of an apparent resistivity profile across a buried hemicylindrical valley is shown in Figure 7.15. The field and modelled profiles are very similar. The mathematical treatment of apparent resistivity profiles across vertical boundaries is discussed in detail by Telford *et al.* (1990).

The important consideration arising from this discussion is that different array types and orientations across an identical boundary between two media with contrasting resistivities will produce markedly different anomaly shapes. Thus interpretation and comparison of such profiles based simply on apparent resistivity maxima or minima can be misleading; for example, if maxima are used to delimit targets, a false target could be identified in the case of maxima doublets such as in Figure 7.14. Similar complex anomalies occur in electromagnetic data (Section 9.4.3). Furthermore, the type of anomaly should be anticipated when considering the geological target so that the appropriate electrode configuration and orientation can be chosen prior to the commencement of the survey.

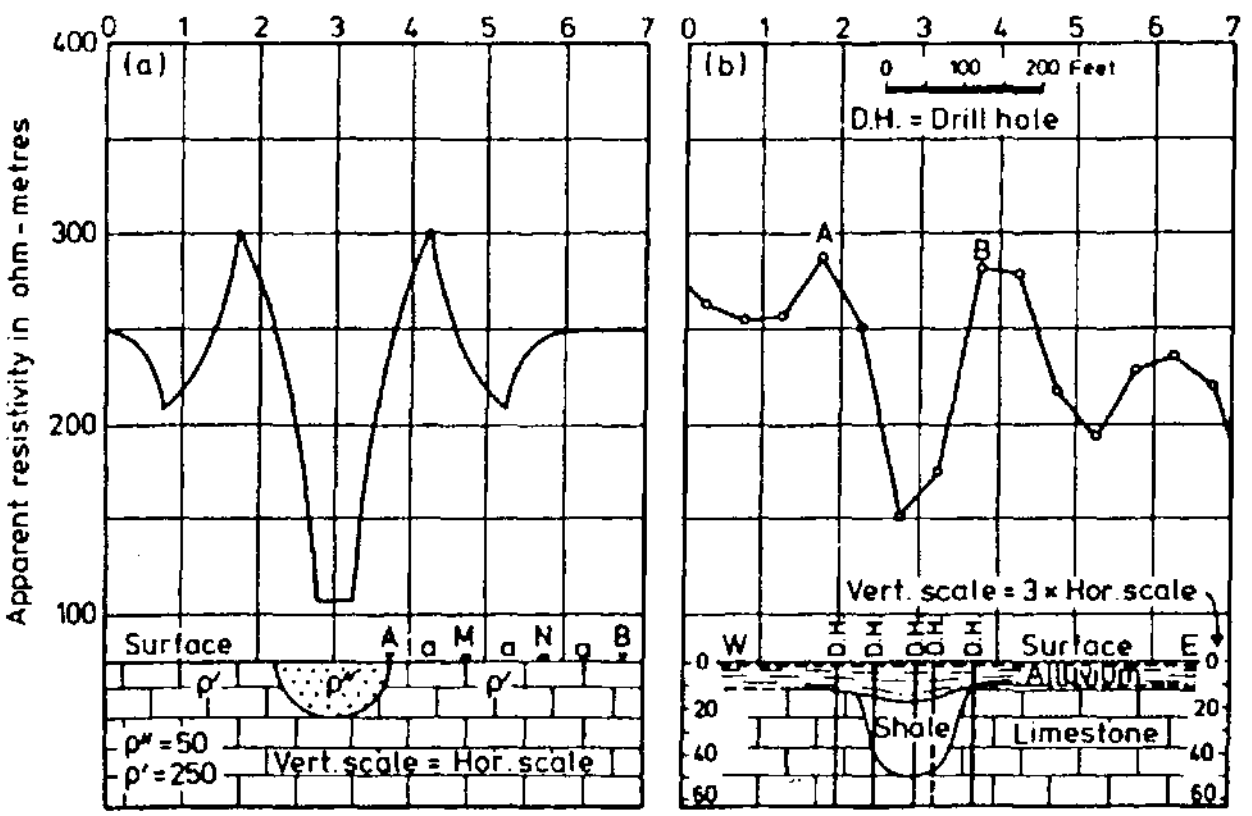

Figure 7.15 Apparent resistivity profiles across a buried valley: (A) theoretical profile, and (B) measured profile. After Cook and van Nostrand (1954) (see Parasnis 1986)

7.4 MODES OF DEPLOYMENT

There are two main modes of deployment of electrode arrays. One is for depth sounding (to determine the vertical variation of resistivity) – this is known as *vertical electrical sounding* (VES). The other is for horizontal traversing (horizontal variation of resistivity) and is called *constant separation traversing* (CST) (also called 'electrical resistivity traversing', ERT). In the case of multi-electrode arrays, two forms are available. Microprocessor-controlled resistivity traversing (MRT) is used particularly for hydrogeological investigations requiring significant depths of penetration. Sub-surface imaging (SSI) or two-dimensional electrical tomography is used for very high resolution in the near-surface in archaeological, engineering and environmental investigations.

7.4.1 Vertical electrical sounding (VES)

As the distance between the current electrodes is increased, so the depth to which the current penetrates is increased. In the case of the dipole–dipole array, increased depth penetration is obtained by increasing the inter-dipole separation, not by lengthening the current electrode dipole. The position of measurement is taken as the mid-point of the electrode array. For a depth sounding, measurements of the resistance ($\delta V/I$) are made at the shortest electrode separation and then at progressively larger spacings. At each electrode separation a value of apparent resistivity (ρ_a) is calculated using the measured resistance in conjugation with the appropriate geometric factor for the electrode configuration and separation being used (see Section 7.3). The values of apparent resistivity are plotted on a graph ('field curve') the x- and y-axes of which represent the logarithmic values of the current electrode half-separation ($AB/2$) and the apparent resistivity (ρ_a), respectively (Figure 7.16). The methods by which these field curves are interpreted are discussed in detail in Section 7.5.

In the normal Wenner array, all four electrodes have to be moved to new positions as the inter-electrode spacings are increased (Figure 7.17A). The offset Wenner system has been devised to work with special multicore cables (Barker 1981). Special connectors at logarithmically spaced intervals permit a Wenner VES to be completed by using a switching box which removes the necessity to change the electrode connections physically. Note that the offset Wenner array requires one extra electrode separation to cover the same amount of the sub-surface compared with the normal Wenner array. When space is a factor, this needs to be considered in the survey design stage.

In the case of the Schlumberger array (Figure 7.17C), the potential electrodes (P_1P_2) are placed at a fixed spacing (b) which is no more

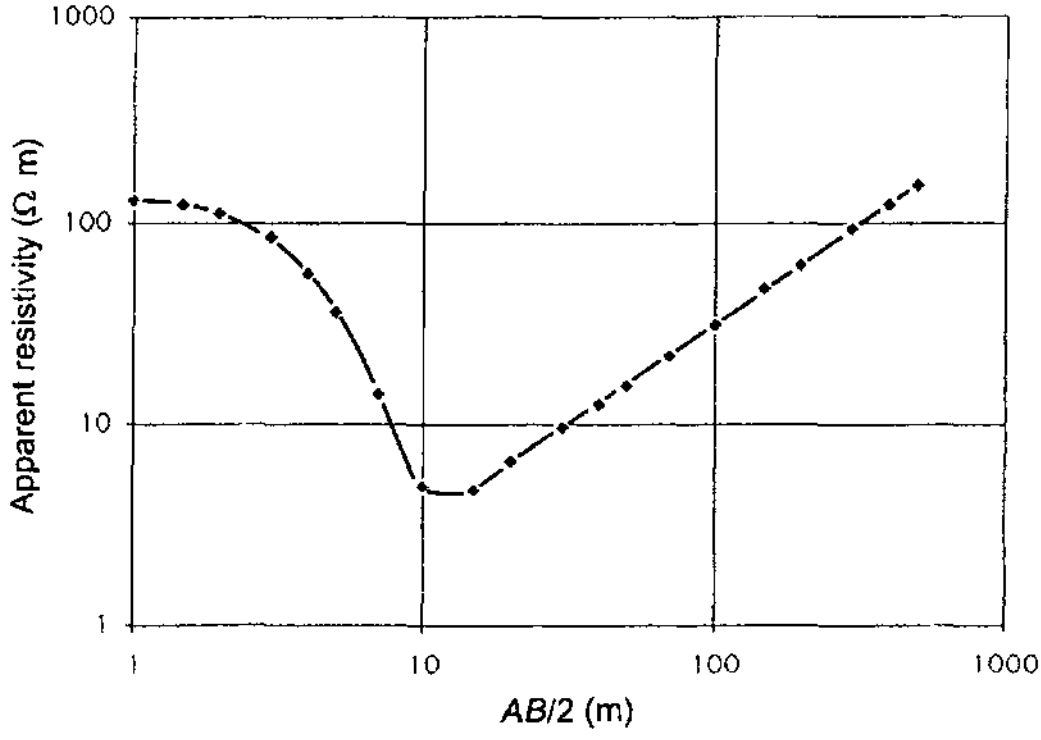

Figure 7.16 A vertical electrical sounding (VES) showing apparent resistivity as a function of current electrode half-separation ($AB/2$)

than one-fifth of the current-electrode half-spacing (a). The current electrodes are placed at progressively larger distances. When the measured voltage between P_1 and P_2 falls to very low values (owing to the progressively decreasing potential gradient with increasing current electrode separation), the potential electrodes are spaced more widely apart (spacing b_2). The measurements are continued and the potential electrode separation increased again as necessary until the VES is completed. The tangible effects of so moving the potential electrodes is discussed at the end of Section 7.4.4. A VES using the Schlumberger array takes up less space than either of the two Wenner methods and requires less physical movement of electrodes than the normal Wenner array, unless multicore cables are used.

The dipole–dipole array is seldom used for vertical sounding as large and powerful electrical generators are normally required. Once the dipole length has been chosen – i.e. the distance between the two current electrodes and between the two potential electrodes the distance between the two dipoles is then increased progressively (Figure 7.17C) to produce the sounding. The square array is rarely used for large-scale soundings as its setting out is very cumbersome (Figure 7.17E). The main advantage of the electrode configuration is the simplicity of the method when setting out small grids. In small-scale surveys investigating the three-dimensional extent of sub-surface targets, such as in archaeology, the square sides are of the order of only a few metres.

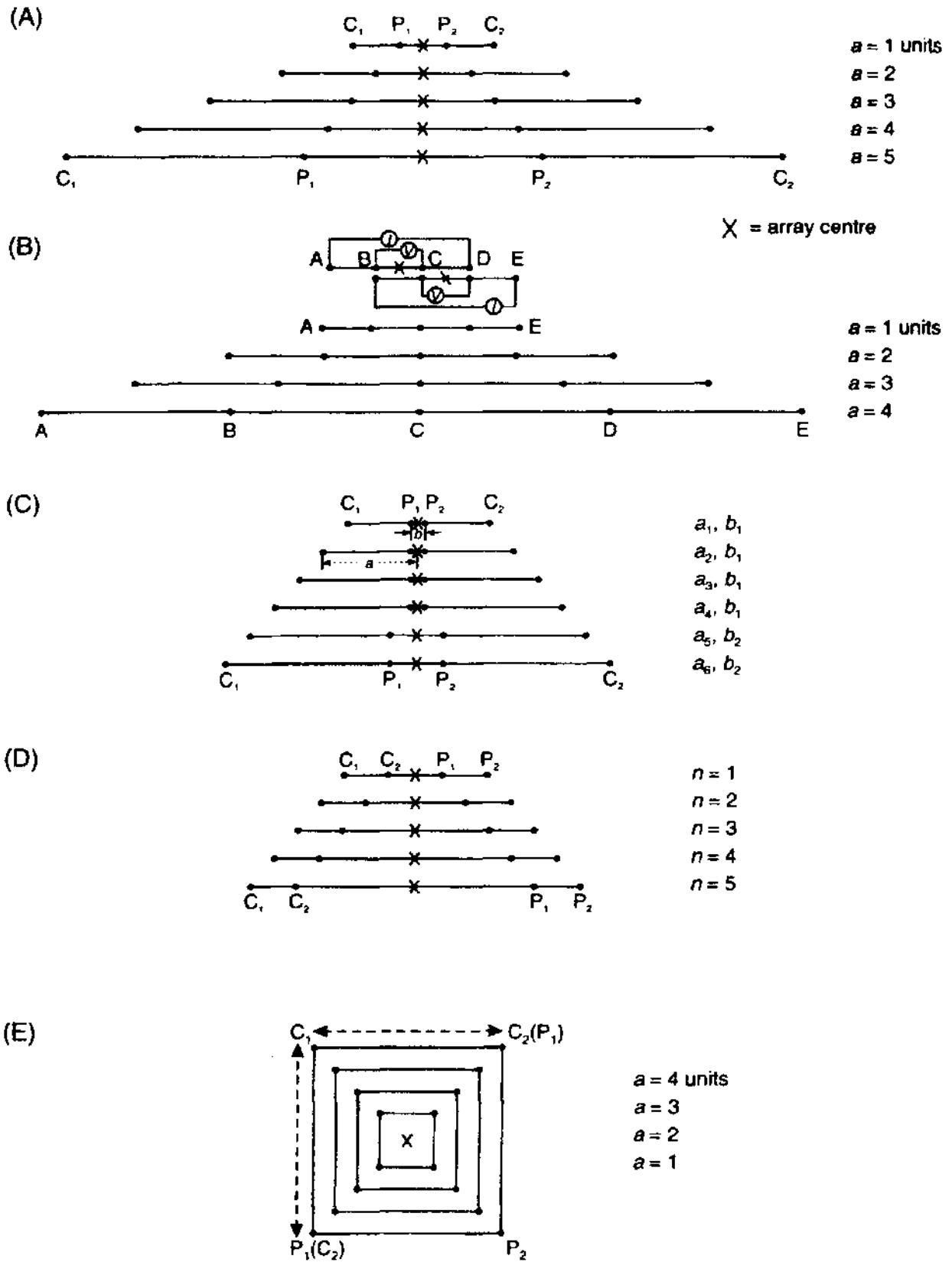

Figure 7.17 Expanded arrays (with successive positions displaced for clarity) for: (A) Wenner, (B) offset Wenner, (C) Schlumberger, (D) dipole–dipole and (E) square arrays

7.4.2 Automated array scanning

In 1981 Barker published details of the offset Wenner array using multicore cables and multiple electrodes for VES investigations. In 1985, Griffiths and Turnbull produced details of a multiple electrode array for use with CST. This theme was developed by van Overmeeren and Ritsema (1988) for hydrogeological applications and by Noel and Walker (1990) for archaeological surveys. For deeper sounding, where multicore cabling would become prohibitively heavy, the cable is wound into 50 m sections on its own drum with an addressable electronic switching unit and power supply mounted in the hub of each cable reel. The switching units are controlled by a laptop computer which can switch any electrode to either of two current or two potential cables which connect the entire array of drum reels. This system is known as the *microprocessor-controlled-resistivity traversing system* (Griffths *et al.* 1990).

In van Overmeeren and Ritsema's *continuous vertical electrical sounding* (CVES) system, an array of multiples of 40 electrodes is connected to a microprocessor by a multicore cable. Using software control, discrete sets of four electrodes can be selected in a variety of electrode configurations and separations and a measurement of the resistance made for each. Instead of using one cable layout for just one VES, the extended electrode array can be used for a number of VES, each one offset by one electrode spacing. If the first VES is conducted with its centre between electrodes 15 and 16, for example, the next VES will be centred between electrodes 16 and 17, then 17 and 18, 18 and 19, and so on. A field curve is produced for each sounding along the array and interpreted by computer methods (see Section 7.5.3) to produce a geo-electric model of true layer resistivities and thickness for each VES curve. When each model is displayed adjacent to its neighbour, a panel of models is produced (Figure 7.18) in which the various resistivity horizons can be delimited. It is clear from Figure 7.18D that the CVES interpretation is closest to the known physical model compared with those for either the tripotential alpha or beta/gamma ratio sections (Shown in Figure 7.18B and C respectively). This particular method requires special equipment and associated computer software, but it highlights a novel application of both field method and data analysis to improve the resolution of shallow resistivity surveys.

In sub-surface imaging (SSI), typically 50 electrodes are laid out in two strings of 25, with electrodes connected by a multicore cable to a switching box and resistance meter. The whole data acquisition procedure is software-controlled from a laptop computer. Similar products have been produced, such as the LUND Automatic Imaging System (ABEM), and MacOhm 21 (DAP-21) Imaging System (OYO), and the Sting/Swift (Advanced Geosciences Inc.), among others.

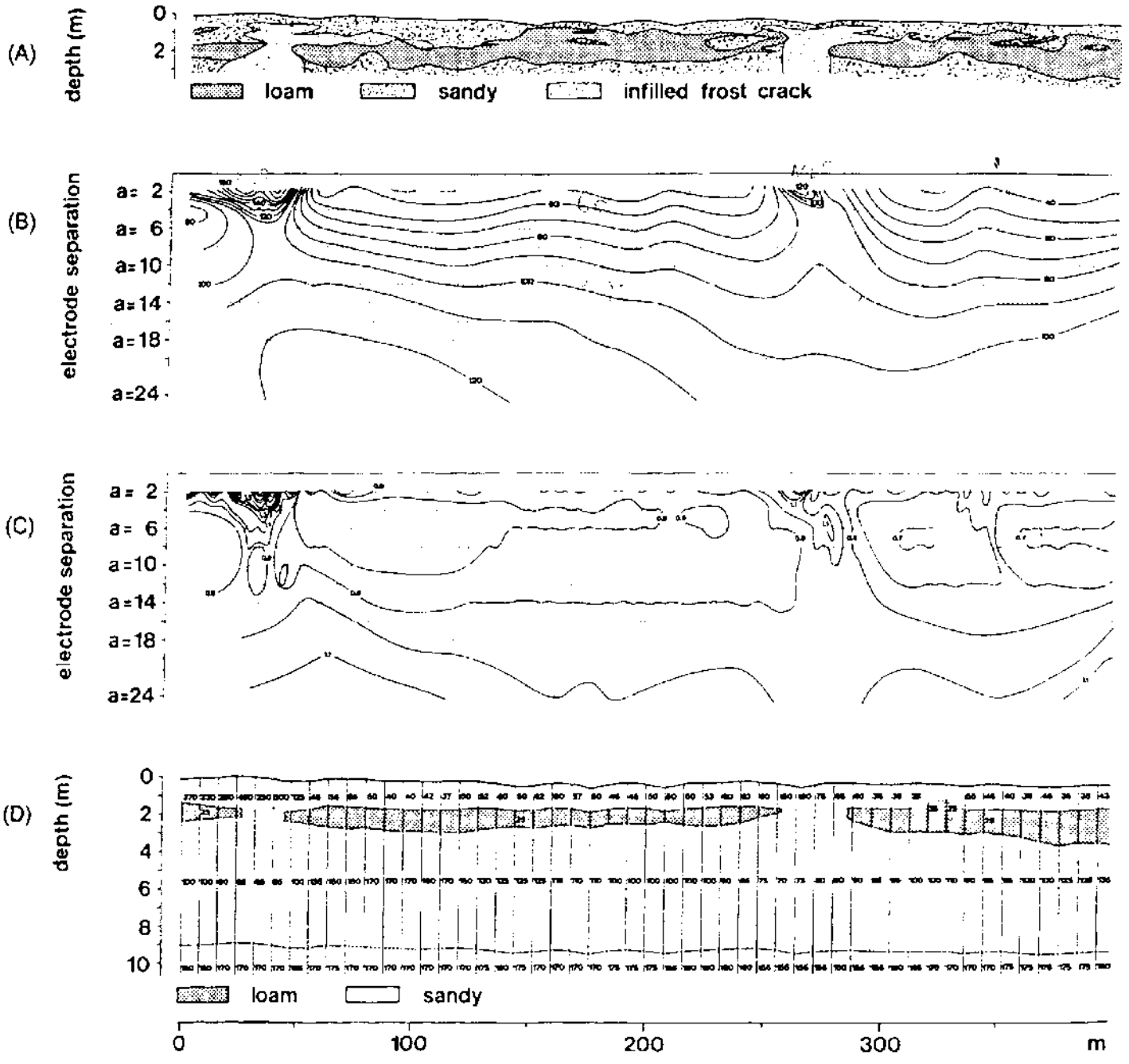

Figure 7.18 High-resolution soil survey using a scanned array. (A) Soil section determined by shallow hand-drilling. Pseudo-sections obtained using (B) Wenner tripotential alpha and (C) beta/gamma arrays. (D) Continuous vertical electrical sounding results with true resistivities indicated. From van Overmeeren and Ritsema (1988), by permission

As with van Overmeeren and Ritsema's CVES method, a discrete set of four electrodes with the shortest electrode spacing ($n = 1$; see Figure 7.19) is addressed and a value of apparent resistivity obtained. Successive sets of four electrodes are addressed, shifting each time by one electrode separation laterally. Once the entire array has been scanned, the electrode separation is doubled ($n = 2$), and the process repeated until the appropriate number of levels has been scanned. The values of apparent resistivity obtained from each measurement are plotted on a pseudo-section (Figure 7.19) and contoured. The methods of interpretation are described in more detail in Section 7.5.6. There are considerable advantages in using SSI or equivalent

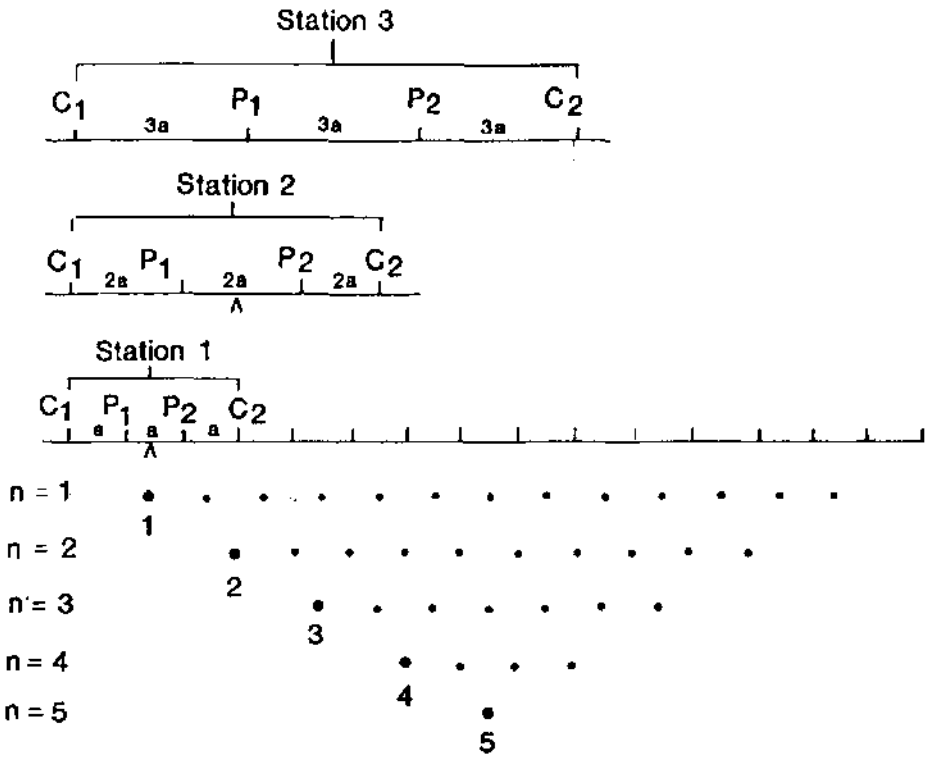

Figure 7.19 Example of the measurement sequence for building up a resistivity pseudo-section. Courtesy of Campus Geophysical Instruments Ltd.

methods. With multicore cable and many electrodes, the entire array can be established by one person. The acquisition of apparent resistivity data is controlled entirely by the software whose parameters are selected at the outset. By changing the inter-electrode spacing between electrodes, the vertical and horizontal resolutions can be specified to meet the objectives of the survey. For example, the horizontal resolution is defined by the inter-electrode spacing, and the vertical resolution by half the spacing. For example, using a 2 m inter-electrode spacing, the horizontal and vertical resolutions are 2 m and 1 m, respectively, for the pseudo-section display. Whether sub-surface features can be resolved at a comparable scale is determined also by the lateral and vertical variations in true resistivity.

7.4.3 Constant-separation traversing (CST)

Constant-separation traversing uses a manul electrode array, usually the Wenner configuration for ease of operation, in which the electrode separation is kept fixed. The entire array is moved along a profile and values of apparent resistivity determined at discrete intervals along the profile. For example, a Wenner spacing of say 10 m is used with perhaps 12 electrodes deployed at any one time at 5 m intervals. Alternate electrodes are used for any one measurement (Figure 7.20) and instead of uprooting the entire sets of electrodes, the connections are moved quickly and efficiently to the next electrode along the line, i.e. 5 m down along the traverse. This provides a CST profile with

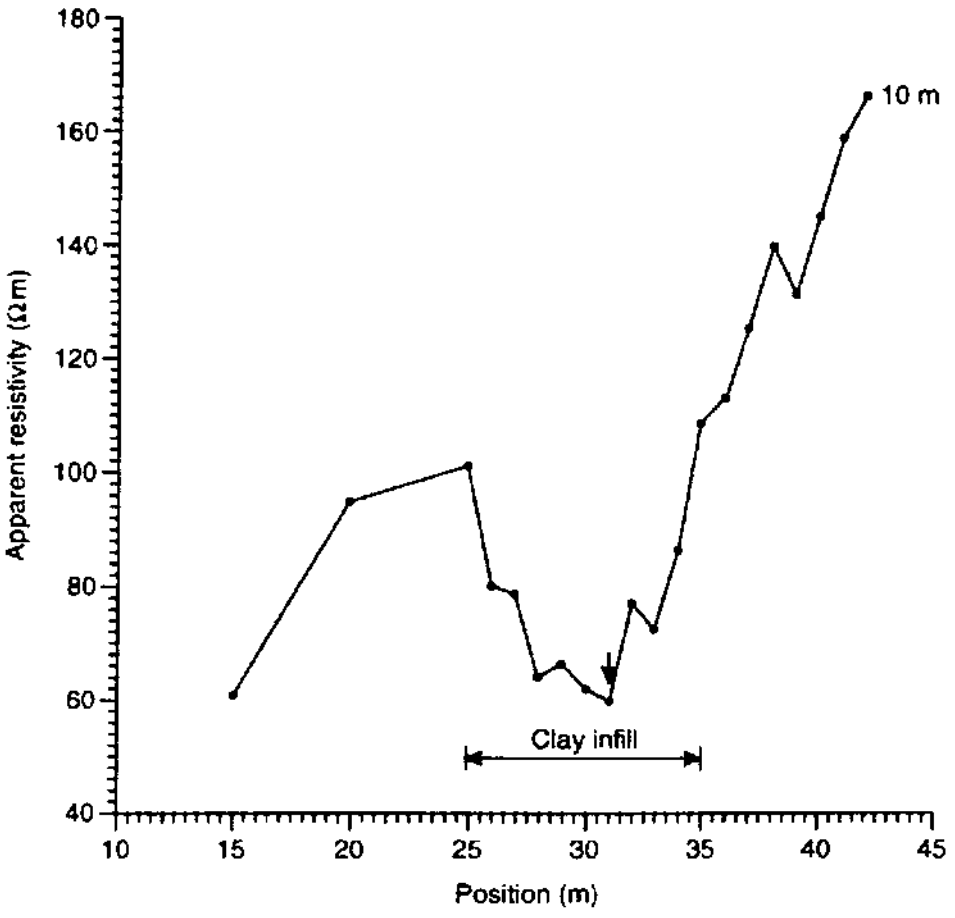

Figure 7.20 A constant-separation traverse using a Wenner array with 10 m electrode spacing over a clay-filled solution feature (position arrowed) in limestone

electrode separation of 10 m and station interval of 5 m. The values of apparent resistivity are plotted on a linear graph as a function of distances along the profile (Figure 7.20). Variations in the magnitude of apparent resistivity highlight anomalous areas along the traverse.

Sörensen (1994) has described a 'pulled array continuous electrical profiling' technique (PA–CEP). An array of heavy steel electrodes, each weighing 10–20 kg, is towed behind a vehicle containing all the measuring equipment. Measurements are made continuously. It is reported that 10–15 line kilometres of profiling can be achieved in a day. The quality of results is reported to be comparable to that of fixed arrays with the same electrode geometry.

7.4.4 Field problems

In order for the electrical resistivity method to work using a collinear array, the internal resistance of the potential measuring circuit must be far higher than the ground resistance between the potential electrodes. If it is not, the potential circuit provides a low-resistance alternative route for current flow and the resistance measured is completely meaningless. Most commercial resistivity equipment has an input resistance of at least 1 MΩ, which is adequate in most cases.

In the case of temperature glacier ice, which itself has a resistivity of up to 120 MΩm, a substantially higher input resistance is required (preferably of the order of $10^{14}\,\Omega$).

Electrical resistivity soundings on glaciers are complicated by the fact that ice does not conduct electricity electronically but by the movement of protons within the ice lattice and this causes substantial polarisation problems at the electrode–ice contact. Consequently, special techniques are required in order to obtain the relevant resistivity data (Reynolds 1982).

Perhaps the largest source of field problems is the electrode contact resistance. Resistivity methods rely on being able to apply current into the ground. If the resistance of the current electrodes becomes anomalously high, the applied current may fall to zero and the measurement will fail. High contact resistances are particularly common when the surface material into which the electrodes are implanted consists of dry sand, boulders, gravel, frozen ground, ice or laterite. If the high resistance can be overcome (and it is not always possible), there are two methods that are commonly used. One is to wet the current electrodes with water or saline solution, sometimes mixed with bentonite. The second method is to use multiple electrodes. Two or three extra electrodes can be connected to one end of the current-carrying cable so that the electrodes act as resistances in parallel. The total resistance of the multiple electrode is thus less than the resistance of any one electrode (see Figure 7.21 and Box 7.12). However, if this method is used, the extra electrodes must be implanted at right-angles to the line of the array rather than along the direction of the profile. If the extra electrodes are in the line of the array, the geometric factor may be altered as the inter-electrode separation (C_1–P_1–P_2–C_2) is effectively changed. By planting the electrodes at right-angles to the line of the array, the inter-electrode separation is barely affected. This problem is only acute when the current electrode separation is small. Once the current electrodes are sufficiently far apart, minor anomalies in positioning are insignificant. This also applies when laying out the survey line to start with.

Box 7.12 Resistances in parallel

Total resistance of multiple electrodes is R_T:

$$1/R_T = 1/R_1 + 1/R_2 + 1/R_3 + \cdots 1/R_n = \sum_{i=1}^{n} (1/R_i).$$

For example, if $r_1 = r_2 = 0.2R$ and $r_3 = r_4 = 0.5R$, then:

$$1/R_T = 1/0.2R + 1/0.2R + 1/0.5R + 1/0.5R + 1/R = 15/R.$$

Thus $R_T = R/15$, and R_T is much less than the lowest individual resistance ($= R/5$).

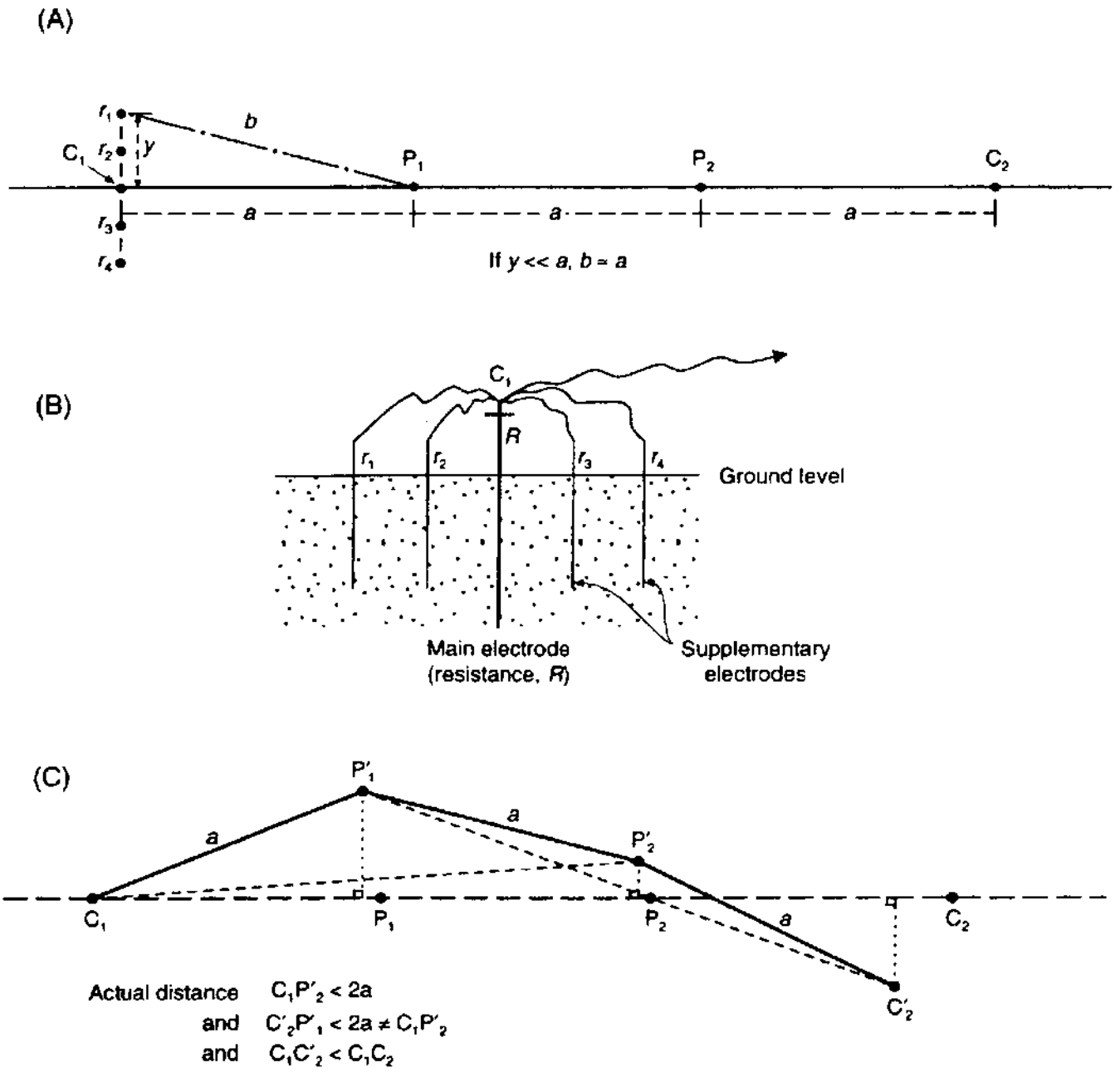

Ideally, a VES array should be expanded along a straight line. If it curves significantly and/or erratically (Figure 7.21C), and no correction is made, cusps may occur in the data owing to inaccurate geometric factors being used to calculate apparent resistivity values. Cusps in VES field curves are particularly difficult to resolve if their cause is unknown. Even if the apparent resistivity values have been calculated correctly with appropriately modified geometric factors, ambiguities may arise in the field curve which it may not be possible to model or interpret. In the case of CST data, if the correct geometric factors are used to derive the apparent resistivities, the CST profile may be interpreted normally. It always pays to keep adequate field notes in addition to recording the geophysical data so that appropriate corrections can be made with recourse to the correct information

Figure 7.21 (A) Supplementary electrodes planted in a straight line at right-angles to the main electrode have minimal effect on the geometric factor as long as the offset $y \uparrow a$. (B) Any number of additional electrodes act as parallel resistances and reduce the electrode contact resistance. (C) An out-of-line electrode array will give rise to erroneous ρ_a values unless the appropriate geometric factor is used. Shortened C_1C_2 produces elevated ΔV between P_1 and P_2 and needs to be compensated for by a reduced value of the geometric factor.

rather than to a rather hazy recollection of what may have been done in the field.

The presence of pipes, sand lenses or other localised features, which are insignificant in relation to the main geological target, can degrade the quality of the field data and thus reduce the effectiveness of any interpretation. If a conductive clay lens is present, for example, then when a current is applied from some distance away from it, the lines of equipotential are distorted around the lens and the current flow lines

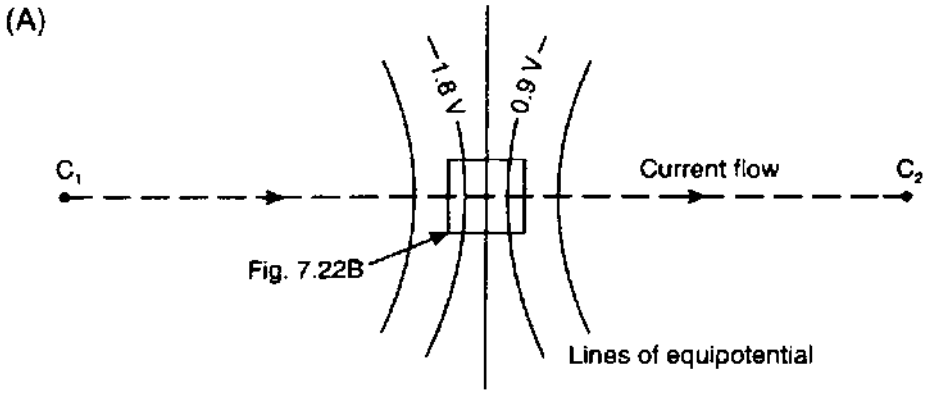

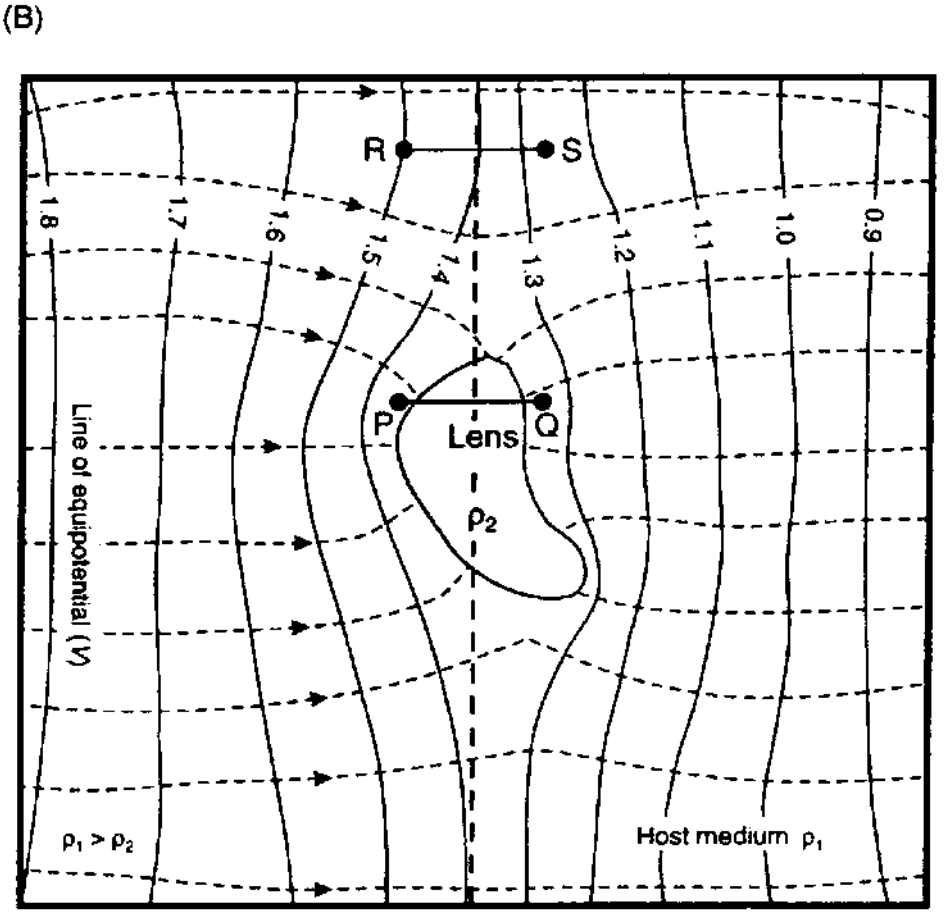

Figure 7.22 Distortion of current flow lines and equipotentials around an anomalous feature. The boxed area in (A) is enlarged to show detail in (B). The magnitude of equipotentials is for illustrative purposes only

are focused towards the lens (Figure 7.22). The potential between P and Q (< 0.1 V) is obviously smaller than that measured between R and S (≈ 0.25 V) which are outside the field of effect of the lens. The apparent resistivity derived using this value of potential is lower than that obtained had the lens not been there, hence the occurrence of a cusp minimum (Figure 7.23A). If the lens has a higher resistivity than the host medium, the current flow lines diverge and the potential between P and Q becomes anomalously high and results in a positive cusp (Figure 7.23B).

Another feature which may occur on VES profiles is current leakage, particularly at large current electrode separations, when the array is aligned parallel to a conductive feature such as a metal pipe or a surface stream. The values of apparent resistivity become increasingly erratic owing to the voltage between the potential electrodes falling to within noise levels and tend to decrease in value (Figure 7.23C). If the position and orientation of a pipe is known, there should be no ambiguity in interpretation. There is no point in extending the VES once it is obvious current leakage is occurring.

A method of reducing the effects of these lateral inhomogeneities using the offset Wenner array has been described in Section 7.3.2. There is, however, no alternative method for the Schlumberger electrode configuration and cusps can be removed by smoothing the curve (dashed lines in Figure 7.23).

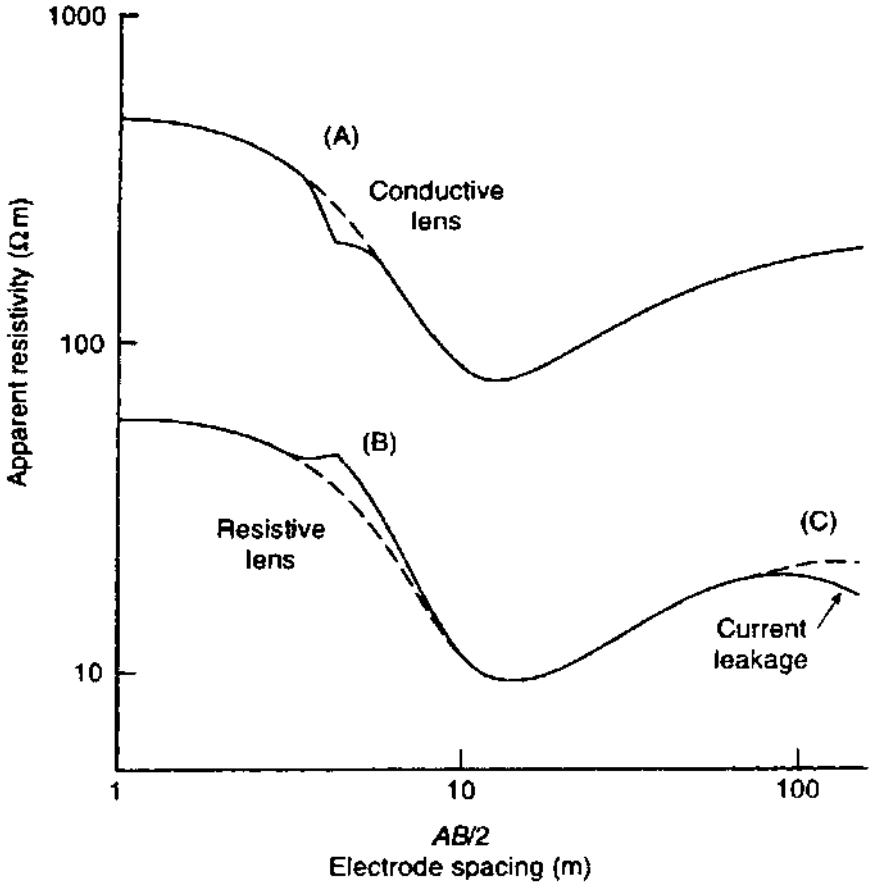

Figure 7.23 Distortion of Schlumberger VES curves due to (A) a conductive lens or pipeline, and (B) a resistive lens. After Zohdy (1974), by permission

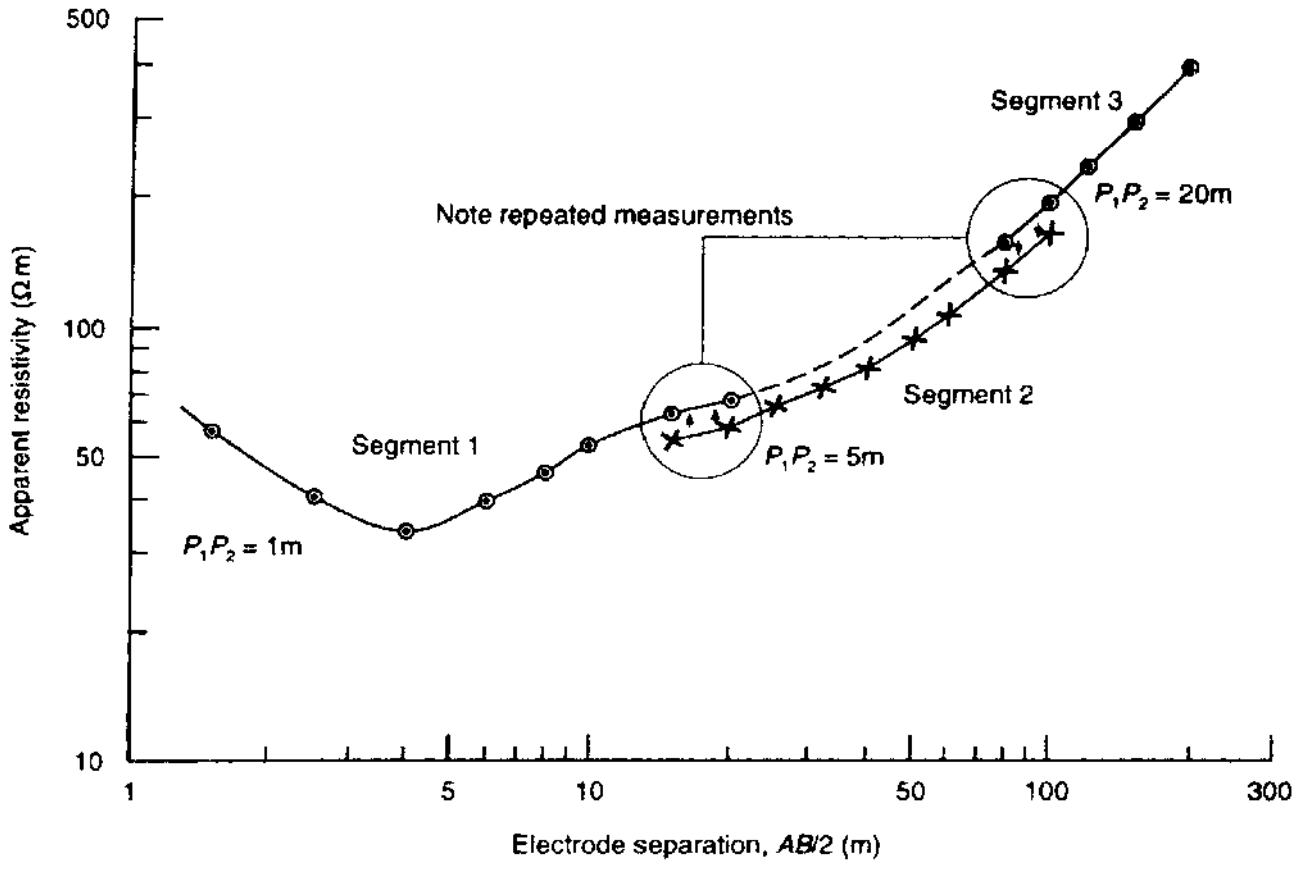

Figure 7.24 Displaced segments on a Schlumberger vertical electrical sounding curve due to different electrode resistances at P_1 and P_2 on expanding potential electrode separations; segment 3 is displaced to fit segment 2 which is in turn displaced to fit segment 1 to produce a smoothed curve

An additional but easily resolvable problem can occur with Schlumberger depth soundings. When the separation of the potential electrode pair is increased (b_1 to b_2 in Figure 7.17C), the contact resistance may change, causing a discrete step up or down of the next segment of the curve (Figure 7.24). Although the value of the apparent resistivity may change from the use of one electrode pair to another, the gradient of the change of apparent resistivity as a function of current electrode half-separation should remain the same. Consequently, the displaced segments can be restored to their correct values and the curve smoothed ready for interpretation. Segments at larger potential electrode separations should be moved to fit the previous segment obtained with a shorter electrode separation. So in Figure 7.24, segment 3 is moved down to fit segment 2 which is moved up to join on the end of segment 1. Measurements of resistance should be repeated at both potential electrode separation when crossing from one segment to the next. As all the electrodes are moved when a manual Wenner array is expanded, there is no discernible displacement of segments of the curve. Instead, the field curve may appear to have lots of cusps and blips through which a smooth curve is then drawn, usually by eye (Figure 7.25). An alternative, preferable, approach is to use the offset Wenner array (see Section 7.3.2) which improves the quality of the acquired field data (Figure 7.25).

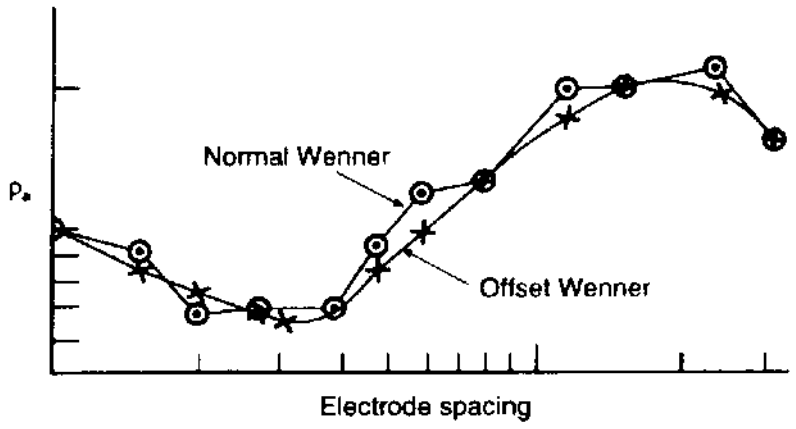

Figure 7.25 The difference in data quality that can be obtained by using an offset Wenner array in place of a normal Wenner array; the normal curve is more noisy

7.5 INTERPRETATION METHODS

Vertical sounding field curves can be interpreted qualitatively using simple curve shapes, semi-quantitatively with graphical model curves, or quantitatively with computer modelling. The last method is the most rigorous but there is a danger with computer methods to over-interpret the data. VES field curves may have subtle inflections and cusps which require the interpreter to make decisions as to how real or how significant such features are. Often a noisy field curve is smoothed to produce a graph which can then be modelled more easily. In such a case, there is little point in spending large amounts of time trying to obtain a perfect fit between computer-generated and field curves. As a general rule, depending on how sophisticated the field acquisition method is, layer thicknesses and resistivities are accurate to between 1% and 10%, with poorer accuracies arising from the cruder field techniques. Furthermore, near-surface layers tend to be modelled more accurately than those at depth, primarily because field data from shorter electrode separations tend to be more reliable than those for very large separation, owing to higher signal-to-noise ratios.

7.5.1 Qualitative approach

The first stage if any interpretation of apparent resistivity sounding curves is to note the curve shape. This can be classified simply for three electrical layers into one of four basic curve shapes (Figures 7.26A–D). These can also be combined to describe more complex field curves that may have several more layers. Note that the curve shape is dependent upon the relative thicknesses of the in-between layers (layer 2 in a 3-layer model; Figures 7.26C, D). The maximum angle of slope that the rising portion of a resistivity graph may have on a log–log graph is 45°, given the same scales on both axes (Figure 7.26A). If the field curve rises more steeply, then this suggests error in the data or that geometric effects due to steeply inclined horizons are distorting the data.

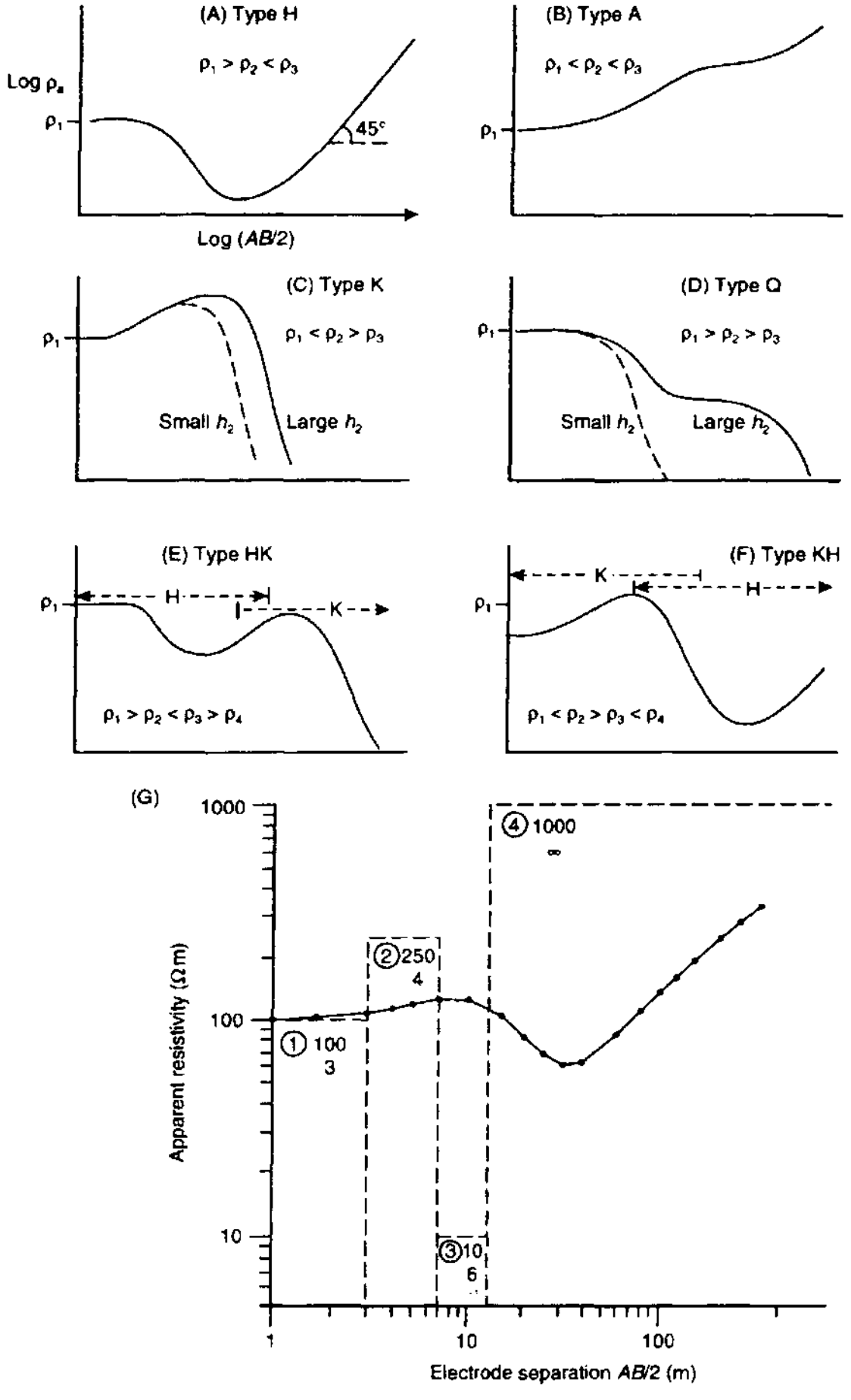
(A) Type H
$\rho_1 > \rho_2 < \rho_3$
Log ρ_a
ρ_1
45°
Log (*AB*/2)
(B) Type A
$\rho_1 < \rho_2 < \rho_3$
ρ_1
(C) Type K
$\rho_1 < \rho_2 > \rho_3$
ρ_1
Small h_2
Large h_2
(D) Type Q
$\rho_1 > \rho_2 > \rho_3$
ρ_1
Small h_2
Large h_2
(E) Type HK
ρ_1
H
K
$\rho_1 > \rho_2 < \rho_3 > \rho_4$
(F) Type KH
K
H
ρ_1
$\rho_1 < \rho_2 > \rho_3 < \rho_4$
(G)
1000
100
10
Apparent resistivity (Ω m)
① 100
3
②250
4
③10
6
④1000
∞
1
10
100
Electrode separation *AB*/2 (m)

The *relative* magnitudes of the true resistivities obtained from the levels of the flat portions or shoulders of the graph are a useful starting point before more involved interpretation. For example, in Figures 7.26A and B, the only difference between the two models is the resistivity of layer 2. In Figure 7.26A, layer 2 resistivity is less than those for both layers 1 and 3. In Figure 7.26B, the second layer resistivity is between those for layers 1 and 3. In the case of Figure 7.26D, if the second layer is very thin (dashed line for small h_2) it may not be evident on the curve that this layer exists, i.e. its effects are 'suppressed'. 'Suppression' is discussed in more detail in Section 7.5.4.

From Figure 7.26G, it can be seen that the number of layers identified is equal to the number of turning points (TP) in the curve, plus one. The presence of turning points indicates sub-surface interfaces, so the number of actual layers must be one more than the number of boundaries between them. However, the coordinates of the turning points in no way indicate the depth to a boundary or provide specific information about the true resistivities (Figure 7.26G). From the curve shape alone, the minimum number of horizontal layers and the relative magnitudes of the respective layer resistivities can be estimated.

Figure 7.26 (*opposite*) Apparent resistivity curve shapes for different resistivity structures: (A) to (D) are three-layer models; (E) and (F) are four-layer models; (G) shows a block model for the layer resistivities and thicknesses and the resulting apparent resistivity curve. Neither the minimum nor the maximum apparent resistivities occur at electrode separations equivalent to the layer depths. To penetrate to bedrock, electrode separation should be about three times the bedrock depth for a Schlumberger array

7.5.2 Master curves

Interpretation of field curves by matching against a set of theoretically calculated master curves is based on the assumptions that the model relates to a horizontally stratified earth and that successively deeper layers are thicker than those overlying. Although this second assumption is rarely valid, the use of *master curves* does seem to provide a crude estimate of the physical model.

Synthetic curves for two-layer models can be represented on a single diagram (Figure 7.27), but for three-layer models the range of graphs is very large and books of master curves have been published (Mooney and Wetzel 1956; European Association of Exploration Geophysicists 1991). It is only practicable to use the master curves method for up to four layers. If more layers are present, the graphical approach is far too cumbersome and inaccurate. Three- and four-layer models can also be interpreted using master curves for two layers with the additional use of auxiliary curves (Figure 7.28) as outlined below.

The field data, smoothed and corrected as necessary, are plotted on a log–log graph on a transparent overlay at the same scale as the master curves. The overlay is placed on the master curves and, keeping the x- and y-axes of the two graphs parallel, the overlay is moved until the segment of the field curve at shortest electrode spacings fits one of the master curves and its k value is noted (Figure 7.29; in this case, $k = -0.3$). The position of the origin of the master curve is marked (A) on the overlay, which is then placed over the auxiliary curve sheet and the line for the same k value is traced on

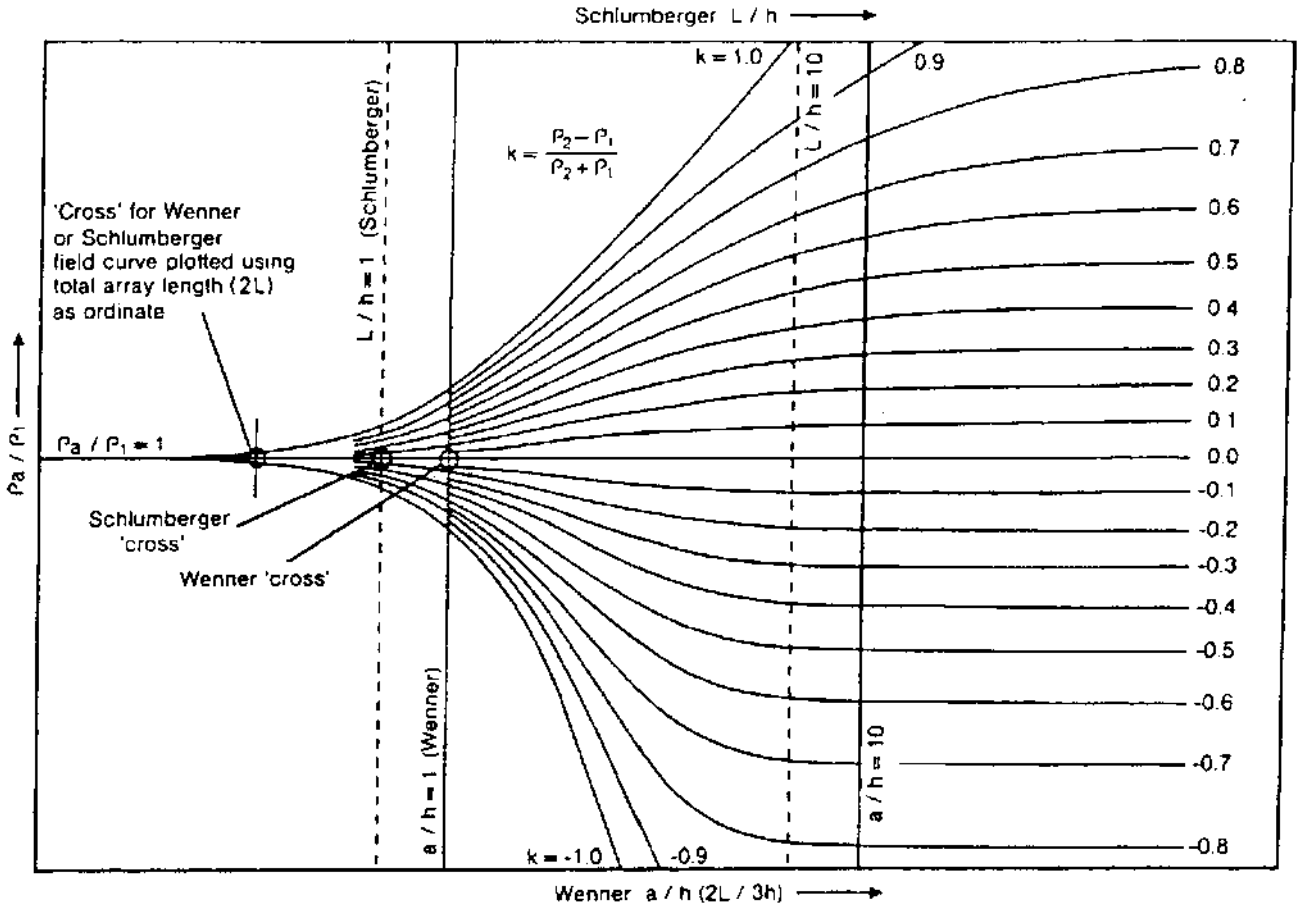

Figure 7.27 Two-layer master curves for Schlumberger and Wenner arrays. From Milsom (1989), by permission

to the overlay. The coordinates of A (which are read off the graph) are first estimates of the true resistivity and thickness of the top layer. Next, the overlay is replaced over the master curve sheet and moved so that the traced auxiliary curve for $k = -0.3$, always lies over the origin of the master curve until the next portion of the field curve is coincident with one of the master curves beneath and the new k value noted; in the example in Figure 7.29 the second k value is $+1.0$. When a fit has been obtained, the new position of the origin of the master curves (B) is marked on to the traced auxiliary curve. The overlay is returned to cover the auxiliary curves and the point B is placed over the origin of the auxiliary curves and the line corresponding to the new k value is again traced on to the overlay. The coordinates of B (also measured off the graph) are first estimates of the resistivity of the second layer and of the total depth to the second interface. The above process is then repeated, going from master curve to auxiliary curves and back again, noting the new k values in each case until the entire field curve has been matched against master curves. The final result should be, for a three-layer case as the example, two points of origin A and B giving ρ_1, t_1 and ρ_r and $(t_1 + t_2)$ and hence t_2. From the first k value, the resistivity of the second layer can easily be calculated (see Box 7.11), and from the second k value, ρ_3 can be estimated, thus completing the determination of the model parameters.

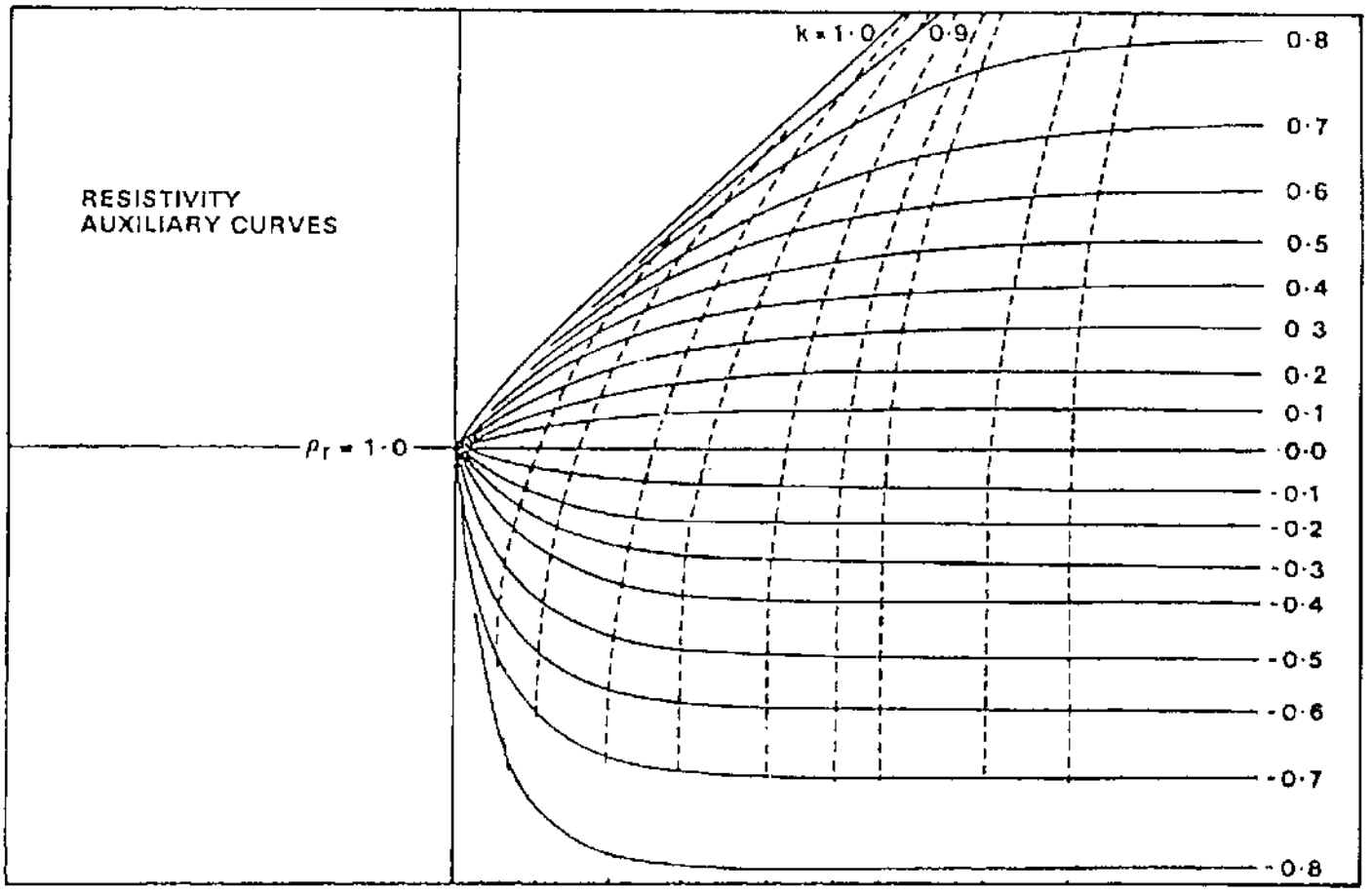

Figure 7.28 Auxiliary curves for a two-layer structure

Curve-matching is constrained to fit the field curve with one calculated from a very limited range of master curves. If the resistivity contrasts do not give rise to a k value that corresponds to one of the master curves, then the accuracy of the fitting (and of the subsequent interpretation) will be reduced. Furthermore, the use of master curves does not allow the problems of equivalence and suppression to be resolved (see Section 7.5.4). Interpretations obtained using this graphical approach should be regarded as crude estimates of the sub-surface layer parameters that can then be put into a computer model to obtain much more accurate and reliable results.

7.5.3 Curve matching by computer

In 1971, Ghosh described a convolution method by which computers can be used to calculate master curves for vertical electrical soundings obtained using either a Wenner or Schlumberger array. The method uses what is called a 'linear digital filter', the details of which are given by Koefoed (1979).

The program synthesises an apparent resistivity profile for an n-layered model in which the variables are layer thickness and resistivity. Model profiles can then be compared with the field curves and

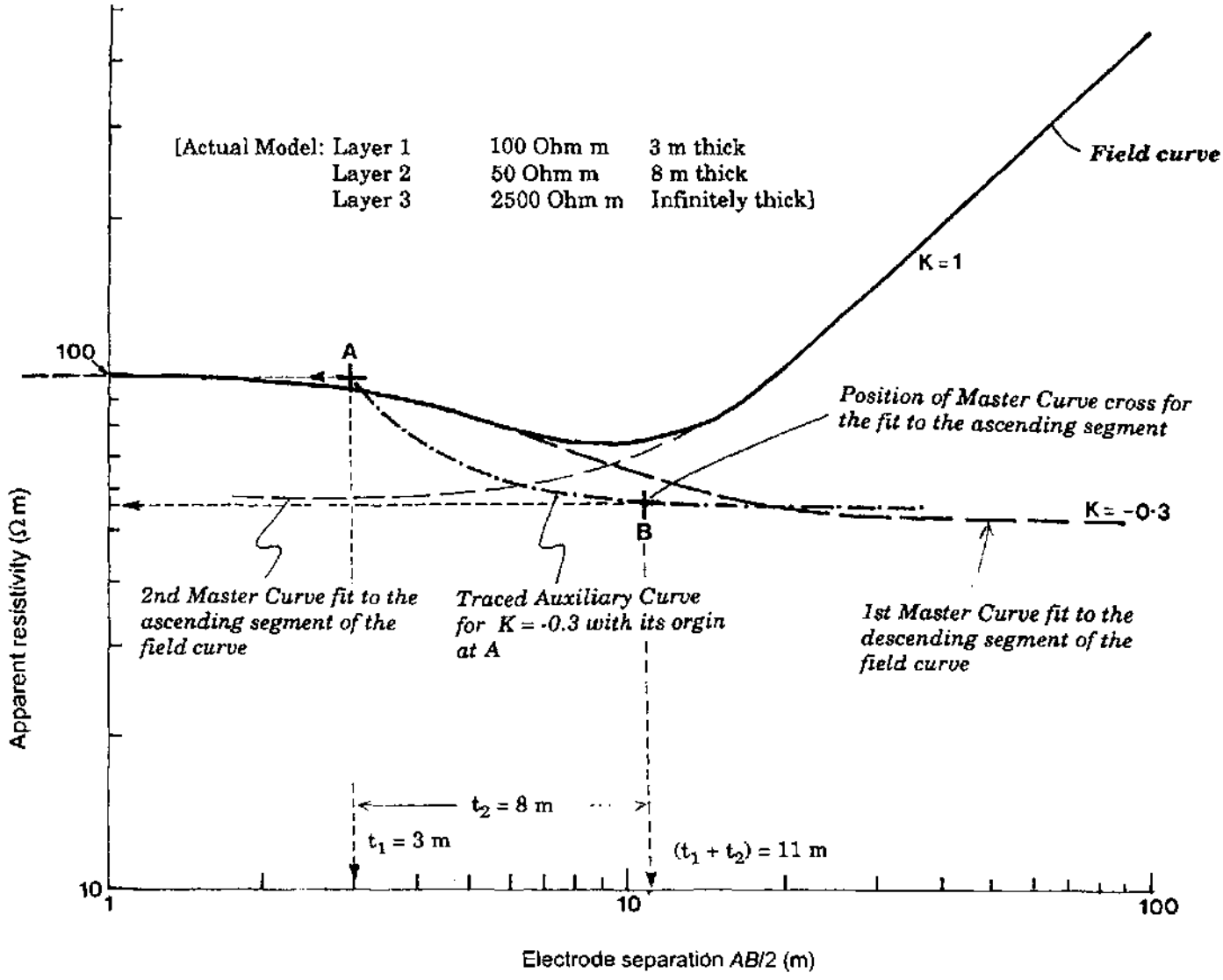

Figure 7.29 Fitting master and auxiliary curves to a Schlumberger VES curve; see text for details

adjustments to the layering and resistivity values can be made by trial and error to obtain as near correspondence as possible to the field curve.

However, in cases where a very good conductor underlies a comparatively resistive layer (where $\rho_1 > 20\rho_2$ and $-1 < k < -0.9$), Ghosh's method was found to produce inaccurate profiles owing to the structure of the filter, which had too few coefficients to track a rapidly falling resistivity curve.

A computer program can easily be checked to see whether it produces erroneous profiles, by obtaining an apparent resistivity curve for a simple two-layer model where the resistivity contrast is at least 20:1 with the lower layer being the more conductive. If the program is unable to cope with such a contrast, the portion of the graph at larger electrode separations will appear to oscillate (Figure 7.30) rather than pass smoothly to the true resistivity of the second layer.

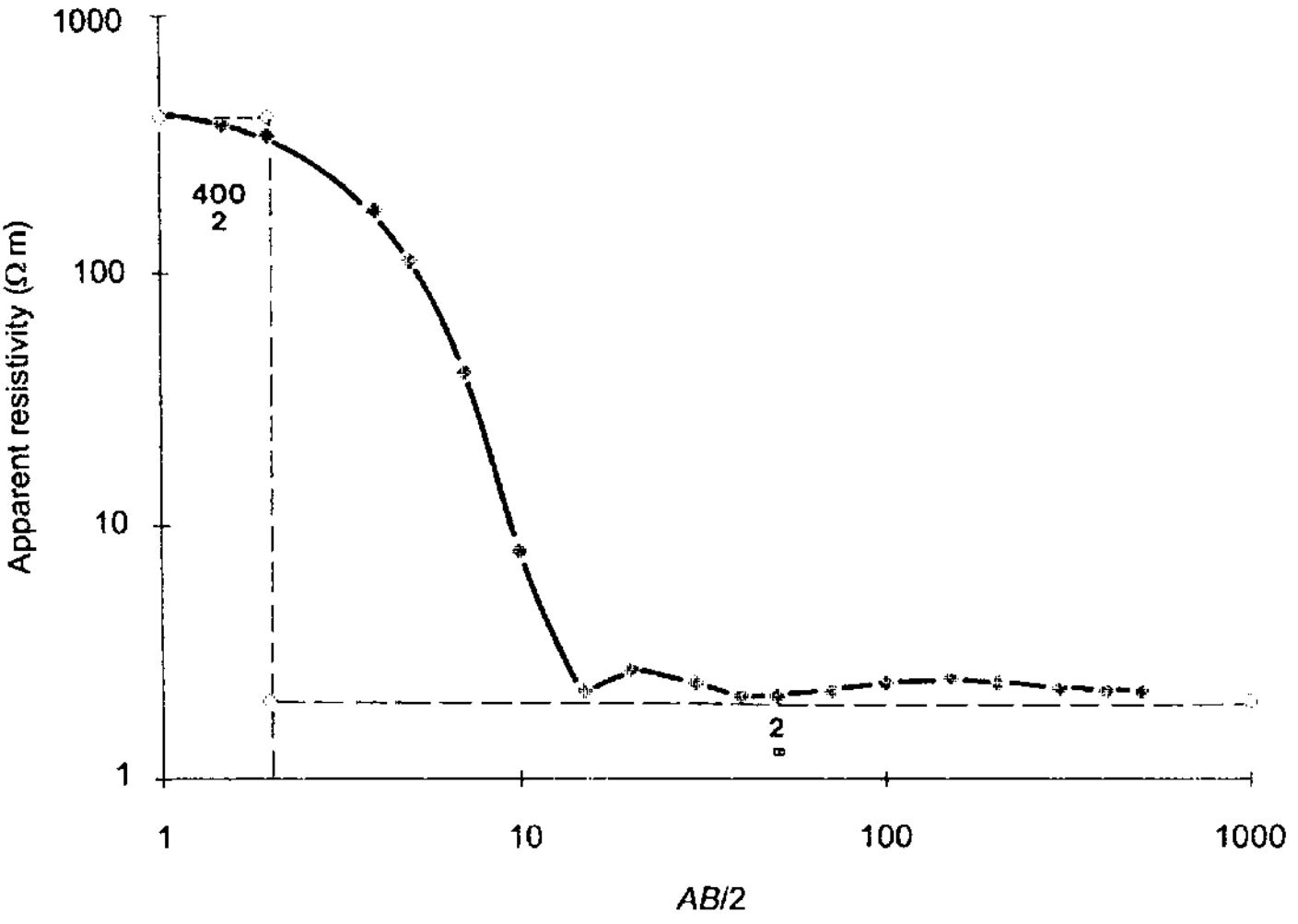

Figure 7.30 Oscillating tail, produced by a computer program that has insufficient coefficients in its linear digital filter to cope with a resistivity contrast of more than 20:1

Much work has gone into the design of linear digital filters to overcome this computational difficulty (e.g. O'Neill and Merrick, 1984), and now modern software packages can cope with even the most extreme resistivity contrasts. Although these packages can deal with as many as 25 layers, 2–6 layers are usually adequate to describe the sub-surface. By increasing the number of layers beyond this, the length of time to produce an acceptable fit is increased dramatically (as there are so many more combinations of layer parameters to try) and, more often than not, the field data do not justify such a level of discrimination and may lead to over-interpretation.

As with master curves, it is always best to fit segments of the field curve at shortest electrode separations first and then to work progressively to greater separations. Once the top layers have been resolved, it is then easier to obtain good estimates of the parameters for the lower layers. The geoelectric basement (the lowest layer) is taken to be semi-infinite in depth and only the layer resistivity is required. Some computer packages display both the field and model curves simultaneously and may produce statistical parameters to describe the closeness of the fit. Optimisation of the interpretation can

be achieved automatically by successive iterations to reduce the degree of misfit until it falls within a specified and acceptable statistical limit.

A major advantage of the computer approach is that it provides an opportunity to investigate the problems of equivalence and suppression quickly and efficiently. See Section 7.5.4 for a more detailed discussion.

With the more sophisticated computer packages, some care has to be taken as to the method by which the convolution method is undertaken as different results may be produced (Figure 7.31). Having said that, as long as the user of the computer program is aware of its advantages and disadvantages, then good and reliable interpretations will be obtained. The danger, as with all uses of computers, is that, for come inexplicable reason, computer-generated results may appear to have greater credibility than those produced by more traditional means, which is not necessarily justified. There is evidently an increasing and undesirable tendency for people to plug data into a computer package, produce a result without thinking about the methodology or of experimental errors or about the geological appropriateness of the model produced. As with all the tools, computers must be used properly. With the availability of laptop computers, at least preliminary interpretation of field curves

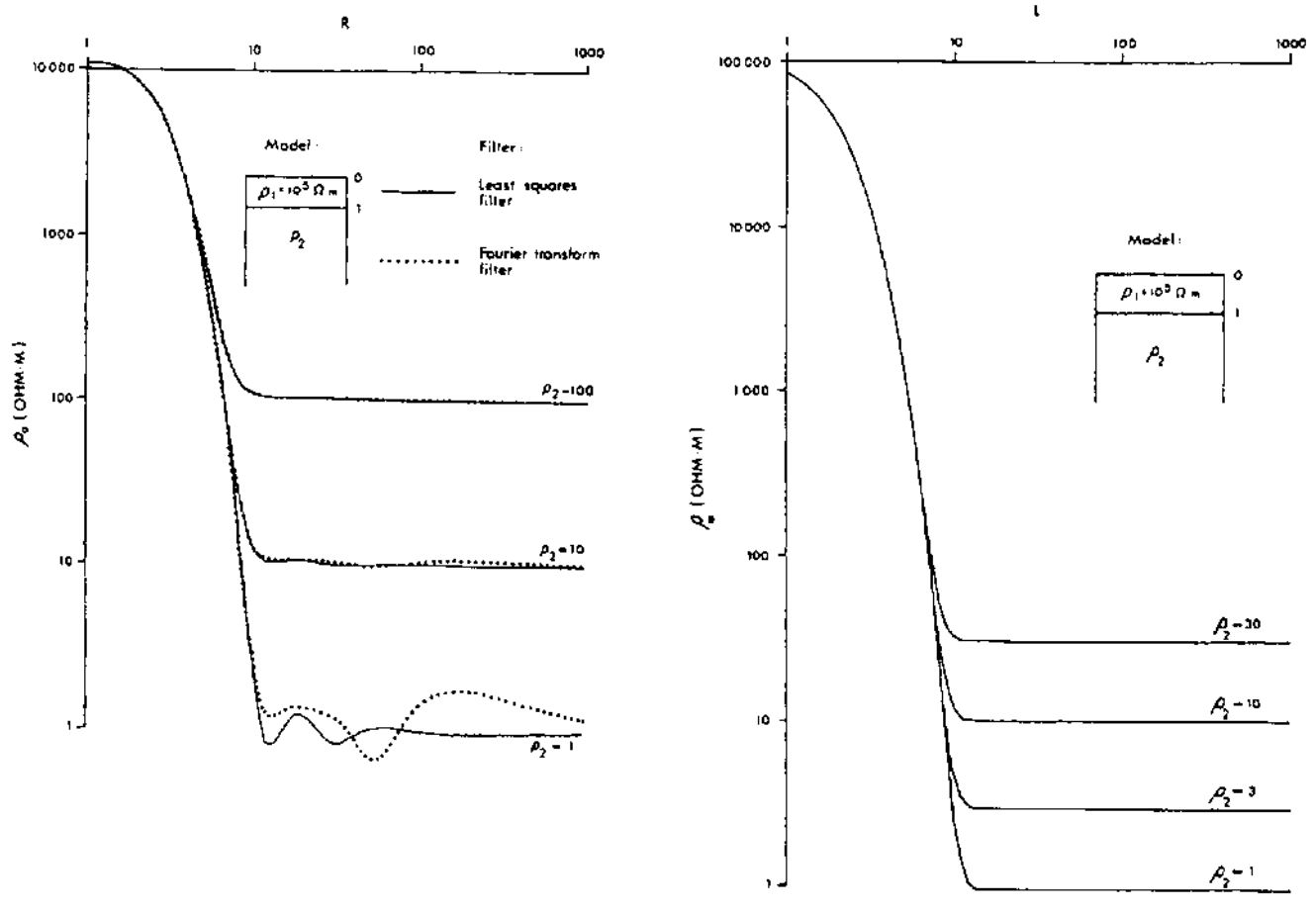

Figure 7.31 Effects of different computational methods on the scale of resistivity contrasts with which the various types of computer program can cope without producing erroneous data. O'Neill and Merrick (1984), by permission

Table 7.4 Material types and their respective resistivity ranges for Kano State, northern Nigeria (Reynolds 1987a)

Material	Resistivity range (Ω m)
Sandy soil with clay	60 100
Clayey sand soil	30–60
Clay	10–50
Weathered biotite granite	50–100
Weathered granite (low biotite)	50–140
Fresh granite	750–8000

Table 7.5 Typical VES interpretation from Kano State, northern Nigeria (Reynolds 1987a)

Layer	Resistivity (Ωm)	Material type
1	95	Very sandy soil
2	32	Clay
3	75	Weathered granite*
4	3500	Fresh granite*

*Granite type also determined from local geological mapping and from local hand-dug wells.

can be done while still in the field, with master and auxiliary curves being used as a backup in case of problems with the computer.

Once an acceptable layer model has been produced for each vertical electrical sounding, the models can be displayed side-by-side much like borehole logs. Between the various VES models, correlations are made between layers with comparable resistivities to build up a two-dimensional picture of both the vertical and lateral variations in resistivity. This can be extended into third dimension so that maps of the individual layer thicknesses, akin to isopachyte maps, can be produced.

The final stage of a resistivity interpretation should be to relate each accepted VES model to the unknown local geology. Tables of resistivities, such as that in Table 7.1, or more geographically specific rock-type/resistivity ranges, can be used instead of referring to layer numbers. The interpretation can then be described in terms of rock units such as those listed in Table 7.4 which are from Kano State in northern Nigeria. Thus a typical resistivity interpretation would consist of perhaps four layers with resistivities as given in Table 7.5.

7.5.4 Equivalence and suppression

In the case of a three-layered model, if the middle layer is conductive relative to those around it, then current flow is focused through and virtually parallel to that layer. The longitudinal conductance S_1 for

this layer is $h_2/\rho_2 = \text{constant}$, and as long as the thickness and resistivity are changed (within limits) so as to maintain that ratio, there will be no appreciable change in the resulting apparent resistivity curve. All the pairs of h_2/ρ_2 are electrically equivalent and no single pair of values is preferable to any other.

However, if computer interpretation of VES curves is undertaken, the range of h and ρ values can be determined so that estimates of the ranges of both thickness and true resistivity can be made. This in itself can be extremely valuable. For example, in northern Nigeria, the subsurface consists of at least three layers – soil, weathered granite and fresh granite. It has been found that weathered granite with a resistivity in the range 50–140 Ω m provides a reasonable source of water (given a saturated thickness >10 m) to supply a hand-pump on a tubewell in a rural village. If the resistivity is less than 50 Ω m, this indicates that there is more clay present and the supply is likely to be inadequate. If the interpretation indicates a second-layer resistivity of 60 Ω m and thickness 12 m, which is characteristic of an acceptable water supply, this layer may be electrically equivalent to only 8 m of material (i.e. too thin) with a resistivity of 40 Ω m (<50 Ω m, thus probably clay rich). This combination could prove to be problematical for a reliable water supply. If, however, the computer models demonstrate that the lowest limit of thickness is 10.5 m and of resistivity is 55 Ω m, then the site could still be used. On the other hand, if the equivalent layer parameters are well into those for the thin clay-rich range, then it is better to try to select another site.

Similarly, if the middle layer is resistive in contrast to those layers surrounding it, then current tends to flow across the layer and thus the product of the layer resistivity and thickness (which is the transverse resistance, T; see Box 7.9) is constant. If, for example, a gravel layer with resistivity 260 Ω m and thickness 2 m is sandwiched between soil ($\rho_1 < 200$ Ω m) and bedrock ($\rho_3 > 4500$ Ω m), then $T_2 = 520$ Ω m^2. If the model thickness is reduced to only 1 m, the gravel layer resistivity must be doubled. Similarly, if the resistivity is reduced the thickness must be increased to compensate. Computer analysis can be used again to resolve the range of layer parameters which produce no discernible change in the apparent resistivity curve.

In the example illustrated in Figure 7.32A, a layer of resistivity 35 Ω m and thickness 2 m is sandwiched between an upper layer of resistivity 350 Ω m and thickness 6 m and the bedrock of resistivity 4500 Ω m (upper bar below curve). The longitudinal conductance S_L for layer 2 is 0.057 siemens (2 m/35 Ω m). The two other models depicted by horizontal bars are extreme values for the middle layer, but which have the same longitudinal conductance and which gave rise to model curves that are coincident with the one shown to better than 0.5%. The depths to bedrock thus range from 7.1 m to 10 m (in the models calculated) and there is no geophysical way of telling which model is 'right'. It is by considering whether a 10 cm thick highly

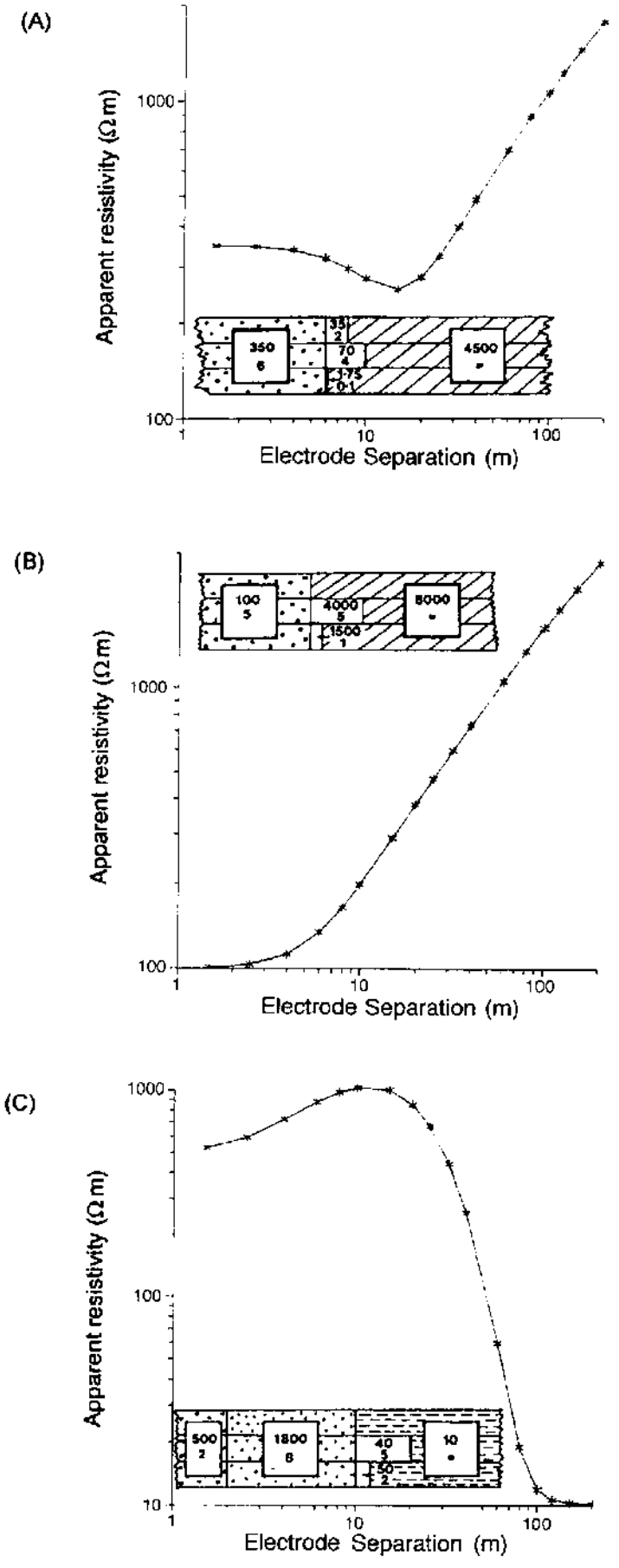

Figure 7.32 (A) Equivalence test on a three-layer model. The models indicated in the lower two horizontal bars are electrically equivalent to the model in the top bar. Pairs of numbers are true resistivity (Ω m) above layer thickness (m). Suppression tests for (B) an ascending curve and (C) a four-layer descending curve

conductive horizon is more geologically reasonable than a far thicker, more resistive band, that the most appropriate model can be chosen.

An additional form of equivalence needs to be borne in mind at the interpretation stage and that is the equivalence between an isotropic and an anisotropic layer. This Doll–Maillet equivalence (see Maillet 1947) results in an overestimate of layer thickness in proportion to the amount of anisotropy which, if present, is of the order of 10–30%.

Apart from equivalence, the other interpretational problem is that of *suppression*. This is particularly a problem when three (or more) layers are present and their resistivities are ascending with depth (*A*-type curve; see Figure 7.26B) or descending with depth (*Q*-type curve; see Figure 7.26D). The middle intermediate layer may not be evident on the field curve and so its expression on the apparent resistivity graph is suppressed. The computer method is invaluable here to estimate (1) if there is a hidden layer present, and (2) if there is, its range of layer parameters. In Figure 7.32B, curves for three-layer models (middle and lower bars) with second layers of resistivity 1500 to 4000 Ω m and thicknesses 1 to 5 m are graphically indistinguishable from that of a two-layer model (top bar). For a layer to be suppressed, its resistivity should approach that of the one below so that the resistivity contrast between the top and the suppressed layer is comparable to that between the top and lowermost layers. The effects of missing such a suppressed layer can have major effects on the estimation of the depth to bedrock. In Figure 7.32C, a similar example is given but for descending resistivities. The curves for models with a suppressed layer (middle and lower bars) fit the three-layer case (top bar) to better than 1% and are indistinguishable graphically.

If the intermediate layers are thin with respect to those overlying, and if either equivalence or suppression is suspected, master curves will provide no solution. However, equivalent or suppressed layers can be modelled very effectively using computer methods in conjunction with a knowledge of what is geologically reasonable for the field area in question.

7.5.5 Inversion, deconvolution and numerical modelling

Zohdy (1989) produced a technique for the automatic inversion of resistivity sounding curves. Least-squares optimisation is used in which a starting model is adjusted successively until the difference between the observed and model pseudo-sections is reduced to a minimum (Barker 1992). It is assumed that there are as many sub-surface layers as there are data points on the field sounding curve (Figure 7.33) and that the true resistivity of each of these assumed layers is that of the corresponding apparent resistivity value. The mean depth of each layer is taken as the electrode spacing at which the apparent resistivity was measured multiplied by some constant. The value of this constant is one which reduces the difference between

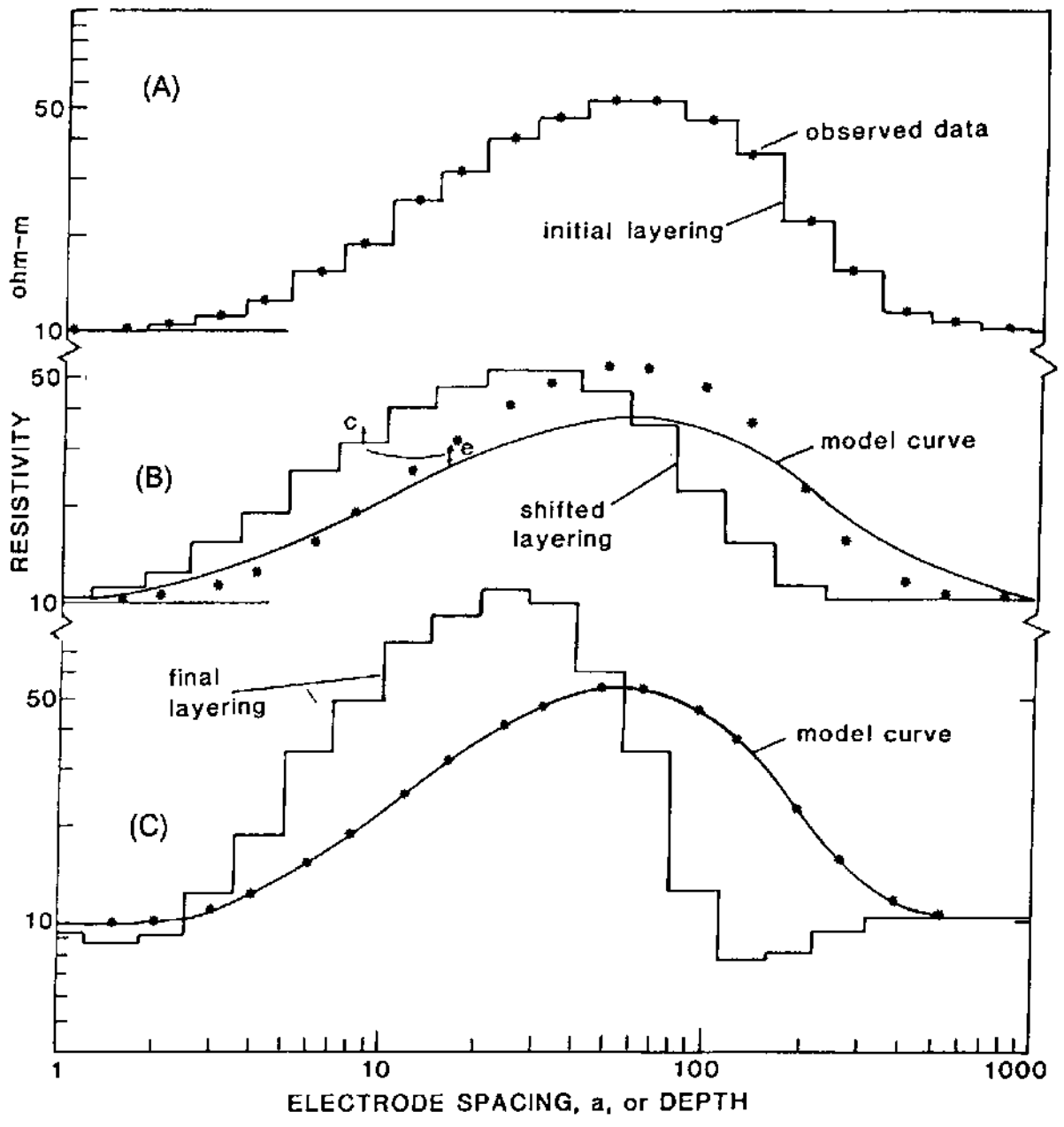

the observed and model resistivity curves to a minimum and is determined by trial and error.

The starting model is used to generate a theoretical synthetic sounding curve which is compared with the field data. An iterative process is then carried out to adjust the resistivities of the model while keeping the boundaries fixed. After each iteration the theoretical curve is recalculated and compared with the field data. This process is repeated until the RMS difference between the two curves reaches a minimum (Figure 7.33).

Zohdy's method has been developed by Barker (1992) for the inversion of SSI apparent resistivity pseudo-sections and more recently by using a deconvolution method (Barker, personal communication). Consequently, it is possible to produce fully automated

Figure 7.33 Automatic sounding inversion technique. (A) Observed data and initial layering. (B) Shifted layering and resulting model sounding curve. The difference (e) between the model and observed curves is used to apply a correction (c) to the layering. (C) The final layering and resulting model curve that is closely similar to the observed data. From Barker (1992), by permission

inversions of SSI pseudo-sections. The final results are displayed also as pseudo-sections in terms of the variations in true resistivity with depth as a function of distance along the array. Examples of inverted pseudo-sections are given in Section 7.7.

In addition to the above inversion routines, others have been produced, often in association with particular equipment, and also as specific developments of true tomographic imaging (e.g. Shima 1990; Daily and Owen 1991; Noel and Xu 1991; Xu and Noel 1993). Commercially available imaging inversion packages are available from a number of sources and are related to a style of data acquisition and equipment. Packages vary from those which can operate easily on a laptop computer, more sophisticated processing may require the computational power of a workstation with full colour plotting facilities.

Finite-element forward modelling can be undertaken using commercially available software. The resistivity response for a two-dimensional model is calculated and displayed as a pseudo-section for comparison with the original field data. This approach is used to help generate realistic sub-surface geometries in definable model structures (e.g. Figure 7.34).

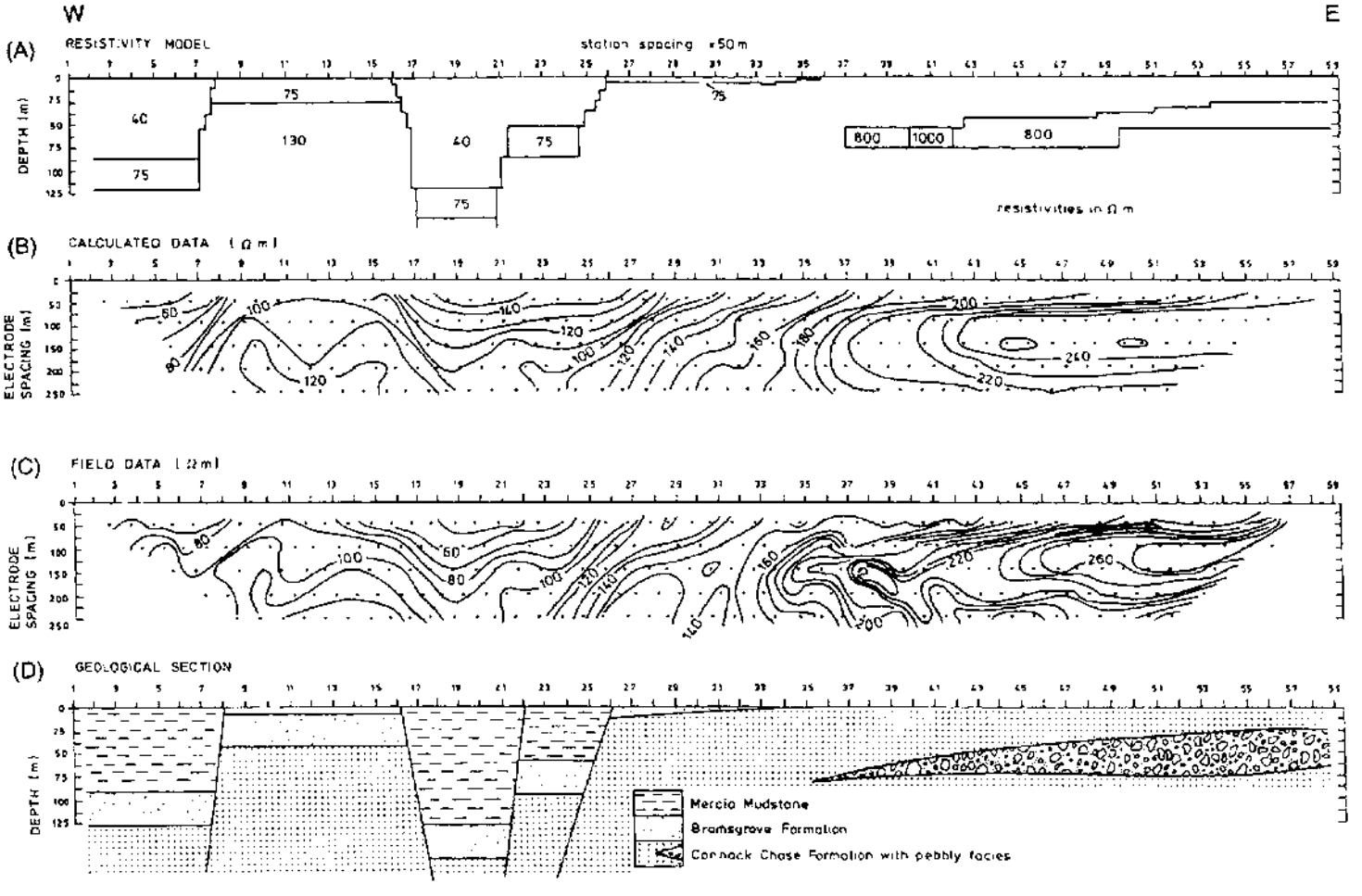

Figure 7.34 Final interpretation of faulted Triassic sequence in Staffordshire, UK. (A) Two-dimensional finite difference model. (B) Computed apparent resistivity pseudo-section. (C) Field data. (D) Geological interpretation based on (A) and additional information. From Griffiths *et al.* (1990), by permission

7.6 MISE-À-LA-MASSE METHOD

The mise-à-la-masse or 'charged-body potential' method is a development of the CST technique but involves placing one current electrode within a conducting body and the other current electrode at a semi-infinite distance away on the surface (Figure 7.35). The voltage between a pair of potential electrodes is measured with appropriate corrections for any self-potentials.

For an isolated conductor in a homogeneous medium, the lines of equipotential should be concentric around the conductor (Figure 7.36A). In reality, lines of equipotential are distorted around an irregularly shaped conductive orebody (Figure 7.36B) and can be used to delimit the spatial extent of such a feature more effectively than using the standard CST method. The mise-à-la-masse method is particularly useful in checking whether a particular conductive mineral-show forms an isolated mass or is part of a larger electrically connected orebody. In areas where there is a rough topography, terrain corrections may need to be applied (Oppliger 1984). There are no general rules that can be applied to mise-à-la-masse data. Each survey is taken on its own merits and a plausible model constructed for each situation, although Eloranta (1984), for example, has attempted to produce a theoretical model to account for the observed potential distributions.

There are two approaches in interpretation. One uses the potential only and uses the maximum values as being indicative of the conductive body. The other converts the potential data to apparent resistivities and thus a high surface voltage manifests itself in a high

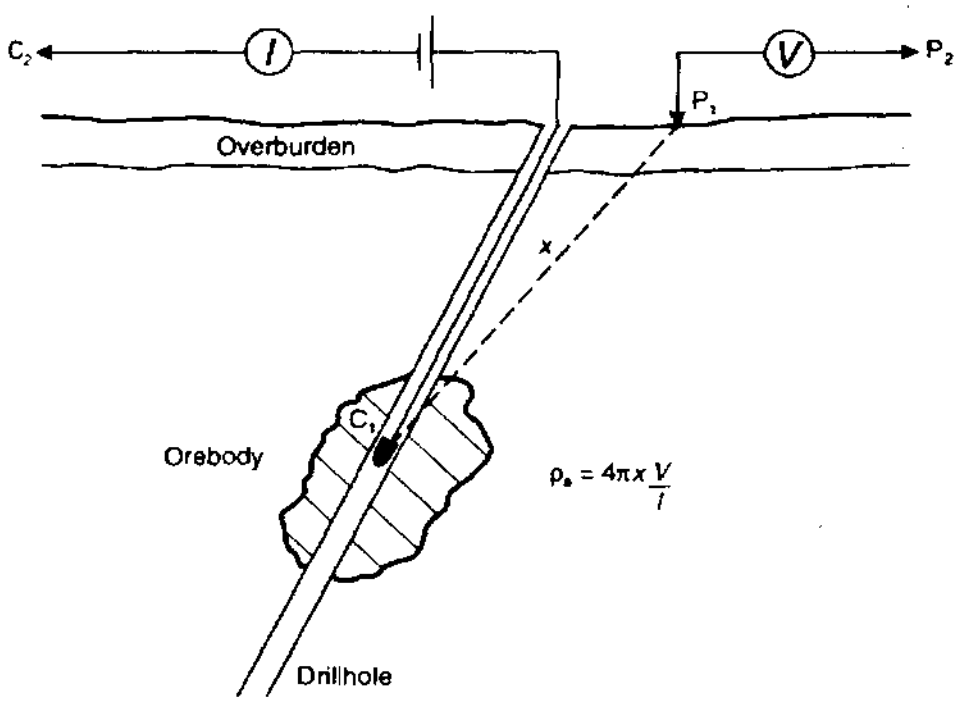

Figure 7.35 Positions of electrodes used in a mise-à-la-masse survey. One form of geometric factor is given where x is the distance between the C_1 electrode down the hole and the P_1 mobile electrode on the ground surface

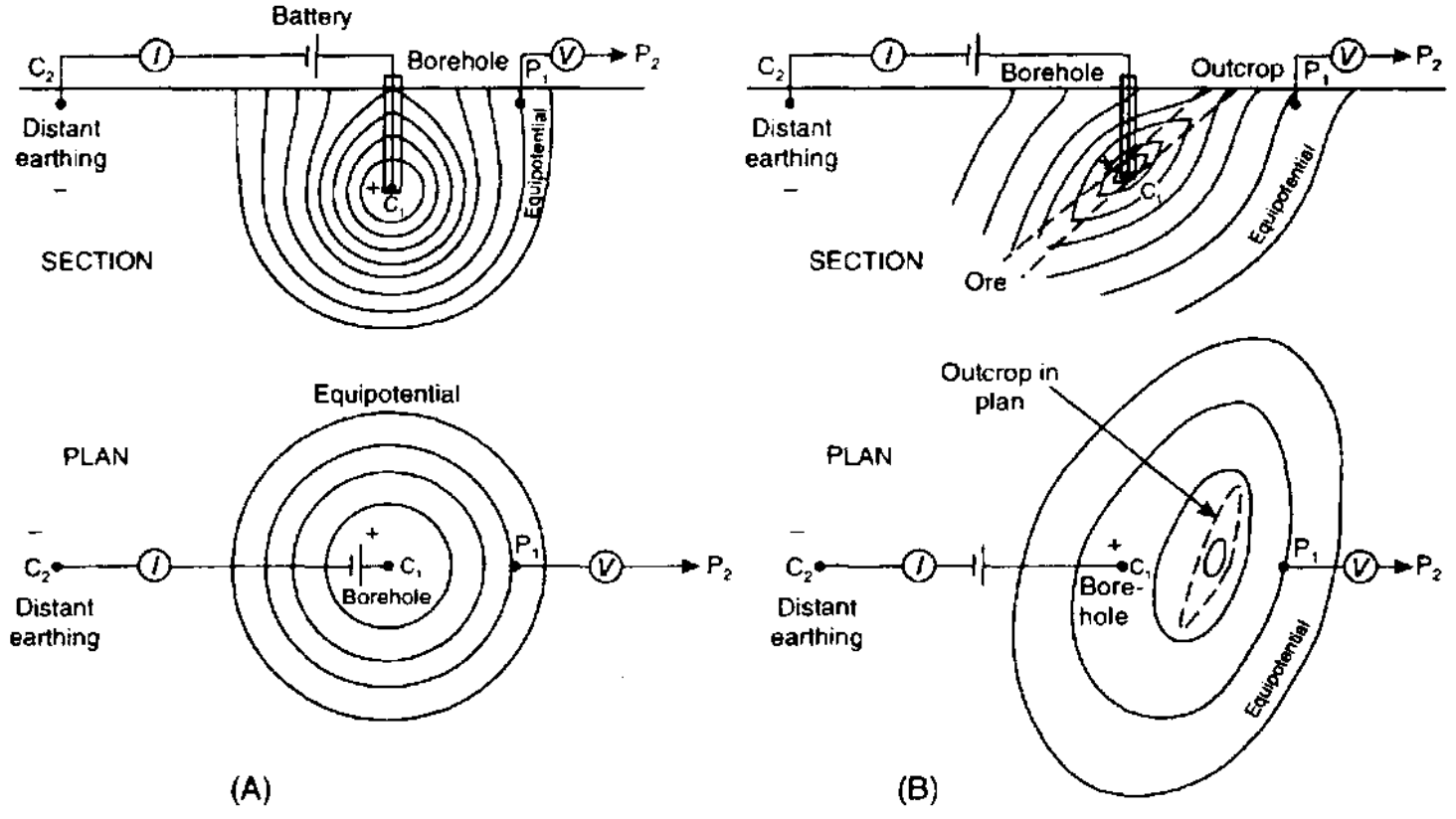

Figure 7.36 (A) Concentric and symmetrical distribution of equipotential lines around a current electrode emplaced within a homogeneous medium. (B) Distortion of equipotentials due to the presence of an orebody. After Parasnis (1966), by permission

apparent resistivity ($\rho_a = 4\pi x\, V/I$, where x is the distance between C_1 and P_1).

An example of a mise-à-la-masse survey in ore prospecting in Sweden is shown in Figure 7.37. One current electrode was placed 65 m below ground, 89 m down an inclined borehole (borehole 33) and the surface potentials mapped (Figure 7.37A). As there were so many boreholes available in this survey, it was possible to determine the vertical distribution of potentials as well as the surface equipotential distribution (Figure 7.37B). Combining all the available data, it was possible to obtain a three-dimensional image of the potential distribution associated with the target orebody and thus delimit its size, strike and structure (Parasnis 1967).

A second example is shown in Figure 7.38, in which the effects of terrain on the surface potentials can be clearly seen. The positive electrode was placed at 220 m depth down a 1 km deep borehole (Figure 7.38A) and the surface potentials mapped (Figures 7.38B and C). Oppliger (1984) found that when terrain slopes exceeds 10°, surface electric potentials can be adversely affected. The terrain-corrected surface potentials are shown in Figure 7.38C. The main differences are that the low of 85 Ω m and the high of 168 Ω m both change in value (to 100 and 150 Ω m respectively) and, in particular, the orientation of the elongate apparent resistivity high is rotated through 30°. The ridge form of this resistive anomaly suggests that

Figure 7.37 (*opposite*) (A) Map of surface potentials obtained in a mise-à-la-masse survey in Sweden with C_1 in borehole 33. The location of Line 2680S is also shown. (B) Potentials in a vertical section through profile 2680S. From Parasnis (1967), by permission

(A)

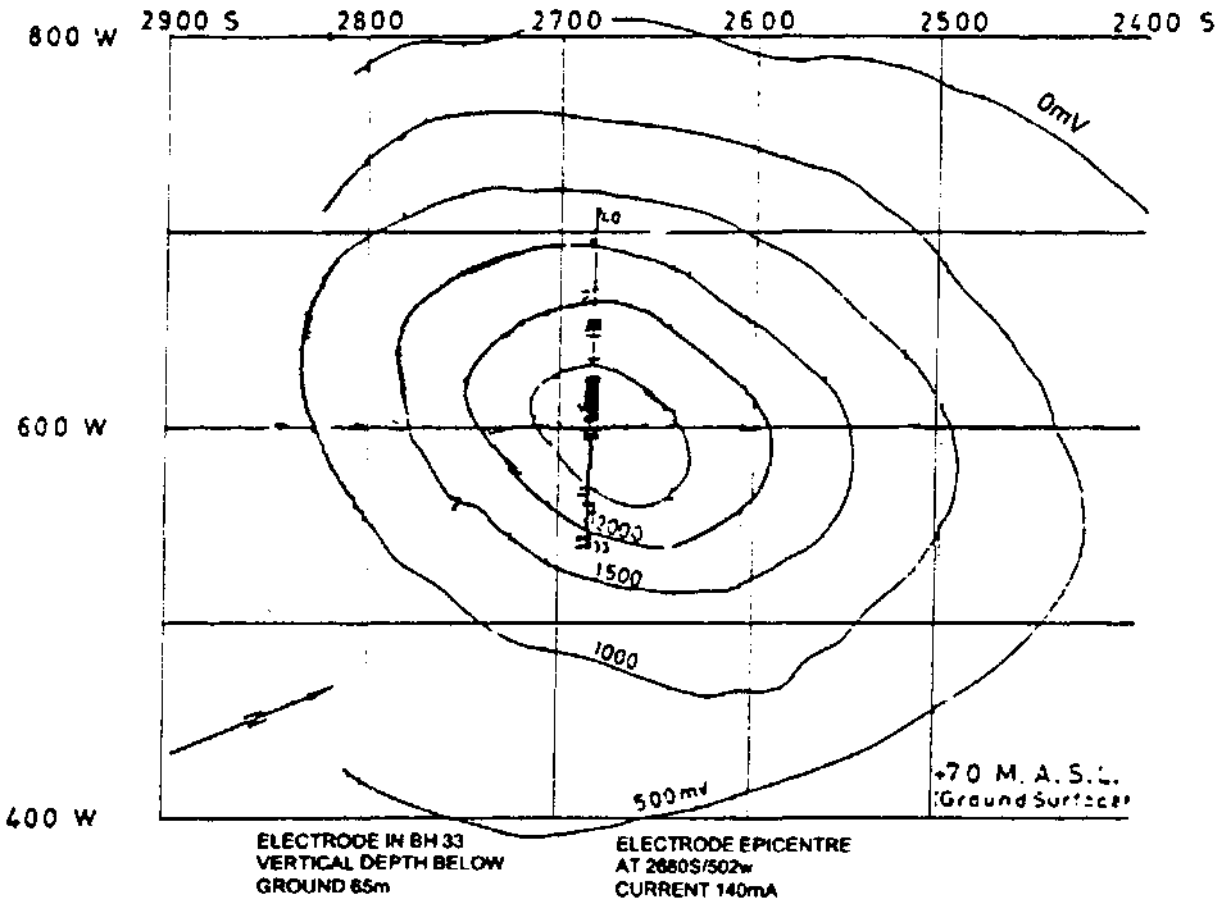
800 W
600 W
400 W
2900 S
2800
2700
2600
2500
2400 S
0mV
3000
1500
1000
500mV
+70 M.A.S.L.
(Ground Surface)
ELECTRODE IN BH 33
VERTICAL DEPTH BELOW
GROUND 65m
ELECTRODE EPICENTRE
AT 2680S/502W
CURRENT 140mA

(B)

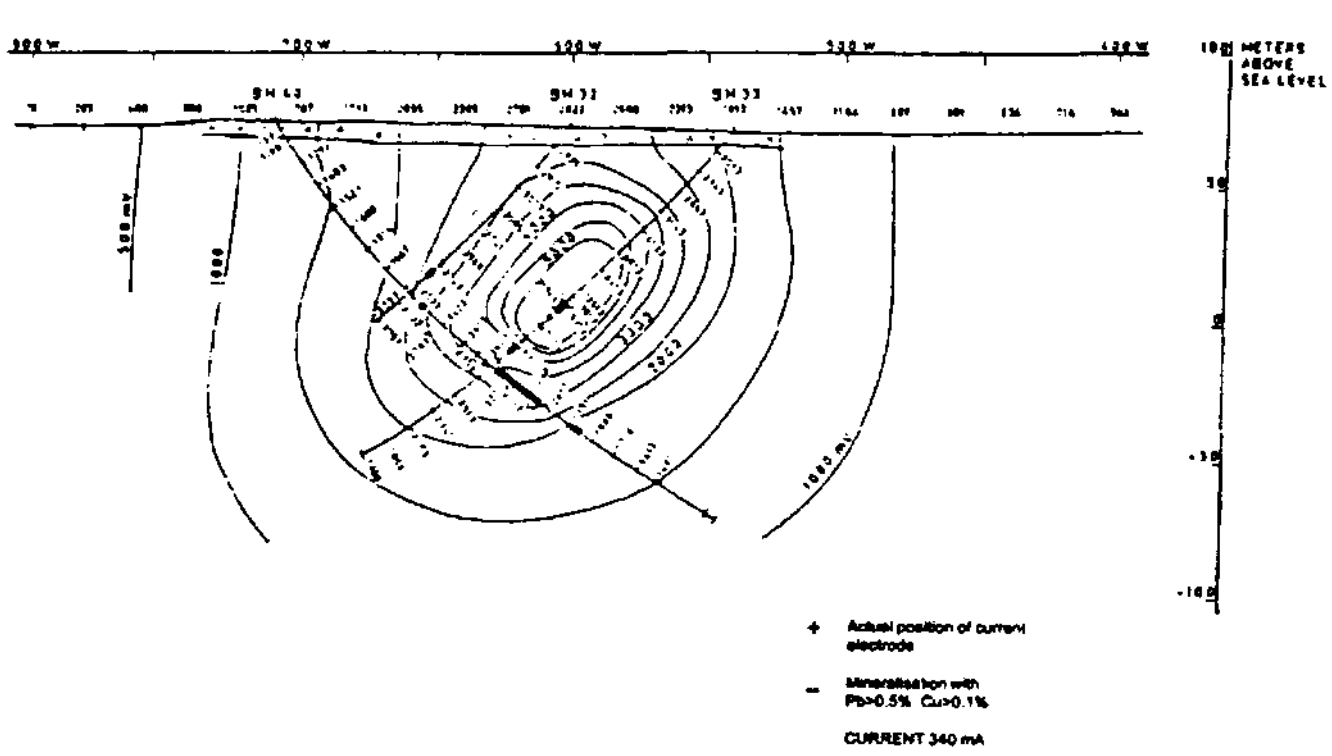
PROFILE 2680 S
BH 33
METERS
ABOVE
SEA LEVEL
Actual position of current electrode
CURRENT 340 mA

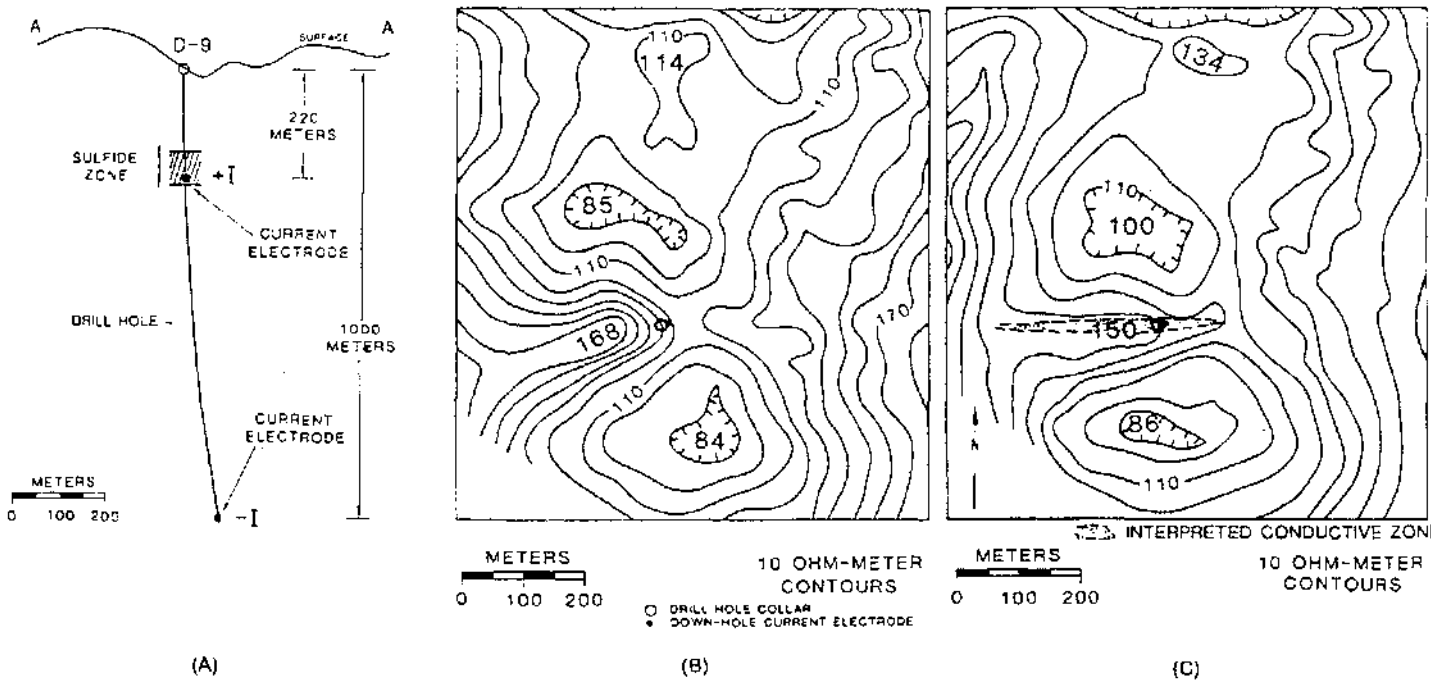

Figure 7.38 (A) Current electrode configurations. (B) Actual mise-à-la-masse apparent resistivities measured on the surface around inclined borehole D-9. Contours are every 10 Ω m. (C) Terrain-corrected apparent resistivities for the same survey with an interpreted conductive zone indicated. From Oppliger (1984), by permission

a conductive body is bounded to the north and south (as indicated by the marked lows) and extends a limited way in an east–west direction. This interpretation has been confirmed by other investigations.

7.7 APPLICATIONS AND CASE HISTORIES

7.7.1 Engineering site investigations

7.7.1.1 Sub-surface collapse features

In a small village in east Devon, a 5 m diameter hole appeared overnight in the middle of the road. The local water main had been ruptured and had discharged for over 12 hours and all the water had disappeared down a fissure into underlying limestone. Several of the local buildings started to crack badly, and on investigation it was found that the rafted foundations of several houses had broken and the houses were literally cracking open at the seams, resulting in the emergency evacuation of the residents.

A resistivity survey was initiated in order to determine the sub-surface extent of the problem prior to drilling. Fortunately, the front gardens of the houses affected were all open-plan so there was no difficulty in access, but space was at a premium. A series of constant-separation traverses was instigated using the Wenner array with electrode separations of 10, 15 and 20 m. The resulting apparent resistivity values were plotted as a contour map (Figure 7.39). It was

Figure 7.39 (*opposite*) (A) Apparent resistivity isometric projection obtained using constant-separation traverses with an electrode separation of 10 m. (B) Modelled microgravity profile that would be expected for the geological model shown in (C): interpreted depth to limestone constrained by drilling. A north–south profile is shown in Figure 7.20. The position of a clay-filled solution feature is arrowed

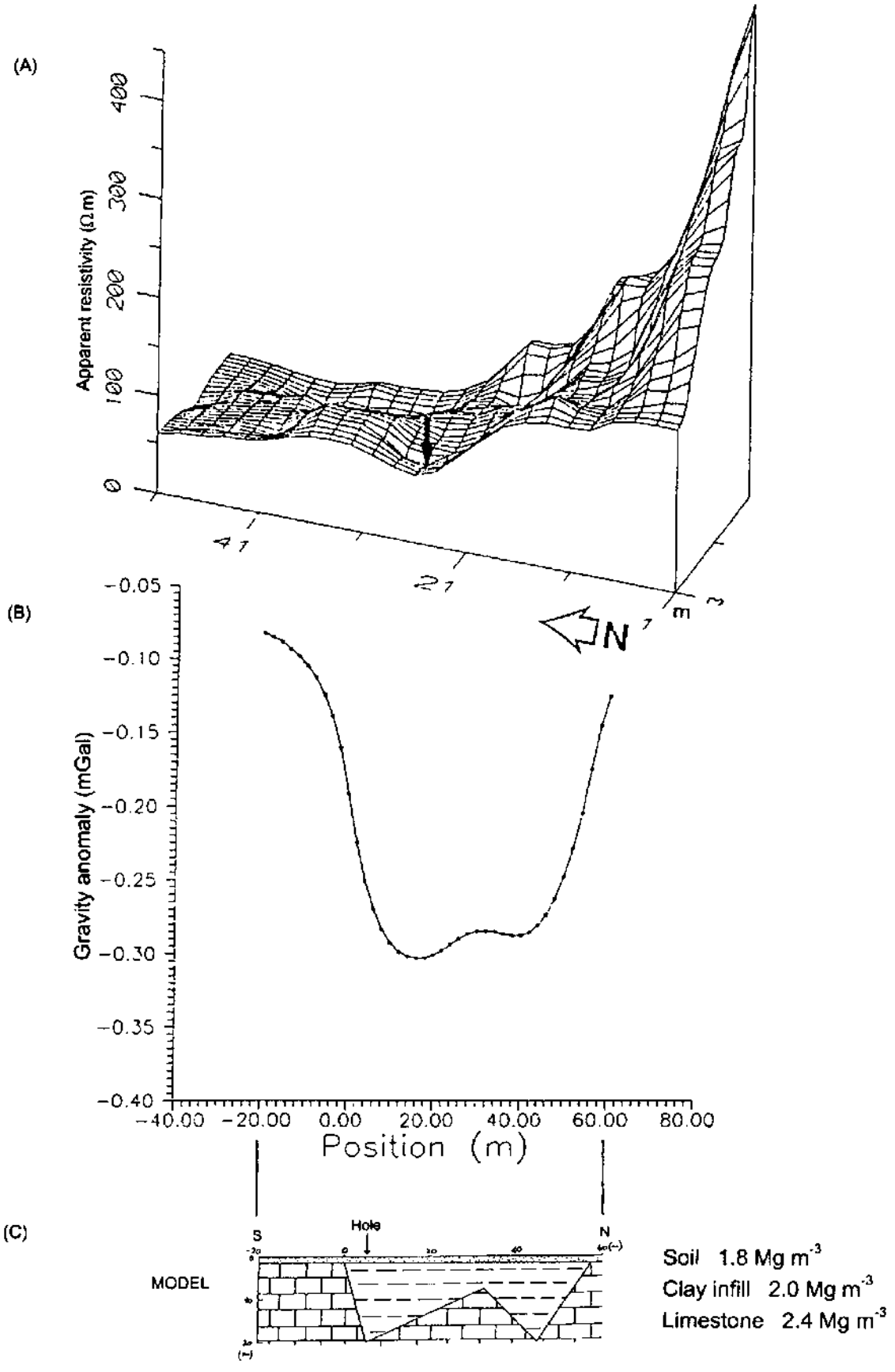
(A)
Apparent resistivity (Ω.m)
0
100
200
300
400
N
m
(B)
Gravity anomaly (mGal)
−0.05
−0.10
−0.15
−0.20
−0.25
−0.30
−0.35
−0.40
−40.00
−20.00
0.00
20.00
40.00
60.00
80.00
Position (m)
(C)
MODEL
S
Hole
N
Soil 1.8 Mg m-3
Clay infill 2.0 Mg m-3
Limestone 2.4 Mg m-3

clear that where the hole had appeared, there was a deep infill of clay. It was this that had slipped through a neck of a fissure into a cave beneath, resulting in subsidence beneath the foundations of the houses and the rupture of the water main. The discharging water disappeared into this newly discovered cavern. The clay depth decreased uphill and suddenly increased again, indicating further clay-filled fissures. On drilling these resistivity anomalies, the depth to limestone was confirmed. One drillhole penetrated the cave but failed to locate the bottom; the cave was at least 20 m deep.

7.7.1.2 Burial of trunk sewer

A route for a proposed new trunk sewer in South Wales was investigated using electrical resistivity methods because access for drilling equipment was not possible. Both vertical electrical soundings and constant-separation traverses were used along the route and compared with available borehole data from the National Coal Board (Prentice and McDowell 1976). The material through which the sewer trench was to have been dug consisted of superficial deposits overlying Coal Measure sandstone and mudstone. The Coal Measure material was anticipated to be massive and strong and thus hard to excavate, while saturated superficial deposits and Coal Measure shales were thought to provide very unstable trench walls. The CST results using a Wenner array with 10 m electrode separation and 10 m station interval revealed locations where sandstone bedrock was interpreted to be close to the surface which would have required

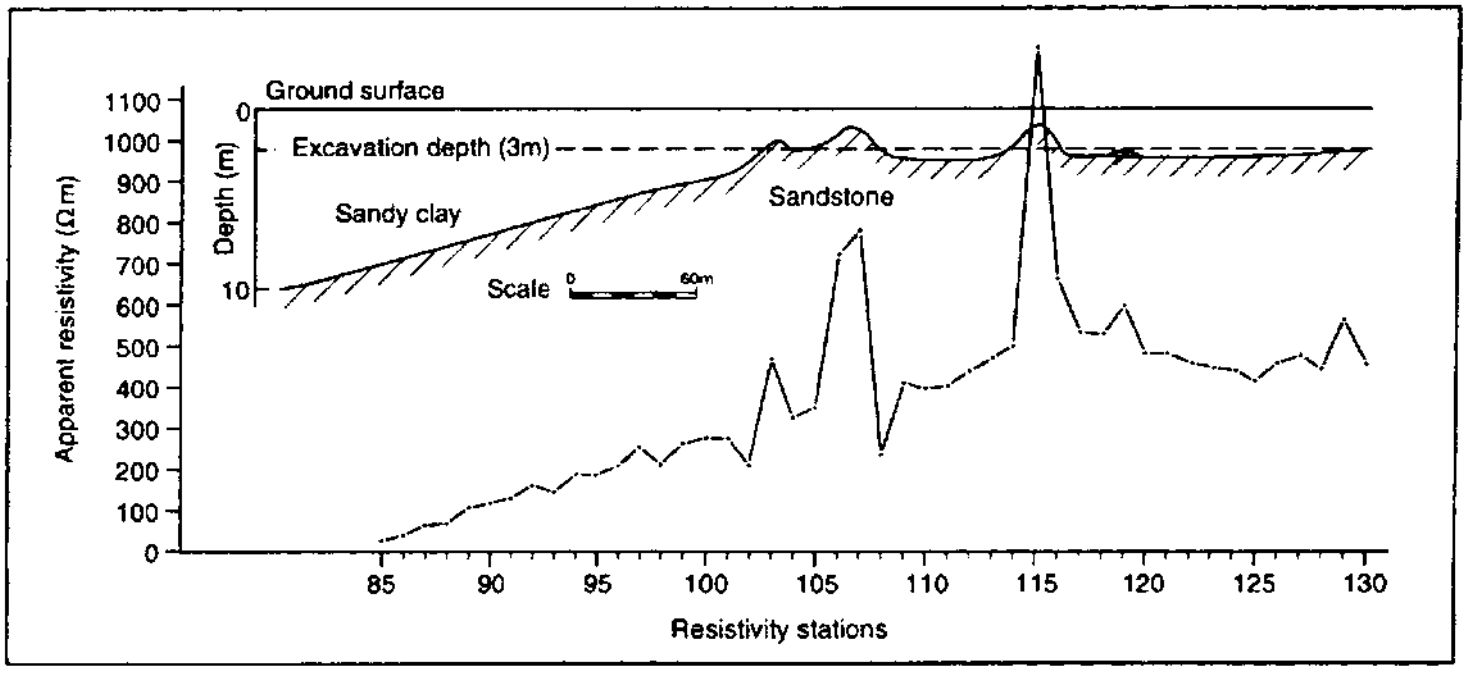

Figure 7.40 Constant-separation traverse data obtained along the proposed route of a new trunk sewer in South Wales, with the interpreted geological section. After Prentice and McDowell (1976), by permission

blasting for the excavation for the new sewer (Figure 7.40). Seismic refraction was also used to obtain acoustic velocities, which in turn were used to determine whether blasting or ripping techniques should be used in the excavation.

7.7.1.3 Location of permafrost

The presence of massive ground ice and frozen ground provides considerable problems to engineers involved in construction projects. First there are the difficulties in excavation, and secondly, substantial problems can emerge with the thawing of such affected ground. It is therefore vital that ice wedges and lenses, and the extent and degree of permafrost, can be determined well in advance.

Ice has a very high DC electrical resistivity in the range from 1 MΩ m to 120 MΩ m (Reynolds and Paren 1984) and therefore forms a particularly resistive target. A variety of geophysical profiles over a proposed road cutting near Fairbanks in Alaska are illustrated in Figure 7.41. Data obtained in the spring show more variability and resolution than when an active layer of thawed ground is present, as in the autumn measurements (Osterkamp and Jurick 1980). Other geophysical methods which are used successfully in this application are electromagnetic profiling, microgravity and ground radar surveying.

7.7.1.4 Location of buried foundations

As part of a trial survey in January 1993, electrical resistivity subsurface imaging was used at a disused railway yard in order to locate old foundations concealed beneath railway ballast. Details of the geophysical survey have been described in more detail by Reynolds and Taylor (1994, 1995) and Reynolds (1995).

The SSI survey was carried out adjacent to a metal chain-link fence and an old diesel tank, and about 3 m from an existing building. It was thought that the remains of two former buildings might still be present beneath the railway ballast and the existing building. The site was totally unsuitable for electromagnetic profiling, because of the above ground structures. It was also unsuitable for ground penetrating radar owing to the coarse ballast and potentially conductive ash also found on site. Despite extremely high electrode contact resistances, a 25 m long array was surveyed with an inter-electrode separation of 1 m. This provided a vertical resolution of 0.5 m or better. The apparent resistivity data were filtered to remove noise spikes and displayed as a pseudo-section (Figure 7.42 A) which was inverted using a deconvolution technique (Barker, personal communication). The final pseudo-section of true resistivities against depth shows a general increase in resistivity with depth (Figure 7.42B). In particular, it revealed two areas of extremely high resistivity (> 125 000 Ω m)

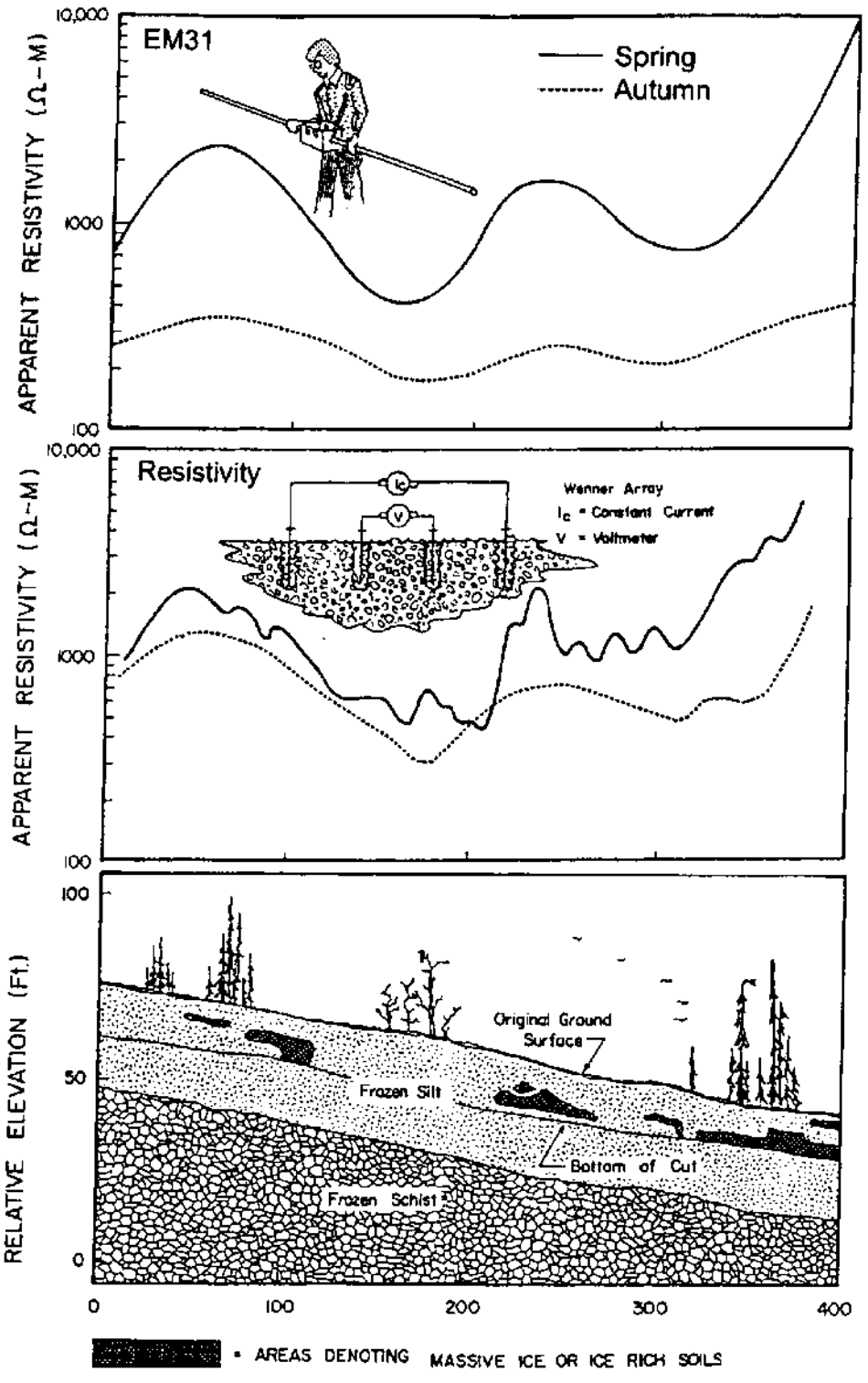

Figure 7.41 Massive ice and frozen ground in a sub-surface profile of a proposed road cut near Fairbanks, Alaska. Also shown are the spring and autumn survey data obtained using electrical resistivity constant-separation traversing and electromagnetic induction (EM31). Massive ground ice produces significant apparent resistivity highs. From Osterkamp and Jurick (1980), by permission

at a depth of about 1 m which had very flat tops to the anomalies. These were interpreted to be due to buried foundations. The main anomaly (between 6 and 11 m along the array) was found to correlate with the outline of one former building on an old plan. The second feature (starting at around 18 m) is thought to be due to the other old building. However, the location was found to be several metres further away from the first building than indicated on the plans. The

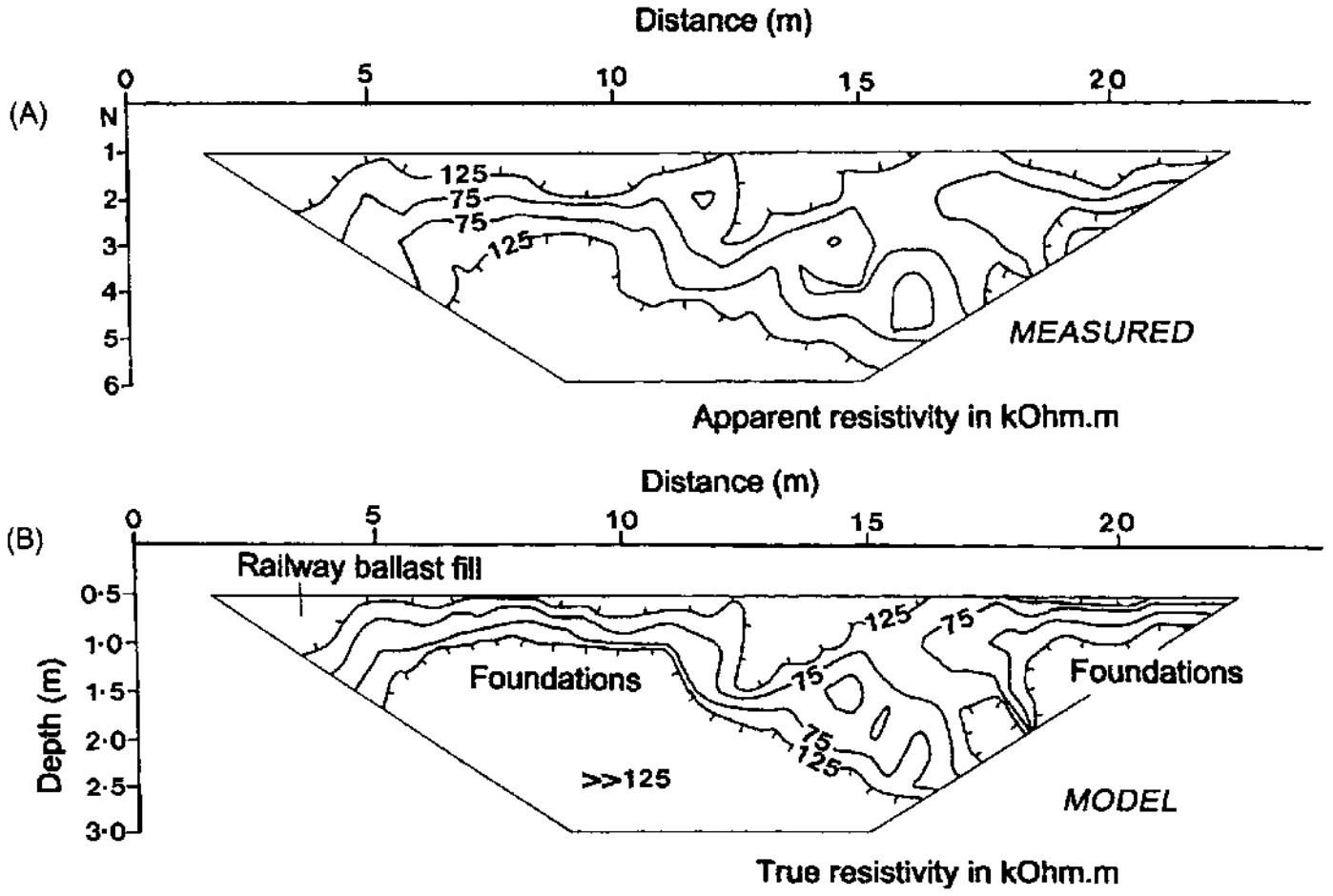

depth to the foundation was thought to be reasonable as adjacent brick slabs excavated a few metres away were found at a comparable depth.

Figure 7.42 Electrical resistivity subsurface imaging pseudo-sections: (A) apparent resistivity profile, and (B) true resistivity–depth profile, over buried concrete slabs at 1 m depth. From Reynolds and Taylor (1995), by permission

7.7.2 Groundwater and landfill surveys

7.7.2.1 Detection of saline groundwater

In the mid-1950s, a comprehensive electrical resistivity survey programme was initiated in order to map out saline groundwater in areas of the Netherlands below or at mean sea level. Figure 7.43 shows schematically the nature of the hydrogeology in the western part of the Netherlands. The vertical electrical soundings provided a means of obtaining information about the vertical distribution of fresh, brackish and saline water bodies and their areal extent (Figure 7.44).

Pockets of saline water were found which were thought to be remnants from before the fifteenth century after which time the present sea-dyke formed, cutting off the sea. To the west of Alkmaar, some 30 m of saline water was found above tens of metres of fresh water separated by an impermeable clay layer. Major demands for construction sand for the building of new roads and urbanisation

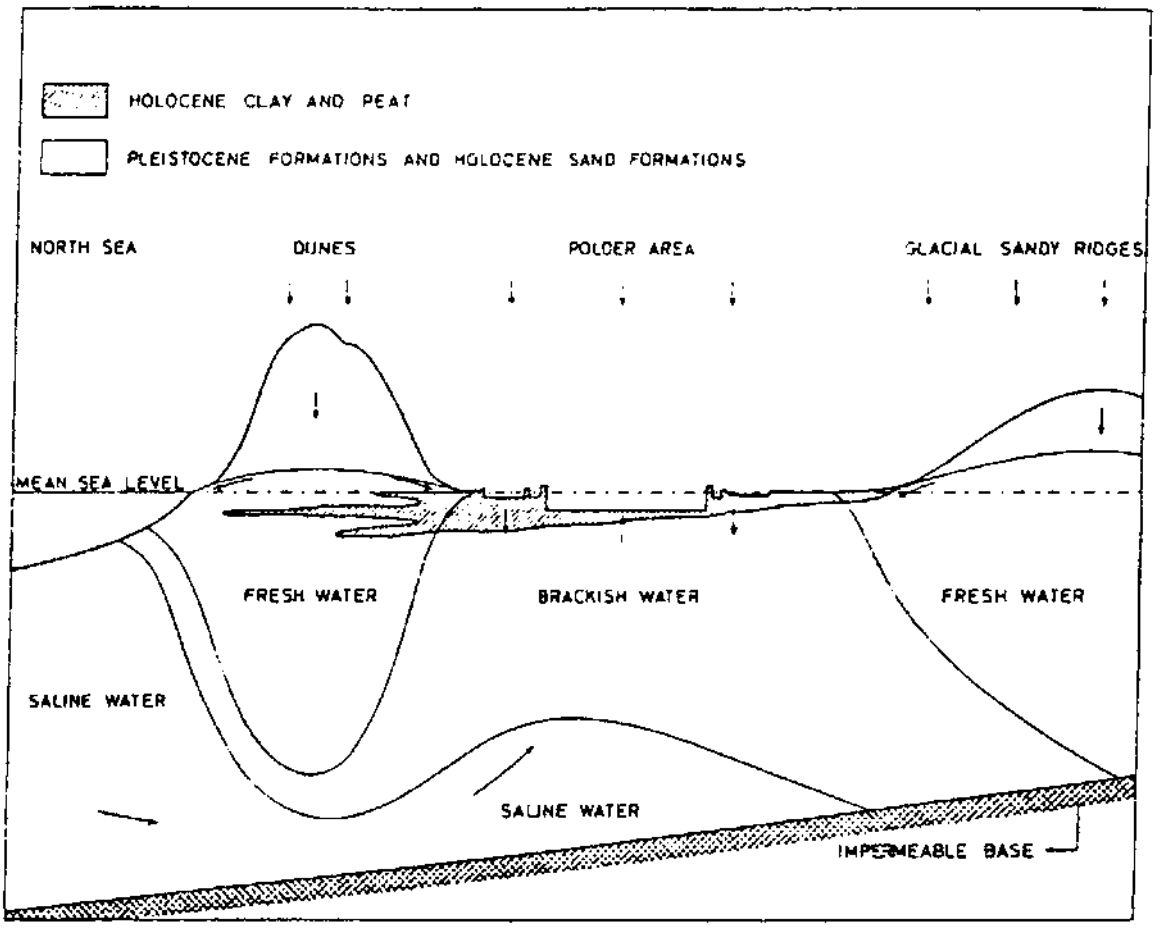

Figure 7.43 Schematic hydrogeological cross-section for the western part of the Netherlands. From van Dam and Meulenkamp (1967), by permission

could have led to the extraction of sands with the demise of the clay barrier. This could have resulted in the mixing of the water bodies and the contamination of an otherwise potable water supply. Furthermore, correlation of resistivities from modelling of VES data with borehole information about groundwater chemistry has led to a relationship between chloride content and resistivity. Consequently, it is possible to determine chloride content of the groundwater from the resistivity data.

7.7.2.2 Groundwater potential

In Kano state, northern Nigeria, an internationally funded aid programme was established in the 1980s to provide tubewells with handpumps for 1000 villages in rural areas. Village populations ranged from several hundred to no larger than 2000 people, but all were in very remote locations. Failure to obtain a reliable supply of water would have resulted in many of the villages being abandoned and the populations moving to the larger towns, thereby compounding the local problems of sanitation and health, education and employment, and the demise of rural culture and skills.

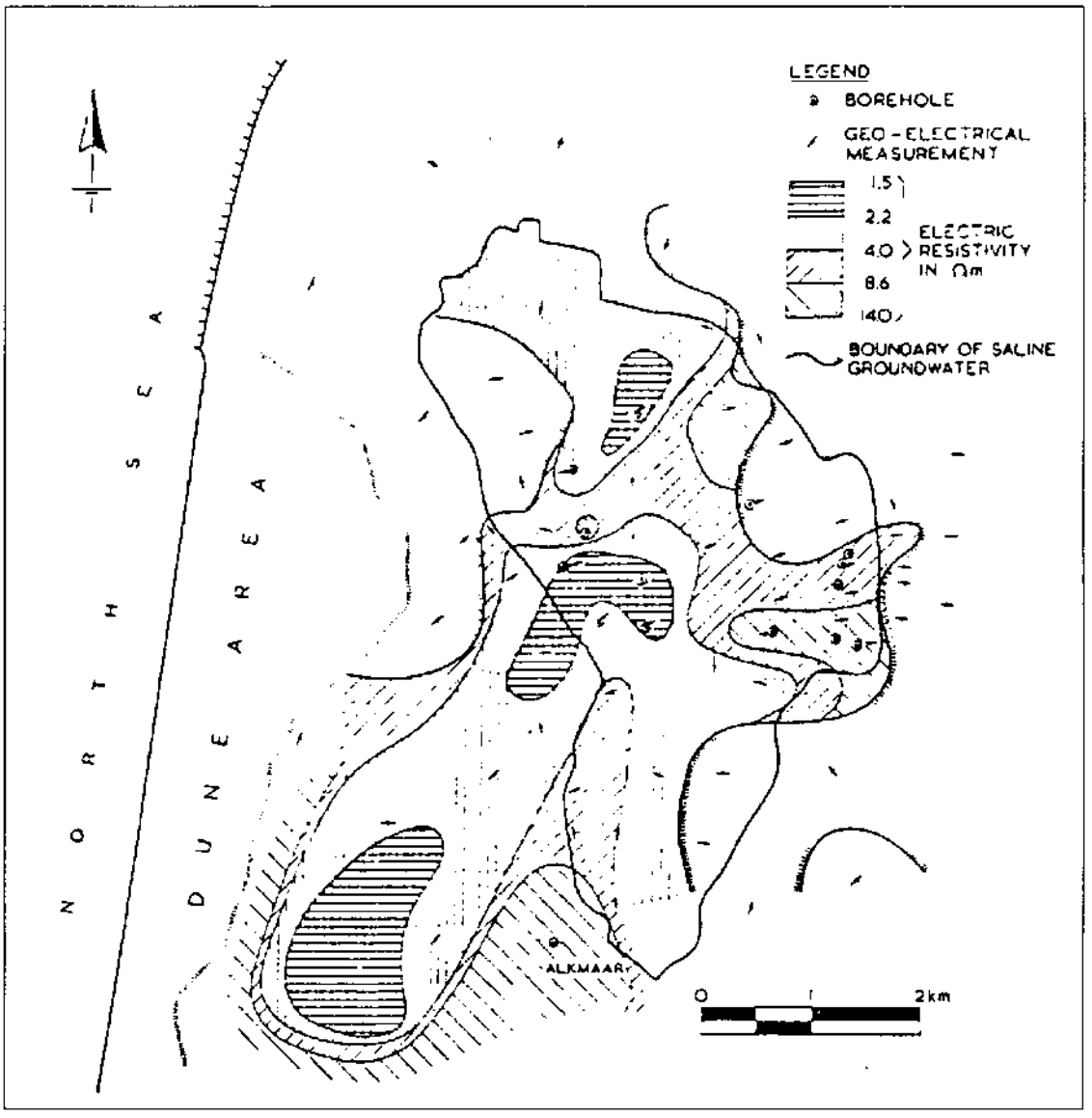

Figure 7.44 Distribution of resistivities of a sand layer with a saline groundwater boundary in Noord Holland as determined by many vertical electrical soundings. From van Dam and Meulenkamp (1967), by permission

It was first recommended that geophysics was unnecessary to locate groundwater; boreholes drilled anywhere would succeed. In practice, borehole failures were in excess of 82% of holes drilled, particularly in the southern areas. Geophysical methods were then called upon to improve the failure rate. Predominantly, vertical electrical soundings were used on sites selected following initial hydrogeological and photogeological inspection. Careful analysis of the VES data with the subsequent borehole information, led to the compilation of a database of typical formation resistivities and their likely hydrogeological potential. It became apparent that certain geographical regions had better and more easily resolved groundwater resources, and six drilling rigs were kept working on these sites. This provided a window of several months in which the more problematic sites could be investigated further until they, too, were ready for drilling.

Use of geophysics to help identify the groundwater potential in areas and to assist in the planning of drilling programmes led to the borehole failure rate falling to 17% of holes drilled and a saving to the project of £5 million – at least 10 times the cost of the geophysical surveys (Reynolds 1987).

7.7.2.3 Landfills

There is an increasing amount of interest in the use of high-resolution resistivity surveys in the investigation of closed landfills, particularly with respect to potential leachate migration. Both resistivity sounding and sub-surface imaging have been used very successfully.

There is no such thing as a typical landfill – some are extremely conductive, others are resistive relative to the surrounding media. There are many variables geophysically (Reynolds and McCann 1992) and care must be taken not to presume a particular geophysical response for any given site. For example, van Nostrand and Cook

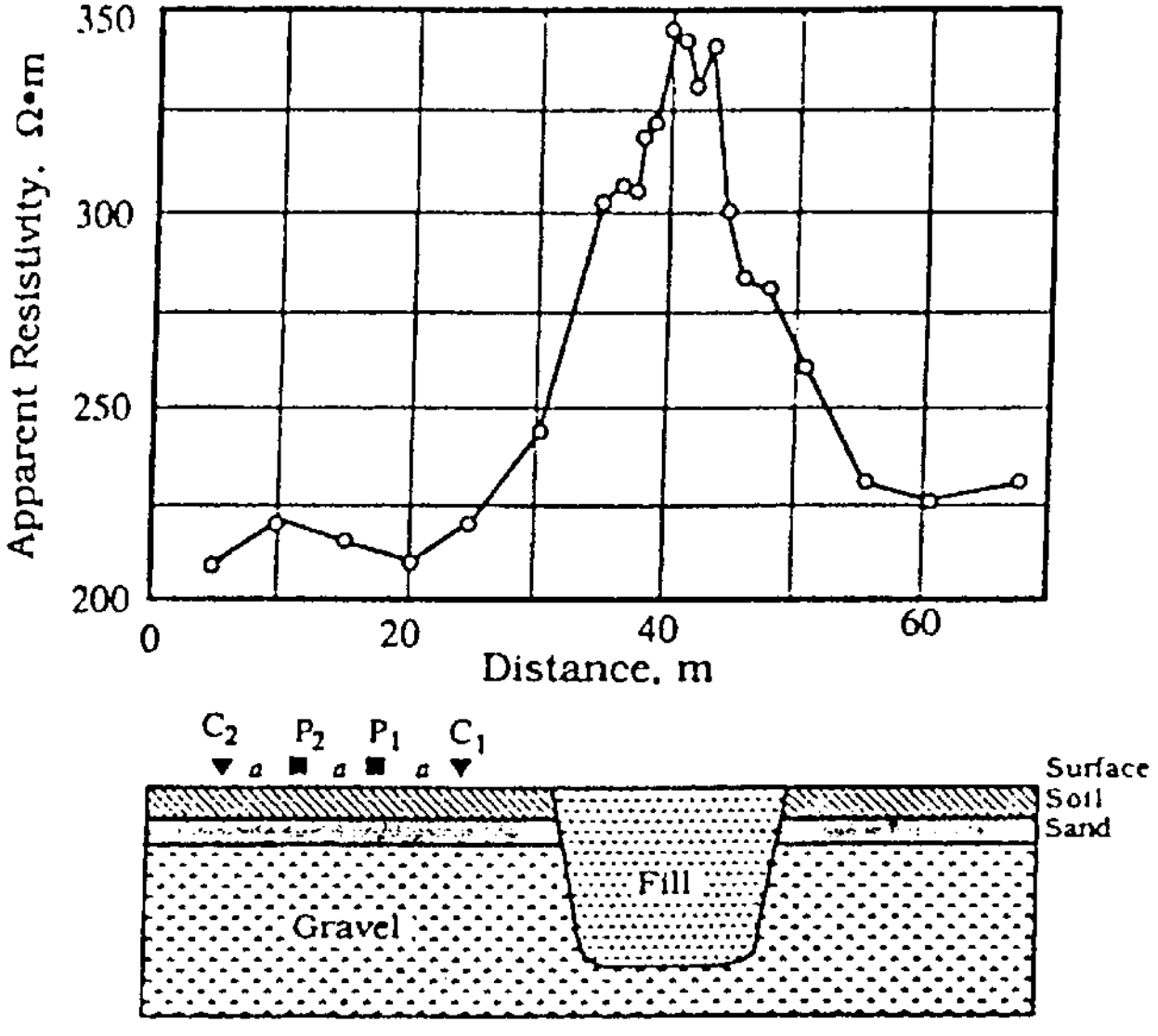

Figure 7.45 Observed apparent resistivity profile across a resistive landfill using the Wenner array. From van Nostrand and Cook (1966), by permission

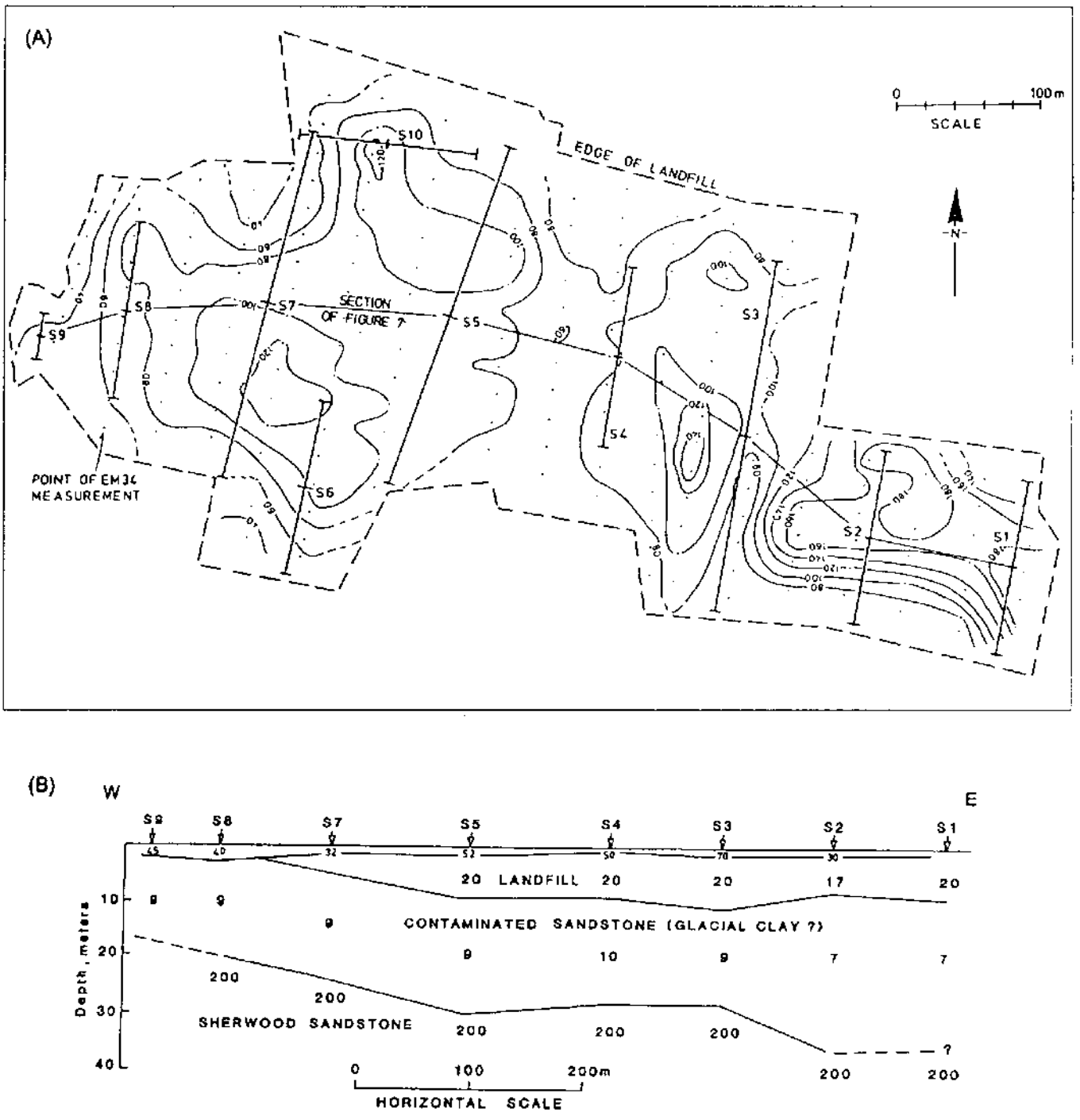

Figure 7.46 (A) Contoured ground conductivity values over a landfill. Solid straight lines represent the positions and orientations of resistivity soundings. Contour interval is 20 ms/m. (B) Geoelectrical section across the landfill based on the soundings in (A). From Barker (1990), by permission

(1966) presented a very clear CST profile of apparent resistivity across a resistive landfill (Figure 7.45). Barker (1990) has shown resistivity sounding results across a landfill in Yorkshire in which the landfill is conductive (around 20 Ω m or less) over a contaminated substrate of sandstone (Figure 7.46). The offset Wenner method was used in this example.

Schlumberger soundings have been used by Monier-Williams *et al.* (1990) as part of a broader geophysical survey around the Novo Horizonte landfill in Brazil. Quantitative analysis of the soundings

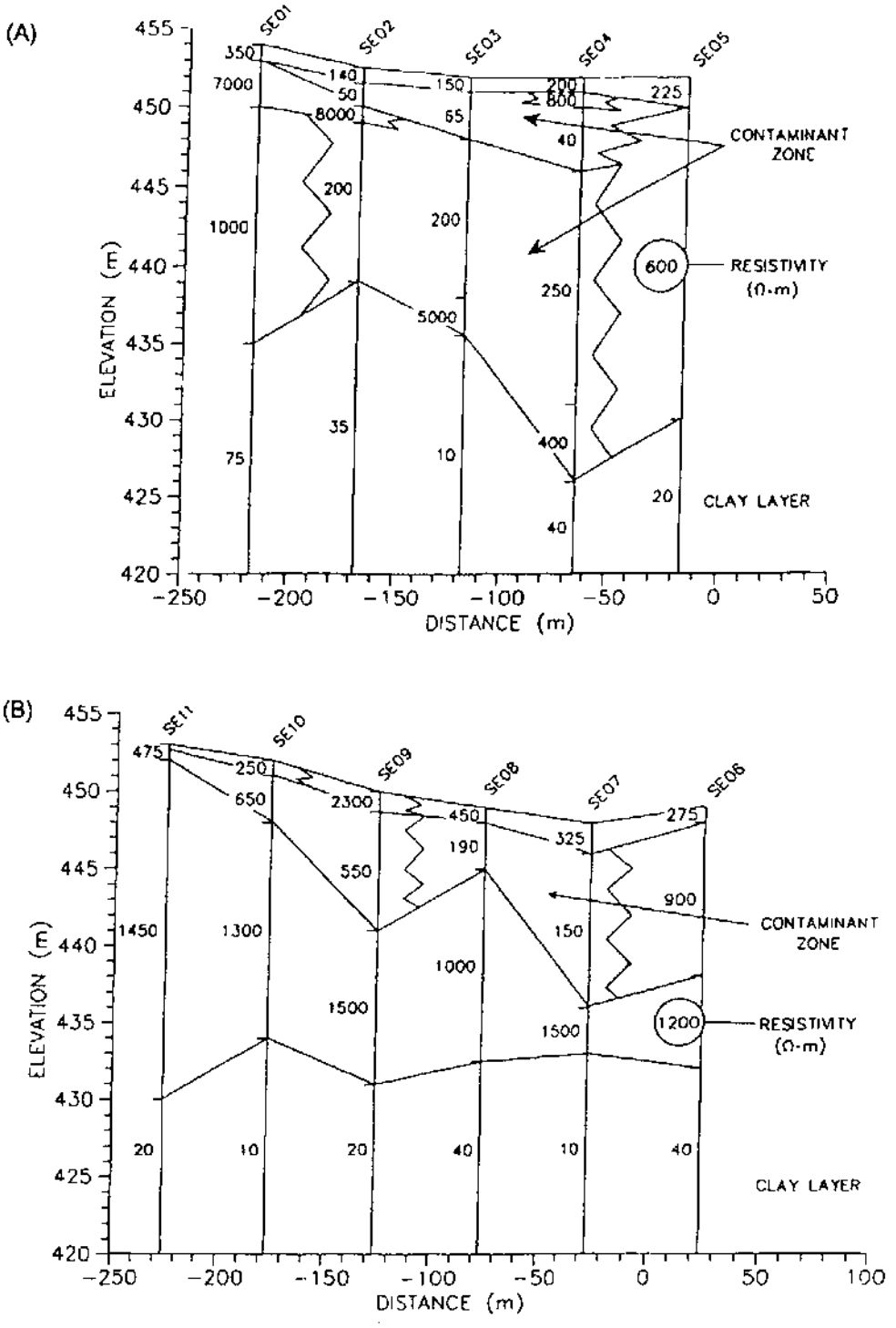

Figure 7.47 Two parallel resistivity sections based on the interpretation of Schlumberger soundings at the Novo Horizonte landfill site, Brazil. The profile in (A) is closer to the landfill than that shown in (B). The background resistivities above the basal clay are high; the lower values in the centre of the sections are assumed to be due to contamination. Note that the conductive zone in (B) is apparently more shallow than in (A). From Monier-Williams *et al.* (1990), by permission

and displays as resistivity panels have revealed significant zones with anomalously low resistivities (Figure 7.47). These have been interpreted as being contaminant plumes arising from the landfill. The displays shown in the figure are orientated parallel to the flank of the landfill, but at 10 m and 70 m distance away from it.

Sub-surface imaging pseudo-sections across a landfill are shown in Figure 7.48. The three panels illustrate the observed apparent

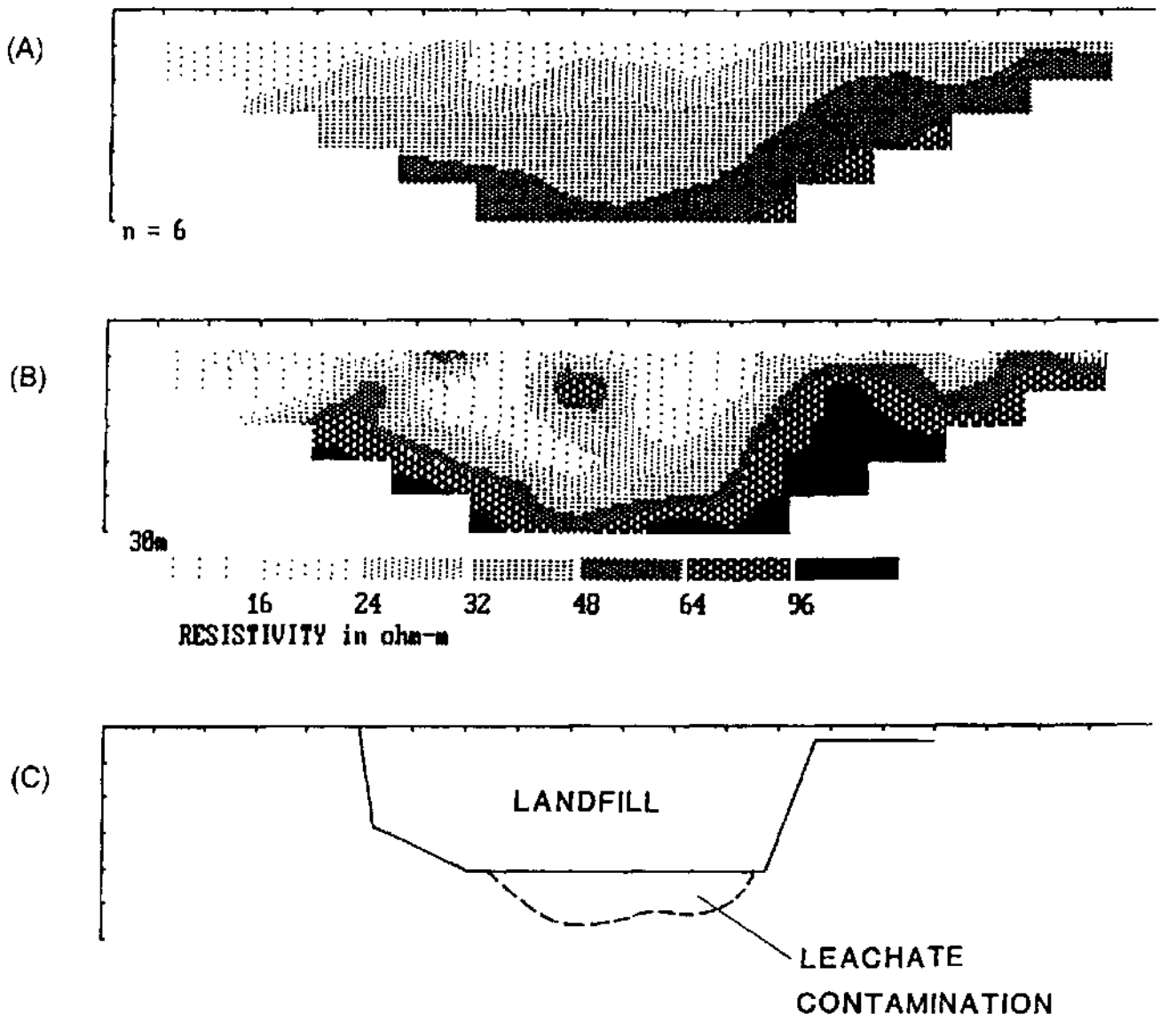

Figure 7.48 (A) Wenner apparent resistivity pseudo-section measured across a landfill. Electrode spacing = 10 m. (B) Resistivity depth section obtained after eight iterations. (C) Approximate section across the landfill based on existing information. From Barker (1992), by permission

resistivity data, the inverted true resistivity–depth model and a schematic interpretation. In this case, the depth and geometry of the landfill were known at the outset. The zone of low resistivity associated with the saturated landfill extends more deeply than had been expected. This is interpreted as indicating the leakage of leachate through the base of the landfill (Barker 1992).

A further example of a sub-surface imaging pseudo-section inverted model is shown in Figure 7.49 (Reynolds 1995). The data were acquired over a closed shallow landfill constructed as a 'dilute and disperse' site over river gravels. The electrical image shows the thin capping material, the waste material and the basal gravels quite clearly. The image is entirely consistent with depths known from boreholes on site.

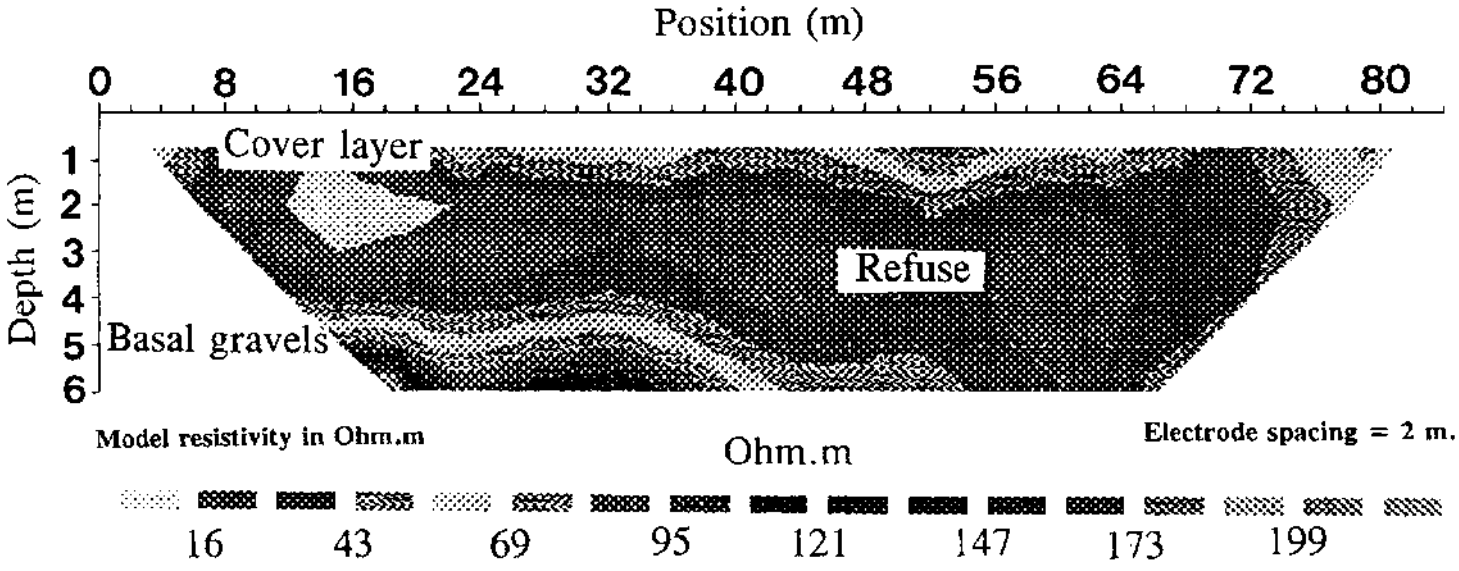

Figure 7.49 Electrical resistivity pseudo-section acquired over a closed landfill in north Wales. From Reynolds (1995), by permission

7.7.3 Glaciological applications

Electrical resistivity methods have been used since 1959 to determine glacier ice thickness. Measurements were first obtained on European glaciers on temperate ice (i.e. ice at its pressure melting point). In 1962, resistivity measurements were made on polar ice (i.e. ice well below its pressure melting point) and were found to be anomalously low by up to three orders of magnitude compared with temperate ice values. Whereas the electrical resistivity behaviour of polar ice is now reasonably understood (Figure 7.50; Reynolds and Paren 1984), the electrical behaviour of temperate ice is still poorly understood. In the 1970s a considerable amount of work was undertaken to develop field data acquisition in Antarctica. Interpretation methods were developed to yield information on vertical thermal profiles through the ice mass and whether or not ice shelves afloat on sea water were melting or freezing at their base. All of these data contribute to an understanding of ice dynamics (rate of ice movement, etc.) and the structure of the ice masses under study.

A series of vertical electrical soundings has been made on George VI Ice Shelf along a flow line of Goodenough Glacier which flows westwards from the Palmer Land Plateau in the Antarctic Peninsula (Figure 7.51). The field curves were modelled to take into account thermal effects and the resulting interpretations are shown in Figure 7.52. The estimated ice thicknesses and rates of bottom melting were in good agreement with those determined independently (Reynolds 1982).

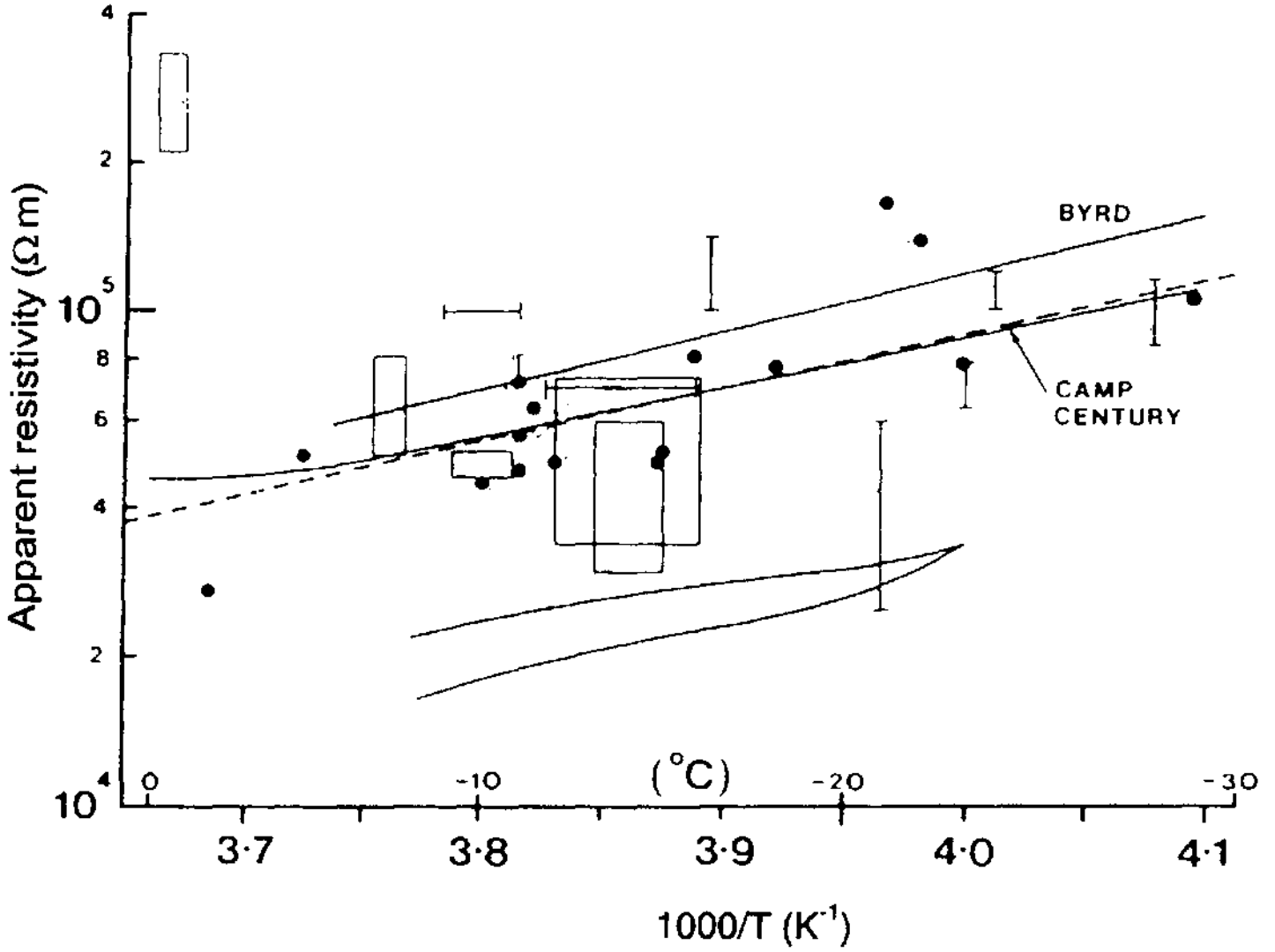

Figure 7.50 Resistivity of ice as a function of temperature. Mean values from georesistivity sounding of ice at 100m or deeper are plotted with estimated uncertainties against the estimated layer temperature from a wide variety of sources. Laboratory measurements on ice cores examined over a range of temperatures are shown by continuous lines. A regression line for the data is given by a dashed line. Given a particular temperature, the ice resistivity can be predicted within a factor of 2 or better. After Reynolds and Paren (1984), by permission

Other uses of resistivity measurements have been made by Haeberli and Fisch (1984) who drilled holes with a hot-water jet drill through Grubengletscher, a local glacier in Switzerland. By using a grounded electrode beyond the snout of the glacier and the drill tip as a mobile electrode, they were able to detect the point at which the drill tip broke through the highly resistive ice into the more conductive substrate (Figure 7.53A). Consequently, they were able to determine the ice thickness much more accurately than by using either the drilling or surface radio-echosounding. With debris-charged ice at the glacier base it is difficult to tell when the glacier sole has been reached judging by thermal drilling rates alone. The radio-echo-sounding depth measurements were found on average to be accurate to within 5%, but generally underestimated the depth. Electrodes were planted at the ice-bed interface at the ends of each of 14 boreholes and standard resistivity depth soundings were undertaken as if the glacier were not there (Figure 7.53B).

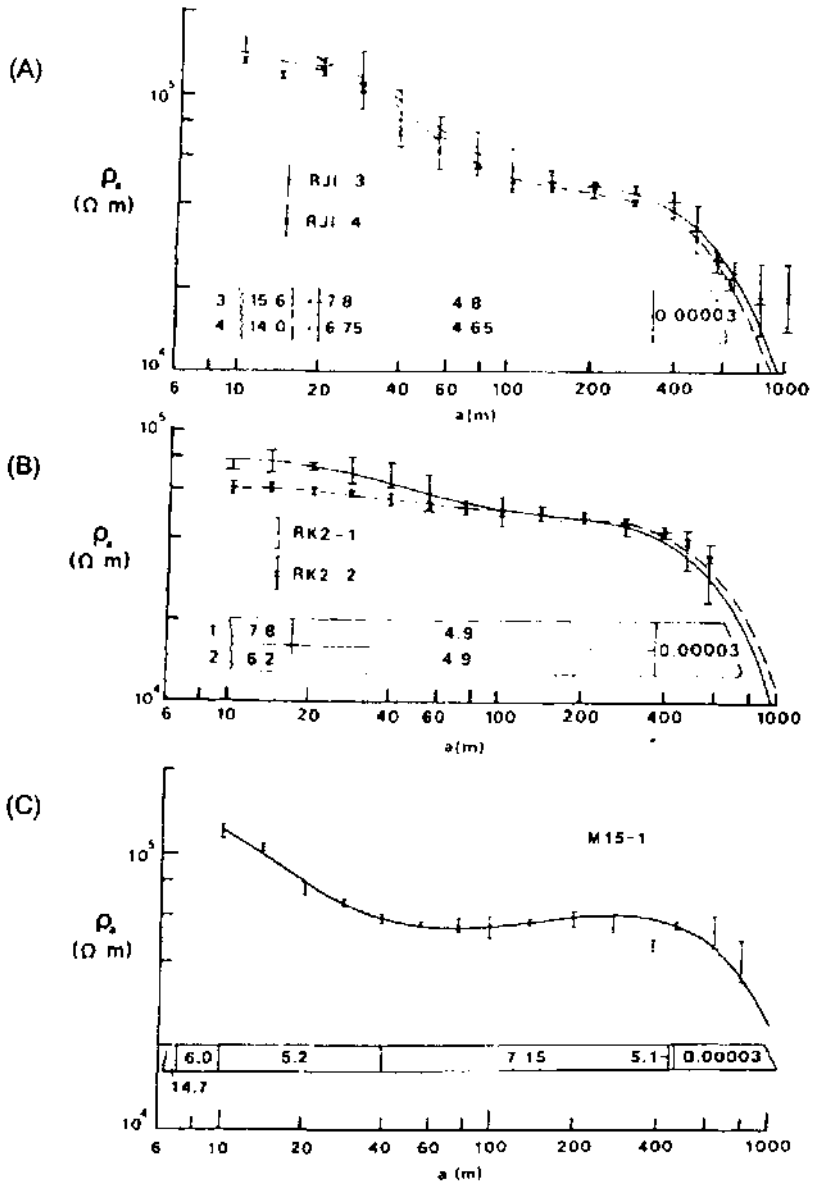

Figure 7.51 Apparent resistivity sounding curves obtained using a Schlumberger array at three sites along a glacial flow line on George VI Ice Shelf, Antarctica. In (A) and (B) two orthogonal soundings are shown at each site. Below each curve is the interpreted model in terms of true resistivities against depth within the ice sheet. The extremely low values of resistivity below the ice shelf indicate that it is afloat on sea water. Model resistivities are given in units of 10 kΩ m. From Reynolds and Paren (1984), by permission

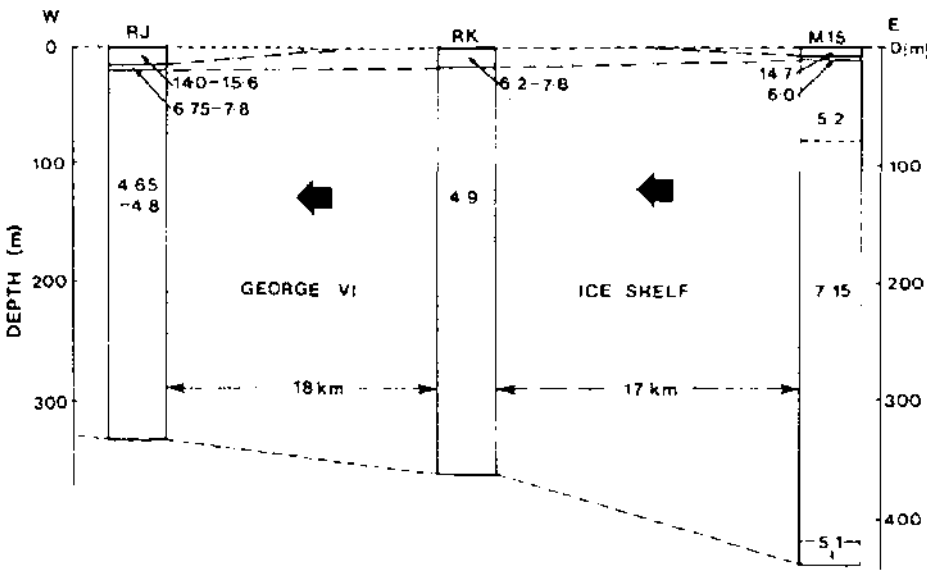

Figure 7.52 Resistivity structure through George VI Ice Shelf along a flow line. Resistivities are in units of 10 kΩ m, and are plotted against depth within the ice sheet. From Reynolds and Paren (1984), by permission

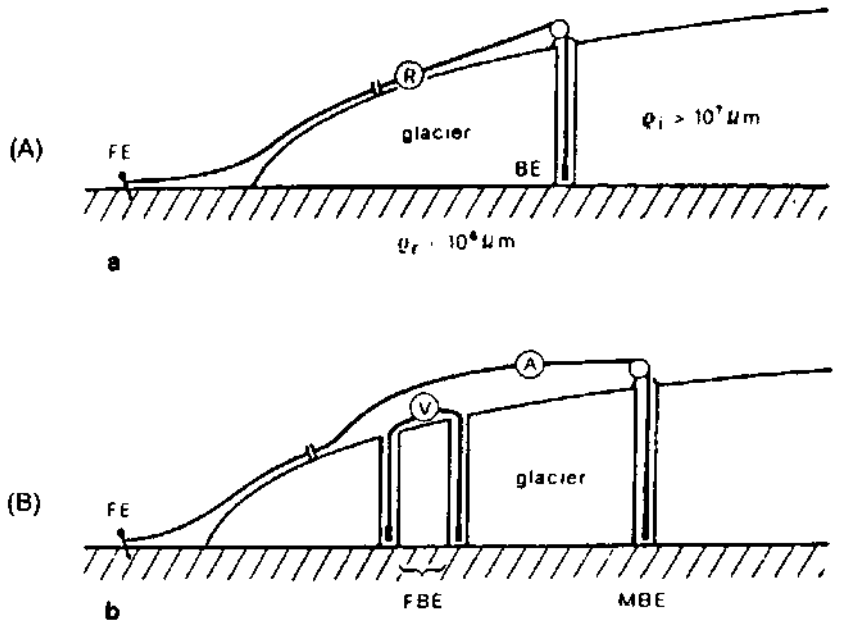

Figure 7.53 Electrode arrays used for the determination of the exact position of the glacier bed (A) and for resistivity soundings of glacier beds (B). FE = fixed electrode outside the glacier margins, BE = borehole electrode for determination of glacier-bed position, FBE = 'fixed' borehole electrodes for resistivity soundings of glacier beds (corresponding to potential electrodes MN in traditional surface soundings), MBE = 'moving' borehole electrode for resistivity soundings of glacier beds. R = resistivity meter, V = voltmeter, A = ammeter. From Haeberli and Fisch (1984), by permission

Haeberli and Fisch discovered that the Grubengletscher was underlain by over 100 m of unconsolidated sediments. It had been thought previously that the glacier was in direct contact with bedrock. This work has demonstrated that by using sub-glacial electrodes, significant new information can be obtained about the nature of the materials underlying the glacier. This can have considerable benefits when trying to understand the sub-glacial hydrogeological regime, for example. This is of particular importance at Grubengletscher because of two proglacial lake outbursts in 1968 and 1970 which caused considerable damage to the nearby village of Saas Balen.

7.8 ELECTROKINETIC (EK) SURVEYING IN GROUNDWATER SURVEYS

When a seismic wave travels through partially or fully saturated porous media, the seismic impulse effectively squeezes the rock, causing the pore fluid to move. This generates a small electrical or electrokinetic signal which can be detected using electrodes implanted at the ground surface, an idea first mooted by Thompson in 1936. Around the same time, Russian workers were experimenting with similar systems (e.g. Ivanov 1939). In 1959, Martner and Sparks reported a systematic study of seismoelectric coupling using explosives at various depths. They were the first to demonstrate that the conversion of seismic to electromagnetic energy at the water table could be detected using surface antennae.

A partially saturated vadose zone generates characteristically electrocapillary signals that are caused by the movement of air/water interfaces in pore throats, and electrophoretic signals that are caused by the displacement of bubbles within the pore fluid. However, fully saturated aquifers generate electrokinetic signals by the displacement of a single fluid (water or brine) when stimulated by a passing seismic wave. The difference between the two types of signal can be identified, leading to the determination of the depth to the water table in unconfined aquifers. The dry zone or basement or any non-aquifer rocks are characterised by the lack of any signal. The method is also referred to as seismoelectric or electroseismic surveying (Thompson and Gist 1993).

The basic data acquisition system consists of a seismic source, usually a sledge hammer or shallow explosives (Figure 7.54). The seismic impulse propagates into the ground and any electrokinetic signals generated by the passage of the P-wave are detected using an electrode-pair dipole with an inter-electrode separation of between 0.5 m and 10 m. Proprietary electronics and software enable the EK data to be converted to indicate permeability and cumulative flow in litres per second (GroundFlow Ltd).

Although the method is described here under 'electrical methods', it is not an active electrical technique. Neither is it purely a seismic method. The technique has been developed recently in the USA under the name Electro-Seismic Prospecting (Thompson and Gist, 1993)

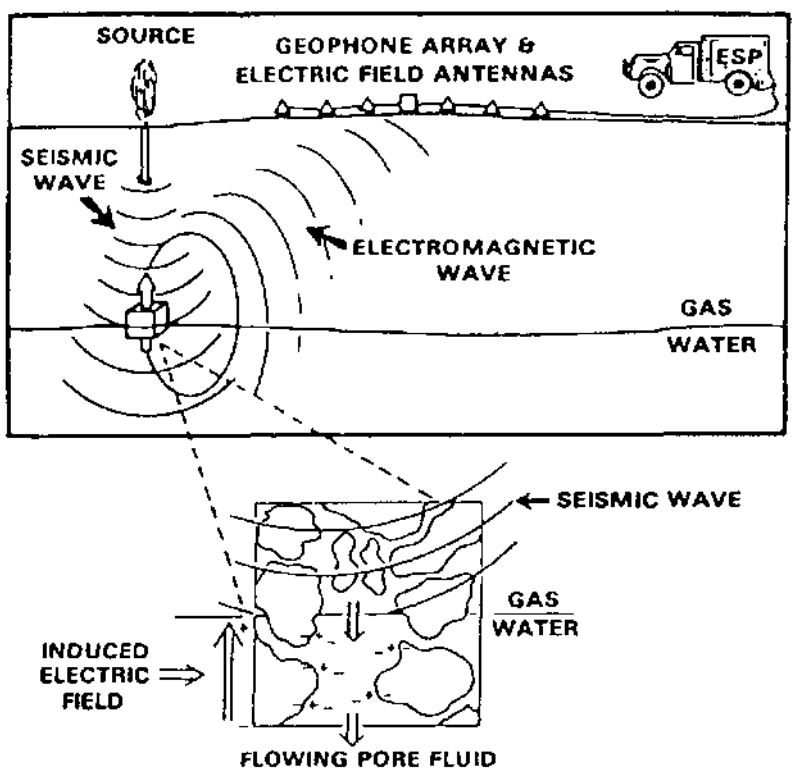

Figure 7.54 Schematic of electro-seismic prospecting as developed by Thompson and Gist (1993). Reproduced by permission

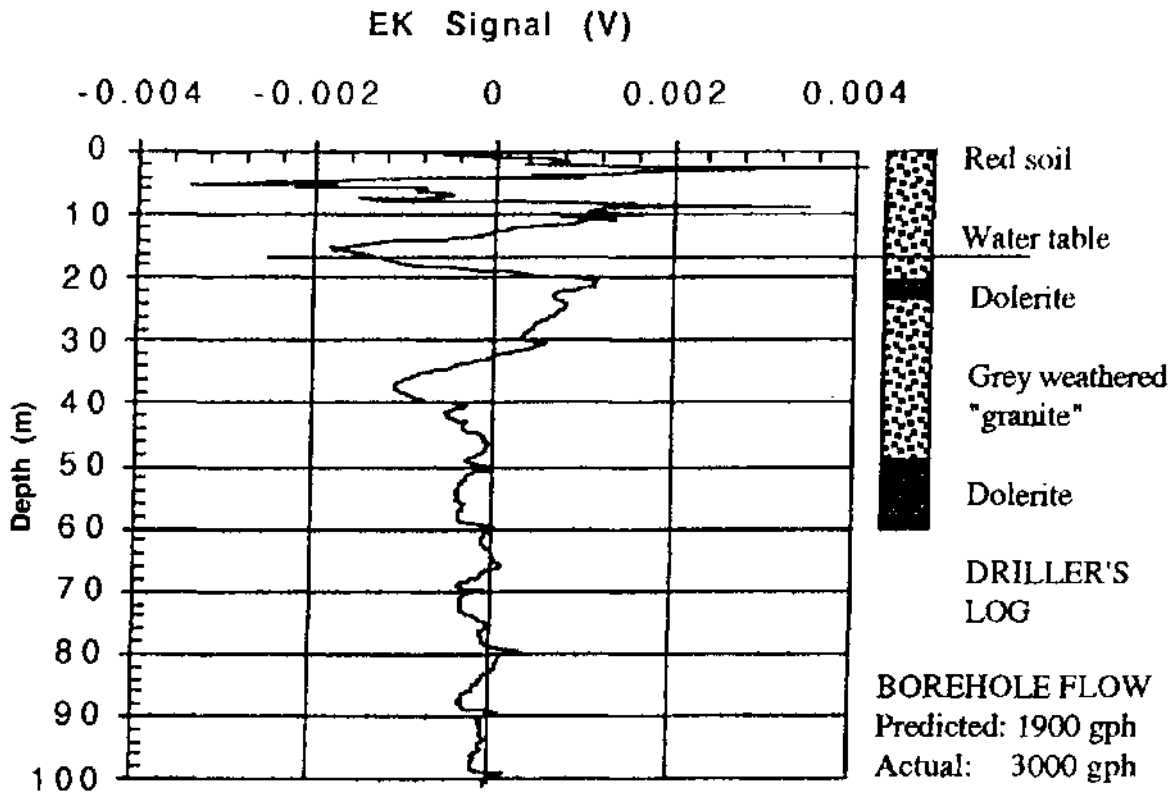

Figure 7.55 Typical electrokinetic signal at a borehole site in Zimbabwe. Courtesy of GroundFlow Ltd

for shallow (< 1 km) hydrocarbon exploration, and in the UK by Clarke and Millar (GroundFlow Ltd; personal communication) for hydrogeological investigations, and by Butler *et al.* (1994) for mapping stratigraphic boundaries. Reference should be made to the various papers to see the fine differences between the various methods proposed by various workers.

An example of the use of EK surveying has been provided by GroundFlow Ltd, UK, and is shown in Figure 7.55. The figure shows the EK response at a borehole site in Zimbabwe. The determination of depth has been undertaken using an assumed P-wave velocity of 1250 m/s. Note the strong EKresponses at and around the position of the water table. Strong electrocapillary signals from the vadose zone are evident above the water table, with electrokinetic signals derived from the saturated zone from 17 m to 50 m. At greater depths, there is very little signal response. The corresponding derived permeability–depth profile and cumulative flow responses are shown in Figures 7.56 A and B, respectively.

Comparison of predicted and actual borehole water flow rates has indicated that the EK-derived values provide a reasonable indication of the actual likely flow rates. However, this method in its modern form is only in its infancy. If the success of early trials is sustained, then this method promises to be a very useful additional tool in hydrogeological investigations.

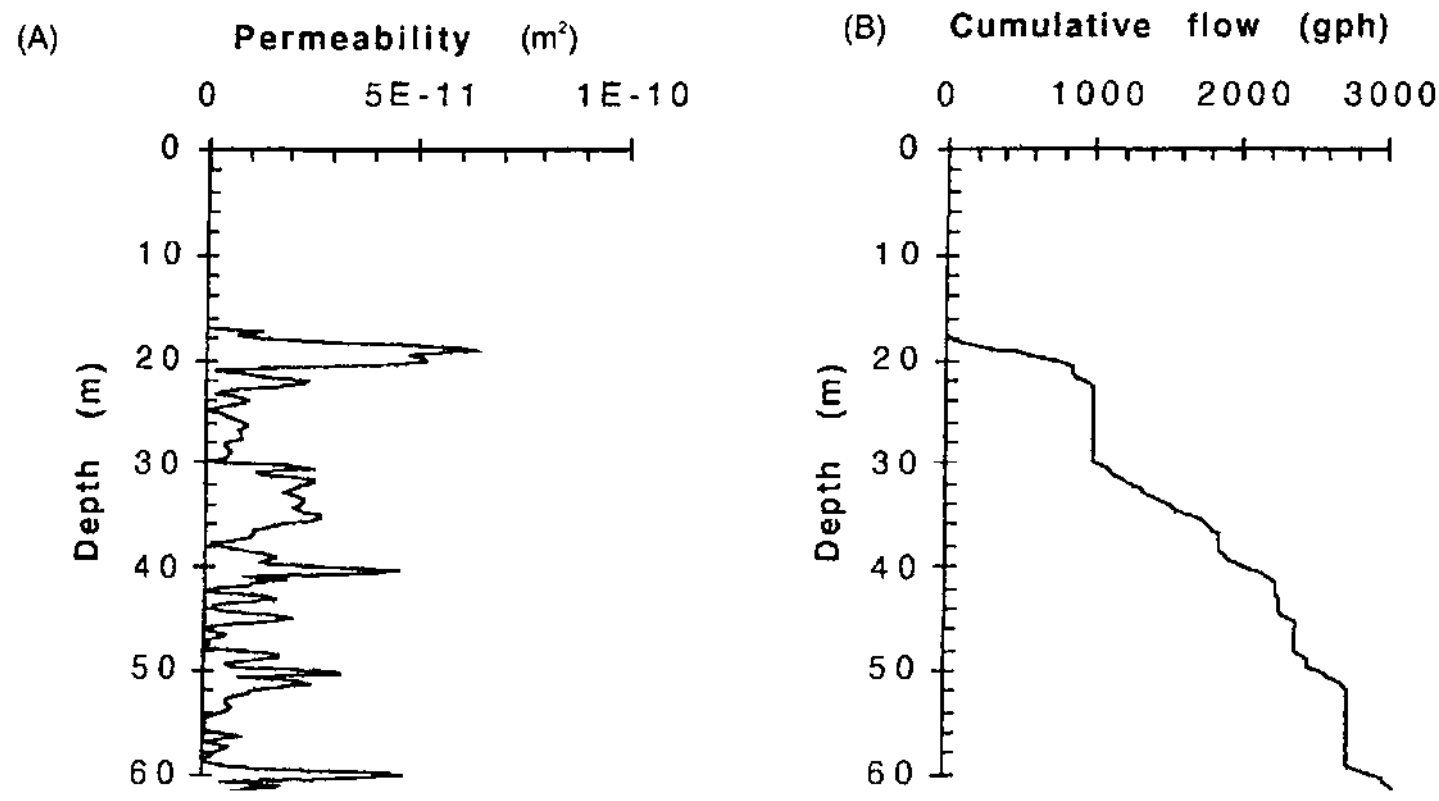

Figure 7.56 (A) Permeability–depth profile, and (B) predicted flow derived from electrokinetic data at a borehole site in Zimbabwe. Courtesy of GroundFlow Ltd

7.9 LEAK DETECTION THROUGH ARTIFICIAL MEMBRANES

The detection of leaks through man-made linings to lagoons and landfills has become increasingly important in the last few years. The intention of lining waste disposal sites is to ensure containment of the waste. However, small tears or cuts in the lining can end up with major leaks of contaminants. Various methods have been developed to try to locate holes in the linings so that they can be repaired or mitigation measures can be taken to remedy the contamination.

The general principle behind all the methods is that the artificial lining (high-density polyethylene (HDPE) geomembrane) is effectively a resistive barrier as long as there are no holes through it. A typical resistivity of an HDPE geomembrane is $> 10^7\,\Omega$m.

Electrical current is passed between two electrodes, one of which is outside the membrane but in contact with the local groundwater, and one is within the waste or in a wet sand layer immediately overlying the geomembrane (Figure 7.57A). The same system can be used in water-filled lagoons (Figure 7.57B). Either a pair of potential electrodes or a roving single potential electrode (with the second one located with the external current electrode) is used to detect anomalous electrical potentials. These occur where electrical current is able to penetrate through holes in the geomembrane. Tears as small as

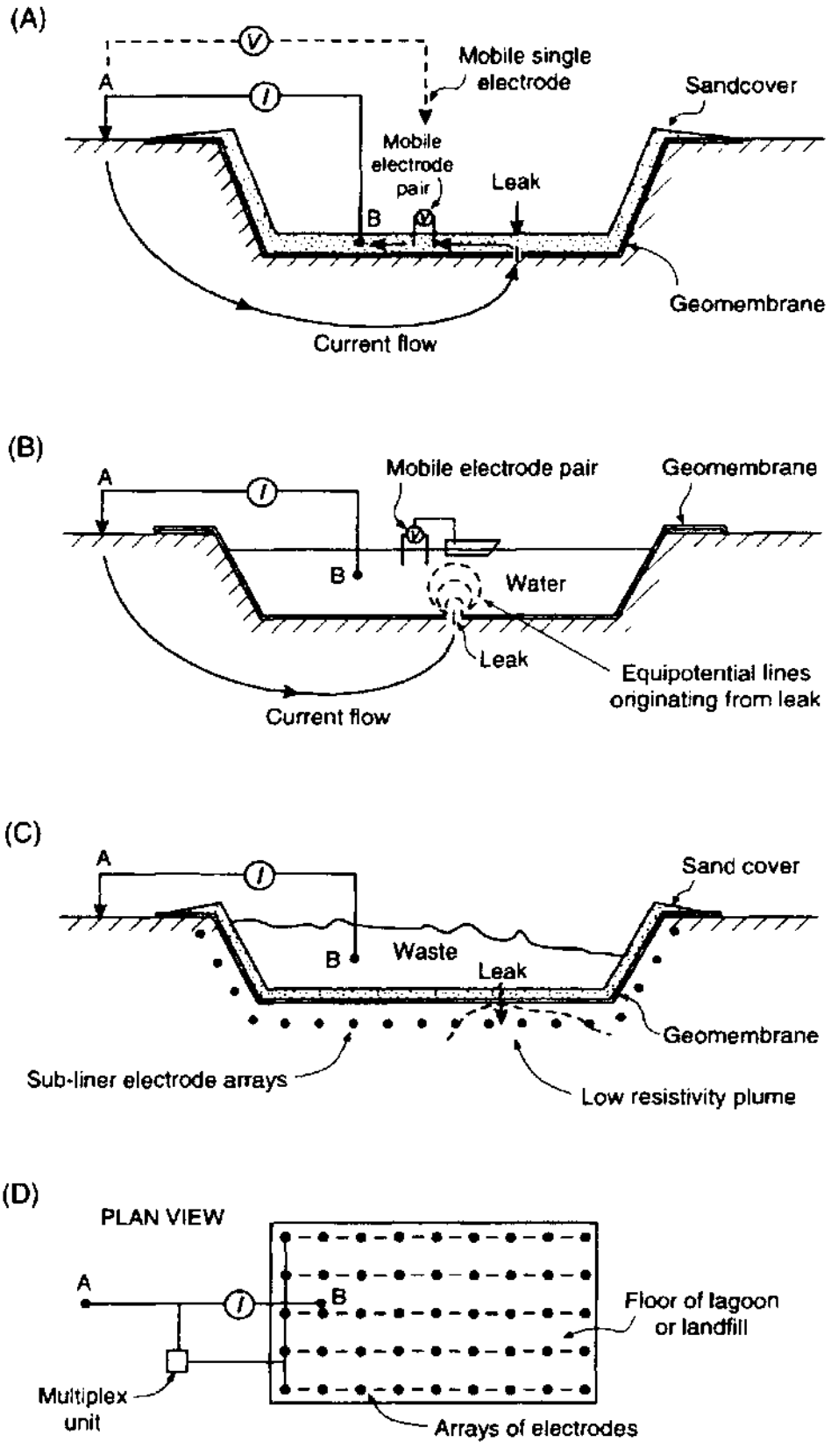

Figure 7.57 Leak detection systems in waste repositories or lagoons with man-made geomembrane liners. The survey layout in the case where (A) the liner is covered with a thin (0.5m) layer of sand and bentonite, and (B) the liner is filled with water. (C) A sub-liner leak detection system that uses permanently installed arrays of electrodes, with a typical plan layout shown in (D)

1 mm at a depth of 0.5 m beneath a sand layer have been located successfully.

In addition to post-construction leak detection, modern containment landfills are being built with sub-liner detection systems installed permanently. Arrays of electrodes connected by sealed multicore cables are buried at a depth of around 1 m below the geomembrane. A current circuit is provided by two electrodes as previously described. At the time of construction, measurements are made to check for holes in the liner so that they can be repaired before the disposal of any waste (Figures 7.57C and D). Instead of measuring potentials above the liner, as in the previous case, this technique permits the measurement of anomalous potentials *below* the liner. In addition, pseudo-sections of resistivity can be obtained by using the sub-liner arrays as sub-surface imaging arrays (see Section 7.4.2), without using the surface current electrode pair. At the construction of the disposal site, baseline measurements can be made when it can be assured that there are no leaks. Once waste has begun to be put into the facility, the sub-liner array can be monitored routinely and repeat pseudo-sections acquired.

The data are normalised so that they display changes in values relative to the baseline dataset. If a leak develops at a later stage in the facility's life, it can be identified from the routine monitoring. By using the array of sub-surface electrodes, the spatial distribution of any sub-liner pollutant plume can be determined so that remedial action can be taken. This may include constructing abstraction wells downstream of a leaking landfill so that the contaminated water can be pumped out and treated. Examples of such leak detection systems have been given by Mazác *et al.* (1990) and by Frangos (1994), among others. Many geophysical contractors are now offering remote leak detection surveys for containment waste repositories. The first landfill in the UK with a sub-liner leak detection system installed was constructed in 1995.